Technische Universität München
TUM School of Engineering and Design

Numerical Simulation of Lifting Surfaces in Rotating Systems

Marco Stuhlpfarrer

Vollständiger Abdruck der von der TUM School of Engineering and Design der Technischen Universität München zur Erlangung des akademischen Grades eines

Doktors der Ingenieurwissenschaften

genehmigten Dissertation.

Vorsitzender :	Prof. Dr.-Ing. Markus Ryll
Prüfer der Dissertation:	1. apl. Prof. Dr.-Ing. Christian W. M. Breitsamter
	2. Prof. Dr.-Ing. Florian Holzapfel

Die Dissertation wurde am 25.05.2021 bei der Technischen Universität München eingereicht und durch die TUM School of Engineering and Design am 16.11.2021 angenommen.

Finally…

CB, AK, AVA, MW, VR, RR, PP, FK, AP, FH, SP, MG, NH, NT, CS

WL, MB, HGF

LTS, FS, LS, MP

Abstract

The fast and accurate prediction of lifting surfaces in rotating systems is crucial for efficient workflows within the design process for various applications. Solutions have to be provided for the classical fields of applications such as helicopters, propeller aircraft, and wind turbines as well as the growing field of urban air mobility. In general, the requirements for a specific method differ for the stages of the design process. During the pre-design stage, the focus is set on predicting the trends of certain design modifications. Within the subsequent stages, the absolute quantities have to be determined correctly. Consequently, the specific needs of a given problem have to be addressed by efficient and reliable simulations with an appropriate fidelity level. The present thesis presents enhanced solutions for several design stages.

At first, the generalized actuator disc concept with certain modifications is provided. The latter are the application of a new Kernel function based on a raised cosine as well as a direct coupling for solving the blade characteristics combined with the continuum simulation. Therefore, the blade characteristics are determined by a panel method coupled with the boundary layer integration method. Furthermore, the multi-domain approach was introduced. For this case, the blade characteristics are directly solved by two-dimensional continuum simulations. For the presented methods, four test cases starting from a two-dimensional cascade test case up to a propeller-fuselage configuration are shown. For the simple test cases, the evaluation of the model specific parameters is of high interest. For the complex scenario, the comparison of the numerical results with experimental data is conducted. In general, a good agreement of the different approaches with the reference data is shown. Moreover, a high speedup of the presented methods is shown.

At second, the flow around a helicopter including rotating rotor-head motion by introducing an analytical, fast, linear-scaling deforming-mesh approach is provided. For the evaluation of the speedup, a simplified test case is designed. The outcome is a significant speedup with respect to the reference method while providing higher mesh quality during the simulation. Furthermore, a complex test case for a scale model of a characteristic twin-engine light utility helicopter featuring collective and cyclic pitch motion of the blade cuffs governed by a fully functional swash plate is shown. Therefore, a comparable speedup as for the simple test case as well as a higher robustness of the simulation is achieved. Moreover, complementary numerical and experimental investigations are presented for two different configurations. The first excludes the tail boom and the stabilizers, while the second includes them. For the configuration without the tail, a detailed description of the flow field as well as a comparison of the latter for several crossflow planes between the numerical results and the experimental data is given. For the configuration with the tail, the convection of the vortical structures is presented qualitatively. In addition, phase-averaged quasi-volumetric particle image velocimetry data for analyzing the wake flow are detailed and compared to the numerical results. In general, a good agreement between the numerical results and the experimental data is achieved. However, for a detailed analysis, the complementary approach is useful.

Zusammenfassung

Die schnelle und genaue Vorhersage von auftriebserzeugenden Flächen in rotierenden Systemen ist entscheidend für effiziente Arbeitsabläufe innerhalb des Auslegungsprozesses für diverse Anwendungen. Lösungen werden in den klassischen Anwendungsbereichen wie Hubschauben, Propellerflugzeuge und Windkraftanlagen, sowie als auch in wachsenden Bereich wie der „Urban Air Mobility“ benötigt. Im Prinzip entscheiden sich die Anforderungen an eine bestimmte Methode für unterschiedliche Phasen im Auslegungsprozess. Während der Vorentwurfsphase liegt das Augenmerk auf der Vorhersage von Tendenzen diverser Änderungen des Entwurfs, wohingegen in den weiteren Phasen, die absoluten Werte von Relevanz sind. Als Konsequenz müssen die speziellen Anforderungen einer Aufgabenstellung mit effizienten und zuverlässigen Methoden angemessenen Gütegrades erfüllt werden. Die vorliegende Arbeit beinhaltet Konzepte zur Lösung für diverse Entwurfsphasen.

Als erstes wird das „Generalized Actuator Disc Concept“ mit bestimmten Veränderungen bereitgestellt. Diese sind die Verwendung einer neuen Kernel Funktion basierend auch einem „Raised Cosine“ sowie eine direkte Kopplung der Lösung für die aerodynamischen Eigenschaften des Blattes mit einer Kontinuumslösung. Die aerodynamischen Eigenschaften des Blattes werden dafür mit einem Panel-Verfahren gekoppelt mit dem Grenzschichtintegrationsverfahren gelöst. Zusätzlich wird der „Multi-Domain“ Ansatz vorgestellt. In diesem Fall werden die aerodynamischen Eigenschaften des Blattes mit einer direkt gekoppelten zweidimensionalen Kontinuumssimulation bestimmt. Die Ergebnisse der Methoden werden anhand von vier Testfällen präsentiert. Diese reichen von einer zweidimensionalen Kaskadenströmung, welche hauptsächlich zur Bestimmung der modellspezifischen Parameter dient, bis hin zu einem komplexen Scenario, wobei der Vergleich der numerischen Ergebnisse mit den Windkanaldaten im Vordergrund steht. Im Prinzip stimmen die Ergebnisse für die unterschiedlichen Ansätze gut mit den Referenzdaten überein. Des Weiteren kann eine große Verringerung der Rechenzeit gezeigt werden.

Als zweites wird die Strömung um einen Hubschrauber mit rotierendem Rotorkopf dargestellt. Dazu wird ein analytischer, schneller, linear skalierender Netzdeformationsansatz vorgestellt. Um die Beschleunigung der Lösung zu demonstrieren wird ein einfacher Testfall generiert, wobei eine signifikante Erhöhung der Lösungsgeschwindigkeit bei höherer Netzqualität während der Simulation im Verglich zur Referenzmethode festgestellt werden kann. Des Weiteren wird ein komplexer Testfall für einen charakteristischen zweimotorigen Leichthubschrauber präsentiert. Dieser enthält einen Rotorkopf mit voll funktionsfähiger Taumelscheibe, welche die kollektive und zyklische Blattverstellung von Blattstummeln vorgibt. Die Erhöhung der Lösungsgeschwindigkeit ist vergleichbar mit jener für den einfachen Testfall mit gleichzeitig robusteren Simulationen. Zusätzlich werden komplementäre numerische und experimentelle Simulationen für zwei verschiedene Konfigurationen durchgeführt. Die Erste inkludiert den Ausleger und die Leitwerke nicht, die Zweite schon. Die Konfiguration ohne Ausleger und Leitwerke wird verwendet um eine detaillierte Beschreibung des Strömungsfeldes sowie einen Vergleich von experimentellen und numerischen Daten in Querströmungsebenen zu geben. Die vollständige Konfiguration wird genutzt um die Konvektion der kohärenten Strukturen qualitative darzustellen. Hierbei werden die experimentellen Daten aus phasengemittelten quasivolumetrischen „Particle Image Velocimetry“ Daten analysiert und mit den numerischen Ergebnissen verglichen. Hierbei wird auch eine gute Übereistimmung zwischen den numerischen und den Experimentellen Daten erhalten. Jedoch erweist sich der komplementäre Ansatz für eine detaillierte Untersuchung als hilfreich.

Table of Content

Table of Content I
List of Figures IV
List of Tables XIV
Nomenclature XV
1 Introduction 1
1.1 Background and Motivation 1
1.2 Objectives and Contribution of the Work 3
1.3 Outline 5
2 Modeling of the Propeller Action 6
2.1 Introduction 6
2.1.1 Wind Turbine Applications 8
2.1.2 Aerospace Applications 13
2.2 Momentum Theory 16
2.2.1 Axial Momentum Theory 16
2.2.2 General Momentum Theory 17
2.3 Blade Element Theory 19
2.4 Blade Element Momentum Theory 21
2.5 Generalized Actuator Disk Model 23
2.5.1 Actuator Disc Model 25
2.5.2 Actuator Line Model 26
2.5.3 Actuator Surface Model 26
2.6 Panel Method Coupled with Boundary Layer Integration Method (PanBL) 27
2.7 Generalized Actuator Disc Approach Coupling with PanBL 29
2.7.1 Solution Strategy 29
2.7.2 Inflow Conditions for the Actuator disc 30
2.7.3 Thrust and Circumferential Force of a Blade Section 37
2.7.4 Source Terms for the Actuator Disc 39
2.7.5 Inflow Conditions for the Actuator Line 43
2.7.6 Source Terms for the Actuator Line 56
2.7.7 Improved Inflow Condition 59
2.8 Generalized Actuator Disc Approach Coupling with Two-Dimensional CFD 60
2.9 Resolved Flow Simulations 62
2.9.1 Steady-State Flow Simulation with Moving Reference Frame 62

2.9.2 Time-Accurate Flow Simulation with the Moving Mesh Approach 62
3 Two-Dimensional Test Case 64
3.1 Test Case Description 64
3.2 Mesh Generation and Numerical Setup 71
3.3 Results and discussion 79
4 Three-Dimensional Test Cases 116
4.1 Three-Dimensional Cascade Test Case 116
4.1.1 Test Case Description 116
4.1.2 Mesh Generation and Numerical Setup 119
4.1.3 Results and Discussion 128
4.2 Three-Dimensional Propeller Test Case 153
4.2.1 Test Case Description 153
4.2.2 Mesh Generation and Numerical Setup 154
4.2.3 Results and Discussion 158
4.2.4 Conclusions 166
4.3 Propeller-Fuselage Configuration 167
4.3.1 Test Case description 167
4.3.2 Measurement Technique and Test Conditions 168
4.3.3 Mesh Generation and Numerical Setup 168
4.3.4 Results and Analysis 170
4.3.5 Conclusions 173
5 Modeling of the Rotorcraft 174
5.1 Introduction 174
5.2 Mesh Motion Method 177
5.3 Analytical Mesh-Deformation Method 179
6 Results of the Rotorcraft Simulation 187
6.1 Test Case Description 187
6.2 Measurement Technique and Test Conditions 189
6.3 Numerical Setup 189
6.3.1 Meshing and Blocking Strategy 189
6.3.2 Application of the Mesh-Deformation Method 193
6.3.3 Solver Settings and Independency Studies 195
6.4 Results and Analysis 198
6.4.1 Validation and Flow Field Description 198
6.4.2 Wake Flow Analysis 208

6.5 Conclusions 214
7 Conclusions and Outlook 215
A Appendix 234
A.1 Normalized Cosine-Squared Function 234
A.2 Panel Method Coupled with Boundary Layer Integration Method 237
A.2.1 Panel Method 237
A.2.2 Boundary Layer Integration Method 238
A.2.3 Coupling of Panel Method with Boundary Layer Integration Method 239
A.3 Propeller Thrust and Torque Calculation with Blade Element Momentum Theory 240
A.4 Wind Tunnel A 242

List of Figures

Figure 1: Boundary streamtube of the flow through the propeller plane. In addition, the local areas for the integration at certain radial positions are presented. 17
Figure 2: Exemplary radial distribution of the sections for the blade element theory. The numbers denominate each section. The cut-planes show the boundaries of the sections and the black solid line the reference airfoil of a section. 19
Figure 3: Forces and velocities on a blade element. The sketch includes the circumferential V_φ and axial inflow V_x velocities as well as the resultant velocity V_{rel}. The sectional thrust ΔT and circumferential force ΔF_φ as well as the sectional lift ΔL an drag forces ΔD are shown. 20
Figure 4: Exemplary radial distribution of the sections for the momentum theory according to a cosine law 22
Figure 5: Different boundary conditions to realize the action of the propeller on the fluid. The principles of boundary condition (left), pressure force (middle), and source term (right) are shown. The blue highlighted regions describe the location of the impact of the propeller action into the fluid domain. 24
Figure 6: Flow chart for the panel method coupled with the boundary layer integration method. 28
Figure 7: Fluent flow chart for the generalized actuator disc approach with PanBL. 30
Figure 8: Methods to obtain the inflow conditions for the modeled propeller. Computational grid points and actuator disc grid points are matching (left) and non-matching (right). 31
Figure 9: Simplified velocity U and radius r of the boundary streamtube for different operating points. 33
Figure 10: Determination of the inflow conditions for the actuator disc. 34
Figure 11: Determination of inflow velocities of an actuator disc segment. The blue highlighted cells are set to be within the associated propeller segment. The finite volume grid with its center points is drawn (grey lines and points) and the propeller segments are represented by the black lines. The vectors show the velocity components of a cell in the different coordinate systems. Velocity components: u, v; Coordinate Systems: Cartesian and cylindrical according to (2.40). 36
Figure 12: Interpolation of source terms of the actuator disk. Source distribution with constant segment value projected to the computational grid (left) and linear interpolation (right). The propeller grid (black lines and points) and the finite volume grid with associated center points (grey lines and points) are visualized. 39
Figure 13: Parameter variation of the distribution function. The axial position of the disc center SR_c, the width of the actuator disc SR_w, and the width of the smoothed cosine part of the actuator disc boundary SR_s is varied. $SR_s/SR_w = 1$ (magenta lines), $SR_s/SR_w = 0.5$ (green lines), and $SR_s/SR_w = 0.25$ (blue lines) are shown for three different widths of the actuator disc SR_w 41
Figure 14: Inflow velocities for the sections of the actuator line approach. The vectors for each section show the resultant as well as the component of the inflow velocity. 44
Figure 15: Force distribution generated by the actuator line approach. The aerodynamic force is acting at the reference point of each section. It is equal to the quarter-chord point

of the reference airfoil of the section. The resultant force (red) as well as the lift (green) and drag (orange) are presented. 45
Figure 16: Position of the averaging region. The blue highlighted box represents the source term region and the black and green highlighted boxes two possible averaging regions with the associated center points. The dashed line shows an airfoil with the quarter chord point coinciding with the source region center point. 46
Figure 17: Determination of the inflow velocities with a squared averaging region. The vector field represents the resulting flow field (top), of a freestream flow with an angle of attack (middle), and a potential vortex (bottom). The length of the vortices in set constant. 47
Figure 18: Determination of the inflow velocities with a rectangular averaging region. The vector field represents the resulting flow field of a freestream flow with an angle of attack and a vortex distribution. The length of the vortices in set constant. 49
Figure 19: Spanwise and vertical position of the averaging region. Streamwise view of a left side of a symmetric lifting surface is presented. The source distribution (blue) is shown in the source region and the translucency represents the local value. The averaging regions with the center points are marked black and one additional averaging region with associated center point is marked green. The dashed lines represent the airfoil shape. 50
Figure 20: Flow field in the crossflow plane for a concentrated vortex. The source distribution (blue) is shown in the source region. The averaging regions with the center points are marked black. The dashed lines represent the airfoil shape. The red point represents the center of the potential vortex. The length of the vectors is set constant. 51
Figure 21: Flow field in the crossflow plane for a vortex distribution. The source distribution (blue) is shown in the source region. The averaging regions with the center points are marked black. The dashed lines represent the airfoil shape. The red line represents vortex sheet. The length of the vectors is set constant. 51
Figure 22: Flow field in the crossflow plane in the vicinity of the blade tip for a vortex distribution. The source distribution (blue) is shown in the source region. The averaging regions with the center points are marked black. The green lines show a different calculation method for the sections. The dashed lines represent the airfoil shape. The red line represents vortex sheet. The length of the vectors is set constant. 52
Figure 23: Determination of inflow conditions for the actuator line segment. The blue highlighted cells are set to be within the associated propeller segment. The finite volume grid with its center points is drawn (grey lines and points) and the propeller segments are represented by the black lines. The vectors show the velocity components of a cell in the different coordinate systems. 54
Figure 24: Interpolation of source terms of the actuator line. Source distribution without smoothing (left) and with smoothing (right) in chordwise direction is shown. The propeller grid (black lines) and the finite volume grid with associated center points (grey lines and points) are visualized. The color blue represents no propeller action. 56
Figure 25: Parameter variation of the distribution function. The position of the disc center $SR_{c,x}$ and $SR_{c,y}$, the width of the actuator disc $SR_{w,x}$ and $SR_{w,y}$, and the width of the smoothed cosinusoidal part of the actuator disc boundary $SR_{s,x}$ and $SR_{s,y}$ are shown.

The green and blue lines represent the action of the propeller in different coordinate directions. 58
Figure 26: Fluent flow chart of the generalized actuator disc with 2D-CFD. 60
Figure 27: Sketch of the two-dimensional test case. Basic description (top) and application of the periodic boundary condition (bottom). 65
Figure 28: Sketch of the two-dimensional test case for the limiting value of $\sigma_{2D} \rightarrow \infty$ 66
Figure 29: Blocking for the resolved cascade simulation. Blocking of the whole domain for a solidity of $\sigma_{2D} = 1/9$ (left) and detailed blocking around the airfoil (right). 71
Figure 30: Mesh for the resolved simulations. Initial mesh (right) and rotated airfoil with deformed mesh (right). 72
Figure 31: Blocking strategy for the actuator disc (left). Whole mesh for the actuator disc simulation with refinement in the actuator region (middle) and detailed view of the actuator region (right). 74
Figure 32: Blocking strategy for the actuator line (left). Whole mesh for the actuator line simulation with refinement in the actuator region (middle) and detailed view of the actuator region (right). 75
Figure 33: Mesh for the actuator disc approach coupled with 2D-CFD in its initial state (left) and with rotated airfoil (right). For each state, on the left hand side the AD disc domain is shown while at the right hand side the resolved airfoil domain is presented. 76
Figure 34: Mesh for the actuator line approach coupled with 2D-CFD. On the left hand side the AL domain is presented, while on the right hand side the resolved airfoil domain in its initial state is shown. 78
Figure 35: Two-dimensional thrust and circumferential force coefficient for one blade depending on the solidity. The advance ratio is set to $J = 0.25$ (top), $J = 0.5$ (middle), and $J = 0.75$ (bottom). Resolved. 82
Figure 36: Contour plot of the normalized relative circumferential velocity for the operating points $(J, \sigma_{2D}, \alpha) = (0.75, 1/3, 7.5°)$ (top, left) and $(J, \sigma_{2D}, \alpha) = (0.75, 0, 7.5°)$ (top, right). Graphs of the circumferential velocity along the lines inserted in the contour plot depending on the vertical direction (Bottom). Red line: $(J, \sigma_{2D}, \alpha) = (0.75, 1/3, 7.5°)$, Blue line: $(J, \sigma_{2D}, \alpha) = (0.75, 0, 7.5°)$. 83
Figure 37: Contour plot of the normalized axial velocity for the operating points $(J, \sigma 2D, \alpha) = (0.75, 1/3, 7.5°)$ (top, left) and $(J, \sigma_{2D}, \alpha) = (0.75, 0, 7.5°)$ (top, right). Graphs of the axial velocity along the lines inserted in the contour plot depending on the vertical direction (Bottom). Red line: $(J, \sigma_{2D}, \alpha) = (0.75, 1/3, 7.5°)$, Blue line: $(J, \sigma_{2D}, \alpha) = (0.75, 0, 7.5°)$. 84
Figure 38: Two-dimensional thrust and circumferential force coefficient for one blade depending on the angle of attack. The advance ratio is set to $J = 0.75$. Resolved. 85
Figure 39: Two-dimensional thrust and circumferential force coefficient for one blade depending on the solidity. The advance ratio is set to $J = 0$. Resolved. 86
Figure 40: Two-dimensional thrust and circumferential force coefficient for one blade depending on the source region width nondimensionalized with the chord length of the blade. The advance ratio is set to $J = 0.25$. AD-PanBL. 87
Figure 41: Two-dimensional thrust and circumferential force coefficient for one blade depending on the averaging region width nondimensionalized with the source region width. The advance ratio is set to $J = 0.25$. AD-PanBL. 88

Figure 42: Two-dimensional thrust and circumferential force coefficient for one blade depending on the smoothing region width nondimensionalized with the width of the region. The advance ratio is set to $J = 0.25$. AD-PanBL. 89
Figure 43: Two-dimensional thrust and circumferential force coefficient for one blade depending on the center of the source and averaging region nondimensionalized with the cell length. The operating point is $(J, \alpha, \sigma_{2D}) = (0.25, 5.0°, 1/3)$. $SRw = 10.5\ l_{cell}$. AD-PanBL. 90
Figure 44: Two-dimensional thrust and circumferential force coefficient for one blade depending on the center of the source and averaging region nondimensionalized with the cell length. The operating point is $(J, \alpha, \sigma_{2D}) = (0.25, 5.0°, 1/3)$. $SRw = 5.5\ l_{cell}$. AD-PanBL. 91
Figure 45: Two-dimensional thrust and circumferential force coefficient for one blade depending on the center of the source and averaging region nondimensionalized with the cell length. The operating point is $(J, \alpha, \sigma_{2D}) = (0.25, 5.0°, 1/3)$. $SRw = 10.9\ l_{cell}$. AD-PanBL. 92
Figure 46: Two-dimensional thrust and circumferential force coefficient for one blade depending on the solidity. The advance ratio is set to $J = 0.25$ (top), $J = 0.5$ (middle), and $J = 0.75$ (bottom). AD-PanBL: Solid line; Res.: Dashed line. 94
Figure 47: Two-dimensional thrust and circumferential force coefficient for one blade depending on the angle of attack. The advance ratio is set to $J = 0.75$. AD-PanBL: Solid line; Resolved: Dashed line. 96
Figure 48: Two-dimensional thrust and circumferential force coefficient for a blade depending on the solidity. The advance ratio is set to $J = 0$. AD-PanBL: Solid line; Resolved: Dashed line 96
Figure 49: Two-dimensional thrust and circumferential force coefficient for one blade depending on the source region width nondimensionalized with the chord length of the blade. The advance ratio is set to $J = 0.25$. AL-PanBL. 98
Figure 50: Two-dimensional thrust and circumferential force coefficient for one blade depending on the averaging region width nondimensionalized with the source region width. The advance ratio is set to $J = 0.25$. AL-PanBL. 100
Figure 51: Two-dimensional thrust and circumferential force coefficient for one blade depending on the smoothing region width nondimensionalized with the width of the region. The advance ratio is set to $J = 0.25$. AL-PanBL. 101
Figure 52: Two-dimensional thrust and circumferential force coefficient for one blade depending on the solidity. The advance ratio is set to $J = 0.25$ (top), $J = 0.5$ (middle), and $J = 0.75$ (bottom). AL-PanBL: Solid line; Res.: Dashed line. 104
Figure 53: Two-dimensional thrust and circumferential force coefficient for one blade depending on the angle of attack. The advance ratio is set to J=0.75. AL-PanBL: Solid line; Resolved: Dashed line. 105
Figure 54: Two-dimensional thrust and circumferential force coefficient for one blade depending on the solidity. The advance ratio is set to J=0. AL-PanBL: Solid line; Resolved: Dashed line. 106
Figure 55: Two-dimensional thrust and circumferential force coefficient for one blade depending on the solidity. The advance ratio is set to $J = 0.25$ (top), $J = 0.5$ (middle), and $J = 0.75$ (bottom). AD-2C: Solid line; Resolved: Dashed line. 108

Figure 56: Two-dimensional thrust and circumferential force coefficient for one blade depending on the angle of attack. The advance ratio is set to J=0.75. AD-2C: Solid line; Resolved: Dashed line. 109
Figure 57: Two-dimensional thrust and circumferential force coefficient for a blade depending on the solidity. The advance ratio is set to J=0. AD-2C: Solid line; Resolved: Dashed line..... 110
Figure 58: Two-dimensional thrust and circumferential force coefficient for one blade depending on the solidity. The advance ratio is set to $J = 0.25$ (top), $J = 0.5$ (middle), and $J = 0.75$ (bottom). AL-2C: Solid line; Resolved: Dashed line. 112
Figure 59: Two-dimensional thrust and circumferential force coefficient for one blade depending on the angle of attack. The advance ratio is set to J=0.75. AL-2C: Solid line; Resolved: Dashed line. 113
Figure 60: Two-dimensional thrust and circumferential force coefficient for one blade depending on the solidity. The advance ratio is set to J=0. AL-2C: Solid line; Resolved: Dashed line..... 114
Figure 61: Sketch of the three-dimensional test case. 117
Figure 62: Blocking for the resolved cascade simulation. Blocking of the whole domain for a solidity of $\sigma_{3D} = 1/9$ (left) and the detailed view of the blocking around the airfoil (right) is shown. 120
Figure 63: Blocking for the actuator disc simulation. Blocking of the whole domain (left) and detailed view of the blocking with mesh in the actuator disc region (right) is shown. 122
Figure 64: Blocking for the actuator line simulation. Blocking of the whole domain for a solidity of $\sigma_{3D} = 1/9$ (left) and detailed view of the blocking with mesh in the actuator line region (right) is shown. 123
Figure 65: Mesh for the actuator disc approach coupled with 2D-CFD. On the left hand side, the AD disc domain is shown while on the right hand side the resolved airfoil domains are presented. The airfoil is shown in its non-rotated state..... 125
Figure 66: Mesh for the actuator line approach coupled with 2D-CFD. On the left hand side, the AL disc domain is shown for a solidity of $\sigma_{3D} = 1/9$ while on the right hand side the resolved airfoil domains are presented. The airfoil is shown in its non-rotated state..... 127
Figure 67: Three-dimensional thrust and circumferential force coefficient for one blade depending on the solidity. The advance ratio is set to $J = 0.25$. Resolved. 130
Figure 68: Normalized, sectional thrust and circumferential force coefficient along the spanwise direction. The results for the angles of attack of $\alpha = 2.5°$ (non-filled symbols) and $\alpha = 5.0°$ (filled symbols) are shown. Resolved. 131
Figure 69: Isosurfaces of the normalized, axial vorticity for a value of $\omega_x b/U_\infty = -10$ are shown in the blade tip region. The top row depicts the suction side and the bottom row the pressure sides of the blades. The left column presents the results for an angle of attack of $\alpha = 2.5°$ and the right column for an angle of attack of $\alpha = 5.0°$. The isosurface for the solidity of $\sigma_{3D} = 1/3$ is orange highlighted, for the solidity of $\sigma_{3D} = 1/9$ is blue highlighted, and for the solidity of $\sigma_{3D} = 0$ is green highlighted..... 132
Figure 70: Slices of the normalized, axial vorticity for values smaller than $\omega_x b/U_\infty \leq -1$. The slices are located in the range of $-1 \leq x/c \leq 2$ with $x/c = 0$ set at leading edge. The distance between two slices equals $\Delta x/c = 0.5$. The angles of attack of $\alpha = 2.5°$ (top) and $\alpha = 5.0°$ (bottom) are provided for the solidities of $\sigma_{3D} = 1/3$ (left), $\sigma_{3D} = 1/9$ (middle) and $\sigma_{3D} = 0$ (right). Resolved..... 133

Figure 71: Distribution of the local thrust coefficient $C_{T,f}$ in the blade tip region. The solidities of $\sigma_{3D} = 1/3$ (left), $\sigma_{3D} = 19$ (middle) and $\sigma_{3D} = 0$ (right) are presented for the angles of attack of $\alpha = 2.5°$ (top) and $\alpha = 5.0°$ (bottom). Additionally, the surface streamlines are inserted. 134
Figure 72: Distribution of the local circumferential force coefficient $C_{Fx,f}$ in the blade tip region. The solidities of $\sigma_{3D} = 1/3$ (left), $\sigma_{3D} = 1/9$ (middle) and $\sigma_{3D} = 0$ (right) are presented for the angles of attack of $\alpha = 2.5°$ (top) and $\alpha = 5.0°$ (bottom). Additionally, the surface streamlines are inserted. 135
Figure 73: Three-dimensional thrust and circumferential force coefficient for one blade depending on the solidity. The advance ratio is set to J=0.25. AD-PanBL: Solid line; Resolved: Dashed line. 136
Figure 74: Normalized, sectional thrust and circumferential force coefficient along the spanwise direction. The results for the angles of attack of $\alpha = 2.5°$ (non-filled symbols) and $\alpha = 5.0°$ (filled symbols) are shown. AD-PanBL: Solid line; Resolved: Dotted line. 138
Figure 75: Slices of the normalized, axial vorticity for values smaller than $\omega_x b/U_\infty \leq -1$. The slices are located in the range of $0 \leq x/c \leq 1$ with $x/c = 0$ set at leading edge. The distance between two slices equals $\Delta x/c = 0.5$. The angles of attack of $\alpha = 2.5°$ (top) and $\alpha = 5.0°$ (bottom) are provided for the solidities of $\sigma_{3D} = 1/3$ (left), $\sigma_{3D} = 1/9$ (middle) and $\sigma_{3D} = 0$ (right). The isosurface (grey) represents the source region. AD-PanBL. 140
Figure 76: Three-dimensional thrust and circumferential force coefficient for one blade depending on the solidity. The advance ratio is set to J=0.25. AL-PanBL: Solid line; Resolved: Dashed line. 141
Figure 77: Normalized, sectional thrust and circumferential force coefficient along the spanwise direction. The results for the angles of attack of $\alpha = 2.5°$ (non-filled symbols) and $\alpha = 5.0°$ (filled symbols) are shown. AL-PanBL: Solid line; Resolved: Dotted line. 142
Figure 78: Slices of the normalized, axial vorticity for values smaller than $\omega_x b/U_\infty \leq -1$. The slices are located in the range of $-1 \leq x/c \leq 2$ with $x/c = 0$ set at leading edge. The distance between two slices equals $\Delta x/c = 0.5$. The angles of attack of $\alpha = 2.5°$ (top) and $\alpha = 5.0°$ (bottom) are provided for the solidities of $\sigma_{3D} = 1/3$ (left), $\sigma_{3D} = 1/9$ (middle) and $\sigma_{3D} = 0$ (right). The isosurface (grey) represents the source region. AL-PanBL. 144
Figure 79: Three-dimensional thrust and circumferential force coefficient for one blade depending on the solidity. The advance ratio is set to J=0.25. AD-2C: Solid line; Resolved: Dashed line. 145
Figure 80: Normalized, sectional thrust and circumferential force coefficient along the spanwise direction. The results for the angles of attack of $\alpha = 2.5°$ (non-filled symbols) and $\alpha = 5.0°$ (filled symbols) are shown. AD-2C: Solid line; Resolved: Dotted line 146
Figure 81: Slices of the normalized, axial vorticity for values smaller than $\omega_x b/U_\infty \leq -1$. The slices are located in the range of $0 \leq x/c \leq 1$ with $x/c = 0$ set at leading edge. The distance between two slices equals $\Delta x/c = 0.5$. The angles of attack of $\alpha = 2.5°$ (top) and $\alpha = 5.0°$ (bottom) are provided for the solidities of $\sigma_{3D} = 1/3$ (left),

$\sigma_{3D} = 1/9$ (middle) and $\sigma_{3D} = 0$ (right). The isosurface (grey) represents the source region. AD-2C. 148
Figure 82: Three-dimensional thrust and circumferential force coefficient for one blade depending on the solidity. The advance ratio is set to J=0.25. AL-2C: Solid line; Resolved: Dashed line. 149
Figure 83: Normalized, sectional thrust and circumferential force coefficient along the spanwise direction. The results for the angles of attack of $\alpha = 2.5°$ (non-filled symbols) and $\alpha = 5.0°$ (filled symbols) are shown. AL-2C: Solid line; Resolved: Dotted line. 150
Figure 84: Slices of the normalized, axial vorticity for values smaller than $\omega_x b/U_\infty \leq -1$. The slices are located in the range of $-1 \leq x/c \leq 2$ with $x/c = 0$ set at leading edge. The distance between two slices equals $\Delta x/c$=0.5. The angles of attack of $\alpha = 2.5°$ (top) and $\alpha = 5.0°$ (bottom) are provided for the solidities of $\sigma_{3D} = 1/3$ (left), $\sigma_{3D} = 1/9$ (middle) and $\sigma_{3D} = 0$ (right). The isosurface (grey) represents the source region. AL-2C. 151
Figure 85: Domain for the resolved propeller simulation. The rotating domain including blades and spinner (left) and the stationary domain including the aft body and the rotating domain (right) is shown. 153
Figure 86: Mesh for the resolved propeller simulation. View showing the spinner and the blades (left) and view showing the aft body (right) is provided. 154
Figure 87: Mesh for the propeller simulation. A detailed view of the spinner and a blade is presented. 155
Figure 88: Generalized Actuator disc approach. Surface of spinner and aft body are present. In contrast to the resolved propeller (left), the propeller blades and the sliding mesh interface are not required (right). 156
Figure 89: Thrust coefficient C_T (left) and efficiency η (right) depending on the advance ratio J for an RBPA of $\theta_{75} = 10°$ simulated with different modeling approaches. Resolved propeller: URANS/RP; Actuator disc: RANS/AD; Actuator line: URANS/AL. 159
Figure 90: Sectional thrust coefficient ΔC_T (left) and circumferential force coefficient ΔC_{Fx} (right) depending on the nondimensionalized radius r/r_{BT} for an RBPA of $\theta_{75} = 10°$ simulated with different modeling approaches. The sectional coefficients are normalized with the corresponding coefficients of the blade. Resolved propeller: URANS/RP; Actuator disc: RANS/AD; Actuator line: URANS/AL. 160
Figure 91: Contour plot of the time-averaged normalized axial velocity for the URANS/RP and the RANS/AD (bottom), and radial distribution of the normalized axial velocity component at three different radial positions downstream of the propeller (top). Cruise flight: $v = 16.67$, $\omega = 261.080$, and $\theta_{75} = 10°$. 161
Figure 92: Contour plot of the time-averaged normalized axial velocity for the URANS/RP and the URANS/AL (bottom), and radial distribution of the normalized axial velocity component at three different radial positions downstream of the propeller (top). Cruise flight: $v = 16.67$, $\omega = 261.080$, and $\theta_{75} = 10°$. 162
Figure 93: Contour plot of the normalized Q criterion in the range of $2.5 \leq Q/n^2 \leq 50$ and cut off below $Q/n^2 = 1$ (top, right) is shown. Isosurface of the normalized Q criterion with an isovalue of $Q/n^2 = 5$ (bottom; right) is exhibited. The isosurface is colored red (resolved propeller) and blue (actuator line). 163

Figure 94: Thrust coefficient C_T (left) and torque coefficient C_Q (right) depending on the disc inflow angle ϕ_D for an RBPA of $\theta_{75} = 10°$ simulated with different modeling approaches. Resolved propeller: URANS/RP; Actuator disc: RANS/AD; Actuator line: URANS/AL. 164
Figure 95: Lateral moment coefficient C_m (left) and vertical moment coefficient C_n (right) depending on the disc inflow angle ϕ_D for an RBPA of $\theta_{75} = 10°$ simulated with different modeling approaches. Resolved propeller: URANS/RP; Actuator disc: RANS/AD; Actuator line: URANS/AL. 165
Figure 96: Isosurface of the normalized Q criterion with an isovalue of $Q/n^2 = 5$ colored by the turbulent kinetic energy for a disc inflow angle $\phi_D = 90°$ and an RBPA of $\theta_{75} = 10°$. Resolved propeller: URANS/RP (left); Actuator disc: URANS/AL (right); 166
Figure 97: Test configuration mounted in the test section of the wind tunnel. View in direction of the nozzle (left) and in the direction of the diffusor (right) is shown. Propeller and spinner are not shown. 167
Figure 98: Configuration for the numerical simulation. The nozzle (orange highlighted), the room including the test section (grey highlighted), the propeller-fuselage configuration mounted on the sting (blue highlighted), the blades of the wind tunnel (red highlighted), and the diffusor (green highlighted) are presented. 168
Figure 99: Blocking of the wind-tunnel domain excluding the diffusor (left) and the aircraft domain (right) is shown. 169
Figure 100: Thrust coefficient C_T depending on the advance ratio J for an RBPA of $\theta_{75} = 10°$ for different modeling approaches and the experimental data (left). Experimental data: W/T; Resolved propeller: URANS/RP; Actuator disc for propeller-fuselage configuration: RANS/AD-W/T; Actuator disc: RANS/AD; Resolved propeller: URANS/RP. Thrust coefficient caused by the drag of the fuselage and the mounting $C_{T,D}$ depending on the advance ratio J for different conditions (right). 171
Figure 101: Test configuration with dismounted propeller (left) and with enabled propeller representing the cruise flight condition (right) is shown. The advance ratio reads $J = 0.286$. Isosurface of the normalized axial velocity with an isovalue of $u/U_\infty = 1.1$ (top) and crossflow plane colored with the normalized axial velocity in the $0.5 \leq u/U_\infty \leq 1.4$ (bottom) is shown. 173
Figure 102: Static mesh (S) and rotating mesh (R) for the sliding mesh approach. Initial state is shown on the left hand side, after rotation on the right hand side. 178
Figure 103: Static mesh (S), deforming mesh (D), and rotating mesh (R) for the deforming mesh approach. Initial state is shown on the left hand side, after rotation on the right hand side. 178
Figure 104: Surface deformation obtained by the analytical mesh-deformation approach. The initial state (top, left), the rotated-only state (top, right), the translation-only state (bottom, left), and the combined rotation-translation state (bottom, right) are presented. 181
Figure 105: Sketch and mesh for the mesh-deformation test case. A sketch showing the region and measures is drawn (top, left). The initial mesh is presented (top, right). The deformed meshes for the maximum deflection within the test case are presented for the diffusion-based method (bottom, left) and the analytical mesh-deformation method (bottom, right). 183

Figure 106: Required wall-clock time t_{WC} for one simulation run obtained by the diffusion-based mesh-deformation method (dashed line) and the analytical mesh-deformation method (solid line) depending on the number of cells for different numbers of cores N_c. 184
Figure 107: Side and top view of the helicopter configuration. The framed parts are associated to the configuration excluding the tail boom and the empennage. 187
Figure 108: Wind tunnel configurations. The full model (left) and the model without tail sting-mounted (right) in the wind tunnel is presented. 188
Figure 109: Helicopter configuration without the empennage mounted on the one-armed mounting sting (middle) is presented. Gray highlighted stationary domain with the green highlighted embedded disc domain is depicted (left). Rotor head with truncated rotor blades is exhibited (right). 190
Figure 110: Blocking of the lower rotor head domain including the swash plate, the mast and the scissors and lower parts of the steering rods (left) and blocking of the upper rotor head domain (right). [5] 191
Figure 111: Blocking of one blade domain (left) and blocking of the disk segment domain with the embedded blade domain (right) [5]. 191
Figure 112: Mesh in the symmetry plane of the helicopter configuration excluding the empennage, but with included mounting sting. 192
Figure 113: Surface mesh of the rotor head. The rotor head includes rotor mast, hubcap, scissors, damper, steering rods, and swash plate. The global view of the whole rotor head (left) and a detailed view of the rotor head (right) is shown. 192
Figure 114: Definition of the deforming regions. Top view of the rotor (left) and view along the blade in direction of the rotor head (right) is presented. The isosurfaces covering the blades represent a deformation function of $F_{def} = 0.01$ (blue highlighted) and $F_{def} = 0.99$ (red highlighted). A sector, associated to a blade, is divided by the green highlighted isosurface. 194
Figure 115: Additional deforming region (left) and actually used deforming region including the mesh (right) is shown. The isosurfaces of the additional deformation function of $F_{defxp} = 0.01$ (blue highlighted) and $F_{defxp} = 0.99$ (red highlighted) are presented (left) 195
Figure 116: Crossflow planes colored by the time-averaged vorticity magnitude in order to determine the dominant flow structures [5]; $Re \approx 1 \cdot 10^6,\ \alpha = \beta = 0°$. 199
Figure 117: Definition of the crossflow planes. [5] 200
Figure 118: Normalized time-averaged axial velocity distribution for the crossflow planes P1, P2, and P3 in the wake flow of the backdoor section is shown [5]; $Re \approx 1 \cdot 10^6,\ \alpha = \beta = 0°$. 201
Figure 119: Surface streamlines obtained by a simulation with the SAS model. Blue highlighted isosurface of the normalized time-averaged axial velocity with the value $u/U_\infty = 0$ is presented. Slice-planes colored and cut off by $0 \leq u/U_\infty \leq 0.9$ are shown. The mounting sting is not included for this investigation; $Re \approx 1 \cdot 10^6,\ \alpha = \beta = 0°$ 202
Figure 120: Normalized time-averaged axial velocity distribution for the crossflow planes P4, P5, and P6 in the wake flow of the rotor head [5]; $Re \approx 1 \cdot 10^6,\ \alpha = \beta = 0°$. 203
Figure 121: Normalized time-averaged axial vorticity distribution for the crossflow planes P4, P5, and P6 in the wake flow of the rotor head [5]; $Re \approx 1 \cdot 10^6,\ \alpha = \beta = 0°$. 204

Figure 122: Turbulence intensity distribution for the crossflow planes P4, P5, and P6 in the wake flow of the rotor head [5]; $Re \approx 1 \cdot 10^6,\ \alpha = \beta = 0°$. 205
Figure 123: Energy spectra for the velocity components in dependence on the spatial wave number k multiplied by the diameter of the hubcap [5]; $Re \approx 1 \cdot 10^6,\ \alpha = \beta = 0°$. 207
Figure 124: Wake structures for the FHC. The vortical structures are designated by the origin of the structure as well as the associated number of the blade (B) if applicable. BTV: Blade tip vortex; HCVP: Hubcap vortex pair; BIV: Inwards of the blade tip located vortex; HTI: Hubcap BTV interaction; $Re \approx 1 \cdot 10^6,\ \alpha = \beta = 0°$..... 209
Figure 125: Quasi-volumetric PIV-setup. The grey highlighted planes show the measured planes, and the blue highlighted cuboid exhibits the volume for the reconstruction of the volumetric data..... 210
Figure 126: Isosurface of the normalized, phase-averaged Q criterion for an isovalue of $Q \cdot \left(l_{ref} / U_\infty \right)^2 = 0.5$ colored by the axial vorticity component in the range of $-1.0 \leq \omega_x \cdot l_{ref}/U_\infty \leq 1.0$. The vortical structures are designated by the origin of the structure as well as the associated number of the blade (B) if applicable. BTV: Blade tip vortex; HCVP: Hubcap vortex pair; BIV: Inwards of the blade tip located vortex; HTI: Hubcap BTV interaction; $Re \approx 1 \cdot 10^6,\ \alpha = \beta = 0°$..... 211
Figure 127: Crossflow planes colored by the phase-averaged, normalized vorticity magnitude in the range of $1.5 \leq \omega \cdot l_{ref}/U_\infty \leq 9.5$ cut off below the lower limit. The vortical structures are designated by the origin of the structure as well as the associated number of the blade (B) if applicable. BTV: Blade tip vortex; HCVP: Hubcap vortex pair; BIV: Inwards of the blade tip located vortex; HTI: Hubcap BTV interaction; $Re \approx 1 \cdot 10^6, \alpha = \beta = 0°$. 212
Figure 128: Crossflow planes colored by the phase-averaged, normalized axial velocity component in the range of $0.4 \leq u/U_\infty \leq 0.9$ cut off above $u/U_\infty \geq 0.95$. The blades are designated (B) ; $Re \approx 1 \cdot 10^6, \alpha = \beta = 0°$. 213
Figure 129: Normalized raised-cosine function for $x \in [-1,1]$. 234
Figure 130: Normalized smoothing function for $x \in [-1.5,1.5]$. 236

List of Tables

Table 1: Relaxation factor for the resolved propeller simulations of the two-dimensional test case. 73
Table 2: Mesh independency study for the resolved simulation of the two-dimensional test case. 73
Table 3: Relative deviation of the thrust and circumferential coefficient for the resolved simulation. 81
Table 4: Relative deviation of the thrust and circumferential coefficient for the resolved and the AD-PanBL simulation. 93
Table 5: Relative deviation of the thrust and circumferential coefficient for the Dependency Test 1 of the AL-PanBL simulation. 99
Table 6: Relative deviation of the thrust and circumferential force coefficient for the Dependency Test 2 of the AL-PanBL simulation. 100
Table 7: Relative deviation of the thrust and circumferential coefficient for the resolved and the AL-PanBL simulation. 103
Table 8: Relative deviation of the thrust and circumferential coefficient for the resolved and the AD-2C simulation. 107
Table 9: Relative deviation of the thrust and circumferential coefficient for the resolved and the AL-2C simulation. 111
Table 10: Relaxation factor for the resolved propeller simulations of the three-dimensional test case. 121
Table 11: Mesh independency study for the resolved simulation of the three-dimensional test case. 121
Table 12: Relative deviation of the thrust and circumferential force coefficient for the AD-PanBL simulation related to the resolved simulation. 137
Table 13: Relative deviation of the thrust and circumferential force coefficient for the AL-PanBL simulation related to the resolved simulation. 142
Table 14: Relative deviation of the thrust and circumferential force coefficient for the AD-2C simulation related to the resolved simulation. 146
Table 15: Relative deviation of the thrust and circumferential force coefficient for the AL-2C simulation related to the resolved simulation. 149
Table 16: Contributions to the thrust coefficient due to the aerodynamic tare. 172
Table 17: Ratio of the wall-clock time of the simulation t_{WC} for the diffusion-based mesh-deformation method related to that of the analytical mesh-deformation method for different numbers of cores and grid resolutions. 184
Table 18: PPG for different numbers of cores. 185
Table 19: PPC for different grid resolutions. 186
Table 20: Force and moment coefficients obtained by the wind-tunnel experiment and the numerical simulation according to Stuhlpfarrer et al. [5]. 198

Nomenclature

Latin Characters

Symbol	Unit	Description
A	m^2	Area
AR_c	m	Averaging regions; Position of the center
AR_s	m	Averaging regions; Widths of the smoothing region
AR_w	m	Averaging regions; Widths of the region
a	$-$	Axial interference factor
a_{ij}	m^{-1}	Influence coefficient matrix
a'	$-$	Rotational interference factor
B	$-$	Number of propeller blades
b	m	Half span
C	$-$	Constant
C	$-$	Courant number
C_D, c_D	$-$	Drag coefficient
C_{Fx}	$-$	Circumferential force coefficient
C_L, c_L	$-$	Lift coefficient
C_Q	$-$	Torque coefficient
C_T	$-$	Thrust coefficient
C_Y	$-$	Side force coefficient
C_l	$-$	Roll-moment coefficient
C_m	$-$	Pitching-moment coefficient
C_n	$-$	Yawing-moment coefficient
c	m	Chord length
c_f	$-$	Skin friction coefficient
c_p	$-$	Specific heat for constant pressure
c_p	$-$	Pressure coefficient
D	N	Drag force
D	m	Diameter
d	m	Distance
F_x, F_ϕ	N	Circumferential force
F_{distr}	$-$	Distribution function
H	$-$	Shape factor
H_1	$-$	Shape factor
J	$-$	Advance ratio
k	m^2/s^2	Turbulent kinetic energy
k	$1/m$	Wave number
l	m	Length; Characteristic length
l, m, n	Nm	Moments
Ma	$-$	Mach number
$\dot{m}$	kg/s	Mass flow rate
N	$-$	Number
n	$-$	Rounds per minute

$\boldsymbol{n}$	$-$	Surface orthogonal vector
PPC	$-$	Parallel performance related to number of cores
PPG	$-$	Parallel performance related to grid resolution
p	$-$	Pressure
Q	$-$	Torque
R	$-$	Radius of vortex ring
Re	$-$	Reynolds number
r	m	Radius
S_i	N/m^3	Source term component
SR_c	m	Source regions; Position of the center
SR_s	m	Source regions; Widths of the smoothing region
SR_w	m	Source regions; Widths of the region
T	N	Thrust
T_C	$-$	Thrust coefficient
t	s	Time
U, V	m/s	Velocity
u, v	m/s	Disturbance velocity components
u, v, w	m/s	Velocity components
V	m^3	Volume
v_{rel}	m/s	Relative velocity magnitude
w	m	Width
x, y, z	m	Cartesian Coordinates
x, φ, z	m	Cylindrical Coordinates
y^+	-	Dimensionless wall distance

Greek Characters

Symbol	Unit	Description
α	°	Angle of attack
α	$-$	Weighting parameter for mesh-deformation method
α_{den}	$-$	Density relaxation factor
α_{mom}	$-$	Momentum relaxation factor
α_p	$-$	Pressure relaxation factor
α_{temp}	$-$	Temperature relaxation factor
α_{tke}	$-$	Turbulent kinetic energy relaxation factor
$\alpha_{u,update}$	$-$	Multi-domain update relaxation factor
α_{ν_t}	$-$	Turbulence eddy viscosity relaxation factor
α_ω	$-$	Turbulence eddy frequency relaxation factor
β	°	Angle of sideslip
Γ	m^2/s	Circulation
γ	m/s	Vortex strength
γ	$-$	Diffusion coefficient
δ	°	Boundary layer thickness

δ^*	°	Displacement thickness
ϵ	m	Characteristic length of the Kernel
η_ϵ	$-$	Kernel function
θ	°	Angle of Incidence
θ	m	Momentum thickness
θ_{75}	°	Angle of incidence at 75 per cent of the blade tip radius
$\theta_{0,}\theta_C, \theta_S$	°	Parameter for the governing law of the pitch angles
Λ	$-$	Aspect ratio
μ	$Pa\ s$	Dynamic viscosity
μ	$-$	Advance ratio
ν	m^2/s	Kinematic Velocity
ν_t	m^2/s	Turbulence eddy viscosity
ρ	kg/m^3	Density
σ	$-$	Solidity
ϕ	°	Inflow angle
ϕ_D	°	Inclination of the disc relative to the inflow condition
ϕ	m^2/s	Potential
φ	°	Polar angle
Ω	$1/s$	Rotational speed
ω	$1/s$	Angular velocity
ω	$1/s$	Turbulence eddy frequency

Subscripts

Symbol	Description
AD	Acuator disc
$AD-2C$	Actuator disc coupled with two-dimensional CFD
AL	Actuator line
$AL-2C$	Actuator line coupled with two-dimensional CFD
AR	Averaging region
amb	Ambient
BT	Blade tip
bf	Blade fixed coordinate system
$Cores$	Computer cores
c	Cell
$cart$	Cartesian coordinate system
$cell$	Cell
cis	Cells in segment
cp	Cross plane
cr	Center of the vortex ring
cr	Cylindrical coordinate system
D	Disc
$distr$	Distribution function
e	End of boundary layer

FHC	Full helicopter configuration
$FM, 0$	Fuselage and mounting sting without propeller
FM	Fuselage and mounting sting with enabled propeller
FOC	Helicopter configuration excluding the tail and empennage
f	Face
G	Grid
Hub	Hubcap
IO	Inlet to outlet
i, j	Indices
in	Inlet
out	Outlet
p	Propeller plane
p	Panel coordinate system
per	Periodic
rel	Relative quantity
res	Resolved blade simulation
rms	root-mean-square quantity
sec	Sections
t	Total quantity
WC	Wall clock
W/T	Wind tunnel
w	Ultimate wake
x, y, z	Cartesian coordinate
∞	Freestream
$2D$	Two-dimensional
$3D$	Three-dimensional

Acronyms

Symbol	Description
AD	Actuator disc
AD-2C	Actuator disc coupled with two-dimensional CFD
AFDD	U.S. Army Aeroflightdynamics Directorate
AL	Actuator line
AL-2C	Actuator line coupled with two-dimensional CFD
ANSYS	Ansys Inc.
AS	Actuator surface
B	Number of a rotor blade
BD	Blade domain
BEM	Blade element momentum
BET	Blade element theory
BEMT	Blade element momentum theory
BIV	Inner vortical structure on a blade
BTV	Blade tip vortex

CAMRAD II	Comprehensive analytical model of rotorcraft aerodynamics and dynamics
CFD	Computational fluid mechanics
CFX	Flow solver by ANSYS
CVFEM	Control-volume finite element method
DD	Disc domain
DS	Disc segment domain
DLR-TAU	Flow solver by DLR (Deutsches Zentrum für Luft- und Raumfahrt)
DNS	Direct numerical simulation
EllipSys	Flow solver by DTU (Technical University of Denmark)
elsA	Flow-Solver by ONERA
Eu	Euler
FHC	Full helicopter configuration
Fluent	Flow solver by ANSYS
FLWB	Forward skid landing gear bottom structure
FLWS	Forward skid landing gear side structure
Flu3M	Flow Solver by ONERA
FOC	Helicopter configuration excluding the tail and empennage
FUN3D	Fully unstructured navier-stokes, Flow solver by NASA
FVM	Finite volume method
GAD	Generalized actuator disc
GIT	Georgia Institute of Technology
HCV	Hubcap vortex
HCVP	Hubcap vortex pair
HOST	Helicopter overall simulation tool
HTI	Interactional vortical structure of hubcap vortex with blade tip vortex
JavaFoil	Panel method coupled with boundary layer method written in Java
LES	Large eddy simulation
LRHD	Lower rotor head domain
LU	Lower-upper
MEXICO	Model experiments in controlled conditions
MFVP	Mast fairing vortex pair
MUSCL	Monotonic upstream-centered scheme for conservation laws
MT	Momentum theory
NACA	National advisory committee for aeronautics
NASA	National aeronautics and space administration
NS	Navier-Stokes
ONERA	Office national d’études et de recherches aérospatiales
OpenFOAM	Open Source Field Operation and Manipulation, Flow solver
PanBL	Panel method coupled with boundary layer integration method
PLU	Lower-upper with partial pivoting
PropPanBL	Momentum theory coupled with PanBL
PUMA	Lifting-line software
RANS	Reynolds-averaged Navier-Stokes
ROBIN	Rotor-body interaction
SD	Static domain
SST	Shear-stress transport

STAR-CD	Flow solver by CD-adapco
TUM	Technical University of Munich
TUM-AER	Chair of aerodynamics and fluid mechanics
URANS	Unsteady Reynolds-averaged Navier-Stokes
URHD	Upper rotor head domain
VAWT	Vertical axis wind turbine
WENO5	Weighted essentially nonoscillatory scheme fifth-order
WBS	Wake between the strakes
WDS	Wake downstream of each strake
WSLG	Wake of the skid landing gear
W/T	Wind tunnel
2C	Two-dimensional Reynolds-averaged Navier-Stokes simulation

1 Introduction

The present chapter provides the background of and the motivation for the thesis, followed by the objectives and contribution of the work as well as the outline. The state of the art is not presented within this chapter. Since this thesis includes one part related to the simplified propeller modeling and another one regarding the deformation of computational fluid dynamic meshes for helicopter rotor heads, the state of the art is presented separated in the corresponding subchapters.

1.1 Background and Motivation

The prediction of lift-generating surfaces in rotational reference systems started more the one hundred years ago. The first attempts to describe the behavior of a propeller used simple analytical methods, nevertheless, with in some cases, appropriate accuracy. The enhancement of the methods, including more features of the real world, lead to an increased complexity and were not able to be solved analytically anymore. Subsequently, a numerical solution was required. Due to the absence of computers at that time, the results were difficult over even not possible to obtain. [1]
With the introduction of computational fluid mechanics (CFD), the flow around lifting surfaces can be calculated in detail. However, such time-accurate, resolved simulations of flows applied for complex geometries require a large computational effort. Consequently, for solving such flows, the limiting calculation power, in particular of a common workstation, is still not sufficient for providing the results within an appropriate wall-clock time. Furthermore, additional conditions, as for example licensed software, require an economical utilization of the available resources. Consequently, fast and efficient methods are highly beneficial. In the following, two examples are given briefly.
Considering the pre-design stage of a new aircraft configuration at first, a lot of different designs have to be calculated, while the focus is not set on predicting the exact value rather than the influence of a modification on the certain quantities. In order to solve this issue for flows around lifting surfaces in rotating frames, a combination a continuum-based CFD simulation with a semi-analytically-based description of the propeller was invented in [2]. After suggesting the method in the late 1980s, several modifications and further developments were conducted. In addition, the fields of application were extended continuously. Although nowadays a lot of variations of the basic method are in use, there is still space for improvements as well as for detailed investigations concerning the model parameters.
While within the pre-design stage the impact of a modification on a specific quantity is of main interest, within subsequent stages of the design process, the focus is set on determining the absolute value as accurate as possible. For some complex configurations, the solution cannot be obtained on a common workstation. However, even for high-fidelity simulations executed on high-performance computers, an efficient solution is beneficial also.
Conclusively, the main goal, arising out of the previous examples, is that for low- as well as high-fidelity simulation the reduction of the numerical effort has to be achieved. Furthermore, for both examples, enhanced solutions shall be provided within this thesis.

Some years ago, the Chair of Aerodynamics and Fluid Mechanics (TUM-AER) of the Technical University of Munich (TUM) contributed to the research project EUROPAS. The focus of the project was set on the technologies for autonomous, unmanned sensor platforms addressing efficient, propulsion systems and ground station control technologies, while the main objective was the

provision of solutions for all-electric, environmentally friendly and inexpensive unmanned aerial systems. TUM-AER dealt on the one hand with the overall aerodynamics of the aircraft and on the other hand with the aerodynamics of the propeller. For both topics, numerical and experimental investigations were conducted. In the course of the project, in particular, the numerical modeling of the propeller gained more and more attention. As mentioned in the last paragraph, the time-accurate simulation of propellers for a large number of operating points is not feasible with limited computational power. However, the project required aerodynamic data of the propeller itself as well as mounted on the aircraft for several advance ratios, blade pitch angles, and Reynolds numbers. As a result, the input data space is large. In order to overcome this issue, the application of the generalized actuator disc approach was suggested. While at first, solely a passive disc with constant disc loading was intended, the a priori unknown forces generated by the propeller lead to the implementation of an active, coupled approach. Furthermore, the geometrical data for the propeller within the project were provided by a three-dimensional scan. The idea was to create a framework that is able to perform the workflow from reading in the geometrical data of the propeller to calculate the generalized actuator disc simulation. In order to cover a wider range of test cases, both, the actuator disc and the actuator line approach are used for the generalized actuator disc within the framework. A detailed study of this framework was presented in [3]. The investigations included several test cases for different flight regimes. The focus was set on the forces and moments for a wide range of operating points. Nevertheless, the local pressure distribution and the wake field were detailed for two operating points also. Although the results show a good agreement to the experimental data, some effects and discrepancies could not be fully understood.
Consequently, a detailed study applying simple test cases, with gradually increasing the complexity, enables the detection of the origins of the effects. For example, a two-dimensional test case aligned within the plane perpendicular to the radial direction of the propeller allows for investigating the impact of the dimensions of the actuator region on the results. Further, the extension to a three-dimensional test case in a steady frame emphasizes, e.g., the influence of the blade tip vortex. Due to the increasing interest of propellers operating in non-axial inflow conditions, the feasibility of the approach for predicting that kind of flows is beneficial also. Conclusively, a comprehensive study of the advantages and disadvantages of the method has to be performed.

At the same time as the aforementioned project, several projects regarding the flows around helicopters were performed at TUM-AER. The emphasis was mainly set on drag reduction and efficiency increase, but other topics, like fluid-structure interaction, were investigated also. The research projects ADHeRo [4] and EcoHC2 [5] dealt with the aerodynamic optimization of a twin-engine light utility helicopter. Within both projects, numerical and experimental investigations have been performed. While the scales as well as the number of blades differ between the considered configurations of the projects, the common feature of both was the application of a fully functional rotor head including a swash plate for governing collective and cyclic pitch motion of the blade cuffs. The main goal was the investigation concerning the drag of the configurations. As reviewed in e.g. [4], the whole blade has not to be incorporated necessarily. The behavior of the drag can even be estimated by including the rotor head and blade cuffs. The latter are obtained by truncating the blade at the radial position of the first effective aerodynamic section. A further difference between the projects was that the tail boom and the stabilizers were included only in the EcoHC2 configuration. After finishing these projects, TUM-AER contributed to the project CHARME. The emphasize was set on aero-mechanical investigations applying the large scale model with the five-bladed rotor head of the ADHero project as well as an added tail boom and stabilizers according to

the EcoHC2 project. The objective was to investigate the interaction of the wake of the fuselage and the rotor head with the tail parts of the helicopter. In the experiments, loads, flow field measurements in the wake, and unsteady pressure probes located at the vertical stabilizer have been evaluated. As a result, a comprehensive database was generated. For the numerical simulation, the flow solvers of ANSYS were applied. Initially, the flow solver ANSYS CFX was applied within the ADHeRo project [6]. The rotor head motion was established with the diffusion-based deforming mesh approach provided by ANSYS CFX. The solution therefore, needed high computational effort, while it was difficult to achieve convergence. Consequently, the solver was changed to ANSYS Fluent for EcoHC2 as well as CHARME due to the better performance for unsteady flows. The computational effort was much less; however, the solution of the mesh-deformation equations required a comparable effort to that of the flow equations. Furthermore, convergence issues were still present. Consequently, a fast and stable mesh-deformation method for the present case is beneficial. Since an analytical prescription of the motion of the rotor head is applied in this case, an analytical function for the mesh deformation can be defined as well. Furthermore, a detailed complementary analysis of the numerical results with the experimental data in the wake flow of the helicopter shall be performed.

1.2 Objectives and Contribution of the Work

Basically, the thesis is structured into two parts. On the hand, the simplified modeling of the propeller by the generalized actuator disc concept and on the other hand, the modeling of the flow around a helicopter including the rotor head motion by introducing a fast, linear-scaling deforming mesh approach and comparing the results with complementary generated experimental data.

At first, the objectives concerning the simplified modeling of the propeller by the generalized actuator disc concept are presented. Although the introduced method shows a good agreement for the complex test case [3], the need for more detailed studies on the occurring effects with simple test cases is stated in the previous section. Therefore, a more detailed description of the therein applied generalized actuator disc method with theoretical considerations is made initially. Furthermore, the distribution function applied for the investigations presented in [3] has to be discussed in detail. In particular, the construction of the new Kernel function with the related model-based parameters is declared. Furthermore, a presentation and description of the newly-introduced multi-domain approach is provided. In addition, a comparison with the resolved propeller simulation and experimental data is included.

The first main objective for the part of the thesis concerning the modeling of the propeller is to investigate the influence of the model-based parameters on the results. Therefore, special designed test cases in two and three dimensions are used. The range of the propeller and flow parameters is based on the requirements needed for real-world applications, while allowing for simply separating, various occurring effects. The test cases focus, in particular, on studies concerning the independence of certain model parameters on the results and consequently, finding an appropriate parameter set, providing a high quality of the prediction for a wide range of propeller and flow parameters.

The second main objective concerns the investigations of the directly-coupled multi-domain approach. Since within the multi-domain approach, solely the calculation of the airfoil data is changed, the same test cases can be simulated to validate the method. The model-based parameters have not to be changed. However, therefore additional questions, like stability and convergence

issues, have to be answered.
The final objective for the part of the thesis concerning the modeling of the propeller is the demonstration of feasibility and applicability for more complex test cases. Therefore, two additional test cases are designed. At first, the feasibility for simulating non-axial inflow conditions with the simplified method has to be proofed and at second, the application for a complex aircraft configuration including the propeller is provided.
In the following, the points beyond the state-of-the-art for the modeling of the generalized actuator disc approach are described briefly:

- **Kernel function:** Instead of the usage of a common Gaussian Kernel function that is not bounded in space, a distribution function based on a raised-cosine function is established. For a Cartesian Grid, in combination with a well-suited parameter set for the distribution function, an almost conservative, but smooth representation of the modeled propeller is obtained.

- **Raised-cosine kernel:** The presented Kernel function is applied not solely for the distribution of the source terms but also for evaluating the inflow conditions to the blade.

- **Direct coupling and multi-domain approach:** In contrast to the widespread approach of taking tabulated airfoil data for calculating the aerodynamic properties of a propeller, a direct coupling of the finite volume simulation with on the one hand, a panel method coupled with a boundary layer integration method and, in particular, on the other hand, a direct coupling with a two-dimensional Reynolds-averaged Navier-Stokes (RANS) simulation within a multi-domain framework is conducted.

At second, the first main objective regarding the modeling of the flow around a helicopter including the rotor-head motion by introducing a fast, linear-scaling deforming-mesh approach is provided. The objective of this part is mainly to demonstrate and give a detailed description, including some special consideration, of the presented method in [5].
The second main objective for this part is the comparison of the results for the wake flow obtained by the numerical approach regarding those of the experimental data based on [5]. This comparison is basically performed with averaged flow results of a scale-adaptive simulation and the data generated by particle image velocimetry. In addition, phase-averaged quasi-volumetric particle image velocimetry data are presented.

Concerning the helicopter simulation, the points beyond the state-of-the-art are as follows:

- **Analytical mesh-deformation:** Application of an analytical function based on a raised cosine to describe the motion of the rotor blades as well as the deformation of the computational grid.

- **Complementary numerical and experimental investigations:** Results of the numerical simulations are compared to the experimental data. The wind-tunnel model features a fully-functional rotor head. Results of the phase-averaged quasi-volumetric particle image velocimetry measurements are presented.

1.3 Outline

As already mentioned above, the thesis consists of two major parts. At first, the modeling of the propeller action is described in chapter 2. The chapter starts with an introduction including a comprehensive literature review in section 2.1. In the following, the basic concepts for calculating the aerodynamic properties of a propeller, like the momentum theory, the blade element theory, and the combination of the latter, the blade element momentum theory, are summarized in the sections 2.2, 2.3, and 2.4, respectively. While the previous concepts do not allow for a detailed investigation of the flow field, the enhancement by connecting the blade element theory with a continuum-based numerical approach do. The result is the generalized actuator disc approach and is presented in section 2.5. The panel method, applied for calculating the airfoil data, is presented in section 2.6. The core element of the thesis, the direct coupling between the methods within one framework as well as the application of the distribution function, is shown in section 2.7 in detail. In section 2.8, solely the necessary modifications for the multi-domain approach by substituting the calculation of the sectional airfoil data are described. Additional information for solving the problem is given within the generic test cases in the next chapter. Finally, in section 2.9, a brief introduction for the resolved simulations is given.
The test cases for investigating the introduced methods are presented in chapters 3 and 4. In chapter 3, the two-dimensional cascade test case is described. This test case is used to find an appropriate set of the parameters for the actuator disc as well as the actuator line for a wide range of operating points. The three-dimensional cascade test case, in section 4.1, represents the extension of the previous test case by one dimension, in order to determine the quality of the prediction by including three-dimensional effects. While the previous test cases are of generic type and emphasize in detail on the behavior of the model, in section 4.2, the three-dimensional propeller test case is presented. The latter is used for two points. On the one hand, an intermethod comparison of the modeled propeller with regard to the resolved propeller simulation is presented. On the other hand, the applicability for inclined inflow conditions is presented qualitatively. Finally, a complex configuration of the propeller mounted on an aircraft is presented in section 4.3. Therein, a validation of the numerical simulations with the experimental data is provided.
In chapter 5, the modeling of the rotorcraft is presented. In section 5.1, the introduction with the literature review is provided. In section 5.2, a general overview of the mesh-motion methods, containing the mostly-used ones, is given. Finally, in section 5.3, the analytical mesh-deformation method is presented. Therefore, the basic considerations are made as well as results for simple examples are described. In addition, a scalability study is presented.
In chapter 6, the results of the rotorcraft simulation is presented. In section 6.1, the test case description is provided. In section 6.2, the test conditions of the numerical setup as well as the measurement techniques are described. The numerical setup is presented in section 6.3. Basically, the meshing and blocking strategy, the application of the analytical mesh-deformation method, and the solver settings are shown. Finally, in section 6.4, a validation of the flow field in the wake is presented for a helicopter configuration excluding the tail. In addition, a characterization of the flow field is given for a helicopter configuration including the tail.

2 Modeling of the Propeller Action

In this chapter, the methods for the modeling of the propeller action are discussed. First, an introduction including the state-of-the-art is provided in Section 2.1. Within this subchapter, an overview of the method and the fields of application are presented. Thereafter, the different basic theories are described in detail. In Section 2.2, the momentum theory (MT) is explained followed by an introduction into the blade element theory (BET) in Section 2.3. The latter methods are then combined to the well-known blade element momentum theory (BEMT) presented in Section 2.4. The complexity is increased and leads to the generalized actuator disk (GAD) approach presented in Section 2.5. In Section 2.6, a brief overview of the panel method coupled with the boundary layer integration method (PanBL) applied within this thesis is provided. In Section 2.7, the generalized AD model developed within this thesis is coupled with PanBL for generating the airfoil data. In Section 2.8, PanBL is substituted with a 2D-CFD simulation for providing the airfoil data and results consequently in a multi-zone approach. The theory concerning resolved simulations is finally presented in Section 2.9. The latter are used for inter-method comparisons.

2.1 Introduction

The calculation of the forces and moments generated by propellers is a challenging task. The main objective of a propeller is the generation of forward thrust. Therefore, the ambient fluid has to be set into backward motion. During this process, losses in useful energy are inevitable caused by the kinetic energy of the fluid downstream of the propeller. Moreover, the rotational motion of the fluid downstream of the propeller is a source of loss. This motion is caused on the one hand by frictional drag of the propeller blade and on the other hand by projection of the lift vector in the circumferential direction. [1].

In order to capture all these effects appropriately, substantial effort has to be made. Since the investigations of propellers have started more than hundred years ago and due to the absence of computational resources at that time, it was not possible to include all effects occurring in the flow around the propeller. In order to circumvent the problem, simplified models and assumptions have been applied. One of the simplest models is the axial momentum theory or 1D momentum theory presented initially by Rankine [7] and further developed by Froude [8]. Within this theory, an ideal propeller is considered. This means that losses induced by the frictional drag of the blade as well as the rotational motion of the slipstream is neglected. Furthermore, this model assumes a constant thrust distribution across the whole disk. Within this model, in generally called Froude´s actuator disc model, the propeller is modeled by a disc with a sudden increase of pressure through the disc while the velocity profile is continuous. [1].

In order to enhance the axial momentum theory, the assumption that no rotation in the slipstream of the propeller occurs has to be dropped. The rotational motion in the slipstream leads to a further loss of useful energy. Including the rotational motion of the flow downstream of the propeller, the general momentum theory is obtained [1]. Nevertheless, for the solution of the equations obtained therein, still some simplifications had to be made. Joukowsky, for example, supposed a constant circulation, since therefore, the flow in the slipstream remains irrotational except along the axis of the propeller [1]. Some of the assumptions have been used as well to derive best efficiency distributions across the disc. As a further refinement of the solution, the influence of the blade drag

has been included, whereas additional simplifications, e.g. constant influence factors along the radial direction of the blade, have been made to allow the originating integrals to be solved analytically. [1].

The results obtained by these theories provide the thrust and torque of the propeller in terms of the increase in momentum of the fluid while passing the propeller disc. Moreover, the solution can also determine the maximum possible efficiency. However, there is no statement made how these integral values are connected to the actual shape of the propeller and consequently, the flow around it. This gap was tried to be closed by W.Froude [9], who estimated the forces on the propeller. Nonetheless, the evaluation of the primitive blade element theory was made by Drzewiecki [10]. The idea of this method is that the blade is divided into several blade elements along the radial direction, whereas each has individual inflow conditions and different geometrical properties. The aerodynamic forces and moments of the section are estimated by considering the section as an airfoil with specified inflow conditions. Summing over all elements, results in the total thrust and torque of the propeller. Difficulties within this method have been found in the determination of the airfoil data and the inflow conditions. It has to be kept in mind, that the airfoil data were generated for finite wings with moderate aspects ratios. Drzewiecki [11] assumed that the axial inflow conditions for the propeller depend on the undisturbed freestream conditions only. Since deviations compared to the experiments have been detected, he has assumed the problem to rely on incorrect airfoil data and suggested to perform tests with specially designed propellers. In contrast, Betz [12] and de Bothezat [13] applied for their approaches the axial inflow velocity resulting from the momentum theory. Moreover, Fage and Collins [14] modified the inflow conditions empirically. Although it was known that the inflow is influenced by both, the global propeller action, and the local effect of one blade, the clarification of the contribution of the effects could not be established until the introduction of Prandtl's airfoil theory. [1].

It is evident that each section of the propeller initiates a change in the circulation when it produces lift. For an assumed constant circulation along the whole propeller blade, in combination with Helmholtz's second theorem, a vortex system is generated. This consists of the bound vortex, the initial vortex, the axial vortex and the helical shaped tip vortex. For determining the inflow conditions, the tip vortex has to be assumed as a vortex sheet. The latter assumption equals the result for the limit of an infinite number of propeller blades. With this simplification and considering symmetry issues, the obtained velocity in the propeller plane is similar to the velocity provided by the momentum theory. This result is very important, since it says that the actual velocity at the propeller plane has to be used as inflow condition for the local blade element. The global and local effects of the flow around the propeller are therefore included. The arisen difficulties within the primitive blade element theory have been avoided by the application of the actual flow data in the propeller plane. However, the measured airfoil characteristics for finite aspect ratios have to be transformed for infinite aspects ratios. Although, the prescribed approach has been derived for a single propeller blade, it can be applied for propellers with more propeller blades as well. This assumption was proved by Glauert [1], who stated that two-dimensional motion of single airfoil could be applied for generating airfoil data for a blade element. With this knowledge, the calculation of thrust and moments of a propeller can be performed. The predictive quality of the approach is appropriate as well. In particular, it is even in usage in the pre-design stage. [1].
However, some drawbacks are contained within the method by the made assumptions. For example, the mutual interference in the wake flow is not covered and problems can arise for heavily loaded discs. The analysis of heavily loaded propellers with a nonlinear actuator disc model was provided by

Wu [15], who solved a partial differential equation for the stream function [16]. Therein, an approach for capturing complex geometries is given. This includes, for example, ducted propellers and propellers with finite hubs. Further improvements therefore were made by Greenberg [17, 18] and Conway [19, 20]. In the context of wind turbine aerodynamics, a nonlinear model was applied by Madsen [21]. An overview of the state-of-the-art for this kind of approaches was given by van Kuik [22]. Therein, the work of Peters [23] for example, is described. The latter mentioned is interesting for the modeling presented in this thesis, since an actuator disc approach with a defined distribution of sources is used which applies hyperbolic cosine and hyperbolic tangent functions. Nevertheless, the interaction with other geometrical parts, like a fuselage, is still not possible to capture with all the previous presented methods.

For this purpose, further enhancements can be made by coupling the blade element theory with the Euler or Navier-Stokes equations. Within this thesis the term generalized actuator disc model [24] denominates the combination of the Navier-Stokes equations for the governing flow and a representation of the propeller action by e.g. source terms. The advantage within this approach is the inherently captured mutual interference between the blade sections as well as the provided induced velocity caused by the blade tip vortices. In addition, the influence of other lift generating parts, e.g. the wing, as well as flow displacing parts, e.g. the fuselage, can be covered. The approach has been applied in different areas of fluid mechanics by several authors. A lot of works have been published in the field of wind turbine aerodynamics, since the approach is very suitable concerning the flow conditions at the operating points. In the field of aerospace engineering, it has also been applied for propeller and rotor flows as well as the simulation of turbomachinery. At last, it has been applied for the propulsion system of ships. Since this method is from major importance within this thesis, the literature review is detailed in the following.

The literature review is started within the field of wind turbines, since the most research has been performed therefore. Review papers have been published by Vermeer [25], Leishman [26], Sanderse [27], and Hansen [28], as well as Sorensen [29], which have been used as a basis for the presented literature survey. Thereafter, the literature related to the field of aerospace engineering is reviewed.

2.1.1 Wind Turbine Applications

The first application of such a combined approach using Navier-Stokes/Euler equations and introducing source terms for the blade action of vertical axis wind turbines (VAWTs) was introduced by Rajagopalan and different co-authors [30, 31, 32]. The first realization of the generalized actuator disc approach for horizontal wind turbines was made by Sorensen [29, 33]. Therein, a constant disc loading was established. Sorensen and Myken [34] improved the model by including non-constant disc loading and azimuthal velocities in combination with airfoil data in tabulated form to estimate the loading. Sorensen and Kock [35] additionally increased the numerical order of the method, invented a filtering of the solution in order to suppress spurious oscillations, and allowed for stretched grids also. The method solves the incompressible, axisymmetric Navier-Stokes equation in vorticity-swirl velocity-stream-function notation by the application of finite differences. Further investigations have been conducted by Masson et al. [36] and Ammara et al. [37] who also solved the two-dimensional, incompressible, axisymmetric Navier-Stokes equation, but applying a Control-Volume Finite Element Method (CVFEM). The influence of a coned rotor was investigated by Madsen

and Rasmussen[1999], Mikkelsen et al. [38] and Masson et al. [39]. Ammara et al. [37] extended the actuator disc (AD) method embedded into the CVFEM method to three dimensions for investigating coned rotors obtaining acceptable results. As a further improvement, approximate models for yaw were presented by Mikkelsen and Sorensen and Masson et al. [39].

Since the axisymmetric solution does not allow a varying distribution in azimuthal direction, a three-dimensional NS-solution had to be applied to circumvent this shortcoming. Although that was made, the fully unsteady behavior could even not be covered. The result for solving that issue was the actuator line (AL) method presented initially by Sorensen and Shen [40]. Within this approach, the action of the propeller is represented as a rotating line force. The force distribution along the blade is calculated with the local inflow conditions in combination with tabulated airfoil data. The principle was adapted as well by Leclerc and Masson [41]. A detailed description of the AD and the AL approach can be found in the dissertation of Mikkelsen [24]. Investigations concerning the wake flow of wind turbines with an emphasis on the tip vortices and the mutual interaction of the wake flow within wind farms are presented in the dissertations of Troldborg [42] and Ivanell [43].

As a further enhancement in the description of the propeller action, the actuator surface (AS) method has been invented. It was originally presented by Shen et al. for VAWTs [44, 45]. The difference between the AL and AS method lies in the representation of the propeller action. According to the descriptive designation of the method, the AS prescribes the force distribution across a rotating surface. In contrast to the actuator line, not only sectional drag and lift coefficients are needed. In order to obtain a varying distribution in chordwise direction also, the local pressure and skin friction at a certain position has to be known. Shen et al. [45] used XFoil for the generation of the airfoil database. A different actuator surface approach was presented by Sibuet Watters and Masson [46, 47]. Therein, inviscid aerodynamic theory was applied to generate pressure and velocity discontinuities across the propeller surface. Subsequently, viscous effects are not included.

In the following, a lot of different implementations for various applications are presented. The different rotor modeling strategies have been coupled with CFD models of different orders of fidelity. A lot of work has been presented, investigating the wake of wind turbines as well as the mutual interference of the wind turbine wakes with other wind turbines. It has been shown, that the methods are well-suited for such investigations. Nevertheless, the focus of the review is based on the modeling of the distribution and generation of the propeller forces.

Rethore [48] presented in his dissertation a different treatment of the forces in EllipSys as it had been used for previous investigations, e.g. Mikkelsen [24]. Instead of a Gaussian distribution function, a pressure jump term acting between adjacent cells was used. The result was a reduced amount of wiggles, while allowed for a decreasing number of nodes in the region where the forces of the propeller were applied. In addition, a method for distributing the forces area-weighted across the cells was presented, which also was intended to speed up the simulation. Finally, a combination of a Large Eddy simulation (LES) with an actuator disc method was presented for a wind turbine located within a turbulent boundary layer, which served as basis to enhance the resolving capabilities of a k-ε turbulence model. Troldborg [42] invented the combination of the actuator line approach with an LES instead of a RANS simulation.

Wu and Porte-Agel [49] tested two different actuator disc models in combination with an LES for wind turbine arrays. One was based on a uniform load distribution according to the axial momentum

theory, while the second used BEMT theory. In comparison to wind-tunnel measurements, it was shown that the inclusion of the BEMT led to better results for the modeling of the rotation within the wake flow. Furthermore, Porte-Agel et al. [50] conducted numerical investigations using an AL method which were in good agreement with the experimental data as well. However, the results for the time-averaged velocities were similar to the AD in combination with the BEMT. Wu and Porte-Agel [51] presented a further validation of the introduced model that was also in good accordance with the experimental data of wake flow measurements. Therefore, the approach using the BEMT showed again more accurate results. Additionally, the publication included a detailed investigation of the layout effect of wind-farms. The interaction of wind farms with the atmospheric boundary layer was investigated by Porte-Agel et al. [52]. The same methods as presented before were applied to evaluate the different heat flux profiles in the boundary layer of the atmosphere as well as the heat flux at the surface caused by the presence of a wind farm. The presented methods used the Gaussian kernel for the distribution of forces.

Shen et al. [53] applied the actuator line method and compared it to experimental data for the MEXICO rotor. Different airfoil data have been used within this work; one original data set and another one including certain corrections (e.g. three-dimensional effects in the stall region). It has been stated that the results including the correction gave a better agreement with the experiment for this case in contrast to the uncorrected data.
An exclusively experimental investigation, which seems to be of interest for numerical modeling, was made by Aubrun et al. [54]. It was shown that the actuator disc approach is appropriate to model the wake field of a wind turbine. Therefore, wake field investigations for an experimental actuator disc (modeled by a porous disc) and a three-bladed wind turbine rotor were conducted. The wake field showed good agreement between both methods.
An enhancement of the numerical treatment was made by Johnstone et al. [55], who conducted a direct numerical simulation (DNS) with an actuator disc approach, including an Ekman boundary layer. Meaningfully, a spectral method was used for this purpose. As kernel for the distribution of the forces a Gaussian curve is applied along the disc axis and an error function in the radial direction to the disc edge. This shows that the method is even suited for fully scale-resolving simulations.
Malki et al. [56] presented a coupling of the blade element momentum approach and a RANS flow solver for evaluating tidal stream turbine performance. With this method, similar results to classical BEMT methods and reasonable agreement with experimental data were obtained. The method used for wind turbines were applied successfully therefore. For this approach, the mesh has to be fitted with the actuator disc shape.
Further investigations concerning AD modeling of the MEXICO rotor were presented by Mahmoodi and Schaffarczyk [57]. Therefore, Fluent 5.7 was applied as flow solver. User-defined functions of Fluent were called to calculate the source terms for the propeller action, by taking into account the local inflow conditions and tabulated airfoil data. For this method, the mesh has to fit to the AD geometry. The results were in good agreement with experimental data. This approach was in the following implemented with slight modifications in OpenFOAM by Jeromin et al. [58]. Therein, the Fluent and OpenFOAM AD results were compared to the results of the resolved CFD simulations with DLR-TAU and the experimental data. It was concluded that similar error bands of all methods regarding the experimental data were obtained for the prediction of the overall thrust and torque. The trend of the overall torque was even better captured by the ADs than by the resolved CFD simulations. Nevertheless, the spanwise distribution of the normal and the tangential force required an improvement.

Castellani and Vignaroli [59] applied a uniform disc distribution for investigating the wake of a wind turbine including the boundary layer. Therefore, a RNG k-ε model was used for the turbulence closure. The comparison to experimental data provided a good agreement and better results than simpler models. Masters et al. [60] applied a coupled BEMT/CFD approach for the wake flow of tidal stream turbines. It was shown that the approach was even well-suited for such applications. The numerical results obtained for the wake flow were in good accordance with the experimental data for different non-uniform inflow conditions caused by different water surface gradients.

Makridis and Chick [61] investigated wind turbine wakes including terrain effects with an AD method based on the approach of Zori and Rajagopalan [62]. The method was implemented in Fluent using source terms in the momentum equation. The obtained results were stated to agree well with experimental data in an overall perspective, whereas at some locations discrepancies were detectable.

Schmitz and Jha [63] presented a turbine-turbine interaction test case as well as a rotor hub wake investigation. The AL model of Sorensen and Shen [40] was coupled with an LES in OpenFOAM therefore. The main objective of the rotor hub wake investigation was to evaluate, if the per-rev harmonics can be represented by modeling the blade with drag forces exclusively. The conclusion was that this goal can be fulfilled with the method appropriately.

Nishino and Willden [64] presented a low-order modeling of blade induced turbulence using an actuator disc within the Fluent framework for RANS calculations. A simple permeable disc was applied, but the objective was to study the effect of a rotor on the turbulence in its wake flow. Therefore, a model for the blade-induced turbulence was developed. The obtained results were in good agreement with the experimental data for appropriately chosen sets of parameters for the tip vortex correction as well as the modeled turbulence of the rotor. Nevertheless, it was stated that further validation studies are needed, in particular, to examine the robustness of the model.

Kim et al. [65] introduced an improved actuator surface method for wind turbine applications. The difference is that the determination of the inflow velocities was fundamentally changed. Instead of extracting the velocity from the flow field at the reference line for a direct estimation of the effective inflow angles, a preceding procedure based on the lifting line theory was applied. Therefore, the blade was divided into spanwise and chordwise elements. For all elements, the bound circulation and the circulation of the shed vortices were determined. The induced velocities of all elements on the reference line were taken into account to correct the inflow conditions. The results were provided for a simple wing test case as well as two wind turbine test cases. The results showed good agreement with the experimental data for all of the test cases. In addition, the dependence on the distance of the reference line relative to the quarter-chord line on the results was small, if the distance was at least greater than one chord length. Furthermore, it was stated that the tip loss correction is not necessary for this model.

Gou et al. [66] conducted a detailed comparison of BEM-CFD and full resolved rotor simulations. Therefore, an implementation in ANSYS CFX was used in accordance with Malki et al. [56]. Within this work, numerical and experimental data for the airfoil characteristics were applied for the BEM. It was found that the prediction of the thrust is comparable, while the power extraction is overestimated by using the numerical data for BEM. The power showed a deviation in the radial distribution for increasing radii. The averaged velocity field in the wake field gave reasonable predictions with the BEM.

A hybrid actuator sector method was invented by Storey et al. [67]. This method represented a combination between the actuator line and the actuator disc approach. The idea was to drop the

restriction for small time steps by the actuator line approach and distribute the forces of the propeller across a certain azimuthal sector. The limiting case for angles tending to zero is the actuator line approach. The other limit results in the actuator disc approach. The prescribed distribution along the azimuthal direction was generated by a trapezoidal function. The obtained wake field results were comparable to the results of the AL approach, while the numerical effort was similar to the AD approach.

Another revised BET-CFD model was presented by Edmunds et al. [68]. Within this model, an additional source term was added. The main idea was to capture the effects of the tip vortex appropriately. The strength of this additional source term was determined by applying the lifting line theory assuming an elliptical distribution function and fulfilling a vanishing effective angle of attack at the blade tip. It was concluded that a good correlation with experimental data was obtained in terms of power, thrust, and wake flow field prediction.

Shives and Crawford [69] adapted two-equation models for AD simulations in order to obtain an appropriated prediction of the wake flow field including the turbulent kinetic energy production due to the breakdown of the trailed vortices. Certain terms were added in the respective equation and resulted in a good agreement compared to the experimental data for various downstream positions concerning the normalized axial velocities as well as the turbulence intensities.

Stevens et al. [70] presented a detailed investigation of the AD and AL approach using an LES and compared the results with the experimental data for an isolated wind turbine as well as a wind farm. The outcome was that in the near field, up to three turbine diameters downstream of a single turbine, the AL captures the wake field better than the actuator disc while further downstream a comparable result is obtained. Furthermore, it was stated that for a near wake prediction the influence of the nacelle and the tower is important.

Baba-Ahmadi and Dong [71, 72] published wake investigations applying the AL method combined with an LES. The wake characteristics as well as a validation were presented. It could be shown that the time-averaged axial velocity profiles as well as the turbulent characteristics were in good agreement with the experimental data.

Elli et al. [73] used a weakly-compressible formulation of the governing equation to simulate the wake of a turbine. In order to reduce the numerical error and suppress the numerical dissipation, a WENO5 scheme was implemented. An AD approach was applied, which results show reasonable agreement with the experimental data. In particular, the preservation of the vortical structures by the WENO5 in contrast to the MUSCL scheme was provided.

Park et al. [74] presented a validation of the model presented by Kim [65] for three test cases. A single wing, three aligned wings as well the ONERA 7A hovering rotor test case were included in the investigation. In addition, the results of this method were compared to results obtained with a Gaussian distribution. In general, the new method showed good agreement with the experimental data for all test cases.

Yang and Sotiropoulus [75] invented an AS method that allowed for accounting the influence of the nacelle within an LES. Another difference within this framework was that instead of a Gaussian distribution, a four-point sine function according to Yang et al. [76] was applied for distributing the propeller forces.

2.1.2 Aerospace Applications

The first application of the generalized actuator disc method for helicopters was performed by Rajagopalan and Lim [2]. They performed steady state calculations with an actuator disc for a helicopter in hover flight and axial translation. The flow was assumed to be laminar and axisymmetric. That is why the flow field was solved in a cylindrical coordinate system. The inflow quantities were extracted from the flow field and tabulated data for the airfoil sections were used to generate the source terms for the momentum equations. Therefore, a good agreement with the experimental data was obtained.

In the following years, Rajagopalan with several co-authors has performed further investigations with this method. Rajagopalan and Moulton [77] investigated the interference of the propeller with a wing and Rajagopalan and Mathur [78, 79] a helicopter rotor in forward flight. Additional information for the latter investigation can be found in the dissertation of Mathur [80]. Furthermore, Zori and Rajagopalan [62] investigated rotor-airframe interaction in forward flight. The applied method uses an intersecting procedure in order to determine the inflow conditions for the rotor blade section depending on the radial and azimuthal position of the cell center of the finite volume cell. Source terms are subsequently used to prescribe the action of the propeller at this position in the NS solution. The details therefore can be found in the Dissertation of Mathur as well [80].

In contrast, Fejtek and Roberts [81] discretized the rotor disc in azimuthal and radial segments. The inflow conditions are averaged over each of the segments. Inflow and outflow boundary conditions are applied for the modeling of the propeller action in the NS-solution. A similar approach using segments has been used by Chaffin and Berry [82], but the pressure jump across the rotor disc was represented by applying an additional mesh using the chimera approach.

In 1997, Poling et al. [83] used the method presented by Rajagopalan for investigations of the flow field of different tilt rotor configurations in hover, which showed well agreement with the experimental data.

Bettschart [84] implemented a steady actuator disc model in the FLU3M code. The distribution of the forces of the actuator disc was realized by a pressure jump at a pre-defined mesh surface. The amount of the rotor forces were set constant as well as determined by an external code that was based on a lifting line method with a prescribed vortex lattice rotor wake.

Further investigations with the method of Rajagopalan were performed by Tong and Sun [85]. Within this publication, investigations with coaxial, tandem, and side-by-side rotors were reported. Comparison with the experiments showed a good agreement for the wake geometry as well as the rotor performance.

A paper supervised by Filippone [86] provided a coupled BEMT-CFD approach within the commercial flow solver Fluent. The aerodynamic characteristics of a blade section were determined by a 2D panel method. It was stated that the latter is independent of the Reynolds Number. Furthermore, it was described that the pressure boundary conditions were used by taken into account the dynamic pressure and the velocity direction to model the propeller action.

Le Chuiton [87] gave a review of the state-of-the-art at that time concerning different possibilities of the representation of the rotor action within such a coupled framework. Calculations were performed with the block-structured flow solver FLOWer, whereby a constant disc loading as well as a non-uniform disc loading computed by a flight mechanics code was prescribed. Results were shown for the BO105 and the Dauphin 365N. Schweikhard [88] implemented this actuator disc method in the unstructured flow solver DLR-TAU using source terms. The flow fields around the EC145 were compared to the FLOWer results and were in good accordance. Further investigations using the

actuator disc with FLOWer were made by Khier [89]. Time-accurate results were opposed to the actuator disc results for the BO105 and the Dauphin 365N configuration.

O'Brian and Smith [90] presented results for various disc loading distributions for a generic configuration as well as the Robin configuration. The paper includes constant and linear disc loading as well as a blade element approach according to Chaffin and Berry [82]. There, the flow solver FUN3D was used. It was shown that a constant disc loading is not appropriate for simulating the rotor-fuselage interaction and at least a linear varying method should be taken into account. Additional information, in particular concerning the implementation, can be found in the dissertation of O'Brian [91]. In contrast to the actuator disc model presented in the paper, also an unsteady actuator surface approach is presented within the thesis and compared to the results obtained by an overset approach. Renaud et al. [92] presented a detailed study using the Dauphin 365N configuration as test vehicle also. Different solvers of AFDD, ONERA, and GIT were used for the investigations. Implicitly, different meshing strategies are taken into account. An isolated fuselage as well as in combination with uniform and non-uniform disc loadings of the actuator disc were applied. The non-uniform loadings were obtained by the lifting line based code HOST [93]. In particular, the pressure coefficients on the surface as well as in the field were compared between the different solvers and showed similar results. The validation with experimental data was in good agreement for the isolated fuselage and the non-uniform disc loading.

Filippone and Mikkelsen [94] investigated the flow around the helicopter in the vicinity of the ground. Therefore, a non-uniform actuator disc according to Sorensen was applied. In particular, the usage of the Gaussian function for reducing spurious oscillations was included. Different forward flight velocities were tested and the flow field in the vicinity of the ground was presented.

Kim and Park [95] carried out numerical simulations with the flow solver STAR-CD in an unsteady manner applying the actuator line approach. Different inflow models were tested and compared to a sliding mesh approach as well as validated with experimental data. A good agreement was found while the numerical effort was reduced to approximately one third. An improvement of this method was presented by Kim and Park [96, 97]. The simulations were conducted with STAR-CD as well. However, instead of using an inflow model, the inflow conditions were extracted from the flow field in a similar manner as it had been performed by Fejtek and Roberts [81]. In particular, it means that the inflow values are obtained by averaging the appropriate cells of the NS-solution in chordwise direction. Additionally, a chordwise force distribution in accordance with the two-dimensional airfoil solution was chosen for representing the source terms. It was stated that for this approach, the influence of the blade tip vortices is inherently covered by the formulation and consequently, a blade tip correction is not required. Kim et al. [98] implemented this approach in the flow solver OpenFOAM and validated the inflow velocities for the ROBIN test case and the GIT test case. The rotor disc was meshed with triangles and the height of the disc was one cell. Nevertheless, the results for both test cases were in good agreement with the experimental data for various advancing ratios.

Zhang et al. [99] investigated a tilt rotor configuration in conversion mode by applying the actuator disc method of Rajagopalan and Mathur [78]. The difference was that for the rotation of the rotor disc during the conversion, an overset grid approach was used. This means that the source terms are calculated initially within a rotor grid with the actuator disc method. The transfer of the rotor action into the stationary background grid is thereafter performed by the overset method. Li et al. [100] applied a validation with this actuator disc method. The results were in good agreement with the experimental data. Furthermore, the actuator disc results were compared to a time-accurate solution of the rotor flow. The objective within these investigations was the XV-15 rotor. Koning et al. [101]

applied RotCFD for actuator disc simulations with the method of Rajagopalan for the same configuration. The results of the actuator disc approach were compared to the results obtained by CAMRAD II [102] as well as validated with experimental data. The investigations have been performed for several tilt angles including hover and axial flight conditions. The results were in good accordance with the experimental data.

A new actuator surface method was presented by Linton et al. [103]. It combined a lifting line blade model with a CFD convected free wake model and was implemented in OpenFOAM. Three test cases, an isolated wing, the Caradonna and Tung rotor, and the UH-60A rotor were investigated. Although, the results show good agreement for the test cases, certain enhancements can be made. In particular, the spanwise load distribution for the Caradonna and Tung rotor can be improved. Raichle [104] presented a conservative discretization of the actuator disc. Therefore, the actuator disc is modeled as a discontinuous surface embedded into the fluid domain. The approach is independent of the mesh topology and developed for axial inflow conditions. The results were compared to experimental data and show a good agreement. Chiew and Aftomis [105] presented a rotor model for steady and unsteady simulations based on the blade element theory. To determine the intersecting cells of computational grid with the rotor disc, some kind of a cut-cell approach was applied. This ensured that only cells within the disc are allowed to act as source terms. In addition, for unsteady simulations a different distribution including a trapezoidal with “smoother edges” was chosen. The validation with the numerical data showed good agreement. Ortun [106] presented a coupled approach between the CFD solver elsA and the lifting-line software PUMA developed by ONERA. In contrast to other methods, the source terms are distributed in axial direction according to the shape of the blade. The strength of the source terms in axial direction is described by a Weibull function. This method shows a good agreement between the reference CFD and the coupled approach results in terms of thrust evolution of a single blade during one revolution. Battai et al. [107] showed the applicability of the actuator disc approach in a fully coupled flight dynamics/CFD simulation of a helicopter. The actuator disc method used the Gaussian distribution that has been presented by Mikkelsen [24] for stabilizing the simulation. The test cases included were starting from hovering flight out of ground effect and were ending up with landing on the deck of a ship. It was concluded that although the results did not match perfectly, the approach was suitable for investigating the coupling methodology.

2.2 Momentum Theory

This subchapter summarizes the momentum theory according to Glauert [1]. Firstly, the axial momentum or 1D momentum theory is described and secondly, the general momentum theory is presented.

2.2.1 Axial Momentum Theory

As stated in the introduction, within the axial momentum theory the rotation of the fluid in the slipstream as well as the frictional drag of the propeller blades is neglected. Furthermore, the load distribution across the disc is constant. The thrust of the propeller can be easily determined with a momentum balance per unit time. It is further assumed that the propeller is fixed in space while the fluid is moving relative to the propeller. The flow velocity far upstream of the propeller is equal to the freestream velocity U_∞. The velocity in the wake far downstream of the propeller is defined as the wake velocity u_w. The change in velocity of the fluid, which flows through the disc, results in the thrust of the propeller. Figure 1 shows exemplarily the boundary streamtube of the flow through the propeller disc with the above described positions. The mass flow through the disc is defined as

$$\dot{m} = \rho\, A_p u_p, \tag{2.1}$$

where ρ is the fluid density, A_P is the area of the propeller disk and u_P is the velocity at the position of the propeller disc. Thus, the thrust of the propeller reads

$$T = \dot{m}\,(u_w - U_\infty) = \rho\, A_p u_p (u_w - U_\infty). \tag{2.2}$$

In addition, the energy balance per unit time between the upstream and downstream location can be established as follows

$$\frac{dE}{dt} = P = \rho\, A_p u_p (u_w^2 - U_\infty^2), \tag{2.3}$$

where E is the kinetic energy and P the power exerted by the propeller. The power of the propeller can be expressed as $P = T\, u_p$ as well. Furthermore, applying the continuity equation and assuming constant density gives

$$A_\infty U_\infty = A_p u_p = A_w u_w. \tag{2.4}$$

Combining these equations provides the velocity u_P in the propeller plane according to

$$u_p = \frac{1}{2}(U_\infty + u_w). \tag{2.5}$$

The same result can be obtained by using the steady, incompressible Bernoulli equation upstream and downstream of the disc independently and determine the pressure jump across the disc. After the integration over the disk area, the thrust of the propeller is obtained [8]. This theory is also referred to as Rankine-Froude theory. It allows estimating the ultimate limit of the efficiency in dependence on the thrust or the power also. Although the equation for the thrust can be applied strictly speaking for the whole propeller only, it is convenient to permit the usage for annular elements as follows

$$dT = \rho\, u_p (u_w - U_\infty)\, dA_p. \tag{2.6}$$

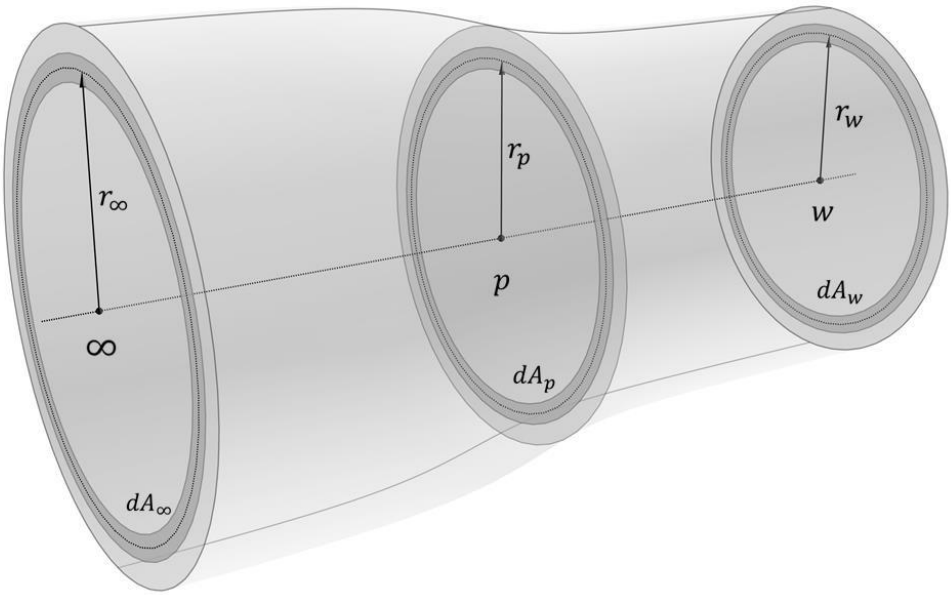

Figure 1: Boundary streamtube of the flow through the propeller plane. In addition, the local areas for the integration at certain radial positions are presented.

2.2.2 General Momentum Theory

In order to enhance the quality of the theory, the rotational motion in the slipstream has to be included. For this purpose, the momentum balance in circumferential direction has to be applied. Evaluating the results for the balance equation at the location of the propeller and far downstream of the propeller in the ultimate wake, it reads

$$\omega_p\, {r_p}^2 = \omega_w\, {r_w}^2. \tag{2.7}$$

In this equation, ω and r represent the angular velocity and the radial position at the location P and W, respectively. The torque of an annular element of the propeller is defined as

$$dQ = \rho\, u_p\, \omega_p\, {r_p}^2\, dA_p. \tag{2.8}$$

This theory can provide a connection between the axial and the radial velocity in the wake, which is described by Glauert [1] and results in the following equation

$$\frac{1}{2}(u_w - U_\infty)^2 = \left[\frac{\Omega - \frac{1}{2}\omega_p}{u_p} - \frac{\Omega - \frac{1}{2}\omega_w}{u_w}\right] u_w \omega_w {r_w}^2. \tag{2.9}$$

Ω denominates the rotational speed of the propeller. The arising problem is that this equation cannot be solved in that form. Therefore, simplifications have been applied. If the flow is considered to be irrotational except along the axis of the propeller, the following equation arises

$$\omega_P \, {r_P}^2 = \omega_w \, {r_w}^2 = C. \tag{2.10}$$

This results in a constant circulation for all radial sections. With this assumption, the constraints for the axial velocity in the propeller plane reads

$$u_p > \frac{1}{2}(U_\infty + u_w). \tag{2.11}$$

Apparently, there is quite a difference between the results for the axial and general theory. Since the latter requires u_p to be greater than the arithmetic mean between the velocities far upstream and far downstream of the propeller plane. This is simply explained by the rotation of the slipstream. Moreover, the torque of the propeller is obtained with this simplification by integration over the disc to

$$Q = \pi \, R_p^2 \, \rho \, u_p \, C. \tag{2.12}$$

However, another important point can be clarified with the previous derived equations. It was shown by Glauert [1] that the increase in u_p is small for moderate Q in comparison to the axial momentum theory. The result justifies neglecting the influence of the rotation of the slipstream. Nevertheless, the results for constant circulation cannot be fulfilled for all sections of the propeller, in particular, the root region.

Since the angular velocity in the slipstream is small compared to the angular velocity of the propeller, higher order terms like ω_p^2 can be omitted [1]. Thus, the incremnetal thrust and the torque of an annular element are

$$d\,T = \, 2\,\pi\,\rho\,\left(\Omega - \frac{1}{2}\omega_p\right)\omega_p\, r_p^3\, dr_p, \tag{2.13}$$

$$d\,Q = \, 2\,\pi\,\rho\, u_p\, \omega_p\, r_p^3\, dr_p, \tag{2.14}$$

respectively. Once the axial interference factor $a = u_p/U_\infty$ and the rotational interference factor $a' = 2\omega_p/\Omega$ are defined, the equations for an ideal frictionless propeller read

$$d\,T = \, 4\,\pi\,\rho\, U_\infty^2 (1+a) a\, r_p\, dr_p, \tag{2.15}$$

$$d\,Q = \, 4\,\pi\,\rho\, U_\infty\, \Omega (1+a) a' r_p^3\, dr_p. \tag{2.16}$$

2.3 Blade Element Theory

This subchapter summarizes the assumptions of the blade element theory as e.g. presented by Glauert [1]. Within this thesis, the blade element theory refers to the term primitive blade element theory invented by Glauert [1]. For the blade element theory, the propeller is divided in several different radial sections in a similar manner as for the momentum theories described in the preceding chapters. The difference of the blade element theory in contrast to the momentum theory is that the action of the propeller blade is of major interest. Figure 2 shows a generic propeller blade or more general a generic wing with n sections. A NACA 0012 airfoil is used with an elliptical chord length distribution along the span. The semi-transparent planes cut the propeller blade at certain radial positions for the division into sections. It has to be noted that within this theory, planes are used instead of cylindrical surfaces. The planes are positioned according to a cosine law depending on the radial coordinate as well to resolve the larger gradients in the vicinity of the blade tip. The dotted lines depict the intersection of the cutting planes and the propeller blade. The solid lines show the reference airfoil for the respective section.

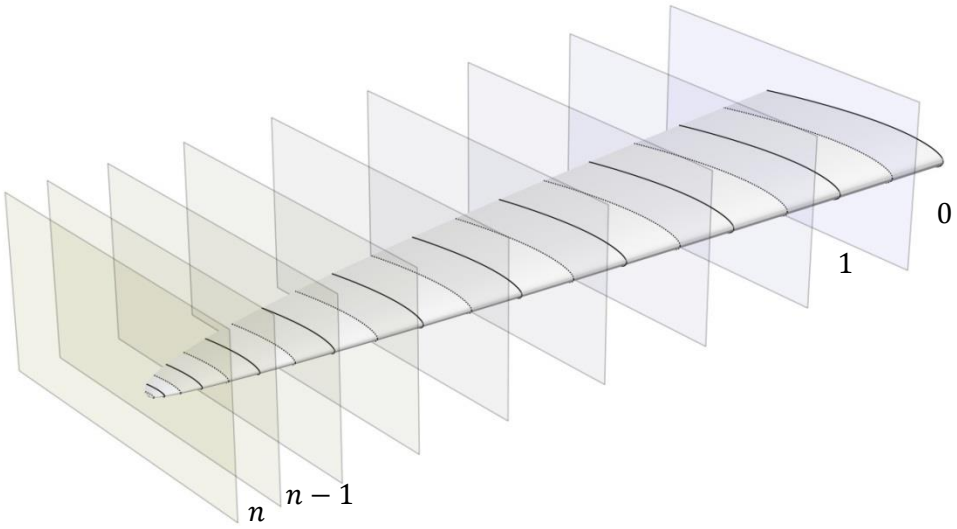

Figure 2: Exemplary radial distribution of the sections for the blade element theory. The numbers denominate each section. The cut-planes show the boundaries of the sections and the black solid line the reference airfoil of a section.

The arising question is on the thrust and circumferential force generated by a certain section. Therefore, the section is assumed as an airfoil as shown in Figure 3. The blade section is inclined with a defined geometric pitch angle θ. The inflow angle at the blade section can be established with the axial inflow velocity V_x and the rotational velocity V_φ to

$$\phi = \arctan\left(\frac{V_x}{V_\varphi}\right). \tag{2.17}$$

The angle of attack of the blade section reads

$$\alpha = \theta - \phi \tag{2.18}$$

and the resultant inflow velocity is denominated as

$$V_{rel} = \sqrt{{V_x}^2 + {V_\varphi}^2}. \tag{2.19}$$

The lift and the drag of a blade section ΔL and ΔD, respectively, are obtained with the associated nondimensional coefficient c_L and c_D as well as the chord length c to

$$\Delta L = \frac{1}{2}\,\rho\, V_{rel}^2 c_L c\, \Delta r_P, \tag{2.20}$$

$$\Delta D = \frac{1}{2}\,\rho\, V_{rel}^2 c_D c\, \Delta r_P. \tag{2.21}$$

The thrust ΔT and the circumferential force ΔF_ϕ of a blade section are established by a change of the reference frame as follows

$$\Delta T = \Delta L\cos(\phi) - \Delta D\sin(\phi) = \frac{1}{2}\,\rho\, V_{rel}^2 c\,(c_L\cos(\phi) - c_D\sin(\phi))\Delta r_P, \tag{2.22}$$

$$\Delta F_\phi = \Delta L\sin(\phi) + \Delta D\cos(\phi) = \frac{1}{2}\,\rho\, V_{rel}^2 c\,(c_L\sin(\phi) + c_D\cos(\phi))\Delta r_P. \tag{2.23}$$

These equations can be integrated along the radial direction in order to obtain the thrust and torque of the propeller blade. Within this theory, the thrust of the whole propeller is calculated by multiplying the thrust of a single blade with the total number of blades.

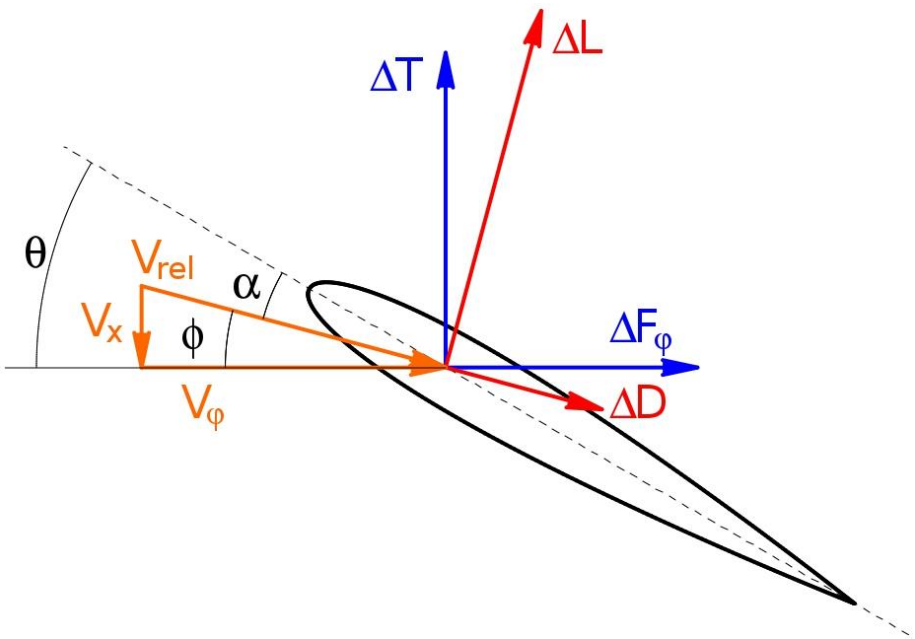

Figure 3: Forces and velocities on a blade element. The sketch includes the circumferential V_φ and axial inflow V_x velocities as well as the resultant velocity V_{rel}. The sectional thrust ΔT and circumferential force ΔF_φ as well as the sectional lift ΔL an drag forces ΔD are shown.

2.4 Blade Element Momentum Theory

As described in the introduction, Drzewiecki [11] adopted the inflow conditions of an undisturbed flow for the equations derived in the previous subchapter. However, the results were not satisfying with this approach. Therefore, the inflow conditions have to be modified according to the suggestion of Betz and Bothezat [12] by including the results of the momentum theory. The combination can be established by comparing the equations for the thrust and circumferential force of the momentum theory and the blade element theory. Writing the equations in dependence of the axial influence factor a as well as the rotational interference factor a' the following system of equations can be provided

$$dT = 4\,\pi\,\rho\,U_\infty^2(1+a)a\,r_P\,dr_p, \tag{2.24}$$

$$dQ = 4\,\pi\,\rho\,\Omega^2(1-a')a'r_P^3\,dr_p = 4\,\pi\,\rho\,U_\infty\,\Omega(1+a)a'r_P^3\,dr_p. \tag{2.25}$$

$$dT = \frac{1}{2}\,\rho\,V_{rel}^2 c\,B(c_L\cos(\phi) - c_D\sin(\phi))\,dr, \tag{2.26}$$

$$dQ = \frac{1}{2}\,\rho\,V_{rel}^2 c\,B\,(c_L\sin(\phi) + c_D\cos(\phi))\,r_P\,dr_P. \tag{2.27}$$

Keeping in mind that c_L, c_D, ϕ, and V_{Rel} can be expressed in terms of the known propeller parameters and the inflow condition, the unknown variables are a, a', dT, and dQ. Thus, the resulting system of equations can be solved. This task has to be executed numerically due to its non-linear behavior. Furthermore, the $d(\cdot)$ has to be changed to $\Delta(\cdot)$ for the discrete numerical calculation. Starting with initial values for a and a', the thrust and moment can be calculated according to equations (2.26) and (2.27). In the next step the equations for thrust and torque (2.24) and (2.25) are adopted to generate the interference coefficients. The new influence coefficients can be used to improve the prediction of the thrust and torque in equation (2.26) and (2.27) again. The described procedure has to be repeated until convergence of the influence factors is obtained. Consequently, the thrust and torque of the whole propeller are determined by summing over all sections of the propeller disc to

$$T = \sum \Delta T, \tag{2.28}$$

$$Q = \sum\,\Delta Q. \tag{2.29}$$

This procedure is often used and the results show acceptable accuracy for moderately loaded propellers in the pre-design stage. Nevertheless, it can be applied for axisymmetric inflow conditions only. Furthermore, the mutual interference between the sections is omitted. For information about non-axial inflow conditions, Appendix A.3 is referred.

A possible division of the propeller plane into several radial sections by a cosine law depending on the radial coordinate is shown exemplarily in Figure 4. For each of these sections, the above presented equation for thrust and torque is evaluated.

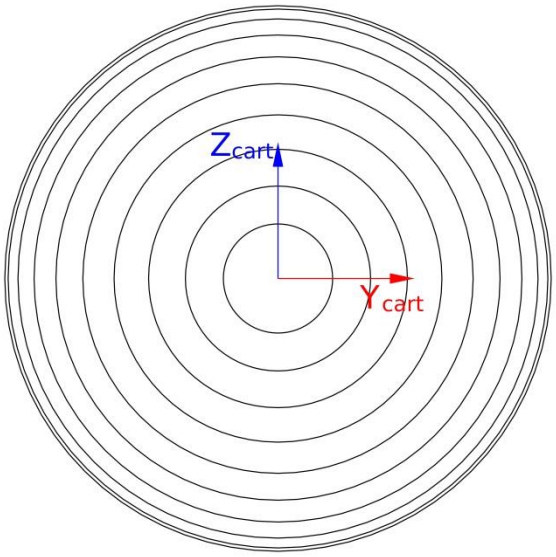

Figure 4: Exemplary radial distribution of the sections for the momentum theory according to a cosine law.

2.5 Generalized Actuator Disk Model

In this chapter, the generalized actuator disk model is described. This application of the method has been presented by several authors in different fields of fluid mechanics as reviewed in the introduction. The principle is to model the action of the whole propeller or one propeller blade and couple it to the flow field that is governed by the Euler or Navier-Stokes equations. This could be realized by different complexities of the propeller model. The simplest propeller model is the actuator disc model, which is well-suited for steady flows. The actuator line approach allows the simulation of unsteady effects also, but the numerical effort is much higher. The most complex approach within this theory is represented by the actuator surface approach. The theory for the approach is provided in the following subchapters. Nevertheless, the numerical treatment for the coupling of all the models is similar. Hence, the basic idea is described at first.

In principle, within the generalized actuator disc method, the action of the propeller is added to the momentum equation. To be exact, if the energy equation is solved also, the action has to be taken into account as well. The momentum equation in its integral form is given as follows

$$\int_V \frac{\partial \rho \boldsymbol{u}}{\partial t}\, dV + \int_A \rho \boldsymbol{u}(\boldsymbol{u} \cdot \boldsymbol{n})\, dA = -\int_A p\boldsymbol{n}\, dA + \int_A \boldsymbol{\tau} \cdot \boldsymbol{n}\, dA + \boldsymbol{F}. \tag{2.30}$$

The last term $\boldsymbol{F}$ on the right hand side in this equation is used for modeling the action of the propeller. As mentioned above, several methods are possible to describe this term.

There are, in general, three different possibilities to couple the action of the propeller within the Eu/NS-equations as summarized by e.g. LeChiton [87]. The force $\boldsymbol{F}$ can be introduced as a boundary condition, as a pressure force, or as a momentum source. The applied method within this thesis is based on the momentum source approach; consequently this one is described in detail. The other two approaches are briefly discussed for clarifying the important differences.

Boundary Condition:

For this approach, the actuator disc geometry has to be taken into account during the mesh generation. Figure 5 (left) shows the blue highlighted actuator disc geometry for a simple two-dimensional mesh. As one can see, the disc has to be cut out of the fluid domain. As detailed in, e.g. LeChituon [87], the boundary conditions at both sides have to be adopted in order to fulfill the required local thrust of the propeller.

Pressure force:

In Figure 5 (middle), the principle of this method is depicted. Therefore, the disc geometry has to be taken into account in general as well during the mesh generation. In this two-dimensional case, the disc is meshed as a line as highlighted in blue in Figure 5 (middle). The local thrust of the propeller results by adding an appropriate pressure jump between the adjacent cells. Another method to avoid the effort of meshing is to cut the cells during the solution and prescribe the pressure forces at the cut faces or lines depending on the dimensions of the case.

Source Term:

For the method with source terms, there are basically no requirements concerning the mesh generation. Figure 5 (right) shows the basic idea. Although the shape of the disc can be included in the mesh generation and consequently, only cells inside a certain physical mesh region are considered to be part of the disc, the description can also be made by functions to check if cells are part of the disc. The action of the propeller is inserted into the fluid domain as a volume specific source term. This leads to the following equation for the source term in the momentum equation

$$\boldsymbol{F} = \int_{V_P \cap V} \boldsymbol{S}\, dV. \tag{2.31}$$

$\boldsymbol{F}$ is the force generated by the propeller at a certain position in the domain. $\boldsymbol{S}$ is the source term, which represents the force per an infinitesimal volume. The integration is performed over the volume of the propeller V_P.
Strictly speaking, the integration has to be performed over the intersection $V_P \cap V$, according to Sanderse [27] applied to volumes. However, the domains are constructed within this thesis in that way that $V_P \subseteq V$. That allows for the simplification made in the following in accordance with $V_P \cap V = V_P \Leftrightarrow V_P \subseteq V$. Furthermore, $\boldsymbol{S}(\boldsymbol{x}) = 0 \; \forall \; \boldsymbol{x} \notin V_P$ is taken for a simpler formulation.

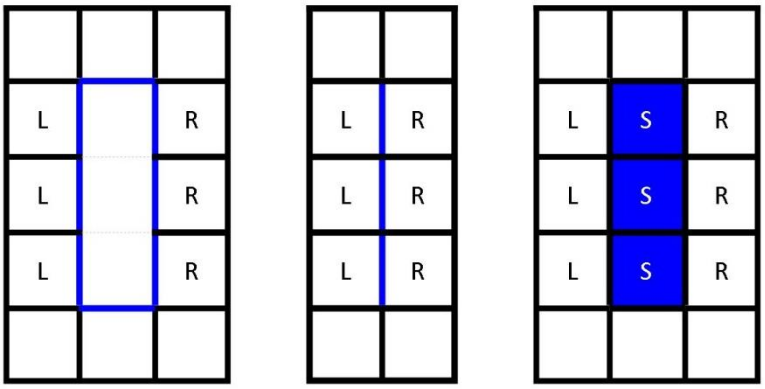

Figure 5: Different boundary conditions to realize the action of the propeller on the fluid. The principles of boundary condition (left), pressure force (middle), and source term (right) are shown. The blue highlighted regions describe the location of the impact of the propeller action into the fluid domain.

Applying the divergence theorem for momentum equation, incorporate incompressibility as well as constant material properties, the differential form of the momentum equation in vector and index notation for the implementation of source terms reads

$$\frac{\partial \boldsymbol{u}}{\partial t} + (\boldsymbol{u} \cdot \nabla)\boldsymbol{u} = -\frac{1}{\rho}\nabla p + \nu \Delta \boldsymbol{u} + \frac{1}{\rho}\boldsymbol{S}, \tag{2.32}$$

$$\frac{\partial u_i}{\partial t} + u_j \frac{\partial u_i}{\partial x_j} = -\frac{1}{\rho}\frac{\partial p}{\partial x_i} + \nu \frac{\partial^2 u_i}{\partial {x_j}^2} + \frac{1}{\rho} S_i. \tag{2.33}$$

2.5.1 Actuator Disc Model

The actuator disk model as a subpart of the generalized actuator disc model means that the whole propeller action is simplified as a disk with a defined local force distribution. Therefore, different methods for establishing the force distribution are possible. Basically, it has to be distinguished between a prescribed and a coupled formulation for the determination of the local force distribution. For the latter, the inflow conditions for the propeller model are dynamically extracted during the simulation from the flow field and serve as input for a propeller solver.

The prescribed formulation is the simplest formulation. Therefore, the load distribution of the propeller disc obtained by an analytical, a numerical, or an experimental approach is fed into the flow field simulation. Consequently, computational effort is low, since the flow field solution does not affect the disc load.

The coupled methods represent an enhancement of the prescribed formulation, but are more computational time-consuming. The term coupled means in this context that the fluid flow solution is directly coupled with the propeller flow solution. Consequently, due the non-linear behavior of the underlying equations, an iterative procedure has to be used to obtain an appropriate solution. The principle of the method is quite simple. The inflow conditions required by the propeller model are extracted from the NS/Eu-solution upstream of the disc. The calculated forces by the propeller model are subsequently fed back into the flow solution by one of the above described methods, e.g. source terms.

For the coupled approach, different complexities in the modeling can be performed. The easiest way is to prescribe, for example, a uniform loaded disc that is represented by a constant thrust coefficient $T_C = const.$ for the whole propeller disc area. A further enhancement is obtained by varying the thrust coefficient $T_C = f(r, \varphi)$ across the propeller disc. Obviously, for unsteady simulations, the thrust coefficient can additionally depend on the time $T_C = f(r, \varphi, t)$. In all cases the thrust of an element of the propeller is obtained as

$$dT = \frac{1}{2}\rho V_{ref}^2 T_C \, dA. \tag{2.34}$$

The reference velocity V_{ref} is extracted from the flow field of the NS/Eu-domain at a certain position upstream of the disc as mentioned above. Logically, the reference velocity can be determined at one defined position for the whole propeller as well as locally for each radial and azimuthal position. By sampling the velocity at each iteration step in an unsteady simulation, time dependency is inherently included. If time dependency has to be suppressed, a temporal filtering (or temporal averaging as filter method) has to be employed additionally. Analog to the thrust coefficient, the circumferential force can be established.

As a further enhancement of the model, the coefficients can be calculated by the blade element theory for each location on the propeller disc. In this case, the local contribution to the total thrust dT and circumferential force dF_φ depend on $(dT, dF_\varphi) = f(r, \varphi, t, c_L, c_D, \boldsymbol{u_P}, c, \rho, B, \omega)$. The lift and drag coefficient, c_L and c_D, are depending on the nondimensional flow parameters $(c_L, c_D) = f(\alpha, Ma, Re)$. Consequently, this method has an increased numerical effort due to the higher amount of dependencies. Reconsidering the basic methods shown in the preceding subchapter, simplifications can be made by dropping certain dependencies, e.g. steady flow $\left(dT, dF_\varphi\right) \neq f(t)$;

rotational symmetry $\left(dT, dF_{\varphi}\right) \neq f(\varphi)$. The solution process is similar as for the uniformly loaded disc. Firstly, the inflow conditions are extracted from the NS/Eu-simulation at a reference position. Secondly, the BEM solver is executed with this data to provide the local thrust and circumferential force. In the last step, the forces are distributed appropriately on the surface of the disc.

2.5.2 Actuator Line Model

In contrast to the actuator disc model presented in the previous chapter, within the actuator line approach, the force is distributed along a defined line. The principle idea is that the line is rotating comparable to the propeller blade. For each single time step, the inflow conditions are determined dynamically out of the NS/Eu-domain on a reference position upstream of the actual position of the line. The local thrust and circumferential force is established by the same methods as declared for the actuator disc method in the preceding subchapter. Mostly, this method is coupled with a BEM solver for the estimation of the local loads. Finally, the results are fed back into the flow domain with the common methods. Preferable are methods, which do not require an adaption of the mesh to the line, e.g. a source term method. Nevertheless, different methods exist that apply, for example, an overset method in combination with an adapted mesh as well. A big advantage of the actuator line method is its possibility to capture the blade tip vortices, instead of producing a vortex sheet as it is obtained by the AD approach. Consequently, the unsteady predictive capabilities of this approach are highly improved. Subsequently, the inflow quantities contain the effect of the blade tip vortex as well, which can be used for the implicit modeling. Nonetheless, time-step restrictions lead to a higher computational effort.

2.5.3 Actuator Surface Model

The actuator surface approach prescribes the forces on a defined surface. This approach represents the extension of the actuator line approach by one dimension. The shape of the surface can be planar as well as curved. In principle, the enhancement of this method is the distribution of the forces along the chord. Therefore, instead of the overall airfoil quantities of a section like c_L and c_D, additional information of the local quantities along the chordwise direction c_p and c_f are required. Obviously, this allows for a more detailed description of the flow. However, models for these distributions have to be applied. While it is possible within the AL approach to use experimental data for the sectional lift and drag, analytical or numerical results have to be used for this approach, since it would require a high effort to determine experimental pressure and skin friction distributions for various inflow conditions. That is why one option for the prescription of the propeller action is the application of certain approximate functions based on potential theory. Therefore, a reference line for determining the inflow conditions is used, like for the lower order approaches, to calculate the pressure and skin friction distribution on the surface. As mentioned above, the forces are distributed according to these results along the chordwise direction. However, methods have been developed that are directly incorporated in the NS/Eu-domain. This means that the pressure and velocity discontinuities across the surface are obtained locally by inserting e.g. a vortex sheet in the domain like in potential methods. The strength of the sheet is determined in that manner that e.g. the kinematic condition is fulfilled.

2.6 Panel Method Coupled with Boundary Layer Integration Method (PanBL)

As stated in the previous sections, the airfoil data have to be determined. These data can be obtained experimentally, analytically as well as by low to high fidelity numerical methods. A low fidelity model is for example the panel method, whereas a high fidelity method is for example CFD. In order to keep the numerical effort at a low level while allowing the actual Reynolds number and Mach number to be considered and adapted during the iteration process of the simulation, the panel method combined with a method for solving the boundary layer represents a good trade off. That is why for the calculation of the airfoil data a panel method coupled with a boundary layer integration method is applied. The latter is used to estimate the frictional drag of the airfoil. Within this chapter, the description of the method is summarized briefly. A more detailed explanation of the method is presented in the Appendix A.2 which is based on the work of Wauquiez [108]. Figure 6 shows the flow chart of the procedure of PanBL.

The linear-strength vortex panel method according to Katz and Plotkin [109] was applied for solving the potential flow around the airfoil. At first, the airfoil data and the inflow conditions are read in as an ordered point cloud. In the next step, the panels are created out of this cloud, whereas each cloud point equals an end panel point. The control points are set in the middle of a panel. Thereafter, a local coordinate system for each panel is generated and the geometrical data of each panel are calculated. Following, the influence coefficients of each panel are calculated and put into the matrix for the influence coefficients. The right hand side is obtained with the knowledge of the inflow conditions. Subsequently, the system can be solved for the vorticity distribution. Consequently, the tangential velocity distribution is determined by using the back substitution. The pressure distribution results by the application of a simplified Bernoulli equation and can be integrated to obtain the lift of the airfoil.

The first step of the boundary layer integration method is a repaneling with an increased number of panels compared to the panel method. The tangential velocities therefore have to be interpolated on the new panels. The stagnation point has to be determined to divide the airfoil in an upper and lower part for the boundary layer integration method. The two boundary layers are solved sequentially in the following. This allows an approximation of the overall frictional drag of the airfoil. In addition, the lift is corrected, if a stall model is used.

Within this investigation, the boundary layer integration method is coupled one way with the panel method. That means that the boundary layer displacement thickness is not fed back into the calculation of the panel method iteratively. In particular, for low Reynolds numbers with large displacement thicknesses, the results can be affected by this omission.

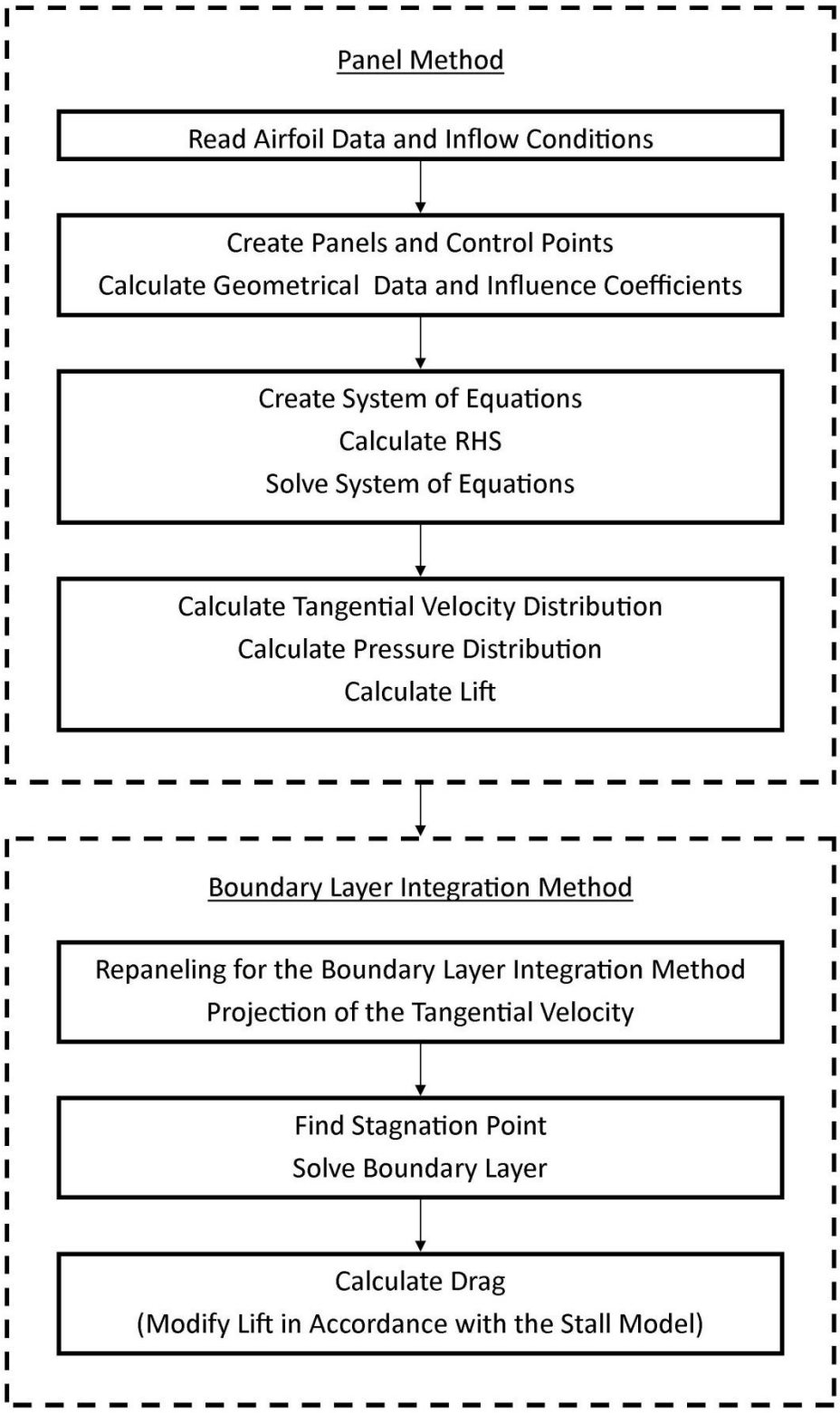

Figure 6: Flow chart for the panel method coupled with the boundary layer integration method.

2.7 Generalized Actuator Disc Approach Coupling with PanBL

Within this subchapter the actually implemented method within this thesis is described. At first, the strategy of the solution process is presented. Secondly, the specified methods and required parameters for each solution step are given. Lastly, the modification for the actuator line approach is presented.

Certain contents of this chapter have been already published by Stuhlpfarrer et al. [3].

2.7.1 Solution Strategy

Within this chapter the applied strategy for the solution is described. It is presented for the actuator disc approach in detail. The differences needed for the actuator line approach are explained briefly, since the general procedure is similar.

The implemented method couples the finite volume method (FVM) for solving the Navier-Stokes equation in three dimensions (3D) with the blade element theory. The applied solver for the NS equation is ANSYS Fluent. The advantage of Fluent is that it allows the compilation and hooking of C-code files in order to provide a complete framework for the propeller simulation within one executable. For this purpose, the functions of the standalone PanBL are compiled within Fluent. The resulting library provides the whole blade element theory capabilities within Fluent.

In the following, an overview of the applied procedure for solving the coupled simulation is given. Since Fluent provides different interface macros at certain run times during the solution process, the appropriate macro has to be chosen for the solution steps. Figure 7 shows the flow chart of the solution procedure in Fluent. The blue highlighted terms refer to the interface for the coupling with PanBL. The steps, mainly associated to one of the two parts of the simulation, are framed and labeled.

At first, Fluent is opened and the case file is loaded. The libraries of PanBL are rebuilt if necessary. In the next step, after the initialization of the flow field for the NS solution, the “User-Defined Init” is performed by the DEFINE_INIT() macro of Fluent. This is used to call additional functions of the PanBL library which allocate storage and read the geometrical data of the specified airfoil sections and its radial positions. After the data have successfully been read, the simulation run is started. At the beginning of each of the iterations, the “User-Defined Adjust” is performed by the DEFINE_ADJUST macro of Fluent. This calls the functions of the PanBL libraries for determining the local aerodynamic coefficients for each section and the resulting local thrust and torque of the propeller. These quantities are used by the DEFINE_SOURCE macros of Fluent to prescribe the strength of the momentum sources for the NS domain. It is called during the “Solve Momentum” sequence. The simulation is stopped if a defined convergence criterion for the flow field quantities and/or the thrust and torque of the propeller is met.

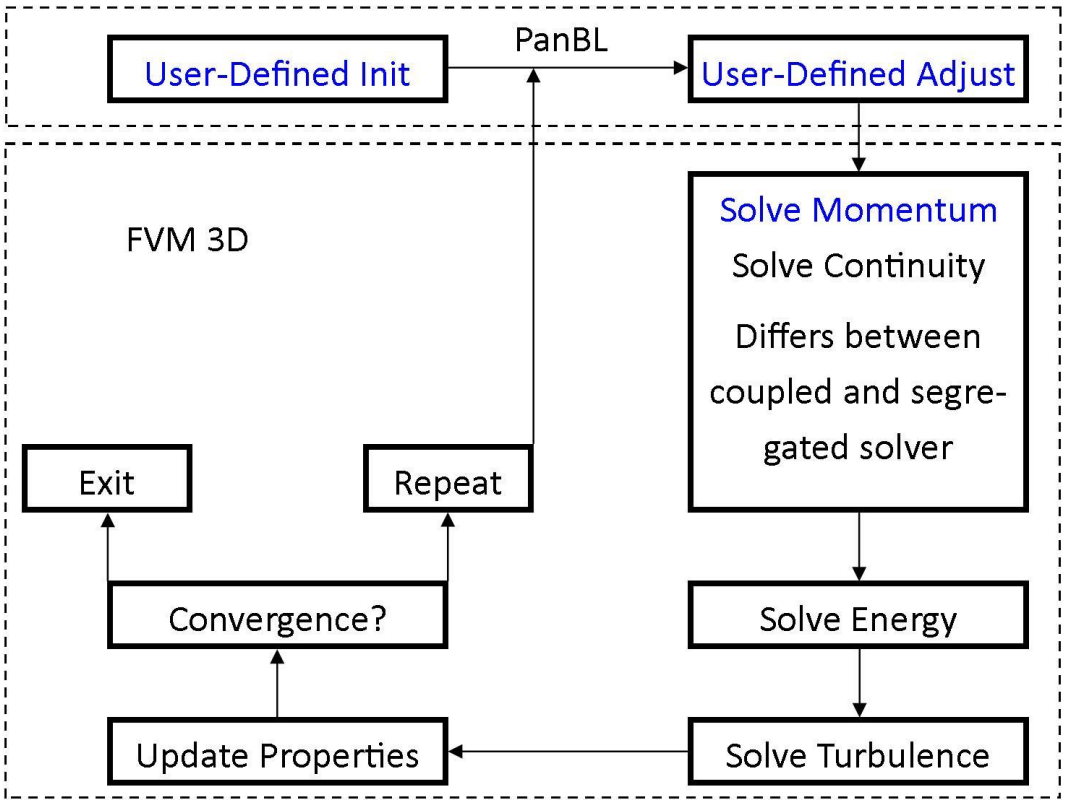

Figure 7: Fluent flow chart for the generalized actuator disc approach with PanBL.

2.7.2 Inflow Conditions for the Actuator disc

Several methods to determine the inflow conditions for the blade element theory have been published since the generalized actuator disc approach has been introduced. The different approaches are logically depending on the type of the generalized actuator disc model.

At first, the developed method for determining the inflow conditions for the actuator disc approach is presented. As detailed in the literature review above, the inflow conditions can be obtained by different methodologies. Apparently, two groups may be distinguished:

- Determination of field values on control points for the actuator disc
- Averaging of values within a certain region of the actuator disc

The first group is in accordance to the method presented by e.g. Rajagopalan and Fanucci [30]. For the determination itself, two different ways are possible and shown in Figure 8. Firstly, if control points for the actuator disc are located at the same position as the mesh points of the computational grid, the values at the points can be employed directly. Secondly, if the mesh points and the control points are located at different physical positions some kind of interpolation has to be used. This can be done in the easiest way by a nearest neighbor search or for a better approximation a linear or a higher order interpolation. An alternative treatment for the determination of the control point values is the usage of an overset method. This method inherently provides the interpolation from the rotor grid to the background grid like it was shown by e.g. Chafin and Berry [82]. The drawback is that an additional grid for the rotor with control points lying on the mesh points has to be generated.

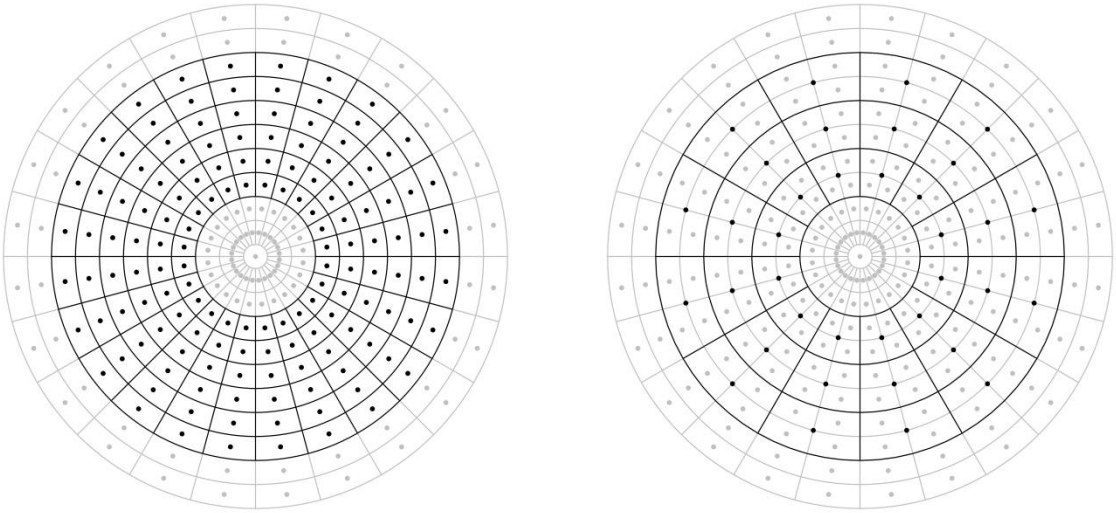

Figure 8: Methods to obtain the inflow conditions for the modeled propeller. Computational grid points and actuator disc grid points are matching (left) and non-matching (right).

The second group is based on the approach of e.g. Fejtek and Roberts [81]. Therefore, two different grids are established, one for the actuator disc and another one for the surrounding flow domain. In this method the actuator disc is divided into several azimuthal and radial divisions. The inflow conditions are obtained by averaging the local inflow quantities over each node point, which is located physically within a certain division.

For the method within this thesis, an approach based on the second group is chosen. Nevertheless, crucial modifications have been made therefore.

In the basic method, a three-dimensional background grid was generated with hexahedral elements. The actuator disc grid was a planar, two-dimensional grid and consisted of quad elements. Due to its circular shape, it was described in polar coordinates. The actuator disc grid was set in the x-y-plane of the background grid. This resulted in a two-dimensional averaging process. In order to be more flexible in terms of the positioning and the orientation of the actuator disc in the physical space (in particular for distributed rotor/propeller configurations), a three-dimensional representation of the disc is appropriate. This can be established on the one hand by an interpolation of the node values of the NS-solution on a two-dimensional actuator disc plane, followed by a two-dimensional averaging. On the other hand, a three-dimensional averaging of the node values within a certain actuator disc volume can be performed.

Within this work, a three-dimensional volume averaging over an actuator disc volume is chosen. The reason for choosing this approach is based on several points:

- Enhanced numerical stability for calculating the sectional coefficients with PanBL and the whole simulation, since the averaging over a certain volume already acts as a low pass filter on the inflow conditions. In particular, for the steady state simulation an increase of the convergence rate can be obtained.
- The implementation as well as the application for unstructured grids is easy to establish.
- The parallelization for arbitrary partitioned meshes is easy as well.

Concerning the consistency with respect to the flow physics by calculating the inflow conditions with a volume averaging along the axial direction, some considerations have been made. According to the axial momentum theory [1], the velocity across the propeller disc along the axial direction is continuous. The actual value of the axial velocity in the propeller plane provided by this theory reads $u_P = \frac{1}{2}(U_\infty + u_w)$.

In the following, a short example for the volume averaging is provided. For this example, only the axial velocity distribution is of interest. Therefore, the flow is assumed to be one-dimensional in the axial direction of the propeller.

Considering the axial momentum theory, rotation is excluded. According to Glauert [1], the flow can be assumed to be governed by a circular vortex sheet from $0 \leq x < \infty$. $x = 0$ is the position of the propeller plane.

The induced axial velocity of one vortex ring along the axes of the ring is obtained by

$$u = \frac{\Gamma}{2\pi}\left(\frac{R^2}{(R^2 + {x_{cr}}^2)^{\frac{3}{2}}}\right). \tag{2.35}$$

Therein, Γ represents the circulation, R the radius of the ring, and x_{cr} the distance along the axis, measured from the center of the ring. In order to simplify the results, the radius is set to $R = 1$. Additionally, it has to be mentioned that units are not taken into account for simplicity in this example. The circulation is substituted by an infinitely small vortex element $d\Gamma = \gamma\, dx_r$, whereby the specific vorticity of the sheet is set to $\gamma = \pi$. This leads to the integral

$$u = \frac{1}{2}\int_0^\infty \left(\frac{1}{(1 + (x - x_r)^2)^{\frac{3}{2}}}\right) dx_r. \tag{2.36}$$

This can be integrated and provides the result for the velocity along the axis as follows

$$u = \frac{1}{2}\left(\frac{x}{\sqrt{x^2 + 1}} + 1\right). \tag{2.37}$$

According to this result, the velocity upstream and downstream of the propeller plane is point-symmetric to the point $x = 0$ located at the axis of the circular vortex sheet. It follows that if the averaging is performed in a symmetric region upstream and downstream of the propeller plane, the value at the propeller plane is obtained. In addition, a freestream velocity U_∞ can be superposed, which leads to the following result

$$U = U_\infty + \frac{1}{2}\left(\frac{x}{\sqrt{x^2 + 1}} + 1\right). \tag{2.38}$$

Both results are in accordance with the relation of the axial momentum theory $u_P = \frac{1}{2}(U_\infty + u_w)$. This result can be easily proofed by evaluating $U_\infty = \lim_{x\to-\infty} U(x)$, $u_P = U(0)$, and $u_w = \lim_{x\to\infty} U(x)$. Nevertheless, it has to be kept in mind that the result differs for the general momentum theory. For a better understanding within this example, the velocity profiles and the local radius of the stream tube are visualized in Figure 9 for different test cases. The local radius is

calculated by the application of the continuity equation and assuming constant density. The static thurst test case is represented by a freestream velocity of $U_\infty = 0$. Therefore, the radius of the stream tube is infinite at an infinite upstream position. The other cases, the propeller case and the wind turbine case are characterized by a freestream velocity of $U_\infty > 0$. The difference is that in the propeller case the fluid is accelerated and in the wind turbine case the fluid is decelerated. Consequently, the axial velocities and the local radii, respectively, show an inverted behavior.

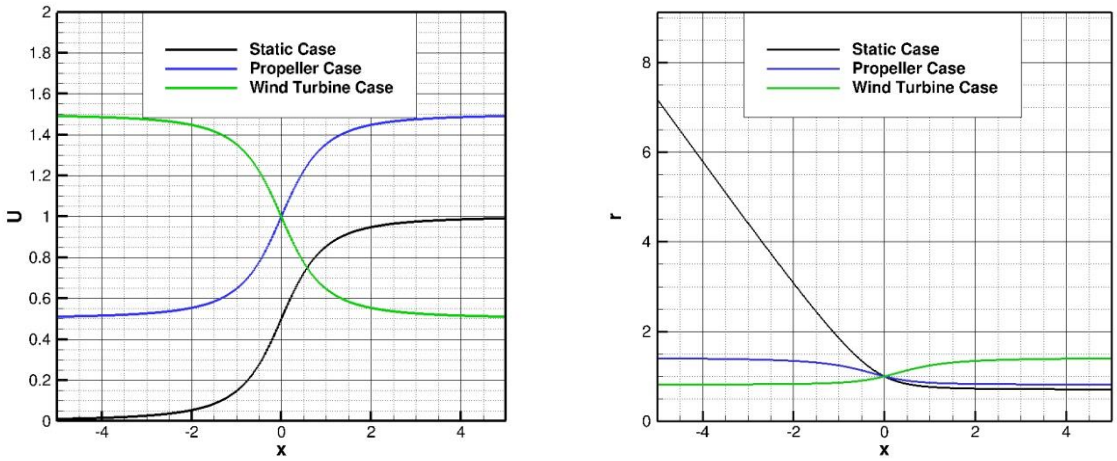

Figure 9: Simplified velocity U and radius r of the boundary streamtube for different operating points.

Furthermore, and in particular, a more important question arises, if u_P is the appropriate velocity, which is needed by PanBL, since the latter requires the undisturbed flow far upstream of the propeller blade. For this purpose, the method provides two additional parameters that can be set. The first is the width of the disc w and the second is the distance of the center of the disc to the center of the propeller d. This allows influencing the resulting inflow conditions in some way. Figure 10 shows a sketch of the important features for a forward flight case with a freestream velocity of $U_\infty > 0$. The velocity profile along the propeller axis (orange line) follows Equation (2.38). The resulting stream tube (black line) is calculated by the application of the continuity equation while assuming constant density. Logically, if the center of the averaging region is not located in the center of the propeller plane the obtained axial velocity is higher or lower depending on the direction. It becomes visible, that an increase in d in upstream direction leads to a smaller inflow velocity obtained by the averaging method and vice versa for a region located downstream. Obviously, if the center of the averaging volume coincides with the propeller plane ($d = 0$), the result of the axial momentum theory is obtained.

Although the vortex sheet within the example has the shape of a circular cylinder, the continuity enforces a flow contraction downstream of the propeller plane. In Figure 10, the averaging volume is drawn enlarged. It has to be mentioned that the example represents a heavily loaded propeller. The latter can be seen due to the massive flow contraction. That is why one difficulty of the averaging process for heavily loaded propellers can be detected, in particular, in the blade tip region. It is obvious, that by averaging in the blade tip region, the reconstructed inflow condition can differ. The averaging is done in axial direction, while the streamlines are inclined towards the axial direction. To overcome this problem, the averaging region has to be fitted locally along the direction of the

incoming streamlines. In addition, a local adaption of the averaging region can be applied as well for non-axial inflow conditions, which will be discussed in the following.

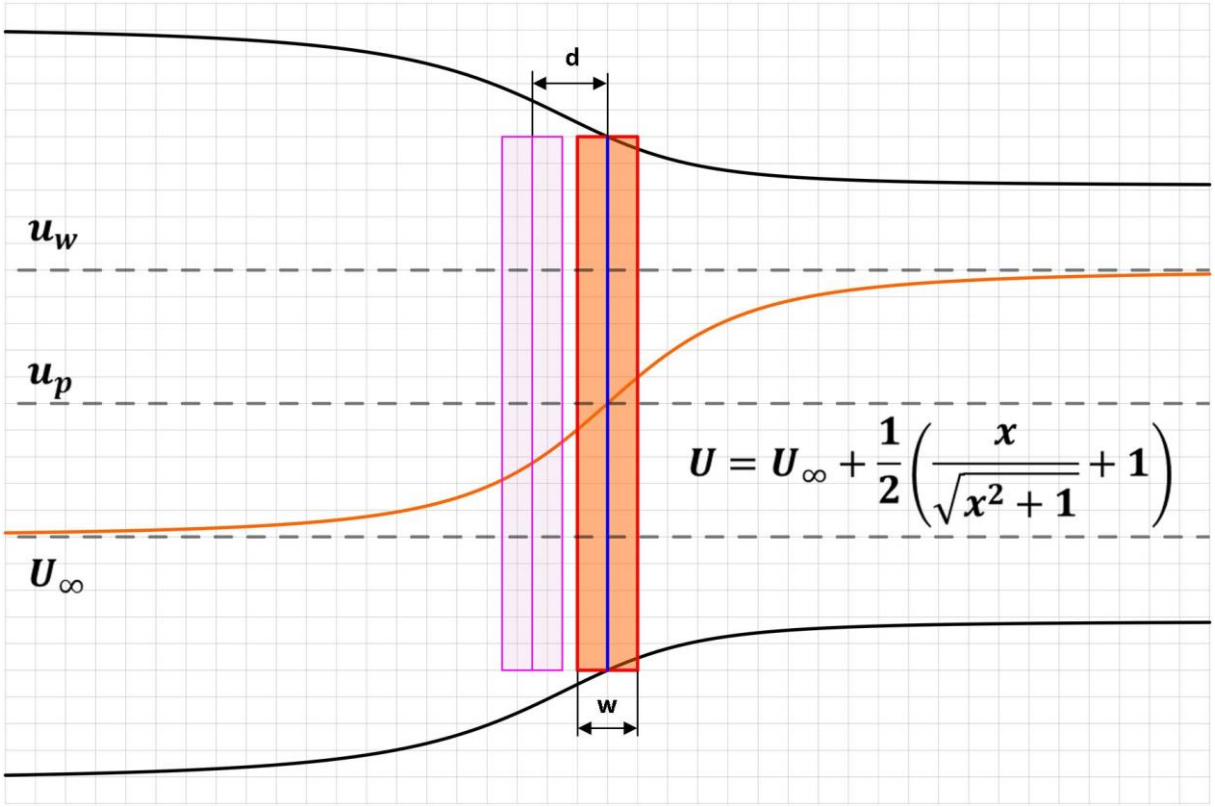

Figure 10: Determination of the inflow conditions for the actuator disc.

Since the basic ideas are presented, in the following the procedure for determining the inflow conditions is declared. Therefore, a step-by-step description is given.

Realization of the Determination of the Inflow Conditions

In order to connect the NS/Eu-Solver with PanBL, the interfaces have to be set appropriately. The implemented actuator disc approach has to be as general as possible. That is why Fluent is running in the three-dimensional version. That means that the three-dimensional Cartesian coordinates are used. Nevertheless, it is suitable to formulate the propeller action in a cylindrical coordinate system. Moreover, the local forces generated by a certain blade section have to be solved in an additional blade-fixed coordination system. This requires two coordinate transformations to obtain the forces of the blade section.

In the following, the procedure is presented on a two-dimensional example. Figure 11 presents a quad mesh drawn by the grey lines. The cell centers are marked by grey points. The black lines show the imaginary propeller mesh. In this case, a segmentation in azimuthal as well as in radial direction is performed, which is necessary to capture non-axial inflow conditions appropriately. At first, the coordinates of the cell centers are transformed into the cylindrical coordinate system as follows

$$\begin{pmatrix} x \\ r \\ \varphi \end{pmatrix}_{cyl} = \begin{pmatrix} x \\ \sqrt{y^2 + z^2} \\ \arctan\left(\frac{z}{y}\right) \end{pmatrix}_{cart} . \tag{2.39}$$

In the following, it is checked, if the cell is a part of a segment of the propeller mesh. Within this approach, the cell is assigned to a segment, if the cell center is located within it. Figure 11 shows that exemplarily for one segment with blue highlighted cells, if the cell is inside the segment. The velocities of all cells located in a segment are transformed as well into the cylindrical coordinate system according to

$$\underbrace{\begin{pmatrix} u \\ v \\ w \end{pmatrix}_{cyl}}_{\boldsymbol{u_{cyl}}} = \underbrace{\begin{pmatrix} 1 & 0 & 0 \\ 0 & \cos(\varphi) & \sin(\varphi) \\ 0 & -\sin(\varphi) & \cos(\varphi) \end{pmatrix}}_{\boldsymbol{M_{cart,cyl}}} \underbrace{\begin{pmatrix} u \\ v \\ w \end{pmatrix}_{cart}}_{\boldsymbol{u_{cart}}} . \tag{2.40}$$

The representing velocity of one section is obtained by the averaging described above. The equation therefore reads

$$u_i = \frac{\sum_{N_{cis}} u_{i,c} V_{i,c}}{\sum_{N_{cis}} V_{i,c}}. \tag{2.41}$$

Therein, the index N_{cis} represents the number of cells in a segment, i a segment, and c a cell in a segment. Consequently, $V_{i,c}$ is the volume of a cell c in a segment i. Obviously, for an equally spaced grid the volume averaging results in an arithmetic mean value. It could be considered also as some kind of mass averaging for incompressible flow or in particular, flow with constant density.

The evaluation of the equation is easily done by using a serial solver. Additional considerations have to be made if the equation is solved in parallel on several compute node processes and consequently, mesh partitioning has to be performed. In this case, the numerator and the denominator have to be evaluated at first for each partition of the mesh by the associated node process. If every process has finished its independent summation, the sum over all processes is made to get the correct sum for the numerator and the denominator of each disc segment. Subsequently, the correct averaged velocity can be determined for each disc segment.

In the following, the averaged velocities have to be transferred into the blade-fixed coordinate system. The sole difference between the two coordinate systems within this application is the rotational speed of the blade fixed coordinate system around the x-axis that superposes a circumferential velocity. In addition, the sign has to be changed, since the velocity of the blade leads to a fluid flow in the opposite direction. Moreover, the vector is multiplied by a combined permutation and reflection matrix to assign the coordinate directions as required by PanBL. Therefore, the transformation reads

$$\underbrace{\begin{pmatrix} u \\ v \\ w \end{pmatrix}_{bf}}_{\boldsymbol{u_{bf}}} = \underbrace{\begin{pmatrix} 0 & 0 & -\mathrm{sgn}(\Omega) \\ -1 & 0 & 0 \\ 0 & 1 & 0 \end{pmatrix}}_{\boldsymbol{M_{PR}}} \cdot \left(-\begin{pmatrix} \Omega \\ 0 \\ 0 \end{pmatrix} \times \begin{pmatrix} 0 \\ r \\ 0 \end{pmatrix} + \underbrace{\begin{pmatrix} u \\ v \\ w \end{pmatrix}_{cyl}}_{\boldsymbol{u_{cyl}}} \right). \tag{2.42}$$

The x_{bf}- and the y_{bf}-coordintate of the blade-fixed coordinate system are then used to estimate the local thrust and torque of a blade section. The reflection has to be made, because the x_{bf}-diection of the blade fixed coordinate system has to point from the leading edge to the trailing edge of the airfoil.

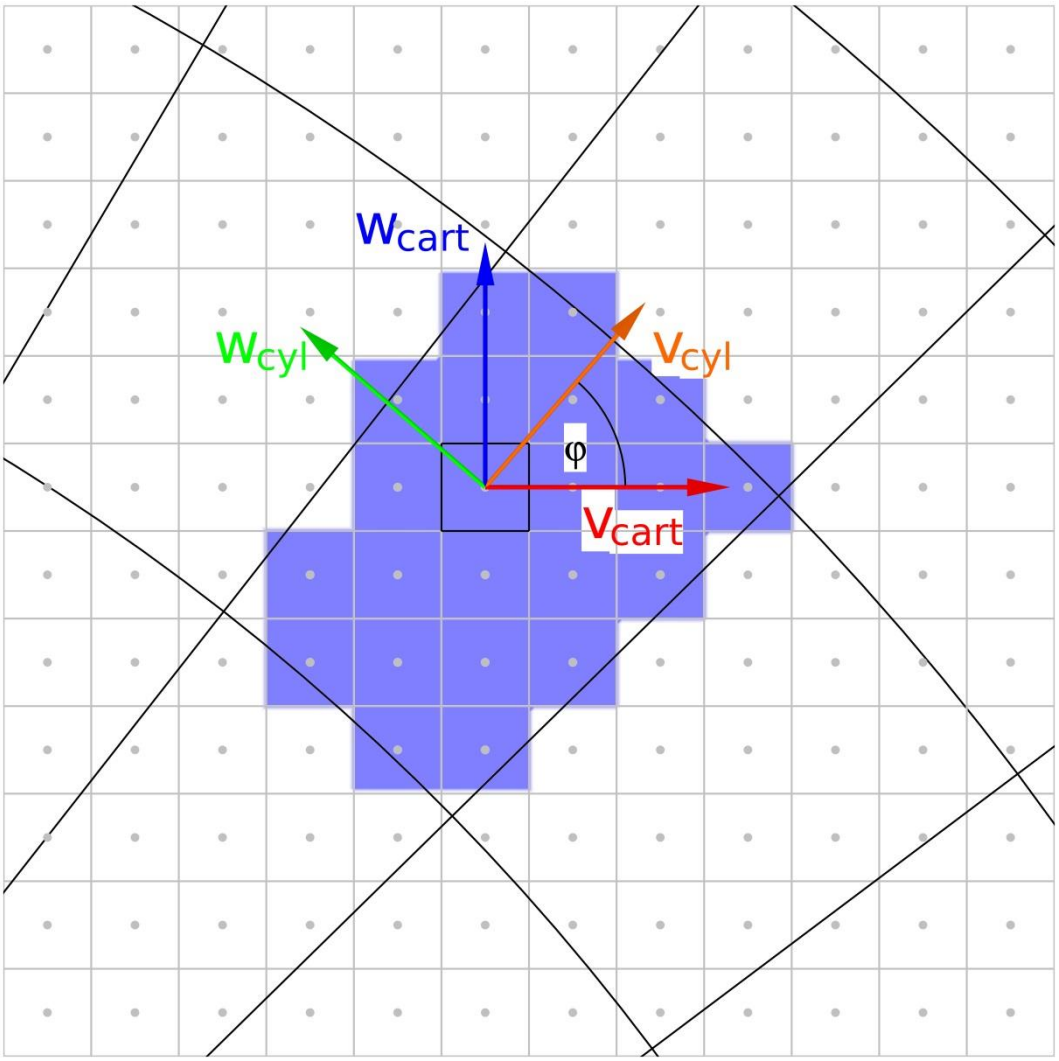

Figure 11: Determination of inflow velocities of an actuator disc segment. The blue highlighted cells are set to be within the associated propeller segment. The finite volume grid with its center points is drawn (grey lines and points) and the propeller segments are represented by the black lines. The vectors show the velocity components of a cell in the different coordinate systems. Velocity components: u, v; Coordinate Systems: Cartesian and cylindrical according to (2.40).

2.7.3 Thrust and Circumferential Force of a Blade Section

The obtained inflow conditions are used to calculate the local forces of a certain segment. The inflow conditions are providing the inflow angle as well as the magnitude of the inflow velocity. The values are fed as input parameters into PanBL and the forces are the output. Within this subchapter, PanBL is assumed to be a black box that determines the lift coefficient c_L and the drag coefficient c_D of a certain segment depending on the inflow conditions. In the following, the important equations of the blade element theory necessary for the applied approach are recalled briefly.

At first, the relations for the inflow conditions are applied to obtain the inflow angle ϕ and the inflow velocity V_{rel}. With the knowledge of the local angle of incidence of the considered section, the angle of attack is determined according to

$$\phi = \arctan\left(\frac{v_{bf}}{u_{bf}}\right), \tag{2.43}$$

$$V_{rel} = \sqrt{{u_{bf}}^2 + {v_{bf}}^2}, \tag{2.44}$$

$$\alpha = \theta - \phi. \tag{2.45}$$

The quantities V_{rel} and α are transferred to PanBL and the lift coefficient c_L and the drag coefficient c_D are calculated. Subsequently, the thrust ΔT and circumferential force ΔF_ϕ of the segment are determined by the following equations.

$$\Delta T_{cyl} = \frac{1}{2}\,\rho\, V_{rel}^2 \frac{B\,c}{2\pi r}\, r\,(c_L\cos(\phi) - c_D\sin(\phi))\Delta r\,\Delta\varphi, \tag{2.46}$$

$$\Delta F_{\varphi,cyl} = \frac{1}{2}\,\rho\, V_{rel}^2 \frac{B\,c}{2\pi r}\, r\,(c_L\sin(\phi) + c_D\cos(\phi))\Delta r\,\Delta\varphi. \tag{2.47}$$

It is visible that the quantities are already written in the cylindrical coordinate frame. Initially, the thrust ΔT and circumferential force ΔF_ϕ for a segment are obtained in the blade fixed coordinate system. However, the forces in the blade fixed and the cylindrical coordinate system are matching for the considered azimuthal angle φ within the modelling approach. Consequently, the formula can be written in the previous form.

In contrast to the equations presented in the description of the blade element theory in Section 2.3, the present equations are valid for a segment instead of a section only. That means that an additional partitioning in circumferential direction is added. This is represented by multiplying the equation with $(r\,\Delta\varphi)/(2\pi r)$, with $\Delta\varphi$ describing the angle of a sector. For a better understanding, the formulas are rearranged additionally that the dependence of the forces on the solidity can be seen directly.

The formulas can be further rewritten that the forces are related to the surface of a segment as follows

$$\frac{\Delta T_{cyl}}{\Delta r\,(r\,\Delta\varphi)} = \frac{1}{2}\,\rho\, V_{rel}^2 \frac{B\,c}{2\pi r}\,(c_L\cos(\phi) - c_D\sin(\phi)), \tag{2.48}$$

$$\frac{\Delta F_{\varphi,cyl}}{\Delta r\ (r\ \Delta\varphi)} = \frac{1}{2}\ \rho\ V_{rel}^2\ \frac{B\ c}{2\pi r}\ \ (c_L \sin(\phi) + c_D \cos(\phi)). \tag{2.49}$$

This formulation is necessary for the determination of the sources presented in the following subchapter.

2.7.4 Source Terms for the Actuator Disc

Since the forces for each of the segments are determined, the source terms have to be established. The procedure, to calculate the source terms, has to be inverted compared to the estimation of the inflow conditions in terms of transformations between the different coordinate systems. This can be performed straightforward. Nonetheless, additional considerations have to be made at first for the realization of an appropriate flow flied solution. As stated above, the forces are calculated for each segment. That means that for all of the cells within a certain segment, the same source term could be applied. Figure 12 shows an exemplary distribution for five segments. Therefore, it is assumed that the underlying source distribution is linearly varying in the vertical direction. In Figure 12 (left), for each segment, all cell values of the associated segment are set according to the reference value of this segment. It becomes visible that at the boundaries between the propeller segments discontinuities arise. The approximation of such jumps by a series of smooth functions, e.g. Fourier series, includes all wave numbers. The term wave numbers instead of frequency is chosen, since a fully spatial problem is considered. Consequently, by applying the source terms in this way, spurious oscillations in the numerical solution occur. Therefore, the convergence rate for a steady solution is smaller and the stability of the simulation is worse. In order to circumvent this behavior, linear interpolation between the reference cell values is performed. The resulting solution is shown in Figure 12 (right). In this case, the discontinuities at the boundaries disappear. It can be argued, that the derivative of the piecewise-linear interpolation is still containing discontinuities. That is true, but due to the large size of the segment of the propeller compared to the cell sizes within this application, the error might be small. A further point that may arise concerns the conservation of momentum of this method. Due to the interpolation, the conservation is not exactly fulfilled, but the error decreases with an increasing number of cells. Within this work, zeroth, first and third order interpolation has been implemented. Investigations have shown that the difference between the results of first and third order approximation is small. Hence, only the thirst order approximation is used.

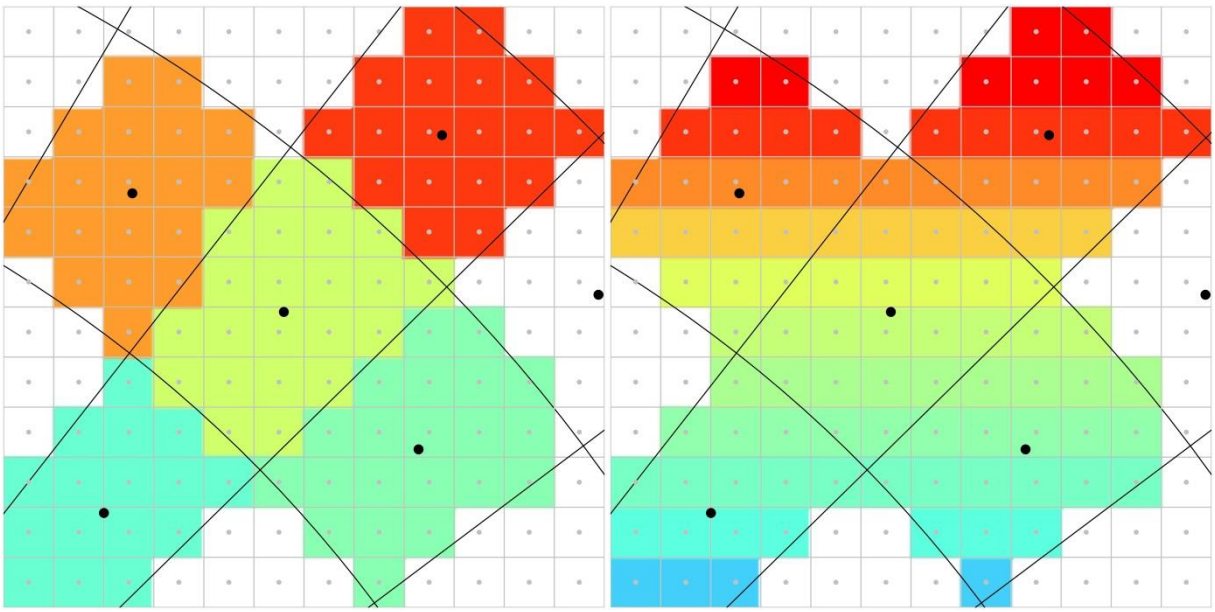

Figure 12: Interpolation of source terms of the actuator disk. Source distribution with constant segment value projected to the computational grid (left) and linear interpolation (right). The propeller grid (black lines and points) and the finite volume grid with associated center points (grey lines and points) are visualized.

The previous example dealt with the interpolation of the source terms in the propeller plane. The next point to be discussed is the treatment of the axial distribution of the source terms. Instead of using a thickness of the source disc of one cell, the actual implementation is based on a volume region similar to the averaging region for the determination of the inflow conditions. This approach is highly flexible in the choice of the propeller disc region and is almost independent of the type and shape of the mesh for the flow solution. The determination if a cell is a part of a volume is executed analogously to the above presented method. Consequently, the same discontinuities appear in the axial direction. In order to prevent the rectangular function in the distribution, a smooth function is applied.

Therefore, a piecewise defined blending function consisting of a normalized raised cosine and a rectangular function is constructed. Detailed information about this function can be found in the Appendix A.1 . This method is used to avoid spurious oscillations in the flow field. In contrast to the widely used Gaussian kernel function as e.g. presented by Sorensen et al. [110], the invented method has been applied, since it is bounded in space.

At first, to be able to reveal the difference between the methods, the basic idea of the Gaussian kernel is described, which reads as follows

$$\eta_\epsilon(|\Delta \boldsymbol{x}|) = \frac{1}{\epsilon^3 \pi^{\frac{3}{2}}} \exp\left[-\left(\frac{|\Delta \boldsymbol{x}|}{\epsilon}\right)^2\right]. \tag{2.50}$$

The function is used to distribute the action of a source at a certain point on several cells and therefore, reduce the amplitude of the spectral velocities at higher wave numbers. The parameter ϵ defines the smoothness of the obtained result in terms of a characteristic length of the kernel. In several publications this parameter has been chosen to vary between one and four characteristic cell lengths l_{cell}. $|\Delta \boldsymbol{x}|$ is the distance from the point of the evaluated propeller action to an arbitrary mesh point. Obviously, the function tends to zero $\lim_{|\Delta \boldsymbol{x}|\to\infty} \eta_\epsilon(|\Delta \boldsymbol{x}|) = 0$ if the distance $|\Delta \boldsymbol{x}|$ is tending against infinity. However, within a finite domain, it will not be zero. Notwithstanding this, it has to be stated that the smearing with this function can be performed for different input spaces of the argument $|\Delta \boldsymbol{x}| \in \mathbb{R}^n$, whereby $n = 1,2,3$ for this application. In its original form, the function is an image according to $\eta_\epsilon: \mathbb{R}^3 \to \mathbb{R}$.

The actual implemented method within this thesis used the piecewise defined function

$$\mathrm{F}_{distr} = \left\{ \begin{array}{c} 0, \qquad |x - SR_c| > SR_2 \\ \frac{1}{SR_w} \cos\left(\frac{\pi}{2} \frac{(|x - SR_c| - SR_1)}{SR_s}\right)^2, |x - SR_c| \geq SR_1 \ \wedge |x - SR_c| \leq SR_2 \\ \frac{1}{SR_w}, \qquad |x - SR_c| < SR_1 \end{array} \right\}, \tag{2.51}$$

$$with\ SR_1 = \frac{SR_w - SR_s}{2}\ and\ SR_2 = \frac{SR_w + SR_s}{2}. \tag{2.52}$$

The mathematical properties of the function can be found in the Appendix A.1 . Nevertheless, the main features are briefly reviewed in the following. Due to its smearing behavior in physical space, spurious oscillations are reduced, and consequently, a smoother result is obtained if certain requirements on the combination of the mesh parameters and the parameters of the distribution

function are fulfilled. Moreover, the function is bounded in finite space in contrast to the Gaussian Kernel function. That allows for a conservative representation of the distribution in a bounded spatial domain.

Within the definition of the distribution function F_{distr}, SR_c is the axial position of the disc center, SR_w is the width of the actuator disc, and SR_s is the width of the smoothed cosine part of the actuator disc boundary. The quantities are visualized in Figure 13. The definition of the parameter SR_s is shown for the green curve exemplarily. All in all, Figure 13 contains nine different parameter variations, which provides the same integrational value of the distribution, as required. Strictly speaking, SR_c is varied as well to get a spatial separation in axial direction of the three discs, which would lead to 12 parameter settings. However, this aspect is not further discussed. Obviously, it can be seen, the smaller the width of the disc, the higher is the amplitude of the peak. For this example, three widths SR_w are applied, whereas the size is bisected from left to right. In addition, for each of these different sizes, three smoothing widths are shown. The ratios of the smoothing width to the disc width are set to $SR_s/SR_w = 1$ for the magenta lines, $SR_s/SR_w = 0.5$ for the green lines, and $SR_s/SR_w = 0.25$ for the blue lines.

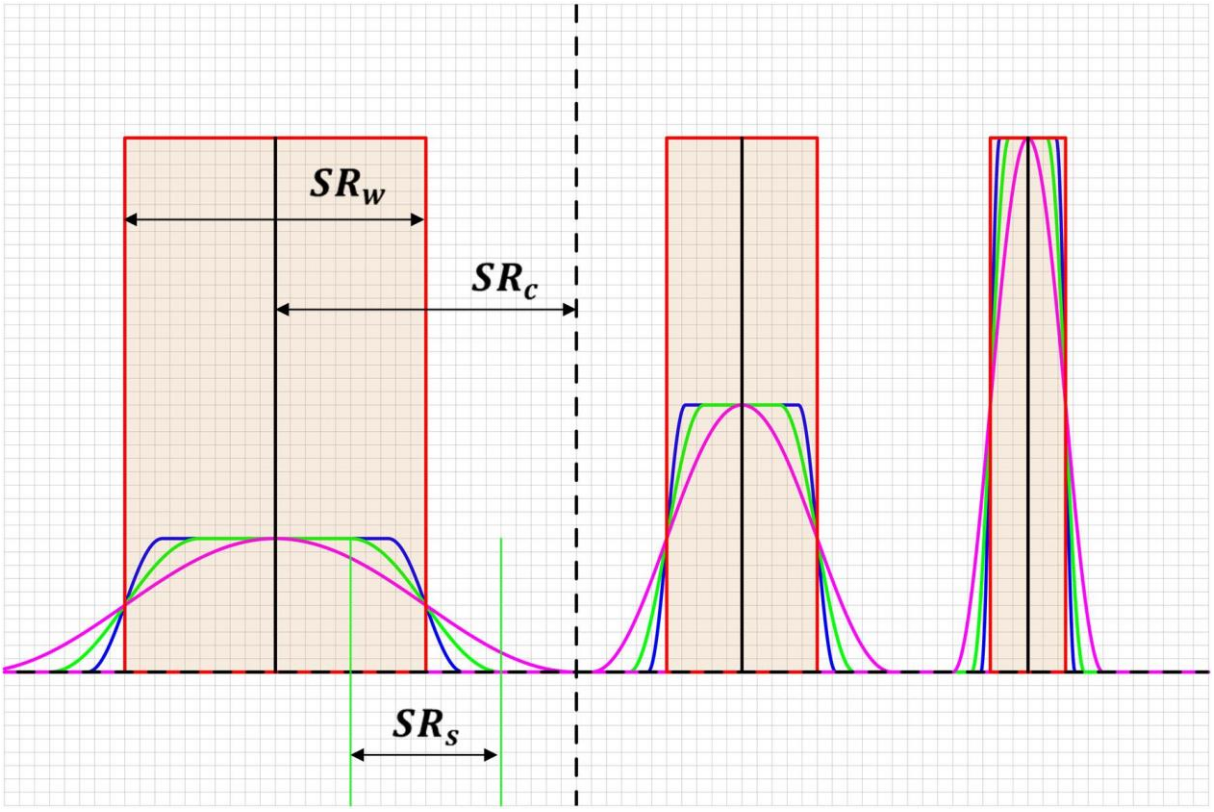

Figure 13: Parameter variation of the distribution function. The axial position of the disc center SR_c, the width of the actuator disc SR_w, and the width of the smoothed cosine part of the actuator disc boundary SR_s is varied. $SR_s/SR_w = 1$ (magenta lines), $SR_s/SR_w = 0.5$ (green lines), and $SR_s/SR_w = 0.25$ (blue lines) are shown for three different widths of the actuator disc SR_w.

It has to be mentioned, that for the simulations $SR_s > 3 \cdot l_{cell}$ should be fulfilled. l_{cell} represents a characteristic cell length. Otherwise, the desired behavior of the distribution is not fully obtained. The smaller the region of the smoothing is chosen, the sharper is the resulting jump in the distribution. Consequently, for $SR_s < l_{cell}$, a rectangular distribution is provided by the function due

to the low-pass filtering property of the underlying finite volume method. In particular, the behavior can be detected on the right hand side in Figure 13 for small disc and smoothing widths (blue curve).

In the next step, the source terms in the Cartesian coordinate system can be determined. Therefore, the specific forces in the cylindrical coordinate system are transferred into the Cartesian coordinate system with the inverse matrix of the one used for the source evaluation. Moreover, the distribution function F_{distr} is scalar multiplied with the transformed quantities to obtain the required smooth solution. Finally, the source terms read

$$\begin{pmatrix} S_x \\ S_y \\ S_z \end{pmatrix}_{cart} = \underbrace{\begin{pmatrix} 1 & 0 & 0 \\ 0 & \cos(\varphi) & -\sin(\varphi) \\ 0 & \sin(\varphi) & \cos(\varphi) \end{pmatrix}}_{\boldsymbol{M_{cyl,cart}}} \begin{pmatrix} \dfrac{\Delta T_{cyl}}{\Delta r\,(r\,\Delta\varphi)} \\ 0 \\ \dfrac{\Delta F_{\varphi,cyl}}{\Delta r\,(r\,\Delta\varphi)} \end{pmatrix}_{cyl} F_{distr}(x, SR_c, SR_w, SR_s). \tag{2.53}$$

These are the principle functions for distributing the forces in the three directions in space within the AD model. For the AL model applied in this work, the axial distribution is kept as for the AD method.

The variation along the chordwise direction is modified. That is evident, as presented in the description of the methods. The AL is a part of an unsteady simulation including a rotating line in contrast to the AD in the course of propeller simulations. Therefore, at each time step the position and strength of the source is varying. In the following, the properties of the AL will be discussed.

It should be stated that the AD can be also applied for unsteady flows. This is of interest, e.g. if the thrust of the propeller is of major importance while the interaction of the tip vortices with an airframe is inferior.

2.7.5 Inflow Conditions for the Actuator Line

Within this subchapter, mainly the differences to the actuator disc approach are described. The determination of the inflow conditions is based on the implemented approach used for the actuator disc. At first, the basic ideas in contrast to the common approaches are presented. In the following, certain special considerations for the parameters are made. Finally, details for the implementation within an unsteady simulation are presented.

As presented in the description of the actuator line method in Chapter 2.5.2, the actuator line is an imaginary line that moves like a propeller through the domain. At this line, a certain number of sample points are located. At each of these points, the local inflow velocities are determined by an interpolation, e.g. tri-linear. This allows for a reconstruction of the inflow conditions. The detailed description therefore is provided, while explaining the presented method.

In contrast to the actuator line approach, the actuator surface approach presented in chapter 2.5.3 requires a line that is located at a defined position upstream of the imaginary propeller surface. This line includes a certain number of sample points as well. But for this case, additional corrections have to be made for an appropriate reconstruction of the inflow conditions. The corrections are required, since the actuator surface induces velocities at the sample points, which distorts the reconstruction of the inflow. This topic is addressed in e.g. Shen et al. [45].

Within this approach, the determination of the inflow conditions is based on a volume averaging around the actuator line. The distribution of forces is made as well on a volume region instead of a line. That means that properties of an actuator disc and an actuator surface have to be considered for the modeling. The applied procedure is quite similar as it is used for the actuator disk simulation. Consequently, certain advantages of the approach are inherited, as for example, the spatial filtering of the quantities. However, in order to highlight the appropriate effects of this method, some basic considerations are necessary, after the principle of the method is presented briefly.

In general, the blade is segmented in a certain number of sections as already presented in the description of the theory in Chapter 2.5.2. Figure 14 illustrates an elliptical wing consisting of NACA 0012 airfoils. The segmentation is visualized by the semi-transparent cut planes. The intersection of the latter with the wing geometry is depicted by the dashed lines. The solid lines represent the actual airfoil sections used for the calculation of the two-dimensional airfoil properties. Within this approach, the velocities are volume-averaged within each section. In contrast to the actuator disc approach, the averaging is bounded in streamwise direction also. As shown above, for the actuator disc approach a circumferential averaging within an annulus is made. In Figure 14, the averaging regions are rectangular boxes. The reason for the choice of the size and shape of the region will be detailed below. Exemplarily, the absolute inflow vectors as well as its components for the sections are depicted in Figure 14. Therefore, constant velocities normal to the chord lines and linearly varying velocities along the radial direction are considered. The averaged velocities are used for the calculation of the forces.

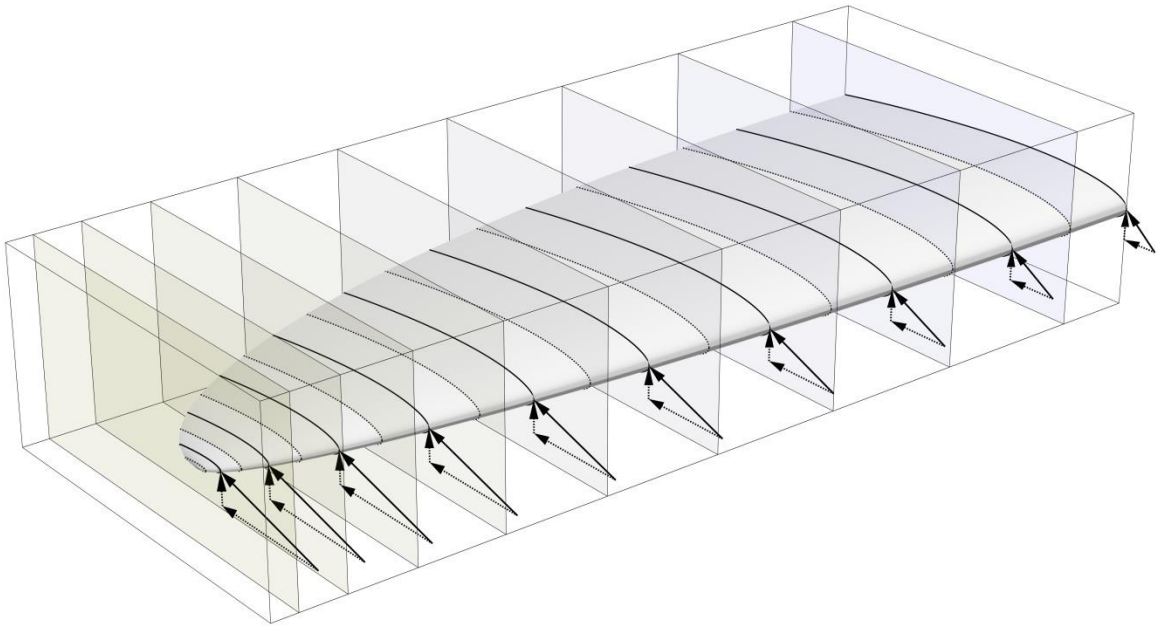

Figure 14: Inflow velocities for the sections of the actuator line approach. The vectors for each section show the resultant as well as the component of the inflow velocity.

The forces, regardless of how these are generated, are acting at the quarter chord points of the airfoil of a respective actuator line segment. This is presented schematically in Figure 15. The blue boxes represent the segments of the actuator line. Within each segment, the black points represent the quarter chord points. At all of these points, the lift (green vectors), the drag (orange vectors), and the resultant force of the section (red vectors) acts. The forces are drawn in accordance to the inflow conditions shown in Figure 15 with the respective angle of attack and velocity magnitude. The resultant forces are subsequently transferred into the finite volume method.

The source terms for the finite volume method are evaluated in a similar way as for the actuator disc approach in the previous chapter. In order to avoid discontinuities in the solution, a distribution function is applied. In the following, the required considerations of the modeling approach are provided. This is demonstrated on two examples.

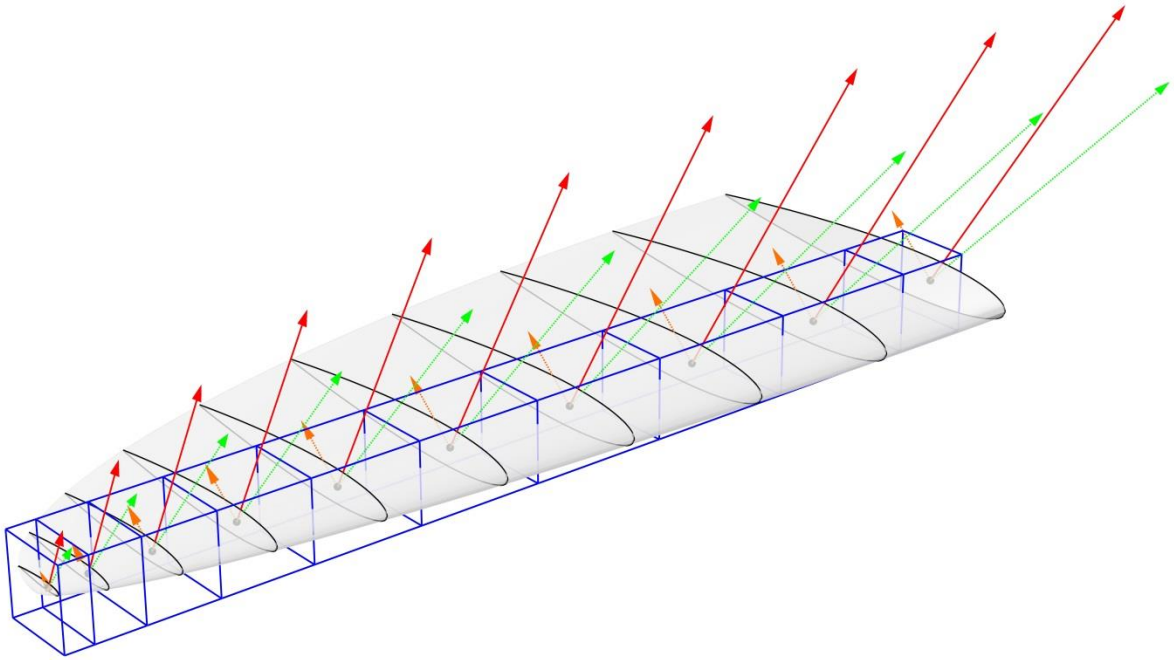

Figure 15: Force distribution generated by the actuator line approach. The aerodynamic force is acting at the reference point of each section. It is equal to the quarter-chord point of the reference airfoil of the section. The resultant force (red) as well as the lift (green) and drag (orange) are presented.

Two-Dimensional Airfoil

The first example concerns the size and position of the averaging region. For simplification issues, this is demonstrated for a two-dimensional case. In Figure 16, a blue highlighted source distribution is depicted. The shape of the NACA 0012airfoil is visualized with the dashed line and its quarter chord point is marked in black. This point represents the center of the source for this example. Furthermore, two averaging boxes with different centers highlighted in green and black are shown. The open question is to find the best possible position for determining the undisturbed inflow conditions of the blade section with the averaging method.

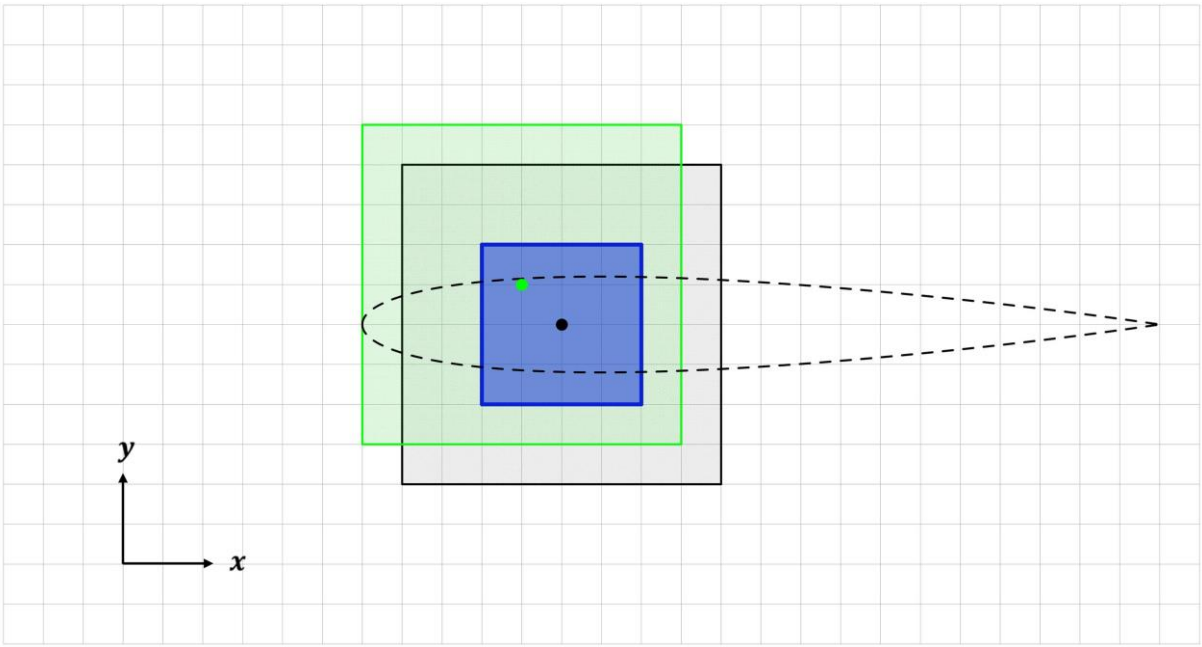

Figure 16: Position of the averaging region. The blue highlighted box represents the source term region and the black and green highlighted boxes two possible averaging regions with the associated center points. The dashed line shows an airfoil with the quarter chord point coinciding with the source region center point.

In the following, it is assumed that the flow fulfills all requirements to be considered as a potential flow. The airfoil section has to produce lift. This can be easily modeled by superimposing a freestream velocity with a potential vortex. The resulting velocity field reads

$$\begin{pmatrix} U \\ V \end{pmatrix} = \underbrace{\begin{pmatrix} U_\infty \\ V_\infty \end{pmatrix}}_{\boldsymbol{U}_\infty} + \frac{\Gamma}{2\pi r}\begin{pmatrix} y \\ -x \end{pmatrix} \; with\, r = \sqrt{x^2 + y^2}. \tag{2.54}$$

Therein, U_∞ and V_∞ are the undisturbed velocity in the freestream. Γ designates the bounded circulation of the airfoil. It is well-known that the circulation for an airfoil is related to the lift L of the airfoil and subsequently to the lift coefficient c_L as follows

$$\Gamma = \frac{c_L\, c\, |\boldsymbol{U}_\infty|}{2}. \tag{2.55}$$

Within this equation, c defines the chord length of the airfoil. In Figure 17 (top) a, the superposed velocity vector field according to the equations is shown. The arrows are drawn with a constant length, since this does not interfere with the conclusions, but allows for a clearer visualization.

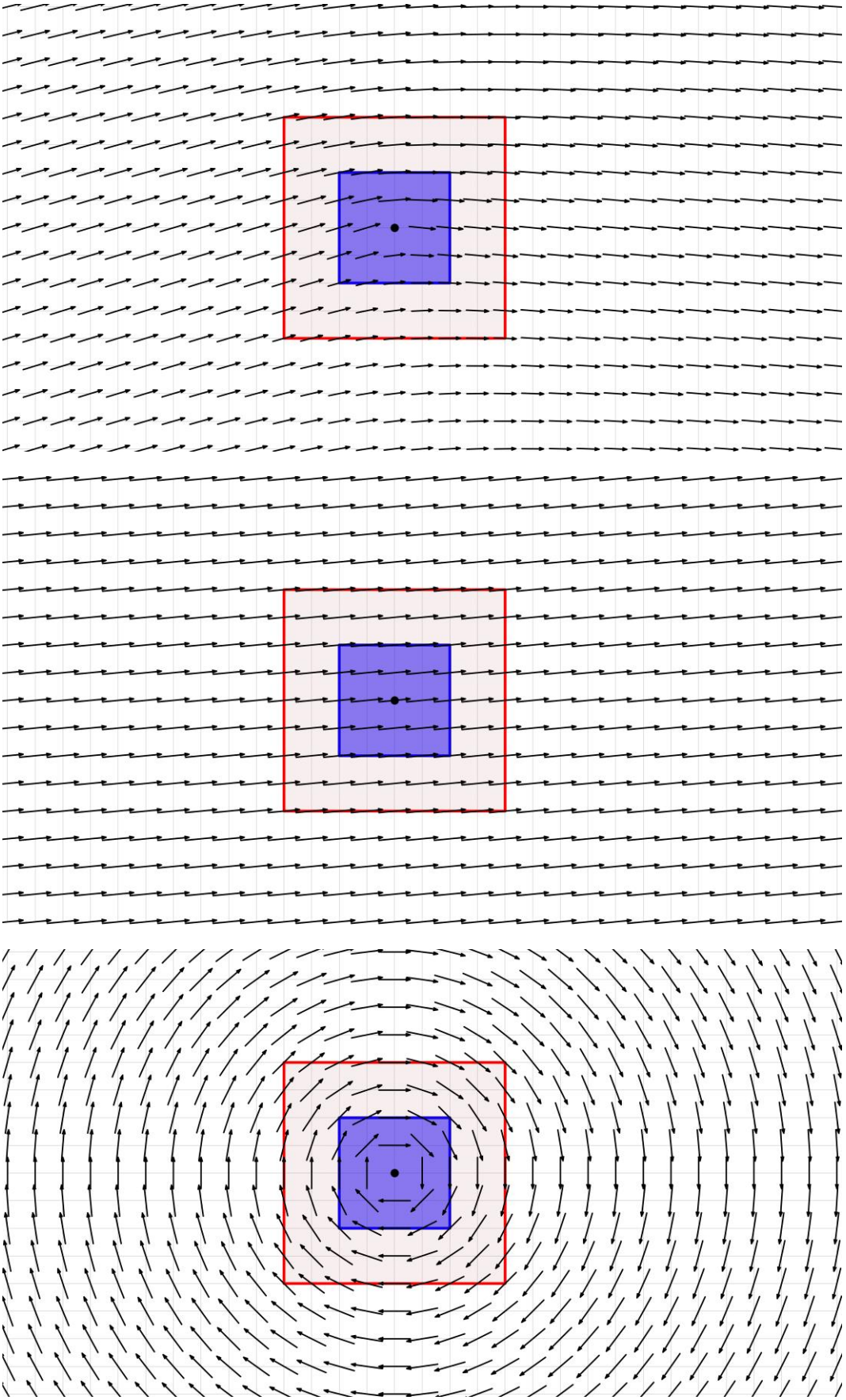

Figure 17: Determination of the inflow velocities with a squared averaging region. The vector field represents the resulting flow field (top), of a freestream flow with an angle of attack (middle), and a potential vortex (bottom). The length of the vortices in set constant.

Since it is obviously difficult to derive any visual information on how to determine the inflow conditions with the averaging method for the actuator line out of the superposed vector field, the undisturbed freestream velocity field as well as the velocity field produced by the bound vortex is shown also. Considering these figures, the result is easy to detect. Without any vortex, the result is logically independent of the position of the averaging region. Regarding the velocity field induced by the bound vortex, it can be seen that the averaged velocity vanishes, if the center of the region is positioned in the center of the vortex and the boundary of the region fulfills point-symmetry about the center of the vortex. Consequently, the answer for the best location of the center is found. In addition, this averaging can be applied and written as follows

$$\begin{pmatrix} u_{AR} \\ v_{AR} \end{pmatrix} = \frac{1}{d_{AL,x}\, d_{AL,y}} \int_{-\frac{d_{AL,x}}{2}}^{\frac{d_{AL,x}}{2}} \int_{-\frac{d_{AL,y}}{2}}^{\frac{d_{AL,y}}{2}} \begin{pmatrix} U_\infty \\ V_\infty \end{pmatrix} dydx = \begin{pmatrix} U_\infty \\ V_\infty \end{pmatrix}, \tag{2.56}$$

$$\begin{pmatrix} u_{AR} \\ v_{AR} \end{pmatrix} = \frac{1}{d_{AL,x}\, d_{AL,y}} \int_{-\frac{d_{AL,x}}{2}}^{\frac{d_{AL,x}}{2}} \int_{-\frac{d_{AL,y}}{2}}^{\frac{d_{AL,y}}{2}} \frac{\Gamma}{2\pi r} \begin{pmatrix} y \\ -x \end{pmatrix} dydx = \begin{pmatrix} 0 \\ 0 \end{pmatrix}. \tag{2.57}$$

For the actuator line models presented in the literature e.g. [24, 40], for which the sample points for evaluating the inflow conditions equals the source points, this result is obtained inherently. This could be imagined by reducing the size of the box to the limit of zero.

Moreover, considering Figure 17 (bottom), some further properties can be detected. If the averaging region is moved in negative x-directon, the obtained averaged velocity in y-direction v_{AR} becomes $v_{AR} > 0$. Consequently, by moving the region in the opposite direction, the averaged velocity in y-direction v_{AR} is obtained to $v_{AR} < 0$. Due to symmetry issues, this is analogue for the other coordinate direction and averaged velocity.

At this point, it has to be mentioned that certain models presented for the actuator surface approach in the literature can counteract this behavior for non-matching center points. Such models, in general, subtract the induced velocity from the actual velocity at the sample point. The induced velocity is calculated by modeling the blade with different vortex models as for example shown by Shen et al. [45]. Due to the averaging made herein, this type of correction has to be slightly modified. The sample point has to be substituted by the center of the averaging region. Although this approach has been tested, it is not further discussed in detail, since there is no need for it if the center points are matching.

Another open question for this approach is what happens if the source distribution is not a squared region anymore. This might be interesting if, at least, the representative blade section has to be positioned inside of the source term region. The answer is similar to the one above for the squared shape of the region. But instead of modeling the action of the source as one vortex it can be considered as a planar vortex distribution. Consequently, the circulation Γ of the bound vortex has to be substituted by the area-specific vortex distribution, which is equal to the vorticity according to $\omega = \frac{\mathrm{d}\Gamma}{dx\, dy}$. The usage of this information for the current example, leads to the equation for the velocity field as follows

$$\begin{pmatrix} U \\ V \end{pmatrix} = \underbrace{\begin{pmatrix} U_\infty \\ V_\infty \end{pmatrix}}_{\vec{U}_\infty} + \int_{-x}^{x}\int_{-y}^{y} \frac{\omega}{2\pi r}\begin{pmatrix} y-y' \\ -(x-x') \end{pmatrix} dy'dx' \;\; with\; r = \sqrt{(x-x')^2+(y-y')^2}. \tag{2.58}$$

The quantities marked with primes represent the position of a vorticity-containing element. The resulting velocity field is shown in Figure 18. Applying the averaging method after separating the superposed velocity field leads to the following equations

$$\begin{pmatrix} u_{AR} \\ v_{AR} \end{pmatrix} = \frac{1}{d_{AL,x}\, d_{AL,y}} \int_{-\frac{d_{AL,x}}{2}}^{\frac{d_{AL,x}}{2}} \int_{-\frac{d_{AL,y}}{2}}^{\frac{d_{AL,y}}{2}} \begin{pmatrix} U_\infty \\ V_\infty \end{pmatrix} dydx = \begin{pmatrix} U_\infty \\ V_\infty \end{pmatrix}, \tag{2.59}$$

$$\begin{pmatrix} u_{AR} \\ v_{AR} \end{pmatrix} = \frac{1}{d_{AL,x}\, d_{AL,y}} \int_{-\frac{d_{AL,x}}{2}}^{\frac{d_{AL,x}}{2}} \int_{-\frac{d_{AL,y}}{2}}^{\frac{d_{AL,y}}{2}} \int_{-x}^{x}\int_{-y}^{y} \frac{\omega}{2\pi r^2}\begin{pmatrix} y-y' \\ -(x-x') \end{pmatrix} dy'dx'\, dydx = \begin{pmatrix} 0 \\ 0 \end{pmatrix}. \tag{2.60}$$

In particular, the second integral can be evaluated by taking into account the symmetry considerations made above. Obviously, that is valid only if the centers of the source and the averaging region are matching. In other cases, it has to be argued like in the single vortex case.

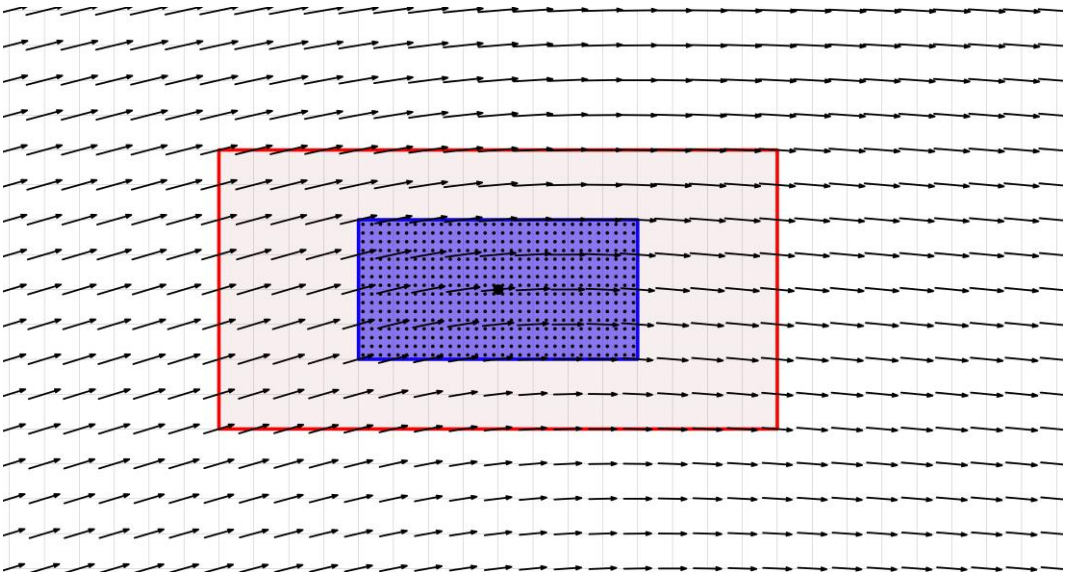

Figure 18: Determination of the inflow velocities with a rectangular averaging region. The vector field represents the resulting flow field of a freestream flow with an angle of attack and a vortex distribution. The length of the vortices in set constant.

A brief additional discussion is provided, concerning the fact that the description of the modeling with a vortex distribution is presented, although a specific force distribution is applied within the CFD simulations. This can be easily declared by imaging that the force induces a pressure jump across the finite volume cell in the direction of the lift within this example. This pressure jump can be modeled in terms of an acceleration potential [111] by a doublet of constant strength positioned in the finite volume cell, while the axis of the doublet is orientated in lift direction. Since for this steady case, the velocity potential is obtained by integrating the acceleration potential along the streamwise

direction, the constant doublet distribution of the acceleration potential will result in a linearly varying doublet distribution in the velocity potential. Furthermore it is known, that the linearly varying doublet distribution is similar to the constant vortex distribution [109]. Consequently, the resulting flow field is similar.

The considerations made above concerns the averaging in the plane of the airfoil section. That is why the two-dimensional airfoil has served as an example. In the following, the averaging in the third dimension is of interest. Therefore, a simple three-dimensional wing is shown.

Three-Dimensional Wing

At first, the principles of setting the position and size of the sections is discussed. In Figure 19, a view in streamwise direction at the left side of a symmetric half-wing configuration is shown. The black points represent the quarter chord points of a section. The local inflow quantities are needed and the geometrical airfoil data at the position of the points are applied for the estimation of the forces for the respective section. In this case, the points are distributed according to a cosine-law depending on the spanwise coordinate y. The averaging regions are marked by the black lines. It has to be noted that the boundary between two regions are set in the arithmetic mean of two quarter points. The green highlighted region shows an exemplarily modified position of an arbitrary selected averaging region. This can affect the result of the averaging procedure and will be discussed in the preceding paragraphs. In addition, the blue highlighted region represents the source term region. The shading represents the strength of the source distribution. Moreover, the black dashed lines are the upper and lower boundary of the wing. The chosen size of the source distribution region is larger than the extension of the wing in vertical coordinate direction. The size of the averaging region in vertical direction is chosen larger than the size of the source terms.

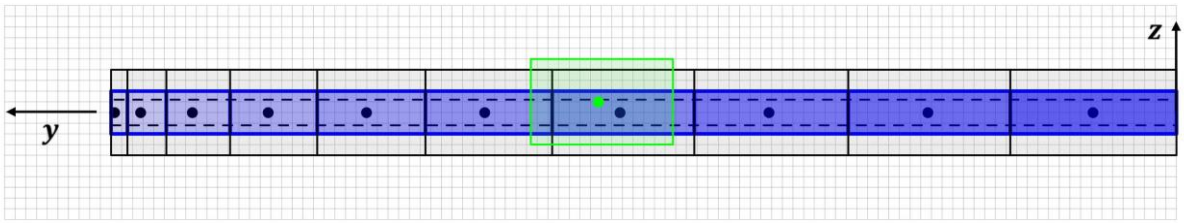

Figure 19: Spanwise and vertical position of the averaging region. Streamwise view of a left side of a symmetric lifting surface is presented. The source distribution (blue) is shown in the source region and the translucency represents the local value. The averaging regions with the center points are marked black and one additional averaging region with associated center point is marked green. The dashed lines represent the airfoil shape.

The detailed description of the chosen distributions, sizes, shapes, and position is presented in the following after a brief discussion of the basic flow properties in a crossflow plane. Therefore, in the following a constant blade loading along the span of the wing is assumed. Consequently, this can be modeled by a bound vortex along the span of the wing, which has no influence on this result since the vortex line is set directly at the considered crossflow plane. The resulting vector field is shown in Figure 20. The vectors have a fixed length and, consequently, provide directional information only. But it is known that the vortex induces magnitudes of the velocities, which are inverse-proportional to the distance of the vortex center, in particular for this two-dimensional example. In Figure 20, the red point marks the center of the vortex. The question is how the inflow conditions have to be determined with this volume-based averaging. Therefore, some considerations are of interest:

- Influence of the height of the averaging region

- Influence of the inclination of the velocity vectors to the surface of the wing
- Influence of the size of the averaging region in spanwise direction

Obviously, the induced velocity by the blade tip vortices is inherently included at every point of the wing. In the vicinity of the symmetry plane, the induced velocity vectors within an averaging volume points almost vertically downwards. As a consequence, the averaged velocity for the region is almost unaffected by its height. Moreover, for these regions the inclination and the size in spanwise direction lead to small deviations of the obtained inflow conditions.

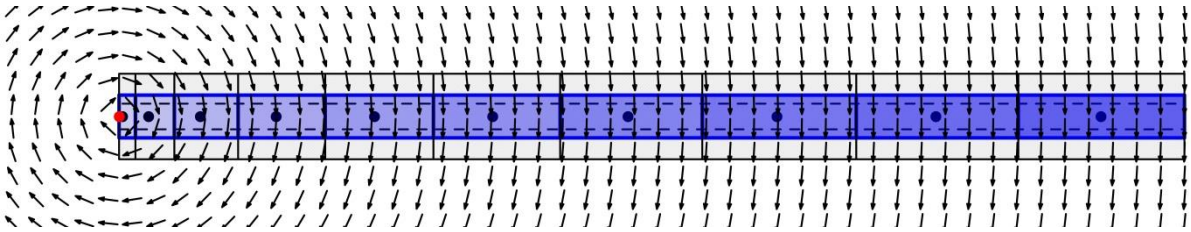

Figure 20: Flow field in the crossflow plane for a concentrated vortex. The source distribution (blue) is shown in the source region. The averaging regions with the center points are marked black. The dashed lines represent the airfoil shape. The red point represents the center of the potential vortex. The length of the vectors is set constant.

But as it can be seen in Figure 21, the situation is different for regions near the wing tip. In order to describe the flow conditions in the tip region, the model of the concentrated vortex is substituted to a vortex distribution in vertical direction. The red line in Figure 21 shows the vortex distribution.

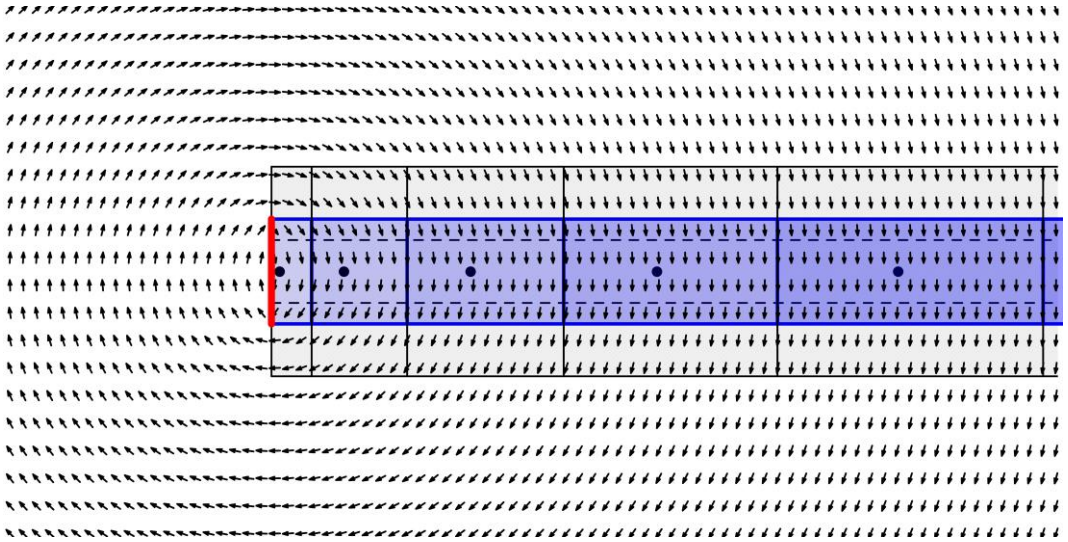

Figure 21: Flow field in the crossflow plane for a vortex distribution. The source distribution (blue) is shown in the source region. The averaging regions with the center points are marked black. The dashed lines represent the airfoil shape. The red line represents vortex sheet. The length of the vectors is set constant.

The axis of each infinitesimal vortex element along the line is oriented perpendicular to the plane. This is valid for a constant source distribution across the whole modeled wing in the CFD simulation. In this case, the whole wing can be modeled in terms of an acceleration potential with a constant doublet distribution with its axis aligned with the vertical direction. Consequently, as shown for the two-dimensional airfoil example above, the modeling can be established by the constant strength vortex distribution along the red line of the blade tip.

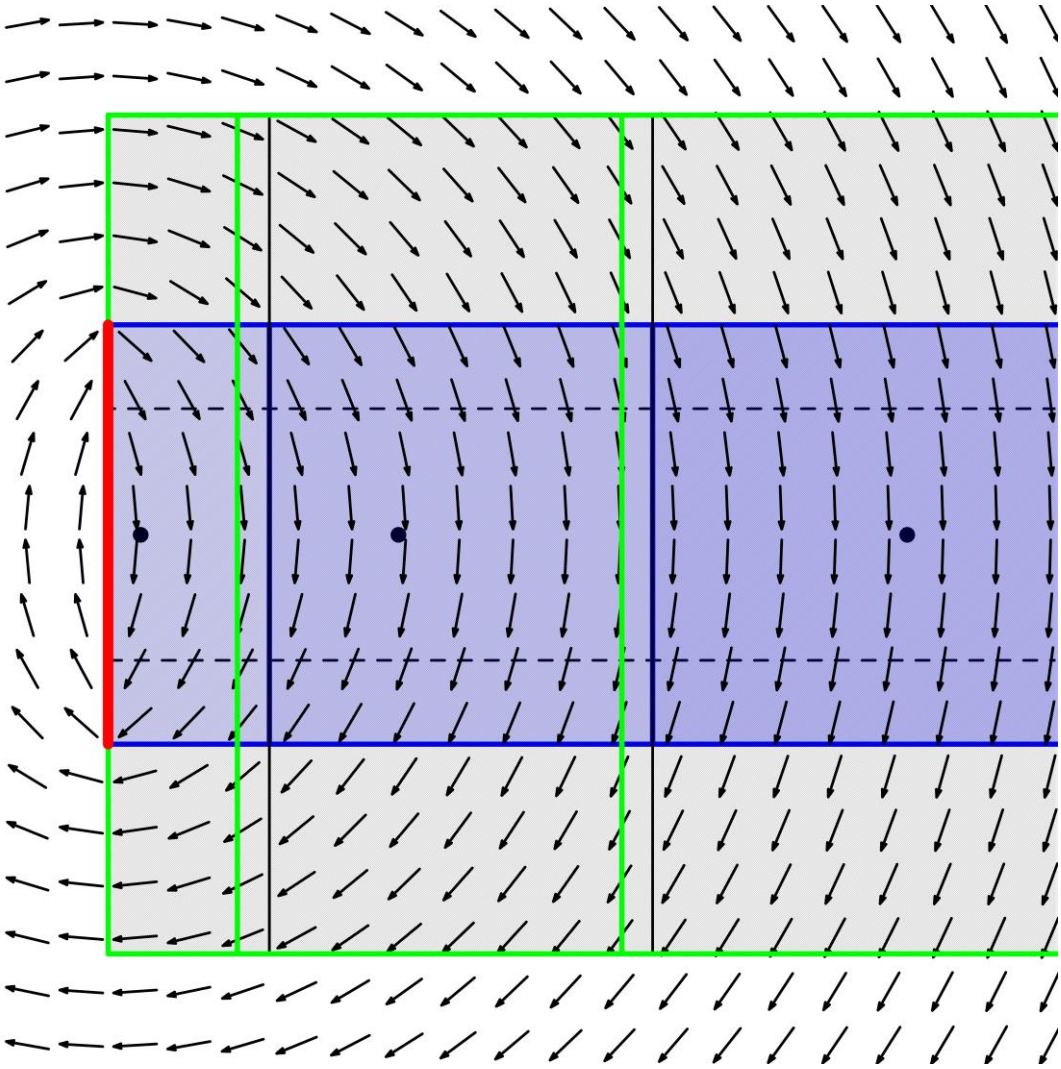

Figure 22: Flow field in the crossflow plane in the vicinity of the blade tip for a vortex distribution. The source distribution (blue) is shown in the source region. The averaging regions with the center points are marked black. The green lines show a different calculation method for the sections. The dashed lines represent the airfoil shape. The red line represents vortex sheet. The length of the vectors is set constant.

A detailed view of the flow field around the blade tip region is provided in Figure 22. The vectors are drawn with a fixed length in this figure also. The smaller the distance from an evaluation point to the wing tip, the greater is the deviation of the vectors from the vertical direction, in particular, at the upper and lower boundary of the averaging region. But due to symmetry of the solution, it can be stated that the spanwise velocity component is vanishing by averaging across one of the sections. The only requirement therefore is that the center of the averaging region is at the same vertical position as the center of the source region (for a symmetric one) or at least the vertical boarders are symmetrically located regarding the center of the source region. Consequently, the size of the region in vertical direction is not important. Considering the vertical velocity component, it is easy to determine that the size in vertical direction influences the averaged velocity. The larger the vertical size of the region, the lower is the averaged velocity due to the nonlinear behavior of the vertical velocity along the vertical direction. Furthermore, it can be seen that the size of the averaging region in spanwise direction is influencing also the result of the averaged vertical velocity. In particular, in the vicinity of the blade tip, the effect is of importance. Consequently, in contrast to the airfoil test case no size or ideal position of the region can be found in order to get an unaffected result for the averaged vertical velocity component. Subsequently, the parameters have to be adjusted.

However, it can be argued that this aspect of the modeling is appropriate for the wing. Consider an airfoil with a non-zero thickness. While for the lifting line theory the induced velocities are taken at the position of the line, which gets the information of the inflow at a certain point only, the real airfoil notices the flow field variation in the vertical direction as well. Concluding, the averaging region includes information of the global flow field around the airfoil. Therefore, the sizes have to be adjusted in accordance with the sizes of the source term region that will be discussed in the next chapter.

For the presented example of the wing, a constant distribution of the source terms is shown. That is an equivalent result to a constant lift distribution along the span, which is usually not obtained within an application. By assuming a varying lift distribution along the spanwise direction (e.g., constant for each section), the source term strengths are varying also. Although the jumps in the source distribution are locally smaller between two sections as for the constant lift distribution at the blade tip, the difficulty with the choice of the size of the averaging region (in particular, in the vertical direction) is in this case present at all sections with high gradients in the lift distribution along the spanwise direction. But for a certain spanwise position, the description made in the previous paragraph may be applied locally.

Realization of the Determination of the Inflow Conditions:

In general, the implemented procedure for the actuator line approach is similar to the actuator disc approach. Therefore, the three-dimensional solver has to be applied and consequently, the Cartesian coordinate frame is the basic frame for the solution. In contrast to the actuator disc, the actual implemented actuator line determines the inflow conditions for the finite volume calculation in a blade fixed coordinate frame. Consequently, the coordinate transformation from the Cartesian to the cylindrical coordinate frame is not performed for the position vectors. But, the position vectors within the Cartesian frame have to be directly transformed into the blade fixed coordinate system. This is established with the following relation

$$\underbrace{\begin{pmatrix} x \\ y \\ z \end{pmatrix}_{bf}}_{\boldsymbol{x_{bf}}} = \boldsymbol{M_{PR}} \cdot \underbrace{\begin{pmatrix} 1 & 0 & 0 \\ 0 & \cos(\Omega t + \Delta\varphi_B) & \sin(\Omega t + \Delta\varphi_B) \\ 0 & -\sin(\Omega t + \Delta\varphi_B) & \cos(\Omega t + \Delta\varphi_B) \end{pmatrix}}_{\boldsymbol{M_{cart,bf}}} \cdot \mathbf{x}_{\boldsymbol{cart}}. \tag{2.61}$$

The matrix $\boldsymbol{M_{PR}}$ is the permutation/rotation matrix as used in the actuator disc approach to reassign the coordinate direction between Fluent and PanBL. The transformation matrix $\boldsymbol{M_{cart,bf}}$ is a time-dependent rotation matrix that includes the angle shift $\Delta\varphi_B$ for multi-bladed rotors.

In the following, the cell to segment assignment is performed in the blade fixed coordinate system. The principle is the same as for the actuator disc. A cell-center-based query is made to decide if a cell is within a segment. In order to allow for applying the code structure from the actuator disc approach, each blade is assigned to a sector and the blade is divided into the radial sections. This allows a fast change between the methods and can be executed even during runtime and if necessary, for example, create an initial steady state result as basis for the unsteady simulation. Figure 23 shows the determination if a cell is part of a segment.

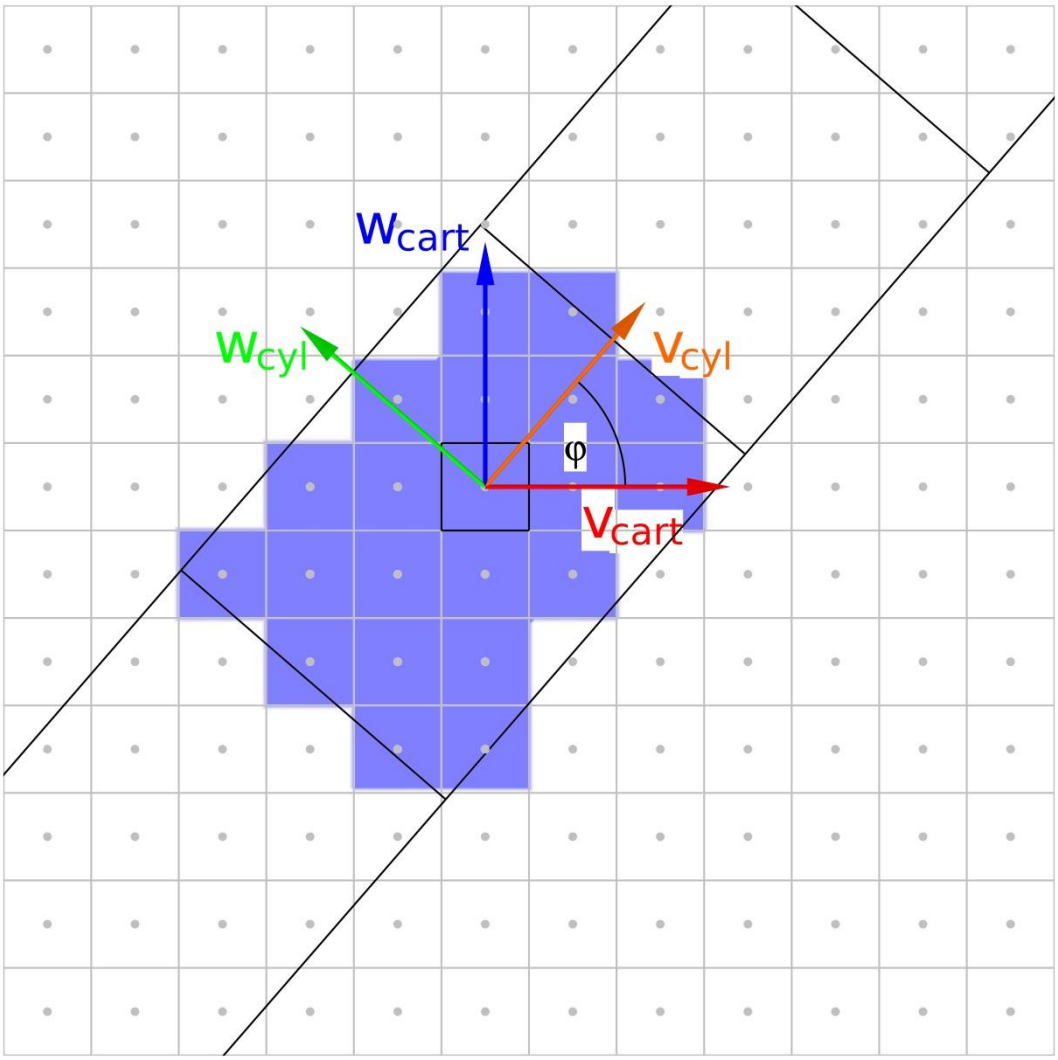

Figure 23: Determination of inflow conditions for the actuator line segment. The blue highlighted cells are set to be within the associated propeller segment. The finite volume grid with its center points is drawn (grey lines and points) and the propeller segments are represented by the black lines. The vectors show the velocity components of a cell in the different coordinate systems.

In the following step, the volume averaged velocity is calculated in the same way as for a segment within the actuator disc approach according to

$$u_i = \frac{\sum_{N_{cis}} u_{i,c} V_{i,c}}{\sum_{N_{cis}} V_{i,c}}. \tag{2.62}$$

In this case the averaging is conducted as well in the cylindrical coordinate frame which is obtained by

$$\boldsymbol{u_{cyl}} = \boldsymbol{M_{cart,cyl}}\, \boldsymbol{u_{cart}}. \tag{2.63}$$

The statements concerning the parallelization have to be applied for these simulations also. Finally, the transformed velocities into the blade-fixed coordinate system are obtained analogously and read

$$\boldsymbol{u_{bf}} = \boldsymbol{M_{PR}} \cdot \left(-\begin{pmatrix} \Omega \\ 0 \\ 0 \end{pmatrix} \times \begin{pmatrix} 0 \\ r \\ 0 \end{pmatrix} + \underbrace{\begin{pmatrix} u \\ v \\ w \end{pmatrix}_{cyl}}_{\boldsymbol{u_{cyl}}} \right) \tag{2.64}$$

Although it has been stated that the method is designed for time-accurate solutions, it can also be used in a rotating frame simulation as well. The procedure is very similar. The only difference relies in the matrix $\boldsymbol{M_{cart,bf}}$, which loses its time dependency, since the blade is not moving. Nevertheless, the velocity calculation remains as it is for the time-accurate solution.

The calculation of forces is completely identical between the actuator line and actuator disc approach, since no model for the calculation of unsteady airfoil effects is included.

2.7.6 Source Terms for the Actuator Line

The determination of the source terms for the actuator line is as well quite similar to the approach used for actuator disc. The forces obtained by PanBL are determined for each section of a blade. In principle, the same inverse procedure in terms of coordinate transformations compared to the workflow for the generation of the inflow conditions has to be performed. Furthermore, the linear interpolation in spanwise direction is applied in order to avoid jumps of the source terms at the section boundaries. The treatment of the sources including the distribution function in the axial direction of the propeller is also applied for a smoother distribution of the sources at the respective boundaries. The main difference occurs at the boundaries of the chordwise direction of the imaginary blade. This might be clear, since the actuator disc is continuous in this direction. Due to discontinuity generated by the actuator line, the same smoothing function is applied as in the axial direction. This fact is briefly described in the following. For a better understanding, Figure 24 (left) shows a linear distribution of the source terms along the spanwise direction of the blade. As it is visible, a linear interpolation is used inside the segments as it has been presented to be a suitable choice within the actuator disc approach. At the chordwise boundaries, no smoothing has been applied in order to visualize the appearing jumps. In contrast, in Figure 24 (right) the smoothing has been applied in chordwise direction with the distribution function F_{distr}. It has to be noted that the axial coordinate of the propeller within the distribution function presented for the actuator disc is substituted by the chordwise coordinate of the propeller for this example. A detailed description of the modified function is provided in one of the following paragraphs. The ratio of the smoothing width and the disc width is $SR_s/SR_w = 0.5$. Logically, the statement for the actuator line remains valid that the proposed minimum number of cells lying in the smoothing region has to be applied as well according to $SR_s > 3 \cdot l_{cell}$. Consequently, the smoother result is well visible. In particular, this behavior has advantages for the unsteady simulations.

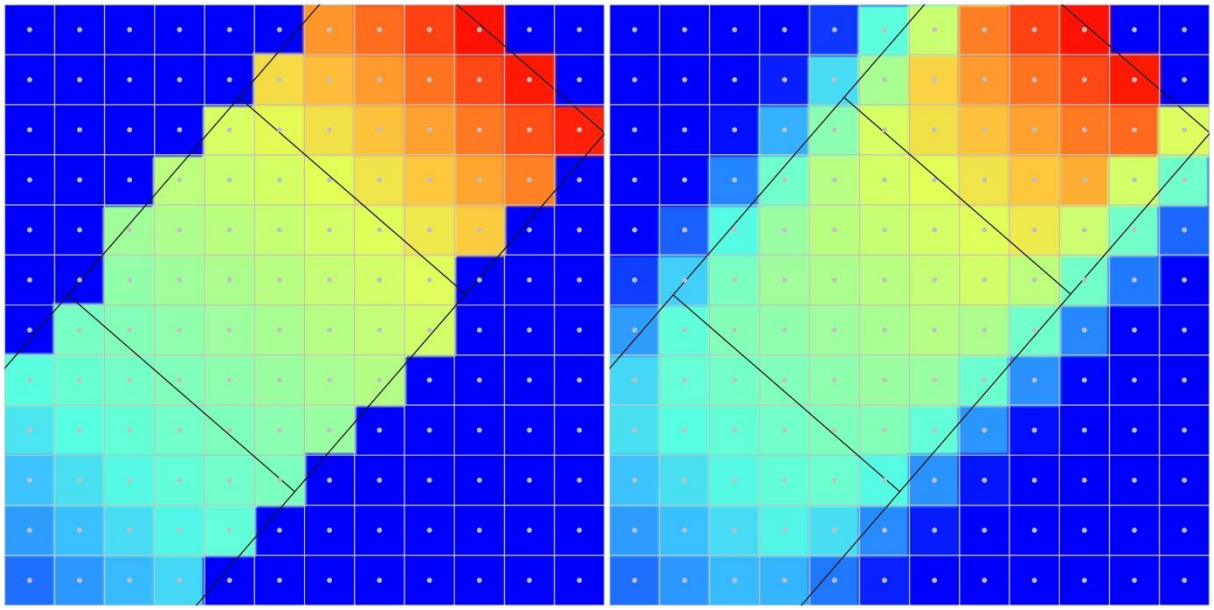

Figure 24: Interpolation of source terms of the actuator line. Source distribution without smoothing (left) and with smoothing (right) in chordwise direction is shown. The propeller grid (black lines) and the finite volume grid with associated center points (grey lines and points) are visualized. The color blue represents no propeller action.

In order to show the principle, it can be assumed that a rotation of the blade with a small azimuthal angle is performed. The rotation shall be that small that at a certain time step t_n one cell center is inside the segment of the blade and the following time step t_{n+1} it lies outside. Consequently, the value of the source term will change abruptly from a non-zero value to a value of zero. This can lead to spurious oscillations and a reduced convergence rate of the solution. Due to the distribution function, this unfavorable behavior is improved. This might be even true for larger time-step sizes.

Since the smoothing function is applied in two coordinate directions, a more general formulation of the distribution function can be provided as follows

$$\mathrm{F}_{distr,x_i} = \begin{Bmatrix} 0, & |x_i - SR_{c,x_i}| > SR_{2,x_i} \\ \frac{1}{SR_{w,x_i}} \cos\left(\frac{\pi}{2} \frac{\left(|x_i - SR_{c,x_i}| - SR_1\right)}{SR_{s,x_i}}\right)^2, & |x_i - SR_{c,x_i}| \geq SR_1 \ \wedge |x_i - SR_{c,x_i}| \leq SR_{2,x_i} \\ \frac{1}{SR_{w,x_i}}, & |x_i - SR_{c,x_i}| < SR_{1,x_i} \end{Bmatrix}, \tag{2.65}$$

$$with\ SR_{1,x_i} = \frac{SR_{w,x_i} - SR_{s,x_i}}{2} \text{ and } SR_{2,x_i} = \frac{SR_{w,x_i} + SR_{s,x_i}}{2}. \tag{2.66}$$

In the following, the coordinates of the general form of the distribution function are set to $x_i = x$ and $x_i = y$ to present some considerations in a simplified manner. These coordinates are described in the blade fixed coordinate system within the current implementation. The important quantity of the function is that it is bounded also for a concurrent application in several coordinate directions according to

$$\int_{-\infty}^{\infty} \int_{-\infty}^{\infty} F_{distr,x}\left(x, SR_{c,x}, SR_{w,x}, SR_{s,x}\right) \cdot F_{distr,y}\left(y, SR_{c,y}, SR_{w,y}, SR_{s,y}\right) dx\, dy = 1. \tag{2.67}$$

This result seems to be obvious. Although the functions are connected by a multiplication, the integration can be performed independently in each coordinate direction due to the unique appearance of the integrational variables in each function.

In Figure 25, the described quantities are visualized. In this example, the parameters of the source region in the x- and y- coordinate direction are set to equal values. This concerns the position of the center of the region regarding the quarter chord point of the representative section $SR_{c,x} = SR_{c,y}$, the width of the region $SR_{w,x} = SR_{w,y}$, and the smoothing width $SR_{s,x} = SR_{s,y}$. The ratio of the smoothing width to the source width is set to $SR_{s,x}/SR_{w,x} = SR_{s,y}/SR_{w,y} = 0.5$. The source distribution in x-direction is highlighted in green, while the blue highlighted curve shows the respective distribution in the y-direction. The detailed description of the influence of the different widths can be found in chapter 2.7.4.

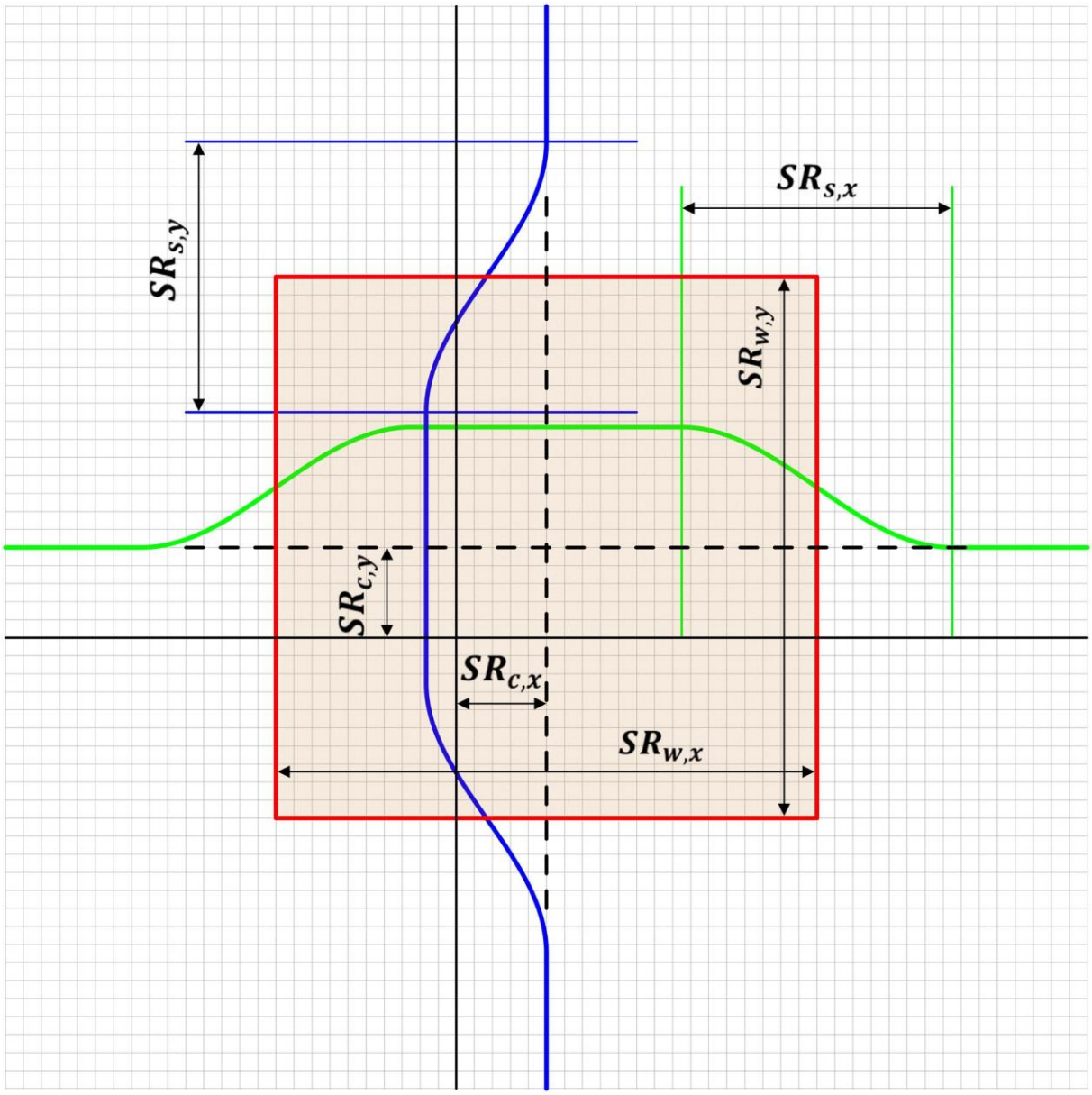

Figure 25: Parameter variation of the distribution function. The position of the disc center $SR_{c,x}$ and $SR_{c,y}$, the width of the actuator disc $SR_{w,x}$ and $SR_{w,y}$, and the width of the smoothed cosinusoidal part of the actuator disc boundary $SR_{s,x}$ and $SR_{s,y}$ are shown. The green and blue lines represent the action of the propeller in different coordinate directions.

In the following, the procedure for the actual implementation of estimating the source terms for each cell is presented. Therefore, the thrust and circumferential force is obtained for a certain segment of the actuator line according to

$$\frac{\Delta T_{cyl}}{\Delta r} = \frac{1}{2}\,\rho\, V_{rel}^2\, \mathrm{c}\,(c_L \cos(\phi) - c_D \sin(\phi)), \tag{2.68}$$

$$\frac{\Delta F_{\varphi,cyl}}{\Delta r} = \frac{1}{2}\,\rho\, V_{rel}^2\, \mathrm{c}\,(c_L \sin(\phi) + c_D \cos(\phi)). \tag{2.69}$$

In contrast to the determination of the source terms for the actuator disc, the thrust and circumferential force is related to the radial increment of the segment solely. The circumferential

distribution is inherently provided by the distribution function $F_{distr,x,bf}$ as it has been presented as well in the axial direction with $F_{distr,x}$ for the actuator disc approach.

In the next step, the source terms are transformed in the Cartesian coordinate frame. Since the thrust and circumferential force are described in the cylindrical coordinate system, the inverse coordinate transformation compared to the determination of the inflow conditions is performed. In addition, the distribution function in both smoothing directions is applied and results in the equation

$$\begin{pmatrix} S_x \\ S_y \\ S_z \end{pmatrix}_{cart} = \underbrace{\begin{pmatrix} 1 & 0 & 0 \\ 0 & \cos(\varphi+\Omega t) & -\sin(\varphi+\Omega t) \\ 0 & \sin(\varphi+\Omega t) & \cos(\varphi+\Omega t) \end{pmatrix}}_{\boldsymbol{M_{cyl,cart}}} \begin{pmatrix} \frac{\Delta T_{cyl}}{\Delta r} \\ 0 \\ \frac{\Delta F_{\varphi,cyl}}{\Delta r} \end{pmatrix}_{cyl} \cdot (F_{distr,x} \cdot F_{distr,y})_{bf}. \tag{2.70}$$

It is important that the distribution functions are applied in the blade-fixed coordinate system. In particular, the distribution function $F_{distr,x,bf}$ only works appropriately in the blade-fixed coordinate frame. Due to the rotation of the blade-fixed frame around the x-axis of the cylindrical frame, an execution in another frame will make the function useless. For the smoothing along the blade-fixed y-axis it is not that crucial, since the coordinates remains the same after transformation. But for consistency, it has to be implemented as well in the blade-fixed frame.

2.7.7 Improved Inflow Condition

Within this chapter a slight modification for the inflow condition is presented. It is intentionally placed at the end of the description of the methods, since the distribution of the source terms and its properties have to be known.

The initial formula for the determination of the inflow condition reads

$$u_i = \frac{\sum_{N_{cis}} u_{i,c} V_{i,c}}{\sum_{N_{cis}} V_{i,c}}. \tag{2.71}$$

As described, the cell is counted to be within a region if its cell center is positioned within the region. Consider a small movement of the mesh or of the cell center in axial direction. For the ideal case, the averaging region shall be symmetric around the point of the source. Due to the discretization of the continuous space, one cell center will drop out of the region on one side, while another center will join the region on the other side. The obtained averaged value will therefore be different. In order to obtain less dependence on the mesh, a multiplication with the symmetric and smooth distribution function F_{distr} can be performed to reduce this behavior for arbitrary meshes. For an equidistant mesh, a correct result is obtained. The resulting equation reads

$$u_i = \frac{\sum_{N_{cis}} u_{i,c} V_{i,c}\, F_{distr}}{\sum_{N_{cis}} V_{i,c}\;\; F_{distr}}. \tag{2.72}$$

2.8 Generalized Actuator Disc Approach Coupling with Two-Dimensional CFD

Within this chapter, a modified method of the previous one is shown. The described method is fast, although drawbacks can be identified. As it is generally known, panel methods, even coupled with boundary layer methods, provide results of moderate quality in some cases. For example, separated flows or flows including transonic flow regimes might be difficult to cover.

For this purpose, a direct coupling between a three-dimensional generalized actuator disc approach and a two-dimensional simulation of the airfoil sections is established. In principle, the determination of the inflow conditions as well as the generation of the source terms is equal. That is why it is not discussed here. Differences are made in the solution strategy and logically, in the thrust and torque calculation. In the following, these topics are addressed for the actuator disc solely. The application for the actuator line is comparable as in the coupling with PanBL and can be implemented in a straightforward manner.

The combined approach is realized completely in Fluent. Basically, the solution of the three-dimensional domain including the generalized actuator disc and the two-dimensional airfoil calculation is made within one single Fluent simulation. Therefore, several domains are loaded and solved in parallel mode. The flow chart for the solution procedure within Fluent for this approach is presented in Figure 26. The blue highlighted tasks present the interfaces for the two domains.

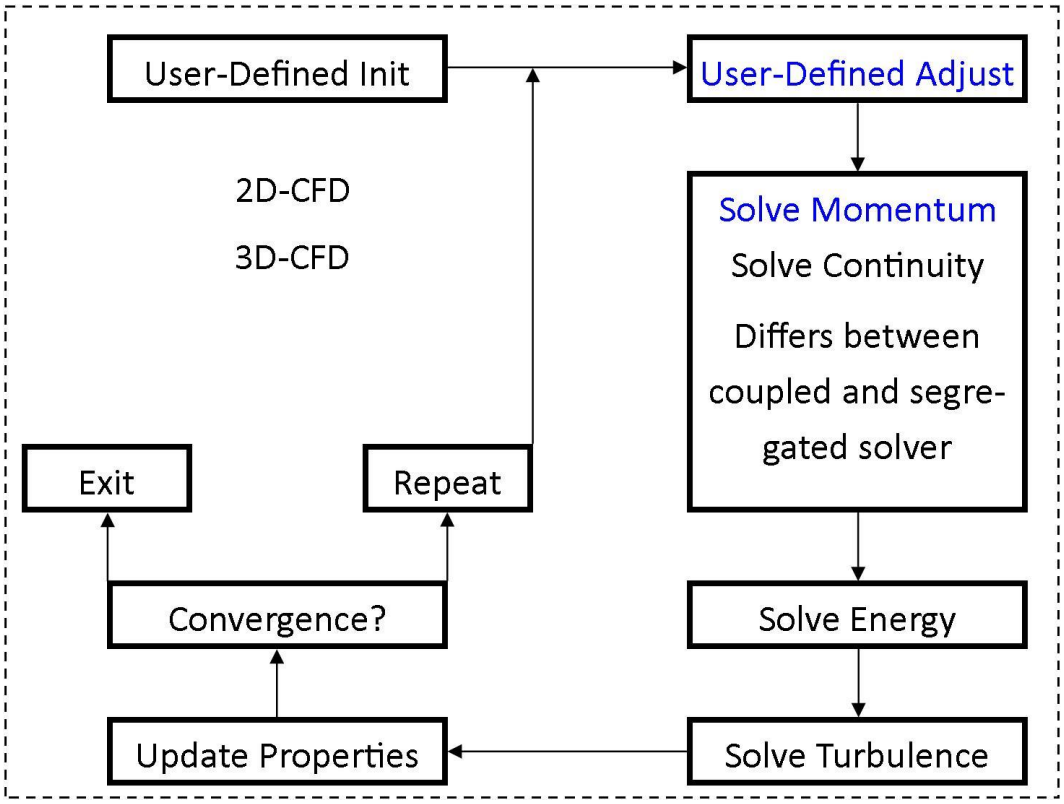

Figure 26: Fluent flow chart of the generalized actuator disc with 2D-CFD.

At first, Fluent is started and a mesh including the multiple domains is loaded. After initializing the flow field in all of the domains appropriately, the calculation is started. The DEFINE_ADJUST macro is used for several tasks at the “User-Defined Adjust” step. Within the actuator disc domain, the inflow quantities to the imaginary blade are sampled and stored. Furthermore, the forces acting on the propeller blade in the two-dimensional blade domain are calculated and stored. Subsequently, the flow field is solved with these values. In the following “Solve Momentum” step, two macros are used. The DEFINE_PROFILE macro updates the inflow conditions of the blade domain with the sampled inflow data of the actuator disc domain. The DEFINE_SOURCE macro is used at this runtime to insert the action of the propeller in the actuator disc domain depending on the forces calculated on the propeller blade. This procedure is repeated until a converged solution of the flow quantities in all domains is established.

2.9 Resolved Flow Simulations

In this section, the fully resolved simulations of the propeller by the application of computational fluid dynamics are presented. There are two different methods available. Firstly, if rotational or translational periodicity is applicable, the flow can be simulated within a moving reference frame. This approach is presented in chapter 2.9.1. Secondly, for non-periodic flows the motion of the propeller has to be captured. For this purpose, the sliding mesh approach is applied within these investigations and is described in section 2.9.2.

2.9.1 Steady-State Flow Simulation with Moving Reference Frame

The steady state flow simulation with the moving frame approach requires less numerical effort in contrast to the time-accurate flow simulation with the moving mesh approach. The latter means that node locations are really moved in physical space, which is presented in the following chapter. The moving reference frame allows an arbitrary motion of an object, while the physical node positions of a mesh remain at its initial position. The motion is imaginary realized by additional terms in the governing equation. The representation of a relative motion of certain parts of the mesh, however, can be hardly realized.

For the applications presented within this thesis, translational as well as rotational moving frames are used. For the simple two-dimensional test cases, the translation of the airfoil is modeled. For these cases, it can be imagined that there is only a velocity superposed. For the more complex three-dimensional cases, the rotation of the propeller is obtained due to the rotation of the rotating reference frame. Caused by the rotation of the frame, in particular, additional forces like centripetal force or Coriolis force are added for each cell. This kind of simulation is applicable for axisymmetric flow solely. It cannot be used for non-axial inflow conditions since it violates the symmetry constraint. A further advantage is the reduced effort for generating a mesh because only one domain is required.

The required formulas for this approach are not described, since no modifications are made and it is assumed as generally known. The implementation can be found in [112].

2.9.2 Time-Accurate Flow Simulation with the Moving Mesh Approach

The time-accurate flow simulation applying the moving mesh approach requires high effort to solve a problem compared to the previously presented moving reference frame approach. First of all, it obviously requires an unsteady simulation, since the nodes of the mesh have to be moved to realize the motion. Subsequently, the node positions have to be updated at each time step. However, in particular the abilities associated to the unsteady solution allow solving arbitrary motions of the mesh. Furthermore, the relative motion of different mesh domains with a sliding mesh interface can be realized. This interface type is able to transfer flow quantities from one domain into another domain with relative motion to each other at a specified surface. Another approach for transmitting the quantities is the overset method. In this case, an interpolation between two volume meshes is performed. Further details of both approaches are presented in chapter 5.

Applied to the simulation of propellers, some points can be summarized. Firstly, the effort in generating the mesh is higher. Therefore, a rotating and a stationary domain have to be meshed. Secondly, the calculation of the solution requires more computational effort. One the one hand the physical position of each cell and node in the rotating domain has to be modified at each time step and on the other hand the non-conformal interface cells using the sliding mesh approach have to be calculated for every single time step. The term non-conformal interface means that the nodes of both sides of the interface have not to be located at the same physical position. Consequently, for the sliding surfaces the intersections have to be recalculated at each time step. Nevertheless, as mentions for the general case of the method, there are fewer restrictions to the simulation setup; e.g. non-axial inflow, time-depending inflow or non-uniform inflow conditions applied within simulations can be performed also.

3 Two-Dimensional Test Case

Within this chapter, investigations for a two-dimensional, generic test case are conducted. Therefore, a two-dimensional cascade test case is presented to investigate the influence of the averaging and source region parameters which are described in chapter 2.7. For the test case, simulations with the generalized actuator disc approach as well as the RANS/URANS simulations are performed and the obtained results are presented and compared.

For this test case, a cascade using NACA 0012 airfoils is presented. The cascade provides a flow field, comparable to the flow in a plane of constant radius for a propeller, but with reduced complexity. Consequently, the modeling approach has to provide a comparable flow field solution and has to be consistent with the underlying physics. Furthermore, the test case is designed as simple as possible, to allow for investigating the influence of certain parameters associated to the cascade, e.g. number of blades, angle of incidence, etc., as well as the parameters regarding the modeling of the generalized actuator disc.

3.1 Test Case Description

General

Figure 27 (top) shows a sketch of the domain used for the simulations as well as the location and types of the boundary conditions. The boundary condition on the upper side of the domain is set to a velocity or pressure inlet. The boundary condition on the lower side of the domain is set to a pressure outlet. On the left and right hand side of the domain, a periodic boundary condition is applied. In order to realize the motion of the blade, a moving reference frame is used for these investigations. This means that the blade in the figure imaginarily moves from right to left and consequently, the relative inflow to the stationary considered blade is from left to right.
In addition, Figure 27 (top) exhibits two airfoils (NACA 0012 airfoil), representing the blade for two different angles of incidence. This dashed black line corresponds to an angle of incidence of $\theta = 0°$ while the dashed orange line shows the same airfoils at an angle of incidence of $\theta = 15°$. The red point is the quarter chord point which is used as the pivot point for the rotation of the blade. Figure 35 (bottom) illustrates the domain for the calculation in the middle and the imaginary adjacent ghost domains, implied by the periodic boundary conditions, to the left and the right hand side.
A measure that includes the number of blades of a propeller in nondimensional form is the solidity. It relates the sum of the chord lengths $c(r)$ of all propeller blades at a certain radial position to the total circumferential length at this radius as follows

$$\sigma = \frac{B\ c(r)}{2\pi r}. \tag{3.1}$$

B represents the number of blades within this relation. For this two-dimensional investigation of the cascade the solidity is defined as

$$\sigma_{2D} = \frac{c}{l_{per}}. \tag{3.2}$$

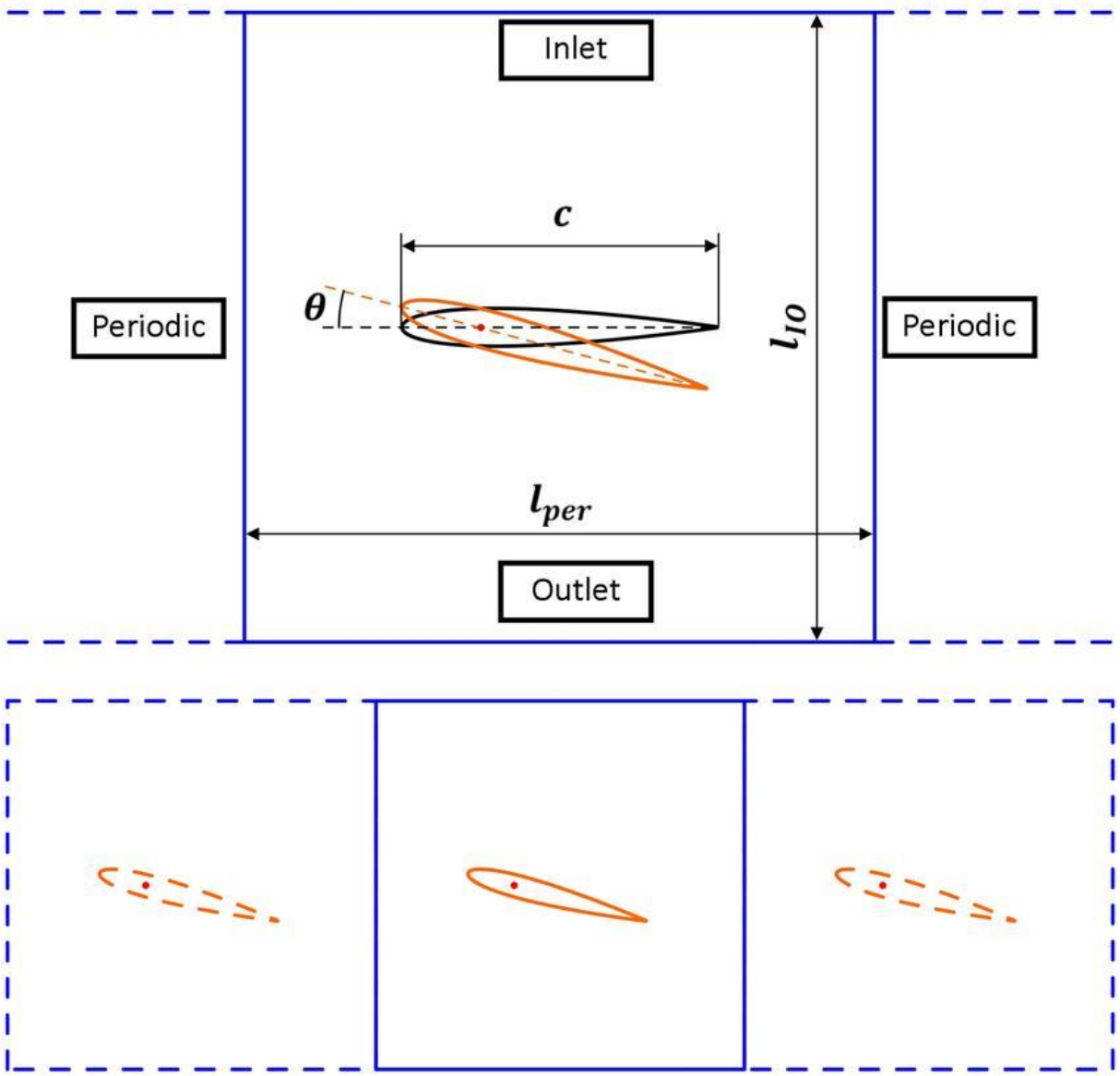

Figure 27: Sketch of the two-dimensional test case. Basic description (top) and application of the periodic boundary condition (bottom).

l_{per} is the periodic length of the domain. The definition of σ_{2D} can be imagined to be the ratio of the length covered by the blade to the distance between the reference points of two adjacent blades. Nevertheless, it should be kept in mind that this parameter is not affected by the pitch angle θ. Strictly speaking, the projection of the chord length on the horizontal axis differs depending on the angle of incidence, but this influence is not accounted here.

The designed simulation setup has been chosen in order to allow for the possibility of setting different solidities within this investigation in an easy manner. Therefore, the solidity can be varied by adjusting the periodic length l_{per}. Considering Figure 27 (bottom), this issue becomes visible in accordance to the above stated pictorial description of the parameter. For simplicity, the chord length is set to $c = 1\ m$ for the results presented in this subchapter.

The limiting case for $\sigma_{2D} \to 0$ results in a periodic length $l_{per} \to \infty$. It is obvious that it is not possible to calculate this solidity with the applied setup, but the resulting case equals an undisturbed stand-

alone airfoil. Consequently, the periodic boundary conditions are modified to an inlet and an outlet boundary condition. The size of this domain has to be large enough that no interaction of the boundary conditions with the airfoil is given. This is proven by checking the pressure field. Within Fluent, for the outlet boundary condition a “pressure outlet” boundary condition or an “outflow” boundary condition can be chosen. It has been tested that the “pressure outlet” boundary condition with “average pressure specification” shows an equivalent result as the outflow boundary condition.

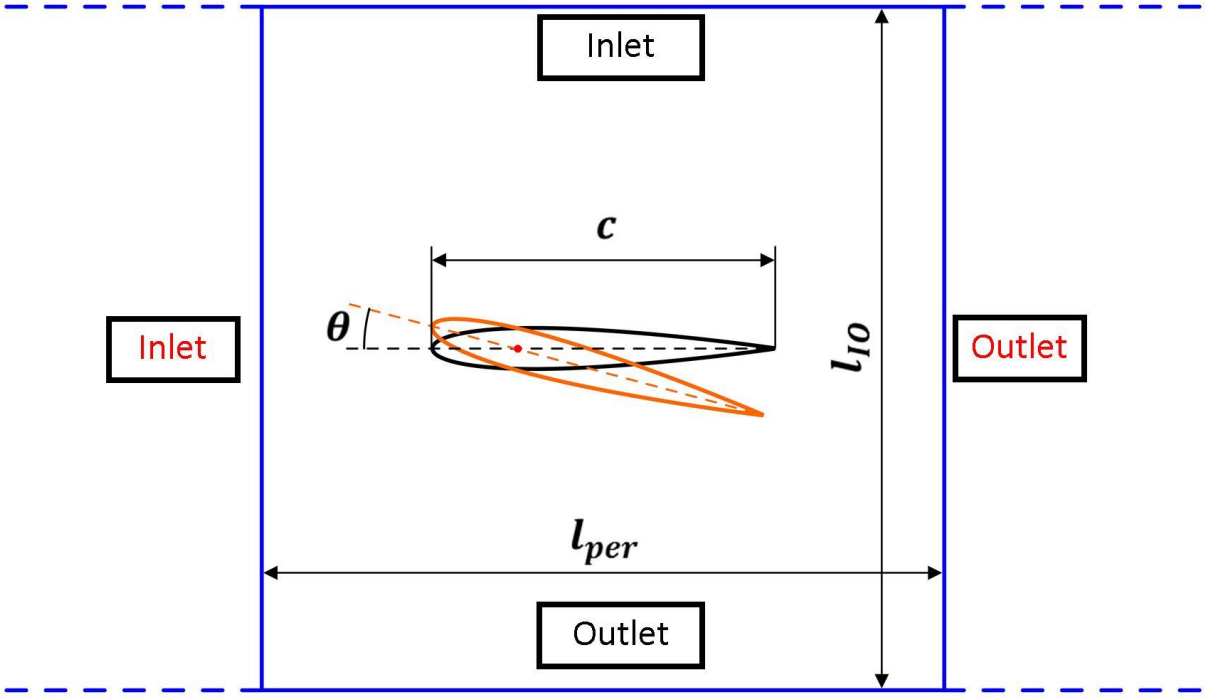

Figure 28: Sketch of the two-dimensional test case for the limiting value of $\sigma_{2D} \rightarrow \infty$.

Definitions: In order to be in conformity with a propeller flow, the velocity in x-direction u represents the circumferential velocity of a propeller simulation. That is why the terms circumferential and horizontal velocity are used synonymously for u. Further, the velocity in y-direction v corresponds to the axial velocity of a propeller simulation. Consequently, the terms axial and vertical velocity are used synonymously for the velocity v. Moreover, as described above, the limiting case is obtained for $\sigma_{2D} \rightarrow 0$. However, for simplicity the case is referred to $\sigma_{2D} = 0$.

Objectives and Parameters

The objective of the investigations is set on the comparison of the results obtained by the fully resolved cascade flow and the modeled ones for certain operating points. Therefore, two different cases are presented. Firstly, a case that corresponds to a forward flight of the propeller is chosen. In this case, a velocity boundary condition is set at the inlet of the domain. Secondly, a case for the determination of the static thrust of a related propeller is considered. The boundary condition at the inlet is set in this case to a pressure boundary condition. That leads to the results, that the velocity at the inlet of the domain is adjusted automatically by the produced thrust of the blades.

Before describing the set of parameters, some basic properties of the test case and its impact on the expected results are reviewed. This is necessary to justify the choice of certain prescribed input parameters as well as the chosen quantities for the discussion of the results.

Firstly, as described in the previous theory chapter, the propeller increases the total pressure across the propeller disc. The force generated by the propeller determines the amount of the increased total pressure downstream of the disc. Obviously, for an infinite thin disc, a discontinuity in the pressure profile along the direction of the propeller axis will arise. Secondly, the continuity equation has to be fulfilled. In particular, the latter has to be discussed for this test case in detail.
As stated above, the flow is considered to be incompressible. Therefore, the continuity equation in its integral and simplified form for the actual flow domain reads as follows

$$\int_{Inlet} v_{in} dx - \int_{Outlet} v_{out}\, dx + \int_{Per\ 1} u_{per,1} dy - \int_{Per\ 2} u_{per,2} dy = 0. \tag{3.3}$$

The applied periodic boundary conditions for this case establishes the velocity at a certain position y to be $u(y)_{per,1} = u(y)_{per,2} \neq C$, although they are allowed to vary in y-direction. Consequently, the last two terms on the left hand side of the equation are vanishing. The resulting equation is

$$\int_{Inlet} v_{in} dx = \int_{Outlet} v_{out}\, dx. \tag{3.4}$$

In general, the velocities at the inlet and the outlet for a certain position x are not equal $v(x)_{in} \neq v(x)_{out}$. However, it can be stated that the averaged velocities or the mass flow rate have the same amount at the inlet and the outlet. Furthermore, it can be assumed that if $l_{IO}$is large enough, the influence of the airfoil on the velocities at the boundaries is negligible and as a consequence $v(x)_{in} = C$ and $v(x)_{out} = C$. In this case the local velocity equals the averaged velocity at the inlet as well as the outlet and has to be equal $v_{in} = v_{out}$. This is important to consider for the choice of the boundary conditions to not overdetermine the set of parameters of the system.

In the following, the momentum equation in the y-direction is reconsidered and written in simplified and reordered form as follows

$$\int_{Inlet} \rho v_{in} v_{in} dx - \int_{Outlet} \rho v_{out} v_{out} dx + \int_{Inlet} p_{in} dx - \int_{Outlet} p_{out} dx + T_{2D} = 0. \tag{3.5}$$

It has to be mentioned that compressibility and viscous effects are not taken into account. In addition, the periodic boundaries are not incorporated due to its designated properties. The thrust T_{2D} is the thrust acting on the propeller that is why the sign is changed. However, one can easily see that the propeller with positive thrust leads to an increase in static pressure or an increased velocity at the outlet. As outlined in the last paragraph, the velocity at the inlet and the outlet will be almost the same and therefore, the thrust causes mainly an increase in the static pressure at the outlet compared to the inlet for this test case.

Furthermore, the momentum equation in the x-direction written in simplified and reordered form reads as follows

$$-\int_{Inlet} \rho u_{in} v_{in} dx + \int_{Outlet} \rho u_{out} v_{out} dx + F_{x,2D} = 0. \tag{3.6}$$

Moreover, the periodic boundaries are not included according to its properties. The circumferential force $F_{x,2D}$ is the force acting on the propeller. Since the velocity at the inlet $u_{in} = 0$, the circumferential force $F_{x,2D}$ can be determined easily.

Consequently, for the evaluation of the forces acting on the blade, the momentum difference between inlet and outlet can be used as well. In addition, by substituting the thrust of the blade by the source term in the actuator disc or actuator line simulation, the presented procedure can be applied in the same way. The same considerations are valid for the circumferential forces also.

The properties of the governing equations applied to this setup allow some conclusions for the test cases.

- For the forward flight test case, applying a velocity at the inlet v_{in} establishes the mass flow through the domain. In this case the solver has to provide a static pressure at the inlet p_{in} that is smaller than at the outlet. The total pressure difference is determined by the propeller-specific parameters like the solidity, angle of incidence and translational speed of the blade. The prescribed parameters for this test case are in order to avoid an overdetermination of the parameters as follows:

    - Velocity at the inlet v_{in}
    - Static pressure at the outlet p_{out}

- For the static thrust test case, the total pressure at the inlet $p_{t,in}$ is set. Therefore, the velocity at the inlet v_{in} is part of the result. The propeller causes as well a difference in total pressure as described at the previous bullet point for the forward flight case. The prescribed parameters are therefore:

    - Total pressure at the inlet $p_{t,in}$
    - Static pressure at the outlet p_{out}

- As presented above, the averaged velocity at the inlet equals the velocity at the outlet $v_{in} = v_{out}$ for a sufficient large domain. Therefore, the pressure difference between inlet and outlet can be easily taken for determining the thrust, or at least for plausibility considerations. In analogy, the force in the translational direction can be established by the x-momentum equation in a simply manner.
- Since for the actuator disc simulation of the cascade, only one cell in x-direction is necessary, it can concluded that the inlet velocity v_{in} equals the velocity through the whole domain $v = v_{in}$. This point has to be kept in mind for setting the regions of the actuator disc.

- The behavior of the velocity u is different. Under the assumptions made, the velocity equals $u_{in} = 0$ upstream of the plane of the blades and downstream the additional x-momentum provided by the blade will lead to a velocity $u \neq 0$.

The quantities used for the comparison between the two methods are the forces produced by one single blade of the cascade. However, other quantities can be chosen due to its relation to each other as presented in detail. They will be used for additional proofs of the results only.

Since the general properties of the test case are presented, the parameter settings for the investigations are discussed. This includes beside the parameters associated with the test case itself, the parameters that are necessary for the AD and the AL modeling. The nondimensional parameters, which are of main interest for the test case, are the following:

- Angle of Incidence θ
- Solidity σ_{2D}
- Advance Ratio J
- Reynolds Number Re
- Mach Number Ma

The first two parameters (θ, σ_{2D}) are corresponding to the geometrical properties of the cascade. The advancing ratio J describes the kinematics of the blade relative to the flow and the last two parameters (Re, Ma) are related to the properties of the flow. Consequently, the spanned parameter space needed to be investigated can be large by considering all possible combinations. Therefore, a reduction of the parameter space is unavoidable. For this purpose, subspaces, which map the requirements for certain real-life applications of the method, have to be defined a priori. Furthermore, simplifications can be considered. For example, the angle of incidence θ can be combined with the advance ratio J resulting in the angle of attack α of the blade.
Nonetheless, the focus of the investigation is set on the influence of the solidity on the resulting forces, since the test case is well-suited for that. The loading of the blade is correlated to the angle of attack which allows the application of the above stated simplification. The Reynolds Number Re and the Mach Number Ma are varying within practical applications that is why the necessary input space has to include these two parameters usually.

The next step is the description of the parameters related to the modeling approach of the actuator disc. According to the previous theory chapter, the actual implemented modeling method requires a defined region for calculating the inflow quantities as well as for inserting the specific forces into the finite volume method domain. These quantities are:

- AR_c: Axial position of the center of the region for determining the inflow conditions
- AR_w: Width of the region for determining the inflow conditions
- AR_s: Width of the smoothing region for determining the inflow conditions
- SR_c: Axial position of the center of the region for distributing the forces
- SR_w: Width of the region for distributing the forces
- SR_s: Width of the smoothing region for distributing the forces

The first parameters (AR_c, AR_w, AR_s) are used to determine the inflow conditions, while the last parameters (SR_c, SR_w, SR_s) are parameters for distributing the action of the propeller to the appropriate finite volumes. The position of the center of the region for distributing the forces SR_c is

set to the position of the corresponding quarter-chord point of the airfoil in the fully resolved simulation. The influence of this position is not investigated.

As stated in the paragraph concerning the distinct properties of this test case above, the velocity v through the cascade for the actuator disc simulation is constant. That means that the position of the region for the averaging of the inflow conditions AR_c has no influence. Nevertheless, since the velocity u is changed due to the action of the blade on the fluid, the position AR_c, the width AR_w, and the smoothing width AR_s of the averaging region relative to the position SR_c, width $SR_w$and smoothing width SR_s used for the source term distribution becomes important.

Therefore, an easy example based on the description in the theory chapter is given. Considering a resulting velocity profile like a Heaviside function. Obviously, the average value will be different if the center of the averaging region is set at the position $AR_c = 0$ or at one side $AR_c < 0 \,||\, AR_c > 0$ of the jump. For this example, it means that a position of the center left of the discontinuity will lead to smaller average values and right of it to larger ones. For arbitrary functions, the parameters of the averaging region have an influence as well. In particular, if the distribution function for the sources which is introduced in the theory chapter is applied, the resulting velocity profile differs from the Heaviside function. In this case, the properties of the averaging function are important also.

The extension of the parameters used for the actuator disc to the actuator line is straightforward by adding one dimension as described in the theory chapter. The parameters therefore read as follows and will not be further discussed within this subchapter:

- $AR_{c,x}$, $AR_{c,y}$
- $AR_{w,x}$, $AR_{w,y}$
- $AR_{s,x}$, $AR_{s,y}$
- $SR_{c,x}$, $SR_{c,y}$
- $SR_{w,x}$, $SR_{w,y}$
- $SR_{s,x}$, $SR_{s,y}$

Conclusively, within this test case, the focus is set on the influence of the interactional effects of the blades within the cascade for certain flow conditions. Therefore, the variation of the solidity for different advance ratios and pitch angles is of major importance. Although, the local flow conditions around the blade are depending on the Mach number Ma and Reynolds number Re, these parameters are set constant within this investigation. It is clearly evident that the latter parameters change the local effects and the resulting lift and drag of the blade, and as a consequence, the wake of the blade. That is why a combination of these parameters is chosen which provides a solution with a comparable local behavior of the flow around the blade for the resolved and modeled method.

3.2 Mesh Generation and Numerical Setup

In the following, the blocking and meshing approaches for the different methods are described. At first, the simulation setup for the resolved blades is presented. In the following, the actuator disc and actuator line approach combined with PanBL are explained and finally, the combination with the two-dimensional CFD for obtaining the airfoil data is provided.

Resolved Propeller

In Figure 29, the blocking strategy for the resolved simulations is shown. The airfoil is surrounded by an O-grid due to its finite trailing edge. In order to realize the different periodic lengths of the domain and consequently different solidities, a block is inserted at the left side of the domain which can be easily extended. Due to the periodic boundary condition, there will be logically no difference if this block is located upstream or downstream of the airfoil, in particular, since a one-to-one connection of the related nodes of each side of the periodic face is established. This means that each node of the one side of the periodic condition has a vertically equally positioned node on the other side. The accuracy of the results of a one-to-one connection has been compared to a general interface without matching nodes. It has been found out that the pressure gradients at the interfaces are represented correctly for a one-to-one connection, while it is not necessarily fulfilled for non-matching nodes at the boundaries. Figure 29 (left) shows the whole domain for the simulation of a solidity of $\sigma_{2D} = \frac{1}{9}$. In Figure 29 (right) the O-grid and the region near the airfoil is detailed. There are visualized the main blocks, while the additional block is cut on the left side of the figure. Furthermore, it is visible that the domain is designed for solidities less than $\sigma_{2D} \leq \frac{1}{3}$. Higher solidities are not considered, since the modeling aims on propeller configurations and not on fans. It is a matter of fact that for propeller configurations with a high number of blades even higher solidities can occur near the spinner, but the amount of the forces and moments produced in this region is small compared to the overall performance. Moreover, in this region several three-dimensional effects that cannot be covered with these modeling approaches occur anyway.

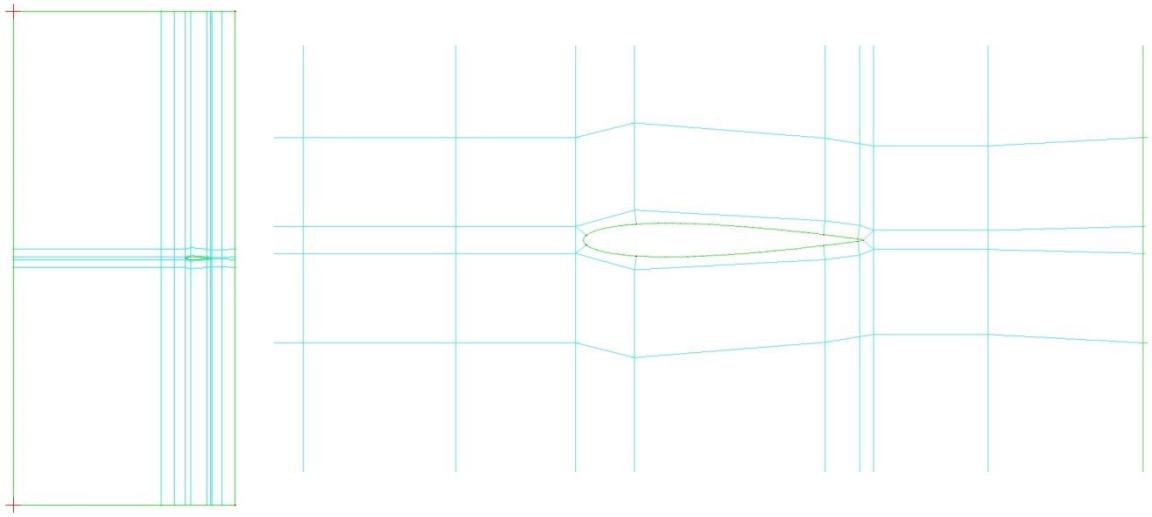

Figure 29: Blocking for the resolved cascade simulation. Blocking of the whole domain for a solidity of $\sigma_{2D} = \frac{1}{9}$ (left) and detailed blocking around the airfoil (right).

The different settings for the angle of incidence of the airfoil are easily performed by applying the mesh-deformation method presented in the chapter 5.3. It is not described within this chapter, since it is used only as a tool for the rotation of the airfoil and the deformation of the adjacent cells of the mesh within this application. Nevertheless, in Figure 30 the original (left) as well as a deformed mesh (right) of this setup is shown exemplarily.

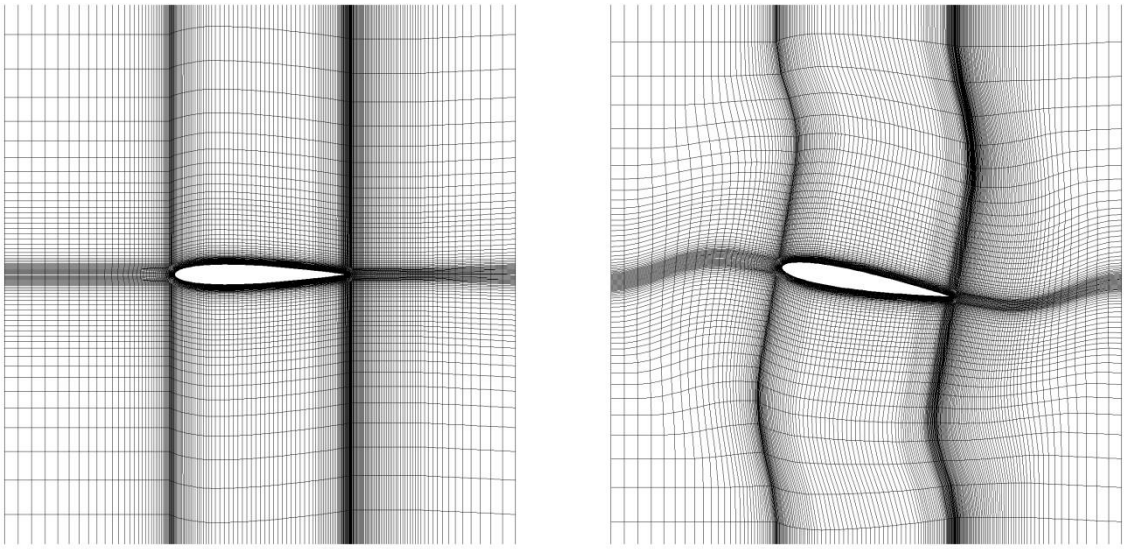

Figure 30: Mesh for the resolved simulations. Initial mesh (right) and rotated airfoil with deformed mesh (right).

In order to proof the independence of the obtained results on the mesh, a mesh independency study is performed. The initial mesh for the fully resolved simulations includes 46 blocks with 40942 cells. These values are for the mesh with a solidity $\sigma_{2D} = \frac{1}{3}$. The number of cells along the chord of the blade is 118. The first cell of the boundary layer is set in order to fulfill a nondimensional wall distance of $y^+ < 1$. The O-grid blocks adjacent to the airfoil are therefore designed to have 80 cells in the direction perpendicular to the surface with a size of $1 \cdot 10^{-5} m$ for the first cell along this direction. That is necessary, to resolve the linear behavior within the viscous sublayer of the boundary layer appropriately. Consequently, the application of a wall function in not required.
In the following, one refined and one coarsened mesh is generated. Respectively, a scaling factor of 1.4 and $\frac{1}{1.4}$ is applied. The initial scaling at the surface of the airfoil is not modified. The quantity of the mesh independency study to be evaluated is the thrust coefficient as well as the circumferential force coefficient of the airfoil.

Prior to the discussion of the results of the mesh independency study, the solver settings are described briefly. As presented above, the flow is considered to be incompressible and steady. Consequently, the two-dimensional, planar, pressure-based, coupled solver is applied for solving the problem. For the velocity formulation, the absolute option is set. The energy equation is not solved within this investigation. The turbulence modeling is performed by the shear-stress transport (SST) turbulence model. The density of the fluid is set to $\rho = 1.225\ kg/m^3$, while the dynamic viscosity reads $\mu = 1.225 \cdot 10^{-5}\ kg/(m\ s)$. The resulting kinematic viscosity is $\nu = 1 \cdot 10^{-5}$. The gradients are evaluated by a least squares cell based method. The second-order pressure discretization scheme is applied. The momentum equations are discretized by the second-order upwind scheme. For the turbulent kinetic energy as well as the specific dissipation rate, first-order upwind schemes are

applied. The set flow Courant number varies between the different simulations. Since the periodic length of the domain l_{per} depends on the solidity, different scales of the Courant number might be necessary due to the variation in the length of the domain. Furthermore, certain angles of attack will show less stable solutions with too high flow Courant numbers. Consequently, the Courant number is adopted for each of the simulations in the range of $5 < C < 100$. The relaxation factors are shown in Table 1. The convergence criteria for all quantities to be solved are set to $1 \cdot 10^{-6}$.

Table 1: Relaxation factor for the resolved propeller simulations of the two-dimensional test case.

Explicit-Relaxation Factors and Under-Relaxation Factors					
Momentum	Pressure	Density	Turbulent Kinetic Energy	Specific Dissipation Rate	Turbulence Eddy Viscosity
$0.1 < \alpha_{mom} < 0.5$	$0.1 < \alpha_p < 0.5$	$\alpha_{den} = 1.0$	$\alpha_{tke} = 0.8$	$\alpha_{\omega} = 0.8$	$\alpha_{\nu_t} = 1.0$

The mesh independency study is performed for the operating point $(J, \sigma_{2D}, \alpha) = \left(0.25, \frac{1}{3}, 5.0°\right)$. This represents a case with strong interaction of the blades and a moderate blade loading. Table 2 provides the thrust and circumferential force coefficient for the three meshes. As it is visible, the deviation between the values even for the course related to the fine mesh is far less than 1%. Nevertheless, the initial grid is taken for the generation of the validation results.

Table 2: Mesh independency study for the resolved simulation of the two-dimensional test case.

	Coarse grid	Initial grid	Fine grid
$C_{T,2D}$	0.492	0.493	0.493
$C_{Fx,2D}$	0.053	0.053	0.053

Actuator Disc Approach with PanBL

For the comparison of the actuator disc (AD) approach coupled with PanBL (AD-PanBL) with the fully resolved cascade, in general, the mesh resolution as well as the applied numerical settings shall be comparable. That is why for the actuator disc simulation a similar mesh resolution in the region of the imaginary blade and its wake is chosen. Considering the properties of this test case for the actuator disc in detail, it can be easily seen that one cell in the circumferential direction of the imaginary blade is sufficient if periodic boundary conditions are used. This results out of the fact that in the circumferential direction of the imaginary airfoil movement, no variation of the forces can be obtained, caused by the averaging procedure within the actuator disc model along the circumferential direction. The periodic length for the one cell in the circumferential direction is set to $l_{per} = 1$. The setting of the solidity is done solely within the calculation as a numerical parameter. The resulting flow field is the same as modifying the periodic length by B, but without generating meshes for each value of the solidity. The procedure for generating the periodicity is equal as for the resolved simulation. The variation of the underlying angle of incidence is performed within the calculation of forces also.

The mesh independency study for the actuator disc simulation is performed in one dimension only. This is obviously sufficient, caused by the periodic boundary condition and one cell only in the

circumferential direction of the blade. The initial mesh consists of 4 blocks with 200 cells. The blocking strategy is shown in Figure 31 (left). In Figure 31 (middle), the distribution of the cells of the mesh is presented. In the region of the actuator disc, a constant spacing of $1 \cdot 10^{-2}\ m$ is applied. Therefore, Figure 31 (right) details the region were the actuator disc acts. In general, the refined region has not to be that fine as well as that large for the actuator disc simulation. However, it is made to allow for investigating different parameters of the actuator disc approach on a part of the mesh with equally distributed cells. Subsequently, a finer and a coarser mesh is generated with a scaling factor of 2 and $\frac{1}{2}$, respectively. The initial scaling is modified in this case as well. The quantities for the comparison of the different mesh resolutions for the actuator disc approach are as well the thrust and circumferential force coefficient as presented for the resolved simulation. However, since for the AD modeling, the mesh resolution is coupled with the modeling parameters of the AD, the results are not provided in this section. A discussion concerning this aspect is presented while analyzing the influence of the modeling parameters in chapter 3.3.

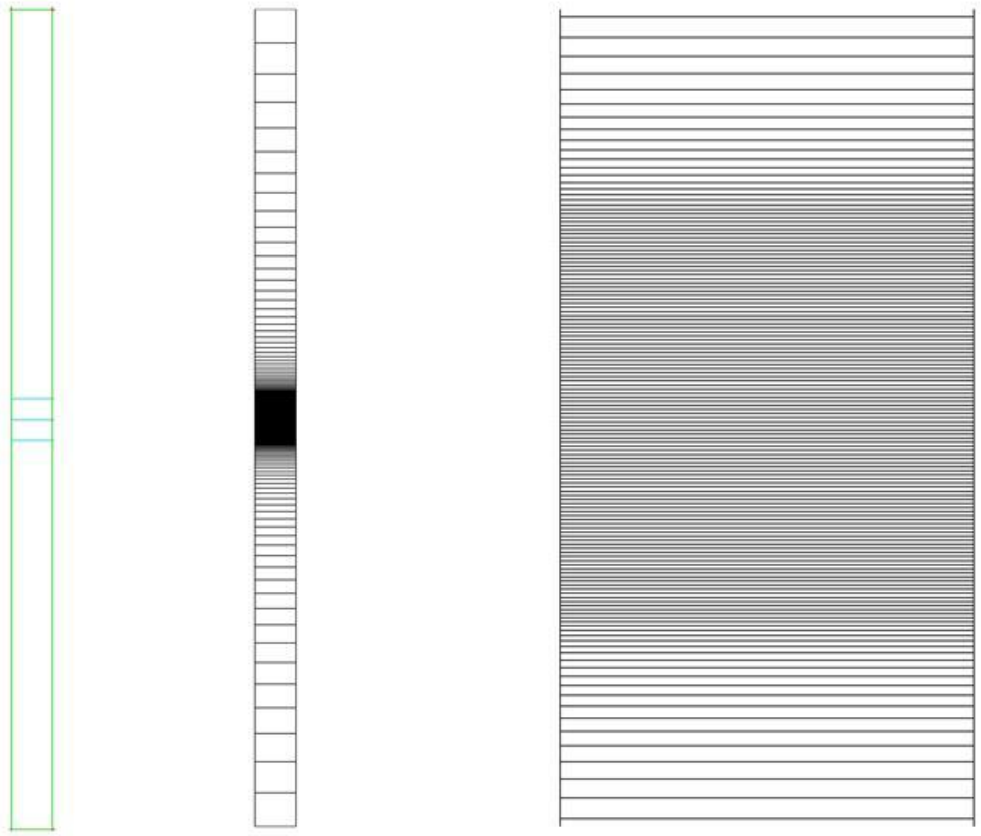

Figure 31: Blocking strategy for the actuator disc (left). Whole mesh for the actuator disc simulation with refinement in the actuator region (middle) and detailed view of the actuator region (right).

The chosen numerical schemes and models are the same as for the resolved configuration. Moreover, for the actuator disc simulation with the smaller periodic length of $l_{per} = 1\ m$, the Courant number C has to be reduced to ensure fast, or in special cases at least convergence. The convergence criteria for all quantities to be solved are set to $1 \cdot 10^{-6}$.

Actuator Line Approach with PanBL

The blocking strategy and the mesh setup for the actuator line (AL) approach coupled with PanBL (AL-PanBL) are based on those of the resolved simulation. In contrast to the actuator disc approach, it is not possible to use one cell only in the direction of motion of the imaginary moving blade. The reason is that the actuator line provides a non-constant distribution along the circumferential direction. However, the periodic boundary condition is applied in the same way as for the previous presented approaches. The setting of the solidity is made by the definition of the periodic length l_{per} of the domain, while the angle of incidence is set within the calculation of forces as a numerical parameter.

The difference in the blocking strategy between the resolved simulation and this approach is attributed to in the blocks in the region of the airfoil which are substituted by a Cartesian grid block. Within this investigation, the choice of the Cartesian grid is justified to reduce the influence of the mesh on the results in the region of the actuator line representation. Figure 32 (left) shows the blocking strategy for this approach. The global view of the mesh is presented in Figure 32 (middle), while in Figure 32 (right), a detailed view of the region containing the actuator line is presented.

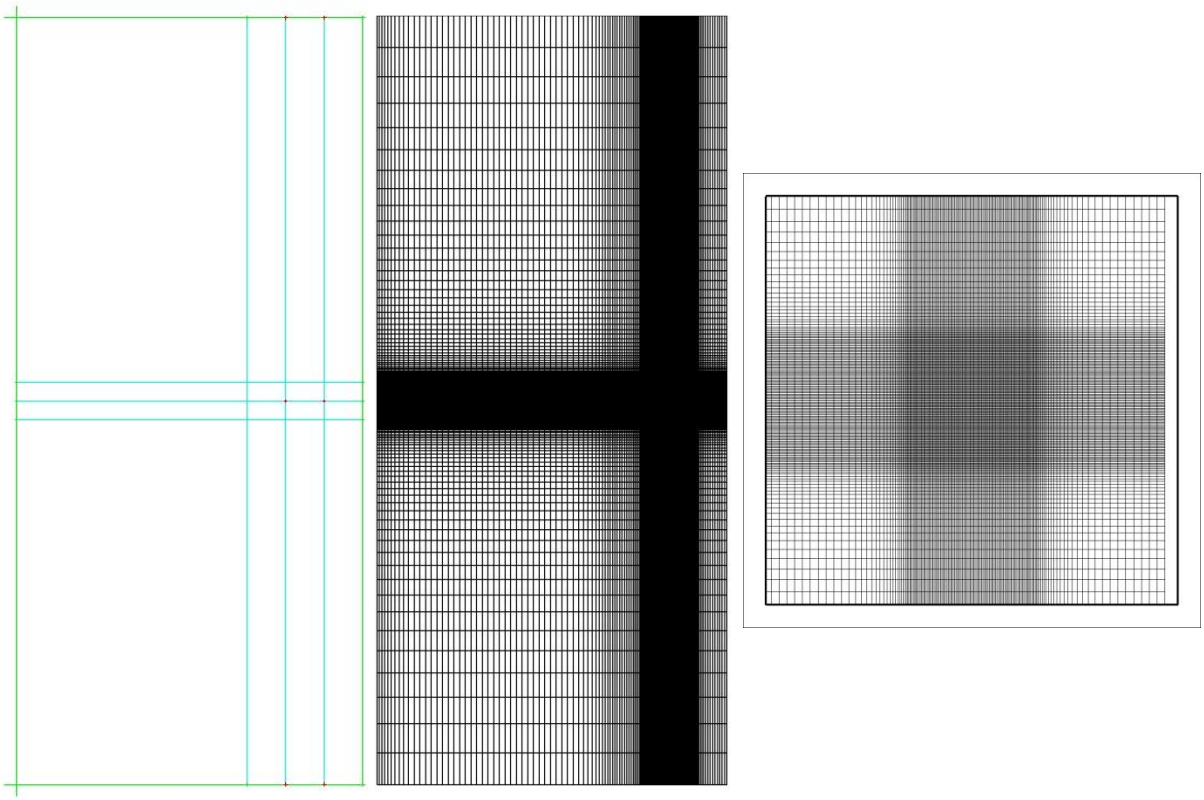

Figure 32: Blocking strategy for the actuator line (left). Whole mesh for the actuator line simulation with refinement in the actuator region (middle) and detailed view of the actuator region (right).

The mesh independency study for this test case is made with three different meshes. However, a scaling in both coordinate directions in the same way as for the resolved cascade simulations is conducted. The initial mesh for $\sigma_{2D} = \frac{1}{3}$ includes 12 blocks and 30800 cells. The resulting resolution in the region of the actuator line is $10\ mm$. Figure 32 (right) shows the mesh in the described region.

The refined and coarsened mesh is obtained by a scaling with a factor of 1.4 and $\frac{1}{1.4}$ in each coordinate direction, respectively. Therefore, the evaluated quantities are like for the other methods the thrust and circumferential force coefficients. For the AL simulation, the statement made for the AD simulation concerning the coupling of mesh resolution and modeling parameters is valid as well. Consequently, the analysis of the mesh resolution is shifted to the discussion of the influence of the parameters on the results in chapter 3.3.

Finally, the settings of the numerical schemes and models are chosen as for the resolved simulation with certain operating-point-dependent modifications of the Courant number.

Actuator Disc Approach with 2D-CFD

As described in the theory chapter, this approach is a combination of the actuator disc and the resolved simulation of a blade in two dimensions. Within this simplified two-dimensional test case, the actuator disc mesh and the resolved cascade mesh are taken as they are. Consequently, the mesh independency study for this simulation has no to be presented, since the results are already included within the description of the other test cases before. Nevertheless, the combination of the meshes for this setup is described briefly. Therefore, Figure 33 shows the meshes of the domains used for the calculation. On the left hand side, the actuator disc domain is represented, while in the domain on the right hand side, the resolved airfoil is embedded. For the actuator disc domain, the periodic mesh of the AD-PanBL simulation is applied, except for the solidity of $\sigma_{2D} = 0$. For that solidity, by definition, no feedback into the AD domain is performed. In this case, the finite force generated by the airfoil is distributed over the imagined infinite periodic length l_{per}. The source in the AD domain obtains the limiting value of zero. It is noted, that the latter behavior is valid for the AD coupled with PanBL as well. For the simulation of the airfoil section, the resolved airfoil mesh is taken. It has to be noted that the mesh for the stand-alone airfoil has to be chosen therefore. Consequently, velocity inlet and outlet boundary conditions are chosen. Moreover, the deforming mesh capabilities are used for describing the appropriate angle of incidence of the airfoil section. The solidity is set within the force calculation like for the AD-PanBL simulations.

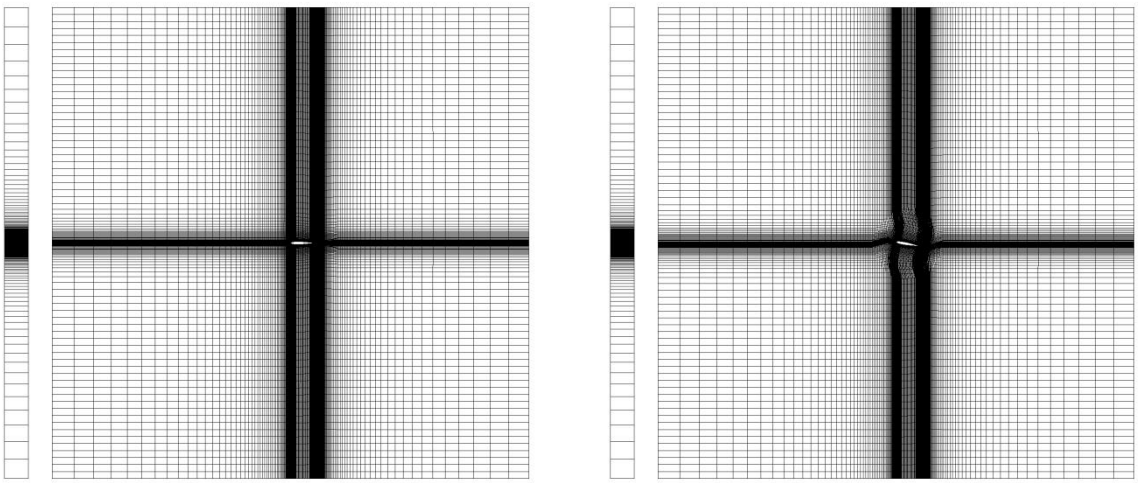

Figure 33: Mesh for the actuator disc approach coupled with 2D-CFD in its initial state (left) and with rotated airfoil (right). For each state, on the left hand side the AD disc domain is shown while at the right hand side the resolved airfoil domain is presented.

The numerical setup and models are taken from the basic cases as well. Nevertheless, some adjustments are necessary in order to obtain a fast, stable, and converging solution. Since the solution is performed within one Fluent task, the same global Courant number is applied for both domains. Furthermore, due to the diverging scales of the domains, in particular in the circumferential direction, the updating of inflow conditions and the sources in the corresponding domain, can lead to oscillations. For example, in Figure 33 is the length of the AD domain set to $1\,m$. The length measured from the inlet to the leading edge of the airfoil in the resolved domain is greater that $10\,m$. The velocity at the inlet of the resolved domain is established by the averaging process executed in the AD domain. Consequently, the velocities are in the same order of magnitude. With the same Courant number and comparable velocities, the propagation of the updated inflow velocities to the position of the airfoil in the resolved domain causes higher numbers of iterations. Consequently, the forces fed back into the AD domain by source terms are delayed in terms of iterations, regarding the change of the inflow conditions. To avoid the declared issue, different updating schemes for forces and inflow conditions in the corresponding domain are executed. For example, the forces or inflow conditions of the corresponding domain are updated only if local convergence is achieved for the previously updated states. In addition, a non-linear relaxation factor has been implemented to limit the maximum change per iteration. The convergence criteria for all quantities to be solved are set to $1 \cdot 10^{-7}$.

Another possibility to avoid this issue is to change the angle of attack by modifying the angle of incidence of the blade with the deforming mesh routine at each updating step. In this case, the delay due to the propagation through the domain is vanished, since the inflow conditions remain in its initial state. The disadvantage is that besides the angle of attack, the magnitude of the velocities changes. Therefore, the inflow velocity has to be changed as well, or the frame motion has to be invented. Although all of these procedures are already included in the framework of Fluent in combination with the UDFs written at AER, the method is not applied here. The convergence is good, even with the updating schemes presented above. Nevertheless, for further improvements and in particular for speeding-up the simulation runs, the method has to be taken into account.

Actuator Line Approach with 2D-CFD

This approach is the straightforward extension of the previous presented combination from the actuator disc to the actuator line. The existing meshes are used as well and therefore, the mesh independency study is not presented as discussed above. Figure 34 shows exemplarily the meshes of the domains used for the calculation. The setup is depicted for a solidity of $\sigma_{2D} = \frac{1}{9}$. On the left hand side, the actuator line domain is shown and on the right hand side, the resolved airfoil domain is presented. The periodic boundary condition is used for the actuator line domain except for $\sigma_{2D} = 0$ as well. However, for the latter mentioned solidity, the source terms are fed back into the AL domain in contrast to the AD approach. Furthermore, since the distribution region is finite in both coordinate directions, a non-zero source term is generated. The velocity inlet and pressure outlet is used for the resolved airfoil domain. The solidity is set with the periodic length of the AL domain and the angle of incidence set with the mesh-deformation routine in the resolved airfoil domain. For the solidity of $\sigma_{2D} = 0$, the inlet and outlet boundary condition is applied for the AL domain instead of the periodic boundary conditions.

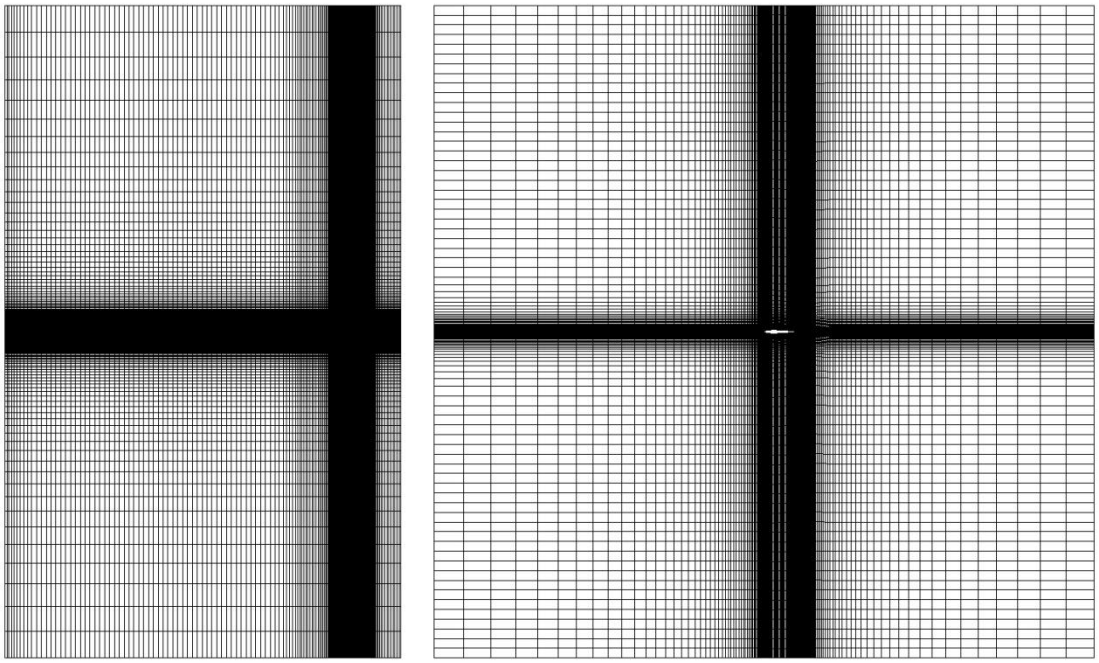

Figure 34: Mesh for the actuator line approach coupled with 2D-CFD. On the left hand side the AL domain is presented, while on the right hand side the resolved airfoil domain in its initial state is shown.

The numerical setting and models are taken as well from the basic cases. For this simulation, the scales of the domain are also strongly varying. Apparently, due to the larger extension of the AL domain compared to the AD domain in the previous description, the convergence is better. For this investigation, the update schemes have to be applied as well; however, the number of iteration for local convergence is less. The non-linear relaxation factor is not applied within these investigations. The convergence criteria for all quantities to be solved are set again to $1 \cdot 10^{-6}$.

3.3 Results and discussion

In the following, the results for the simulations concerning the variation of the solidity σ, the angle of attack α and the advance ratio J are discussed. The investigation is, at first, performed for the resolved cascade to clarify the general effects appearing within the test case. Therefore, the thrust and the circumferential forces are presented. The further steps are to evaluate the quality of each of the presented modeling approaches for certain model parameters. Finally, an overall comparison of the approaches and conclusions are provided.

In order to obtain dimensionless coefficients, the following definitions are applied. It has to be noted that the definition of the coefficients within this investigation differs from the common notation for propeller investigations. The forces are considered only for one single blade. Furthermore, the definitions are made in two-dimensional space.

Two-dimensional thrust coefficient of a blade:

$$C_{T,2D} = \frac{T_{2D}}{\frac{1}{2}\,\rho\, v_{rel}^2\, c} \tag{3.7}$$

Two-dimensional circumferential force coefficient of a blade:

$$C_{Fx,2D} = \frac{F_{x,2D}}{\frac{1}{2}\,\rho\, v_{rel}^2\, c} \tag{3.8}$$

Advance ratio:

$$J = \pi \cdot \frac{v}{u} \tag{3.9}$$

Segment loading:

$$SL = \frac{T_{2D}}{l_{per}} = \frac{T_{2D}}{c}\sigma_{2D} \tag{3.10}$$

The advance ratio is defined including the π, in order to be consistent with the definition of J for propellers and consequently, obtaining comparable inflow angles for certain values of J.

Relative deviation of force coefficients between two certain solidities:

$$\Delta C_{i,2D,rel,\sigma}(\alpha, J) = \frac{C_{i,2D}\left(J, \sigma_{2D,1}, \alpha\right) - C_{i,2D}\left(J, \sigma_{2D,2}, \alpha\right)}{C_{i,2D}\left(J, \sigma_{2D,1}, \alpha\right)}, with\ i = \{T, Fx\} \tag{3.11}$$

This relative deviation is analyzed to quantify the influence of the solidity on the forces. The value is chosen instead of the derivative of the forces with respect to the solidity, since within this investigation mainly the deviation between the highest and smallest solidity is of interest.

Resolved Propeller

At first, the results for the forward flight test case are presented. Therefore, the set of the advance ratio is $J = \{0.25, 0.5, 0.75\}$. Since the influence of the solidity on the forces generated by the cascade is of main interest within this investigation, the two-dimensional solidity is the dependent variable. The computed values of the solidity are $\sigma_{2D} = \left\{\frac{1}{3}, \frac{1}{6}, \frac{1}{9}, \frac{1}{12}, \frac{1}{25}, 0\right\}$. In addition, the angles of attack $\alpha = \{0.0°, 2.5°, 5.0°, 7.5°\}$ are applied to obtain results for different blade loadings. In Figure 35, the two-dimensional thrust and the circumferential force coefficient of a single blade depending on the solidity are presented. The advance ratio J is varied ascending from Figure 35 (top) to Figure 35 (bottom) and each curve represents an angle of attack.

The influence of the solidity and the angle of attack on the force coefficients is discussed starting with an advance ratio of $J = 0.25$. It can be seen that the thrust as well as the circumferential force coefficient has a distinct dependence on the solidity, in particular, with increasing angles of attack. The reason for the reduction of the forces with higher solidities σ_{2D} relies in the interaction of the blade with the wake flow of the upstream blades. Obviously, the smaller the distance between two blades, corresponding to higher solidities, the greater is the reduction of the forces at the downstream positioned blade. The reason is the modified inflow condition of the blade. Moreover, the higher the angle of attack, the higher is the lift of the blade. Subsequently, the greater is the deflection of the flow downstream of the blade also. Consequently, the more pronounced is the effect of the solidity for higher angles of attack. For an angle of attack of $\alpha = 0°$, almost no influence can be detected. In this case, the dominating effect responsible for generating the wake flow is introduced by the friction of the airfoil. Therefore, the force vector is aligned with the inflow velocity vector and as a result, the flow in the wake of the blade is not deflected. This can be seen in Figure 35 for the point $(J, \sigma_{2D}, \alpha) = (0.25, 0, 0°)$. In contrast, for higher solidities the thrust coefficient gets smaller $C_{T,2D}\left(0.25, \frac{1}{3}, 0°\right) < C_{T,2D}(0.25, 0, 0°)$ although the global inflow conditions are the same. This effect is explained by the effective inflow conditions of the blade. For an advance ratio of $J = 0.25$, the inflow angle equals $\phi = 4.55°$. The angle of incidence is set to $\theta = 4.55°$ to obtain the required undisturbed angle of attack $\alpha = 0°$. Along the direction of the chord line upstream, the adjacent blade upstream is located on the left hand side while the adjacent blade downstream is located on the right hand side. In this case, the asymmetric blocking effects due to the blade and its wake are sufficient to change the local inflow condition that the produced lift, and subsequently the thrust, becomes slightly negative. The effect is more pronounced the higher the solidity. Due to the contribution of the lift to the circumferential force, the latter is as well decreasing for higher solidities. Considering higher angles of attack, this effect is still valid. The reaction of the thrust deflects the fluid downstream of the blade downwards which amplifies the reduction of thrust. In general, the similarity of the slopes of the thrust and the circumferential force is explained by the dominating fraction of the lift to the circumferential force also. Since even for an angle of attack of $\alpha = 2.5°$, the fraction of the lift acting in circumferential direction dominates the drag of the airfoil.

In order to get a more quantitative representation of the behavior, the relative deviation $\Delta C_{i,2D,rel,\sigma}$ between the quantities for $\sigma_{2D,1} = 0$ and $\sigma_{2D,2} = \frac{1}{3}$ related to the result for $\sigma_{2D,1} = 0$ are provided. The relative deviation of the thrust coefficients for the respective set of angles of attack $\alpha = \{0.25°, 0.5°, 0.75°\}$ read $\Delta C_{T,2D,rel,\sigma} = \{5.06\,\%, 8.25\,\%, 12.22\,\%\}$. The angle of attack of $\alpha = 0°$ is intentionally not shown, since the absolute value is too small for useful results after

normalization. Consequently, the trends could not be shown representatively. However, the above described reduction is well visible. The corresponding relative deviation of the circumferential force coefficients are $\Delta C_{Fx,2D,rel,\sigma} = \{3.04\ \%, 4.12\ \%, 6.00\ \%\}$, which shows the same trend.
The global behavior of the forces for the advance ratios of $J = 0.5$ and $J = 0.75$ is similar as for those of the advance ratio of $J = 0.25$. Nevertheless, differences are present. Due to the rotation of the inflow vector for different advancing ratios, the thrust as well as the circumferential forces is changed. In the present test case, the corresponding inflow angles for advance ratios of $J = \{0.25, 0.5, 0.75\}$ are $\phi = \{4.55°, 9.04°, 13{,}43°\}$. Consequently, for the applied advance ratio range, the impact of the rotation is mainly detectable for the circumferential force. Considering exemplarily the ratio of the thrust coefficients $\frac{C_{T,2D}(0.75,0,7.5°)}{C_{T,2D}(0.25,0,7.5°)} = 0.97$ and the ratio of the circumferential force coefficients $\frac{C_{Fx,2D}(0.75,0,7.5°)}{C_{Fx,2D}(0.25,0,7.5°)} = 2.57$, the statement is proofed. Furthermore, the slopes of the forces depending on the solidity are getting steeper with higher advance ratios. This indicates a stronger interaction of the blade with the adjacent blades and the corresponding wake flows.
Before providing a more detailed explanation of the occurring effects, the quantitative analysis for the remaining advance ratios $J = 0.5$ and $J = 0.75$ is presented. Therefore, the relative deviation of the thrust and circumferential coefficient is calculated as for the advance ratio of $J = 0.25$ in one of the preceding paragraphs. The set of angles of attack is as well $\alpha = \{0.25°, 0.5°, 0.75°\}$. For a better structuring, the results for all advance ratios are summarized in Table 3. Obviously, the results coincide with the above made statements. However, one interesting point is that the relative deviation of the thrust coefficient depending on the angle of attack is increasing stronger the higher the angle of attack. For the circumferential force coefficient that behavior is observed just for the advance ratios of $J = 0.25$ and $J = 0.50$, while for $J = 0.75$ a local minimum at $\alpha = 5.0°$ is detected. The increase of the deviation of the force coefficients depending on the advance ratio, however, is almost constant.

Table 3: Relative deviation of the thrust and circumferential coefficient for the resolved simulation.

J	$\Delta C_{T,2D,rel,\sigma}$			$\Delta C_{Fx,2D,rel,\sigma}$		
	$\alpha = 2.5°$	$\alpha = 5.0°$	$\alpha = 7.5°$	$\alpha = 2.5°$	$\alpha = 5.0°$	$\alpha = 7.5°$
0.25	5.06 %	8.25 %	12.22 %	3.04 %	4.12 %	6.00 %
0.50	11.43 %	12.72 %	15.67 %	8.27 %	8.50 %	9.97 %
0.75	16.81 %	16.81 %	19.12 %	13.31 %	12.69 %	13.73 %

Basically, the effective inflow conditions can be imagined as a combination of the effective inflow angle and the effective inflow velocity. However, to determine an appropriate inflow condition for a blade is not trivial. While the determination is still possible for a single blade, the complex flow field through a cascade including interactional effects, in particular for high solidities, do not allow this. Since the understanding of these effects is necessary for the modeling approach, the flow field is briefly discussed for two certain points. One point, for a single blade excluding mutual blade interaction $(J, \sigma_{2D}, \alpha) = (0.75, 0, 7.5°)$, and another one $(J, \sigma_{2D}, \alpha) = (0.75, \frac{1}{3}, 7.5°)$, for the highest obtained interaction within the investigated parameter field.

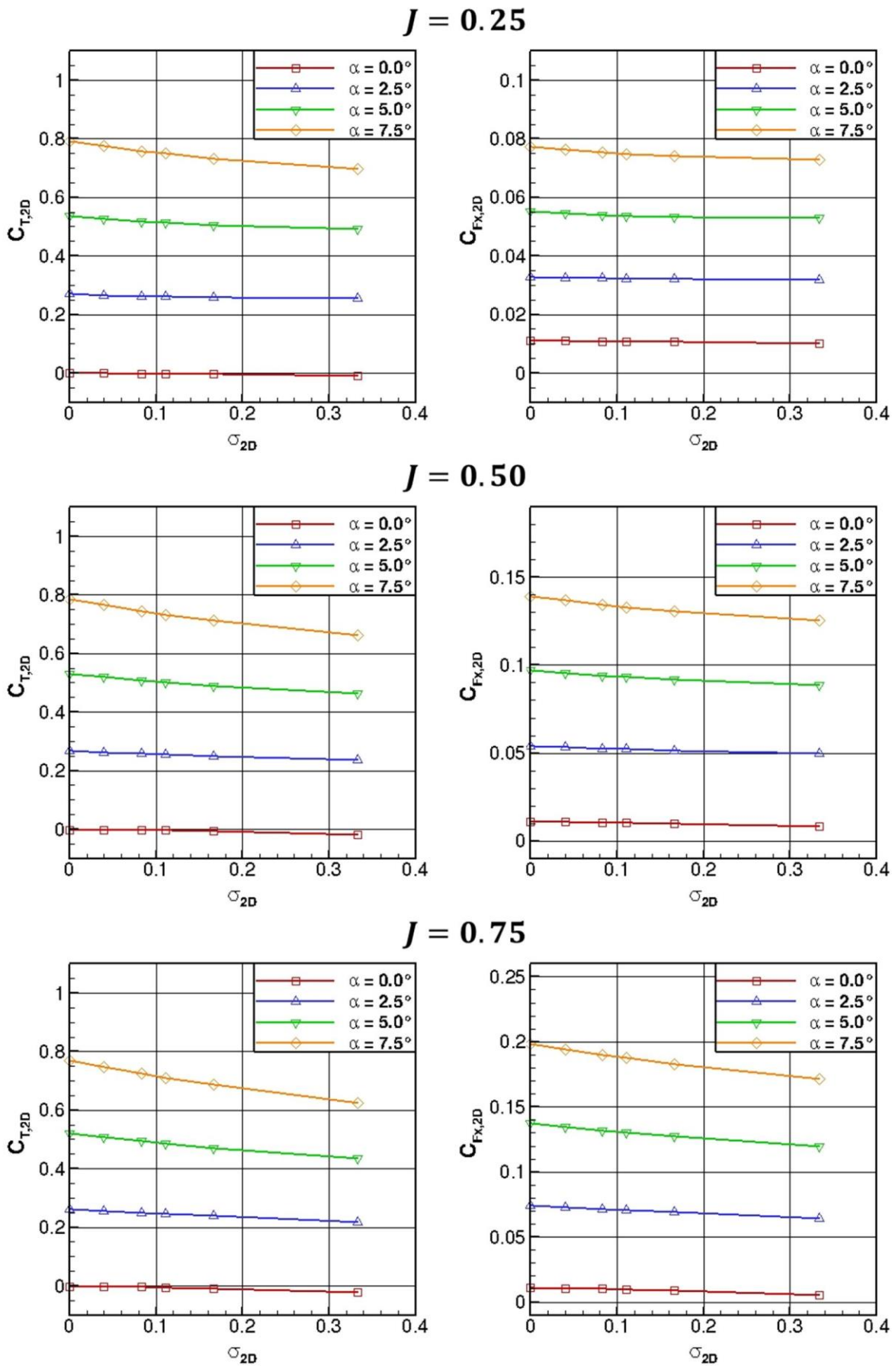

Figure 35: Two-dimensional thrust and circumferential force coefficient for one blade depending on the solidity. The advance ratio is set to $J = 0.25$ (top), $J = 0.5$ (middle), and $J = 0.75$ (bottom). Resolved.

In Figure 36, a contour plot of the normalized relative circumferential velocity is shown for the point $(J, \sigma_{2D}, \alpha) = (0.75, \frac{1}{3}, 7.5°)$ (top, left) and for the point $(J, \sigma_{2D}, \alpha) = (0.75, 0, 7.5°)$ (top, right) to present the qualitative behavior. For the quantitative discussion, three graphs (bottom) depict the relative circumferential velocity along the lines inserted in the contour plots. Considering the contour plot, the distinct behavior of the relative circumferential velocity across the blade row is well visible. The stand-alone airfoil without interaction generates only a small local disturbance in the relative circumferential velocity along the y-axis. For $y \to \pm\infty$, the disturbance in the velocity will almost vanish. In contrast, the flow field for the blade row with, in particular, high solidities shows two different velocities far upstream and far downstream of the blade row. The reduction of the relative circumferential velocity across the blade row is well visible in the graphs in Figure 36 (bottom). The velocity decreases almost monotonically for the case with interaction, globally. In addition to the global influence on the flow field, the wakes of the blades are detectable as well. The case without interaction shows only the mentioned local change in velocity.

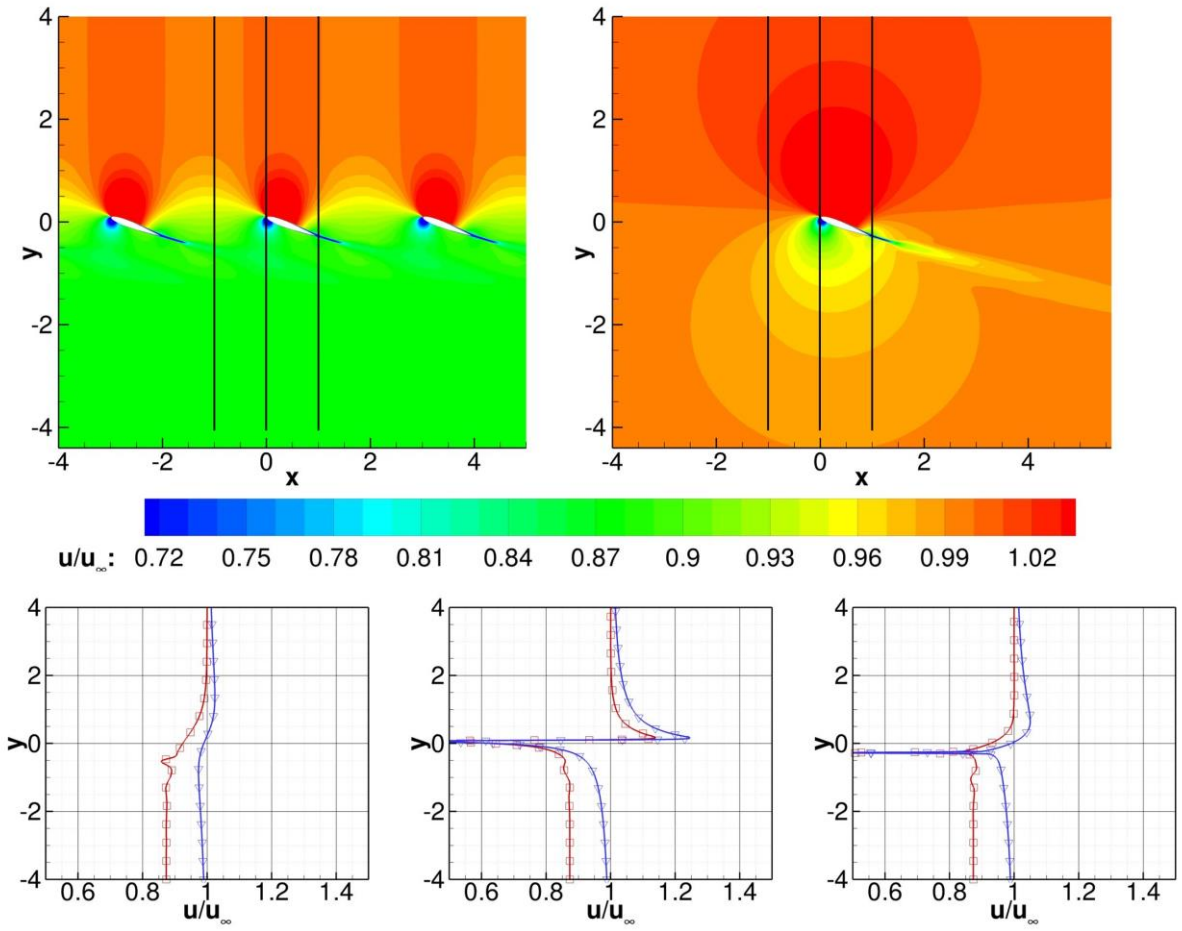

Figure 36: Contour plot of the normalized relative circumferential velocity for the operating points $(J, \sigma_{2D}, \alpha) = (0.75, \frac{1}{3}, 7.5°)$ (top, left) and $(J, \sigma_{2D}, \alpha) = (0.75, 0, 7.5°)$ (top, right). Graphs of the circumferential velocity along the lines inserted in the contour plot depending on the vertical direction (Bottom). Red line: $(J, \sigma_{2D}, \alpha) = (0.75, \frac{1}{3}, 7.5°)$, Blue line: $(J, \sigma_{2D}, \alpha) = (0.75, 0, 7.5°)$.

In Figure 37, a contour plot of the velocity v is shown for the point $(J, \sigma_{2D}, \alpha) = (0.75, \frac{1}{3}, 7.5°)$ (top, left) and for the point $(J, \sigma_{2D}, \alpha) = (0.75, 0, 7.5°)$ (top, right). Additionally, the graphs of the velocity along the inserted lines are presented (bottom). The biggest difference arises due to the periodic

boundary condition. As it is visible, for the stand-alone airfoil without interaction, downstream of the airfoil, the downwash of the latter has increased the magnitude of the axial velocity. For the periodic case, the flow velocity downstream and upstream of the blade is the same if the circumferential distance between two points for a constant vertical position equals $\Delta x = l_{per}$. Furthermore, due to continuity, the mass flux in vertical direction, related to the area obtained with the periodic length l_{per}, is constant. Consequently, in both cases, the velocity far upstream and downstream of the blade is equivalent in a global consideration. Moreover, the local change in the velocity is less for the higher solidity of $\sigma_{2D} = \frac{1}{3}$ caused by the fixed flux. As a remark, the influence of the wake of the upstream located blades is detectable as well for the latter solidity.

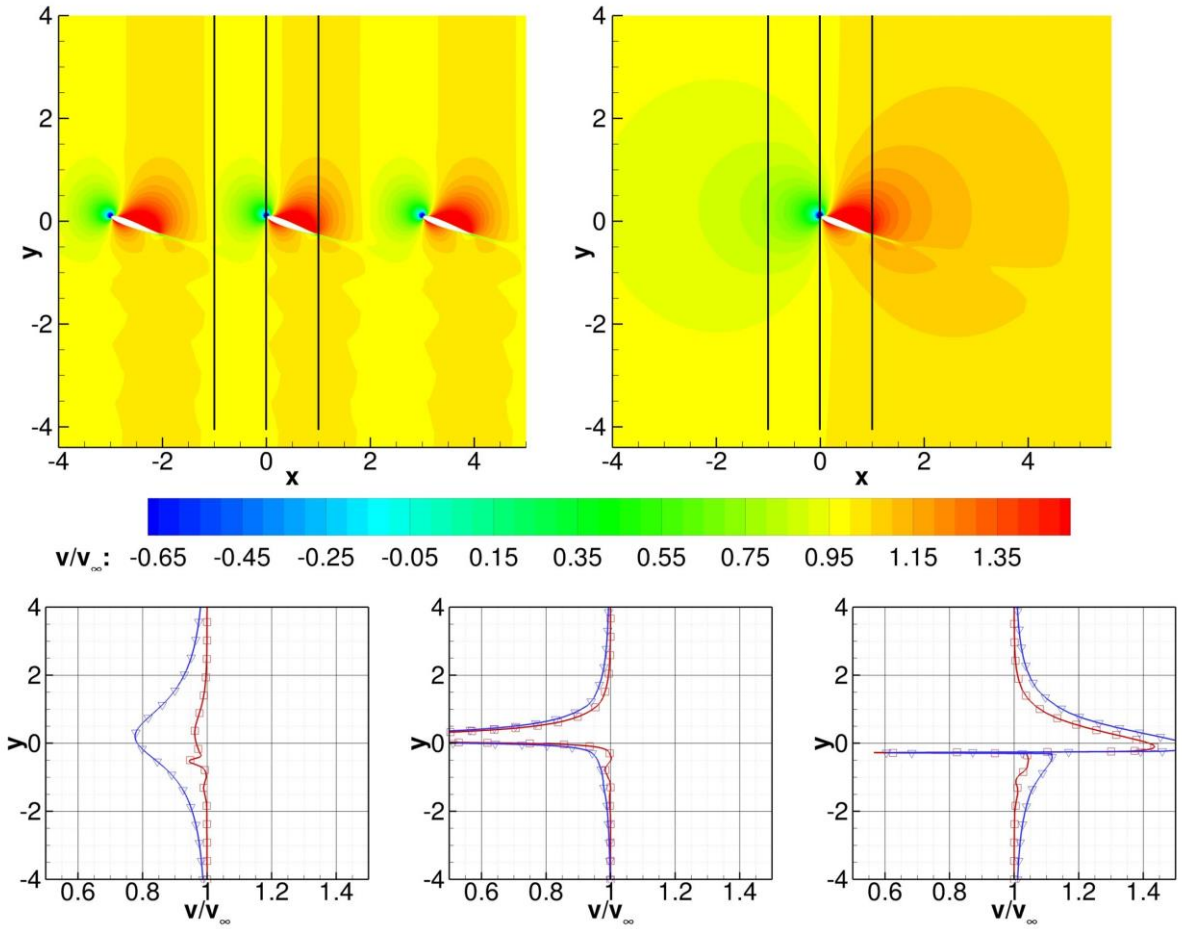

Figure 37: Contour plot of the normalized axial velocity for the operating points $(J, \sigma_{2D}, \alpha) = (0.75, \frac{1}{3}, 7.5°)$ (top, left) and $(J, \sigma_{2D}, \alpha) = (0.75, 0, 7.5°)$ (top, right). Graphs of the axial velocity along the lines inserted in the contour plot depending on the vertical direction (Bottom). Red line: $(J, \sigma_{2D}, \alpha) = (0.75, \frac{1}{3}, 7.5°)$, Blue line: $(J, \sigma_{2D}, \alpha) = (0.75, 0, 7.5°)$.

The next point to be discussed is the dependence of the forces on the angle of attack for different solidities. For this purpose, the thrust and circumferential force coefficient versus the angle of attack are shown in Figure 38. The advance ratio is chosen to be $J = 0.75$, since as presented above, the highest interaction is visible for this operating condition. The chosen solidities are $\sigma_{2D} = \frac{1}{3}$ and $\sigma_{2D} = 0$. Since the latter is imagined as a stand-alone airfoil, some statements can be made to explain the behavior. The applied symmetrical airfoil has a point-symmetric lift curve depending on

the angle of attack. The drag of the airfoil is non-linear. However, the lift of the airfoil dominates the drag for the shown angle of attack range by at least one order of magnitude. Consequently, the thrust polar is almost point-symmetric as well, since the fraction of the lift vector provides the dominating contribution to the thrust for the chosen advancing ratio. For the circumferential force, the influence of the non-linear drag is much higher, hence, it is clearly visible that there is no point symmetry, although the fraction of the lift still dominates the fraction of drag. The next step is to consider the solidity $\sigma_{2D} = \frac{1}{3}$ and discuss the changes in the result. The slope of both forces deviates more for the different solidities the higher the magnitude of the angle of attack. The higher the angle of attack, the higher is the lift and consequently, the deflection of the flow in the wake of the blade. Subsequently, the inflow conditions are changed more. In particular, the circumferential velocity is modified. For high positive angles of attack, this issue leads to a reduction of the thrust and for high negative angles of attack to an increase of the magnitude of the thrust. The circumferential force shows a similar behavior due to the dominating influence of the fraction of the lift.

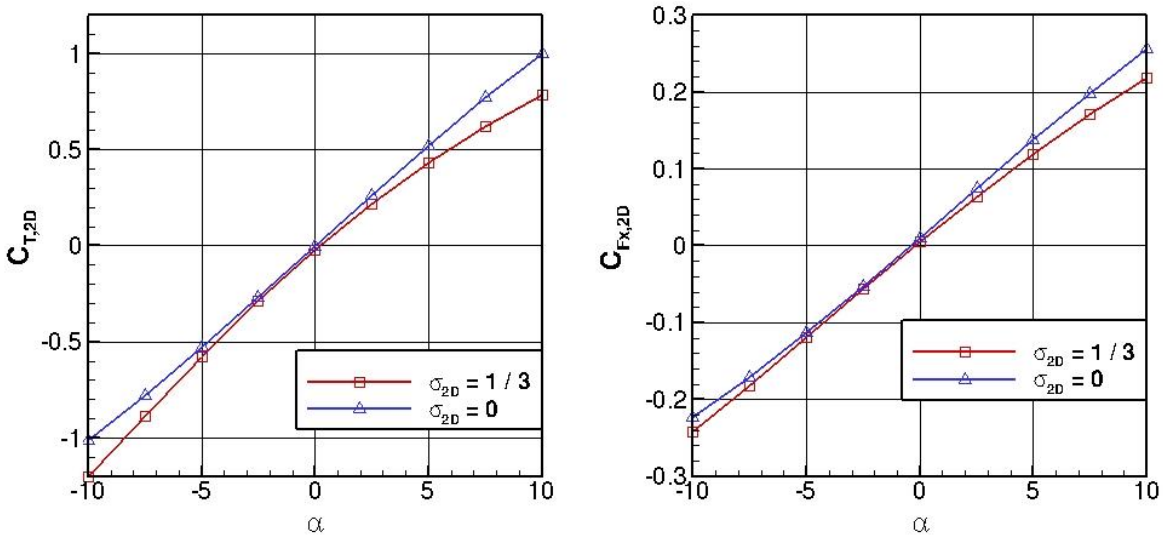

Figure 38: Two-dimensional thrust and circumferential force coefficient for one blade depending on the angle of attack. The advance ratio is set to $J = 0.75$. Resolved.

Finally, the results for the static thrust test case are presented. For this test case, the pressure at the inlet is set while the velocity at the inlet results as part of the solution. This is comparable to a static thrust test case of a propeller. Consequently, the value of the advance ratio would result in $J = 0$. Subsequently, the inflow angle refers to $\phi = 0°$ and the angle of attack α meets the angle of incidence θ. Therefore, the variation is made within this investigation for different angles of incidence θ. Nonetheless, it is evident that the actual inflow velocity is non-zero and as a result, the effective angle of attack differs from the angle of incidence.

In Figure 39, the thrust and circumferential force depending on the solidity are presented for three different angles of incidence. The basic trend of all curves shows, the greater the solidity the smaller are the forces produced by the blade. Since the velocity is not fixed at the inlet, the resulting velocity is proportional to the square root of the segment loading SL. This relation can be simply determined with the momentum equations. The segment loading can be expressed by the solidity multiplied by the thrust. Furthermore, the higher the axial velocity v, the smaller is the angle of attack and consequently, the lift of the blade. Subsequently, the thrust of the segment is reduced. Although the

segment loading is implicitly reduced as well, the thrust of the segment is finally less for higher solidities. The complexity of the case with its implicit connections, therefore, requires a well-thought solution procedure with appropriate initial condition to obtain a converged and fast solution.
Nevertheless, for higher angles of incidence, the lift increases and as result the thrust increases as well. Moreover, due to the above described connection, the negative slope is steeper with higher angles of incidence. Lastly, for low solidities and high angles of incidence, the angles of attack are high due to the low induced velocity which will lead to the stall of the blade. The latter is well visible for the angle of incidence $\theta = 30°$. The circumferential force shows a similar characteristic, since the lift of the blade has a dominating influence due to the high inflow angles. It has to be kept in mind that for the static thrust test case, the variation of the inflow angles is much greater than in the forward flight case due to the implicit set of the induced velocity.

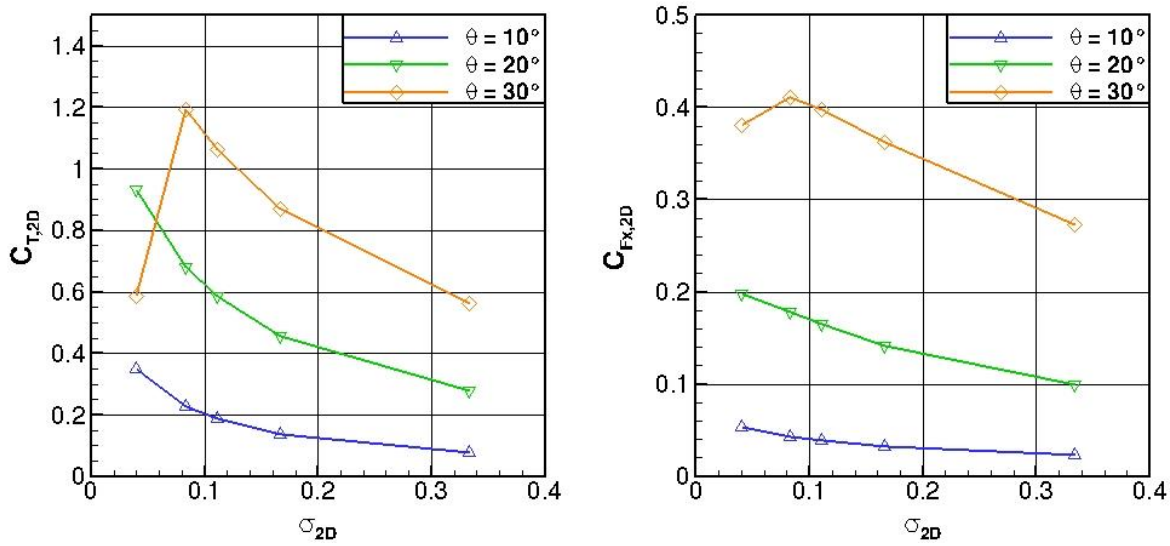

Figure 39: Two-dimensional thrust and circumferential force coefficient for one blade depending on the solidity. The advance ratio is set to $J = 0$. Resolved.

Conclusion and required modeling capabilities: The test case is basically designed for evaluating the influence of the solidity and the related interactional effect on the integral quantities as well as on the flow field. The interaction of the blade with the wake flow leads to a reduction of the forces with increasing solidity. Moreover, the higher the angle of attack, the higher is the reduction of the forces. Consequently, the capabilities shall be fulfilled by appropriate models. Nevertheless, the model shall provide appropriate solutions for the limiting case of a single airfoil also.

Actuator Disc Approach with PanBL

This subsection starts with the investigation of the modeling parameter for the actuator disc coupled with PanBL. As described in the corresponding theory chapter, some adjustable parameters of the model are available. The model includes parameters for the calculation of the inflow conditions as well as the distribution of the sources. As it is described in the theory chapter, the position of the centers of both regions should be coincident and not be modified. Consequently, the data set to be investigated is reduced to the width of the regions (AR_w, SR_w) and the width of smoothing of the regions (AR_s, SR_s). The investigations are performed for selected points in the field only. Finally, with the obtained parameters, the whole field is calculated and compared to the resolved simulation results.

Dependency Test 1: At first, the influence of the widths of the regions (AR_w, SR_w) is investigated. For this investigation, the width of the averaging and the source region is set to be equal $AR_w = SR_w$. In addition, the widths of the smoothing of the regions are set to be equal and constant, $AR_s = SR_s = C$. The required condition that the distribution function is wider than three characteristic cell lengths is fulfilled as well. For the first three investigations, three operating points are chosen. The first point is $(J, \alpha, \sigma_{2D}) = (0.25, 5.0°, \frac{1}{3})$. In order to obtain, on the one hand, results for less interactional effects and on the other hand for less blade loading, the points $(J, \alpha, \sigma_{2D}) = (0.25, 5.0°, \frac{1}{25})$ and $(J, \alpha, \sigma_{2D}) = (0.25, 2.5°, \frac{1}{3})$ are chosen, respectively. In Figure 40, the thrust and circumferential force coefficient for the three points are plotted depending on the width of the source region SR_w nondimensionalized by the chord length of the airfoil. It is visible, that almost no influence, neither for the thrust nor for the circumferential force, can be detected. The maximum relative deviation between the largest and smallest region width related to the largest region width is for all shown calculation points less than $\Delta C_{T,2D,rel} < 0.4\%$ for the thrust and less than $\Delta C_{Fx,2D,rel} < 0.2\%$ for the circumferential force. Consequently, the result can be seen as independent of the size of the region. The number of cells to be fully accounted within the regions is between $5 \leq N_c \leq 30$.

$AR_w = SR_w \neq C$	$AR_s = SR_s = 0.1\ c = 10\ l_{cell}$	$AR_c = SR_c = 0$

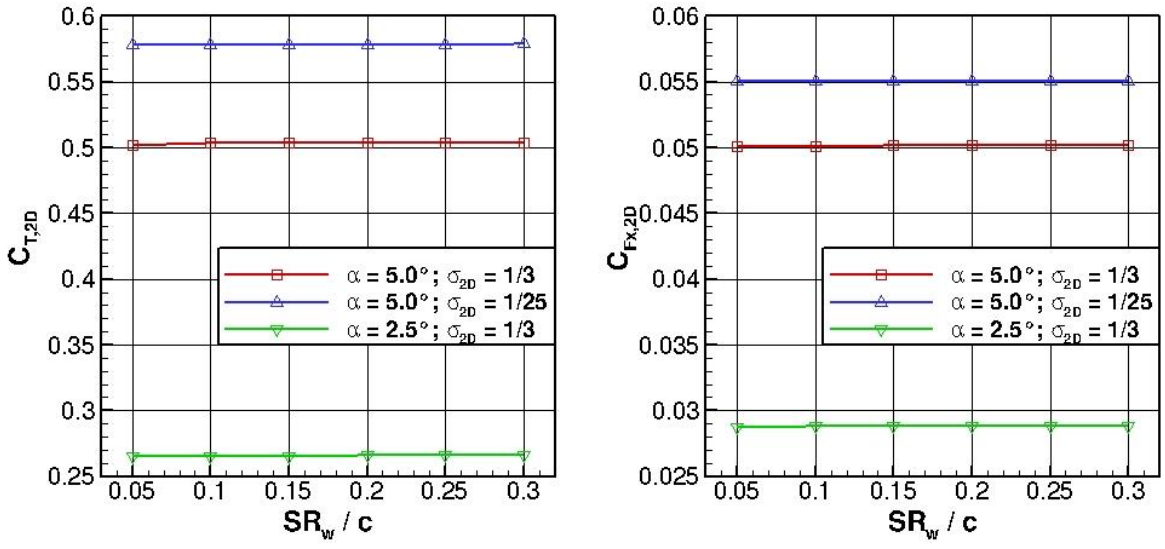

Figure 40: Two-dimensional thrust and circumferential force coefficient for one blade depending on the source region width nondimensionalized with the chord length of the blade. The advance ratio is set to $J = 0.25$. AD-PanBL.

Dependency Test 2: The second investigation deals with the width of the averaging region AR_w. Therefore, the width of the source term region is set to be constant $SR_w = C$. The width of the smoothing region for the averaging region as well as for the source term region is also not varied $AR_s = SR_s = C$. The condition for the width of the smoothing region relative to the characteristic cell length is fulfilled here as well. As stated for the first investigation, the same three operating points are chosen. Figure 41 shows the thrust and circumferential force coefficient for the operating points depending on the ratio of the averaging region width related to the source region width. Within this investigation, a rather independent solution is obtained also. The maximum relative deviation of thrust between the largest and the smallest ratio is less than $\Delta C_{T,2D,rel} < 0.1\%$, while for the circumferential force it is less than $\Delta C_{Fx,2D,rel} < 0.05\%$ regarding the largest ratio. The number of cells to be fully accounted within the averaging region is between $5 \leq N_c \leq 20$.

$AR_w \neq C, \quad SR_w = 0.1\ c\ = 10\ l_{cell}$	$AR_s = SR_s = 0.1\ c = 10\ l_{cell}$	$AR_c = SR_c = 0$

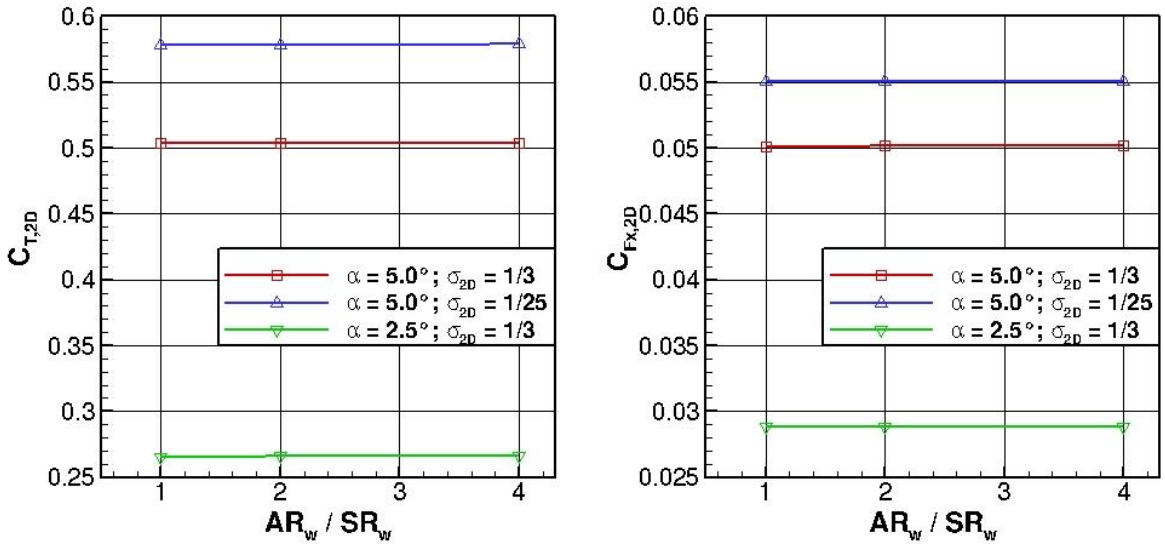

Figure 41: Two-dimensional thrust and circumferential force coefficient for one blade depending on the averaging region width nondimensionalized with the source region width. The advance ratio is set to $J = 0.25$. AD-PanBL.

Dependency Test 3: Within the third investigation, the influence of the width of the smoothing function is evaluated. For this purpose, the widths of the smoothing function for the averaging and the source region are set to be equal, but varying $AR_s = SR_s$. The width of the source and the averaging region is kept constant $AR_w = SR_w = C$. In Figure 42, the thrust and circumferential force coefficient for the above described operating points depending on the ratio of the width of the smoothing function related to the width of the source region are presented. There is also almost no influence of the numerical parameter on the predicted forces. However, is has to be stated as well that the size of the smoothing function is greater than three characteristic cell lengths. The maximum relative deviation between the smallest and the largest width of the smoothing function is for the thrust less than $\Delta C_{T,2D,rel} < 0.025\%$ and for the circumferential force less than $\Delta C_{Fx,2D,rel} < 0.015\%$ regarding the largest ratio. The number of cells to be fully accounted within the smoothing region is between $5 \leq N_c \leq 20$.

$AR_w = SR_w = 0.2\ c\ = 20\ l_{cell}$	$AR_s = SR_s \neq C$	$AR_c = SR_c = 0$

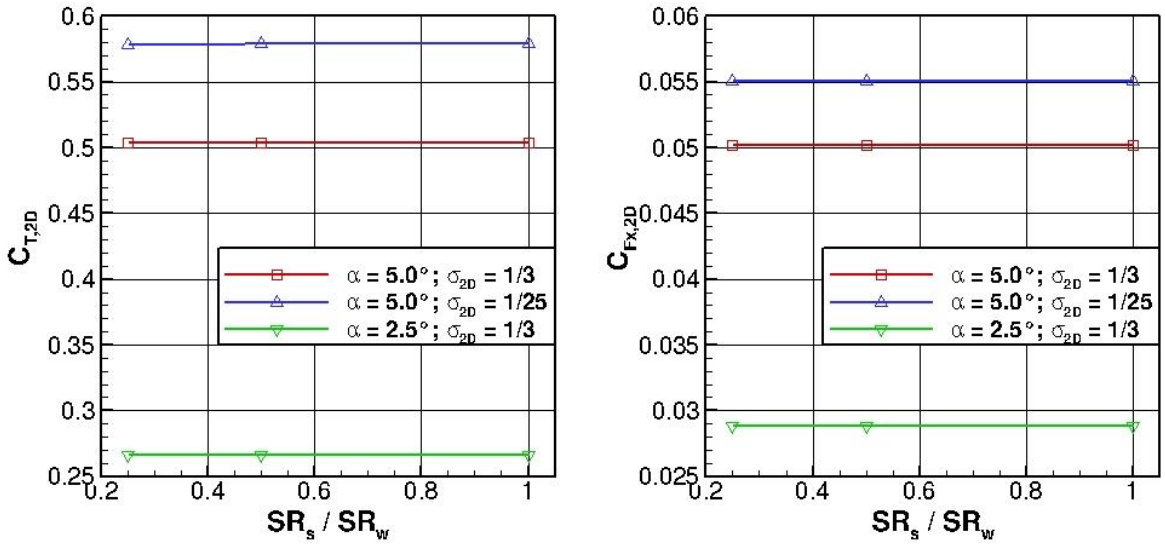

Figure 42: Two-dimensional thrust and circumferential force coefficient for one blade depending on the smoothing region width nondimensionalized with the width of the region. The advance ratio is set to $J = 0.25$. AD-PanBL.

Dependency Test 4: Finally, the centers of the source and averaging region are varied coincidently, relative to the grid. Therefore, three difference widths of the smoothing function are applied, however, the width of the smoothing region for the averaging and the source region is equal $AR_s = SR_s$. The width of the averaging and the source region is set to be equal and constant $AR_w = SR_w = C$. The idea of this test is mainly to demonstrate the influence of the smoothing function on the results. For this investigation, one operating point is presented only, since it is sufficient to declare the numerical effects induced by the method. The chosen point is $(J, \alpha, \sigma_{2D}) = (0.25, 5.0°, \frac{1}{3})$.

At first, the width of the averaging and the source region is set to $AR_w = SR_w = 10.5\ l_{cell}$. Within this setup, the shared cell face of two considered, adjacent cells is set in coincidence with the center of the source region $SR_c = 0$. Consequently, the cell centers of the adjacent cells are located at $y = \pm\ 0.5\ l_{cell}$. The cell centers of the sixth cell in positive and negative direction are at the position $y = \pm\ 5.5\ l_{cell}$. Recalling, the method counts a certain cell to be part of a region if its cell center is located within the region. For this example, the cell centers have to be at the positions according to $|y| \leq \frac{SR_w}{2} = 5.25\ l_{cell}$ to be located within the source region. The statements are made solely for the source region, but they are valid as well for the averaging region. In the initial state, five cells in positive and negative direction are included. Considering a movement of the center of the source region $0 < \Delta SR_c < 0.25\ l_{cell}$, the obtained result is the same. However, if the displacement of the center of the region is between $0.25\ l_{cell} \leq \Delta SR_c \leq 0.75\ l_{cell}$, the sixth cell in the positive direction is included also. For proofing this fact, the limiting value of $\Delta SR_c = 0.25\ l_{cell}$ is applied. The resulting constraint for the position of the cell center to be within the region reads $-\frac{SR_w}{2} + \Delta SR_c = -5.0\ l_{cell} \leq y \leq \frac{SR_w}{2} + \Delta SR_c = 5.5\ l_{cell}$. Consequently, eleven instead of ten cells are counted for the region. The influence on the forces is provided in Figure 43. The latter shows the thrust and circumferential force coefficient for the blade depending on the center of the regions related to the cell size. Since the actual volume of the cells within the region is not accounted, severe changes of the resulting forces are observed without smoothing. It has to be remarked that the calculated

specific forces to be fed into the finite volume solution are related to the ideal volume of the actuator disc as presented in the theory of the method. It can be argued, that the actual sum of cell volumes within the disc region can be used for renormalization. Applied to this example, for $0 < \Delta SR_c < 0.25\ l_{cell}$ the obtained volume within the disc region equals the volume of ten cells and for $0.25\ l_{cell} \leq \Delta SR_c \leq 0.75\ l_{cell}$, it equals the volume of eleven cells. Executing with the renormalization, the change of the magnitude of the forces is smaller at the position of the discontinuities, but the discontinuities do not vanish. Although the forces of the modeled disc are conservatively transferred into the finite volume domain after renormalization, the inflow conditions are different and subsequently the predicted forces. Including the smoothing function, a smooth solution for the forces is obtained. Implicitly, the conservation is fulfilled on equidistant grids also. The renormalization is not applied for the investigations within this thesis except in this section. The latter can be applied if the grid is strongly distorted. That is why the procedure is not activated for these investigations since Cartesian meshes are made in the actuator region. The maximum relative deviation of the maximum and the minimum value related to the maximum value gives for the thrust $\Delta C_{T,2D,rel} = 7.92\ \%$ and for the circumferential force $\Delta C_{Fx,2D,rel} = 8.22\%$ excluding the smoothing function $SR_s = 0$. In contrast, the maximum relative deviation including the smoothing function $SR_s = SR_w$ read for the thrust $\Delta C_{T,2D,rel} = 1.52 \cdot 10^{-6}$ and the circumferential force $\Delta C_{Fx,2D,rel} = 1.95 \cdot 10^{-7}$. As an additional fact, excluding the smoothing function $SR_s = 0$ and using the renormalization provides a relative deviation of $\Delta C_{T,2D,rel} = 0.26\ \%$ for the thrust and $\Delta C_{Fx,2D,rel} = 0.04\%$ for the circumferential force. The application of smoothing function and renormalization is equal to the results for activating the smoothing function only.

$AR_w = SR_w = 0.105\ c\ = 10.5\ l_{cell}$	$AR_s = SR_s \neq C$	$AR_c = SR_c \neq C$

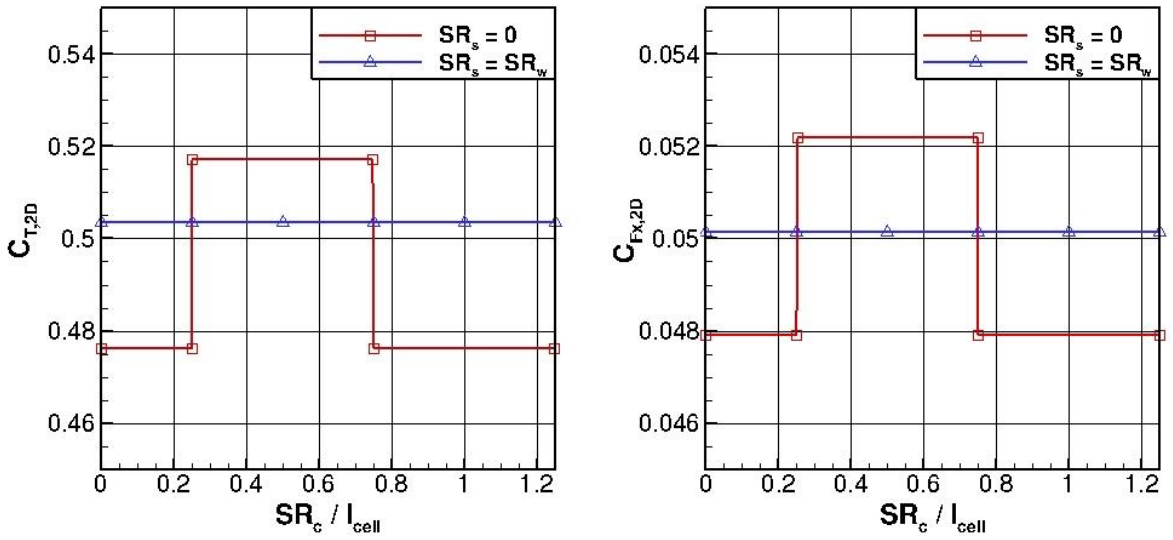

Figure 43: Two-dimensional thrust and circumferential force coefficient for one blade depending on the center of the source and averaging region nondimensionalized with the cell length. The operating point is $(J, \alpha, \sigma_{2D}) = (0.25, 5.0°, \frac{1}{3})$. $SR_w = 10.5\ l_{cell}$. AD-PanBL.

Secondly, a reduction of the width of the regions is performed. Therefore, the width of the source and the averaging region is set to $AR_w = SR_w = 5.5\ l_{cell}$. This should represent the half of the width, but the value has to fulfill $(i + 0.5) l_{cell}$ whereby $i \in \mathbb{Z}$ in order to have the discontinuities for the same center position displacement as in the previous example. In Figure 44, the thrust and

circumferential force coefficient of a blade depending on the center of the regions related to the cell size are provided. It is obvious, that in conjunction with the above declared issues, the occurring changes in magnitude of the forces at the discontinuities are greater for the smaller region width by excluding the smoothing function $SR_s = 0$. The reason is that the ratio of the ideal disc volume related to the volumes of cells accounted to be within the disc differs more the smaller the number of cells involved. In the present case, five or six cells are detected to be within the region, while in the previous case ten or eleven cells are included. Consequently, the maximum relative deviation of the maximum and the minimum value related to the maximum value reads for the thrust $\Delta C_{T,2D,rel} = 15.22\ \%$ and for the circumferential force $\Delta C_{Fx,2D,rel} = 15.22\%$. Including the smoothing function $SR_s = SR_w$, the related values are $\Delta C_{T,2D,rel} = 2.88 \cdot 10^{-5}$ and $\Delta C_{Fx,2D,rel} = 4.27 \cdot 10^{-6}$. In addition, the deviation with renormalization and excluding the smoothing function $SR_s = 0$ is calculated to $\Delta C_{T,2D,rel} = 1.81\ \%$ and $C_{Fx,2D,rel} = 0.31\%$. It becomes visible, that the deviation for the smaller region width is higher, even, with the smoothing function compared to the previous presented setting. Further facts have briefly to be discussed. Although this test shall show only the arising discontinuities, the following additional statements are of interest for the modeling. As visible in Figure 44, the thrust predicted with the smoothing function $SR_w = SR_s$ differs strongly from the average of the minimum and maximum without the smoothing function $SR_s = 0$. Considering the normalization, it could be expected that the minimum and the maximum thrust for $SR_s = 0$ differs from the thrust obtained for $SR_w = SR_s$ only by the ratios $\frac{5.5}{6}$ and $\frac{5.5}{5}$, respectively. However, the obtained inflow conditions are changed as well. This is partially caused by the changing width of the averaging region as already clarified in the theory chapter of the actuator disc. Moreover, it is found that for high specific forces, the velocity v through the disc is not smooth anymore, although converge down to 10^{-7} is achieved for all solved quantities. This behavior disagrees mathematically and physically with the periodic boundary condition for this particular test case but is provided by the present flow solver. Consequently, the averaged process could not obtain the correct velocity.

$AR_w = SR_w = 0.055\ c\ = 5.5\ l_{cell}$	$AR_s = SR_s \neq C$	$AR_c = SR_c \neq C$

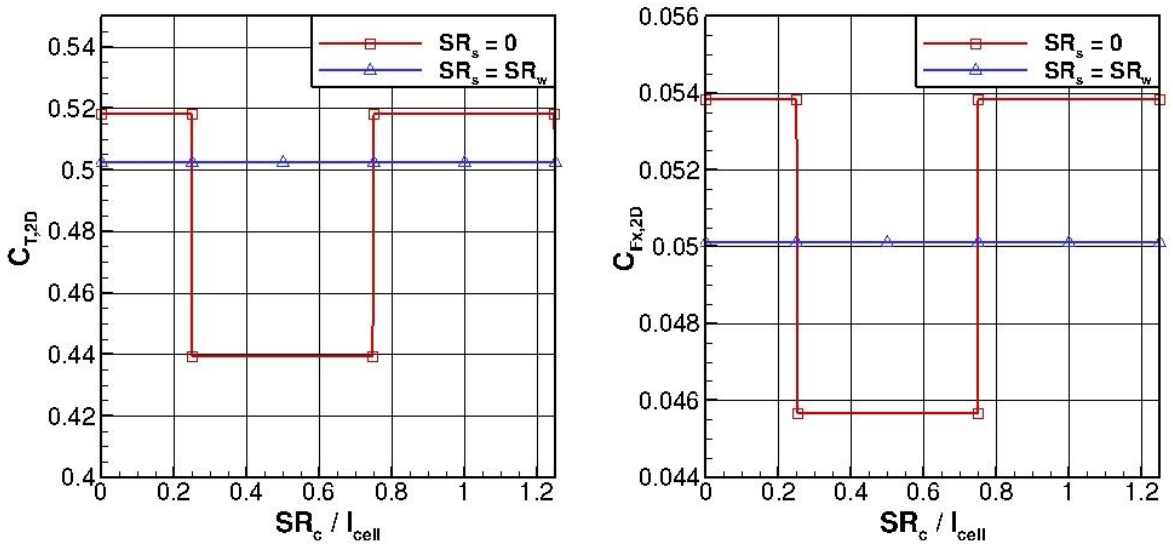

Figure 44: Two-dimensional thrust and circumferential force coefficient for one blade depending on the center of the source and averaging region nondimensionalized with the cell length. The operating point is $(J, \alpha, \sigma_{2D}) = (0.25, 5.0°, \frac{1}{3})$. $SR_w = 5.5\ l_{cell}$. AD-PanBL.

Moreover, it has to be mentioned that for this fourth dependency test the disc widths are chosen intentionally small to better see the effects and the discontinuities. Considering the first dependency test, the herein applied widths of the region are located at the lower boundary of the parameter space for which independency is not achieved. This leads to the next reason why the values of thrust differ from the expected ratios with and without applying the smoothing function. Since the test is made for small widths of the disc SR_w, the activation of the smoothing function with $SR_s = SR_w$ implicitly increases the width of the distribution function of the disc as well. Comparing the results for the smallest presented width SR_w in Figure 40, the increasing of the thrust with the width can be detected. The issue is not visible in this distinctness for the circumferential force.

Finally, the averaging and the source region width are set to $AR_w = SR_w = 10.9\, l_{cell}$. This is made to confirm the above made statements, in particular, for region widths which are almost integral multiples of the cell size. Therefore, the thrust and circumferential force coefficient of a blade depending on the center of the regions related to the cell size for this setting are provided in Figure 45. Consider at first the case with inactive smoothing function $SR_s = 0$. By moving the center region, the periods with high thrust are nine times larger than for the low thrust. The changes in magnitude of thrust at the positions of the discontinuities are comparable to the case with $AR_w = SR_w = 10.5\, l_{cell}$ as well. That seems to be obvious, since the involved number of cells is the same. The maximum relative deviation of the maximum and the minimum value related to the maximum value results for the thrust coefficient in $\Delta C_{T,2D,rel} = 7.96\,\%$ and for the circumferential force in $\Delta C_{Fx,2D,rel} = 8.24\%$. In contrast, the related results with activated smoothing function are $\Delta C_{T,2D,rel} = 6.62 \cdot 10^{-5}$ and $\Delta C_{Fx,2D,rel} = 6.88 \cdot 10^{-5}$. Due to the difference in the obtained inflow conditions, the minimum as well as the maximum thrust without smoothing function are smaller than the thrust obtained with smoothing function.

$AR_w = SR_w = 0.109\, c\ = 10.9\, l_{cell}$	$AR_s = SR_s \neq C$	$AR_c = SR_c \neq C$

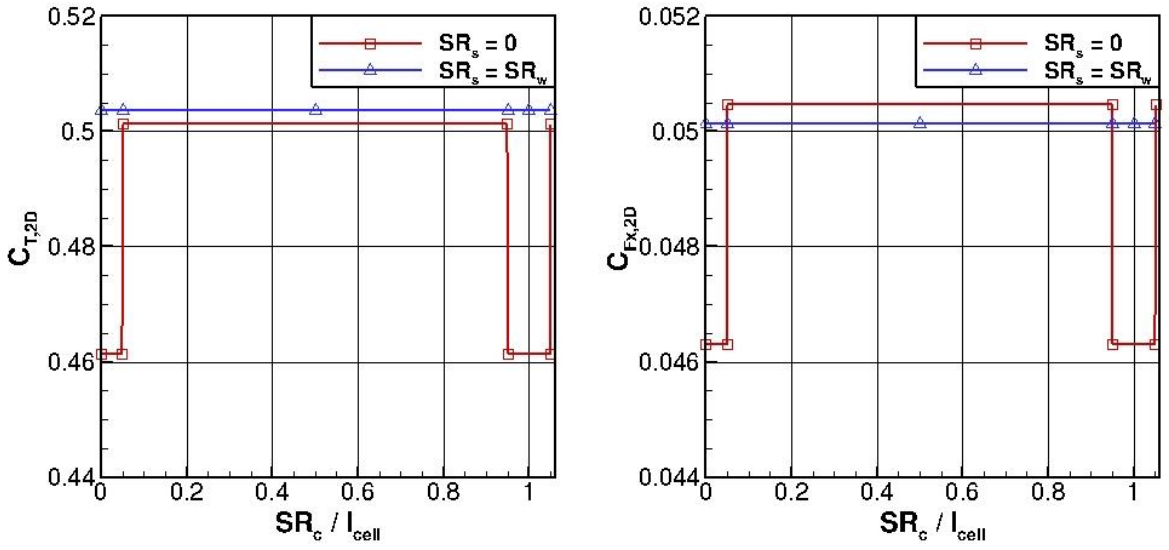

Figure 45: Two-dimensional thrust and circumferential force coefficient for one blade depending on the center of the source and averaging region nondimensionalized with the cell length. The operating point is $(J, \alpha, \sigma_{2D}) = (0.25, 5.0°, \frac{1}{3})$. $SR_w = 10.9\, l_{cell}$. AD-PanBL.

Comparing the results of the three widths with activated smoothing function, the relative deviation reads for the thrust approximately $\Delta C_{T,2D,rel} \approx 0.25\,\%$ and for the circumferential force $\Delta C_{Fx,2D,rel} \approx 0.07\,\%$.

Conclusively, the important points are summarized. For this test case, the independency of the forces is obtained if the source region width is at greater than $SR_w > 0.1\,c$. Moreover, no dependence on the width of the averaging region is the detected if it is equal or greater than the width of the source region $AR_w \geq SR_w$. Furthermore, there is no impact of the width of the smoothing region if the last two requirements are fulfilled. As described in detail, the smoothing function has to be applied to obtain smooth results. Subsequently, an appropriate parameter set of the method for calculating the whole physical parameter field is $AR_w = SR_w = 0.2\,c$, $AR_s = AR_s = 0.1\,c$, and $AR_c = SR_c = 0\,c$. The reference data for this investigation are taken from the resolved simulations.
As already mentioned in the description of the test case, the influence of the cell sizes on the result is connected to the widths of the actuator disc. The presented results confirm that statement. Consequently, the results of the mesh independency study are not shown, because the results to not provide additional information. The important aspects for the modeling approach are the ratios of the actuator disc widths related to the cell sizes.

Parameter field calculation: In order to check the requirements on the method, the same parameter field as provided for the resolved simulation is calculated and presented. At first, the forward flight test case is discussed. The set of the advance ratio is $J = \{0.25, 0.5, 0.75\}$, for the solidity it is $\sigma_{2D} = \left\{\frac{1}{3}, \frac{1}{6}, \frac{1}{9}, \frac{1}{12}, \frac{1}{25}, 0\right\}$, and for the angle of attack it is $\alpha = \{0.0°, 2.5°, 5.0°, 7.5°\}$. In Figure 46, the two-dimensional thrust and the circumferential force coefficient of one single blade depending on the solidity are shown. The advance ratio of J are in ascending order from Figure 46 top to bottom. The global behavior of the results is similar to the resolved simulation. With increasing angle of attack α, the thrust and the circumferential force coefficients are increasing. However, with increasing solidities σ_{2D}, the thrust coefficient as well as the circumferential force coefficient is reduced. Furthermore, for increasing advance ratios, the slope of the thrust and circumferential force coefficient depending on the solidity becomes more negative. Consequently, the global effects are represented correct. For a more quantitative consideration concerning the prediction of the interaction, the relative thrust and circumferential force coefficients for the actuator disc simulation are compared to the results for resolved simulation and presented in Table 4.

Table 4: Relative deviation of the thrust and circumferential coefficient for the resolved and the AD-PanBL simulation.

J	$\Delta C_{T,2D,rel,\sigma,res}$			$\Delta C_{T,2D,rel,\sigma,AD}$		
	$\alpha = 2.5°$	$\alpha = 5.0°$	$\alpha = 7.5°$	$\alpha = 2.5°$	$\alpha = 5.0°$	$\alpha = 7.5°$
0.25	5.06 %	8.25 %	12.22 %	11.25 %	14.67 %	18.24 %
0.50	11.43 %	12.72 %	15.67 %	14.08 %	17.06 %	20.07 %
0.75	16.81 %	16.81 %	19.12 %	17.00 %	19.63 %	22.25 %
J	$\Delta C_{Fx,2D,rel,\sigma,res}$			$\Delta C_{Fx,2D,rel,\sigma,AD}$		
	$\alpha = 2.5°$	$\alpha = 5.0°$	$\alpha = 7.5°$	$\alpha = 2.5°$	$\alpha = 5.0°$	$\alpha = 7.5°$
0.25	3.04 %	4.12 %	6.00 %	7.88 %	10.13 %	12.19 %
0.50	8.27 %	8.50 %	9.97 %	10.91 %	12.97 %	14.39 %
0.75	13.31 %	12.69 %	13.73 %	13.96 %	15.57 %	16.85 %

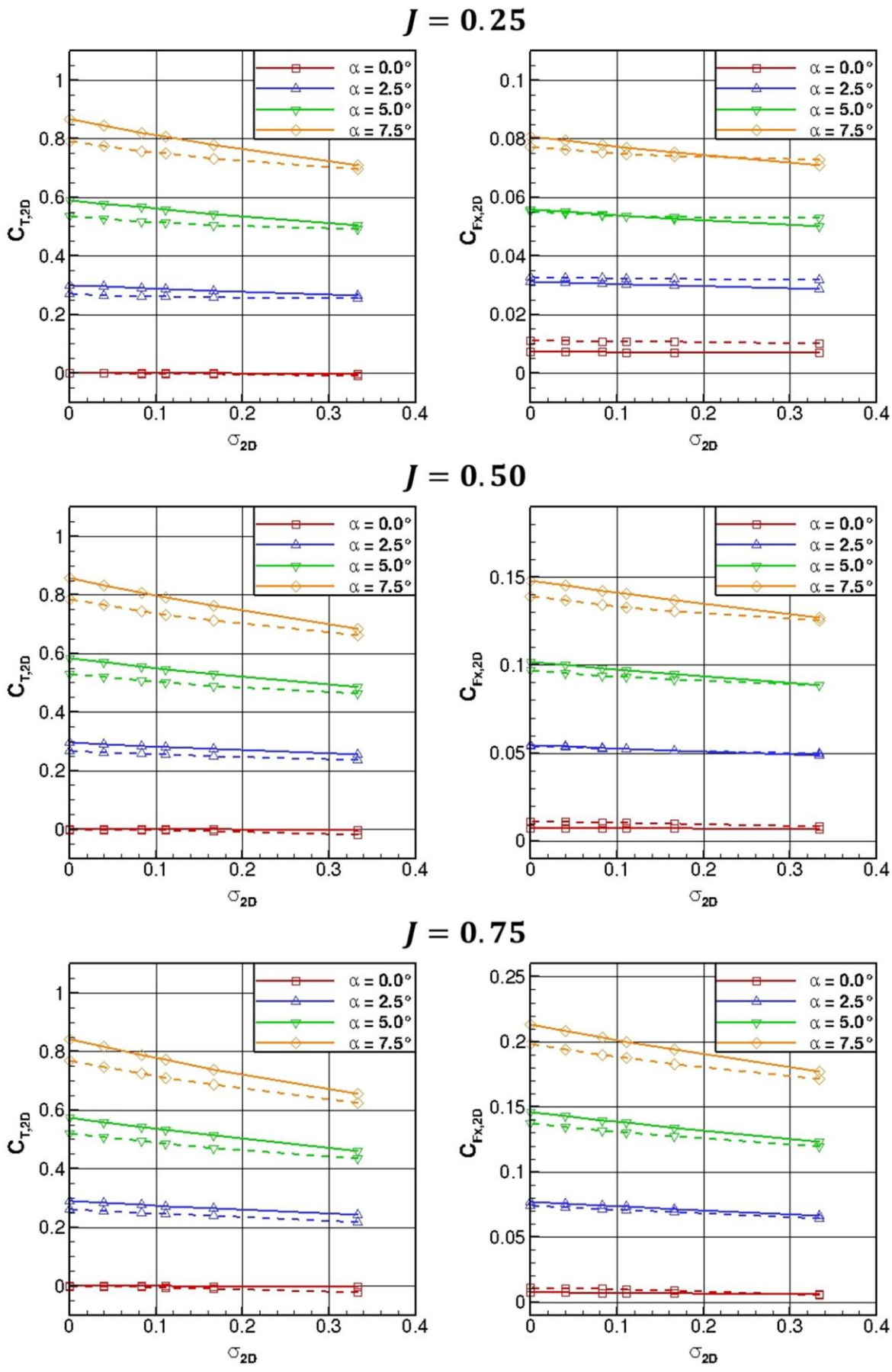

Figure 46: Two-dimensional thrust and circumferential force coefficient for one blade depending on the solidity. The advance ratio is set to $J = 0.25$ (top), $J = 0.5$ (middle), and $J = 0.75$ (bottom). AD-PanBL: Solid line; Res.: Dashed line.

The coefficients are calculated according to (3.11), with the corresponding solidities of $\sigma_{2D,1} = 0$ and $\sigma_{2D,2} = \frac{1}{3}$. At first, the thrust is discussed. The reduction of thrust for the whole parameter range is overestimated by the actuator disc method. The biggest difference is obtained for the medium angle of attack and the smallest advance ratio with $\approx 6.4\%$, while the smallest difference occurs for the smallest angle of attack and the greatest advance ratio with $\approx 0.2\%$. The progressive increase of the reduction of thrust with increasing angle of attack is not provided by the actuator disc method. Considering the circumferential force, the biggest difference is predicted for the smallest advance ratio and the highest angle of attack with $\approx 6.2\%$ while the smallest difference takes place for the smallest angle of attack and the greatest advance ratio with $\approx 0.7\%$. In general, it can be stated, the higher the interaction, the better is the prediction of the actuator disc. The difficulty within this test case is for the actuator disc that a variation of the velocity v is not allowed due to continuity, periodic boundary condition, and only one cell in x-direction. The resolved simulation includes the first-mentioned two constraints as well, but the extension in x-direction allows a variation of the circumferential velocity u locally. Consequently, the prediction is more accurate, the higher the influence on the circumferential velocity u. This is provided for higher advance ratios due to the rotation of the vectors of lift and drag, as well as for small angles of attack as a result of the smaller lift.

In the following, the dependence of the thrust and the circumferential force on the angle of attack is analyzed. Therefore, in Figure 47 the corresponding coefficients are plotted for the solidities $\sigma_{2D} = 0$ and $\sigma_{2D} = \frac{1}{3}$. The range of the angle of attack is extended to $\alpha = \pm 10°$ and the advance ratio is set to $J = 0.75$. For $\sigma_{2D} = 0$, by definition, the inflow conditions are set to the undisturbed freestream conditions. Comparing the resulting thrust coefficient of the actuator disc simulation with that of the resolved simulation, the first difference relies in the slopes of the thrust depending on the angle of attack. Although the Reynolds number for the investigations equals $Re = 10^6$, the derivative of the lift with respect to the angle of attack is smaller for the resolved simulation due to the presence of the boundary layer. The behavior cannot be modeled with the one-way coupling of PanBL. For the angle of attack $\alpha = 10°$, the thrust coefficient obtained by the actuator disc simulation reads $C_{T,2D,AD}(0.75, 0, 10°) = 1.08$, while the related thrust coefficient for the resolved simulation equals $C_{T,2D,res}(0.75, 0, 10°) = 1.0$. Evidently, the thrust is overestimated by approximately $8\,\%$. Considering the value for an angle of attack of $\alpha = -10°$, the corresponding coefficients are $C_{T,2D,AD}(0.75, 0, -10°) = -1.09$ and $C_{T,2D,res}(0.75, 0, -10°) = -1.01$. The deviation is as well approximately $8\,\%$. That seems to be correct for the symmetric airfoil and the small inflow angle. The values for the circumferential force are not provided, since the amount of the deviation is comparable due to the dominating contribution of lift.

The influence of the interactional effects on the forces depending on the angle of attack is captured well by the actuator disc approach for the solidity $\sigma_{2D} = \frac{1}{3}$. With increasing angle of attack, the thrust is reduced compared to the stand-alone airfoil. The thrust coefficient for an angle of attack $\alpha = 10°$ reads for the actuator disc approach $C_{T,2D,AD}(0.75, \frac{1}{3}, 10°) = 0.82$. The reference value of the resolved simulation equals $C_{T,2D,res}(0.75, \frac{1}{3}, 10°) = 0.78$. The deviation between the values is approximately 5%. Caused by the overpredicted reduction of the thrust with increasing solidities and the overprediction of the absolute values of the thrust by PanBL, the overall deviation of the thrust is less for higher solidities.

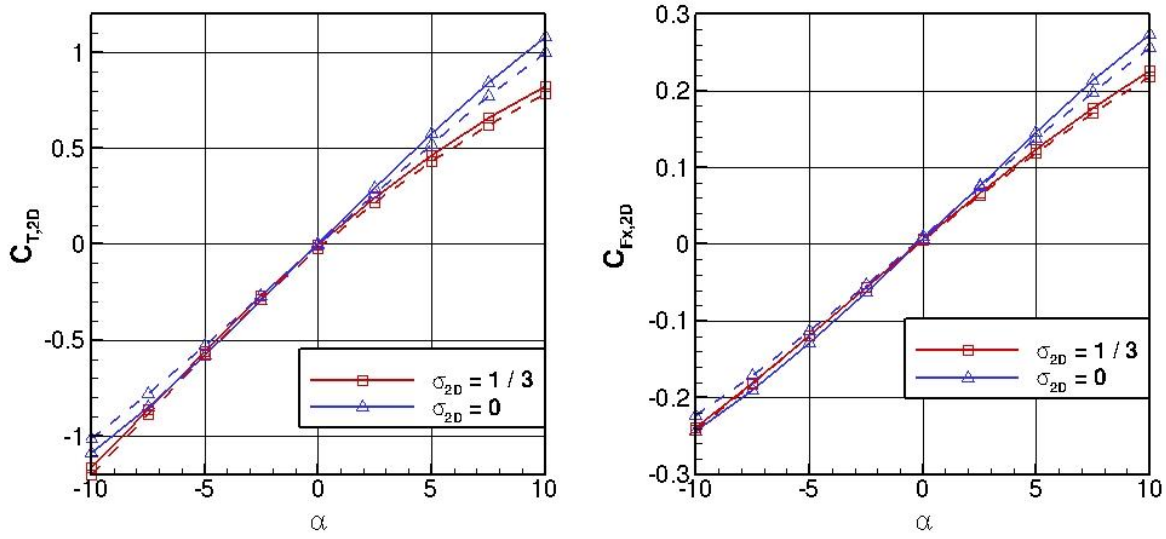

Figure 47: Two-dimensional thrust and circumferential force coefficient for one blade depending on the angle of attack. The advance ratio is set to $J = 0.75$. AD-PanBL: Solid line; Resolved: Dashed line.

Finally, the static thrust test case is discussed. In Figure 48, the thrust and circumferential force coefficient is presented depending on the solidity for the angles of incidence $\theta = \{10°, 20°, 30°\}$. Considering the global trends, a good agreement with the resolved simulation is obtained for the angles of incidence $\theta = 10°$ and $\theta = 20°$. For the angle of incidence of $\theta = 30°$, the behavior is in good agreement as well, while the stall of the blade is not represented correctly. This is caused by the simple stall model included in PanBL which does not capture the stall appropriately.

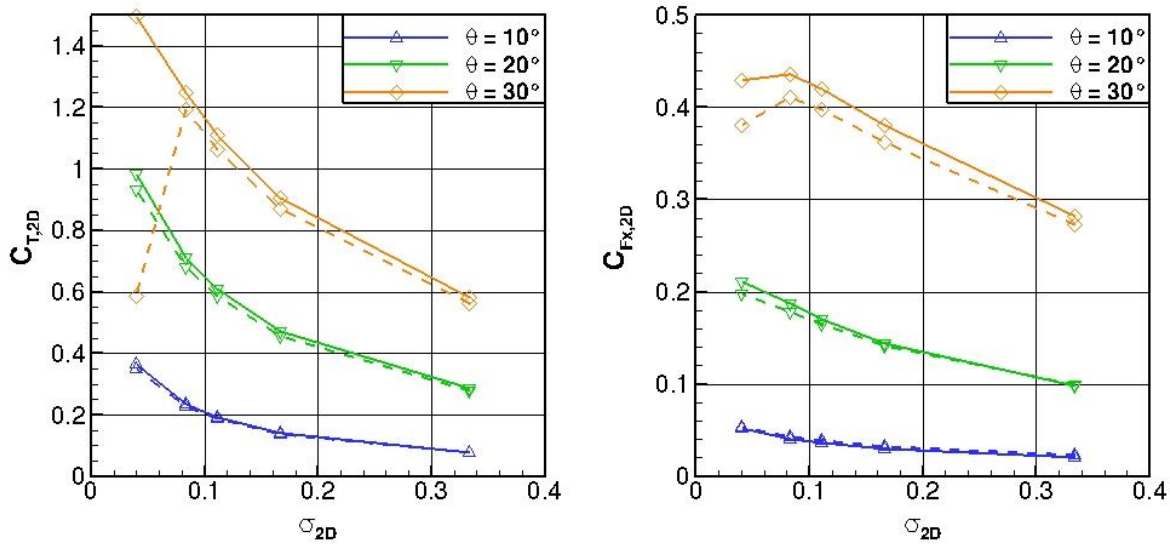

Figure 48: Two-dimensional thrust and circumferential force coefficient for a blade depending on the solidity. The advance ratio is set to $J = 0$. AD-PanBL: Solid line; Resolved: Dashed line.

For this investigation, the quantitative discussion is made with the relative deviation of the force coefficients obtained by the AD simulation related to the corresponding one of the resolved simulation. The slope is not discussed, since it is not caused by the interactional effects only, rather due to the implicit setting of the velocity governed by the thrust. The maximum deviation for the

outlier reads $\Delta C_{T,2D,rel} = 156.06\%$ in the thrust and $\Delta C_{Fx,2D,rel} = 12.57\%$ in the circumferential force. Excluding the outlier, the mean deviation over all solidities for $\theta = \{10°, 20°, 30°\}$ reads for the thrust $\overline{\Delta C_{T,2D,rel}} = \{3.44\%, 4.07\%, 4.22\%\}$ and for the circumferential force $\overline{\Delta C_{Fx,2D,rel}} = \{-7.67\%, 3.10\%, 5.43\%\}$. Conclusively, the results show a good agreement.

Actuator Line Approach with PanBL

Within this subsection, the investigations concerning the influences of the parameters for the two-dimensional extension of the above presented actuator disc approach, the actuator line, are provided. Comparing the theory of the actuator disc with that of the actuator line, for all method-specific parameters, merely the directional information in the circumferential direction is added. For simplicity, the parameters are kept equal for the different dimensions within the present investigations. This fact results in squared regions. Moreover, the position of the center of the averaging and source region is set to be equal for both dimensions $AR_{c,x} = SR_{c,x}$, $AR_{c,y} = SR_{c,y}$. That is why in this section the following definitions are applied: $AR_{c,x} = AR_{c,y} = AR_c$, $SR_{c,x} = SR_{c,y} = SR_c$, $AR_{w,x} = AR_{w,y} = AR_w$, $SR_{w,x} = SR_{w,y} = SR_w$, $AR_{s,x} = AR_{s,y} = AR_s$, $SR_{s,x} = SR_{s,y} = SR_s$. For the comparison with the resolved simulation, the centers are positioned at the quarter chord point of the airfoil. Finally, the whole cascade parameter field is calculated and compared.

Dependency Test 1: The first investigation deals with the influence of the width of the averaging and the source regions AR_w and SR_w. As conducted for the similar investigation of the actuator disc approach, the width of the source and averaging region is set to be equal, but not constant $AR_w = SR_w$. However, the widths of the smoothing kernels are set to be equal and constant $AR_s = SR_s = C$. Additionally, the required condition that the smoothing function is wider than three characteristic cell lengths is fulfilled in both directions. In order to obtain comparable results to the actuator disc approach in the previous chapter, the same operating points are taken for the investigation with the actuator line. The points are $(J, \alpha, \sigma_{2D}) = (0.25, 5.0°, \frac{1}{3})$ as initial state, $(J, \alpha, \sigma_{2D}) = (0.25, 5.0°, \frac{1}{25})$ for less interactional effects, and $(J, \alpha, \sigma_{2D}) = (0.25, 2.5°, \frac{1}{3})$ for less blade loading. Therefore in Figure 49, the thrust and circumferential force coefficient depending on the width of the source region SR_w nondimensionalized by the chord length of airfoil are shown.

$AR_w = SR_w \neq C$	$AR_s = SR_s = 0.1\ c = 10\ l_{cell}$	$AR_c = SR_c = 0$

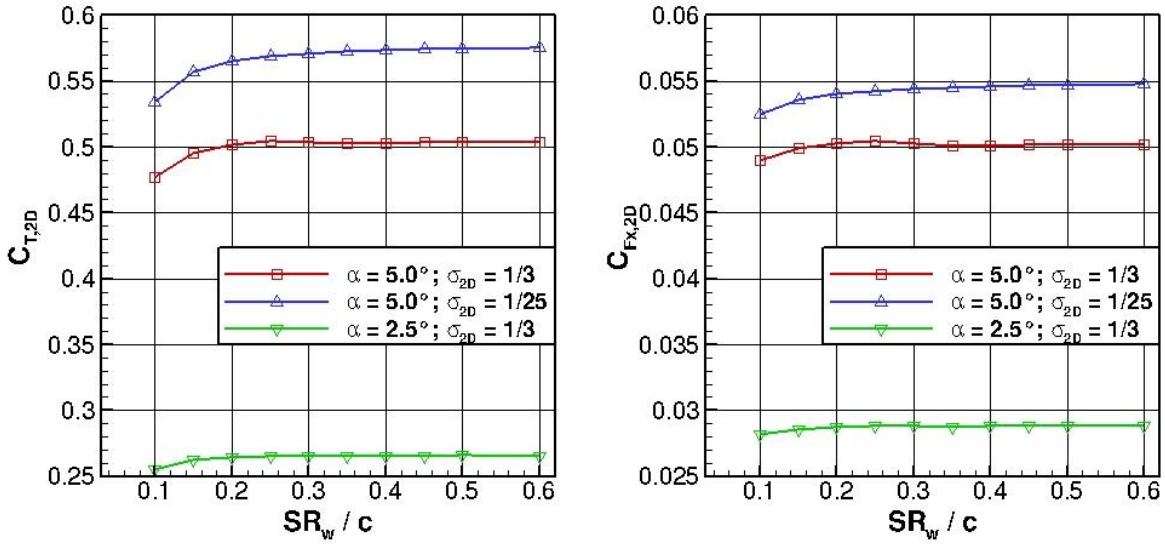

Figure 49: Two-dimensional thrust and circumferential force coefficient for one blade depending on the source region width nondimensionalized with the chord length of the blade. The advance ratio is set to $J = 0.25$. AL-PanBL.

In contrast to the actuator disc approach, a dependence on the width of the region is detected, in particular, for small widths of the region. The higher the loading of the blade, the greater is the reduction of both forces. High blade loading leads to high specific forces in the finite volume domain. The arising problem is that the center of the vortex as described in the theory chapter differs from the real center of the vortex in the simulation if the specific forces become higher. Consequently, the averaging procedure, which is based on the theory, provides incorrect inflow conditions. An opportunity to overcome this issue is a local adaption of the averaging region. For this purpose, the center of the vortex has to be localized and the center of the region has to be shifted to the center of the vortex within each of the iterations. For the presented investigations, the procedure is not included.

In the following, the quantitative description is given. The relative deviation of the thrust from the largest ($SR_w = 0.6\ c$) to the smallest ($SR_w = 0.1\ c$), related to the largest calculated width of the region is presented in Table 5. The above stated behavior that the deviation increases with higher loadings is well visible. Nevertheless, the influence of the parameter on the forces is too high to consider the result to be independent of the mesh, e.g. $\Delta C_{T,2D,rel}\left(0.25, \frac{1}{25}, 5.0°\right) = 7.31\ \%$. Ideally, the extension of the region shall be as small as possible, e.g. for real-life applications if bodies are in vicinity of the blade or for small errors in the three-dimensional case as presented in the theory chapter. Considering Figure 49 again, a good compromise between a small region width and small deviation to the independent result seems to be $SR_w = 0.2\ c$. For larger widths $SR_w > 0.2\ c$, the slope of the curves reduces fast to almost zero. That is why the relative deviation of the thrust and circumferential force coefficient for $SR_w = 0.2$ is printed in Table 5 as well. It is detectable, that all relative deviations are acceptable for the modeling approach, however, the higher the blade loading the greater is the deviation. In contrast, the dependence of the results on the mesh for the actuator disc is negligible in the comparable investigation if $SR_w > 0.1\ c$. The number of cells to be fully accounted within the source region is $10 \leq N_c \leq 60$.

Table 5: Relative deviation of the thrust and circumferential coefficient for the Dependency Test 1 of the AL-PanBL simulation.

	$\left(0.25, \frac{1}{3}, 5.0°\right)$	$\left(0.25, \frac{1}{25}, 5.0°\right)$	$\left(0.25, \frac{1}{3}, 2.5°\right)$
$SR_w = 0.1$			
$\Delta C_{T,2D,rel}$	5.31 %	7.31 %	3.86 %
$\Delta C_{Fx,2D,rel}$	2.40 %	4.28 %	2.29 %
$SR_w = 0.2$			
$\Delta C_{T,2D,rel}$	0.34 %	1.88 %	0.42 %
$\Delta C_{Fx,2D,rel}$	−0.21 %	1.39 %	0.12 %

Dependency Test 2: The second investigation is addressed to the width of the averaging region AR_w. The width of the source term region is set to be constant $SR_w = C$. Furthermore, the width of the smoothing function for the averaging as well as the source region is set to a constant value $AR_s = SR_s = C$. The minimum required width of the smoothing function related to the characteristic cell length is fulfilled as well. For reasons of comparison, the same operating points as in the previous test are chosen. In Figure 50, the thrust and circumferential force coefficient for the operating points are plotted against the ratio of the width of the averaging region to the width of the source region. In contrast to the actuator disc simulation, a distinct influence of the size of the averaging region can be

detected. The smaller the width of the averaging region, the smaller is the generated force. Furthermore, the higher the force, the more pronounced is the reduction. For a larger width of the region, the averaging procedure reduces the influence of the local modified velocity within the wake, e.g. caused by the drag of the blade, for the determination of the inflow conditions. As a result, the obtained inflow velocity is higher and the force as well.

$AR_w \neq C, \quad SR_w = 0.1\,c\, = 10\,l_{cell}$	$AR_s = SR_s = 0.1\,c = 10\,l_{cell}$	$AR_c = SR_c = 0$

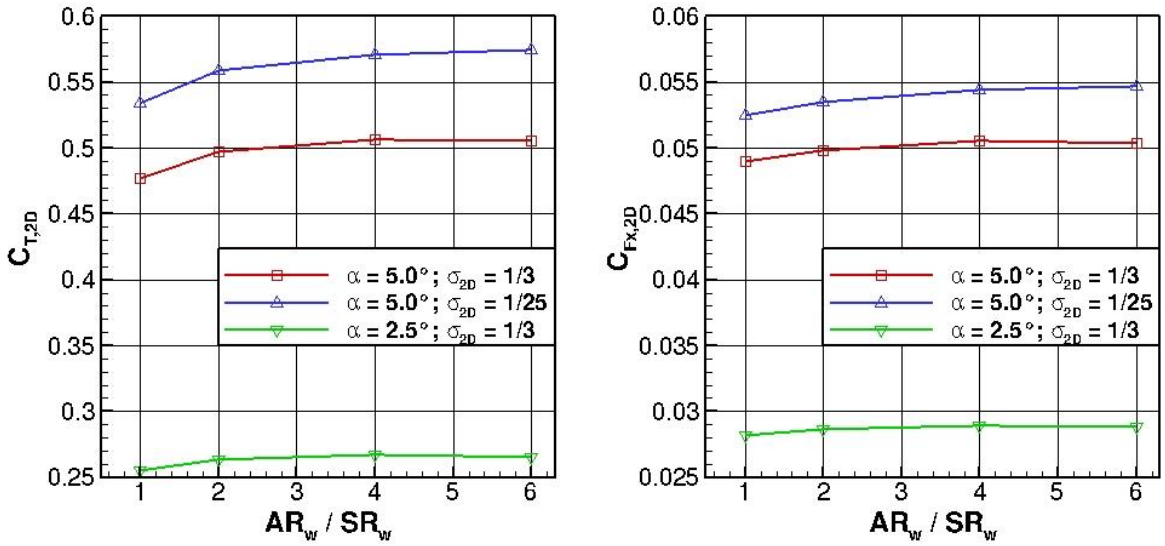

Figure 50: Two-dimensional thrust and circumferential force coefficient for one blade depending on the averaging region width nondimensionalized with the source region width. The advance ratio is set to $J = 0.25$. AL-PanBL.

For the quantitative discussion, the relative deviation of the thrust and circumferential force for the largest ratio $\frac{AR_w}{SR_w} = 6$ to the smallest ratio $\frac{AR_w}{SR_w} = 1$, related to the largest $\frac{AR_w}{SR_w} = 6$ ratio is calculated and summarized in Table 6. In this test, the relative deviation shows no independence of the mesh for $\frac{AR_w}{SR_w} = 1$ as well. That is why the relative deviation for $\frac{AR_w}{SR_w} = 2$ is inserted in Table 6 also. Although the relative deviation is even greater than 2% for one operating point, the ratio can be seen to be acceptable. It has to be kept in mind that the width of the source region SR_w for this test is the smallest presented width of the previous study. As it is shown in the latter, the deviation is smaller with larger widths of the regions. Consequently, by increasing the size of the source region the deviation for comparable ratios becomes even smaller. The number of cells to be fully accounted within the averaging region is $10 \leq N_c \leq 60$.

Table 6: Relative deviation of the thrust and circumferential force coefficient for the Dependency Test 2 of the AL-PanBL simulation.

	$\left(0.25, \frac{1}{3}, 5.0°\right)$	$\left(0.25, \frac{1}{25}, 5.0°\right)$	$\left(0.25, \frac{1}{3}, 2.5°\right)$
$AR_w/SR_w = 1$			
$\Delta C_{T,2D,rel}$	5.56 %	7.10 %	3.73 %
$C_{Fx,2D,rel}$	2.82 %	4.11 %	2.25 %
$AR_w/SR_w = 2$			
$\Delta C_{T,2D,rel}$	1.64 %	2.72 %	0.59 %
$C_{Fx,2D,rel}$	1.29 %	2.17 %	0.37 %

Dependency Test 3: Finally, within the third investigation, the influence of the width of the smoothing function SR_s is presented. The width of the smoothing function of the source and the averaging region is equal $AR_s = SR_s$ and the width of the source and the averaging region is set to be equal and constant $AR_w = SR_w = C$. In Figure 51, the thrust and circumferential force coefficient depending on the ratio of the width of the smoothing function to the width of the source region are plotted for the above described operating points. The requirement on the minimum width of the smoothing function related to the characteristic cell length is fulfilled as well. As it is visible, almost no influence of the mesh on the resulting forces can be detected. The maximum relative deviation between the smallest and the largest width related to the largest width of the smoothing function reads $\Delta C_{T,2D,rel} = 1.05\%$ and for the circumferential force $\Delta C_{Fx,2D,rel} = 0.64\%$. The number of cells to be fully accounted within the smoothing region is between $10 \leq N_c \leq 60$.

$AR_w = SR_w = 0.2\ c\ = 20\ l_{cell}$	$AR_s = SR_s \neq C$	$AR_c = SR_c = 0$

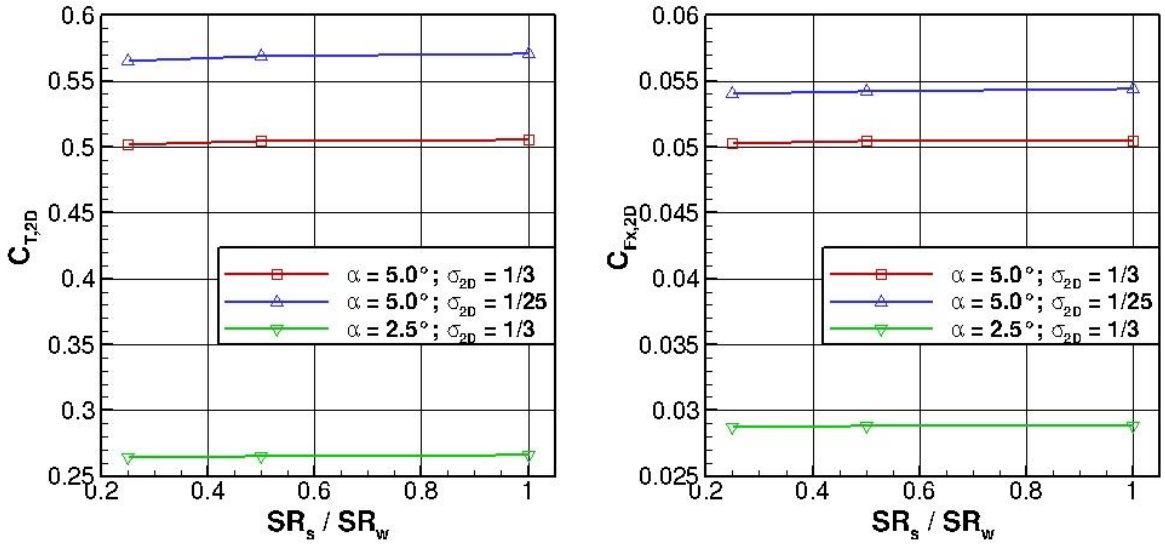

Figure 51: Two-dimensional thrust and circumferential force coefficient for one blade depending on the smoothing region width nondimensionalized with the width of the region. The advance ratio is set to $J = 0.25$. AL-PanBL.

As conclusion, the important facts resulting out of the dependency tests are summarized. In contrast to the results obtained with the actuator disc method, a stronger dependence on the widths of the method is apparent. Due to the requirement, to have small regions for certain modeling issues as well as small deviations from the independent solution, the source region width has to be at least equal or greater than $SR_w \geq 0.2\ c$. The size of the averaging width related to the source region width has to be at least equal or greater than $\frac{AR_w}{SR_w} \geq 2$. The result is obtained for very small source regions SR_w. For greater source widths, the ratio can be smaller, since the result is somehow affected by the absolute size of the width of the region. The smallest influence on the results is obtained by the width of the smoothing function. This can be seen independent of the width for all tested sizes. Consequently, the chosen parameter set for the calculation of the physical parameter field is $AR_w = SR_w = 0.2\ c$, $AR_s = AR_s = 0.1\ c$, and $AR_c = SR_c = 0\ c$. The parameter set is the same as for the actuator disc simulation with the extension in the second coordinate direction. It has to be mentioned that the choice of the parameter set for the actuator disc simulation has been influenced by the results of the actuator line also. Otherwise, the widths for the AD can be chosen

smaller. The reference data for the comparison are taken from the resolved simulations. The results of the mesh independency study are also not shown as described for the actuator disc approach.

Parameter field calculation: The description of the calculation of the parameter field is structured in the same way as for the previous methods. At first, the forwards flight test case is discussed analogously. Therefore, the advance ratios are set to $J = \{0.25, 0.5, 0.75\}$, the solidities to $\sigma_{2D} = \left\{\frac{1}{3}, \frac{1}{6}, \frac{1}{9}, \frac{1}{12}, \frac{1}{25}, 0\right\}$, and the angles of attack to $\alpha = \{0.0°, 2.5°, 5.0°, 7.5°\}$. The two-dimensional thrust and the circumferential force coefficient of a single blade depending on the solidity are presented in Figure 52. The advance ratios are arranged in ascending order from Figure 52 top to bottom. The global behavior predicted by the actuator line is comparable to that of the resolved simulation. Evidently, the thrust and circumferential force coefficients are increasing with the angle of attack α. In contrast, the higher the solidity σ_{2D}, the smaller is the thrust and circumferential force coefficient. In addition, the slope of the thrust and circumferential force coefficient depending on the solidity is more negative for higher advance ratios. Although the global trends agree well, the points without interactional effects, corresponding to $\sigma_{2D} = 0$, show too small forces for all presented advance ratios. Comparing with the resolved simulation, the forces predicted by the actuator line calculation are still higher. However, for these points the slope of the curve changes its sign for small solidities. The reason relies in the calculation of the inflow conditions. In contrast to the actuator disc approach, the inflow condition for $\sigma_{2D} = 0$ are obtained by the application of the averaging procedure as for the remaining solidities. By definition, the inflow conditions for the actuator disc approach for $\sigma_{2D} = 0$ are set to the conditions of the undisturbed inflow. However, the averaging procedure for the actuator line provides incorrect values, in particular, for the circumferential velocity of a stand-alone airfoil. In this case, the local influence of the drag results in an underestimated relative circumferential velocity and consequently, in underestimated forces. The underestimation is caused by the finite extension of the averaging and the source region. The idea of the averaging procedure is basically based on inviscid flows. Due to the drag of the blade, in particular, the relative circumferential velocity downstream of the blade is reduced. As stated above, the source region is embedded within the averaging region. Consequently, the averaging procedure provides a reduced velocity. Reconsidering the discussion of the flow field obtained for the resolved propeller within a cascade above, the relative circumferential velocity downstream of the blade is reduced significantly compared to the stand-alone airfoil caused by the wakes of the blades. Furthermore, the velocity along the circumferential direction is periodic. Conclusively, it can be imagined that the inflow conditions for a certain blade contain the information of the wakes of the upstream located blades. The actuator line approach includes this information, caused by the averaging procedure, but even for a stand-alone blade. That is why the representation of the inflow velocities is captured better for the cascade flow and, in particular, for higher solidities.

For the actuator line, the quantitative discussion is made is the same manner as for the actuator disc. Therefore, the relative thrust and circumferential force coefficients for the actuator disc simulation are compared to the results for the resolved simulation and presented in Table 7. The coefficients are calculated according to (3.11) for the solidities $\sigma_{2D,1} = \frac{1}{25}$ and $\sigma_{2D,2} = \frac{1}{3}$. In contrast to the investigation for the actuator disc approach, the solidity representing less interactional effects is not set to $\sigma_{2D,1} = 0$, since this is not representative for the interaction within this investigation, due to the reasons declared in the last paragraph. Starting the discussion with the thrust coefficient, it is visible that the actuator line overestimates the reduction of the thrust for almost the whole

parameter range. The biggest difference is obtained for the smallest angle of attack and the smallest advance ratio with $\approx 5.1\%$. The smallest discrepancy can be detected for the smallest angle of attack and the highest advance ratio with approximately -0.4%. The deviation of the actuator line regarding the resolved calculation shows a comparable behavior as for the actuator disc method. For the circumferential force, the biggest difference is predicted for the smallest advance ratio and the medium angle of attack with $\approx 4.1\%$, while the smallest difference is detectable for the greatest advance ratio and the smallest angle of attack with $\approx 0.1\%$. For the circumferential force, also a comparable behavior for the deviation of the actuator line as for the AD, compared with that of the resolved simulation, is obtained. Obviously, the statement made for the actuator disc approach that the prediction of the forces is more accurate the higher the interactional effects of the blade are, is still valid. In contrast to the actuator disc approach, the periodic boundary condition in combination with the continuity does not prohibit a variation of the axial velocity v along the circumferential direction x. This is basically enabled by the number of cells to be greater than one in the latter mentioned direction for the actuator line method.

Table 7: Relative deviation of the thrust and circumferential coefficient for the resolved and the AL-PanBL simulation.

J	$\Delta C_{T,2D,rel,\sigma,res}$			$\Delta C_{T,2D,rel,\sigma,AL}$		
	$\alpha = 2.5°$	$\alpha = 5.0°$	$\alpha = 7.5°$	$\alpha = 2.5°$	$\alpha = 5.0°$	$\alpha = 7.5°$
0.25	3.49 %	6.43 %	10.11 %	8.60 %	11.21 %	13.56 %
0.50	9.73 %	10.85 %	13.62 %	11.75 %	14.27 %	16.62 %
0.75	14.81 %	14.62 %	16.69 %	14.46 %	16.70 %	18.80 %
J	$\Delta C_{Fx,2D,rel,\sigma,res}$			$\Delta C_{Fx,2D,rel,\sigma,AL}$		
	$\alpha = 2.5°$	$\alpha = 5.0°$	$\alpha = 7.5°$	$\alpha = 2.5°$	$\alpha = 5.0°$	$\alpha = 7.5°$
0.25	2.03 %	2.95 %	4.70 %	5.55 %	7.04 %	7.87 %
0.50	7.02 %	7.18 %	8.61 %	8.93 %	10.50 %	11.56 %
0.75	11.71 %	10.98 %	11.92 %	11.78 %	13.15 %	14.04 %

The following discussion focuses on the dependence of the thrust and circumferential force on the angle of attack generated by the actuator line approach. In Figure 53, the thrust and circumferential force coefficient for the soldities $\sigma_{2D} = 0$ and $\sigma_{2D} = \frac{1}{3}$ are plotted. The range of the angle of attack is set to $\alpha = \pm 10$ for an advance ratio of $J = 0.75$. Although for the discussion of the slope above, the solidity $\sigma_{2D} = \frac{1}{25}$ is applied for representing the flow with less mutual interaction, the solidity $\sigma_{2D} = 0$ is chosen for this discussion. As detected during the discussion on the slope of the curve, the latter mentioned point can be seen as an outlier. However, for the discussion of the dependence on the angle of attack, the choice is appropriate. The thrust as well as the circumferential force coefficient obtained by the actuator line approach shows a good agreement with the corresponding coefficients of the resolved simulation. In contrast to the actuator disc simulation, the slope is captured better, in particular, for the case with no interaction. However, this is a result of two counteracting trends. On the one hand, as described in the preceding paragraph, the averaging procedure provides inflow conditions which results in reduced forces. On the other hand, PanBL overestimates the forces due to the lack of the modeling caused by the one-way coupling. The latter behavior is well visible for the result of the solidity $\sigma_{2D} = 0$ obtained by the AD simulation in Figure 47. Therefore, equivalent inflow conditions for the resolved and the AD method are present. Conclusively, the occurring deviation can be addressed solely to the modeling approach of the blade.

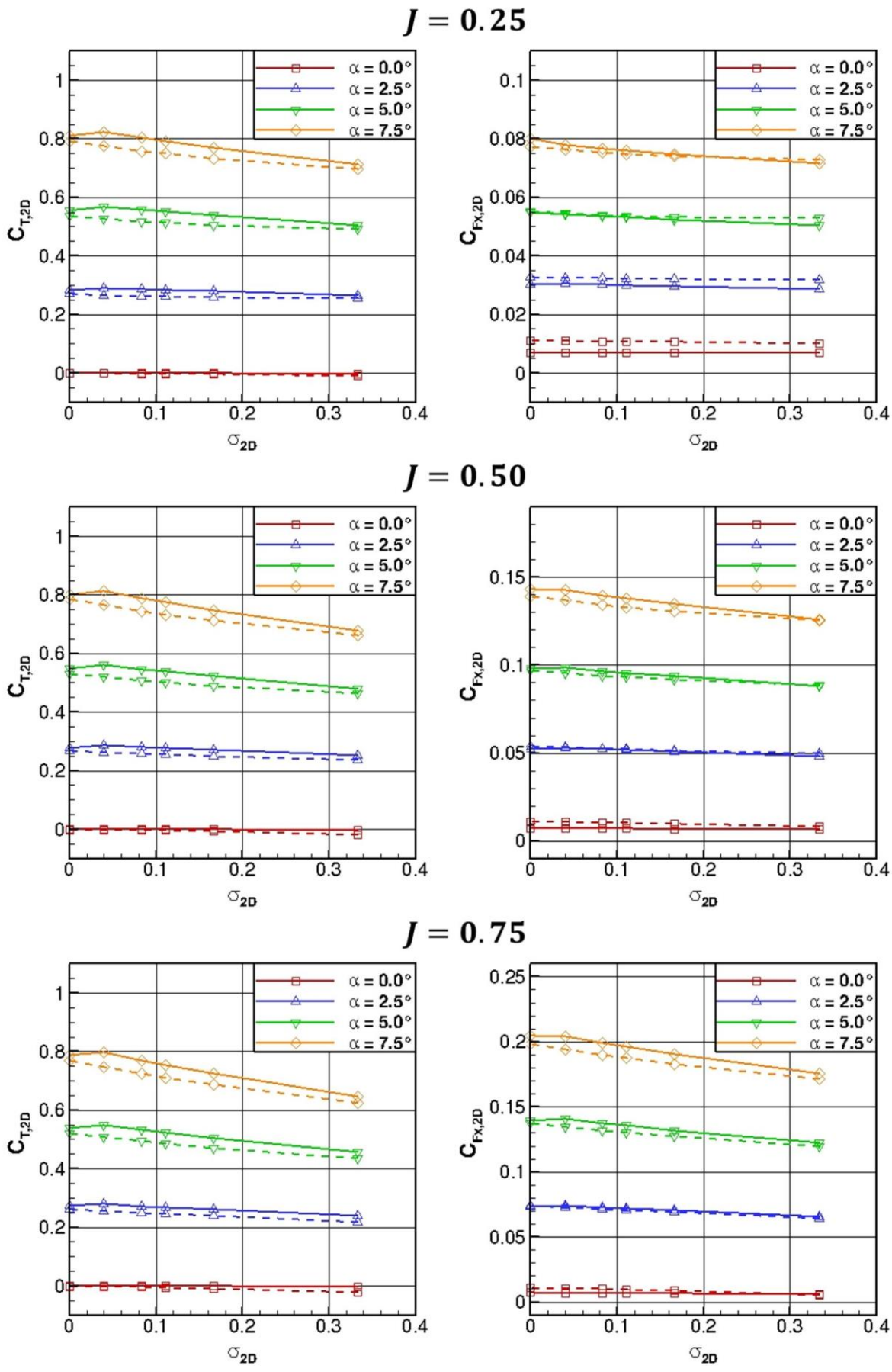

Figure 52: Two-dimensional thrust and circumferential force coefficient for one blade depending on the solidity. The advance ratio is set to $J = 0.25$ (top), $J = 0.5$ (middle), and $J = 0.75$ (bottom). AL-PanBL: Solid line; Res.: Dashed line.

The quantitative discussion is started for the stand-alone blade for an angle of attack of $\alpha = 10°$. The thrust coefficient provided by the actuator line simulation equals $C_{T,2D,AL}(0.75, 0, 10°) = 1.0$, while the related thrust coefficient for the resolved simulation reads $C_{T,2D,res}(0.75, 0, 10°) = 1.0$ also. As already mentioned in the qualitative description, the thrust is in very good accordance caused by two counteracting effects. Reconsidering, the value of thrust for the actuator disc approach reads $C_{T,2D,AD}(0.75, 0, 10°) = 1.08$. As described, this value is obtained if the actual freestream conditions are submitted to PanBL. Consequently, PanBL overestimates the thrust at this operating point by approximately 8%. Conclusively, the averaging procedure of the actuator line underestimates the thrust by approximately 7%. The effects are comparable for an angle of attack $\alpha = -10°$. The corresponding coefficients are $C_{T,2D,AL}(0.75, 0, -10°) = -1.0$ and $C_{T,2D,res}(0.75, 0, -10°) = -1.01$. The deviation is approximately $1\ \%$. Taken into account the corresponding thrust coefficient of the actuator disc $C_{T,2D,AL}(0.75, 0, -10°) = -1.09$, the influence of the counteracting trends on the results is comparable to the positive angle of attack of $\alpha = 10°$. The values for the circumferential force are not discussed, since the trends are similar due to the contribution of the lift.

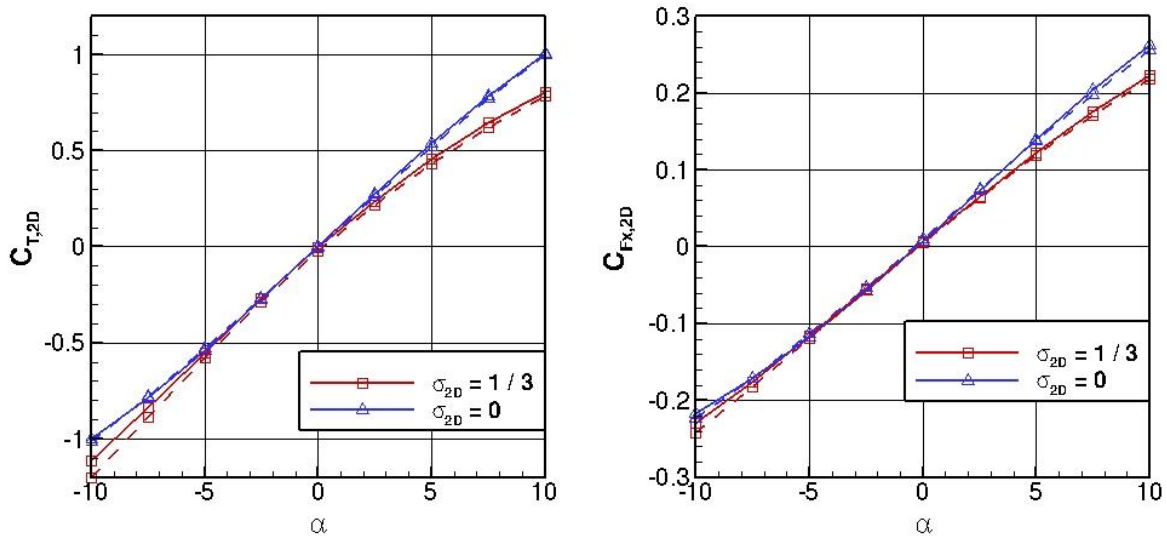

Figure 53: Two-dimensional thrust and circumferential force coefficient for one blade depending on the angle of attack. The advance ratio is set to J=0.75. AL-PanBL: Solid line; Resolved: Dashed line.

In the following, the solidity $\sigma_{2D} = \frac{1}{3}$ representing a strong interaction is discussed quantitatively. For an angle of attack of $a = 10°$, the thrust coefficient for the actuator line simulation reads $C_{T,2D,AL}(0.75, \frac{1}{3}, 10°) = 0.81$, while the resolved simulation provides a coefficient of $C_{T,2D,res}(0.75, \frac{1}{3}, 10°) = 0.78$. The deviation is approximately 4%. The thrust coefficient obtained by the actuator disc approach for this operating point is $C_{T,2D,AL}(0.75, \frac{1}{3}, 10°) = 0.82$. Consequently, the reduction of thrust caused by the averaging procedure is almost not present for the smaller solidities as already stated in the qualitative description of the trends.

The final discussion addresses the static thrust test case. In Figure 54, the thrust and circumferential force coefficient depending on the solidity for the angles of incidence $\theta = \{10°, 20°, 30°\}$ are shown. The global behavior, predicted by the actuator line approach, agrees well with the results of the resolved simulation for the angles of incidence of $\theta = 10°$ and $\theta = 20°$. For the angle of incidence of

$\theta = 30°$, the global trend is represented correct also, unless the blade stalls. The reason for the reduced thrust in this case is not caused by the stall model of PanBL only. Another reason for the reduction of the thrust is the averaging procedure of the actuator line method. As already mentioned, the drag causes an underestimated prediction of the circumferential velocity during the averaging process. Although this aspect leads to a higher angle of attack, the thrust is decreased as a result of the dominating effect of the reduced velocity magnitude. Furthermore, the influence of moved center of the bound vortex for higher specific loadings leads to a reduction of the thrust.

The quantitative discussion is conducted with the relative deviation of the force coefficients obtained by the AL simulation related to the corresponding quantity of the resolved simulation. The slope is not discussed as for the AD simulation, since it is not caused majorly by the interactional effects. The maximum deviation for the outlier is established by $\Delta C_{T,2D,rel} = 111.97\,\%$ in the thrust and $\Delta C_{Fx,2D,rel} = -8.47\,\%$ in the circumferential force coefficient. Excluding the outlier, the mean deviation over all solidities for the angles of incidence $\theta = \{10°, 20°, 30°\}$ reads for the thrust coefficient $\overline{\Delta C_{T,2D,rel}} = \{2.98\,\%, 3.09\,\%, 2.42\,\%\}$ and for the circumferential force coefficient$\overline{\Delta C_{Fx,2D,rel}} = \{-8.34\,\%, 1.87\,\%, 3.03\,\%\}$. Conclusively, the results of the actuator line are in good accordance with those of the resolved simulation.

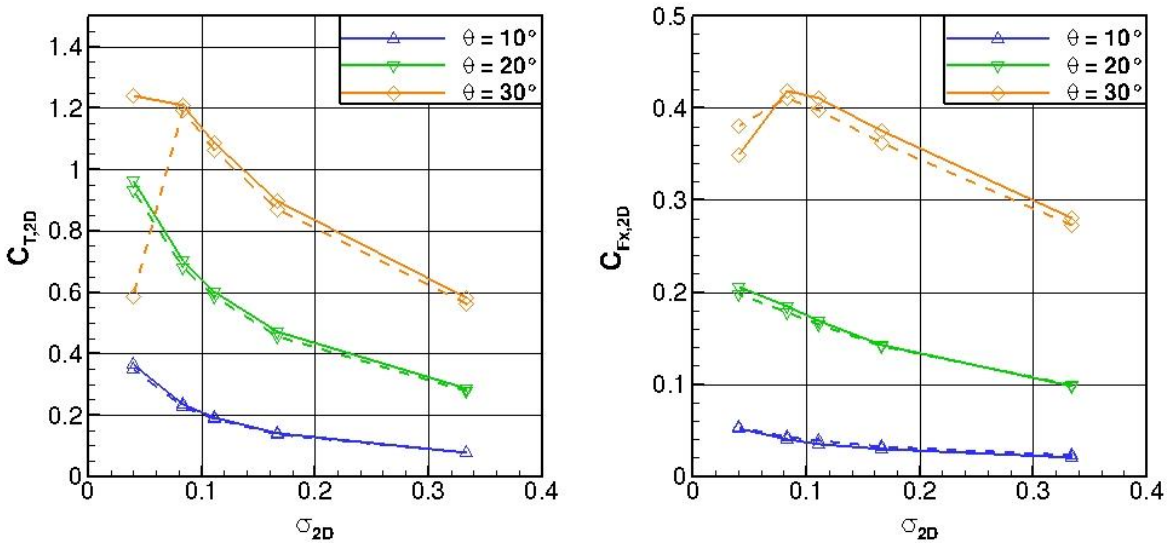

Figure 54: Two-dimensional thrust and circumferential force coefficient for one blade depending on the solidity. The advance ratio is set to J=0. AL-PanBL: Solid line; Resolved: Dashed line.

Actuator Disc Approach with 2D-CFD

Within this subsection, the results for the actuator disc simulations coupled with 2D-CFD (AD-2C) for generating the airfoil data are presented. For this approach, a parameter variation of the actuator disc parameters is not necessarily performed. Since the major difference is solely the generation of the blade forces. That is why within this study, the parameters for the actuator disc are taken from the simulation of the actuator disc coupled with PanBL. The same parameter field points are chosen for the simulation and compared to the resolved simulation.

Parameter field calculation: The structure of this section is the same as in the preceding subsections. Consequently, the forward flight test case is discussed, at first, for the set of advance ratios $J = \{0.25, 0.5, 0.75\}$, of the solidities $\sigma_{2D} = \left\{\frac{1}{3}, \frac{1}{6}, \frac{1}{9}, \frac{1}{12}, \frac{1}{25}, 0\right\}$, and of the angles of attack $\alpha = \{0.0°, 2.5°, 5.0°, 7.5°\}$. The two-dimensional thrust and the circumferential force coefficient of one blade depending on the solidity are presented in Figure 55. The advance ratio of J are in ascending order from Figure 55 top to bottom. The global trend of the forces is comparable to that of the resolved simulation. The increasing forces with higher angles of attack α, the reduction of forces with higher solidities as well as the more negative slope of the forces depending on the solidity with increasing advance ratios are captured correctly. By the definition of the actuator disc approach, the inflow conditions for $\sigma_{2D} = 0$ are matching the conditions for a stand-alone airfoil. In combination with the generation of 2D airfoil data calculated with the same mesh as for the resolved simulation, the corresponding results of the resolved approach and the actuator disc approach are equal for $\sigma_{2D} = 0$. The quantitative description is conducted with the relative deviation of the thrust and circumferential force coefficient. In Table 8, the deviations for the corresponding solidities $\sigma_{2D,1} = 0$ and $\sigma_{2D,2} = \frac{1}{3}$ are presented. The choice of the solidities is in accordance with the applied solidities for the AD-PanBL simulation.

Table 8: Relative deviation of the thrust and circumferential coefficient for the resolved and the AD-2C simulation.

J	$\Delta C_{T,2D,rel,\sigma,res}$			$\Delta C_{T,2D,rel,\sigma,AD-2C}$		
	$\alpha = 2.5°$	$\alpha = 5.0°$	$\alpha = 7.5°$	$\alpha = 2.5°$	$\alpha = 5.0°$	$\alpha = 7.5°$
0.25	5.06 %	8.25 %	12.22 %	11.91 %	14.63 %	17.77 %
0.50	11.43 %	12.72 %	15.67 %	14.12 %	16.54 %	19.28 %
0.75	16.81 %	16.81 %	19.12 %	16.74 %	18.84 %	21.24 %
J	$\Delta C_{Fx,2D,rel,\sigma,res}$			$\Delta C_{Fx,2D,rel,\sigma,AD-2C}$		
	$\alpha = 2.5°$	$\alpha = 5.0°$	$\alpha = 7.5°$	$\alpha = 2.5°$	$\alpha = 5.0°$	$\alpha = 7.5°$
0.25	3.04 %	4.12 %	6.00 %	7.95 %	9.98 %	11.97 %
0.50	8.27 %	8.50 %	9.97 %	10.37 %	12.15 %	13.78 %
0.75	13.31 %	12.69 %	13.73 %	13.10 %	14.63 %	15.98 %

The reduction of the thrust is overestimated for almost the whole parameter range by the actuator disc approach coupled with 2D-CFD. The biggest difference occurs for the smallest angle of attack and the smallest advance ratio with ≈ 6.9 %. The smallest difference can be detected for the smallest angle of attack and the highest advance ratio with ≈ -0.1 %. This is a similar result to the AD-PanBL approach. The maximum of the deviation for AD-PanBL and AD-2C results distinguishes by approximately 1 %. The higher the interaction, the better is the prediction. Nonetheless, the dependence of the thrust on the solidity is almost not affected by the airfoil data generation.

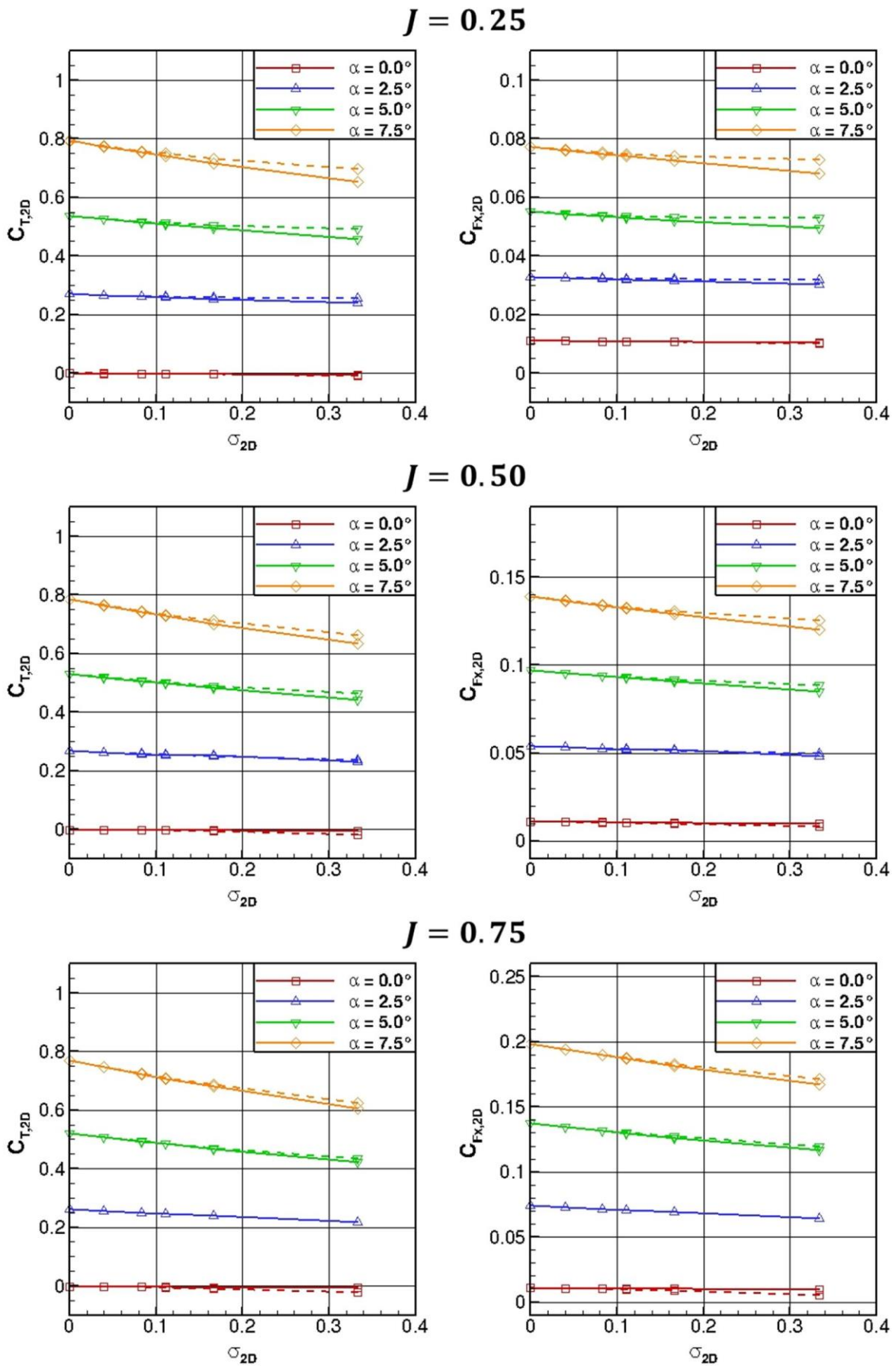

Figure 55: Two-dimensional thrust and circumferential force coefficient for one blade depending on the solidity. The advance ratio is set to $J = 0.25$ (top), $J = 0.5$ (middle), and $J = 0.75$ (bottom). AD-2C: Solid line; Resolved: Dashed line.

The biggest difference in the circumferential force is obtained for the smallest advance ratio and the highest angle of attack with $\approx 6.0\%$. The smallest difference is predicted for the smallest angle of attack and the highest advance ratio with $\approx -0.2\ \%$. The difference between the values generated by the AD-PanBL and AD-2C approach is below $1\ \%$. Consequently, the impact of the airfoil data generation can be seen to be negligible for the dependence of the circumferential force on the solidity as well. The statements concerning the interaction made for the AD-PanBL approach are valid here also.

The next point to be discussed is the dependence of the thrust and circumferential force on the angle of attack. In Figure 56, the related coefficients are shown for the solidities $\sigma_{2D} = 0$ and $\sigma_{2D} = \frac{1}{3}$. The range of the angle of attack is set to $\alpha = \pm 10$ and the advance ratio equals $J = 0.75$. As noted, for the actuator disc approach, the inflow conditions are set to the undisturbed freestream conditions for $\sigma_{2D} = 0$. Consequently, the resulting forces for the latter mentioned solidity are equal for both presented methods. In order to investigate the effects caused by the interaction of the blades, the results for the solidity $\sigma_{2D} = \frac{1}{3}$ are discussed. The behavior of both forces is captured well by the actuator disc simulation, in particular, for positive angles of attack $\alpha > 0$.

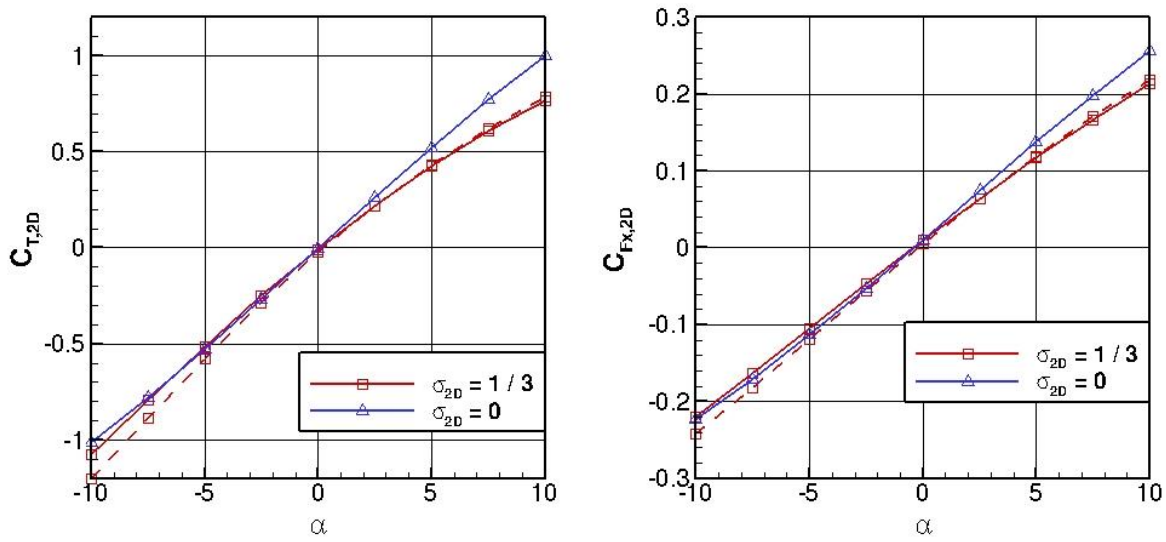

Figure 56: Two-dimensional thrust and circumferential force coefficient for one blade depending on the angle of attack. The advance ratio is set to J=0.75. AD-2C: Solid line; Resolved: Dashed line.

For an angle of attack of $\alpha = 10°$, the thrust coefficient for the actuator disc simulation reads $C_{T,2D,AD}(0.75, \frac{1}{3}, 10°) = 0.77$, while the resolved simulation provides a coefficient of $C_{T,2D,res}(0.75, \frac{1}{3}, 10°) = 0.78$. Subsequently, the deviation is approximately 1%. In contrast, for an angle of attack of $\alpha = -10°$, the corresponding coefficients read $C_{T,2D,AD}\left(0.75, \frac{1}{3}, -10°\right) = -1.08$ and $C_{T,2D,res}\left(0.75, \frac{1}{3}, -10°\right) = -1.20$. The resulting deviation is approximately 10%. Reconsidering the results of the AD-PanBL approach, the deviation between the thrust coefficients obtained by the actuator disc and the resolved simulation is similar for the angle of attack $\alpha = -10°$ and $\alpha = 10°$. However, in the present investigation, the range of positive angles of attack is captured much better. The reason is the overestimation of the lift by PanBL.

The final point to be discussed is the static thrust test case. Therefore, in Figure 57 the thrust and circumferential force coefficient depending on the solidity for the angles of incidence $\theta = \{10°, 20°, 30°\}$ are presented. For this test case, a very good agreement for the whole parameter range is obtained with the actuator disc method. Even for the angle of incidence of $\theta = 30°$ in combination with small solidities and occurring stall, the trend is represented correctly. One the one hand, the underlying 2D-CFD simulation for generating the airfoil data can handle the stall behavior. In addition, the resolved simulation and the airfoil data generation for the actuator disc is performed on the same mesh. On the other hand, the determination of the correct inflow condition seems to be appropriate accurate in accordance with this result.

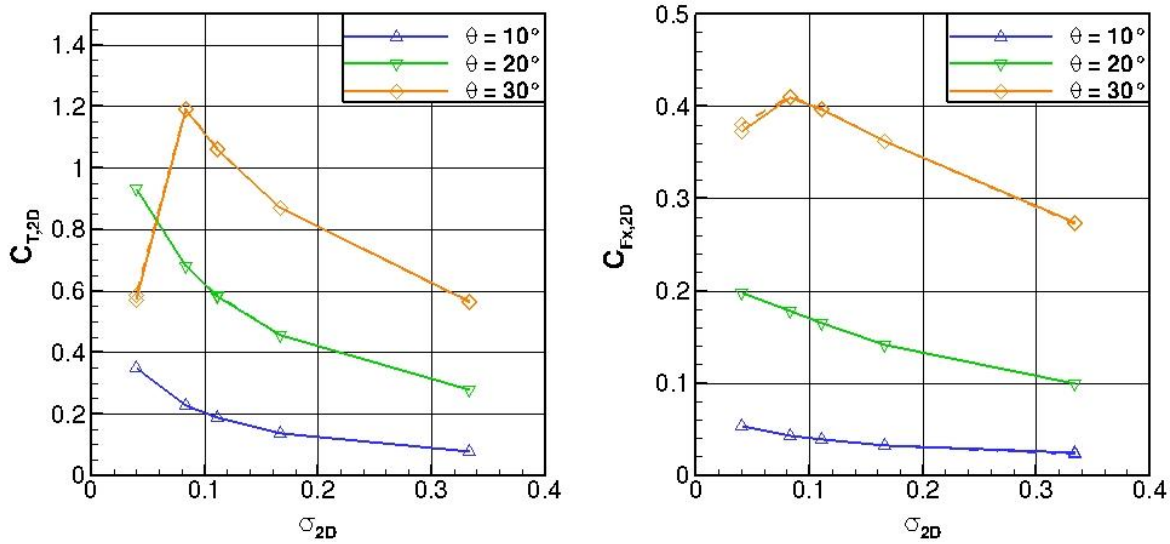

Figure 57: Two-dimensional thrust and circumferential force coefficient for a blade depending on the solidity. The advance ratio is set to J=0. AD-2C: Solid line; Resolved: Dashed line.

For this investigation, the quantitative discussion is conducted as well with the relative deviation of the force coefficients obtained by the AD simulation related to the corresponding quantity of the resolved simulation. The discussion of the slope is also not made caused by the above declared reason. Due to the good agreement, instead of a mean deviation applied for the previous methods, the maximum deviation is presented for this comparison. The maximum deviation over all solidities for the angles of incidence $\theta = \{10°, 20°, 30°\}$ reads for the thrust coefficient $\Delta\widehat{C_{T,2D,rel}} = \{0.83\ \%, 0.19\ \%, 0.40\ \%\}$ and for the circumferential force coefficient $\Delta\widehat{C_{Fx,2D,rel}} = \{0.95\ \%, 0.48\ \%, 0.64\ \%\}$. Conclusively, the results of the actuator disc coupled with 2D-CFD are in very good agreement with those of the resolved simulation in the quantitative consideration also.

Actuator Line Approach with 2D-CFD

Within this subsection, the investigations of the actuator line calculations coupled with 2D-CFD (AL-2C) for generating the airfoil data are presented. The parameters obtained for the actuator line approach coupled with PanBL are taken, since as declared in the previous section for the actuator disc approach coupled with 2D-CFD, solely the generation of the blade forces differs for the corresponding methods. For comparison issues, the investigations are performed for the same field points as in the previous investigations and compared to the resolved simulation.

Parameter field calculation: For consistency, the structure of this section is built in the same way as for the preceding parameter field calculations for the other approaches. At the beginning of the investigation, the forward flight test case is discussed for the advance ratios $\mathrm{J} = \{0.25, 0.5, 0.75\}$, the solidities $\sigma_{2\mathrm{D}} = \left\{\frac{1}{3}, \frac{1}{6}, \frac{1}{9}, \frac{1}{12}, \frac{1}{25}, 0\right\}$, and the angles of attack $\alpha = \{0.0°, 2.5°, 5.0°, 7.5°\}$. In Figure 58, the two-dimensional thrust and the circumferential force coefficient acting on one blade depending on the solidity are presented. The advance ratios J are in ascending order from Figure 58 top to bottom. The global trend of the forces is predicted similar compared to the that of resolved simulation. This means in particular, the higher forces for higher angles of attack α, the smaller forces for higher solidities as well as the more negative slopes of the forces depending on the solidity with increasing advance ratios are represented appropriately. Considering the point for the solidity $\sigma_{2D} = 0$, including no interactional effects, the same statements as made during the discussion for the actuator line approach coupled with PanBL are valid. For the present method, the deviation is even better detectable. For the AL-PanBL approach, the overestimation of the forces caused by the airfoil data generation of PanBL partially overcompensates the underestimation of the forces due to the averaging process. For the present method, the airfoil generation performed by 2D-CFD provides the same airfoil data as for the resolved simulation for a certain inflow condition. Consequently, the forces within this investigation are underestimated compared to the resolved simulation for almost the whole parameter range. The biggest deviation is obtained for solidity $\sigma_{2D} = 0$, due to the above mentioned reasons. The quantitative description is made with the relative deviation of the thrust and circumferential force coefficient. In Table 9, the deviations for the corresponding solidities $\sigma_{2D,1} = \frac{1}{25}$ and $\sigma_{2D,2} = \frac{1}{3}$ are shown. The choice of the solidities is in accordance with the applied solidities for the AL-PanBL simulation.

Table 9: Relative deviation of the thrust and circumferential coefficient for the resolved and the AL-2C simulation.

J	$\Delta C_{T,2D,rel,\sigma,res}$			$\Delta C_{T,2D,rel,\sigma,AL-2C}$		
	$\alpha = 2.5°$	$\alpha = 5.0°$	$\alpha = 7.5°$	$\alpha = 2.5°$	$\alpha = 5.0°$	$\alpha = 7.5°$
0.25	3.49 %	6.43 %	10.11 %	8.65 %	10.61 %	12.75 %
0.50	9.73 %	10.85 %	13.62 %	11.48 %	13.53 %	15.72 %
0.75	14.81 %	14.62 %	16.69 %	13.99 %	15.80 %	17.79 %
J	$\Delta C_{Fx,2D,rel,\sigma,res}$			$\Delta C_{Fx,2D,rel,\sigma,AL-2C}$		
	$\alpha = 2.5°$	$\alpha = 5.0°$	$\alpha = 7.5°$	$\alpha = 2.5°$	$\alpha = 5.0°$	$\alpha = 7.5°$
0.25	2.03 %	2.95 %	4.70 %	5.00 %	6.28 %	7.25 %
0.50	7.02 %	7.18 %	8.61 %	8.14 %	9.63 %	10.81 %
0.75	11.71 %	10.98 %	11.92 %	10.78 %	12.11 %	13.16 %

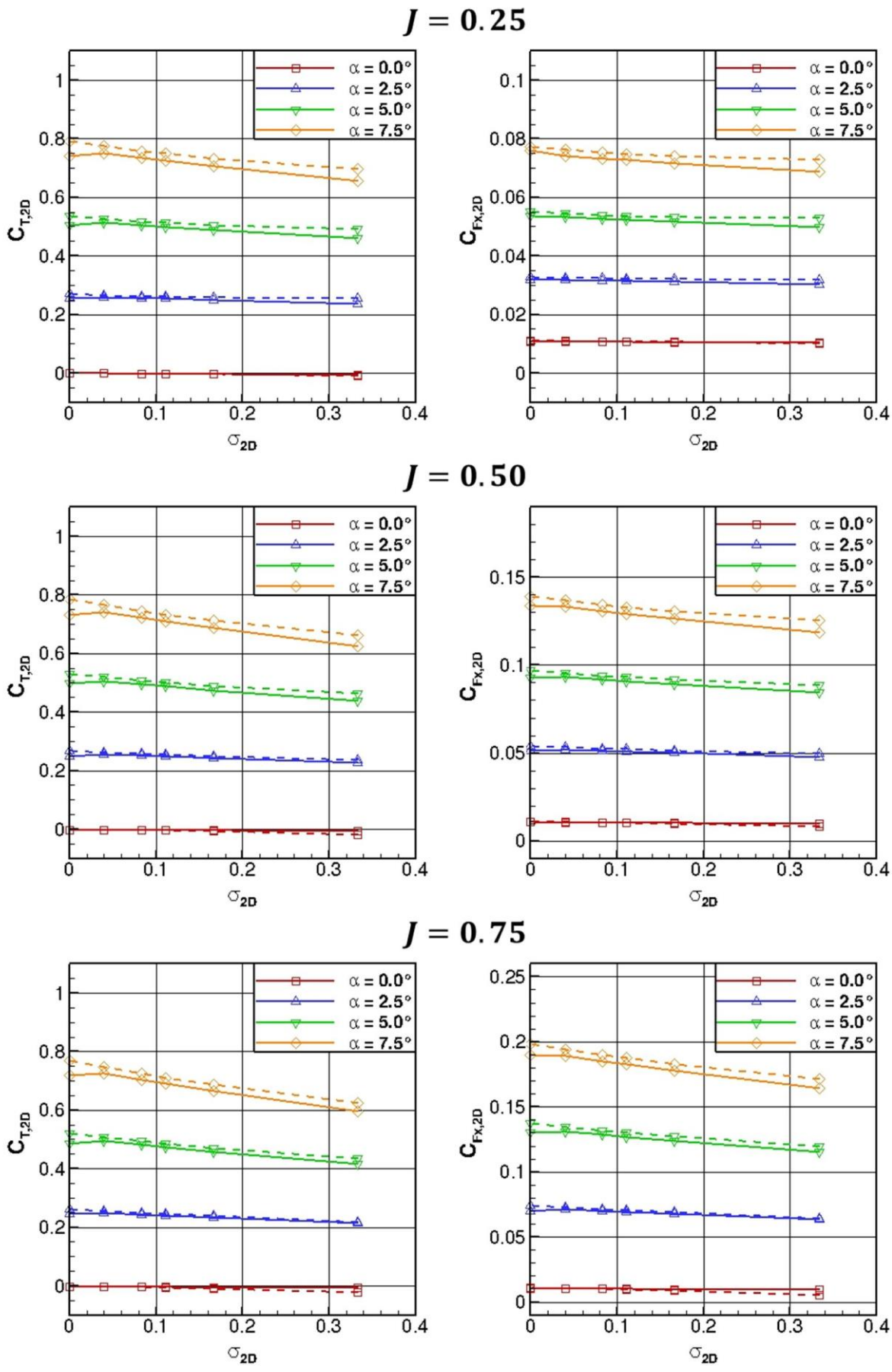

Figure 58: Two-dimensional thrust and circumferential force coefficient for one blade depending on the solidity. The advance ratio is set to $J = 0.25$ (top), $J = 0.5$ (middle), and $J = 0.75$ (bottom). AL-2C: Solid line; Resolved: Dashed line.

For the actuator line approach coupled with 2D-CFD, the reduction of thrust is overestimated for almost the whole parameter range. The biggest discrepancy is obtained for the smallest angle of attack and the smallest advance ratio with $\approx 5.2\ \%$. The smallest difference occurs for the smallest angle of attack and the greatest advance ratio with $\approx -0.8\ \%$. This is a comparable result to the AL-PanBL approach. The maximum of the deviation for AL-PanBL and AL-2C distinguishes by approximately $1\ \%$. Furthermore, the higher the interaction, the better is the prediction within this investigation and the dependence of the thrust on the solidity is almost not affected by the airfoil data generation as well. The biggest difference in the circumferential force is detected for the smallest advance ratio and the medium angle of attack with $\approx 3.3\%$. The smallest difference is obtained for the smallest angle of attack and the greatest advance ratio with $\approx -0.9\ \%$. The maximum discrepancy between the values generated by the AD-PanBL and AD-2C approach is approximately $1\ \%$. The airfoil data generation can be assumed to be negligible for the dependence of the circumferential force on the solidity also. The statements concerning the interaction made for the AL-PanBL approach are valid for the AL-2C also.

In the following, the dependence of the thrust and circumferential force on the angle of attack is presented. In Figure 59, the related coefficients are plotted for the solidities $\sigma_{2D} = 0$ and $\sigma_{2D} = \frac{1}{3}$. The range of the angle of attack is set to $\alpha = \pm 10$ and the advance ratio equals $J = 0.75$. The choice of the solidity $\sigma_{2D} = 0$ for representing the low interaction test case is in accordance with the choice made for the AL-PanBL approach. In this case, the effect of the averaging procedure of the actuator line approach on the resulting forces is obtained directly. The airfoil data generation for the actuator line method uses the same numerical mesh and setup as the resolved simulation. Consequently, the discrepancies between the solutions can be attributed to the inflow conditions provided by the averaging procedure of the actuator line method.

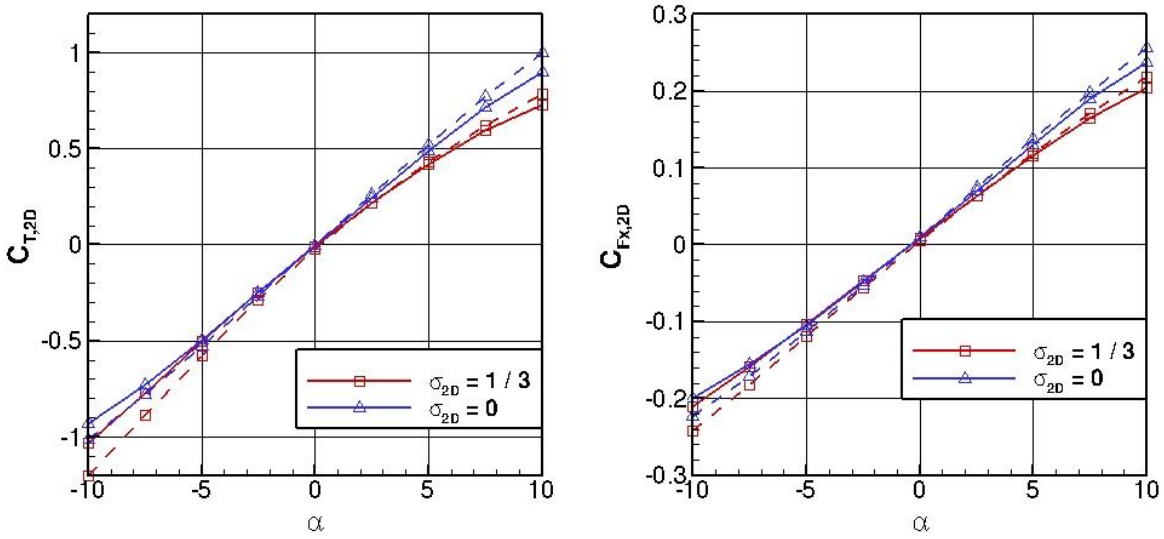

Figure 59: Two-dimensional thrust and circumferential force coefficient for one blade depending on the angle of attack. The advance ratio is set to J=0.75. AL-2C: Solid line; Resolved: Dashed line.

Considering the thrust for the solidity $\sigma_{2D} = 0$, it is visible that the actuator line approach underestimates the magnitude of the thrust for the whole angle of attack range. The reason therefore is caused by the determination of the inflow conditions as stated above. For an angle of attack $\alpha = 10°$, the thrust coefficient provided by the actuator line simulation reads $C_{T,2D,AL}(0.75, 0, 10°) = 0.9$, while the related thrust coefficient for the resolved simulation equals

$C_{T,2D,res}(0.75, 0, 10°) = 1.0$. The thrust predicted by the actuator line approach is underestimated by approximately $10\,\%$. For the angle of attack of $\alpha = -10°$, the related coefficient are $C_{T,2D,AL}(0.75, 0, -10°) = -0.93$ and $C_{T,2D,res}(0.75, 0, -10°) = -1.01$. As a result, the magnitude of the thrust is underestimated by approximately $8\,\%$. Comparing with the results for the AD-PanBL and the AL-PanBL, the effects of the different approaches are clearly visible. While the AD-PanBL approach overestimates the thrust due to the overprediction of the airfoil forces by PanBL and the present approach underestimates the thrust solely caused by the averaging procedure, the AL-PanBL includes both contradicting deviations. That is why the latter method shows the best agreement for this type of investigation. The results for the strong interaction of the blades are presented for the solidity $\sigma_{2D} = \frac{1}{3}$. A good agreement for the both forces is detected. It is visible, that the prediction is better for positive angles of attack $\alpha > 0$. The thrust coefficient for the actuator line simulation equals for the present solidity $C_{T,2D,AL}(0.75, \frac{1}{3}, 10°) = 0.73$. The related thrust coefficient for resolved simulation equals $C_{T,2D,res}\left(0.75, \frac{1}{3}, 10°\right) = 0.78$. Subsequently, the deviation is calculated to be approximately 5%.

Finally, the static test case is discussed. In Figure 60, the thrust and circumferential force coefficient depending on the solidity for the angles of incidence $\theta = \{10°, 20°, 30°\}$ are presented. A good agreement of the forces generated by the actuator line method with respect to the resolved simulation concerning the global behavior is obtained for the angles of incidence $\theta = 10°$ and $\theta = 20°$. However, the forces for the operating points with occurring stall on the blade are not predicted appropriately, e.g. for the combination of small solidities σ_{2D} and the high angle of incidence $\theta = 30°$. The presented behavior is comparable as for the AD-2C approach, but the stall is predicted for higher solidities of $\sigma_{2D} \leq \frac{1}{12}$ instead of $\sigma_{2D} \leq \frac{1}{25}$ also. Nevertheless, the reduction of the forces, if stall occurs, is captured better. Although the underlying airfoil data generation is performed with the same numerical setup and allows therefore the prediction of the stall behavior, the averaging procedure leads to discrepancies in the determination of the inflow conditions and consequently in the forces.

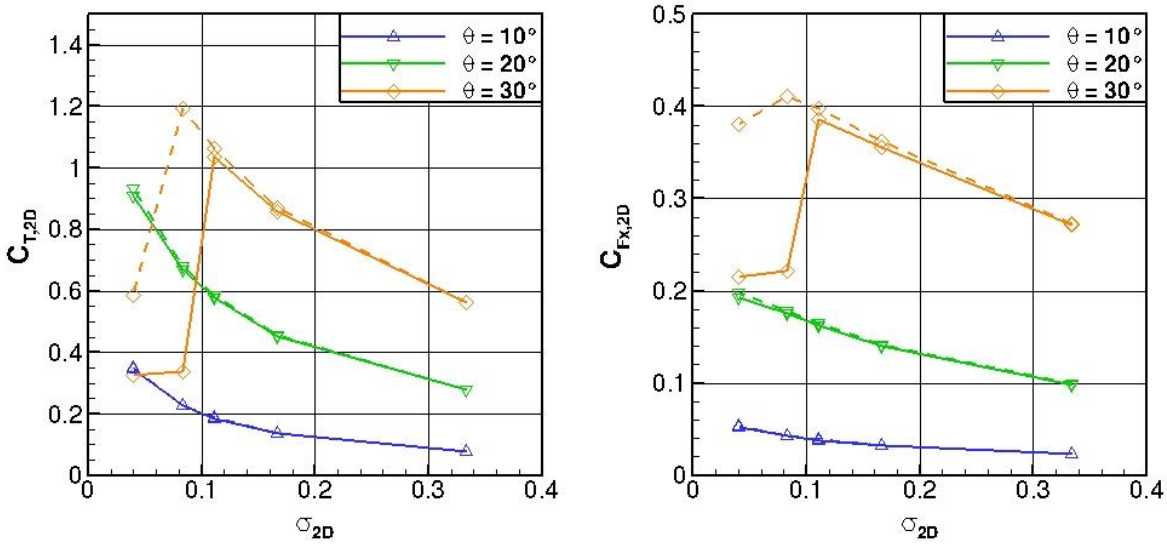

Figure 60: Two-dimensional thrust and circumferential force coefficient for one blade depending on the solidity. The advance ratio is set to J=0. AL-2C: Solid line; Resolved: Dashed line.

As the last point of this subsection, the quantitative discussion is conducted also with the relative deviation of the force coefficients obtained by the AL simulation related to the corresponding quantities of the resolved simulation. The discussion of the slope is also not presented due to the above declared reason. In analogy to the results obtained for the actuator disc approach coupled with 2D-CFD, the maximum deviation is chosen for the comparison. The maximum deviation over all solidities in the stall region for $\theta = 30°$ reads for the thrust $\Delta C_{T,2D,rel} = -71.74\ \%$ and for the circumferential force $\Delta C_{Fx,2D,rel} = -46.08\ \%$. Excluding these points, the maximum deviation over all solidities for the angles of incidence $\theta = \{10°, 20°, 30°\}$ reads for the thrust coefficient $\Delta\widehat{C_{T,2D,rel}} = \{-1.28\ \%, -2.32\ \%, -2.40\ \%\}$ and for the circumferential force coefficient $\Delta\widehat{C_{Fx,2D,rel}} = \{-1.76\ \%, -2.93\ \%, -2.86\ \%\}$. Conclusively, the results of the actuator line coupled with 2D-CFD are in good agreement with those of the resolved simulation for the quantitative consideration also.

Overall Comparison and Conclusions

Before the results between the different methods are compared, a brief review of the important aspects obtained by the resolved simulations for this test case is provided.

For the forward flight test case, the dependence of the forces on the solidity, the angle of attack as well as the advance ratio is investigated. Basically, the higher the solidity, the smaller are the forces. In contrast, the higher the angle of attack, the higher are the forces. For increasing advance ratios, the slope of the forces depending on the solidity becomes more negative. In general, all modeling approaches show the trends correctly. The PanBL-based models overestimate the lift and underestimate the drag which leads to different absolute values. Consequently, the thrust is overestimated for all operating points. For the circumferential force, however, it is depending on the amount of the contribution of the lift and the drag for the considered operating point. For the AL-based models, the underestimated angle of attack obtained by the averaging procedure, in particular, for higher blade loadings results in a more positive slope of the forces depending on the solidity. Both issues can be detected in the plots of the forces depending on the solidities as well as in those depending on the angle of attack.

For the static thrust test case, the dependence of the forces on the solidity and the angle of incidence is investigated. Basically, the higher the solidity, the smaller are the forces and the higher the angle of incidence, the higher are the resulting forces. However, the slope of the forces depending on the solidity is more negative than for the forward flight test case. The trends are representing correctly by the modeling approaches for this case also. The two issues concerning the PanBL-based and the AL-based methods are detectable for the static thrust test case also. Furthermore, additional effects occur. Since the PanBL-based approaches cannot handle the stall appropriately, the thrust is massively overpredicted for low solidities and high angles of incidence. The AL-based approaches, however, underpredict the thrust for low solidities and high angles of incidence. In particular, the higher the calculated drag, the smaller is the predicted thrust due to an underpredicted inflow velocity by the averaging procedure.

Conclusively, the methods show a good agreement for a wide range of input parameters. Moreover, the results obtained by the modeled approaches predict the results of the resolved simulation well for the forward flight case as well as for the static thrust test case.

4 Three-Dimensional Test Cases

This chapter includes the results of the propeller simulations for the generic test case and the complex configuration test cases. The generic test case is chosen in order to investigate the principle effects of the presented modeling approach in detail. The complex test cases have been investigated within the research project EUROPAS [3] in detail and delivers validation data in addition. For all of the test cases, simulations with the generalized actuator disc approach as well as the RANS/URANS simulations are performed and the obtained results are presented and compared. In chapter 4.1, the three-dimensional cascade test case is shown to investigate the modeling approach in spanwise direction. In chapter 4.2, the three-dimensional propeller is used to demonstrate, e.g. non-axial inflow conditions. Finally, the complex test case is discussed in chapter 4.3.

Certain contents of this chapter have been already published by Stuhlpfarrer et al. [3].

4.1 Three-Dimensional Cascade Test Case

The three-dimensional test case is based on the two-dimensional test case by adding a finite wing span with a certain aspect ratio. That means that the geometrical data as well as the numerical setup is very similar. The purpose of this investigation is to proof the quality of the methods including three-dimensional effects. In particular, the influence of the model parameters in the blade tip region, as it is described in the theory chapter, is of interest. The three-dimensional cascade is chosen instead of the propeller, at first, as a simplification within a non-rotating frame.

4.1.1 Test Case Description

General

Figure 61 shows a sketch of the domain used for the simulations as well as the location and types of the boundary conditions. Due to the straightforward extension to the third dimension, the boundary conditions are kept, as far as possible, the same as for the two-dimensional investigations. Consequently, the boundary condition on the upper side of the domain is set to a velocity inlet. The boundary condition on the lower side of the domain is set to a pressure outlet. For the boundaries in chordwise direction, a periodic boundary condition is applied. In spanwise direction, for the symmetry plane a symmetry boundary condition is chosen, while on the opposite boundary a free-slip wall is applied. In order to realize the motion of the blade, a moving reference frame is used for these investigations in the same way as for the two-dimensional test case.
Moreover, Figure 61 exhibits the blade with an aspect ratio of $\Lambda = 20$. The applied airfoil is also the NACA 0012. The angle of incidence is set to $\theta = 0°$. The red line represents the quarter chord line which is used as rotation axis for the blade. The definition of the angle of incidence is in accordance with Figure 27.

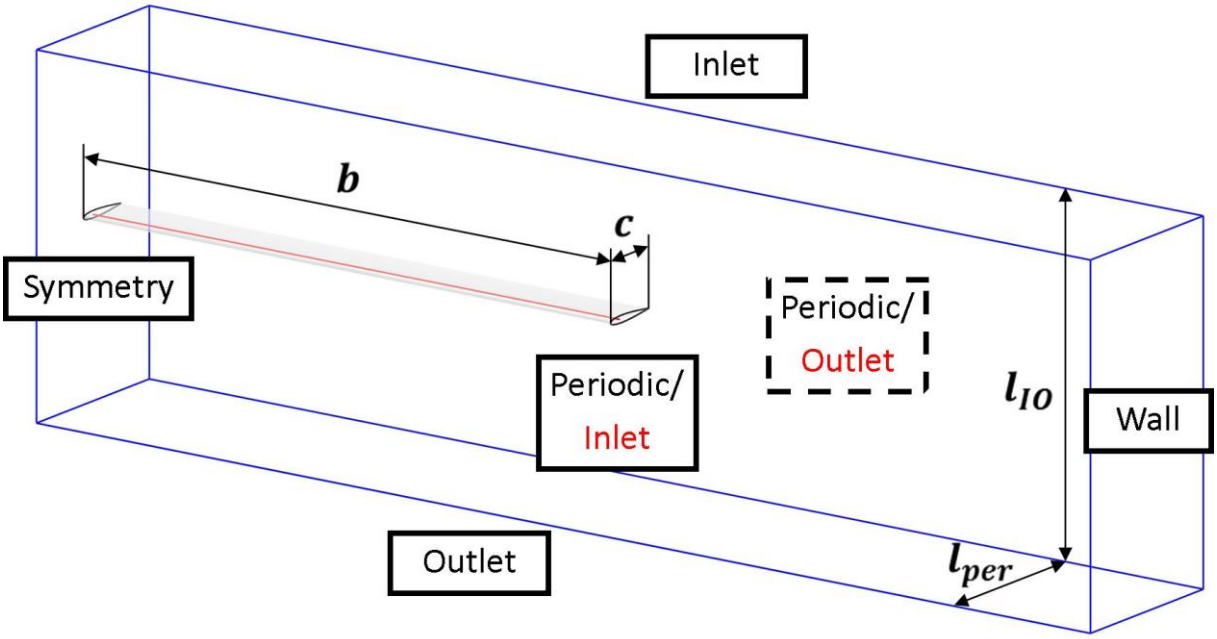

Figure 61: Sketch of the three-dimensional test case.

Although this test case is three-dimensional, however, the definition of the applied solidity is taken over from the two-dimensional test case. This is possible, since the third dimension is established solely by a finite extrusion of the airfoil of the two-dimensional test case. Moreover, the underlying idea of the test cases, to apply a translational motion only, is the same. Consequently, the parameter allows for covering all the effects to be investigated. In addition, a direct comparison with the results of the previous chapter can be made. Nevertheless, the subscript is substituted for a better distinction.

$$\sigma_{3D} = \frac{c}{l_{per}} \tag{4.1}$$

$\mathrm{l_{per}}$ remains the periodic length of the domain and c the chord line of the blade. The chord length is set to $\mathrm{c} = 1\ \mathrm{m}$ as well. For more details concerning the settings of the parameter and its properties, 3.1 is referred.

As stated, the limiting case for $\sigma_{2D} \rightarrow 0$ results in a periodic length $\mathrm{l_{per}} \rightarrow \infty$. In order to simulate this special case for $\sigma_{3D} \rightarrow 0$, the periodic boundary conditions are modified to an inlet and an outlet boundary condition, comparable to the two-dimensional test case. The modification is remarked in Figure 61 also. The size of the domains for the different investigations is similar to the two-dimensional test case. Consequently, the influence of the boundary conditions on the results is comparable small.

Definitions: The applied terms for this test case are in accordance with the two-dimensional test case, see 3.1. The only change is the subscript. The limiting case $\sigma_{3D} \rightarrow 0$ is referred to $\sigma_{3D} = 0$ within this test case.

Objectives and Parameters

The objective of the investigations emphasizes as well on the comparison of the results obtained by the fully resolved cascade flow and the modeled ones for certain operating points. For the three-dimensional investigation, solely the forward flight test case is presented. The reasons are that the results for the two-dimensional test show for the static thrust case similar predictive quality as for the forward flight case. As a consequence, the static thrust case would not provide an added value. Furthermore, due to the higher computational effort in three dimensions in contrast to two dimensions, a reduced number of total simulations is intended.

For the present test case, the description of the properties and its impact on the expected results is discussed briefly. Due to the application of the symmetry and the free-slip wall boundary condition, the derived relations for the two-dimensional test case, see 3.1, are applicable by substituting the line integral with a surface integral, e.g. $\int(\cdot)dx \rightarrow \int(\cdot)dxdz$. Evidently, the added boundaries do not contribute to the equations caused by the orthogonality; neither to the continuity nor to the momentum equation. The statements, concerning the influence of the periodic conditions made in the description for two-dimensional case, remains valid as well. However, the fact that the axial velocity $v(x,z)$ at the inlet and at the outlet is equal for a large length l_{IO} of the domain is not fulfilled. The finite span of the blade with the resulting induced vortex sheet, if aerodynamic forces are generated by the blade, provides different axial velocities downstream of the blade in dependence on the spanwise position. Consequently, the forces are determined only by the integration of the appropriate quantities over the surface of the blade within this investigation.

Since only the forward flight is investigated for this test case, the appropriate set of boundary conditions is presented briefly. Like for the two-dimensional test case, the velocity v_{in} is set at the inlet and the static pressure p_{out} is set at outlet. The static pressure at the inlet p_{in} is a part of the solution and determined implicitly by the propeller-specific parameters.

In the following, the parameter settings for this test case are presented. At first, the propeller-specific parameters are shown and secondly, the parameters assigned to the AD and AL modeling. The nondimensional parameters associated to the propeller are the following

- Angle of Incidence θ
- Solidity σ_{3D}
- Advance Ratio J
- Reynolds Number Re
- Mach Number Ma

In the course of this test case, only the angle of attack α of the blade and the solidity σ_{3D} is varied. Consequently, the influence of different blade loadings as well as different mutual interferences between the blades is presented. The angle of attack α can be imagined as a linear-combination of the angle of incidence θ and the inflow angle ϕ caused by the advance ratio J. The influence of the Reynolds Number Re and the Mach Number Ma is not investigated. For more details concerning the parameters see 3.1. It is noted that the set of parameters investigated within the three-dimensional test case is a subset of the two-dimensional one, in order to allow for simple comparison. Since the blade for the present test case is designed with zero twist, the parameters are constant along the blade and consequently, a reference position is not needed.

The parameters associated with the AD and AL modeling are the same as for the two-dimensional test case, see 3.1. Although the parameters are able to vary along the spanwise direction, this matter of fact is not taken into account for the investigations. The reason is that the blade has constant geometrical properties along the spanwise direction, e.g. chord c, angle of incidence θ. Moreover, the investigations concerning the required widths for the two-dimensional test case, in order to obtain a mesh-independent result, are related to the chord. Consequently, constant widths of the regions along the spanwise direction are justified. In addition, although the actuator line allows for different widths in each coordinate direction, within a plane perpendicular to the spanwise direction, see 3.1, the widths are set equal within the two-dimensional test case. Subsequently, it is set equal within the present test case also and the parameters can be concluded to:

- AR_c: Axial position of the center of the region for determining the inflow conditions
- AR_w: Width of the region for determining the inflow conditions
- AR_s: Width of the smoothing region for determining the inflow conditions
- SR_c: Axial position of the center of the region for distributing the forces
- SR_w: Width of the region for distributing the forces
- SR_s: Width of the smoothing region for distributing the forces

4.1.2 Mesh Generation and Numerical Setup

In the following, the blocking and meshing approaches for the different methods are described as for the two-dimensional test case. At first, the simulation setup for the resolved blades is presented. In the following, the actuator disc and actuator line approach combined with PanBL are explained and finally, the combination with the two-dimensional CFD for obtaining the airfoil data is provided. Since the three-dimensional meshes and setups are based on its two-dimensional counterpart, the descriptions are made briefly and if necessary, the corresponding chapter is referred.

Resolved Propeller

The blocking strategy for the resolved propeller is based on the two-dimensional test case. The blade is embedded in an O-grid, except at the symmetry plane. Figure 62 shows the blocking. The application of the periodic boundary condition, with a one-to-one node-connection, and the settings of the solidity is in accordance with 3.2. These settings are obtained also by inserting a block upstream of the blade. The applicable range of solidities is from $\sigma_{3D} = \frac{1}{3}$ to $\sigma_{3D} = 0$. For the different settings of the angle of incidence, the deformation method is applied as well. Therefore, a constant deformation is applied along the spanwise direction, starting from the symmetry plane and ending at the wall. In Figure 62 (left), the whole domain for the simulation of a solidity of $\sigma_{3D} = \frac{1}{9}$ is shown. In Figure 62 (right), the O-grid and the region near the airfoil is detailed.

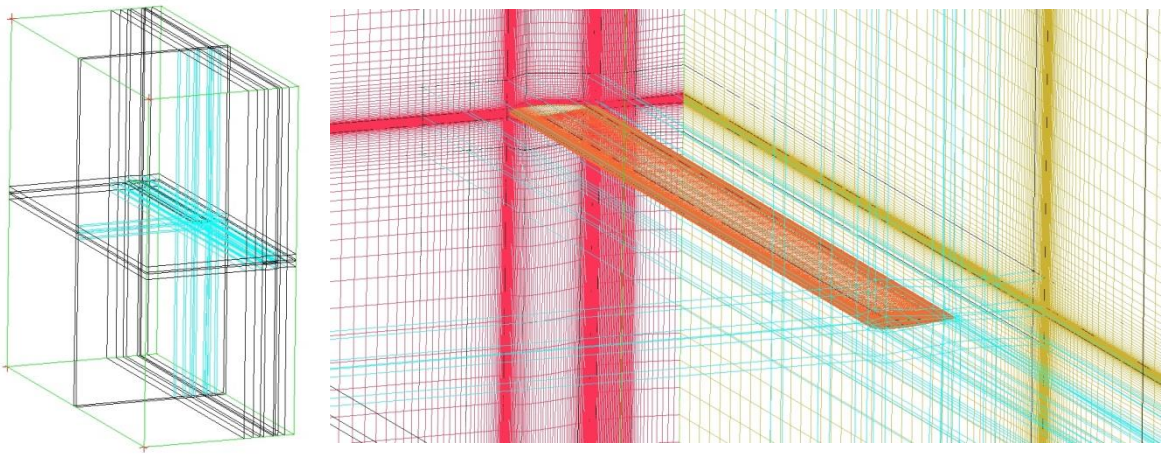

Figure 62: Blocking for the resolved cascade simulation. Blocking of the whole domain for a solidity of $\sigma_{3D} = \frac{1}{9}$ (left) and the detailed view of the blocking around the airfoil (right) is shown.

A mesh independency study is performed as follows. The initial mesh includes 151 blocks with $4.81\ Mio.$ cells for the mesh with a solidity $\sigma_{3D} = \frac{1}{3}$. The number of cells along the chord is 71. The height of the first cell within the boundary layer is set to fulfill a nondimensional wall distance of $y^+ = 1$, in order to resolve the linear behavior within the viscous sublayer appropriately. The O-grid blocks, adjacent to the blade, include 58 cells in the direction perpendicular to the surface with a height of the first cell of $2 \cdot 10^{-5}\ m$. In comparison to the two-dimensional test case, the number of cells is reduced to decrease the numerical effort. Subsequently, the refined and coarsened mesh with a scaling factor in each coordinate direction of 1.25 and $1/1.25$, respectively, is generated. The initial scaling at the surface of the blade is not modified. The evaluated quantities are the thrust as well as the circumferential force coefficient.

In analogy to the two-dimensional test case, the solver settings are described prior to the discussion of the results obtained by the mesh independency study. The settings are basically taken over from the two-dimensional test case. The flow is considered to be incompressible and steady. Consequently, the three-dimensional, pressure-based, coupled solver with absolute velocity formulation is applied. The turbulence model and the numerical schemes are the same as for the two-dimensional test case, see 3.2. Furthermore, the properties of the fluid are unchanged. The Courant number between the simulations is varied in the range of $5 < C < 100$, in order to obtain fast and converging results. The relaxation factors are presented in Table 10. The convergence criteria for all quantities are set to $5 \cdot 10^{-5}$. However, for the solidity of $\sigma_{3D} = 0$, only values less than $6 \cdot 10^{-5}$ for an angle of attack $\alpha = 2.5°$ and values less than $7 \cdot 10^{-5}$ for an angle of attack $\alpha = 5.0°$ are achieved. A detailed study using different explicit-relaxation factors as well as different Courant numbers has been made and shows that the average pressure specification used for the outlet boundary condition hampers convergence. Nevertheless, force convergence is achieved for every result.

As a side node, although for the periodic case the average pressure specification at the outlet is not applied intentionally, an additional test for the operating points $\left(0.25, \frac{1}{3}, 2{,}5°\right)$ and $\left(0.25, \frac{1}{3}, 5.0°\right)$ is performed including it. Interestingly, no parameter set is found to realize at least force convergence with that boundary type due to almost non-damped numerical oscillations.

Table 10: Relaxation factor for the resolved propeller simulations of the three-dimensional test case.

Explicit-Relaxation Factors and Under-Relaxation Factors					
Momentum	Pressure	Density	Turbulent Kinetic Energy	Specific Dissipation Rate	Turbulence Eddy Viscosity
$\alpha_{mom} = 0.3$	$\alpha_p = 0.3$	$\alpha_{den} = 1.0$	$\alpha_{tke} = 0.8$	$\alpha_\omega = 0.8$	$\alpha_{\nu_t} = 1.0$

The mesh independency study is performed for the same operating point as for the two-dimensional case $(J, \sigma_{2D}, \alpha) = \left(0.25, \frac{1}{3}, 5.0°\right)$, representing strong interaction and moderate blade loading. Table 11 provides the thrust and circumferential force coefficient for the three meshes. Resulting, the initial grid is applied for the present investigations.

Table 11: Mesh independency study for the resolved simulation of the three-dimensional test case.

	Coarse grid	Initial grid	Fine grid
$C_{T,3D}$	0.172	0.173	0.173
$C_{Fx,3D}$	0.035	0.035	0.035

Actuator Disc Approach with PanBL

The mesh for the three-dimensional actuator disc (AD) simulation coupled with PanBL (AD-PanBL) is based on the two-dimensional counterpart as well. The mesh resolution in the region of the actuator disc is similar to that of the resolved simulation for comparability. Taking into account the periodicity, one cell in the circumferential direction is sufficient for this test case, see 3.2. In the axial direction, the distribution law is like in the two-dimensional test case. For the spanwise direction, a refinement is established in the region of the blade tip. The blocking and the mesh are shown in Figure 63. The periodic length for the one cell in the circumferential direction is set to $l_{per} = 1\ m$ and the setting of the solidity as well as the angle of incidence is performed as numerical parameter within the calculation. The periodicity is established in the same way as for the resolved simulation.

For the present investigation, the mesh independency study is not conducted. The reason therefore is the connection of the sizes of the cells with the width of the distribution function. As described in 3.3, the ratio of the width of the distribution function related to the size of the cell is more important than the absolute size of the cell for obtaining mesh-independent results.
The applied mesh consists of 8 blocks with 10400 cells. The blocking strategy is presented in Figure 63 (left). In the region of the actuator disc, a constant spacing of $2 \cdot 10^{-2}\ m$ is established in the vertical direction. For the spacing in the spanwise direction, a non-linear distribution of the nodes is applied. At the blade tip, almost squared cells are obtained. Therefore, Figure 63 (right) details the region where the actuator disc acts.

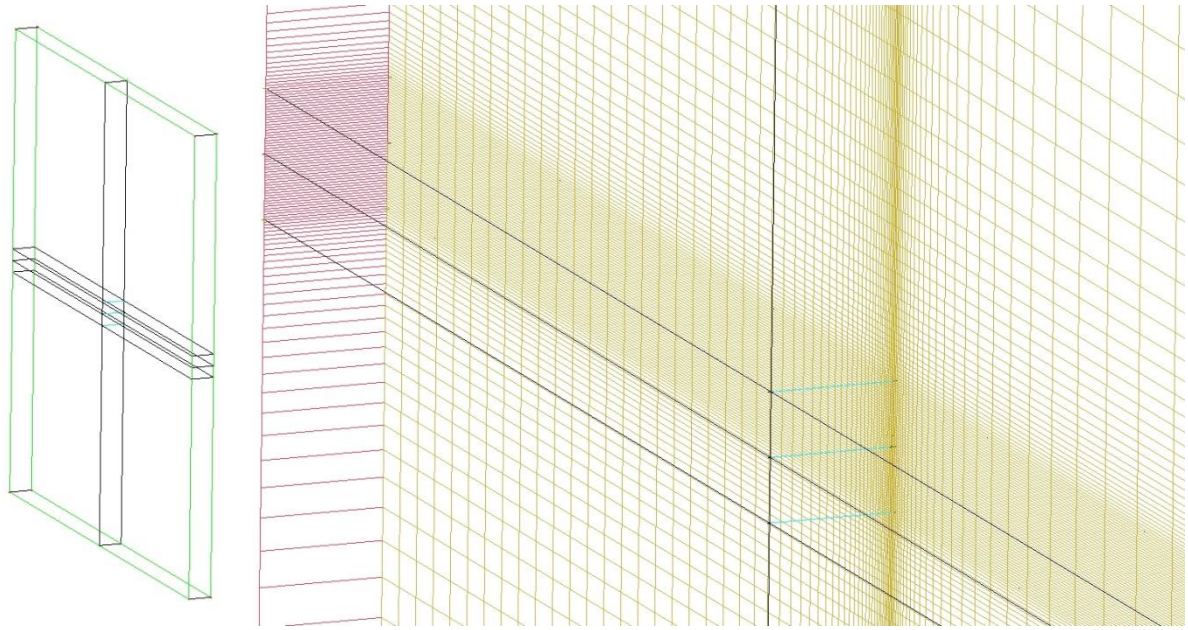

Figure 63: Blocking for the actuator disc simulation. Blocking of the whole domain (left) and detailed view of the blocking with mesh in the actuator disc region (right) is shown.

The chosen numerical schemes and models are the same as for the resolved configuration. The Courant number is set to $C = 5$ and the relaxation factors for momentum and pressure to $\alpha_{mom} = \alpha_p = 0.3$. For the distribution of the actuator disc, a cosine-law with 10 sections is applied in spanwise direction.

For this method, an independency study of the residuals is performed as well. Recalling the two-dimensional test case, a more scientific, strict criterion is chosen. Due to the higher numerical effort of the three-dimensional test case and with regard to modeling a complex real-world application with limited computational power, the influence of the convergence criterion on the results has to be investigated. Therefore, the thrust and circumferential force coefficients are evaluated. The convergence criteria are set to 10^{-4}, 10^{-5}, and 10^{-6} for all residuals. The simulations are made for all operating points presented in the discussion of the results in the next section. The maximum relative deviation of the thrust and circumferential force, by taking into account all points, results for the criteria 10^{-4} related to the criteria 10^{-6} in less than $\Delta C_{T,3D,rel} < 4{,}8 \cdot 10^{-4}$ and $\Delta C_{Fx,3D,rel} < 4{,}21 \cdot 10^{-5}$, respectively. Consequently, the criteria of 10^{-4} is sufficient. Nevertheless, since the results are calculated for the stricter criterion anyway, the discussion is made with the results for the criterion of 10^{-6}.

Actuator Line Approach with PanBL

The blocking strategy and the mesh setup for the actuator line approach (AL) simulation coupled with PanBL (AL-PanBL) are based on those of the resolved simulation. The modifications follow the workflow as provided within the two-dimensional test case, see 3.2. The periodic boundary condition is applied also. The setting of the solidity is conducted by the definition of the periodic length l_{per} of the domain and the angle of incidence is set within the calculation of forces as a numerical parameter.

Basically, the blocks in the region of the airfoil are substituted by a Cartesian grid block, but with equal and constant spacing solely in plane perpendicular to the spanwise direction. In order to keep the modifications between the different approaches as small as possible, the blocking is generated by extruding the blocking of the two-dimensional AL approach along the spanwise direction and prescribing the spanwise distribution of the three-dimensional AD approach. Consequently, comparisons between the different approaches can be made easily. Figure 64 (left) shows the blocking strategy for this approach. In Figure 64 (right), a detailed view of the region containing the actuator line is presented.

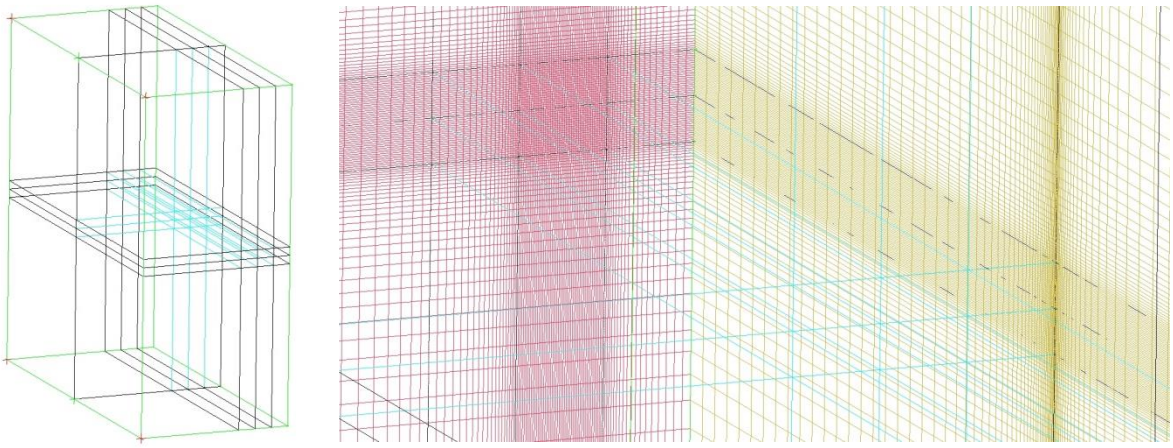

Figure 64: Blocking for the actuator line simulation. Blocking of the whole domain for a solidity of $\sigma_{3D} = \frac{1}{9}$ (left) and detailed view of the blocking with mesh in the actuator line region (right) is shown.

The mesh independency study is also not conducted for the present investigation. The arguments are the same as for the AD approach of the three-dimensional test case in the previous section. Reconsidering therefore the results generated by the actuator line approach within the two-dimensional test case as presented in 3.3. The outcome is that the ratio of the width of the distribution function related to the size of the cell is more important than the absolute size of the cell for obtaining mesh-independent results. Obviously, the statement is applicable for the AD as well as the AL approach. Nevertheless, the mesh for $\sigma_{3D} = \frac{1}{3}$ includes 24 blocks and 915200 cells. The resulting resolution in the region of the actuator line is $2 \cdot 10^{-2}\ m$.

Finally, the settings of numerical schemes and models are chosen as for the resolved simulations with certain case-dependent modifications of the Courant number. For the latter, in addition, an iteration-step depending scheme is applied. The initial value reads $C = 100$. If after a certain target of iterations convergence is not reached, the number is successively reduced. This procedure allows at the beginning a fast convection of the initial perturbation through the domain and when reaching the end of the simulation, convergence can be achieved easier. Nevertheless, most simulations within this investigation do not make use of this procedure, since convergence is obtained at first. The relaxation factors for momentum and pressure are set to $\alpha_{mom} = \alpha_p = 0.3$. The convergence criterion is set to 10^{-5} for all residuals. Therefore, force convergence is achieved as well. For the distribution of the actuator line, a cosine-law with 10 sections is applied in spanwise direction.

Actuator Disc Approach with 2D-CFD

According to the theory chapter, the present approach is a combination of the actuator disc and the resolved simulation of a blade section in two dimensions (AD-2C). In contrast to the AD-PanBL simulation, for this test case, the airfoil data generation is substituted by two-dimensional simulations of resolved blades (2C) for all sections. For comparability issues, the mesh including the actuator region is taken from the AD-PanBL simulation. For the two-dimensional resolved airfoil, the mesh of the resolved airfoil simulation of the two-dimensional test case is taken, see 3.2. Subsequently, it is extruded in spanwise direction by one cell, in order to enable the solving within the three-dimensional Fluent solver. Consequently, a mesh independency study is not conducted, since studies are performed or arguments for its necessity are already provided for the underlying cases. Figure 65 shows the mesh of the different domains. On the left hand side, the actuator disc domain is presented. On the right hand side, the multiple domains for each section of the two-dimensional resolved airfoil simulation are provided. For the actuator disc domain, the periodic mesh of the AD-PanBL simulation is applied, except for the solidity of $\sigma_{2D} = 0$. It has to be noted that for the simulation of the blade section, the mesh of the stand-alone airfoil of the two-dimensional test case, with inlet and outlet boundary conditions, serves as basis. In addition, the deforming mesh capabilities are used for describing the appropriate angle of incidence of the airfoil section. As a side note, a non-constant twist of the blade could be established easily as well for the three-dimensional case with this capability. The solidity is set within the force calculation like for the AD-PanBL simulations.

Before starting the description of the numerical setup, some aspects on the generation of the mesh and the workflow are provided. The idea of the approach is to simulate all domains within one multiple-domain solver run. At first, the domain including the actuator region is inserted. Thereafter, the first domain including the first blade section is added at a translated position. This is not necessary for solving the problem, but enables easier post-processing. Subsequently, the domains are copied several times according to the number of sections needed. These allows for simulations on the exactly same mesh for each section which is necessary for fast convergence. The tasks are fully automated within the developed framework.

The principal numerical setup and models are taken from the basic cases. However, due to the high effort for generating the setup manually, the developed framework allows a fully automated generation of the numerical setup as well. The executed tasks are:

- Loading the mesh
- Renumber boundary condition in accordance to UDF
- Loading material database and setting materials for the domains; allows, for example, to calculate with constant density within the AD domain and with ideal gas within the resolved blade section domain to cover compressible effects
- Setting models, e.g. turbulence model
- Setting boundary conditions, e.g. inlet velocity, and linking with UDF
- Setting domain parameters, e.g. source terms, and linking with the UDF
- Setting initial values in the appropriate coordinate frame

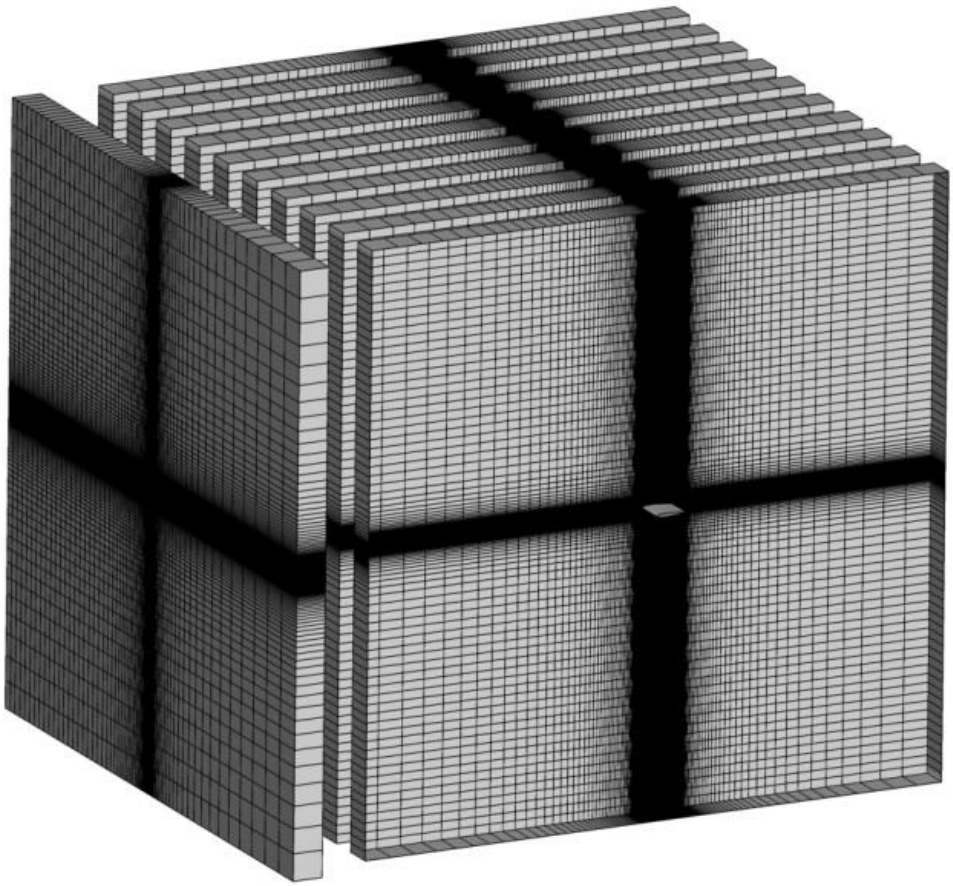

Figure 65: Mesh for the actuator disc approach coupled with 2D-CFD. On the left hand side, the AD disc domain is shown while on the right hand side the resolved airfoil domains are presented. The airfoil is shown in its non-rotated state.

These tasks are necessary for the two-dimensional test case as well, but due to the high number of domains, the automation provides a huge advantage. Considering the whole workflow, starting with the mesh generation, it is ensured that each domain has the same properties. For the present test case, an investigation on the equality of the results over the domains is performed as well. The study is made in serial as well as parallel mode of the solver. Therefore, constant quantities are set and initialized for all domains. The result is that in serial as well as in parallel mode the results are equal to an appropriate number of digits; far more than required for the result. In particular in the parallel mode, the final digits may differ, caused by the application of the dissection method within the domains.

As discussed for the two-dimensional test case, the diverging scales of the domain require some special treatment to obtain at first, stable and at second, fast converging solutions, see 3.2. A further increase in the complexity arises that for the three-dimensional case not solely two domains are involved. Since for every considered section, a two-dimensional simulation within a separate domain is performed, the number of domains equals the number of sections plus one. Consequently, a stable and fast converging solution has to be obtained for each individual simulation in order to avoid an oscillating global solution, basically. In addition, to allow for convergence in the domain of the modeled blade, the distribution along the spanwise direction should not include oscillations. That is why for the present method different update scheme for the forces and the inflow conditions are applied as well. However, due to the higher complexity and the higher number of degrees of freedom of the system, the scheme is formulated stricter as for the two-dimensional case. In general,

at first the flow field in the AD domains is calculated by a one-way coupling. Therefore, the inflow conditions in the domains for each blade section are kept constant and the resulting forces are fed into the AD domain as appropriate source terms. If the flow is developed, the two-way coupling is enabled and the inflow conditions for each domain of a section are updated appropriately. For the inflow velocities, the relaxation factor of $\alpha_{u,update} = 0.05$ is applied. The usage of the non-linear relaxation factor, as presented for the two-dimensional test case of this approach in 3.2, is not implemented, since the estimation of the factor in three dimensions is more difficult. However, the solution itself is not affected; solely, an additional simulation speed-up can be achieved by the implementation. The update interval is determined in order to achieve a certain local convergence prior to the following update. As a side note, the described method to change the angle of attack at each update cycle by rotating the airfoil with the application of the mesh-deformation method instead of the modifying the inflow conditions of a section, see 3.2, can be considered. Occasionally, higher convergence speeds can be achieved.

The settings of the Courant number and the explicit-relaxation factors for momentum and pressure are for the current approach in accordance with the applied ones for the AD-PanBL approach. The quantities read $C = 5$ and $\alpha_{mom} = \alpha_p = 0.3$. The convergence criteria for the residuals are set to 10^{-6}, generally. However, for certain operating points with well-suited initial condition, force convergence is not obtained. In this case, the simulations are extended to achieve a convergence criterion of $5 \cdot 10^{-7}$ for all residuals. For the distribution of the actuator disc, a cosine-law with 10 sections is applied in spanwise direction.

Actuator Line Approach with 2D-CFD

Finally, the combination of the actuator line with the simulation of the resolved airfoils in two dimensions (AL-2C) is detailed. Since it is the extension of the AD-2C approach presented in the last paragraph by one dimension as well as for comparability issues, the meshes are overtaken as far possible from the previous cases. The mesh embedding the actuator line is taken from the AL-PanBL simulation, while the meshes for the different blade sections are taken from the AD-2C simulation. The mesh independency study is also not conducted due to the clarification of its necessity stated for the underlying basic meshes. Figure 66 shows the assembly of the meshes. On the left hand side, the actuator line domain is depicted. The setup is shown for a solidity of $\sigma_{3D} = \frac{1}{9}$. The boundary conditions are set depending on the solidity. On the right hand side, the multiple domains for the resolved airfoil sections are provided. For each domain, the setup of the resolved simulation applied for the two-dimensional test case serves as basis. The further modifications are conducted as for the AD-2C simulation. The setting of the angle of incidence is performed by the deforming mesh routine and the solidity is set by the periodic length l_{per}.

The generation of the mesh for the present test case is performed in analogy to the previous described workflow for the AD-2C approach. Therefore, the same automated mesh generation process is applied. Consequently, only the AL domain is different. Moreover, the automatic generation of the numerical setup of the test case is executed as well. Since the domains for the airfoil sections remain unchanged related to the AD-2C simulation, the equality of the results for each section using, in particular, the parallel solver is not investigated.

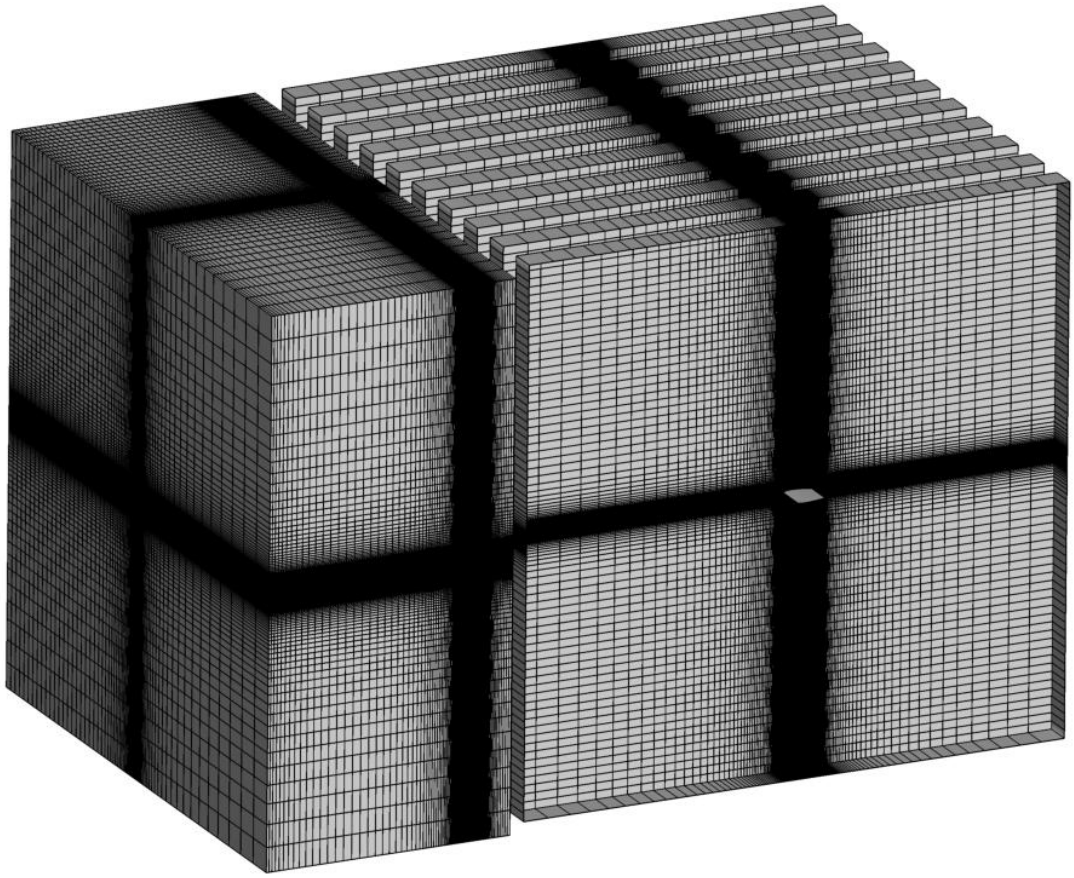

Figure 66: Mesh for the actuator line approach coupled with 2D-CFD. On the left hand side, the AL disc domain is shown for a solidity of $\sigma_{3D} = \frac{1}{9}$ while on the right hand side the resolved airfoil domains are presented. The airfoil is shown in its non-rotated state.

The numerical setup is similar to the AD-2C approach. The difficulties concerning the difference in the scales of the domains as well as the possibility for an unintended oscillating solution described for the AD-2C approach have to be considered for this approach also. Basically, the update scheme described for the AD-2C simulation is applied for the present investigation. The relaxation factor for the inflow conditions reads $\alpha_{u,update} = 0.1$. The actuator line allows a more aggressive setup of the explicit-relaxation factor and the Courant number. This is, among others, caused by the dimensioning of the domain. The setting for the Courant number and the explicit-relaxation factors can be taken over from the AL-PanBL approach applied to this test case. The initial Courant number is set to $C = 50$. In contrast to the AL-PanBL simulation, the step-wise modification of the Courant number is not required due to better convergence behavior. Obviously, the applied update procedure has a similar effect on the solution. The values for explicit-relaxation factor for momentum and pressure are $\alpha_{mom} = \alpha_p = 0.3$. For the distribution of the actuator line, a cosine-law with 10 sections is applied in spanwise direction.

4.1.3 Results and Discussion

In the following, the results for the simulations concerning the variation of the solidity σ and the angle of attack α for a constant advance ratio J are discussed. At first, the investigation is conducted for the resolved cascade to clarify the general effects occurring within the test case. Therefore, the thrust and the circumferential forces are presented comparably to the two-dimensional test case. The further steps are to evaluate the quality of each of the presented modeling approaches followed by an overall comparison of the approaches and a conclusion.

In order to obtain dimensionless coefficients, the following definitions are applied. It has to be noted that the definition of the coefficients within this investigation is an extension of the two-dimensional test case and differs from the common notation for propeller investigations as well. The forces are considered only for one single blade.

Thrust coefficient of a blade:

$$C_{T,3D} = \frac{T_{3D}}{\frac{1}{2}\,\rho\, v_{rel}^2\, c\, b} \tag{4.2}$$

Circumferential force coefficient of a blade:

$$C_{Fx,3D} = \frac{F_{x,3D}}{\frac{1}{2}\,\rho\, v_{rel}^2\, c\, b} \tag{4.3}$$

Advance ratio:

$$J = \pi \cdot \frac{v}{u} \tag{4.4}$$

Segment loading:

$$SL = \frac{T_{3D}}{l_{per}\, b} = \frac{T_{3D}}{c\, b}\sigma_{3D} = \frac{T_{3D}}{A}\sigma_{3D} \tag{4.5}$$

Normalized, sectional force coefficients for the resolved simulation:

$$C_{F,3D,i} = \frac{\sum_{N_{fis}} F_{i,f}}{\frac{1}{2}\,\rho\, v_{rel}^2\, c\, b}\frac{c\,\Delta z}{\sum_{N_{fis}} A_{i,f}} \tag{4.6}$$

Normalized, sectional force coefficients for the modeled simulations:

$$C_{F,3D,i} = \frac{\sum_{N_{cis}} S_{i,c}\, V_{i,c}}{\frac{1}{2}\,\rho\, v_{rel}^2\, c\, b}\,\frac{A_{cp}\,\Delta z}{\sum_{N_{cis}} V_{i,c}\, F_{distr}}, with\ A_{cp} = \begin{cases} SR_w\, l_{per}, & AD \\ SR_w^2, & AL \end{cases} \tag{4.7}$$

The advance ratio is defined including the π, in order to be in consistent with the definition of J for propellers and consequently, obtaining comparable inflow angles for certain values of J.

Resolved Propeller

As presented in the general description of the test case, only the forward flight test case is presented. Therefore, six operating points are chosen. The advance ratio equals $J = 0.25$. The solidities are set to $\sigma_{3D} = \left\{\frac{1}{3}, \frac{1}{9}, 0\right\}$ and the angles of attack to $\alpha = \{2.5°, 5.0°\}$. The parameter space covers a variation of the mutual interaction effects of the blades as well as different blade loadings. The advance ratio is not varied, since at it is shown for the two-dimensional test case, mainly the rotation of the force vectors caused by the variation of the inflow angle change the results.

In Figure 67, the thrust and the circumferential force coefficient of a single blade depending on the solidity are presented for an advance ratio of $J = 0.25$. In addition, the corresponding results for the two-dimensional test case, see Figure 35, are added. Basically, for the three-dimensional test case, a distinct dependence of the forces on the solidity is detected. For higher angles of attack, the reduction of the forces is more pronounced. Compared to the two-dimensional results, the maximum values for the whole range of the solidity are smaller and the slopes depending on the solidity are more negative for the three-dimensional case. At first, the deviation of the maximum value is discussed. The maximum of the thrust and circumferential force is obtained for the solidity $\sigma_{3D} = 0$. Taking into account the common formula for the decrease of the lift slope depending on the aspect ratio for an elliptical wing, derivated from the extended lifting-line theory, the reduction of the lift can be approximated [113]. The ratio of the lift slopes for a finite wing with an aspect ratio of $\Lambda = 20$ and an infinite wing reads approximately $\frac{C_L}{C_{L\infty}} \approx 0.9$. Applying the ratio to the two-dimensional lift, the result of the three-dimensional test case is still slightly smaller. However, it also has to be mentioned that the lift slope depending on the aspect ratio is smaller for the rectangular wing than for the elliptical wing and the efficiency of the airfoil reduces the lift slope as well. Due to the contribution of the lift to the thrust and circumferential force, the reduction of the coefficient is visible in both quantities. After describing the maximum value, the slope of the thrust and circumferential force coefficient depending on the solidity is discussed. As stated above, the trends of the forces for the two-dimensional as well as the three-dimensional case are similar, but the gradients differ. The difference is mainly caused by the design and properties of the test cases. For the two-dimensional test case, the inflow velocities for a certain blade are varying slightly for different section loadings, while the mass flow through the domain is constant. For the three-dimensional test case, the mass flow through the domain is constant as well. However, the difference occurs due to the finite wing. Considering two planes, offset parallel from the symmetry plane. One plane is positioned within the wing span and one outside. Evidently, the finite lift-generating wing produces a downwash and blade tip vortices. For an infinite number of blades, the vortices can be imagined as vortex sheet, separating the higher downwash velocity in the wake of the blade from the velocity outside of the wing region. The higher the segment loading, which is proportional to the solidity, the higher is the axial inflow velocity to the blade and subsequently, the reduction of the lift of the blade is higher. Although the mass flow, and consequently the mean axial velocity are equal for the test cases, the differing velocity distribution along the spanwise direction leads to this result. The curves can also be compared to the result for the two-dimensional static thrust test case, see Figure 43. For the static thrust, the inlet velocity is not fixed, by definition, and the velocity is adjusted automatically depending on the segment loading. The resulting curve shows a similar trend as the three-dimensional test case with fixed inflow velocity in forward flight. However, the slope is even more negative than for the three-dimensional test case. It can be imagined, that the restriction

for the change of, in particular, the axial velocity is at highest starting from the two-dimensional forward flight test case via the three-dimensional flight test case to the two-dimensional static thrust test case. This aspect declares the slopes of the curves. Moreover, the plausibility of the results can be checked with this relation. In contrast to the two-dimensional forward flight test case, a measure for the reduction of the forces depending on the solidity, e.g. see (3.11), is not provided. As stated above or according to the detailed description of the two-dimensional static-thrust test case, see 3.3, the different segment loading is dominating the trend on the forces in the present case.

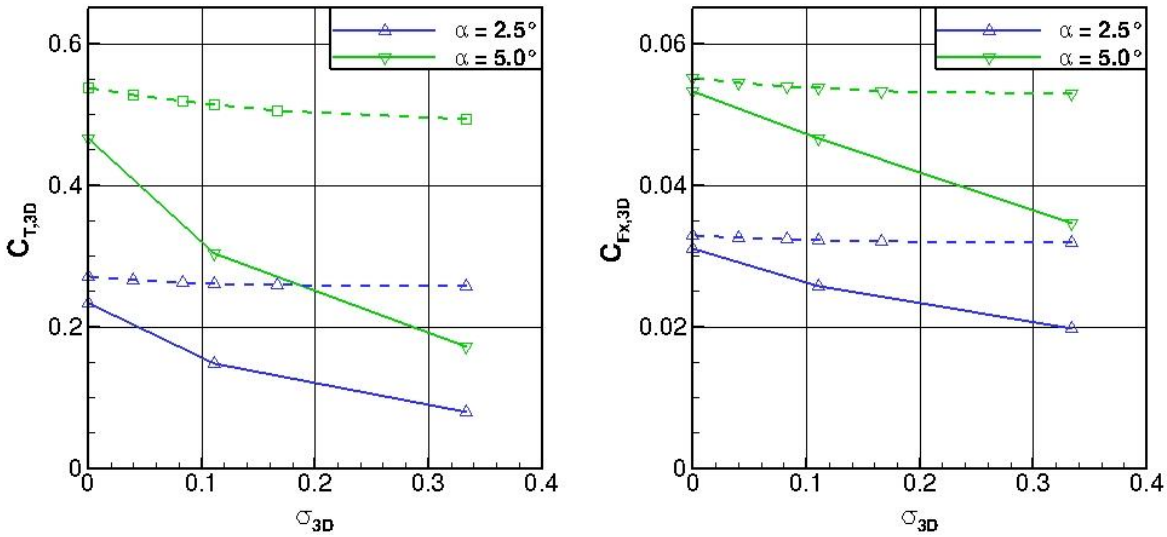

Figure 67: Three-dimensional thrust and circumferential force coefficient for one blade depending on the solidity. The advance ratio is set to $J = 0.25$. Resolved.

After discussing the global quantities obtained for test case, the spanwise distribution is provided. Therefore, the normalized, sectional force coefficients are calculated according to (4.6). Before starting the analysis of the results, some notes on the basic ideas for the determination of the quantity are described briefly.

The coefficient is used to present the spanwise distribution of the forces for a certain number of sections N_{sec} for the evaluation. The distribution of the sections, within these investigations, is constant in spanwise direction with $N_{sec} = 20$. Furthermore, the coefficient has to provide results for the resolved simulation as well as for the modeled simulation for allowing comparison. For the resolved simulation, the forces are obtained by surface integration, while for the modeled simulations, the forces result out of volume integration. Due to the discretization, the integration is substituted by a sum. In order to check if the force of a certain element, face or cell, contributes to a certain section, the centroid of the element is considered. Is the latter positioned within the region, the whole elements contributes to the section. The principle is comparable to that applied for the velocity averaging and the source distribution of the modeled approaches. Since the cells of the mesh are not continuously distributed along the spanwise direction, one section can include more cells than the adjacent section and consequently, the obtained forces for the section are higher. In order to prevent this behavior, the forces are related to the effective projected area or effective volume within the section, respectively. In addition, for the modeled approaches the volumes are multiplied with the local value of the distribution function, since the source terms inherently include the weighting. Finally, the results are extended by the ideal area or volume within a section. This

volume is different between the AD and AL approach, due to the definition of the ideal quantity. The representative radius for a certain section is the mean radius of each section. The latter is used for plotting the spanwise position of the corresponding normalized, sectional force coefficient.
In Figure 68, the distribution of the normalized, sectional thrust and circumferential force coefficient along the spanwise direction is presented. At first, the distributions associated to a solidity of $\sigma_{3D} = 0$ are considered. For both angles of attack, a common distribution known of a wing is obtained. The values of the thrust coefficient scale almost linear with the angle of attack from $\alpha = 2.5°$ to $\alpha = 5.0°$. This result is caused by the dominating contribution of the lift to the thrust. For the circumferential force, the scaling is evidently non-linear. In the next step, the results for the solidity of $\sigma_{3D} = 1/3$, representing strong mutual interaction, are considered. In a global view, for both angles of attack, the sectional forces are decreased in comparison to the non-influenced case with a solidity of $\sigma_{3D} = 0$. The description therefore is already provided within the discussion for the overall coefficients and is caused by the modified inflow conditions, induced by the upstream located blade. However, the sectional thrust and circumferential force are increased locally in the vicinity blade tip. The higher loading occurs due to the interaction of a certain blade with the blade tip vortices of the upstream located blades. Due to the contraction of the flow in streamwise direction, the blade tip vortices are shifted to smaller spanwise positions and consequently, the interaction of the vortices with the downstream located blades takes place on the blade surface. For spanwise positions, greater than those of the axes of the vortices, the induced velocity of the latter increases the local angle of attack and subsequently, the lift in this region. The effect is more pronounced the higher the angle of attack of the blade. Due to the contribution of the lift to the thrust as well as to the circumferential force, the increasing local loading is detectable in both distributions. In addition, the drag is increasing as well with higher angles of attack caused by the interaction with the vortices. The results for the solidity $\sigma_{3D} = 1/9$ show the same trend, but reasonably, not that pronounced.

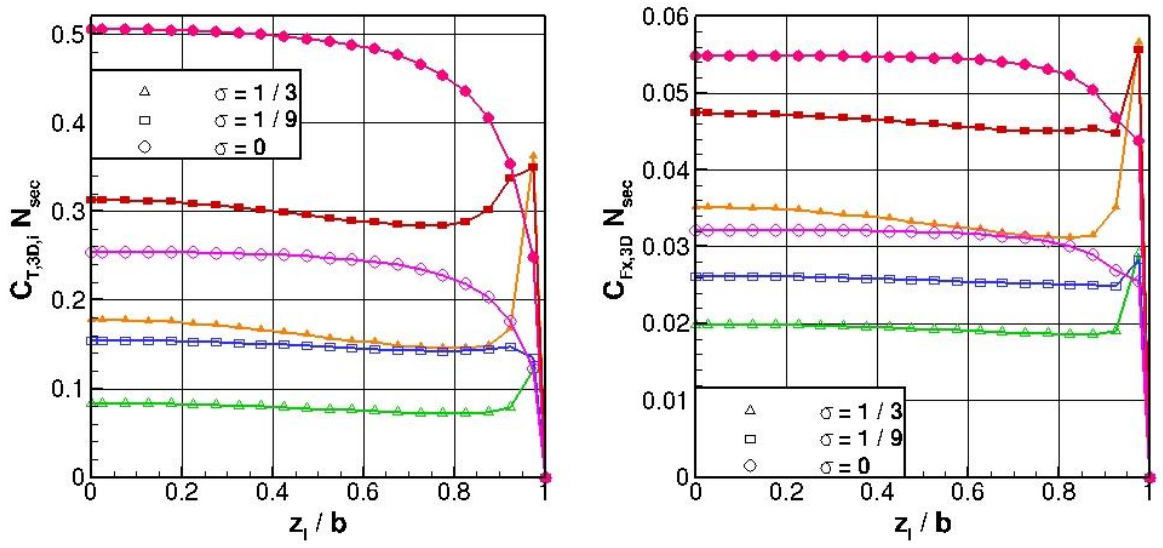

Figure 68: Normalized, sectional thrust and circumferential force coefficient along the spanwise direction. The results for the angles of attack of $\alpha = 2.5°$ (non-filled symbols) and $\alpha = 5.0°$ (filled symbols) are shown. Resolved.

For a better visual imagination of the flow field, in Figure 69, isosurfaces of the normalized, axial vorticity for a value of $\frac{\omega_x b}{U_\infty} = -10$ are plotted. In particular, the influence of the solidity on the vortex formation shall be illustrated. Therefore, the isosurface associated with the solidity of $\sigma_{3D} = \frac{1}{3}$

is orange highlighted, with the solidity of $\sigma_{3D} = \frac{1}{9}$ is blue highlighted, and with the solidity of $\sigma_{3D} = 0$ is green highlighted. Comparing the results for the smaller angle of attack of $\alpha = 2.5°$ (left) with that of the higher angle of attack of $\alpha = 5.0°$ (right), it is evident the cross section of the isosurface is larger which is related to a higher vorticity inside. Moreover, the deflection of the vortices in negative spanwise direction with increasing angle of attack, caused by the contraction of the flow, is detectable. The same trend is visible for higher solidities also. Basically, the higher the angle of attack and the solidity, the stronger is the interaction of the blade with the vortices of the upstream located blades. The highest interaction occurs for the angle of attack of $\alpha = 5.0°$ and the solidity of $\sigma_{3D} = \frac{1}{3}$. For this operating point, the vortex of the upstream located blade, represented by the isosurface, matches the surface of the blade. For the smaller angle of attack of $\alpha = 2.5°$ and the same solidity, the vortex is located more downwards. A similar behavior, but with a different strength of the vortex, is obtained for the angle of attack of $\alpha = 5.0°$ and the solidtiy of $\sigma_{3D} = \frac{1}{9}$. Comparing the results with the distribution of the forces presented in Figure 68, the described local increase of the forces in the blade tip region is proofed.

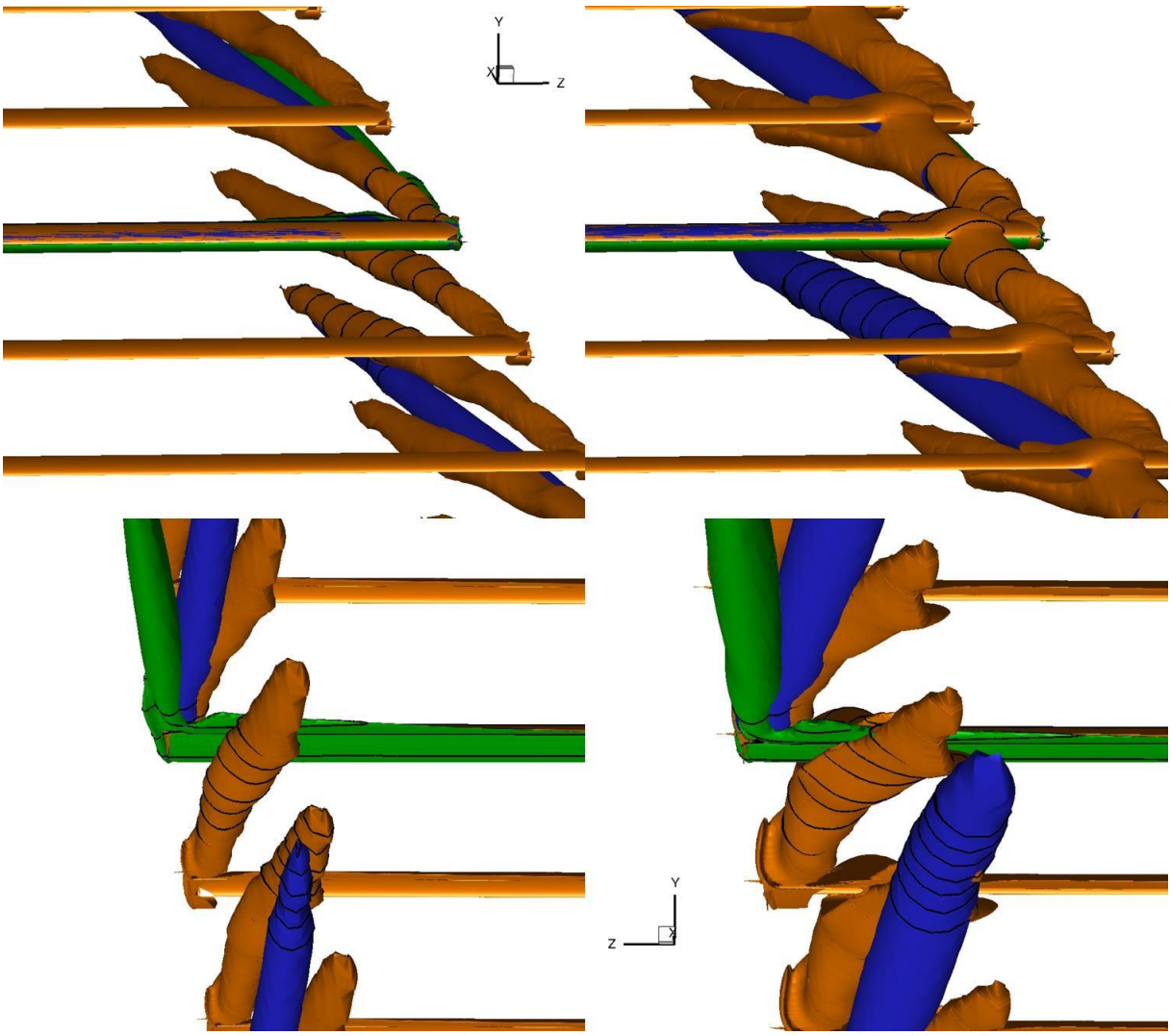

Figure 69: Isosurfaces of the normalized, axial vorticity for a value of $\frac{\omega_x b}{U_\infty} = -10$ are shown in the blade tip region. The top row depicts the suction side and the bottom row the pressure sides of the blades. The left column presents the results for an angle of attack of $\alpha = 2.5°$ and the right column for an angle of attack of $\alpha = 5.0°$. The isosurface for the

solidity of $\sigma_{3D} = \frac{1}{3}$ is orange highlighted, for the solidity of $\sigma_{3D} = \frac{1}{9}$ is blue highlighted, and for the solidity of $\sigma_{3D} = 0$ is green highlighted.

Although the isosurface shows the location of the vortices relative to the blade appropriately, in Figure 70, slices of the normalized, axial vorticity for values smaller than $\frac{\omega_x b}{U_\infty} \leq -1$ are shown and contoured to present the strength of the vortices more detailed and allow for a better visualization of the contraction of the flow. Recalling (4.5), the segment loading is proportional to the thrust of a single blade and the solidity. According to the momentum theory, the contraction of the flow is higher for higher segment loadings. In addition, the strength of the vortices is also higher for higher segment loadings. The highest segment loading within the present investigation is obtained for an angle of attack of $\alpha = 5.0°$ and a solidity of $\sigma_{3D} = \frac{1}{3}$. As it is visible in Figure 70 (bottom, left), the contraction of the flow is the highest compared to the other operating points. The same statement can be made for the strength of the vortices. In particular, the above declared interaction of the vortices with the blade is well detectable. An interesting aspect concerning this operating point is that due to the interaction of the upstream vortex with the blade a larger diameter of the vortex core appears. Finally, the stand-alone wing shows a commonly increased strength of the vortices for higher angles of attack, obviously.

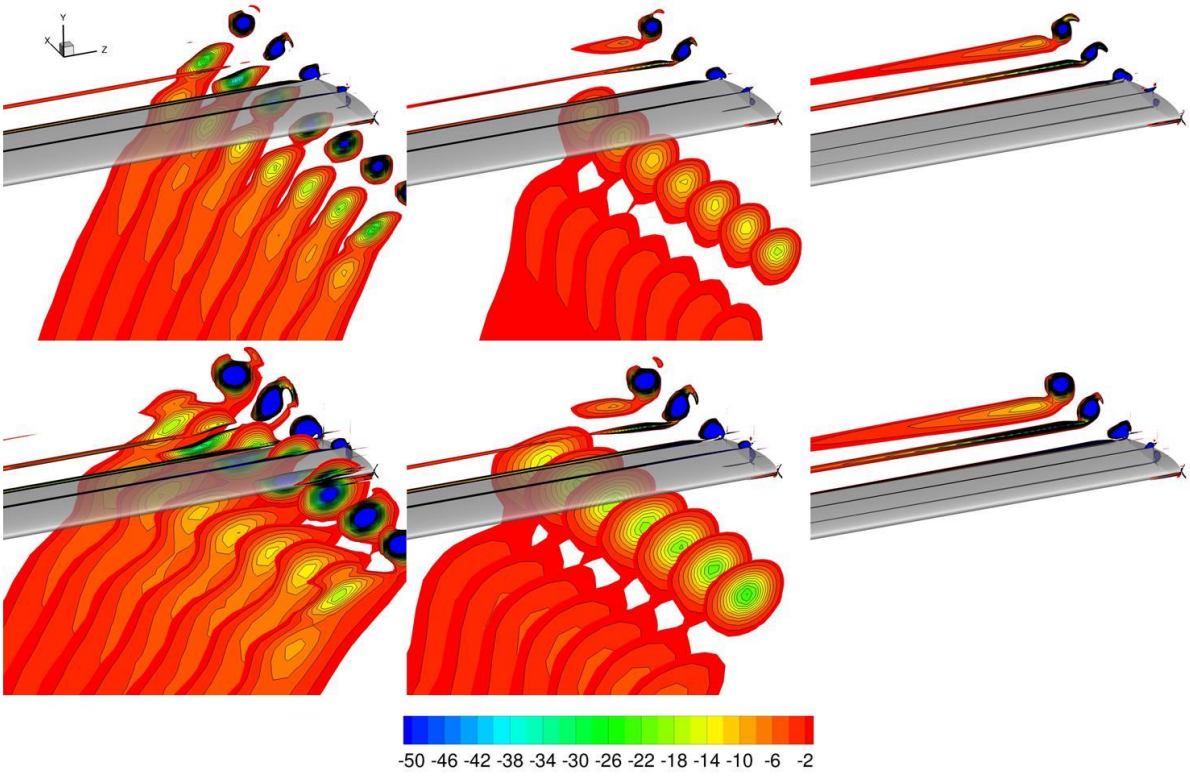

Figure 70: Slices of the normalized, axial vorticity for values smaller than $\frac{\omega_x b}{U_\infty} \leq -1$. The slices are located in the range of $-1 \leq \frac{x}{c} \leq 2$ with $\frac{x}{c} = 0$ set at leading edge. The distance between two slices equals $\frac{\Delta x}{c} = 0.5$. The angles of attack of $\alpha = 2.5°$ (top) and $\alpha = 5.0°$ (bottom) are provided for the solidities of $\sigma_{3D} = \frac{1}{3}$ (left), $\sigma_{3D} = \frac{1}{9}$ (middle) and $\sigma_{3D} = 0$ (right). Resolved.

In addition, for the resolved blade simulation, the distribution of the local thrust and circumferential force coefficient is presented in order to detail the result of the interaction on the blade. In Figure 71, the local thrust distribution is shown for the angles of attack of $\alpha = 2.5°$ (top) and $\alpha = 5.0°$

(bottom). The depicted solidities are $\sigma_{3D} = \frac{1}{3}$ (left), $\sigma_{3D} = \frac{1}{9}$ (middle), and $\sigma_{3D} = 0$ (right). In the blade tip region, surface streamlines are included to visualize the influenced region of the vortical structures. For both angles of attack, the increased local thrust in the vicinity of the blade tip, for higher solidities, is detectable. In particular, the interaction of the blade with the vortex provides at the leading edge an increased contribution to the thrust for higher solidities due to the aforementioned local increase of the angle of attack caused by vortex. In addition, the interaction shows a larger influenced region considering the surface streamlines for higher solidities.

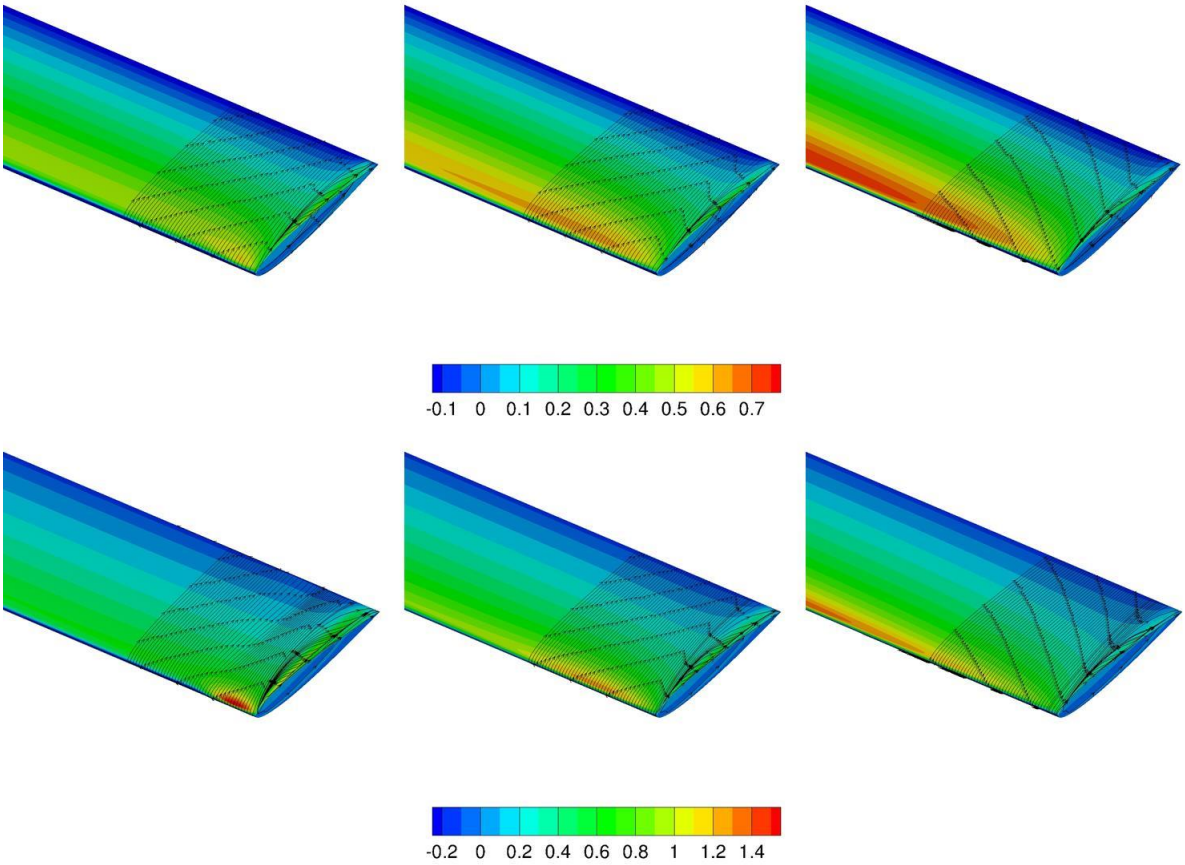

Figure 71: Distribution of the local thrust coefficient $C_{T,f}$ in the blade tip region. The solidities of $\sigma_{3D} = \frac{1}{3}$ (left), $\sigma_{3D} = \frac{1}{9}$ (middle) and $\sigma_{3D} = 0$ (right) are presented for the angles of attack of $\alpha = 2.5°$ (top) and $\alpha = 5.0°$ (bottom). Additionally, the surface streamlines are inserted.

For the distribution of the local circumferential force coefficient, in Figure 72, the same layout is chosen as in the previous Figure 71. The local circumferential force is increased in the blade tip region as well as the local thrust caused by the interaction with the vortices. In contrast to the local thrust, which is increased mainly at the leading edge of the blade, the local circumferential force is increased on the whole suction side of the blade. The main reason therefore, is the reduced pressure caused by the vortices on the suction side. The influence becomes more pronounced, the higher the angle of attack and the solidity, because the strength of the vortices is higher and they are located closer to the surface of the blade. The topology of the vortices can be detected with help of the surface streamlines as well.

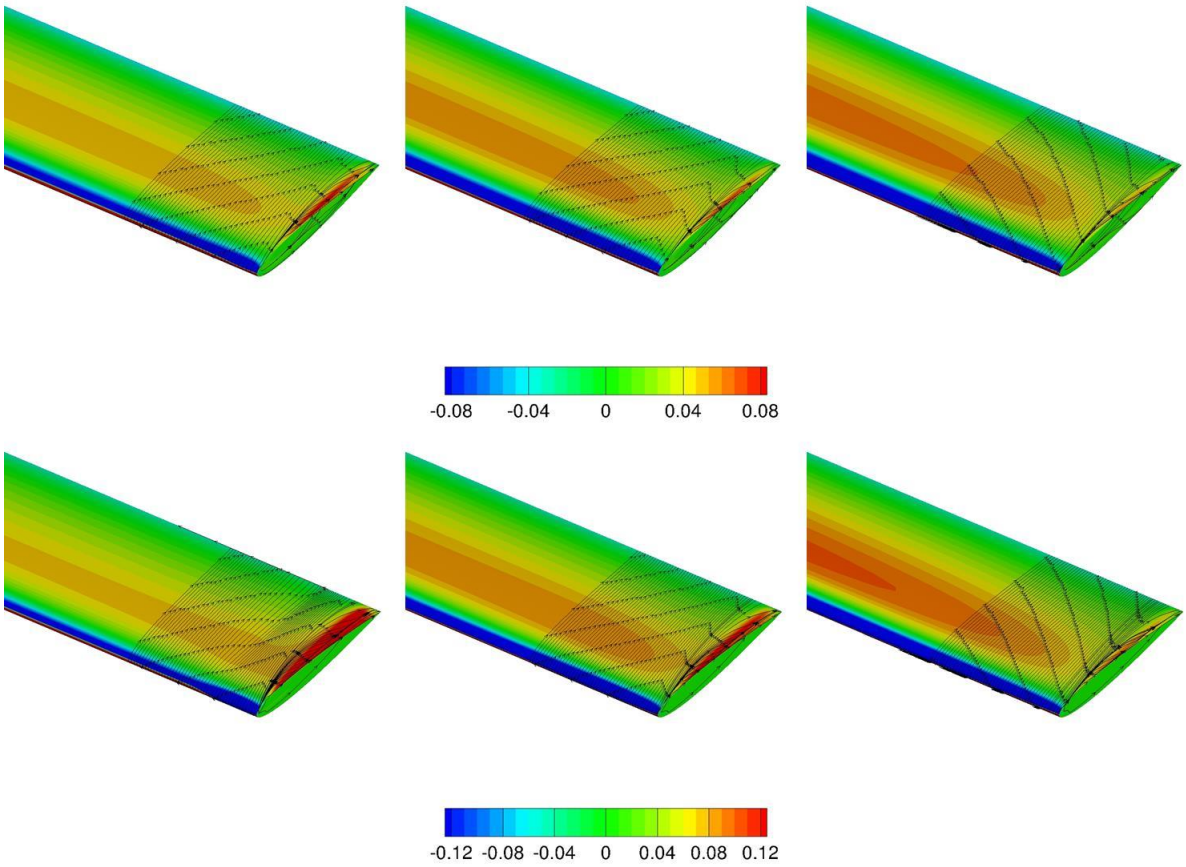

Figure 72: Distribution of the local circumferential force coefficient $C_{Fx,f}$ in the blade tip region. The solidities of $\sigma_{3D} = \frac{1}{3}$ (left), $\sigma_{3D} = \frac{1}{9}$ (middle) and $\sigma_{3D} = 0$ (right) are presented for the angles of attack of $\alpha = 2.5°$ (top) and $\alpha = 5.0°$ (bottom). Additionally, the surface streamlines are inserted.

Conclusion and required modeling capabilities: This test case is based on the two-dimensional test case and is designed for evaluating the influence of the three-dimensional effects. The interaction leads to a reduction of the forces with increasing solidities and increasing angles of attack. In particular, the spanwise distribution of forces is changed due to the influence of the mutual interaction of the blades. Consequently, the modeled approach shall predict the overall forces as well as the spanwise distribution appropriately. In addition, the wake field shall be captured appropriately also.

Actuator Disc Approach with PanBL

In this subsection, the results of the actuator disc coupled with PanBL are presented and compared to those of the resolved simulation. The parameter set for the present investigation is extended in contrast to the resolved simulation. While the advance ratio and the set of angles of attack is kept equally, with $J = 0.25$ and $\alpha = \{2.5°, 5.0°\}$, respectively, the set of the solidity equals $\sigma_{3D} = \left\{\frac{1}{3}, \frac{1}{9}, \frac{1}{25}, \frac{1}{50}, \frac{1}{100}\right\}$. In addition, the limiting value of the two-dimensional test case is inserted according to $\sigma_{2D} = \sigma_{3D} = 0$, to obtain the result for the non-influenced wing. The parameters for actuator disc are taken over from the two-dimensional test case and read $AR_w = SR_w = 0.2\ c$, $AR_s = SR_s = 0.1\ c$, and $AR_c = SR_c = 0\ c$.

In Figure 73, the thrust and the circumferential force coefficient of a single blade depending on the solidity are presented for an advance ratio of $J = 0.25$. Considering the thrust coefficient, the global behavior obtained by the AD-PanBL approach agrees appropriately with that of the resolved simulation. Apparently, the higher the solidity, the better is the prediction of the approach. In the next step, an additional description concerning the choice of the set of solidities is provided. For both approaches, the resolved and the actuator disc, the set includes the solidities $\sigma_{3D} = \left\{\frac{1}{3}, \frac{1}{9}\right\}$. Consequently, a one-to-one comparison of the resulting coefficient is legitimated. For the resolved simulation, the solution for the solidity of $\sigma_{3D} = 0$ is calculated by a modification of the boundary condition to obtain the stand-alone blade. For the actuator disc model, the result for the latter solidity represents, basically, a stand-alone blade solution as well. However, due to the definition of the inflow condition for the actuator disc approach, the disturbance of the other blades as well as the influence of the blade itself vanishes if the solidity tends to zero. Subsequently, the influence of the self-induced velocity of the considered blade is not captured by the approach. The result is a flow around the blade with constant, non-disturbed inflow conditions along the spanwise direction. Consequently, the resulting coefficients for the solidity in two and three dimensions $\sigma_{2D} = \sigma_{3D} = 0$ are equivalent. In order to proof the behavior of the coefficients while converging the limit, the solidities of $\sigma_{3D} = \left\{\frac{1}{25}, \frac{1}{50}, \frac{1}{100}\right\}$ are added in the input space.

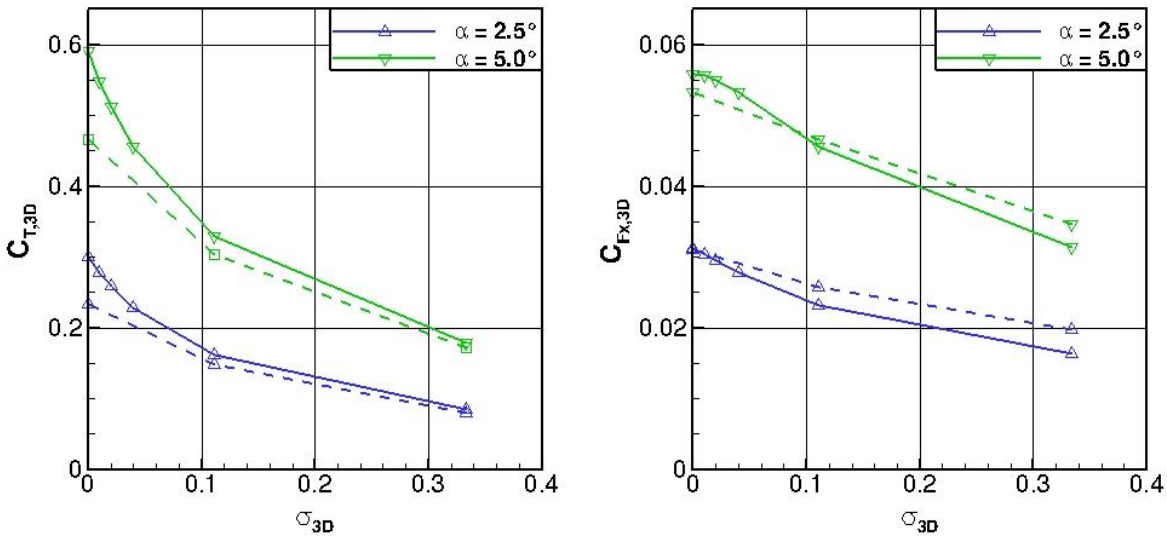

Figure 73: Three-dimensional thrust and circumferential force coefficient for one blade depending on the solidity. The advance ratio is set to J=0.25. AD-PanBL: Solid line; Resolved: Dashed line.

It is visible that the thrust coefficient converges smoothly to the result of the two-dimensional test case. The discrepancy of the results for lower solidities can be declared with the above stated relationships as well. The trend of the circumferential force coefficient shows a reasonable agreement between the approaches. However, the circumferential force coefficient converges smoothly to result for the limiting value also.

For a detailed quantitative discussion, in Table 12, the deviations of the thrust and circumferential force coefficient obtained by the actuator disc related to the results of the resolved simulation are shown. At first, consider the relative deviation of the thrust coefficient. While the quantities obtained by the different models agree well for high solidities, the prediction for the lower ones is worse. The relative deviation for the solidity $\sigma_{3D} = 0$ reads $\Delta C_{T,3D,rel,AD}(0.25{,}0, 2.5°) = 28.15\%$ and $\Delta C_{T,3D,rel,AD}(0.25{,}0, 5.0°) = 26.88\%$. In the following, the reasons for the discrepancy are provided. As discussed in the previous subsection, the two-dimensional thrust coefficient for the resolved simulation is evidently higher than the three-dimensional one. For the present operating points the ratios of the coefficients reads $\frac{C_{T,2D,res}}{C_{T,3D,res}}(0.25{,}0, 2.5°) = 1.158$ and $\frac{C_{T,2D,res}}{C_{T,3D,res}}(0.25{,}0, 5.0°) = 1.155$. Furthermore, within the two-dimensional test case, it is described that the AD-PanBL overestimates the thrust coefficient compared to the resolved simulation by approximately 8%, see 3.3. Although the advance ratio differs, the value can still be used for a rough estimation. Taking into account both aspects, the thrust coefficients for the present operating points can be estimated to be too high by approximately 25%. Obviously, the reasons for the deviations are detected. As stated in the description of the state-of-the-art, for propellers, a tip loss factor can be invented. This factor can increase the accuracy of the prediction for the actuator disc method, in particular for low solidities, by taking into account the finite number of blades by the distance between the wake sheets of two adjacent blades, see [1]. For the present test case, the application of the propeller tip loss factor is not intended, since the properties of the approaches can be investigated easier by excluding that additional effect. Considering higher solidities, the agreement with the resolved simulation is better, reasonably. On the one hand, for higher solidities, the influence of the induced flow around the blade, caused by the blade itself as well as the mutual interaction of all blades within the cascade, is captured better. In addition, as already detected within the two-dimensional test case, the AD-PanBL approach provides a more negative slope of the thrust over the solidity than it is obtained for the resolved simulation.

Table 12: Relative deviation of the thrust and circumferential force coefficient for the AD-PanBL simulation related to the resolved simulation.

σ_{3D}	$\Delta C_{T,3D,rel,AD}$		$\Delta C_{Fx,3D,rel,AD}$	
	$\alpha = 2.5°$	$\alpha = 5.0°$	$\alpha = 2.5°$	$\alpha = 5.0°$
$1/3$	$6.19\ \%$	$3.68\ \%$	$-17.33\ \%$	$-9.38\ \%$
$1/9$	$9.39\ \%$	$8.61\ \%$	$-9.94\ \%$	$-2.16\ \%$
0	$28.15\ \%$	$26.88\ \%$	$0.85\ \%$	$4.77\ \%$

While the results for thrust coefficient of the two approaches are in good agreement for high solidities, the results for the circumferential force coefficient show an inverted behavior. In this case, the discussion is started with the high solidity of $\sigma_{3D} = \frac{1}{3}$, to declare the reason for the large deviation at first. Obviously, the discrepancy of the force coefficients between the two approaches is almost doubled for an angle of attack of $\alpha = 2.5°$ in contrast to an angle of attack of $\alpha = 5.0°$. However, the absolute deviation of the value is comparable. Recall the results of the two-

dimensional test case for the advance ratio of $J = 0.25$. The circumferential force coefficient shows for the AD-PanBL and the resolved simulation for an angle of attack of $\alpha = 0°$ a comparable absolute deviation as for this test case, see Figure 46. The difference occurs due to the underestimation of the zero-lift drag by PanBL with respect to the resolved simulation. For lower solidities, the deviation of the circumferential force coefficients gets smaller. As discussed for the thrust coefficient, the lift is overestimated by the actuator disc approach for lower solidities. Due to the contribution of the lift to the circumferential force, the underestimation of the latter caused by the zero-lift drag is partly compensated by the overestimated lift. It has to be remarked, that the discrepancy is smaller for higher advance ratios, assuming moderate of lift coefficients. Therefore, the contribution of the lift dominates that of the drag to the circumferential force, in general.

In the following, the spanwise distribution of the forces is discussed. The normalized, sectional thrust coefficient according to (4.7) is calculated for this purpose. The same constant distribution as for the resolved simulation with $N_{sec} = 20$ is applied. For the investigation, solely a subset of the operating points is discussed. Therefore, the points allowing a one-to-one comparison are taken. These are the points for the solidities of $\sigma_{3D} = \left\{\frac{1}{3}, \frac{1}{9}\right\}$. Although for the operating point with the solidity of $\sigma_{3D} = 0$ a one-to-one comparison is possible as well, the distribution does not give any additional information. While for the resolved simulation a common distribution of a finite wing is obtained, the actuator disc simulation results into a constant distribution along the spanwise direction. In Figure 74, the distribution of the normalized, sectional thrust and circumferential force coefficient along the spanwise direction is shown.

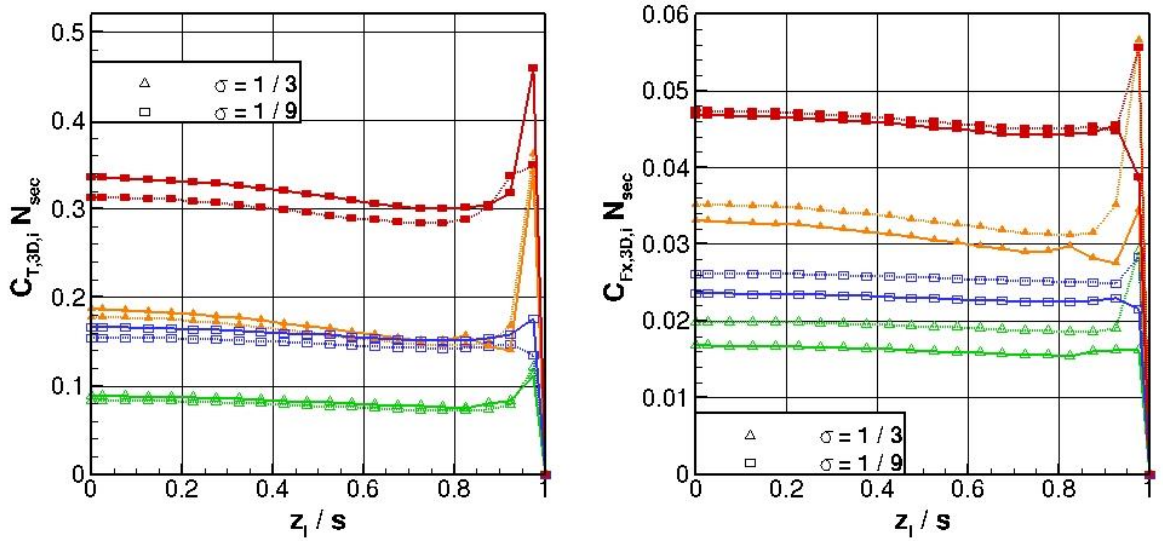

Figure 74: Normalized, sectional thrust and circumferential force coefficient along the spanwise direction. The results for the angles of attack of $\alpha = 2.5°$ (non-filled symbols) and $\alpha = 5.0°$ (filled symbols) are shown. AD-PanBL: Solid line; Resolved: Dotted line.

At first, the distribution of the thrust coefficient for the solidity of $\sigma_{3D} = \frac{1}{3}$ is discussed. For an angle of attack of $\alpha = 2.5°$, the sectional thrust coefficient is in good agreement with the resolved simulation along the spanwise direction. In particular, the higher loading in the region of the tip is represented correctly. For an angle of attack of $\alpha = 5.0°$, the results matches well also. While the actuator disc shows a slightly higher loading over the whole wing span, in the vicinity of the blade tip, the sectional thrust is predicted well. Considering the solidity of $\sigma_{3D} = \frac{1}{9}$, the agreement is not that

good. For an angle of attack of $\alpha = 2.5$, the prediction along the spanwise direction is provided appropriately by the actuator disc regarding the resolved simulation. However, in the vicinity of the blade tip, the actuator disc highly overestimates the thrust. For the higher angle of attack of $\alpha = 5.0°$, the sectional thrust coefficient is overestimated over the whole span and in particular, in the vicinity of the blade tip. The discrepancy between the results in the blade tip region is mainly associated to the actuator disc model, whereas the deviation along the spanwise direction is caused by the overpredicted lift by PanBL. In the following, the distribution of the circumferential force coefficient is discussed. Excluding the tip region, the latter is underestimated by the actuator disc approach regarding the resolved simulation for each presented operating point. As stated for the overall coefficients above, the difference of the predicted zero-lift drag is the reason therefore, in particular, the lower the contribution of the lift. Considering the circumferential force in the vicinity of the blade tip, solely for the advance ratio $\sigma_{3D} = \frac{1}{3}$ and an angle of attack of $\alpha = 5.0$, at least, the trend is represented correctly. The absolute values are predicted too small for all operating points. As described for the resolved simulation, a distinct increase of the circumferential forces is obtained in the blade tip region due to the interaction of the flow with the blade tip vortices of the other blades. The actuator disc approach cannot capture the effect appropriately. In the resolved simulation, the interaction of the vortex with the blade leads to a complex flow field. Depending on the position of the axis of the vortex with respect to the blade, the induced velocity at the surface of the blade is modified and the local pressure distribution as well. Furthermore, due to the pressure field, separation of the flow can occur. The actuator disc approach condenses the whole information, introduced by the vortex, into inflow conditions for a section. In particular, the vortex is changing the local inflow angle for a section. Consequently, the angle of attack of the blade is modified as well. The angle of attack influences mainly the lift of the section. The drag of the section, provided from two-dimensional airfoil data, is that of an airfoil for non-disturbed inflow conditions. Occasionally, local regions of separated flow occur at the blade due to the local pressure distribution within the cascade, while occurring not for the undisturbed airfoil at the same angle of attack. Resulting, the increase of the lift is appropriately captured and the drag is underdetermined. In addition, a modified inflow angle, leading to an increased angle of attack, provides a decreased fraction of lift added to the circumferential force. Putting those aspects together, the underestimation of the circumferential force caused by the interaction is declared.

In Figure 75, slices of the normalized, axial vorticity for values smaller than $\frac{\omega_x b}{U_\infty} \leq -1$ are shown and contoured for the actuator disc approach. Basically, the three slices show the same result for one operating point. This is caused by the definition of the actuator disc approach which does not allow a variation in circumferential direction. The trend of the contraction of the flow is represented correctly regarding the resolved simulation. The higher the segment loading, the higher is the contraction. Furthermore, the increased strength of the vortex sheet with higher segment loading is visible also. Nevertheless, the result is expected like this, since the overall forces also show the correct trend. An interesting fact is that the higher loading in the region of the blade tip is predicted correctly by the actuator disc approach for the operating points with higher segment loading. Recalling the basic principles of the approach according to the theory chapter and considering a crossflow plane, the circulation in the vicinity of the blade tip, in particular for a constant load distribution, is introduced by vertical vortex sheet aligned with the tip of the blade. Consequently, solely a downwards induced velocity along the span is obtained. However, for non-constant load distributions, the center of the rotation moves and consequently, the local induced velocity in

vertical direction can change the sign along the spanwise direction. Considering the operating point for the advance ratio $\sigma_{3D} = \frac{1}{3}$ and an angle of attack of $\alpha = 5.0$, it is visible that the vortical region moves in spanwise direction inwards. As a result, the induced velocity in the blade tip region is pointing upwards and leads to a smaller inflow angle, higher angle of attack, higher lift, and finally, to an increased thrust. The result is in accordance with the force distribution along the spanwise direction. Furthermore, the strength of the vorticity for the different operating points is correlated with the level of the peak at the blade tip.

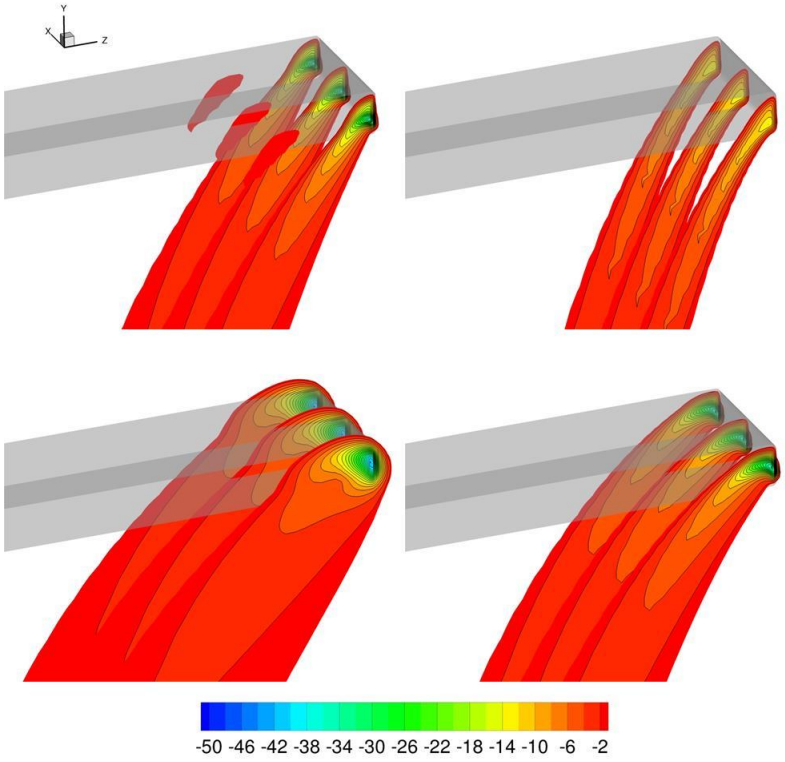

Figure 75: Slices of the normalized, axial vorticity for values smaller than $\frac{\omega_x b}{U_\infty} \leq -1$. The slices are located in the range of $0 \leq \frac{x}{c} \leq 1$ with $\frac{x}{c} = 0$ set at leading edge. The distance between two slices equals $\frac{\Delta x}{c} = 0.5$. The angles of attack of $\alpha = 2.5°$ (top) and $\alpha = 5.0°$ (bottom) are provided for the solidities of $\sigma_{3D} = \frac{1}{3}$ (left), $\sigma_{3D} = \frac{1}{9}$ (middle) and $\sigma_{3D} = 0$ (right). The isosurface (grey) represents the source region. AD-PanBL.

Actuator Line Approach with PanBL

This subsection provides the results for the actuator line approach coupled with PanBL and a comparison with the resolved simulation. The parameter set for this investigation is the same as for the resolved simulation. Consequently, the advance ratio reads $J = 0.25$, the solidities are set to $\sigma_{3D} = \left\{\frac{1}{3}, \frac{1}{9}, 0\right\}$, and the angles of attack to $\alpha = \{2.5°, 5.0°\}$. The model specific parameters for the actuator line are based on the two-dimensional test case and read $AR_w = SR_w = 0.2\,c$, $AR_s = SR_s = 0.1\,c$, and $AR_c = SR_c = 0\,c$. Furthermore, all regions are equally spaced in both direction of the line, e.g., $AR_{w,x} = AR_{w,y} = AR_w$.

Figure 76 shows the thrust and the circumferential force coefficient of a single blade depending on the solidity for an advance ratio of $J = 0.25$. Similar to the AD-PanBL simulation, the prediction of

the AL-PanBL for the thrust coefficient is appropriate with respect to that of the resolved simulation. Basically, the higher the solidity, the smaller is the deviation. The trends obtained for the circumferential force coefficient are comparable to those of the AD-PanBL simulation also.

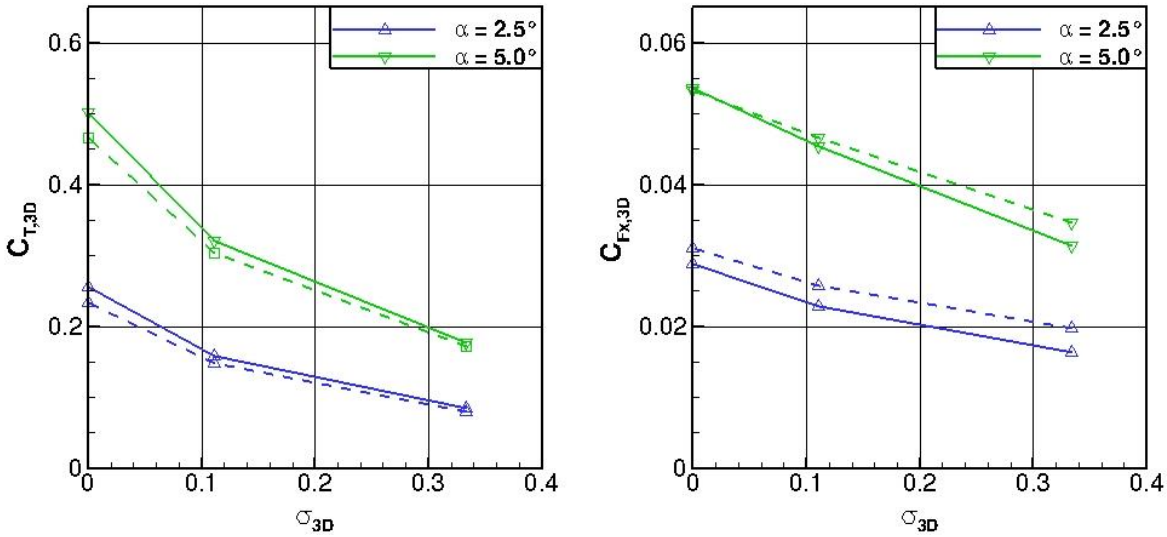

Figure 76: Three-dimensional thrust and circumferential force coefficient for one blade depending on the solidity. The advance ratio is set to J=0.25. AL-PanBL: Solid line; Resolved: Dashed line.

In the following, the quantitative discussion is provided. Therefore in Table 13, the deviations of the thrust and circumferential force coefficient determined by the actuator line related to the results for the resolved simulation are presented. In contrast to the actuator disc approach, the results for the solidity $\sigma_{3D} = 0$ can be determined directly. Considering the thrust coefficient, the highest deviation is obtained for the latter solidity. The reason for the deviation can be declared basically by the overestimation of the lift by PanBL. By definition of the actuator line approach, the induced velocity of blade tip vortex is included in the determination of the inflow conditions. Consequently, if the approach is consistently implemented, mainly the airfoil data causes the deviation. Recalling from the last subsection, the overestimation of the thrust coefficient by PanBL obtained for the two-dimensional test case reads ≈ 8. For the stand-alone blade, the deviations for the operating points read $\Delta C_{T,2D,rel,AL}(0.25,0,2.5°) = 9.07\%$ and $\Delta C_{T,2D,rel,AL}(0.25,0,5.0°) = 8.02\%$. Obviously, the deviation is comparable. Nevertheless, this comparison should serve only as a rough estimation, since the advance ratios are not identical. However, due to the resulting small difference in the inflow angles the made conclusion is justified. As an additional effect that has to be taken into account, recall the results of the two-dimensional test case by AL-PanBL. For the solidity of $\sigma_{2D} = 0$, the thrust coefficient shows a better agreement the higher the loading of the airfoil due to two counteracting effects. On the one hand, PanBL overestimates the lift for a certain angle of attack and on the other hand, the averaging procedure establishes a too small angle of attack. For the present loading in the symmetry plane of the wing, the deviation caused by the averaging procedure, found for a comparable loading by the two-dimensional test case, can be estimated to be less than 4%. Subsequently, the thrust obtained by the AL-PanBL approach includes this reduction, in particular, for spanwise positions with higher sectional loading. Considering higher solidities, the deviation of the predicted thrust between the approaches is smaller. This trend is detected for the AL-PanBL approach in the two-dimensional case as well.

Table 13: Relative deviation of the thrust and circumferential force coefficient for the AL-PanBL simulation related to the resolved simulation.

σ_{3D}	$\Delta C_{T,3D,rel}$		$\Delta C_{Fx,3D,rel}$	
	$\alpha = 2.5°$	$\alpha = 5.0°$	$\alpha = 2.5°$	$\alpha = 5.0°$
$1/3$	5.68 %	2.63 %	−17.68 %	−9.50 %
$1/9$	6.85 %	5.97 %	−11.51 %	−2.81 %
0	9.07 %	8.02 %	−6.87 %	0.57 %

Concerning the deviation of the circumferential force coefficient, an inverted trend related to that of the thrust coefficient is shown, as already described for the AD-PanBL approach in the previous subsection. The discussion is started with the solidity of $\sigma_{3D} = \frac{1}{3}$. The deviation for this solidity is the highest with respect to the resolved simulation, but it is comparable to that of the AD-PanBL approach for both angles of attack. The reason therefore is, as described for the AD-PanBL approach, the underestimation of the zero-lift drag by PanBL related to the resolved simulation. For the lower solidities, the deviation is smaller compared to the AD-PanBL. Since the lift is overpredicted in this case as well, the contribution of the lift to the circumferential force compensates the underestimated zero-lift drag in parts also. In particular for the solidity of $\sigma_{3D} = 0$, the overestimation of the lift by the actuator line is much smaller than by the actuator disc. Consequently, the contribution of the lift to the circumferential force is smaller also. This fact declares the spreading of the deviations between the AD and AL approach with respect to the resolved simulation.

After presenting the overall quantities, in the next step, the distribution of the forces along the spanwise direction is presented. The discussion is made with the normalized, sectional thrust coefficient according to (4.7). Consistently, the constant distribution with $N_{sec} = 20$ is applied. For the present investigation, the same operating points as for the resolved simulation are shown. Therefore, in Figure 77 the distribution of the normalized, sectional thrust and circumferential force coefficient along the spanwise direction is provided.

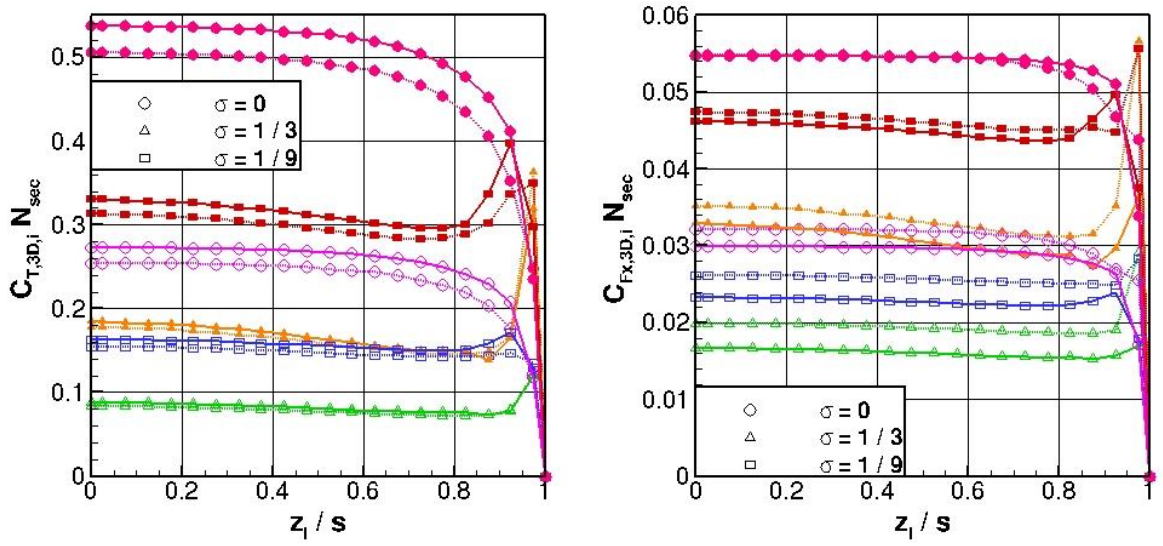

Figure 77: Normalized, sectional thrust and circumferential force coefficient along the spanwise direction. The results for the angles of attack of $\alpha = 2.5°$ (non-filled symbols) and $\alpha = 5.0°$ (filled symbols) are shown. AL-PanBL: Solid line; Resolved: Dotted line.

At first, the distribution of the thrust coefficient for the stand-alone blade represented by a solidity of $\sigma_{3D} = 0$ is discussed. For both angles of attack, $\alpha = 2.5°$ and $\alpha = 5.0°$, the known distribution of a wing is obtained, reasonably. However, the actuator line approach overestimates the sectional thrust with respect to the resolved simulation for almost the whole range distinctly. The reason therefore is the already stated overprediction of the lift by PanBL. In the next step, the sectional thrust coefficient for the solidity of $\sigma_{3D} = \frac{1}{3}$ is discussed. For an angle of attack of $\alpha = 2.5°$, the result obtained by the AL-PanBL simulation is in very good agreement with respect to that of the resolved simulation. The distribution along the spanwise direction as well as the blade tip region is captured correctly. For the angle of attack of $\alpha = 5.0°$, the agreement is well also, evenly, in the blade tip region. Nevertheless, it can stated, the higher the loading, the worse is the agreement of the AL-PanBL with respect to the resolved simulation. For this solidity, including strong interactional effects, the overestimation of the sectional thrust coefficient by PanBL is slightly compensated by the overpredicted interactional effects of the actuator line method which is already observed for the two-dimensional test cases. The distribution of the thrust coefficient along the spanwise direction for the solidity of $\sigma_{3D} = \frac{1}{9}$ agrees acceptable between the modeled and the resolved approach. Along the spanwise direction, the overpredicted lift of PanBL leads to higher thrust values, while in the blade tip region, the impact of the interaction with the vortices is underestimated. In the following, the distribution of the circumferential force coefficient is analyzed. Considering a solidity of $\sigma_{3D} = \frac{1}{3}$ and an angle of attack of $\alpha = 2.5°$, the impact of the underestimation of the zero-lift drag by PanBL becomes visible along the spanwise direction at most. The discrepancy in the region of the blade tip, however, is associated to the actuator line modeling. As described for the actuator disc in the previous subsection in detail, solely the inflow conditions for a section represent the behavior of a section. Consequently, the complex vortex field in the presence of a vortex cannot be handled exactly by condensing the whole information into inflow conditions only. Nevertheless, as already detected for the actuator disc approach in the previous section, the contribution of the overestimated lift, in particular for the operating points with lower solidities, compensates the underestimated zero-lift drag in parts.

In Figure 78, slices of the normalized, axial vorticity for values smaller than $\frac{\omega_x b}{U_\infty} \leq -1$ are shown and contoured for the actuator line approach. In contrast to the actuator disc approach, the ability to resolve the vortices is well visible. In general, the trends are represented correctly compared with the resolved simulation. This concerns the contraction of the flow as well as the higher strength of the vortices for higher segment loadings. Comparing the vortices of the actuator line simulation with those of the resolved simulation, it is detectable that the position of the cores is predicted appropriately, while the size differs. For the advance ratio of $\sigma_{3D} = \frac{1}{3}$ and an angle of attack of $\alpha = 5.0$, the tip vortex of a certain line even merges with the tip vortex of the upstream located line slightly downstream of this certain line. Consequently, the positions of the vortices predicted by the different methods do not match for this operating point. The reason therefore is the overestimated size of the vortices which is caused by the origin of the vortex. For the resolved simulation, the vortex arises from a separation of the flow at the blade tip. Consequently, the initial scale of the vortex is dominated by the size of the boundary layer. In contrast, for the actuator line approach, the vortex arises due to the source term region and is mainly dominated by its width SR_w. By reducing the width, the initial core size could be reduced as well, depending on the resolution of the mesh. As already stated, the cell sizes for this test case are set smaller than necessary for the generalized actuator disc approach to avoid an influence of the mesh on the results and allow for an investigation

of the model parameters. From this point of view, the width can be reduced. On the other hand, the results of the independency study for the actuator width show a minimum required width to obtain an independent result. Furthermore and in particular for real-world applications, the prediction has to provide appropriate accuracy for coarse meshes to save computational effort. Nevertheless, according to the obtained forces, the quality of the prediction is good enough. As a side note, comparing the interaction of the vortex with the actuator line with that of the vortex with the resolved blade for the advance ratio of $\sigma_{3D} = \frac{1}{3}$ and an angle of attack of $\alpha = 2.5$, a similar behavior is detected. In both cases is the vortical structure divided into two smaller structures. While it is known that the presence of the solid wall causes this effect, the presence of the source term results in a similar effect. Finally, the stand-alone airfoil is discussed briefly. The basic behavior is captured appropriately. Both, the tip vortex as well as the vortex sheet emanating from the trailing edge is captured. Nevertheless, the larger scale of the width of the actuator line compared to the trailing edge results in a different representation of the vortex sheet. While the vorticity is locally high for the resolved blade, a wider-distributed result with lower vorticity is obtained for the actuator line.

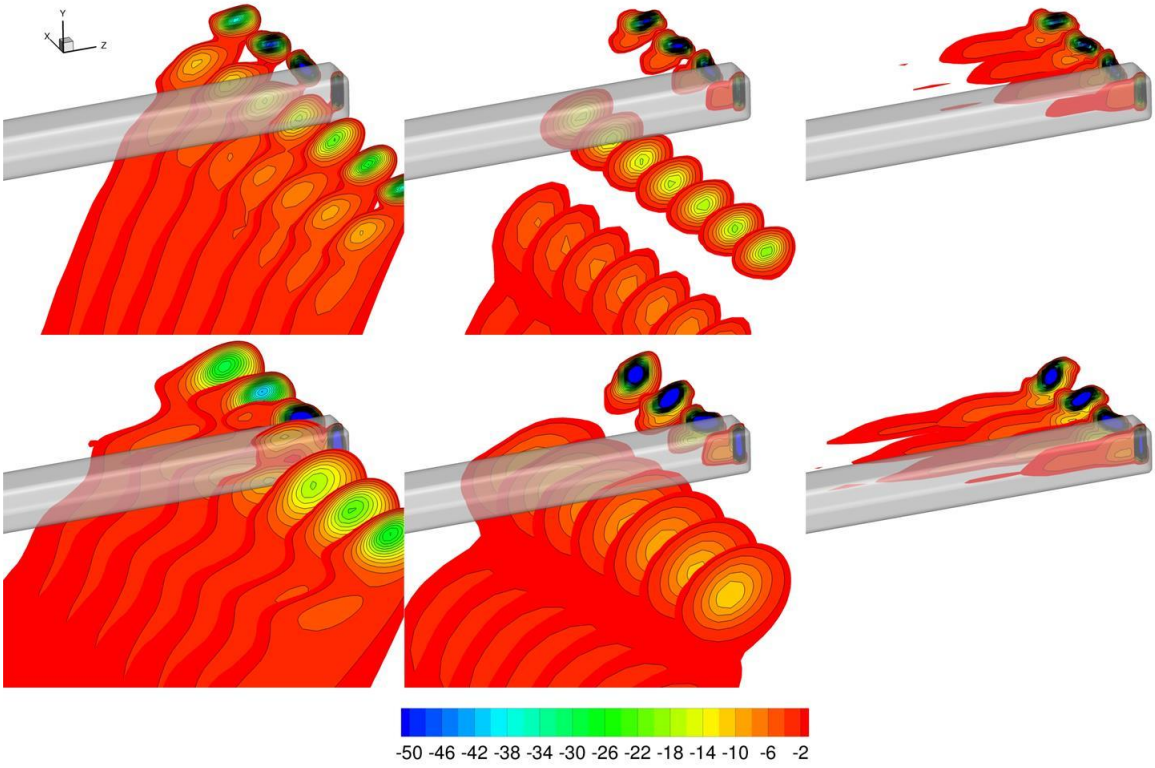

Figure 78: Slices of the normalized, axial vorticity for values smaller than $\frac{\omega_x b}{U_\infty} \leq -1$. The slices are located in the range of $-1 \leq \frac{x}{c} \leq 2$ with $\frac{x}{c} = 0$ set at leading edge. The distance between two slices equals $\frac{\Delta x}{c} = 0.5$. The angles of attack of $\alpha = 2.5°$ (top) and $\alpha = 5.0°$ (bottom) are provided for the solidities of $\sigma_{3D} = \frac{1}{3}$ (left), $\sigma_{3D} = \frac{1}{9}$ (middle) and $\sigma_{3D} = 0$ (right). The isosurface (grey) represents the source region. AL-PanBL.

Actuator Disc Approach with 2D-CFD

In this subsection, the results of the actuator disc coupled with 2D-CFD are presented and compared to those of the resolved simulation. The parameter set used for this investigation is in accordance to that applied for the AD-PanBL approach. The advance ratio reads $J = 0.25$, the angles of attack $\alpha = \{2.5°, 5.0°\}$, and the set of the solidity equals $\sigma_{3D} = \left\{\frac{1}{3}, \frac{1}{9}, \frac{1}{25}, \frac{1}{50}, \frac{1}{100}\right\}$. The actuator disc parameters are kept the same for as well are set to $AR_w = SR_w = 0.2\ c$, $AR_s = SR_s = 0.1\ c$, and $AR_c = SR_c = 0\ c$. The choice of the parameters is motivated within the description of the AD-PanBL simulation.

The thrust and the circumferential force coefficient of a single blade depending on the solidity are presented for an advance ratio of $J = 0.25$ in Figure 79. The global trend of the thrust coefficient agrees well between the AD-2C approach and the resolved simulation. Even the global behavior of the circumferential force coefficient is represented appropriately. Primarily, the made statements are valid for the operating points that allow for a one-to-one comparison. These points are related to the solidities of $\sigma_{3D} = \left\{\frac{1}{3}, \frac{1}{9}\right\}$. For the lower solidities, the lack of capturing three-dimensional effects leads to the discrepancy. The additional operating points for the solidities of $\sigma_{3D} = \left\{\frac{1}{25}, \frac{1}{50}, \frac{1}{100}\right\}$ provide a continuous convergence of the forces to the limit for the solidity of $\sigma_{3D} = 0$.

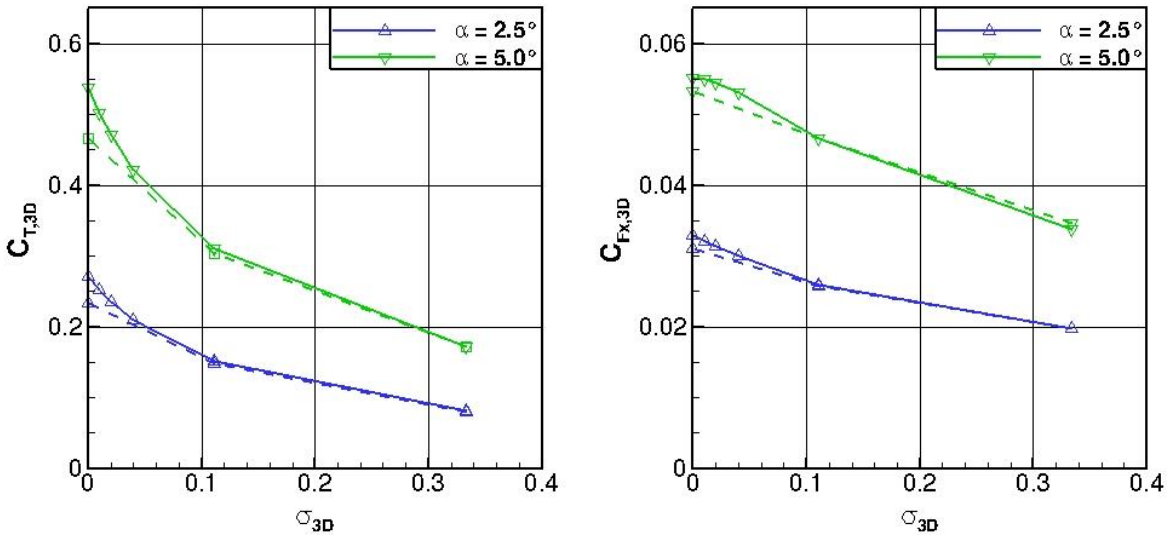

Figure 79: Three-dimensional thrust and circumferential force coefficient for one blade depending on the solidity. The advance ratio is set to J=0.25. AD-2C: Solid line; Resolved: Dashed line.

In the following, the quantitative discussion is presented. Therefore, in Table 14, the deviations of the thrust and circumferential force coefficients obtained by the actuator disc related to the results of the resolved simulations are shown. The relative deviation of the thrust coefficient for the solidity of $\sigma_{3D} = 0$ is caused by the three-dimensional effects. Obviously, since the numerical method for generating the airfoil data is identical, solely the dimensions differ. For the clarification of the three-dimensional effects, the description within the presentation of the resolved simulation is referred. The higher the solidity, the better is the prediction of the thrust by the actuator disc approach. Therefore, the flow around the blade, induced by itself, and the mutual interaction of all blades within the cascade is captured better. The better prediction for higher solidities is detectable for the AD-PanBL simulation also. However, since the airfoil data is calculated by the execution of the same

solver within the present investigation, the deviation can be addressed mainly to the actuator disc approach. The more negative slope of the thrust over the solidity, as already stated for the two-dimensional test case, is visible for both angles of attack as well.

Table 14: Relative deviation of the thrust and circumferential force coefficient for the AD-2C simulation related to the resolved simulation.

σ_{3D}	$\Delta C_{T,3D,rel,AD-2C}$		$\Delta C_{Fx,3D,rel,AD-2C}$	
	$\alpha = 2.5°$	$\alpha = 5.0°$	$\alpha = 2.5°$	$\alpha = 5.0°$
$1/3$	$1.16\ \%$	$-0.66\ \%$	$-0.48\ \%$	$-2.59\ \%$
$1/9$	$2.37\ \%$	$2.08\ \%$	$0.74\ \%$	$-0.24\ \%$
0	$15.77\ \%$	$15.45\ \%$	$6.16\ \%$	$3.51\ \%$

In contrast to the coupling with PanBL, the coupling with the 2D-CFD shows a good agreement for the circumferential force coefficient as well. Due to the application of the same numerical method for both, the calculation of the section within the actuator disc approach as well as the whole blade within the resolved simulation, the zero-lift drag for the airfoil is equal. Resultantly, the deviation can be attributed mainly to the actuator disc modeling. Considering the deviation of the circumferential force coefficient for the solidity of $\sigma_{3D} = 0$, the contribution of the overestimated lift is clearly visible. For the higher solidities, of $\sigma_{3D} = \left\{\frac{1}{3}, \frac{1}{9}\right\}$, the influence of the lift appears also. Nevertheless, the circumferential force coefficient is predicted slightly too small for the highest solidity and the highest angle of attack. A reason therefore is that the additional, interactional drag, caused by the complex flow field within the cascade, is not captured appropriately.

In the following, the distribution of the forces along the spanwise direction is provided. Therefore, the normalized, sectional thrust coefficient according to (4.7) is calculated with the same constant distribution as for the resolved simulation with $N_{sec} = 20$. In accordance to the investigation of the AD-PanBL approach, solely a subset of the operating points, allowing a one-to-one comparison, is considered. These are the points for the solidities of $\sigma_{3D} = \left\{\frac{1}{3}, \frac{1}{9}\right\}$.

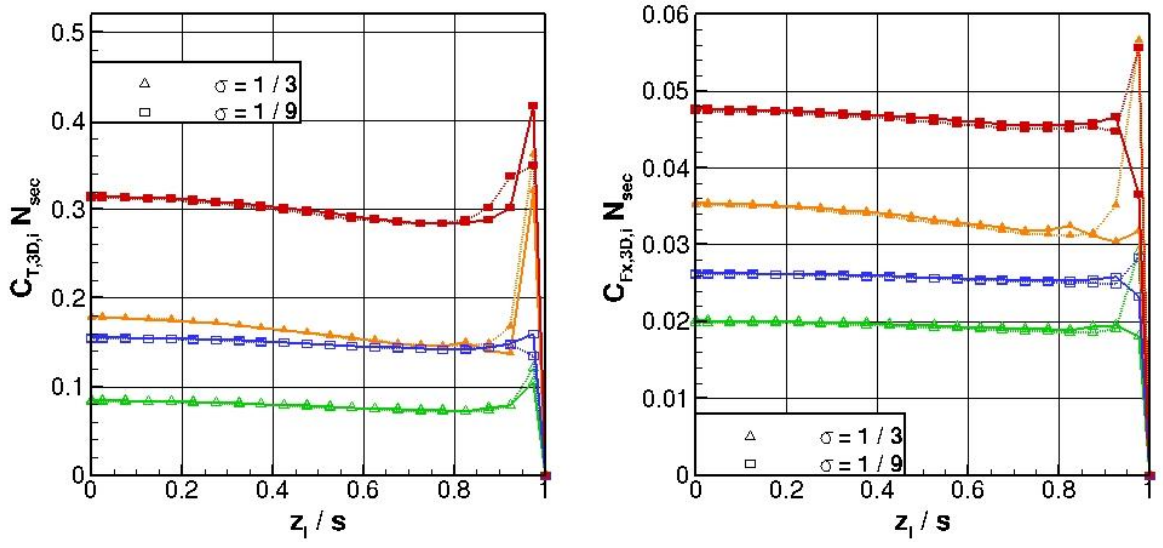

Figure 80: Normalized, sectional thrust and circumferential force coefficient along the spanwise direction. The results for the angles of attack of $\alpha = 2.5°$ (non-filled symbols) and $\alpha = 5.0°$ (filled symbols) are shown. AD-2C: Solid line; Resolved: Dotted line.

The analysis is started with the thrust distribution for the solidity of $\sigma_{3D} = \frac{1}{3}$. Excluding the blade tip region, a very good agreement between the actuator disc and the resolved simulation is achieved. For the angle of attack of $\alpha = 2.5°$, the higher loading in the tip region is predicted appropriately, although the value itself is provided too low compared to the resolved simulation. A comparable behavior is obtained for the higher angle of attack of $\alpha = 5.0°$. For the solidity of $\sigma_{3D} = \frac{1}{9}$, the thrust coefficient obtained by the actuator disc approach meets that of the resolved simulation also very well for both angles of attack, except in the blade tip region. In the latter, the prediction of the actuator disc shows a slightly higher loading for the angle of attack of $\alpha = 2.5°$. For the angle of attack of $\alpha = 5.0°$, the actuator disc approach overestimates the thrust in the blade tip region also. Interestingly, the region with increased loading is predicted wider and with a lower local maximum by the resolved simulation related to the actuator disc. Nevertheless, the statement made for the AD-PanBL approach that the discrepancy between the resolved and the actuator disc simulation in the blade tip region is caused mainly by the actuator disc modeling and in the remaining regions of the wing mainly by the airfoil data generation is still valid. Rather, it evenly can be confirmed by the herein presented results. Since for both simulations, a CFD calculation with the same solver on a comparable mesh is included, the deviation due to the generation of airfoil data vanishes and consequently, the spanwise distributions of the thrust coefficient, excluding the blade tip region, are almost coincident. For the distribution of the circumferential force coefficient, a similar behavior as for that of the thrust coefficient is obtained. Excluding the blade tip region, a very good agreement between the actuator disc approach and the resolved simulation is shown. In contrast to the AD-PanBL simulation that underestimates the zero-lift drag caused by PanBL, the present method including a CFD calculation with the same solver on a comparable mesh provides appropriate drag data. Considering the blade tip region, the shortcomings in modeling the three-dimensional effects, as detailed for the AD-PanBL simulation, are visible. For each presented operating point, the higher circumferential force obtained by the resolved simulation in blade tip region is not predicted by the actuator disc simulation.

In Figure 81, slices of the normalized, axial vorticity for values smaller than $\frac{\omega_x b}{U_\infty} \leq -1$ are shown and contoured for the actuator disc approach coupled with two-dimensional CFD. In general, the trends of the contraction of the flow and the strength of the vortices for higher segment loadings are comparable to those obtained by the AD-PanBL simulation. The absolute values for the vorticity are predicted smaller by the AD-2C simulation caused by the overestimation of lift by PanBL.

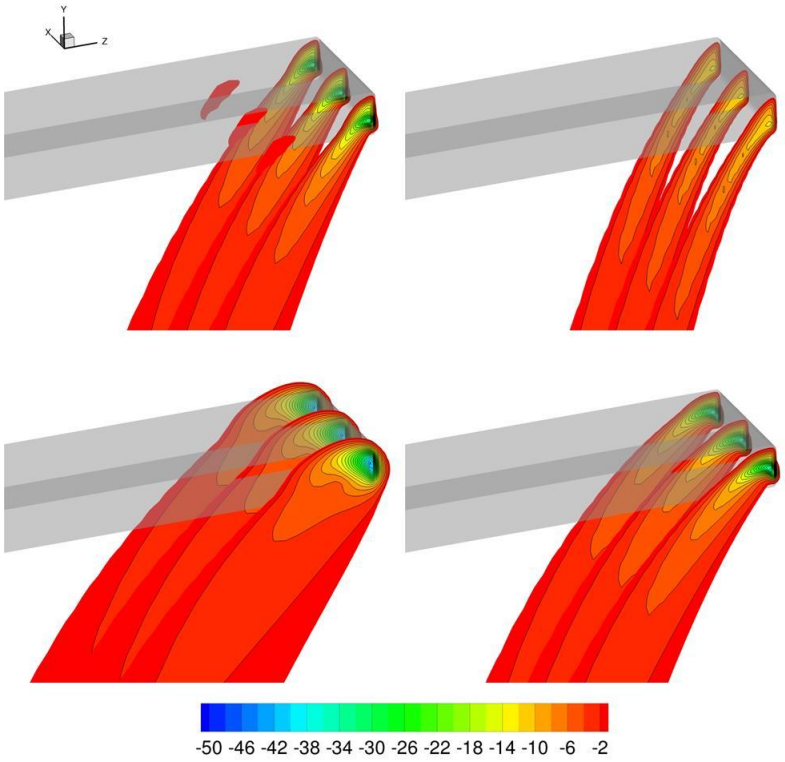

Figure 81: Slices of the normalized, axial vorticity for values smaller than $\frac{\omega_x b}{U_\infty} \leq -1$. The slices are located in the range of $0 \leq \frac{x}{c} \leq 1$ with $\frac{x}{c} = 0$ set at leading edge. The distance between two slices equals $\frac{\Delta x}{c} = 0.5$. The angles of attack of $\alpha = 2.5°$ (top) and $\alpha = 5.0°$ (bottom) are provided for the solidities of $\sigma_{3D} = \frac{1}{3}$ (left), $\sigma_{3D} = \frac{1}{9}$ (middle) and $\sigma_{3D} = 0$ (right). The isosurface (grey) represents the source region. AD-2C.

Actuator Line Approach with 2D-CFD

This subsection includes the results for the actuator line approach coupled with 2D-CFD as well as the comparison with the resolved simulation. The parameter set is taken over from the resolved simulation and equals that applied for the AL-PanBL simulation. The advance ratio reads $J = 0.25$, the solidities are set to $\sigma_{3D} = \left\{\frac{1}{3}, \frac{1}{9}, 0\right\}$ and the angles of attack to $\alpha = \{2.5°, 5.0°\}$. The model specific parameters for the actuator line are in accordance to that applied for the AL-PanBL approach and read $AR_w = SR_w = 0.2\ c$, $AR_s = SR_s = 0.1\ c$, and $AR_c = SR_c = 0\ c$. Furthermore, all regions are equally spaced in both direction of the line, e.g., $AR_{w,x} = AR_{w,y} = AR_w$.

Figure 82 presents the thrust and the circumferential force coefficient of a single blade depending on the solidity for an advance ratio of $J = 0.25$. The prediction of the AL-2C for the thrust coefficient is in excellent agreement with respect to that of the resolved simulation. For the present approach, even the circumferential force coefficient is predicted well.

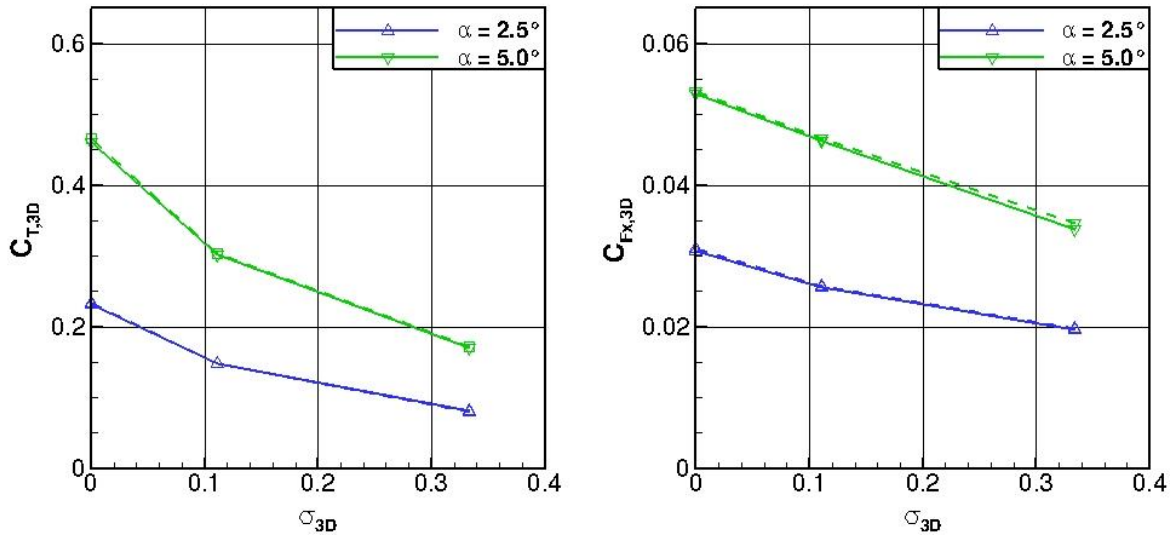

Figure 82: Three-dimensional thrust and circumferential force coefficient for one blade depending on the solidity. The advance ratio is set to J=0.25. AL-2C: Solid line; Resolved: Dashed line.

In the following, the quantitative discussion is provided. The deviation of the thrust and circumferential force coefficient determined by the actuator line related to the results for the resolved simulation is presented in Table 15. Considering the deviation of the thrust coefficient at first, the excellent agreement is confirmed. Since the AL-2C includes the three-dimensional effects as well as the airfoil data obtained by CFD, the greatest sources for the deviations, found out in the previous subsections, are remedied. Since trends of the deviations are not distinctively detectable and several counteracting effects occur, the clarification of the origins is made by discussing the spanwise distribution. For the present test case, the statements made for the thrust coefficient are valid for the circumferential force coefficient also.

Table 15: Relative deviation of the thrust and circumferential force coefficient for the AL-2C simulation related to the resolved simulation.

σ_{3D}	$\Delta C_{T,3D,rel,AL-2C}$		$\Delta C_{Fx,3D,rel,AL-2C}$	
	$\alpha = 2.5°$	$\alpha = 5.0°$	$\alpha = 2.5°$	$\alpha = 5.0°$
$1/3$	$1.07\ \%$	$-1.19\ \%$	$-0.58\ \%$	$-2.56\ \%$
$1/9$	$0.18\ \%$	$-0.25\ \%$	$-0.96\ \%$	$-0.84\ \%$
0	$-0.73\ \%$	$-0.96\ \%$	$-1.08\ \%$	$-0.55\ \%$

The distribution of the forces along the spanwise direction is presented in the following. The discussion is made again with the normalized, sectional thrust coefficient according to (4.7) using the constant distribution with $N_{sec} = 20$. The same operating points as for the AL-PanBL simulation are shown. Therefore, in Figure 83 the distribution of the normalized, sectional thrust and circumferential force coefficient along the spanwise direction is provided.

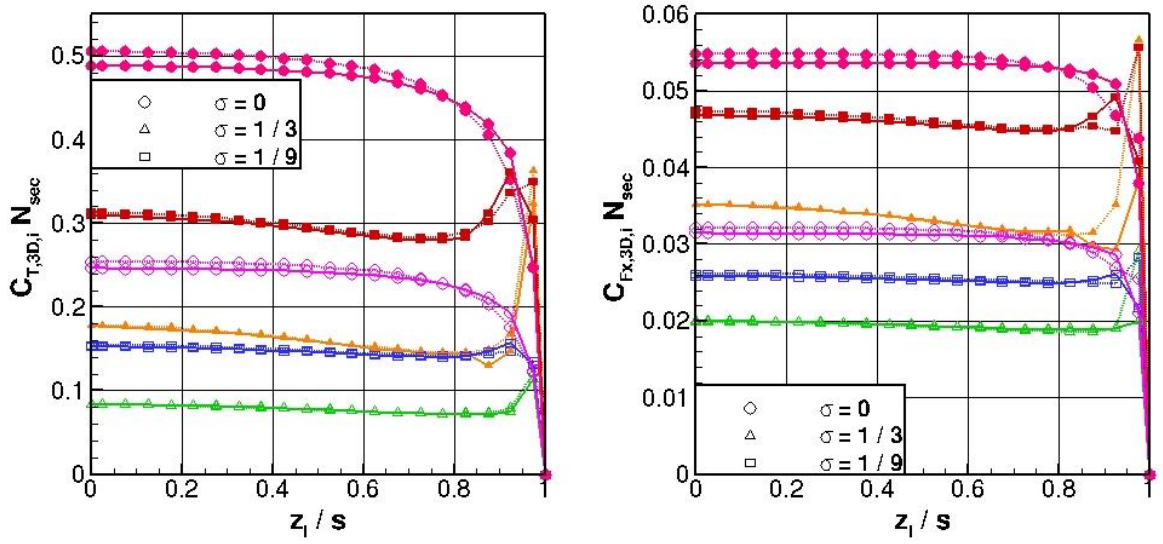

Figure 83: Normalized, sectional thrust and circumferential force coefficient along the spanwise direction. The results for the angles of attack of $\alpha = 2.5°$ (non-filled symbols) and $\alpha = 5.0°$ (filled symbols) are shown. AL-2C: Solid line; Resolved: Dotted line.

Considering the distribution of the thrust coefficient for the solidity of $\sigma_{3D} = \frac{1}{3}$, an excellent agreement is achieved between the AL-2C and the resolved simulation for the angle of attack of $\alpha = 2.5°$. For the angle of attack of $\alpha = 5.0°$, in particular, discrepancies occur in the vicinity of the blade tip. The latter is caused by the modeling of the actuator line approach. As described before, the condensation of the complex flow field into an inflow condition is not able to capture all occurring effects. The slightly underpredicted thrust coefficient along the spanwise direction is associated as well with the actuator line approach. However, the reason therefore is already found out within the investigation of the two-dimensional test case that the averaging procedure of the actuator line provides a too small angle of attack for higher loadings of the blade. For the solidity of $\sigma_{3D} = \frac{1}{9}$, the underestimation of the thrust along the spanwise direction is visible for both angles of attack as well. While for the angle of attack of $\alpha = 2.5°$ the flow characteristics in the blade tip region are represented appropriately, for the angle of attack of $\alpha = 5.0°$, the maximum of the coefficient is predicted at a more inboards located position. The sources of the deviations are the same as described for the higher solidity above. For the solidity of $\sigma_{3D} = 0$, the underestimation of the thrust coefficient along the spanwise direction as well as the small shortcomings in modeling the three-dimensional flow in the blade tip region are visible. Considering the circumferential force coefficient, a very good agreement between the actuator line and the resolved simulation is obtained by excluding the blade tip region. However, the smaller the solidity, the greater is the deviation due to the contribution of the lift. The underestimation of the latter, caused by the averaging procedure of the actuator line approach, is the reason therefore. The local maximum of the circumferential force in the blade tip region is provided less distinctively by the actuator line approach compared to the resolved simulation for solidities including mutual interaction ($\sigma_{3D} > 0$).

In Figure 84, slices of the normalized, axial vorticity for values smaller than $\frac{\omega_x b}{U_\infty} \leq -1$ are shown and contoured for the actuator line approach coupled with two-dimensional CFD. In general, the trends of the contraction of the flow and the strength of the vortices for higher segment loadings are

comparable to those obtained by the AL-PanBL simulation. The absolute values for the vorticity are predicted at lower levels by the AL-2C simulation caused by the overestimation of lift by PanBL.

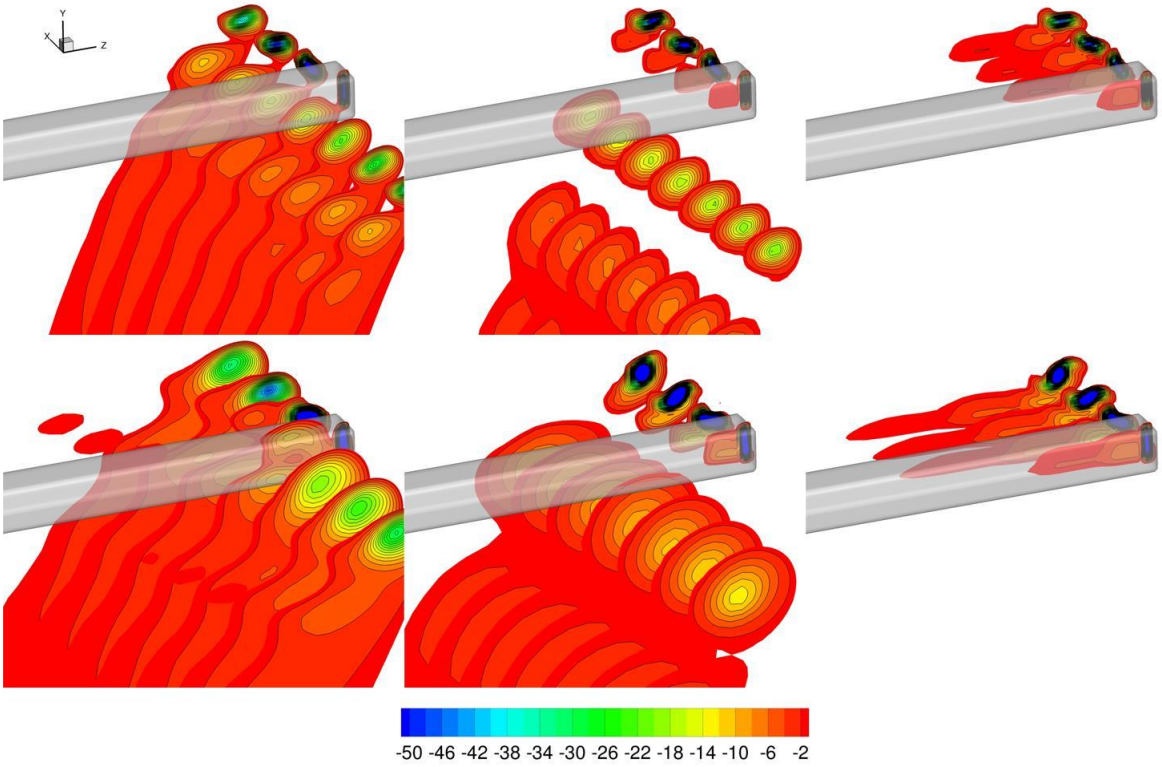

Figure 84: Slices of the normalized, axial vorticity for values smaller than $\frac{\omega_x b}{U_\infty} \leq -1$. The slices are located in the range of $-1 \leq \frac{x}{c} \leq 2$ with $\frac{x}{c} = 0$ set at leading edge. The distance between two slices equals $\frac{\Delta x}{c}$=0.5. The angles of attack of $\alpha = 2.5°$ (top) and $\alpha = 5.0°$ (bottom) are provided for the solidities of $\sigma_{3D} = \frac{1}{3}$ (left), $\sigma_{3D} = \frac{1}{9}$ (middle) and $\sigma_{3D} = 0$ (right). The isosurface (grey) represents the source region. AL-2C.

Overall Comparison and Conclusions

Before the results between the different methods are compared, a brief review of the important aspects obtained by the resolved simulations for this test case is provided.
For the three-dimensional test case, solely the forward flight test case is investigated, but besides the overall forces, the force distribution along the spanwise direction and the flow field are detailed. Concerning the overall forces, the principal behavior is comparable to that of the two-dimensional test case. The higher the solidity, the smaller the forces generated by one blade. Further, the higher the angle of attack, the higher the forces. Basically, the modeled approaches capture the trends well. As already remarked for the two-dimensional test case, the PanBL-based methods overpredict the lift and underpredict the drag. Resultantly, the absolute values of the thrust are overpredicted and for the circumferential force the prediction is depending on the considered operating point. Furthermore, the influence of the reduced angle of attack obtained by the averaging procedure for the AL-based approaches is visible also. An additional effect, occurring in the three-dimensional test case, is the overestimation of the lift by the AD-based methods for low solidities, since the three-dimensional effects are not accounted sufficiently.

Considering the spanwise distribution, the principal behavior of the forces is represented appropriately also. The effects described in the previous paragraph, in particular those related to two dimensions, are influencing the distributions of both forces along the spanwise direction distinctly. Nevertheless, the absolute values are represented appropriately also by all approaches. Obviously, the agreement with the resolved simulation is better captured by the 2C-based method. In the blade tip region, the prediction of the characteristic of the thrust is provided appropriately, but the AL-based method captures the three-dimensional effects better. The distribution of the circumferential force in the blade tip region is predicted reasonable. Although the AL-based approaches agrees better with the resolved simulation, both the AD-based as well as the AL-based approaches cannot handle the increasing drag of the blade caused by the blade vortex interaction for higher solidities.

The representation of the wake field is predicted appropriately by all modeled methods. The principal behavior of the wake, like the flow contraction with increased segment loading, is provided also. By definition, the AD-based methods show only a vortex sheet while the AL-based methods capture each vortex. The agreement of the predicted positions of the vortices by the latter is good related to the resolved simulations. However, the sizes of the vortex cores are presented too large depending on the widths of the actuator line. The application to the stand-alone wing shows a too large extension of the vortex sheet in the wake of the wing as well.

4.2 Three-Dimensional Propeller Test Case

As further increase in the complexity of test cases, the three-dimensional propeller test case is presented. In contrast to the above presented test cases, the applied propeller is not of generic type. Therefore, a three-bladed fixed-pitch propeller, investigated within the research project EUROPAS [3] is applied. The investigation includes the resolved propeller simulations for generating reference data as well as modeled simulations using the AD-PanBL and the AL-PanBL approach. The multi-domain coupling is not applied for this test case.

4.2.1 Test Case Description

As mentioned in the introduction, the propeller is the same as used within the research project EUROPAS [3]. The three-bladed fixed-pitch propeller allows for a manual adjustment of the reference blade pitch angle. Nevertheless, for the present investigation, the angle is kept constant. The reference blade-pitch angle defined at 75% of the tip radius (RBPA) reads $\theta_{75} = 10°$. The purpose of the test case is, on the one hand, a comparison of the results between the different approaches, and on the other hand, to show the reasonability of the prediction for inclined inflow conditions regarding the propeller disc. For this reason, the angle of the disc relative to the inflow is set in the range of $0 \leq \phi_D \leq 90°$. For the calculation of the airfoil data, only PanBL is applied within this investigation. The propeller is presented in Figure 85 (left). The whole calculation domain is presented in Figure 85 (right). The diameter of the propeller is $D = 1.4\ m$. The configuration includes an aerodynamically-shaped aft body. The latter is basically invented to avoid wake shedding of the spinner. The length and shape of the aft body is designed in order to reduce the region of separated flow. The dimensions of the domain are $15D$ in the axial direction and $10D$ in the other directions. The range of the freestream velocity reads $16.67\frac{m}{s} \leq u_\infty \leq 33.34\frac{m}{s}$ and the range of the rotational speed is set to $25\ s^{-1} \leq n \leq 41.667\ s^{-1}$. The associated range of the Reynolds number based on the chord at 75% span of the blade reads $4.74 \cdot 10^5 \leq Re \leq 7.97 \cdot 10^5$.

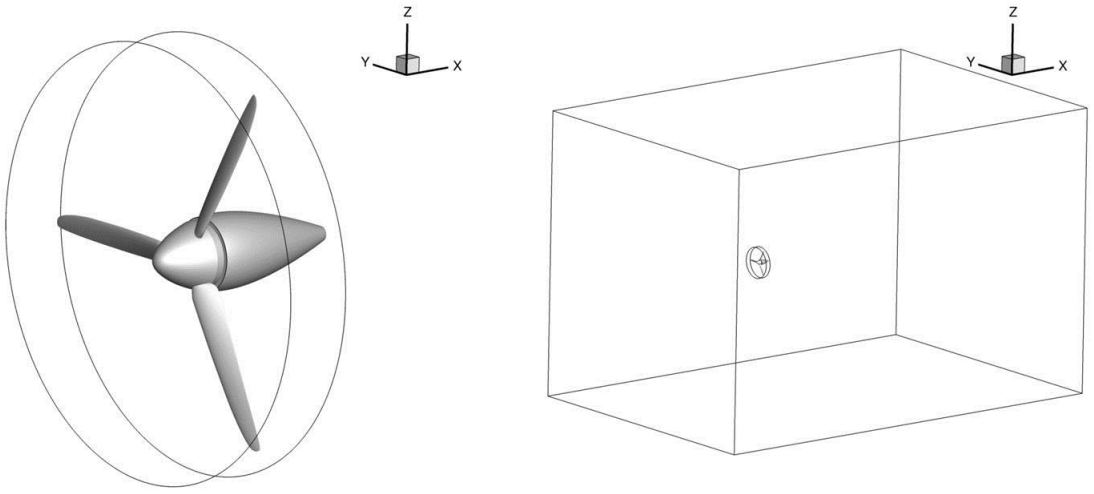

Figure 85: Domain for the resolved propeller simulation. The rotating domain including blades and spinner (left) and the stationary domain including the aft body and the rotating domain (right) is shown.

4.2.2 Mesh Generation and Numerical Setup

In the following, a short description of the meshing strategy and the numerical setup is given. Firstly, the setup for resolved propeller, secondly, that for actuator disc approach coupled with PanBL, and lastly, that for the actuator line coupled with PanBL is presented.

Resolved Propeller

The blocking strategy and mesh generation are employed as detailed in [3]. The computational grid is of block-structured hexahedron type. The blocking consists of two domains. The static domain, including the aft body, embeds the rotational domain. The latter contains the propeller blades as well as the spinner. Furthermore, the boundary layer is resolved in order to prevent the application of a wall function. Therefore, the dimensionless wall distances for the cell centers of the wall-adjacent cells are set to approximately $y^+ \approx 1$. In addition, the number of cells in the boundary layer along the direction perpendicular to the wall is approximately 20. Taking into account the rotational periodicity of the three-bladed propeller, only a sector of $120°$ is meshed, copied, and rotated to obtain the mesh for the full disc. The rotating domain is inserted into the static domain and connected by a sliding mesh interface [112]. The static domain consists of 151 blocks with $6.4 \cdot 10^6$ cells while one-third of the rotational domain includes 598 blocks with $2.3 \cdot 10^6$cells. In order to suppress spurious oscillations at the sliding mesh interface, the ratios of the edge lengths of the cells on both sides of the interface are set close to one. Figure 86 shows the mesh of the resolved propeller.

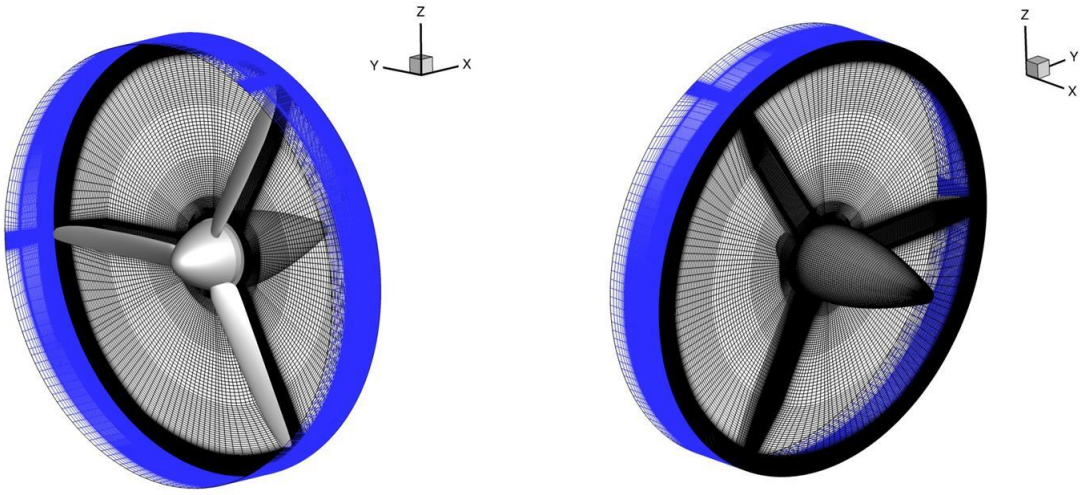

Figure 86: Mesh for the resolved propeller simulation. View showing the spinner and the blades (left) and view showing the aft body (right) is provided.

In Figure 87, the surface mesh of the blade is exhibited in detail. In addition, the mesh of the spinner is presented.

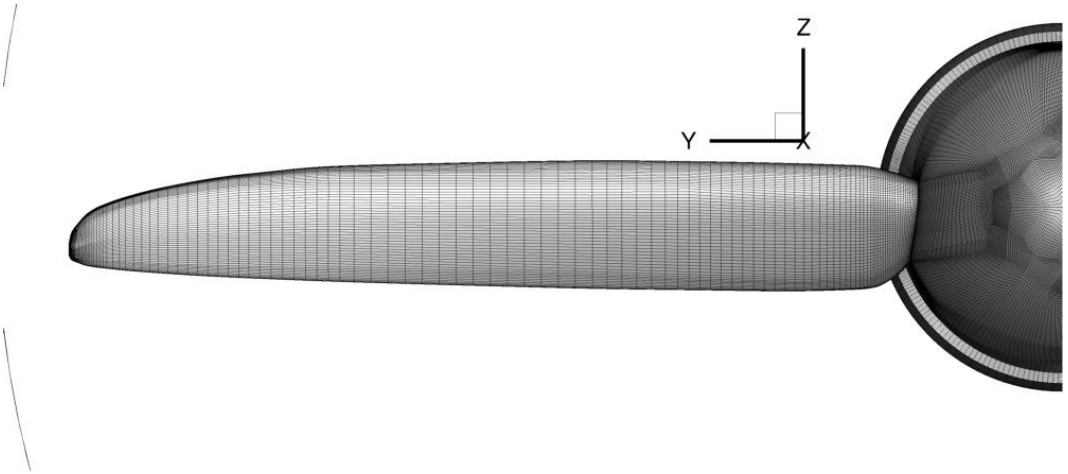

Figure 87: Mesh for the propeller simulation. A detailed view of the spinner and a blade is presented.

For the resolved propeller, the URANS equations are solved by applying the $k-\omega$ shear-stress transport model (SST) [114]. Zonal LES results of the resolved propeller and LES results of the actuator line can be found in Stuhlpfarrer et. al [115, 116]. Due to maximum blade tip velocity of $u_{BT} = 183\,m/s$, the blade tip Mach number exceeds $Ma > 0.3$. Consequently, the compressible pressure-based solver is chosen. For the SST model, viscous heating, compressibility effects, and a production limiter are included [114]. Furthermore, the absolute velocity formulation is applied for all domains. Although time-accurate simulations are conducted, for speeding-up the simulation, a steady-state solution is calculated in the first step as part of a two-step solution. The steady-state solution sets, besides the steady-state flow field, the turbulence decay appropriately. In the second step, the solver switches to the unsteady mode automatically. The pressure-velocity coupling is enabled by the SIMPLE algorithm. For the spatial discretization of the momentum, density, and energy equation, a second-order upwind scheme is applied in order to reduce the numerical dissipation. A bounded second-order implicit scheme is chosen for the temporal discretization. The scheme enables a solution-depending blending between a first-order and second-order spatial scheme to suppress spurious oscillations. A detailed study of the effect of spatial and temporal discretization schemes on the results and, in particular, on capturing the convection of vortices is presented in [116]. The transport equations related to the turbulence modeling, like the turbulent kinetic energy and the turbulence eddy frequency, are discretized by a first-order upwind scheme. The determination of the required gradients is established by the least-squares cell-based method. The under-relaxation factors for the pressure and the temperature are set to $\alpha_p = \alpha_{temp} = 0.2$, respectively, for the steady-state simulation and for the first 10 time steps of the unsteady simulation. Thereafter, the factors are increased to $\alpha_p = 0.3$ and $\alpha_{temp} = 1.0$. The under-relaxation factors for the momentum, density, turbulence eddy viscosity, turbulent kinetic energy, and the specific dissipation rate read $\alpha_{mom} = 0.7$, $\alpha_{den} = \alpha_{vt} = 0.2$, $\alpha_{tke} = \alpha_{\omega} = 0.8$, respectively. For the resolved simulation, air, complying with the ideal gas law, a specific heat of $c_p = 1006.43\,\frac{J}{kg\,K}$, a molecular viscosity $\mu = 1.7895 \cdot 10^{-5} Pa\,s$, and a thermal conductivity of $\lambda = 0.0242\,\frac{W}{m\,K}$ is applied as fluid. The chosen boundary condition for all inlets is a velocity inlet boundary condition. The velocity vector at the inlet is $\boldsymbol{u}_{in}$, the pressure at the inlet equals $p_{in} = 101325\,Pa$, and the temperature $T_{in} = 293.15\,K$. The turbulence intensity and the turbulence eddy viscosity ratio at the inlet is calculated by the application of the analytical description of the turbulence decay, in order to

establish the turbulence quantities as in the wind-tunnel tests, see 4.3.2. For all outlets, the pressure boundary condition with a pressure of $p_{out} = 101325\ Pa$ and a temperature of $T_{out} = 293.15\ K$ is set. For the pressure far-field boundary condition, a pressure of $p_{pf} = 101325\ Pa$ and a temperature of $T_{pf} = 293.15\ K$ is prescribed. For the outlet and the far field, the temperature is provided as a total quantity. The pressure is prescribed locally as a total quantity in case of backflow in the domain. Furthermore, the direction of the backflow in the domain is determined from the neighboring cell inside the domain and the turbulence quantities are prescribed approximately by the quantities at the position of the propeller. Due to the compressible formulation, the non-reflecting acoustic wave model is applied for all pressure-based boundary conditions. The physical surfaces are set to no slip and adiabatic walls. The motion of all parts is in compliance with the wind-tunnel configuration, see 4.3.2.

Generalized Actuator Disc Approach

The blocking strategy and mesh generation for the generalized actuator disc approach are associated closely with the resolved simulation to enable an adequate comparison. For the static domain, the mesh of the resolved propeller is taken over. The blocking strategy for the propeller domain differs, since the mesh needs not to capture the geometry of the propeller, see Figure 88, and the sliding mesh interface can be omitted, because the mesh does not rotate. Basically, the mesh can be generated as one single domain also, but local refinements of the mesh are applied in the propeller region in some cases for this investigation.

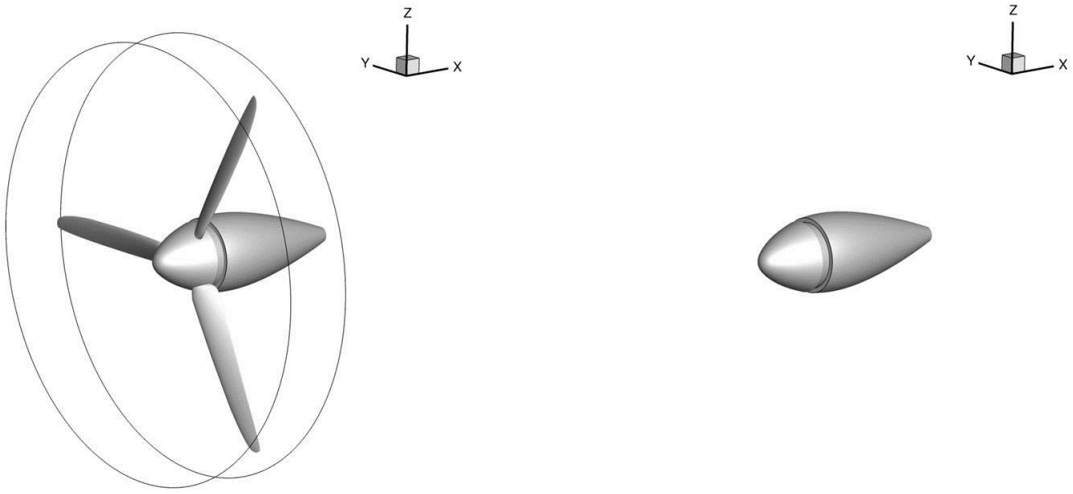

Figure 88: Generalized Actuator disc approach. Surface of spinner and aft body are present. In contrast to the resolved propeller (left), the propeller blades and the sliding mesh interface are not required (right).

For comparison issues, the solver settings and the models are based on the resolved propeller simulation, but with certain modification. For the actuator disc approach, a steady-state simulation is conducted due to the application of the averaging procedure. Furthermore, the compressibility effects are assumed to take place solely in the near field of the blade. The latter effects are modeled by PanBL and consequently, the simulation is conducted incompressible and the energy equation is not solved. The under-relaxation factors of the steady-state calculation in the first step of the resolved propeller simulation are taken.

For the actuator disc and the actuator line approach, a study of the parameters is conducted. However, the widths of the averaging and source region are set to be equal for this test case

($AR_{i,j} = SR_{i,j}$). The resulting widths for the averaging region of the actuator disc approach read $AR_{w,x} = 0.05\ m$ and $AR_{s,x} = 0.025\ m$. The widths in the axial direction are the same for the actuator line approach. For the latter, the widths of the averaging region in circumferential direction are set to $AR_{w,y} = 0.1\ m$ and $AR_{s,x} = 0.05\ m$. The center of the disc and line is determined in order to coincide with the center of the resolved propeller.

The applied constant density for the investigation is $\rho = 1.2\,\frac{kg}{m^3}$. The boundary conditions are comparable as well, whereas the information related to the energy equation is not applied.

Mesh Independency Study

The mesh and time-step size independency study is performed for the resolved propeller and for the generalized actuator disc approach. For the resolved propeller, a systematic variation of the grid size as well as the time step size is performed. Since for the actuator disc approach a steady-state simulation is conducted, solely a mesh independency study is required. For the actuator line approach, however, a mesh and time-step size independency study has to be performed. The operating conditions of the operating point for the study are a freestream velocity of $U_\infty = 16.67\ m/s$ and a rotational speed of $\omega = 209.44\ rad/s$. The RBPA is set to $\theta_{75} = 10°$. The quantity to be investigated is the thrust.

The study for the resolved propeller is conducted for three different numbers of cells and five different time-step sizes. The number of cells of the coarse, medium, and fine grid are $6.9\ Mio.$, $12.9\ Mio.$, and $25\ Mio.$, respectively. Therefore, a systematic refinement over all domains is performed. The time-step sizes in terms of azimuthal propeller angle per time step are $0.25°$, $0.5°$, $1.0°$, $2.0°$, and $4°$. For the evaluation of the thrust and to assess convergence, the mean values for periods of two, one, and a half propeller revolution are considered. If the values for the different periods are converged, the final result is achieved. The basic idea is to find a minimum of necessary revolutions to be calculated for reducing the computational effort. For the present case, the deviation between the mean values for one and for a half propeller revolution at five propeller revolutions is in the order of magnitude of minus four. Consequently, five propeller revolutions are chosen for the simulations. The medium mesh in combination with a time-step size of $2°$ azimuthal propeller angle per time step is applied for the simulations. Although the thrust coefficient is still decreasing slightly for smaller time-step sizes and a higher mesh resolution, the deviation is less than one per cent compared to the fine grid in combination with the smallest time-step size. Taken into account the smaller computational effort, the choice is justified [3].

Initially, the mesh independency study for the actuator disc approach is conducted for three different mesh resolutions. The difference of the thrust coefficient between the course and the fine mesh is less than one per cent [3]. However, as detailed for the generic test case, the more important quantity is the width of the actuator disc region compared to the characteristic cell length which is set appropriately. Furthermore, the constraint concerning the characteristic cell length in relation to the width of the smoothing function is fulfilled. Since the medium mesh is applied for the resolved propeller simulation, for comparison issues, the medium mesh is taken for the actuator disc simulation also.

The independency study for the actuator line approach is conducted for three different time-step sizes in combination with the different widths of the line. However, an independence of the time-step size is achieved, if the distance of the blade tip covered per one time step is less than the width of the actuator line. For the applied widths, the time-step size is set to size of $2°$ azimuthal propeller angle per time step.

4.2.3 Results and Discussion

In this section, the results for the generalized actuator disc approach and the resolved blade simulations are presented. At first, the integral coefficients for axial inflow conditions are provided. Thereafter, the distribution of the thrust along the radial direction of the blade is presented for one operating point. For the latter, the wake flow field is analyzed. Finally, the applicability of the generalized actuator disc approach for non-axial inflow conditions is described.

In order to obtain dimensionless coefficients, the following definitions are applied.

Thrust coefficient:

$$C_T = \frac{T}{\rho\, n^2\, D^4} \tag{4.8}$$

Torque and moment coefficients:

$$C_Q = \frac{Q}{\rho\, n^2\, D^5},\ C_m = \frac{m}{\rho\, n^2\, D^5}, C_n = \frac{n}{\rho\, n^2\, D^5} \tag{4.9}$$

Advance ratio:

$$J = \frac{U_\infty}{n\, D} \tag{4.10}$$

Efficiency:

$$\eta = \frac{J}{2\,\pi} \cdot \frac{C_T}{C_Q} \tag{4.11}$$

Sectional force coefficients for the resolved simulation:

$$\Delta C_F = \frac{\Delta F}{\rho\, n^2\, D^4}, with\ F = T, F_x \tag{4.12}$$

In Figure 89, the thrust coefficient (left) and the efficiency (right) are shown depending on the advance ratio J. The RBPA is set to $\theta_{75} = 10°$. The results are presented for the URANS simulation of the resolved propeller (URANS/RP), the RANS simulation applying the actuator disc approach (RANS/AD), and the URANS simulation applying the actuator line approach (URANS/AL). At first, the thrust coefficient is considered. The global trend of the results for the modeled approaches is in accordance to that of the resolved propeller simulation. Nevertheless, the slope is different between the approaches. The modeled approaches provide a similar slope, while it is less negative for the resolved simulation. The reason therefore is the overestimated lift slope depending on the angle of attack. This issue can be derived by taking into account the derivative of the angle of attack regarding the advance ratio as well as that of the thrust coefficient regarding the angle of attack. Otherwise, it can be tested by a BEMT code applying different lift slopes. The modeled approaches show a good agreement with the resolved simulation for the advance ratios associated to the climb flight. In general, if the simulated advance ratio is closer to the design advance ratio, the result is better. In this case, the local angles of attack along the radius of the blade are in a region that can be predicted

appropriately with PanBL. In the following, the efficiency depending on the advance ratio is considered. The modeled approaches provide a similar trend. In contrast, the resolved simulation shows a reduced efficiency for low advance ratios and an increased efficiency for high advance ratios. This aspect is reasonable by taking into account the definition of the efficiency as well as the trends of the thrust coefficient depending on the advance ratio. Nevertheless, the maximum of the efficiency is predicted for the same advance ratios with all methods, although the maximum value differs. In [3], the results for four different RBPAs reading $\theta_{75} = 8°$, $\theta_{75} = 10°$, $\theta_{75} = 12°$, and $\theta_{75} = 14°$ were presented. Moreover, a quantitative discussion is provided therein. In contrast to the results shown here, the distribution function is solely applied for the sources, but it is not included for the averaging procedure. However, the differences of the results are small. For the estimation of the thrust and efficiency, the RANS/AD simulation is approximately 400 times faster than the URANS/RP.

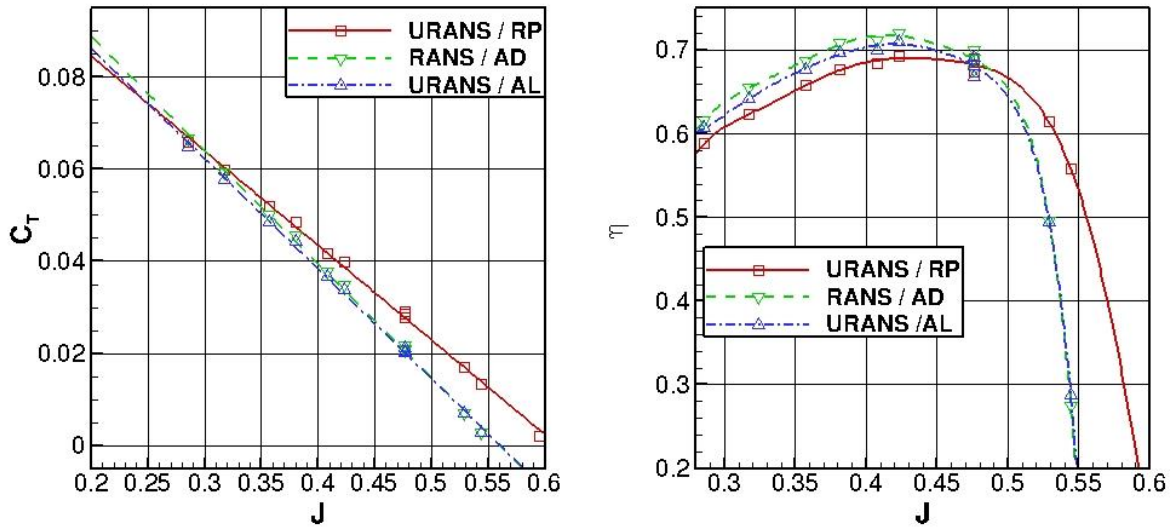

Figure 89: Thrust coefficient C_T (left) and efficiency η (right) depending on the advance ratio J for an RBPA of $\theta_{75} = 10°$ simulated with different modeling approaches. Resolved propeller: URANS/RP; Actuator disc: RANS/AD; Actuator line: URANS/AL.

In order to assess the quality of the prediction for the distribution of the forces along the blade, in Figure 90, the sectional thrust and circumferential force coefficient depending on the radial direction are presented. The sectional coefficients are related to the corresponding integral coefficient of the blade. The operating point is associated to the climb flight with a freestream velocity of $U_\infty = 16.67\, m/s$, a rotational speed of $\omega = 261.80\, rad/s$, and the RBPA is set to $\theta_{75} = 10°$. The corresponding advance ratio reads $J = 0.286$. For the sectional thrust, a very good agreement of the modeled approaches with the resolved propeller simulation is detectable. Slight differences occur for the prediction of the maximum and in the blade tip region. The behavior of the thrust, in the vicinity of the blade tip, is captured better by the actuator line approach than by the actuator disc approach regarding the resolved simulation. Considering the circumferential coefficient, a very good agreement of the modeled approaches with the resolved simulation is found also. Solely for one section, the circumferential force coefficient is provided slightly smaller for the resolved simulation. The behavior in the blade tip region is represented well by the modeled approach regarding the resolved propeller simulation also. It has to be noted that the local angles of attack are moderate for the considered operating point. As a side note, in [3], an additional operating point representing the

cruise flight was shown. For this operating point, the local angle of attack is high in some regions. Although the applied method in [3] differs, as remarked in the preceding paragraph, it was shown that the sectional thrust coefficient is not captured appropriately in the vicinity of the spinner for higher advance ratios. In this region, the actuator disc provides a negative thrust, while the resolved propeller simulation provides a thrust close to zero.

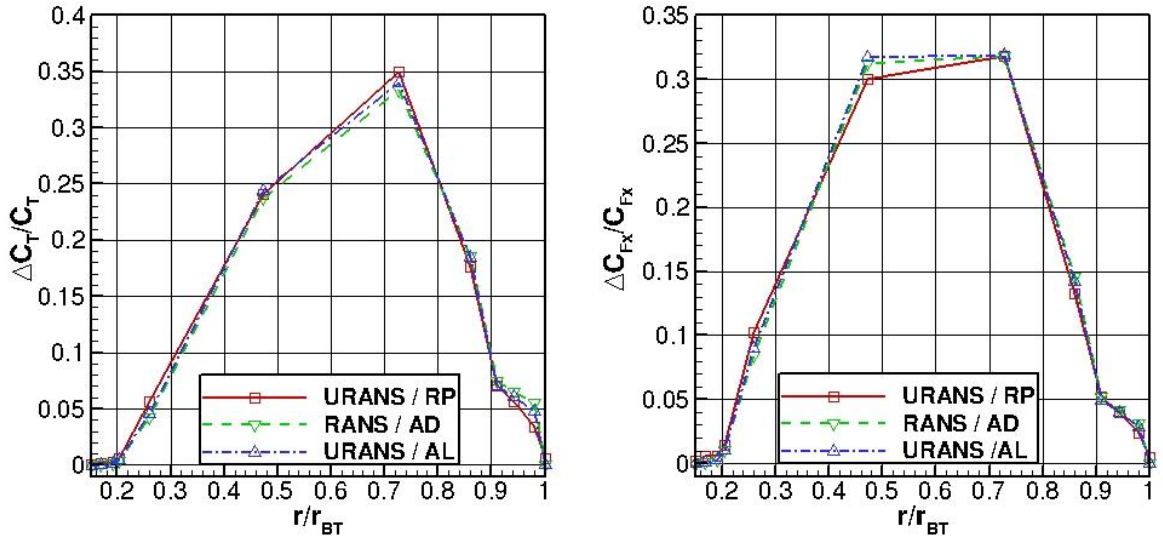

Figure 90: Sectional thrust coefficient ΔC_T (left) and circumferential force coefficient ΔC_{Fx} (right) depending on the nondimensionalized radius r/r_{BT} for an RBPA of $\theta_{75} = 10°$ simulated with different modeling approaches. The sectional coefficients are normalized with the corresponding coefficients of the blade. Resolved propeller: URANS/RP; Actuator disc: RANS/AD; Actuator line: URANS/AL.

In the following, the wake flow field obtained by the resolved propeller simulation is compared qualitatively and quantitatively to that of modeled approaches. The operating point associated to the climb flight is used as well. In Figure 91 (bottom), the time-averaged normalized axial velocity distribution for the URANS/RP and the RANS/AD is depicted. The contour plot shows upstream as well as downstream of the propeller a qualitatively good agreement between both approaches. Differences are visible mainly in the wake flow of the aft body. The region of separated flow at the aft body is predicted smaller by the resolved URANS/RP. The size of the region of separated flow is influenced by the state of the boundary layer downstream of the propeller. Basically, crucial differences in the boundary layer are present between the approaches. For the resolved propeller simulation, the flow is disturbed B times per revolution, while the actuator disc acts continuously on the flow. Furthermore, the velocity field of the resolved propeller simulation is time-averaged. The influence of the periodic wake of the blade cannot be captured fully by the steady actuator disc simulation, in particular, for the boundary layer. It is remarked that the velocity in the propeller domain is averaged in the rotating frame. As a result, the blade tip vortex is visible. For the quantitative comparison, the time-averaged normalized axial velocity is provided along the radial direction for three different downstream positioned lines in Figure 91 (top). The axial positions are exhibited in the contour plot also. In general, a good agreement is achieved for the RANS/AD compared to the URANS/RP for each downstream location. The RANS/AD overestimates the velocity radially outwards and underestimates the velocity radially inwards. Furthermore, the influence of the linear interpolation between the sections can be detected in the flow field. The higher velocity deficit in the vicinity of the aft body, provided by the RANS/AD, is well visible for the most upstream located

line. Moreover, the higher velocity deficit at the propeller axis can be identified for the downstream located lines. For the estimation of the wake flow field, the RANS/AD simulation is approximately 800 times faster than the URANS/RP. In order to obtain a converged flow field for a downstream distance of three propeller diameters, ten revolutions have to be calculated by the URANS/RP simulation.

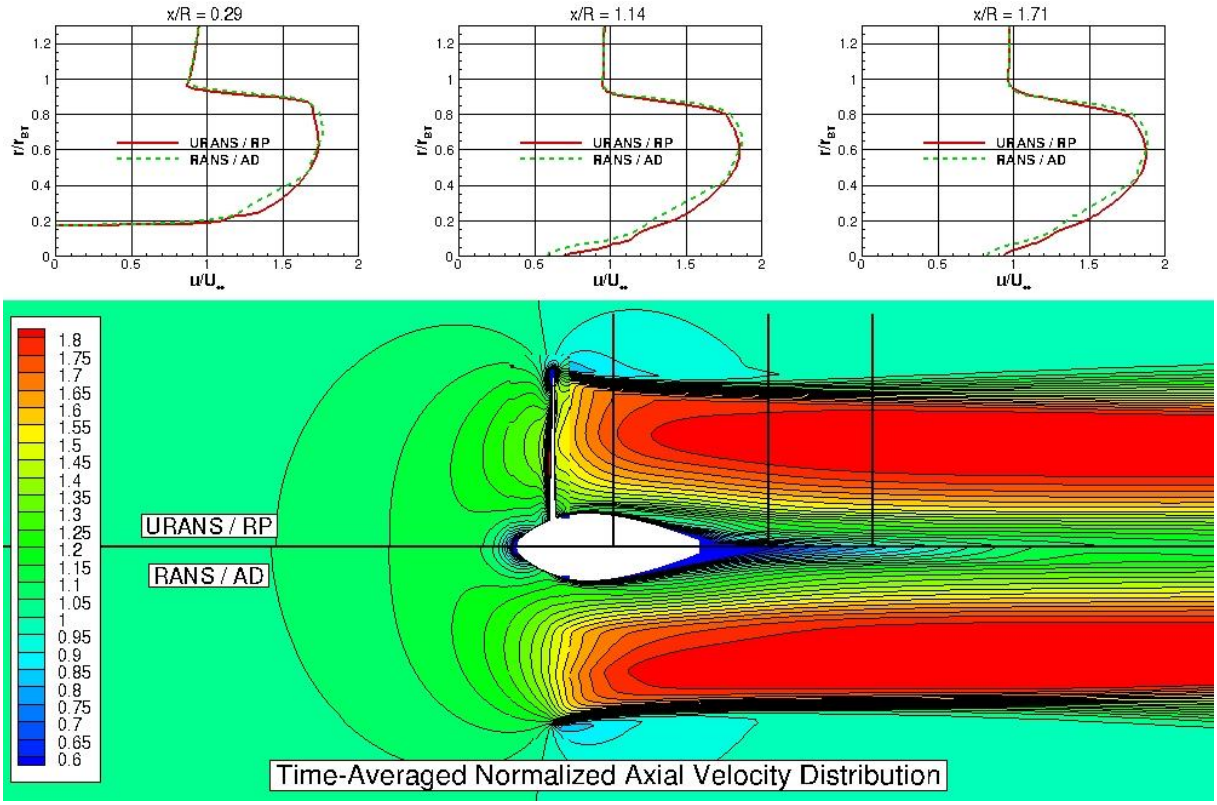

Figure 91: Contour plot of the time-averaged normalized axial velocity for the URANS/RP and the RANS/AD (bottom), and radial distribution of the normalized axial velocity component at three different radial positions downstream of the propeller (top). Cruise flight: $v = 16.67$, $\omega = 261.080$, and $\theta_{75} = 10°$.

In Figure 92 (bottom), the time-averaged normalized axial velocity distribution for the URANS/RP and the URANS/AL is depicted. While the contour plot shows qualitatively a good agreement between both approaches downstream of the propeller, upstream of the propeller, slight deviations are noticeable. Apparently, the velocity upstream of the propeller is predicted slightly lower by the URANS/AL. Taken into account that the thrust is provided smaller by the latter also, the results are reasonable. In accordance to the results obtained by the RANS/AD simulation, differences between the modeled approach and the resolved propeller simulation are visible in the wake of the aft body as well. The size of the region of separated flow is predicted larger by the URANS/AL. The reason therefore is the interaction of the modeled propeller with the boundary layer of the aft body like for the RANS/BET. However, the modeled blade acts for the URANS/AL B times per revolution on the flow like the resolved propeller blade. By comparing the flow field downstream of the connection of the blade with the spinner, the velocity deficit is predicted higher for the URANS/AL compared to the URANS/RP and consequently, the boundary layer includes less momentum. For the quantitative comparison, the time-averaged normalized axial velocity is provided along the radial direction for three different downstream positioned lines in Figure 92 (top). In general, a good agreement is achieved for the URANS/AL regarding the URANS/RP for each downstream location. The region of the blade tip and the outer part of the blade is predicted better by the actuator line than by the actuator disc. The velocity inwards is underpredicted by the URANS/AL compared to the resolved propeller

simulation. The influence of the linear interpolation as well as the higher velocity deficit in the wake can be addressed also.

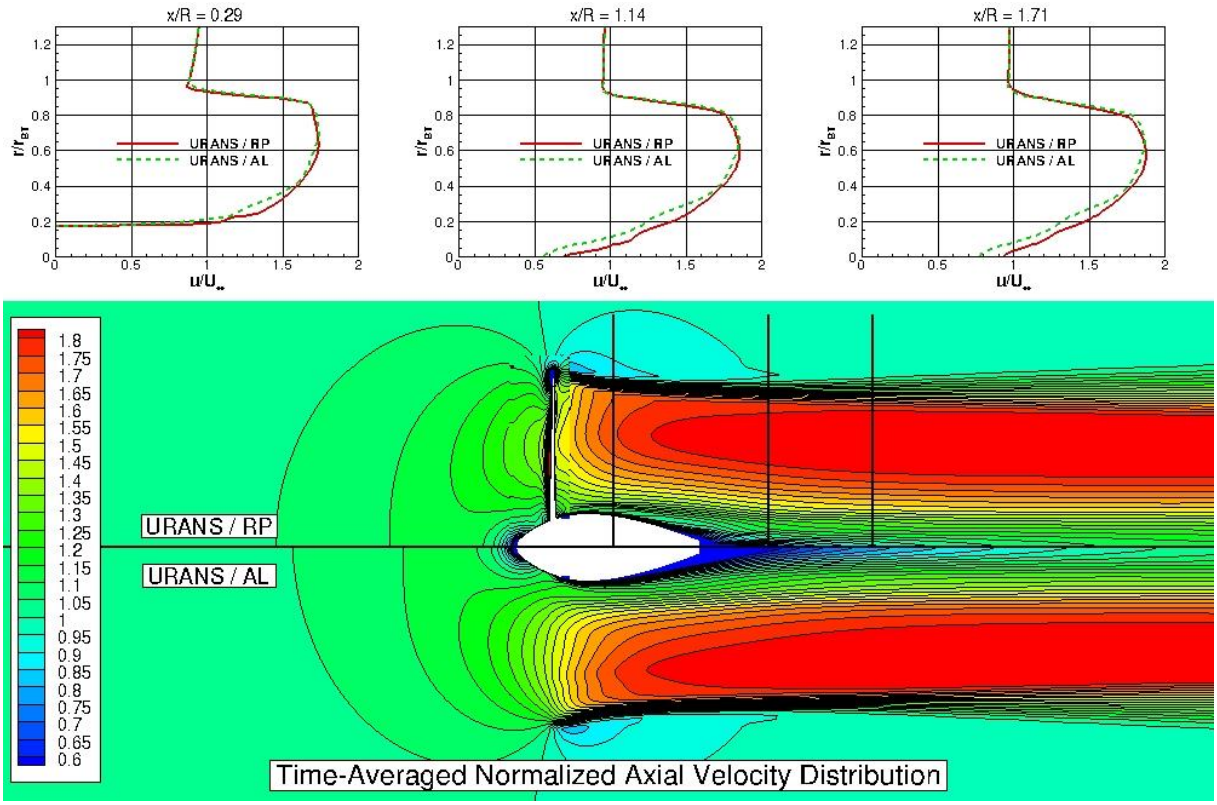

Figure 92: Contour plot of the time-averaged normalized axial velocity for the URANS/RP and the URANS/AL (bottom), and radial distribution of the normalized axial velocity component at three different radial positions downstream of the propeller (top). Cruise flight: $v = 16.67$, $\omega = 261.080$, and $\theta_{75} = 10°$.

Besides the time-averaged distribution, the actual flow field at a certain time is presented for the actuator line and the resolved propeller simulation only. The discussion is conducted basically in order to investigate the occurring coherent structures. Therefore, the Q criterion is applied. In Figure 93 (top, left), the contour plot of the normalized Q criterion in the range of $2.5 \leq \frac{Q}{n^2} \leq 50$ and cut off below $\frac{Q}{n^2} = 1$ is exhibited. The plane is defined by the axis of the propeller and the radial direction of the blade. On the upper side, the result for the resolved simulation and on the lower side, that for the actuator line is shown. The detectable coherent structures are the blade tip vortices, the blade hub vortices, and the wakes of the blades. The location as well as the strength of the blade tip vortices is represented well by the URANS/AL in comparison to the URANS/RP. Moreover, the prediction of the wakes of the blades is provided well by the actuator line approach. The biggest discrepancy is detectable for the blade hub vortices. While the resolved simulation shows the vortical structures separated for the aft body and with higher strength, the actuator line approach provides the structures weaker and with more interaction to the aft body. Consequently, the higher influence on the boundary layer is visible as mentioned above. Furthermore, the larger region of separated flow is predicted by the actuator line approach. In addition to the contour plot, the isosurface of the normalized Q criterion for a value of $\frac{Q}{n^2} = 5$ is presented in Figure 93. The side view is included in Figure 93 (top, right) and three-dimensional views are shown in Figure 93 (bottom). The isosurface for the resolved simulation is highlighted red and that of the actuator line is highlighted in blue. It has to be remarked that the results for the actuator line are mirrored. In general, this view shows the

good agreement of the results as well. In particular, the blade tip vortices are captured similarly between the approaches. Nevertheless, the structures meet well even in the aft body region. Due to the larger extent of the actuator line in axial direction of the propeller, the shear layer is represented larger.

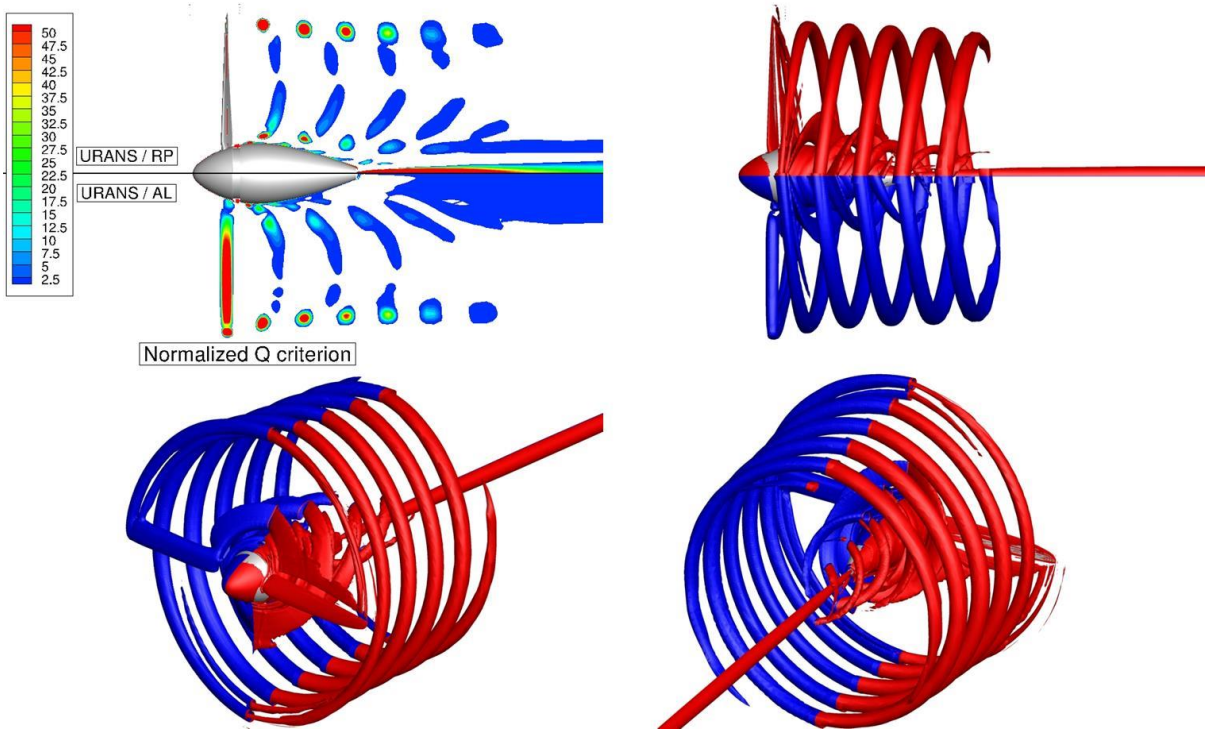

Figure 93: Contour plot of the normalized Q criterion in the range of $2.5 \leq \frac{Q}{n^2} \leq 50$ and cut off below $\frac{Q}{n^2} = 1$ (top, right) is shown. Isosurface of the normalized Q criterion with an isovalue of $\frac{Q}{n^2} = 5$ (bottom; right) is exhibited. The isosurface is colored red (resolved propeller) and blue (actuator line).

In the following, the discussion on the applicability to non-axial inflow condition is provided. Therefore, the thrust and torque as well as the remaining moments are discussed for disc inflow angles in the range of $0 \leq \phi_D \leq 90°$. An angle of $\phi_D = 0°$ represents axial inflow and an angle of $\phi_D = 90°$ an inflow aligned with the z-axis. The inflow conditions are a freestream velocity of $U_\infty = 16.67\, m/s$, a rotational speed of $\omega = 261.80\, rad/s$, and the RBPA of $\theta_{75} = 10°$. The corresponding axial advance ratio reads $J = 0.286$. In Figure 94, the thrust and the torque coefficient depending on the inflow angle are depicted for the URANS/RP, the RANS/AD, and the URANS/AL. At first, the thrust coefficient is considered. A good agreement between the approaches can be detected for an inflow angle of $\phi_D = 0°$. With increasing disc inflow angle, the modeled blade approaches predicts a higher thrust than the resolved propeller simulation. While a reasonable agreement is still obtained for a disc inflow angle of $\phi_D = 30°$, for $\phi_D = 60°$, and $\phi_D = 90°$ the agreement becomes worse. However, the difference between the modeled approaches is small for the whole range of the disc inflow angle. The reason for the discrepancy between the modeled and the resolved approaches is found in the estimation of the airfoil data for a section with PanBL. The identified drawbacks of PanBL within the two-dimensional test case are the overpredicted slope of the thrust coefficient depending on the advance ratio as well as the incorrect stall behavior. For the present investigation, on purpose, a rather large RBPA is applied in order to demonstrate this issue. For higher disc inflow angles, the axial inflow velocity component is lower. Moreover, the lateral inflow component leads to an increased angle of attack on the retreating blade side. However, the

angle of attack on the advancing blade side is reduced. Nevertheless, if the angle of attack is too high within the resolved simulation, the blade stalls. Since the stall model in PanBL does not cover the blade stall correctly, [usually it occurs for much higher angles of attack than for the resolved simulation,] the maximum predicted thrust is higher. Due to the higher thrust, the induced velocity is higher. The latter causes a reduced angle of attack for the operating point and consequently, higher disc inflow angles can be realized without the blade stall. Regarding the torque coefficient, the global trend is presented correctly by both modeled blade approaches. The discrepancy for $\phi_D = 0°$ is associated to the underestimation of the drag by PanBL in contrast to the resolved blade simulation. The difference between the approaches for higher disc inflow angles is caused by the blade stall and modified inflow conditions. Although the global trends are represented well, the effects leading to the behavior are different. Therefore, the variation of the torque for the disc inflow angle of $\phi_D = 60°$ to $\phi_D = 90°$ is considered. For the actuator disc, the reduction is caused for upwind positions of the blade, associated to azimuthal propeller angles in the range of $180° \leq \varphi \leq 330°$, with its peak at $\varphi = 240°$. For the resolved propeller simulation, in contrast, the reduction occurs for azimuthal propeller angles in the range of $240° \leq \varphi \leq 330°$ with no distinct peak. Moreover, the radial position of the contribution to the reduction is different. While the reduction of the torque takes place in the center of the blade for the resolved simulation, it is located in the blade tip region for the actuator disc simulation. For the latter, the torque can be even negative. As already stated for the simplified three-dimensional test case, the actuator disc condenses the information of the complex flow field around the blade to an inflow condition of a blade section only. Moreover, the interaction of the blade with the blade tip vortex of the upstream located blade induces a velocity in negative x-direction. Consequently, the local angle of attack is increased and due to the lack of the appropriate modeling of the separation by PanBL, high local lift is obtained. In addition, the inflow angle becomes negative and provides a negative torque.

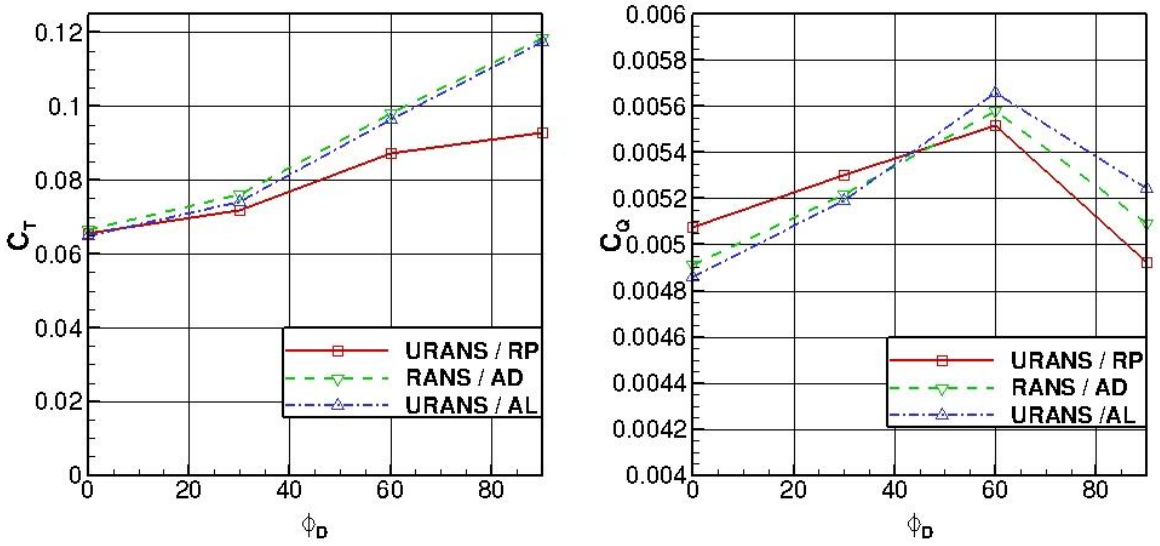

Figure 94: Thrust coefficient C_T (left) and torque coefficient C_Q (right) depending on the disc inflow angle ϕ_D for an RBPA of $\theta_{75} = 10°$ simulated with different modeling approaches. Resolved propeller: URANS/RP; Actuator disc: RANS/AD; Actuator line: URANS/AL.

In particular for the mechanical design, the moments around the remaining axes are of interest. Therefore in Figure 95, the lateral moment coefficient (y-axis) and the vertical moment coefficient (z-axis) depending on the disc inflow angle are provided. Consider the lateral moment coefficient at

first. The overall trend is represented well by the modeled approaches. For disc inflow angles of $\phi_D \leq 60°$, the agreement of the generalized actuator disc with the resolved propeller simulation is good. For $\phi_D = 90°$, the modeled approaches overestimate the moment. The reason therefore is the above stated lack of modeling the lift slope accurately and the blade stall reasonably. Considering the vertical moment, the overall trend is not represented correctly. The deviation between the modeled approaches and the resolved propeller simulation increases with higher disc inflow angles. In particular, the moment for a disc inflow angle of $\phi_D = 90°$ is provided differently. For the latter angle, the thrust of the blade on the advancing blade side is predicted much higher by the generalized actuator disc approach compared to that of the resolved propeller simulation. Again, the issue is addressed to the modeling of the airfoil characteristics by Pan BL. The better agreement of the results for the lateral moments compared to those of the vertical moments is caused by the smaller influence of the disc inflow angle on the local conditions along the circumferential direction of the blade. Obviously, the difference in the local inflow conditions between the advancing and the retreating blade side is higher than that between the upwind and downwind blade side.

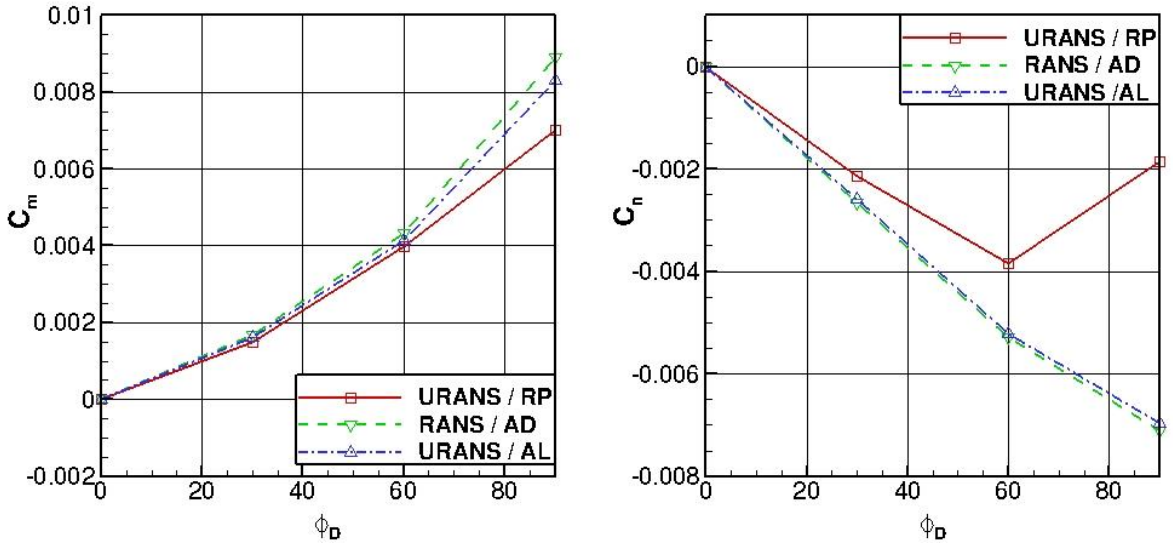

Figure 95: Lateral moment coefficient C_m (left) and vertical moment coefficient C_n (right) depending on the disc inflow angle ϕ_D for an RBPA of $\theta_{75} = 10°$ simulated with different modeling approaches. Resolved propeller: URANS/RP; Actuator disc: RANS/AD; Actuator line: URANS/AL.

Finally, the occurring coherent structures are compared between the actuator line approach and the resolved propeller simulation. The actuator disc approach is not shown, since the coherent structures are not comparable due to the averaging. Therefore, the isosurface of the normalized Q criterion with an isovalue of $\frac{Q}{n^2} = 5$, colored by the turbulent kinetic energy, is exhibited in Figure 96 for a disc inflow angle $\phi_D = 90°$ and an RBPA of $\theta_{75} = 10°$. The results for the resolved propeller simulation are presented in Figure 96 (left) and for the actuator line simulation in Figure 96 (right). In general, the previously discussed issues for the integral coefficients become visible. In both simulations, the blade tip vortices are captured. Furthermore, the interaction of the blade with the tip vortex of the previous blade is presented well on the advancing and the retreating blade side by the actuator line approach. The induced velocity and the increased angle of attack in the blade tip region can be imagined easily by considering the figure. Moreover, a chaotic wake, due to local separations of the flow at the blades, is depicted for resolved propeller simulation. Due to the higher thrust provided by the actuator line approach, the greater deflection of the flow is exhibited.

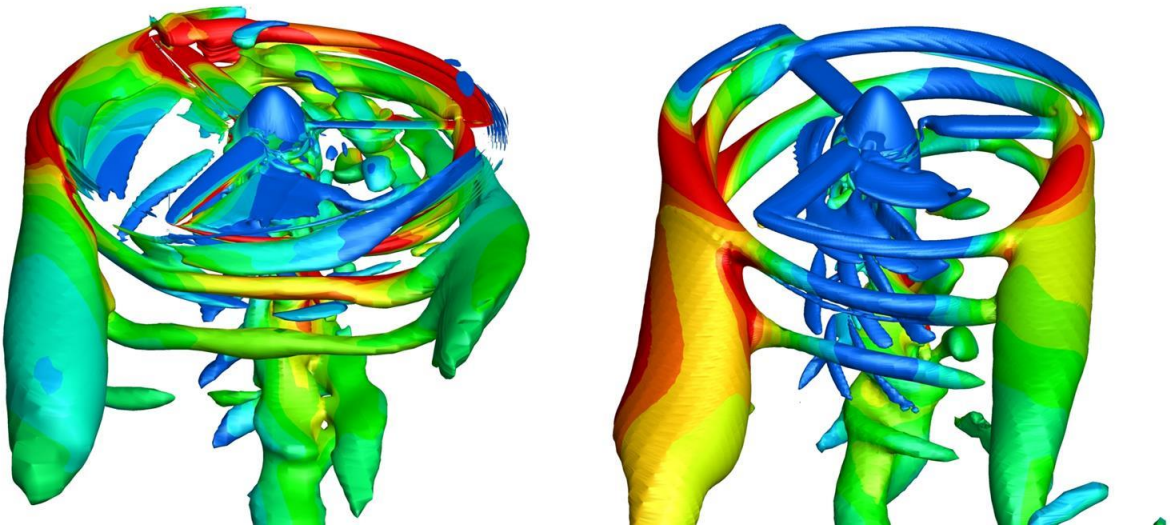

Figure 96: Isosurface of the normalized Q criterion with an isovalue of $\frac{Q}{n^2} = 5$ colored by the turbulent kinetic energy for a disc inflow angle $\phi_D = 90°$ and an RBPA of $\theta_{75} = 10°$. Resolved propeller: URANS/RP (left); Actuator disc: URANS/AL (right);

4.2.4 Conclusions

Within this test case, the application of the generalized actuator disc model for a three-bladed propeller is provided. Therefore, the thrust and efficiency, the distribution of the forces along the blade, and the wake was investigated for axial inflow conditions. In addition, the applicability of the method for non-axial inflow was presented.

Basically, the results for the thrust and efficiency of the modeled approach show a good agreement with those of the resolved propeller blade simulations. Furthermore, the distribution of the forces along the blade is represented well. Discrepancies occur mainly due to the prediction of the airfoil data by PanBL. The overpredicted lift slope leads to the more negative slope of the thrust coefficient depending on the advance ratio. Although the magnitude of the efficiency is not predicted correctly by the modeled approaches compared to that of the resolved propeller simulation, the advance ratio for the maximum is. Concerning the wake flow field, a good agreement of both modeled approaches with the resolved simulation is found also. The biggest differences in the results are detected in the wake of the aft body, since the interaction of the modeled blades with the boundary layer of the latter is not captured appropriately. The strength and position of the blade wakes as well as of the blade tip vortices are in good agreement between the modeled approach and the resolved propeller simulation. The application of the methods for non-axial inflow angles demonstrated a good agreement for moderate disc inflow angles regarding the forces and moments. For high disc inflow angles, the airfoil data are not provided appropriately by PanBL and consequently, the forces and moments are overestimated.

4.3 Propeller-Fuselage Configuration

A complex scenario is represented by the configuration that has been investigated within the research project EUROPAS. Within this project, complementary numerical and experimental investigations were performed for the propeller of an electrically powered ultra-light aircraft. Furthermore, the overall aerodynamic characteristics of the aircraft were evaluated. The experimental data are applied, in particular within this thesis, to validate the numerical results. Within this thesis, a reduced data set of the results presented in [3] is provided. For more details concerning the comprehensive database refer to [3]. In contrast to the publication, the distribution function for the averaging of the inflow conditions is applied only herein.

4.3.1 Test Case description

The numerical as well as the experimental investigations are conducted for a real full-scale ultra-light aircraft without the wing and the horizontal tail. The reason therefore is that the initial objective of the wind-tunnel campaign was the evaluation of the electric propulsion system in freestream conditions. The expected results should include information about, for example, the cooling system and the battery system. Nevertheless, the setup is also suitable for validating the numerical methods and to determine the influence of the wind tunnel on the results.
The numerical investigations are carried out on a propeller-fuselage configuration with the three-bladed propeller presented in section 4.2.1. The complementary wind-tunnel tests have been conducted for the same configuration. The latter has been sting-mounted in the wind tunnel A of the Chair of Aerodynamics and Fluid Mechanics of the Technical University of Munich. The length of the propeller-fuselage configuration reads approximately $5.5\ m$. Figure 97 shows the propeller-fuselage configuration mounted in the test section. The mounting is realized by a specific cranked sting that connects the wing attachment shaft to the six-component underfloor balance. In order to limit possible occurring oscillations of the aircraft, a wire connects the tail of the aircraft with the collector of the wind tunnel on the upper side and with the floor on the lower side. As a side note, the influence of this wire on the forces has been tested for low wind speeds with no remarkable effect. For this test case, only force and moment measurements for the configuration have been conducted.

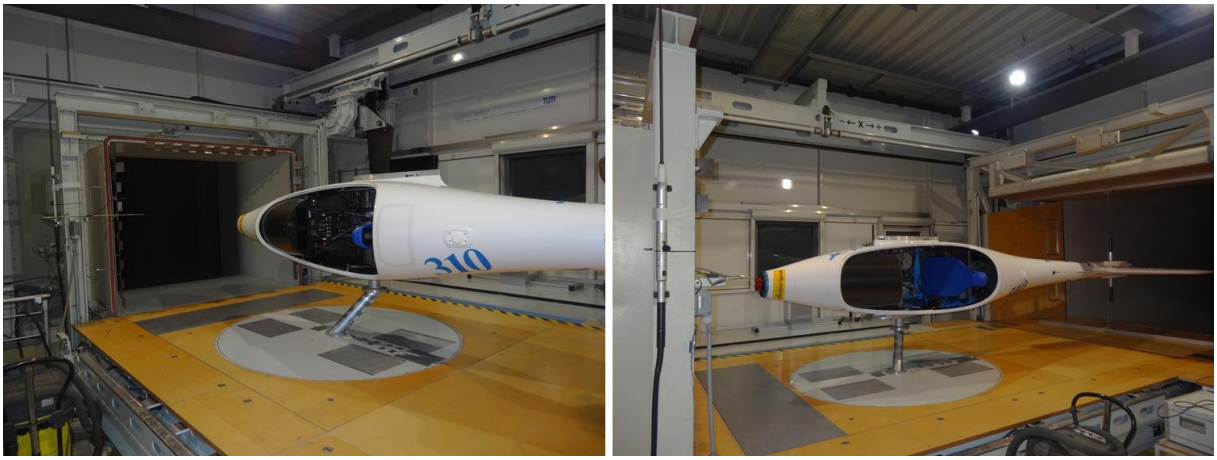

Figure 97: Test configuration mounted in the test section of the wind tunnel. View in direction of the nozzle (left) and in the direction of the diffusor (right) is shown. Propeller and spinner are not shown.

Within this thesis, the emphasis of the test case is set on validating the numerical results obtained by the different methods with the wind-tunnel data. Basically, three different numerical setups are applied; at first, the RANS/AD, at second, the RANS/AD-W/T, and at last the URANS/RP. The first and the last are already described within the previous chapter. The RANS/AD-W/T, however, is presented herein. Basically, the method is the same as for the RANS/AD, but the setup includes the propeller-fuselage configuration as well as the major parts of the wind tunnel in the numerical simulation also. The applied geometry for the numerical simulation is exhibited in Figure 98. Therein, the nozzle (orange highlighted), the room including the test section (grey highlighted), the propeller-fuselage configuration mounted on the sting (blue highlighted), the blades of the wind tunnel (red highlighted), and the diffusor (green highlighted) are presented.

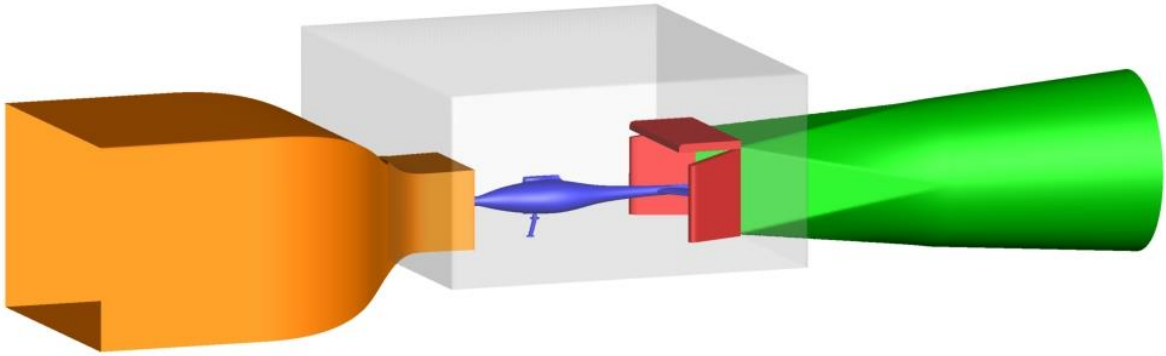

Figure 98: Configuration for the numerical simulation. The nozzle (orange highlighted), the room including the test section (grey highlighted), the propeller-fuselage configuration mounted on the sting (blue highlighted), the blades of the wind tunnel (red highlighted), and the diffusor (green highlighted) are presented.

4.3.2 Measurement Technique and Test Conditions

The experimental investigations have been conducted in the large low-speed facility A of TUM-AER. The force and moment measurements have been performed with a six-component underfloor balance. Details concerning the facility and the measurements of forces and moments can be found in the Appendix A.4. The maximum blockage for the mounted configuration in the wind tunnel is approximately 15%. The uncertainty in the drag and the thrust coefficient is established to be below $3.5\ \%$ based on the actual loads and repeatability tests.

4.3.3 Mesh Generation and Numerical Setup

The blocking strategy and mesh generation are employed as reported in Stuhlpfarrer et al. [3]. The computational grid is of block-structured hexahedron type and the blocking consists of three domains. The blocking for the wind tunnel is separated into two domains for a simplified mesh generation. One domain includes the nozzle, the room around the test section, and the collector blades at the entry of the diffusor. The other domain includes solely the diffusor. The wind-tunnel domain excluding the diffusor is exhibited in Figure 99 (left). The test section domain is embedded in the latter. The test section domain includes the model to be investigated. The idea of separating the

domains in this way is to allow for changing the model easily in the “numerical wind-tunnel”. For the present investigation, the propeller-fuselage configuration, the mounting sting and the test section floor is included within this domain. In Figure 99 (right), the test section domain is presented. The domains are finally connected by a non-conformal interface [112]. In general, the boundary layer is resolved for all domains in order to prevent the application of a wall function. Consequently, the dimensionless wall distance for the cell centers of the wall-adjacent cells are approximately $y^+ \approx 1$. The wind-tunnel domain excluding the diffusor consists of 490 blocks and $2.16 \cdot 10^6$ cells. The diffusor domain includes 9 blocks with $8.47 \cdot 10^5$ cells. The test section domain is made of 2883 blocks and $2.73 \cdot 10^6$cells. The actuator disc parameters are in accordance to those described in 4.2.2.

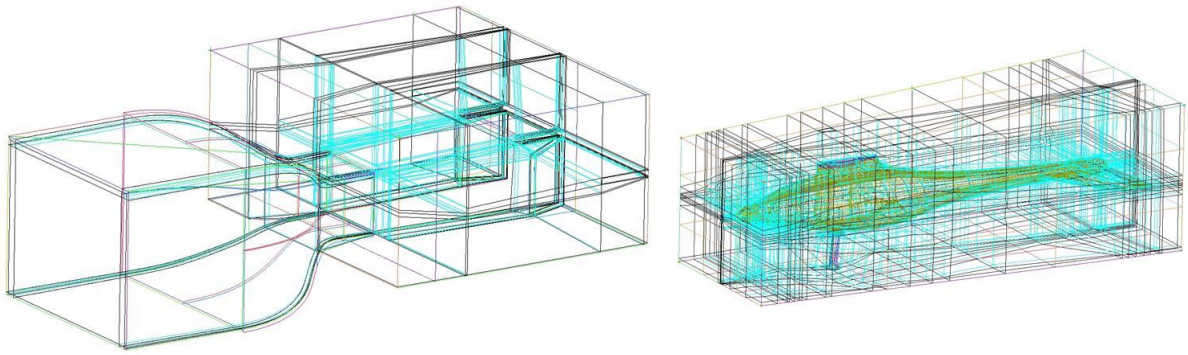

Figure 99: Blocking of the wind-tunnel domain excluding the diffusor (left) and the aircraft domain (right) is shown.

The settings of the numerical schemes are based on that of the generalized actuator disc approach for the three-dimensional propeller test case described in section 4.2.2. Since just RANS/AD calculations are performed, exclusively steady-state simulations are analyzed. A difference of the settings is found in the discretization of the equations. Due to the complex flow field and the fact that solely steady-state simulations are conducted, a first-order upwind scheme is used for the momentum equation. The pressure is discretized by a second-order scheme. Moreover, the coupled solver is applied instead of the SIMPLE algorithm. The Courant number is set to $C = 20$, and the explicit-relaxation factors for the pressure and momentum are set to $\alpha_p = \alpha_{mom} = 0.3$.

The applied boundary conditions are a velocity inlet boundary condition at the inlet of the nozzle and a pressure outlet boundary condition at the outlet of the diffusor. The velocity at the inlet is adjusted in order to achieve the required velocity at the exit of the nozzle. The velocity at the exit of the nozzle is considered to be the freestream velocity for the propeller-fuselage configuration. The turbulence quantities are set in order to obtain comparable conditions at the inlet of the test section as for the wind-tunnel experiments. For the outlet, the pressure is set to $p_{out} = 101325\ Pa$. The boundary conditions for the room around the test section are modeled by free-slip walls.

4.3.4 Results and Analysis

Within this section, the thrust obtained by the different numerical approaches is compared to the experimental data generated in the wind tunnel. Moreover, a brief analysis of the influence of the wind tunnel on the estimation of forces is provided.

The present investigations are conducted for an RBPA of $\theta_{75} = 10°$ only. In Figure 100 (left), the thrust coefficient depending on the advance ratio is exhibited. The thrust coefficient is provided for the experimental data of the propeller-fuselage configuration (W/T), the RANS simulation applying the actuator disc approach for the propeller-fuselage configuration (RANS/AD-W/T), the RANS simulation applying the actuator disc approach for the aft body configuration (RANS/AD), and the URANS simulation of the resolved propeller for the aft body configuration (URANS/RP). The idea for choosing this order is to allow for a step-by-step comparison. At first, the difference of the thrust for the W/T and the RANS/AD-W/T is presented. While the thrust coefficients meet well for moderate advance ratios, discrepancies are detected for low and high advance ratios caused by the different slope of the thrust coefficient depending on the advance ratio. The reason therefore is identified for the three-dimensional propeller test case by the inappropriate prediction of the lift slope by PanBL. Since the geometry for the numerical simulation and the experiment is similar, the calculation of the thrust is performed comparable as well. For the measurements of the wind-tunnel configuration, the direct estimation of the thrust of the propeller is not possible. Obviously, the force obtained by the six-component underfloor balance contains the drag of the fuselage as well as the thrust of the propeller. Furthermore, the aerodynamic force acting on the mounting sting is included also. Usually, an aerodynamic tare is conducted for revising the wind-tunnel data. Consequently, the procedure of the aerodynamic tare is applied to the RANS/AD-W/T too. In general, two different measurement setups are required therefore. For the first, the propeller is dismounted and for the second, the propeller is mounted and the required advance ratios are set. Finally, the thrust of the propeller is determined by subtracting the force resulting for the setup with the dismounted propeller from that with the enabled propeller. It has to be remarked that the aerodynamic tare does not capture the influence of the higher velocity in the slipstream and subsequently the higher drag of the downstream located components appropriately. An estimation of the deviation can be found in [3]. Therein, the axial momentum theory was applied for determining the induced velocity and subsequently, the drag of the fuselage and the mounting sting was interpolated for the resulting velocity. The deviation increases with the increase of the thrust coefficient. It was shown that for small advance ratios, the thrust coefficient is underestimated up to 10%. This issue results in a less negative slope of the thrust coefficient depending on the advance ratio. However, the blockage of the fuselage downstream of the propeller and the small distance of the blade tip to the floor of the test section are influencing the results also. For these effects, a simple estimation of the deviation is not applicable. Comparing the results of the thrust coefficient for the RANS/AD-WT and the RANS/AD, a good agreement for the considered range is visible. It has to be recalled that for the RANS/AD solely the force on the blades is considered for the calculation of the thrust. Consequently, the underestimated thrust caused by the interaction of the slipstream of the propeller with the fuselage and the mounting sting is compensated by the overestimation of the thrust due to the blockage of the fuselage and the small distance to the test section floor. Comparing the results of the URANS/RP with those of the RANS/AD, the slope of the thrust coefficient depending on the advance ratio is predicted less negative. The slope for the URANS/RP is comparable to that obtained by the experimental data. It is noted that for the URANS/RP solely the thrust on the blades is taken into

account as for the RANS/AD. Nevertheless, the influence of the different measurement procedures does not affect the result much, as shown previously. Consequently, a good agreement between the W/T and the URANS/RP is stated. In contrast to the RANS/AD, the URANS/RP is able to predict the local aerodynamic characteristics of an airfoil section better.

In the following, the drag of the fuselage and the mounting sting, required for the aerodynamic tare, are discussed. Therefore, the contributions of the drag on the revised thrust coefficient are exhibited in Figure 100 (right). That means that the thrust coefficient is calculated by substituting the thrust with the drag in the equation. For all curves, a polynomial fit with the order of two is applied. The drag of the fuselage and the mounting sting with dismounted propeller is shown for the experimental data ($D_{FM0,W/T}$) and for the numerical results (D_{FM0}). In general, both methods provide the same trend. The result is reasonable, since with increasing J, the drag is increased. Furthermore, by extrapolating the curves for $J = 0$, a drag of $C_{T,D} \approx 0$ is obtained. Nevertheless, the experimental data provide a higher drag than the numerical results. However, certain parts generating noticeable drag are not captured in the numerical simulation. For example, the cylindrical mounting of the horizontal stabilizer, see Figure 97, is not included. The drag of the fuselage and the mounting sting with the enabled propeller (D_{FM}) is presented for the numerical results only, since it is not possible to determine the contribution with the actual experimental configuration. The drag of the fuselage with the enabled propeller is increasing as well with higher J. For $J = 0$, however, the drag is non-zero due the induced velocity in the slipstream of the propeller. Another plausibility proof can be made by comparing the advance ratio for the intersection of D_{FM0} and D_{FM} with the advance ratio for zero thrust in Figure 100 (right). If no thrust is produced, the induced velocity of the propeller equals zero. Differences can be present, since even if the overall thrust of the propeller is zero, the local thrust can be non-zero and influences the drag of the fuselage. Finally, the difference of D_{FM} and D_{FM0} is calculated (ΔD_{FM}). Obviously, if the thrust coefficient is zero, the difference is almost zero as well. Furthermore, the above noticed underestimation of the thrust coefficient with approximately 10% is detectable.

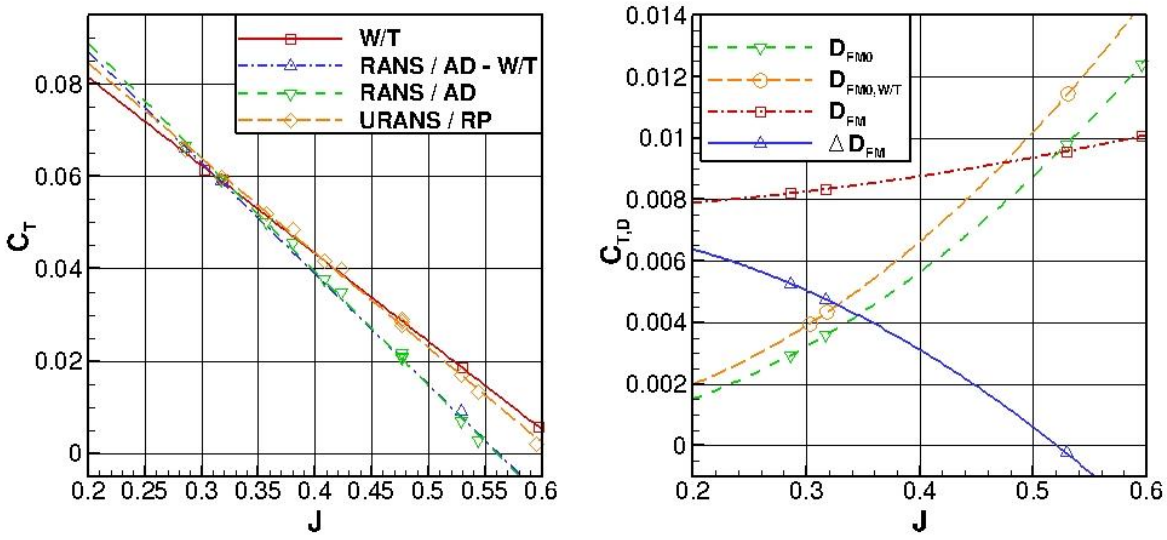

Figure 100: Thrust coefficient C_T depending on the advance ratio J for an RBPA of $\theta_{75} = 10°$ for different modeling approaches and the experimental data (left). Experimental data: W/T; Resolved propeller: URANS/RP; Actuator disc for propeller-fuselage configuration: RANS/AD-W/T; Actuator disc: RANS/AD; Resolved propeller: URANS/RP. Thrust coefficient caused by the drag of the fuselage and the mounting $C_{T,D}$ depending on the advance ratio J for different conditions (right).

For one operating point, a quantitative description is provided. A rather small advance ratio of $J = 0.317$ is chosen in order to enable a better demonstration of the effects. The associated axial velocity and the rotational speed read $U_\infty = 16.67 \frac{m}{s}$ and $\omega = 235.619\, s^{-1}$, respectively. The velocity in the experiment is slightly higher which leads to a slightly higher advance ratio. In Table 16, the contributions to the thrust coefficient are presented for the RANS/AD-W/T, the W/T and the RANS/AD. The table shows entries only for those boxes where values can be obtained. The contribution to the thrust coefficient caused by the drag of the fuselage and the mounting sting with dismounted propeller $C_{T,D_{FM0}}$ is slightly underestimated by the numerical simulations. As described above, not all parts of the experimental setup are included in the numerical simulation. Considering the thrust coefficient caused by the drag of the fuselage and the mounting sting with enabled propeller $C_{T,D_{FM}}$, solely the RANS/AD-WT allows to determine the value. The drag of the fuselage and the mounting sting is more than doubled, comparing the results for the enabled propeller with those for the dismounted propeller, $\frac{C_{T,D_{FM}}}{C_{T,D_{FM0}}} = 2.31$. Considering the thrust coefficient of the propeller blades only $C_{T,Prop}$, the propeller produces for the wind-tunnel configuration approximately 10% more thrust related to the stand-alone propeller. The resulting thrust coefficient for the propeller-fuselage configuration, consisting of the propeller thrust as well as the drag of the fuselage and the mounting sting $C_{T,FM}$, is overpredicted by the numerical simulation $\Delta C_{T,FM,rel} = 0.57\,\%$. For the final result with the completed procedure of the aerodynamic tare, the thrust coefficient is underestimated by the numerical simulation by $\Delta C_{T,rel} = -0.69\,\%$. However, even by taking into account the isolated blade only, the absolute deviation of the thrust coefficient is still less than 3%.

Table 16: Contributions to the thrust coefficient due to the aerodynamic tare.

	J	$C_{T,D_{FM0}}$	$C_{T,D_{FM}}$	$C_{T,Prop}$	$C_{T,FM}$	C_T
RANS/AD-WT	0.317	0.0036	0.0083	0.0637	0.0554	0.0590
W/T	0.318	0.0043			0.0551	0.0594
RANS/AD	0.317			0.0578		0.0578

Finally, a brief analysis of the flow field obtained in the test section of the wind tunnel is made. In Figure 101 (top), the isosurface of the normalized axial velocity for a value of $\frac{u}{U_\infty} = 1.1$ is shown. The results for the RANS simulation without propeller (left) and the RANS/AD (right) with enabled propeller are exhibited. The operating point for the cruise flight with an advance ratio of $J = 0.286$ is chosen. For the configuration with the dismounted propeller, the isosurface of the increased velocity is detectable in the vicinity of the largest cross section of the fuselage only, whereas for the configuration with the enabled propeller, the increased velocity is obtained within the slipstream of the propeller. For both configurations, the wake of the sting mounting is well visible. Moreover, the distribution of the normalized axial velocity is shown for a crossflow plane in Figure 101 (bottom.) Therefore, the influence of the enabled propeller is well visible also. The slipstream caused by the propeller is well visible. In addition, considering the case with the propeller disabled, the shear layer of the caused by wind tunnel can be detected. By enabling the propeller, the shear layer is shifted slightly downwards.

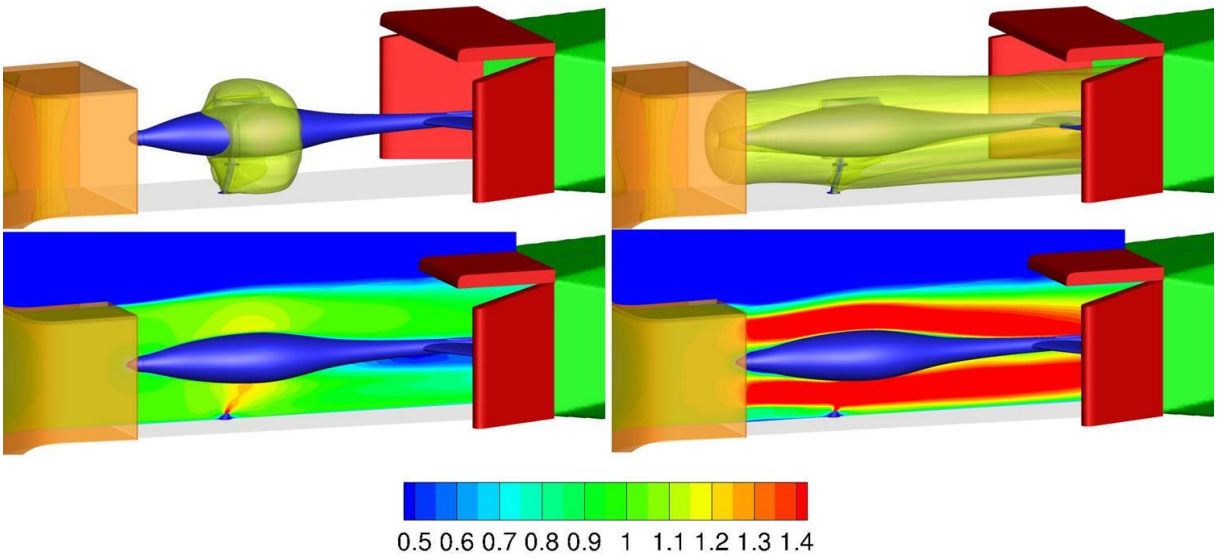

Figure 101: Test configuration with dismounted propeller (left) and with enabled propeller representing the cruise flight condition (right) is shown. The advance ratio reads $J = 0.286$. Isosurface of the normalized axial velocity with an isovalue of $\frac{u}{U_\infty} = 1.1$ (top) and crossflow plane colored with the normalized axial velocity in the $0.5 \leq \frac{u}{U_\infty} \leq 1.4$ (bottom) is shown.

4.3.5 Conclusions

Within this test case, a complex scenario used for the validation was presented. Therefore, the propeller-fuselage configuration was investigated experimentally and numerically. Furthermore, the procedure of the aerodynamic tare was discussed in detail.

The URANS/RP results show from the numerical approaches the best agreement with the W/T data. In particular, the slope of the thrust coefficient depending on the advance ratio is represented very well. The AD-based approaches provide a different slope caused by the representation of the airfoil data by PanBL. The thrust of the propeller-fuselage configuration in the “numerical wind-tunnel”, obtained by the application of the aerodynamic tare, is in accordance with that produced by the modeled propeller for the isolated propeller configuration. The detailed investigation of the contribution of forces, taken into account the aerodynamic tare, shows that the increasing drag of the fuselage for higher thrust levels is compensated by the higher thrust due to the blockage of the fuselage and the small distance of the propeller to the floor of the test section.

5 Modeling of the Rotorcraft

Within this chapter, the theoretical basis for the applied modeling approach of a full helicopter configuration is presented. Therefore, at first an introduction including the review of the state-of-the-art of flow simulations for helicopter configurations is presented. The focus of the investigations is set on the methods used for the rotation of the rotor head including the blades and that is why the state-of-the-art for this topic is detailed. Secondly, the actual mesh-deformation approach applied within this thesis is presented. Finally, a study on the scalability of the deformation method is provided.

Certain contents of this chapter have been already published by Stuhlpfarrer et al. [5].

5.1 Introduction

The accurate prediction of the wake flow of a helicopter is important concerning the interaction of the wake flow with the downstream located parts of the helicopter [117]. However, the realization of this requirement is challenging by the application of computational fluid dynamics. In general, different flow regimes (i.e., laminar, transitional, or turbulent boundary layers) as well as regions of attached and separated flows are present for a common helicopter configuration. In particular, the flow resulting for complex geometries, including laminar-turbulent transition, cannot be resolved by the standard turbulence models such as the Spalart-Allmaras, the $k-\epsilon$, or the $k-\omega$ turbulence models appropriately. Besides the modeling concerning the physical effects, the numerical loss of information due to the temporal and spatial discretization schemes affects the convection of the flow structures also [118]. Consequently, scale-resolving turbulence models in combination with low-dissipative and low-dispersive numerical schemes have to be applied to enhance the quality of the simulation.

In the last years, a variety of works have been published regarding the wake flow of helicopters. In general, the wake flow of parts of the fuselage as well as that of the rotor and the rotor head were investigated. However, for the interaction of the wake with downstream located parts of the helicopter, the flow structures originating on the upper side of the helicopter are more important. As a consequence, the majority of the investigations have been conducted for the wake on the upper side of the helicopter including the rotor head as well as the rotor. For the present thesis, the wake flow on the upper side of the helicopter is of higher importance as well.

Nevertheless, a brief description of the investigations concerning the wake flow of the fuselage is provided. Vogel [119] provided aerodynamic analyses for two helicopter configurations. The focus was set on the origin and the action of the aerodynamic forces and moments depending on the angle of attack and the angle of sideslip. Therefore, numerical and experimental investigations were conducted. Besides the forces and moments, the surface pressure distribution as well as the wake flow field was presented. Although the numerical results meet the experimental data appropriately, it was stated that the application of scale-resolving turbulence models on refined meshes as well as the inclusion of the rotor-head motion is beneficial. A complementary experimental and numerical study concerning the wake flow of parts of the fuselage in combination with an optimization focusing on the parasite drag was presented by e.g. Grawunder [4] at TUM-AER for a twin-engine light utility

helicopter. Therefore, experimental and numerical investigations were conducted to describe the flow topology in the wake in detail. The optimization of the parasite drag was conducted by Grawunder et al. for the skid landing gear [120] and for the aft body by the application of passive flow control [121]. For both optimizations, a detailed explanation of the wake flow field is presented also. For the numerical simulations, the Reynolds stress model was applied. The complementary results show a good agreement.
A recently published and comprehensive experimental study was conducted for a large transport helicopter configuration by De Gregorio [122]. For the helicopter blunt fuselage model, the effectiveness of the active flow control in the ramp region by alleviating the flow separation was demonstrated. Therefore, drag reduction was obtained with a little negative impact in terms of negative lift in some instances. In addition, particle image velocimetry (PIV) measurements of the wake flow are presented.

In contrast to the wake of the fuselage, a large number of investigations concerning the wake of the rotor and the rotor hub can be found in the literature. Since the wake of the rotor head is of higher importance for this thesis, the focus of the review is set thereon. Shenoy et al. [123] conducted numerical simulations for a moderately complex rotor hub. The results were used to investigate scaling effects. Furthermore, the results were compared to experimental data and show a good agreement. Grawunder et al. [6] investigated the wake flow of a fully-functional rotor-head featuring cyclic and collective pitch motion. Complementary numerical simulations and experiments were conducted and a validation of the results stating good agreement was provided.
A comprehensive and detailed review of the numerical and experimental efforts as well as an investigation of the hub was provided by Reich et al. [124]. The result was that complementary numerical and experimental investigations are an adequate tool. Moreover, information of small-scale hubs can represent the qualitative behavior of full-scale hubs although Reynolds number effects have to be kept in mind, in particular, for cylindrical and spherical components. Finally, a static analysis is found to be not sufficient to predict the hub drag. For further investigating the complex flow field in the hub region, in the course of the first rotor hub flow prediction work shop, the emphasis was set on the precise prediction of the flow around the rotor hub and its wake. An overview of the experimental and numerical contributions is provided by Schmitz et al. [125]. The reference data were provided by experiments of a model helicopter rotor hub in the water tunnel in order to enable higher Reynolds numbers in contrast to a wind tunnel by Reich et al. [126]. The model consists of a notional helicopter hub of a large helicopter. However, blade cuffs and as a consequence, the ability for a cyclic pitch motion is not featured. Coder and Foster [127] provided numerical simulations with a second-order temporal and a fifth-order spatial discretization scheme. A grid refinement in the wake was performed in order to reduce the error caused by the discretization. It is stated that the results capture a wide spectrum of turbulent scales, but discrepancies with the time-averaged quantities obtained by the experiment require further investigations. Moreover, a scale-resolving hybrid RANS/LES turbulence model was applied to avoid the overprediction of the turbulence eddy viscosity. Furthermore, Coder et al. [128] investigated different turbulence modeling strategies for rotor hub flows. Basically, two scale resolving models were considered, a delayed detached eddy simulation and the hybrid RANS/LES simulation combining the SST model with a Smargorinsky-type LES sub-grid scale model. That outcome was that the hybrid RANS/LES simulation is less dissipative and the results for the higher harmonics agree better with the experiment.
Although a quite large number of contributions concerning the wake flow of the rotor hub is

available, complementary numerical and experimental investigations capturing cyclic pitch motion can be found only to a limited extent [124].

Besides the detailed investigations of the rotor head above, in the following, a brief review of selected works of the flow around the helicopter configuration including the whole rotor is provided. Although this is not the focus of the thesis, some methods and test cases have to be mentioned, in particular, the scale resolving simulations. Furthermore, works are considered solely if the simulation incorporates the rotor head.
A numerical simulation of the UH-60A airloads rotor mounted in the wind tunnel was conducted by Lee-Rausch and Biedron [129]. The model includes a fuselage, a very simple rotor hub, and the rotor. The trends of the solidity-weighted propulsive force and the power coefficients match the experimental trends over the range of advance ratios. Kowarsch et al. [130] presented aeroacoustic simulations of a complete H145 helicopter in descent flight. Therefore, a fifth-order WENO-Z scheme is applied in order to reduce the numerical error of the spatial discretization, whereas for the temporal discretization a second-order scheme was used. The simulated noise was compared to flight test data and shows a good agreement. With the same numerical method, but with a strongly refined mesh, consisting of $485\ mio.$ cells, Schäferlein (nè Kowarsch) et al. [131], investigated the tail shake phenomenon by including the structural dynamics as well. The presented approach resolves the excitation of low-frequency tail-boom eigenmodes with good agreement compared to the flight test data. However, due to the weak tail shake of the helicopter, only candidates can be identified. A detailed investigation of the UH-60A rotor/wake interaction using adaptive grids was published by Chaderjian [132]. Therefore, as well high-order spatial numerical schemes are applied. The finest grid consists of $1.8\ billion$ cells. The combination of high-order schemes with fine grids allows for capturing the vortices even for long wake ages. The results were used to investigate the loads as well as the flow field containing blade-vortex interactions. Experimental data have been used for validation and a good accordance is shown.

The previously presented review is based on the flow around a helicopter. Since this thesis introduces an analytical mesh-deformation method also, a review of the treatment of relative moving parts of the mesh is provided in the following. It is obvious that the appropriate capturing of the wake flow requires a detailed representation of the rotor-head geometry as well as the cyclic pitch motion. The latter leads to a relative motion of the blades related to the rotor head. For computational fluid dynamics, two different modeling approaches have been applied to adapt the mesh, as summarized, for example, by Steijl et al. [133]. One approach is the Chimera or overset grid approach. Basically, for the overset grid or Chimera approach, at least two different grids are applied. One grid is moving, for example, with each of the rotor blades and the other one, the background mesh, is stationary. In addition, the grid of the blade can be deformable. At the Chimera boundaries, the two mesh regions are overlapping and an interpolation of the flow quantities of the different solution spaces has to be performed. Some advantages of the method can be identified. If the mesh of the blade is solely rigidly moved and consequently not deformed, the quality remains as set up initially. Moreover, the generation of the background mesh is simple and enables high quality meshes. Ideally, Cartesian grids can be generated and in combination with higher-order spatial and temporal discretization schemes, the numerical error of the flow solution can be reduced. An investigation including several applications of the method in the field of rotorcraft is provided by Renzoni et al. [134]. Pahlke and van der Wall [135] applied the approach for a simulation of multibladed rotors in high-speed forward flight with weak fluid-structure-coupling. The results show

an improved solution with respect to the experimental data by incorporating the elastic blades. Pomin and Wagner [136, 137] investigated the flow of a helicopter rotor in hover and forward flight featuring aeroelastic behavior and enabling deformable meshes. The loads as well as the deformation agree fairly well. Potsdam et al. [138] investigated the UH-60 rotor by the application of the chimera method using a loose aerodynamic/structural coupling obtaining a good agreement with the flight test data. Dietz et al. [139] used vortex-adapted chimera grids to improve tip vortex conservation of the main rotor.

The other approach is the deforming mesh approach. Therefore, different deformation types can be applied [e.g. transfinite interpolation (TFI), spring analogy, diffusion-based mesh-deformation, or finite element methods]. As a side note, the deforming mesh approach is applied to realize the cyclic motion of the blade; the rotation is realized by a combined sliding mesh approach. Dubac et al. [140] presented the TFI for a two-dimensional test case that shows that the deformation of the grid do not significantly influence the results compared to a rigid motion of the grid. Park and Kwon [141] applied the spring analogy for the mesh deformation. The results of the numerical simulation show a good agreement with experimental data. Steijl et al. [133] introduced a novel mesh-deformation approach by combining rigid mesh motion for the blocks attached to the blades and a deforming mesh for the remaining blocks. The deformation is performed by the TFI. The main idea was to keep the quality in the vicinity of the blades high, while requiring low computational costs due to the application of the TFI. Daheze and Barakos [142] presented a hybrid method combining the constant tetrahedron method, the TFI, as well as the spring analogy method for simulating deforming rotor blades. The approach combines the advantages of underlying approaches and the outcome was that the convergence is not affected by the deformation. Grawunder et al. [6] investigated the wake flow of a fully-functional rotor-head featuring cyclic and collective pitch motion by applying the diffusion-based mesh-deformation. Although the results match well with the experimental data, the computation effort is high and bad convergence was detected.

5.2 Mesh Motion Method

For the method presented in this thesis, the relative motion between the different parts of the rotor head is captured with a combination of the sliding mesh and a deforming mesh approach. If there is enough space, the sliding mesh approach is a well-suited technique; in particular, if rigid body motions are included exclusively. The advantage of this method is that the flow quantities have not to be interpolated in contrast to e.g. the Chimera approach between the different meshed, since the flux on a certain face can be calculated directly. Furthermore, since the sliding surfaces are in two-dimensional space, the evaluation of the intersecting surfaces is simple, even for a three-dimensional mesh. Consequently, for a two-dimensional configuration the intersecting surface degenerates to a curve. Such a two-dimensional example is show in Figure 102. The static domain (S) is fixed, while the rotating domain (R) is rotated from the initial state (left) about the axis normal to the plane of the paper to obtain the rotated state (right). Nevertheless, one major drawback is that both sliding surfaces must have the same geometrical shape. That may be difficult to obtain in regions with small physical spaces or complex geometries.

The deforming mesh approach, however, provides the capabilities to work appropriately in such regions. Therefore, the treatment of the governing equation might be more complex, since the change of the control volume has to be included. Nevertheless, it is necessary for the treatment of the rotor head motion caused by the high-level geometric complexity. In addition, the deforming

mesh approach allows for elastic surface motion as well. Nonetheless, in order to obtain a similar result for a rotation as presented for the sliding mesh approach above, the methodology differs. Figure 103 presents a rotation with the deforming mesh approach. Therefore a simple quad mesh is applied that is divided into three subdomains, the static (S), the deforming (D), and the rotating domain (R). The static domain remains in its initial state, while the rotating domain discovers a rotation with a certain angle ϕ, merely. The angle can depend on the solution time also. The deforming zone has to fulfill the required motion of the boundary to both adjacent domains. Obviously, the approach cannot handle too large rotational angles.

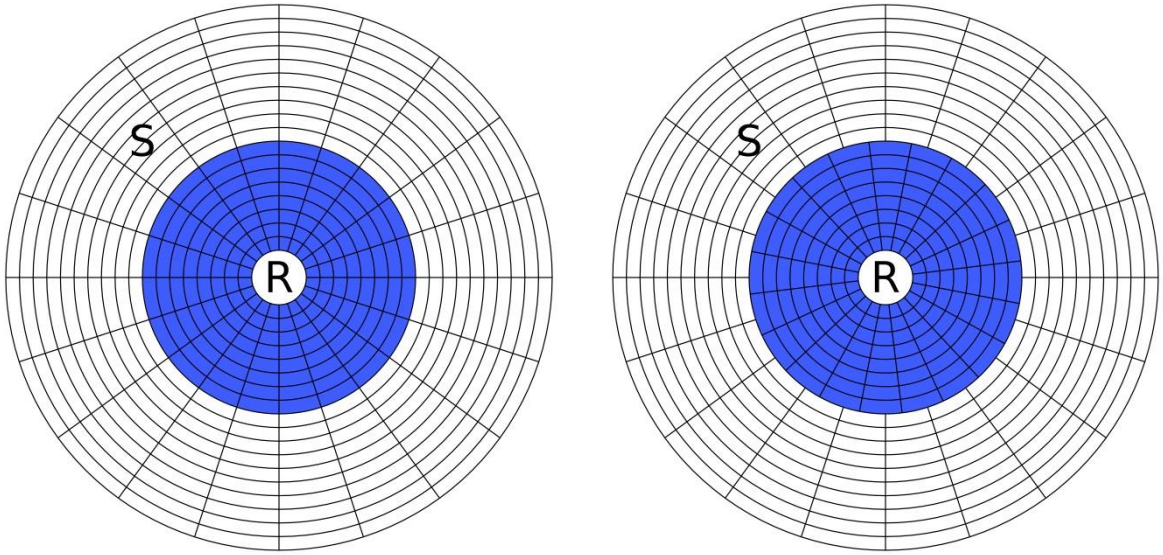

Figure 102: Static mesh (S) and rotating mesh (R) for the sliding mesh approach. Initial state is shown on the left hand side, after rotation on the right hand side.

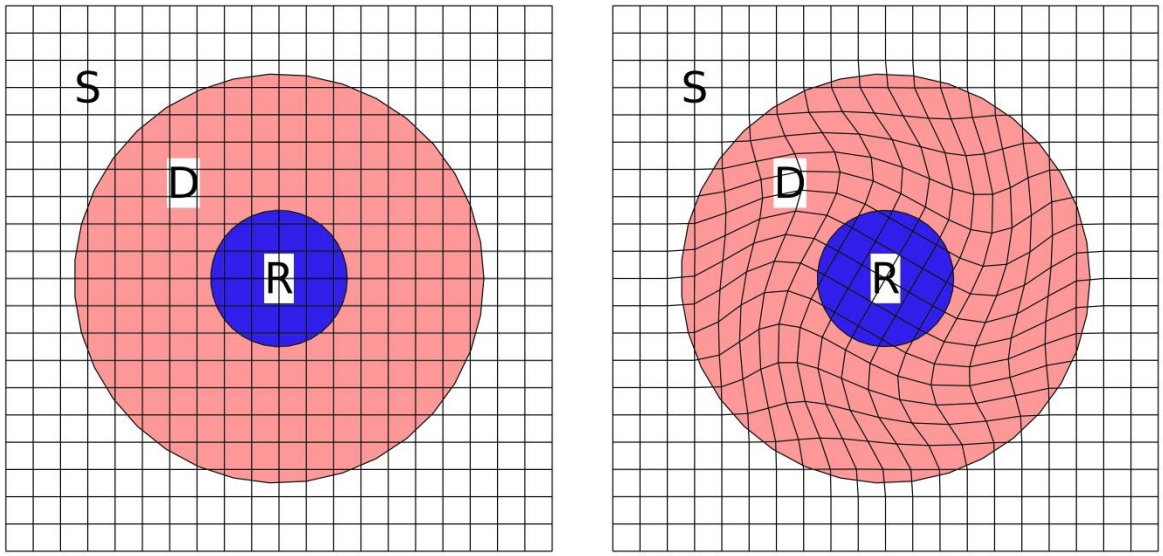

Figure 103: Static mesh (S), deforming mesh (D), and rotating mesh (R) for the deforming mesh approach. Initial state is shown on the left hand side, after rotation on the right hand side.

Initially, the standard deforming mesh approaches provided by Fluent have been tested. In the course of this investigation, the diffusion-based method has been applied. In contrast to the other methods of Fluent, like the spring analogy and the finite element based method, it provides the most stable results with best mesh quality. The diffusion based method relies on the diffusion equation with a diffusion coefficient γ, in order to set the local influence of, e.g. the normalized cell volume or the normalized distance from the boundary layer. The diffusion equation reads

$$\nabla \cdot (\gamma \nabla \boldsymbol{u}) = 0. \tag{5.1}$$

The diffusion coefficient can be described according to

$$\gamma = \begin{cases} \frac{1}{V^{\alpha}}, & for\ the\ normalized\ cell\ volume \\ \frac{1}{d^{\alpha}}, & for\ the\ normalized\ boundary\ distance \end{cases} \tag{5.2}$$

depending on the chosen method. An additional input parameter $\alpha \geq 0$ can be set in order to weight the influence of the cell size or the boundary distance. It is obvious that the diffusion equation will be transformed into the Laplace equation for the velocity if the input parameter is set to $\alpha = 0$. Since the parameter is set globally, difficulties in solving the system can arise if the mesh velocities and the length scales within the mesh are strongly varying. The result is a low convergence rate, or in the worst case, divergence of the simulation run. Furthermore, the computational effort for solving the system of equations scales with the order of magnitude of two related to the number of cells. This issue is a drawback, in particular, for highly resolved mesh regions. Another drawback is that the mesh is not periodic in time, even for an underlying periodic problem. This issue is caused by the diffusion equation which is applied for each time step depending on the present mesh. As a result, the quality of the mesh can be worse for increasing solution times and finally, this issue can lead to divergence of the simulation. Consequently, the analytical mesh-deformation method is developed.

5.3 Analytical Mesh-Deformation Method

At first, the idea of the analytical mesh-deformation is described. Secondly, the speed-up is presented. The application for the complex test case is shown in chapter 6.

The basic principle of the approach is to describe the motion of the parts of the rotor head and the rotor blades as well as the motion of the nodes of the surrounding computational grid with one analytical function. Furthermore, a combination of rigid and deforming mesh regions is applied, but in contrast to [133], independent of the blocking. In general, the governing law for a pitching motion of the rotor blades in terms of the pitch angle θ reads

$$\theta(\psi) = \theta_0 + \theta_c \cdot cos(\psi) + \theta_s \cdot sin(\psi). \tag{5.3}$$

Apparently, the motion of the rotor blades is described by an analytical function. For the other parts of the rotor head connected to the blade, an analytical function can successively be found also.

Nevertheless, the mesh between the moving and the stationary part has to be transformed dynamically. Considering the diffusion function, the adaption of the mesh between two relatively moving parts is realized by a time-dependent transition depending on the velocities of the individual parts. However, there is no restriction to move the nodes of the mesh by an analytical function for each time step that provides a comparable result. In the present case, a smooth function based on a raised cosine is applied. Basically, the function uses the construction applied for the Kernel function of the generalized actuator disc approach within chapter 2.

In the following, the principle is clarified with some examples. Therefore, the application of the mesh deformation is described for a two-dimensional rotation as illustrated in Figure 103. The deformation function F_{def} is defined depending on the radius. F_{def} shall be smooth at the inner and outer boundary of the deforming domain and it shall fulfill the constraints $F_{def}(r_{in}) = 1$ *and* $F_{def}(r_{out}) = 0$. The angle of the rotation of the rotating mesh (R) shall be ϕ. The analytical deformation function for this case reads

$$F_{def}(r) = \left\{ \begin{matrix} 0, & r > r_{out} \\ cos\left(\frac{r - r_{in}}{r_{out} - r_{in}} \cdot \frac{\pi}{2}\right)^{2n}, & r \geq r_{in} \ \wedge r \leq r_{out} \\ 1, & r < r_{in} \end{matrix} \right\}. \tag{5.4}$$

The resulting rotation of the whole mesh is determined by the angle $\phi_{def} = F_{def} \cdot \phi$. The analytical deformation function acts, in this example, on the angle of the rotation. In general, the method is implemented in a node-based manner. Consequently, if a node is located within a certain region, the associated function is applied for the node regardless of the position of the cell center.

The position of the nodes is finally obtained by performing a coordinate transformation. Due to the choice of the smooth function, a smooth transition of the mesh lines is preserved at the boundaries between the stationary and the deforming domain as well as between the deforming and the rotating domain. The smooth transition is visible, in this example, at the radial positions r_{in} and r_{out}. In addition, the parameter n is included in this equation. The latter allows for modifying the shape of the smoothing function. Basically, the higher the value of the parameter n, the smaller is the region of the deformation. In general, the value is set to $n = 1$ which results in a point-symmetric function around $r = \frac{r_{out} - r_{in}}{2}$. It has to be kept in mind that a smooth transition on both limits is obtained only for values of $n \geq 1$. Nevertheless, $n = 0.5$ can be used if the mesh at the lower limit is located on a mesh boundary, where it does not matter if the mesh lines change its orientation. Obviously, the inverse behavior of the function providing $F_{def}(r_{in}) = 0$ *and* $F_{def}(r_{out}) = 1$ can be obtained by substituting the cosine by a sine for certain applications.

For the translational motion, a similar function can be applied. In this case, the deformation is acting directly on the coordinate for the motion according to $x_{def} = F_{def} \cdot x$. The deformation function therefore reads as follows

$$F_{def}(x) = \left\{ \begin{matrix} 0, & |x| > x_{out} \\ cos\left(\frac{|x| - x_{in}}{x_{out} - x_{in}} \cdot \frac{\pi}{2}\right)^{2n}, & |x| \geq r_{in} \ \wedge |x| \leq x_{out} \\ 1, & |x| < x_{in} \end{matrix} \right\}. \tag{5.5}$$

As a side note, while for the rotational motion, in most cases, a cosine distribution with a parameter value of $n = 1$ is applied, for the translational motion a sine distribution with a parameter value of $n = 0.5$ is useful. The latter value is, in particular, of interest if an extension of the first cell is not prohibited and therefore, the quality within the mesh can be kept higher.

Furthermore, the rotational as well as the translational motion can be superposed. Therefore, a further example combining a translation with a rotation is provided and illustrated in Figure 104.

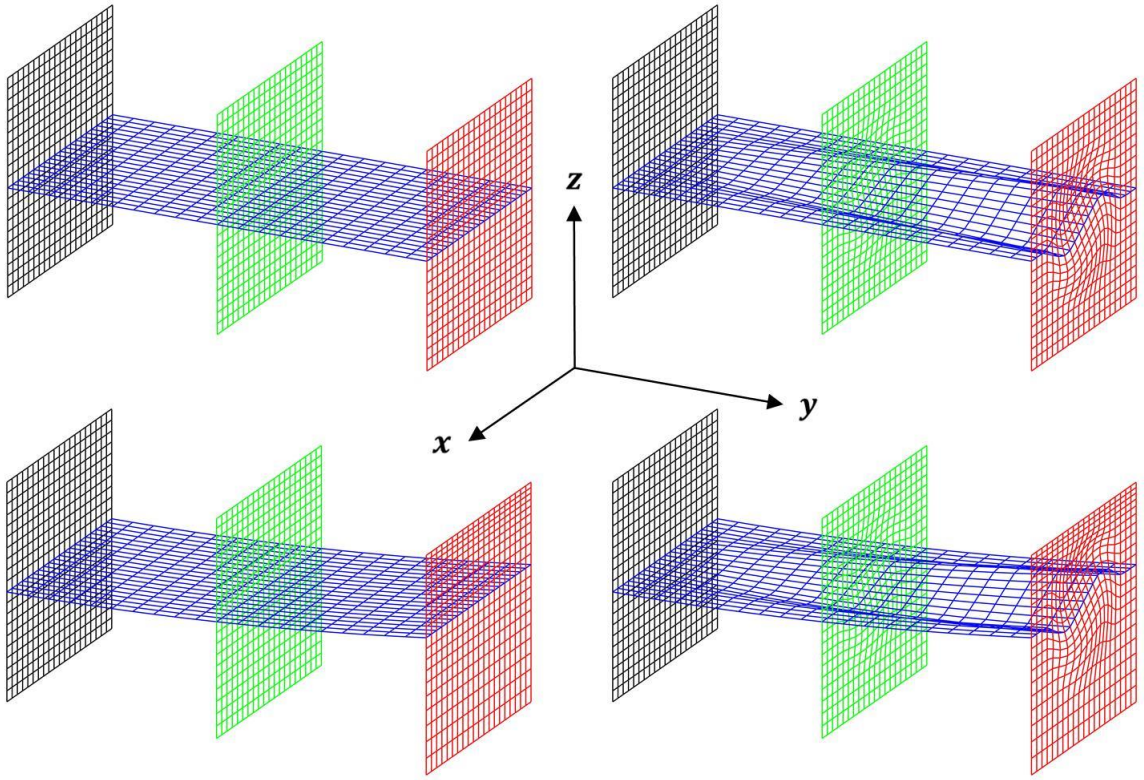

Figure 104: Surface deformation obtained by the analytical mesh-deformation approach. The initial state (top, left), the rotated-only state (top, right), the translation-only state (bottom, left), and the combined rotation-translation state (bottom, right) are presented.

In Figure 104 (top, left), the initial state of a mesh is presented. The ranges of the shown region are $[-x_{min}, x_{max}] = [-1,1]$, $[-z_{min}, z_{max}] = [-1,1]$ and $[-y_{min}, y_{max}] = [0,4]$. The mesh-deformation function shall perform a linear increasing rotation of the mesh around the y-axis depending on the latter according to $\phi(y) = \frac{\phi_{max}}{y_{max}} \cdot y$. y_{max} represents the location of the red highlighted plane and $\phi_{max} = 30°$, the maximum angle of the rotation. The center of the rotation is positioned in the center of the xz-plane (black). The rotation shall be performed within a cylinder of $r \leq 0.25$ and the mesh shall remain in its initial state for $r \geq 0.75$. Between the limiting radii, the analytical mesh-deformation is applied for a cosine distribution with $n = 1$. Furthermore, a non-linear translation in z-direction depending on the y-coordinate shall be conducted according to $z(y) = 0.25 \cdot \left(\frac{y}{y_{max}}\right)^2$. In Figure 104 (top, right), the result of the rotation is well visible. A smooth transition of the mesh is obtained. Furthermore, the quality of the mesh remains well, even for the rotation of $\phi_{max} = 30°$. The mesh after conducting the non-linear translation function is depicted in Figure 104 (bottom, left). Therefore, the quality of the mesh remains also well. Obviously, while for the rotation the cells are mostly skewed, for the translation, the cells are mostly stretched or

compressed. Finally, in Figure 104 (bottom, right), the superposed result of the rotation and translation is provided.

For these simple examples, the position of the boundaries, e.g. r_{in} and r_{out}, are kept constant. Nevertheless, additional dependencies can be set. For example, the radius can be varied depending on the y-coordinate according to $r_{in}(y)$ which is useful for a flapping rotor blade. Moreover, the radius can be adapted locally in order to obtain elliptical or piecewise curved shapes according to $r_{in}(\phi)$, with ϕ being the two-dimensional polar angle. This adaption might be necessary if in certain regions only less physical space is available, e.g. between the rotor blade and the steering rods.

Before a study of the performance of the method is given, a brief description concerning the implementation and the workflow is presented. The mesh deformation is coded in standard C. Since the commercial flow solver ANSYS Fluent is applied, the user-defined functions (UDFs) are used to hook the code of the mesh-deformation function. For the investigations within this thesis, multi-block meshes are used and converted to unstructured ones. As mentioned, the method allows for the utilization of unstructured meshes also. That is obvious, due to the node-based definition and the analytical description of the regions, the determination if a certain node is associated to a deforming or non-deforming region is independent of the shape and location of any blocks. The function is designed usually in such a manner that the mesh is considered to be rigid in the vicinity of boundaries and further away it is deformed. The sizes of the deforming region can be changed easily.

In the following, an example concerning the computational effort and the resulting speedup of the method compared to the diffusion-based method is provided. Therefore, a simple test case based on Figure 103 is presented. A sketch of the test case is presented in Figure 105 (top, left). However, for the present test case, the rotating domain is excluded and the action is modeled solely by a motion of the boundary nodes. The dimensions of the domain are $[-x_{min}, x_{max}] = [-1,1]$, $[-y_{min}, y_{max}] = [-1,1]$ and $[-z_{min}, z_{max}] = [0,2]$. The inner radius is set to $r_{in} = 0.25$. The outer radius is varied and reads $r_{out} = 0.75$ and $r_{out} = 1.0$. The latter is solely necessary for the analytical deformation function. For the diffusion-based mesh-deformation, the whole region between r_{in} and the outer boundary is deformed. The two different radii are presented for two reasons. On the one hand, the comparison of the computational effort between the two methods is only fair if in both cases the whole domain is deformed. Although this is even not fulfilled for $r_{out} = 1.0$, but almost the whole domain is deformed. On the other hand, it is demonstrated that the mesh quality is still high if $r_{out} = 0.75$ and it allows to reduce the size of the deforming region. In Figure 105 (top, right), the initial mesh is presented. The mesh for the maximum deflection obtained by the diffusion-based method is shown in Figure 105 (bottom, left) and the mesh provided by the analytical mesh-deformation function for $r_{out} = 0.75$ is exhibited in Figure 105 (bottom, right). It is well visible that the size and shape of the cells on the rotating surface are almost not modified and the angles of the cells at the surface remain almost perpendicular for the latter. The angle of the rotation is governed by $\phi(t) = \phi_{max} \cdot \sin(\omega\, t)$, with $\phi_{max} = 30°$ and $\omega = 2\pi \frac{1}{20} \frac{\text{rad}}{\text{s}}$. Consequently, 20 time steps with a time-step size of $1\ s$ are required for one period. Finally, the wall-clock time is determined for the simulations of one period with both methods. For the investigations, a coarse, a medium, and a fine mesh with $0.12\ Mio.$, $1\ Mio.$, and $8\ Mio.$ cells, respectively, are generated. In addition, the number of cores is set to 1, 2, 4, 8, 16, and 32. Due to the large computational effort of the diffusion-based method for the finest grid with $8\ Mio.$ cells, only two time steps are calculated. The time step with

less elapsed wall-clock time, in this case the second one, is chosen and multiplied by twenty to estimate the required wall-clock time for the whole simulation.

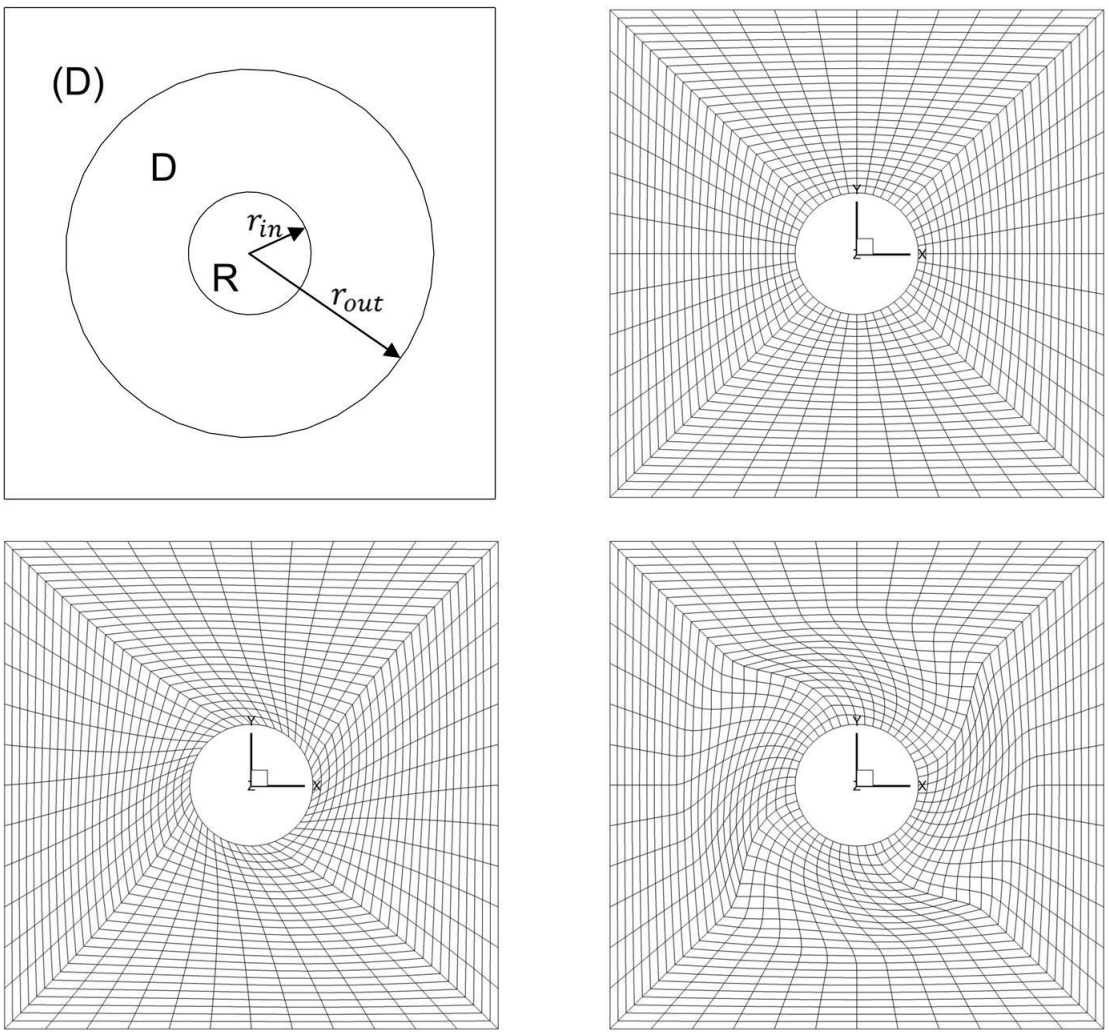

Figure 105: Sketch and mesh for the mesh-deformation test case. A sketch showing the region and measures is drawn (top, left). The initial mesh is presented (top, right). The deformed meshes for the maximum deflection within the test case are presented for the diffusion-based method (bottom, left) and the analytical mesh-deformation method (bottom, right).

In Figure 106, the wall-clock time required for one run is presented for the diffusion-based mesh-deformation method and the analytical mesh-deformation method. For the following comparisons, the results for the radius $r_{out} = 1.0$ are chosen. The magnitude of the relative deviation of the wall-clock time for $r_{out} = 0.75$ and $r_{out} = 1.0$ is less than $1.5\,\%$. In addition, repeatability tests are conducted showing a magnitude of the relative deviation of the wall-clock time of less than $1.1\,\%$. Due to the large difference of the computational effort between the two methods, a logarithmic scale has been chosen. The speedup of the analytical mesh-deformation method related to the diffusion-based is up to an order of magnitude of two. Concerning the number of cores, a similar behavior is provided by both methods. For both methods, the slope is comparable. The reduction of the wall-clock time for higher numbers of cores as well less numbers of cells is obtained. The parallel performance drops for both methods if the number of cores is too high and the number of cells is too low. Obviously, since the boundary cell count ratio gets bad for these points. The absolute wall-clock time t_{WC} is discussed for the medium mesh, since the mesh size is representative for a complex test

case and in contrast to the fine mesh, all points are calculated. The range of the wall-clock time for the analytical mesh-deformation method is given by $8.2\ s \leq t_{WC} \leq 46.7\ s$, whereas the wall-clock time for the diffusion-based mesh-deformation mesh reads $771.5\ s \leq t_{WC} \leq 6091.8\ s$, depending on the number of cores used. Nevertheless, even by applying the serial solver with the analytical method, in contrast to the parallel solver with the diffusion-based method, a big advantage in terms of wall-clock time is shown.

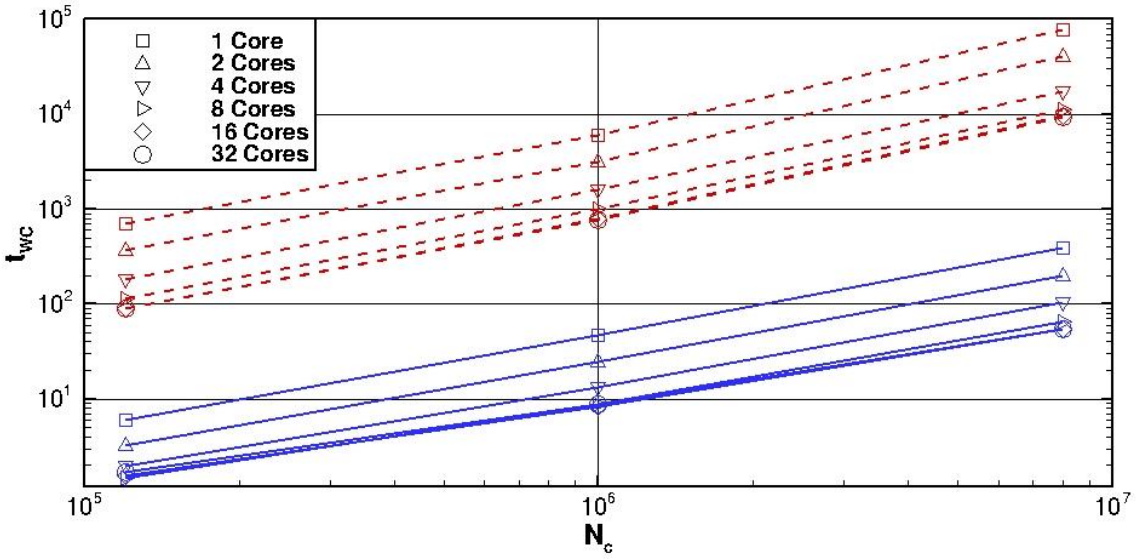

Figure 106: Required wall-clock time t_{WC} for one simulation run obtained by the diffusion-based mesh-deformation method (dashed line) and the analytical mesh-deformation method (solid line) depending on the number of cells for different numbers of cores N_c.

In order to quantify the speedup of the analytical methods, the ratios of the wall-clock times for the diffusion-based mesh-deformation method related to those of the analytical mesh-deformation are presented for different numbers of cores and grid resolutions in Table 17. The values marked with (*) are obtained by the multiplication of the wall-clock time needed for one time step with the maximum number of time steps as described above. In general, the speedup is at least one order of magnitude. Nevertheless, for most combinations the speedup is in the order of magnitude of two. The speedup for high numbers of cores on the coarse grid is the smallest. It has to be remarked that the wall-clock time for the coarse grid is less than $2\ s$ for the calculations with 4, 8, 16, and 32 cores and the overhead caused by serial processes cannot be determined exactly. Consequently, long computational time for serial processes will affect the results strongly.

Table 17: Ratio of the wall-clock time of the simulation t_{WC} for the diffusion-based mesh-deformation method related to that of the analytical mesh-deformation method for different numbers of cores and grid resolutions.

Number of Cores	Coarse	Medium	Fine
1	117.24	130.53	200.96*
2	112.43	130.71	205.81*
4	93.77	123.85	167.63
8	76.87	114.60	172.86
16	57.11	94.95	174.49
32	53.43	88.37	174.29

In the following, a brief description and a comparison of the parallel performance for both methods are provided. Therefore, two different approaches are presented. On the one hand, the number of cores is kept constant and the size of the problem is increased and on the other hand, the size of the problem is kept constant and the number of cores is increased. Instead of applying the formulation for weak and strong scaling, a simplified approach is used. For the first investigation concerning the variation of the size of the problem, the wall-clock time of the simulation t_{WC} related to the number of cells N_c is calculated for two different grids. Subsequently, the ratio of the quantities for the coarser to the finer grid is evaluated according to

$$PPG = \frac{t_{WC,G1}}{N_{c,G1}} \cdot \left(\frac{t_{WC,G2}}{N_{c,G2}} \right)^{-1}. \tag{5.6}$$

The results for different numbers of cores are shown in Table 18. If the wall-clock time per cell is equal for larger problems, the result of the ratio equals $PPG = 100\%$. Considering the diffusion-based mesh-deformation method, the ratio is less than $PPG < 100\%$ for all calculated points. Consequently, the higher the number of cells, the longer is the required wall-clock time. In addition, almost no influence of the number of cores is visible. For the analytical mesh-deformation method, in contrast, the simulation speedup is in some cases $PPG > 100\%$ or needs approximately the same time $PPG \approx 100\%$. The highest speedup is, in particular, obtained for a large number of cores on a coarse gird. In this case, the boundary cell count ratio is high. By increasing the number of cells, the ratio gets smaller and as a result, less information has to be transferred relatively during one time step. The effect is more pronounced for the analytical mesh-deformation method, since the computational effort for deforming the mesh is low compared to the other tasks to be executed during one time step.

Table 18: PPG for different numbers of cores.

	Diffusion-based mesh-deformation method		Analytical mesh-deformation method	
Number of Cores	Coarse to medium	Medium to fine	Coarse to medium	Medium to fine
1	95%	62%*	106%	96%*
2	96%	62%*	111%	98%*
4	94%	75%	124%	102%
8	94%	72%	140%	108%
16	94%	65%	156%	120%
32	98%	65%	162%	134%

The second investigation deals with the variation of the number of cores. Therefore, the wall-clock time of the simulation t_{WC} related to the number of cores N_{Cores} is calculated for two different numbers of cores. In this case, the ratio of the quantities for the lower to the higher number of cores is evaluated according to

$$PPC = \frac{t_{Cores1}}{N_{Cores1}} \cdot \left(\frac{t_{Cores2}}{N_{Cores2}} \right)^{-1}. \tag{5.7}$$

The results for different numbers of cores are shown in Table 19. If the wall-clock time per core is equal for larger problems, the result of the ratio equals $PPC = 100\%$. The results for this comparison are similar. Nevertheless, the speedup is even slightly higher for some points by the diffusion-based mesh-deformation method, in particular, the coarser the resolution of the grid and the smaller the number of cores. Due to the high computational effort of the diffusion-based mesh-deformation method per time step in contrast to the analytical mesh-deformation method, the influence of the effort for the data transfer is comparably low. Consequently, the resulting speedup for the coarse mesh is higher.

Table 19: PPC for different grid resolutions.

	Diffusion-based mesh-deformation method			Analytical mesh-deformation method		
Cores	Coarse	Medium	Fine	Coarse	Medium	Fine
1 to 2	95%	96%	95%*	91%	96%	98%*
2 to 4	100%	98%	119%*	83%	93%	97%*
4 to 8	81%	81%	77%	66%	75%	80%
8 to 16	64%	64%	58%	47%	53%	59%
16 to 32	49%	51%	51%	46%	47%	51%

6 Results of the Rotorcraft Simulation

Within this chapter, the results of the numerical and experimental investigations of the rotorcraft simulations are presented. At first, the test case description in combination with the experimental setup is provided. At second, the numerical setup is described. The latter includes the blocking strategy, the generation of the mesh, and the description of the application of the invented deforming mesh approach. Lastly, the results and discussion of the test case is presented.

Certain contents of this chapter have been already published by Stuhlpfarrer et al. [5].

6.1 Test Case Description

The investigations are conducted with a 1:5 scale model of a characteristic twin engine light (TEL) utility helicopter as presented in Figure 107. Major parts of the detailed model contain front and main cabin section, backdoor section, upper cowling, mast fairing, 5-bladed rotor head, skid landing gear, tail boom, as well as vertical and horizontal stabilizer. The fuselage parts of the model are manufactured of composite material and are connected to an inner load-bearing frame made of aluminum. The tail boom is made of plastic and the vertical as well as the horizontal stabilizer is milled from an aluminum block. The latter are connected to the inner load-bearing frame also. For connecting the model frame to the model support, a tail sting element located inside of the tail boom and the vertical stabilizer is used. The rotor head features collective and cyclic pitch motion of the blade cuffs governed by a fully functional swash plate in combination with steering rods. The blade cuffs are obtained by truncating the blade at the radial position of the first effective aerodynamic blade section. The model is based on Airbus Helicopters Green Rotorcraft Demonstrator Bluecopter [143]. The key parts are an aerodynamically optimized shape at the backdoor section including contoured strakes, a faired skid landing gear as well as a T-tail. The strakes originated from and adjoint-based optimization method by Zhang et al. [144].

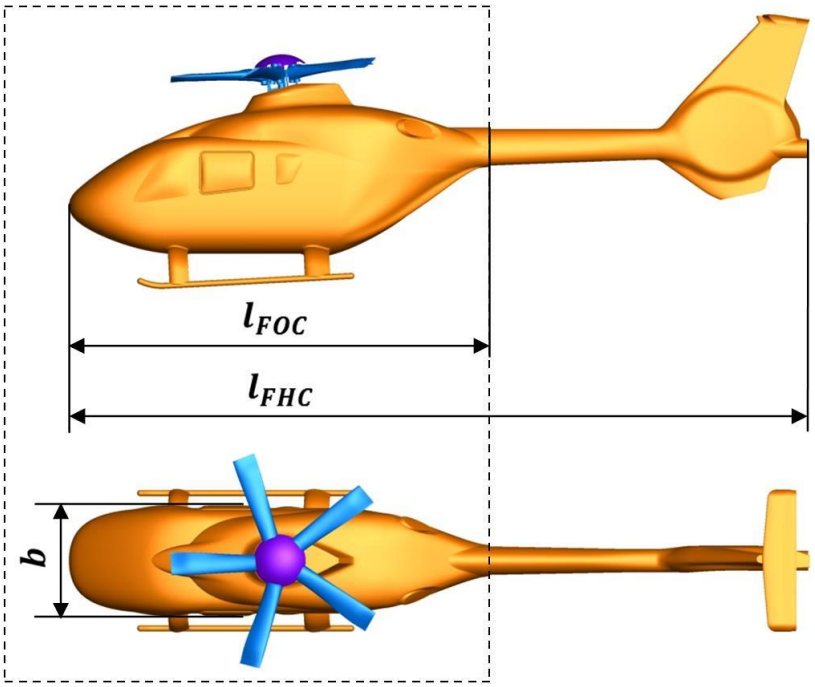

Figure 107: Side and top view of the helicopter configuration. The framed parts are associated to the configuration excluding the tail boom and the empennage.

Basically, investigations for mainly two different setups have been conducted. The first setup contains all above mentioned parts and the second excludes the tail boom and the vertical as well as the horizontal stabilizers. Due to the varying sizes of the models, different mountings are used. Figure 108 (left) presents the full helicopter configuration (FHC) mounted in the test section of the wind tunnel A. The model is sting mounted via the tail sting and a two-armed frame on a six-component underfloor balance. In Figure 108 (right), the configuration excluding the tail and empennage (FOC) is shown. The latter is mounted via a tail sting on a one-armed frame on the six-component underfloor balance. The reason for the different mountings is, on the one hand, the resulting loads and on the other hand, to position of the fuselage in the center of the test section. Both frames are covered aerodynamically in order to prevent an influence of the flow on the measured forces. The underfloor balance, in combination with a second actuator included within the cover of the mounting sting, is used for setting the angle of attack and the angle of sideslip for both setups. The length of the FHC model equals $l_{FHC} = 2.19\ m$ and the fuselage width is $b = 0.33\ m$. The length of the model excluding the tail boom and the empennage (FOC) equals $l_{FOC} = 1.24\ m$. The FOC is applied, in particular, for the presented validation of the numerical results, while the FHC is used to demonstrate the quasi-volumetric particle image velocimetry results.

Figure 108: Wind tunnel configurations. The full model (left) and the model without tail sting-mounted (right) in the wind tunnel is presented.

For the validation of the numerical results, the freestream velocity is set to $U_\infty = 40\ m/s$ and the angular velocity of the rotor equals $\omega = 100.8\ rad/s$ in order to fulfill an advance ratio of $\mu = 0.35$ at ambient pressure and temperature. The freestream Reynolds number of $Re \approx 1 \cdot 10^6$ is based on a characteristic length of the fuselage derived from the model cross section. The angle of attack and the angle of sideslip for the conducted investigations are set to $\alpha = \beta = 0$. The governing law for the pitch motion reads $\theta(\psi) = \theta_0 + \theta_c \cdot \cos(\psi) + \theta_s \cdot \sin(\psi)$, $\theta_0 = 11.5°$, $\theta_c = 2.0°$, $and\ \theta_s = -8.8°$ representing a level flight condition. The azimuthal angle of $\psi = 0°$ corresponds to the back blade, and the angle of $\psi = 90°$ to the advancing blade. The angles are associated to a level flight at maximum takeoff weight and are computed by a flight mechanics code. The governing law for the pitching motion differs slightly for the FHC.

6.2 Measurement Technique and Test Conditions

The experimental investigations have been conducted in the large low speed facility A of the TUM-AER. The force and moment measurements have been performed with a six-component underfloor balance. Details concerning the facility and the measurements of forces and moments can be found in the Appendix A.4. The resulting maximum error for the coefficients within the present investigation is determined to $\Delta C_D = 2.8 \cdot 10^{-3}$, $\Delta C_Y = \Delta C_L = 5.7 \cdot 10^{-3}$, $\Delta C_m = 2.5 \cdot 10^{-3}$, and $\Delta C_l = \Delta C_n = 3.5 \cdot 10^{-3}$.
The determination of the velocities in the wake is conducted with Stereo-PIV. For the generation of the time-averaged wake flow field needed for the validation data, the laser is operating with an averaged double pulse frequency of approximately $12\ Hz$. Therefore, the camera and the recording frequency are equivalent. However, the recoding rate for the phase-averaged measurements is obtained as the least common multiple of the blade passing frequency, the laser frequency, and the camera frequency. For the investigations concerning the validation data, the images are recorded by two sCMOS cameras with a resolution of 2560 x 2160 pixels, resulting in a spatial resolution of approximately $\Delta d \approx 3.5\ mm$ $(\Delta d/b = 0.011)$ [145]. The light sheet thickness is obtained to approximately $3\ mm$.
The size of the measurement windows is chosen in order to capture the whole wake of the rotor head on the upper side and the whole wake of the cabin backdoor section and the skid landing gear on the lower side of the tail boom. The velocity fields are determined by averaging over 400 time-accurate data samples.

In order to proof the independence of the averaged values depending on the number of samples, the difference of the dimensionless root-mean-square (rms) values for the axial velocity between 350 and 400 samples, evaluated for one plane in the wake of the rotor head, are calculated according to $(\mathrm{u}_{\mathrm{rms},400} - \mathrm{u}_{\mathrm{rms},350})/\mathrm{u}_\infty \lessapprox 0.005$. The corresponding relative deviation therefore reads $(\mathrm{u}_{\mathrm{rms},400} - \mathrm{u}_{\mathrm{rms},350})/\mathrm{u}_{\mathrm{rms},400} \lessapprox 0.05$. The maximum error for all velocity components related to the freestream velocity is established to $\Delta u_i/u_\infty \leq 2\%$ [5].

6.3 Numerical Setup

This section provides, at first, the meshing and blocking strategy. Secondly, the application of the mesh-deformation method for this test case is described. Finally, the solver settings are presented.

6.3.1 Meshing and Blocking Strategy

Within this section, a detailed description of the blocking and meshing strategy is presented. Basically, the mesh is subdivided in several domains. This separation is conducted, on the one hand, to simplify the mesh generation by using, for example, periodicities and on the other hand, to realize the relative motion between certain parts of the mesh.

The whole domain for the simulation is divided into three parts that are connected by a sliding mesh interface. The sliding mesh interface allows for a time-accurate solution at nonconformal boundaries. The adjacent cell faces of each part of the mesh are intersected and the mass, momentum, and energy fluxes through each of the resulting faces are determined. The domains are the static domain (SD), the rotating disc domain (DD), and the blade domains (BDs). The static domain contains the

helicopter configuration excluding the rotor head. The rotating disc domain is embedded in the static domain. This domain includes the rotor head related parts as well as the inner parts of the blade cuffs. Furthermore, the blade domains are inserted for providing the cyclic motion of the blade cuffs. The model parts for the simulation are in accordance with the experimental setup. However, although the numerical representation of the rotor head shows simplifications, the important parts are featured. For the mesh generation, the blocking is subdivided additionally. In the following, the individual parts are presented. In general, each part of the mesh is generated block-structured and consists of hexahedral elements exclusively.

Figure 109 (middle) depicts the FOC including the one-armed mounting sting. In Figure 109 (left), the surrounding static domain around the helicopter configuration is shown. The dimensions of the domain are chosen for a negligible influence of the boundary conditions on resulting forces as well as on the wake flow field. For this purpose, the resulting pressure field is checked mainly. Although, the mounting sting is present, the wind-tunnel floor is not. The green highlighted disc in Figure 109 (left) represents the rotating disc domain. Therein, the rotor head including the truncated rotor blades is located. As mentioned above, the DD embeds the BDs to allow for the pitching motion of the blades. Before describing the domains, in Figure 109 (right) the rotor head with the truncated rotor blades is shown in detail. The rotor head consists of the rotor mast, hubcap, scissors, damper, steering rods, and the swash plate. Due the high complexity of the detailed geometrical representation of the rotor head, the latter is divided into several mesh parts that are connected by non-conformal interfaces. As far as possible, periodicity is used for the mesh generation and the resulting mesh is copied and rotated. That is why the DD is divided in the upper rotor head and hubcap domain (URHD), the lower rotor head domain (LRHD), and in disc segment domains (DSs). The periodicity is applicable for the URHD and the DD. The LRHD has to be meshed without applying periodicity due to the two-armed scissors.

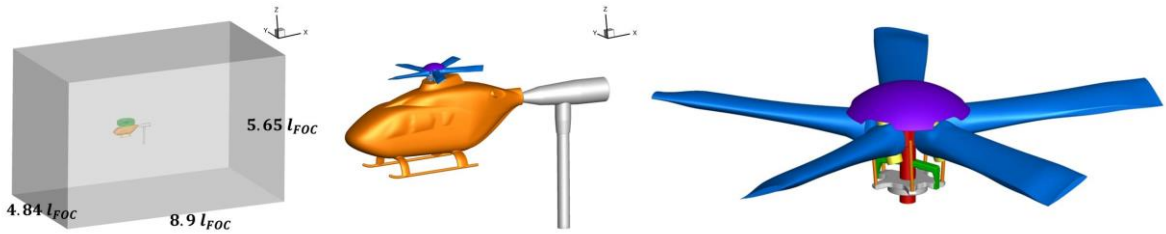

Figure 109: Helicopter configuration without the empennage mounted on the one-armed mounting sting (middle) is presented. Gray highlighted stationary domain with the green highlighted embedded disc domain is depicted (left). Rotor head with truncated rotor blades is exhibited (right).

Figure 110 (left) exhibits the blocking of the LRHD. The related parts to this domain are the swash plate, the lower part of the mast and the steering rods, and the scissors. It is clearly visible that no periodicity can be used for this domain. The domain performs a rotation only. In Figure 110 (right), the blocking of the URHD is presented. The domain includes the hubcap, the upper part of the mast and the steering rods, the dampers, the inner part of the blade, and a simplified connection of the blade and the mast. Obviously, periodicity can be considered for this domain. For the mesh in this domain, the deforming mesh method is applied. The truncated rotor blades and the dampers fulfill the cyclic pitch motion in combination with a rotation of the rotor head, while the remaining parts of the domain are performing a rotation only. Consequently, a relative motion occurs. However, due to the small space between the different parts, the sliding mesh approach does not work. For the latter, it is not possible to include the required interface surface without intersecting the geometry. The

deforming mesh method handles the motion of the boundaries as well as the motion of the nodes of the mesh.

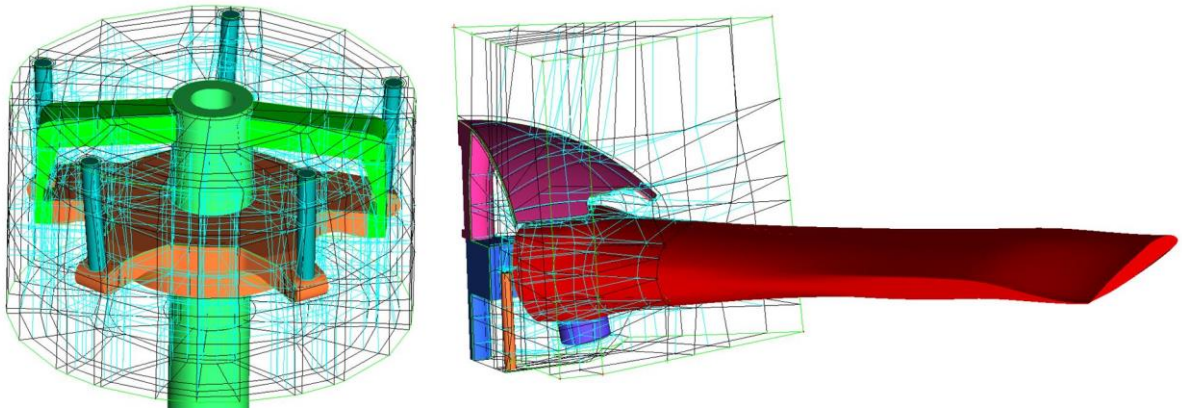

Figure 110: Blocking of the lower rotor head domain including the swash plate, the mast and the scissors and lower parts of the steering rods (left) and blocking of the upper rotor head domain (right). [5]

In Figure 111 (left), the blocking of one BD is shown. Since the blade is considered to be rigid in the present case, solely a rotation depending on the prescribed cyclic pitch angle relative to the rotor head is required. There is enough space for the application of the sliding mesh approach. Figure 111 (right) depicts the blocking of one DS as well as the embedded BD. The DS domain is designed by the inclusion of the periodicity. Finally, the LRHD, URHD, and DS are taken to build the DD. Therefore, the URDH and the DS are copied and rotated four times and connected with the LRHD. The connection of the aforementioned domains is realized by nonconformal interfaces, but without allowing for a relative motion between the domains. However, a one-to-one connection of the nodes is established if possible. The BDs are copied and rotated four times also, but the connection between the BDs and the DD is established by a sliding mesh interface to enable the cyclic pitch motion. In particular, this concerns also the interfaces of the BDs with the DSs as well as with the URHD. The presented approach captures the cyclic and the collective pitch motion of the blade. Furthermore, the motion of the steering rods and the swash plate could be realized also. Nevertheless, in the course of this investigation, the swash plate is not inclined and the scissors and the steering rods perform a rotational motion only.

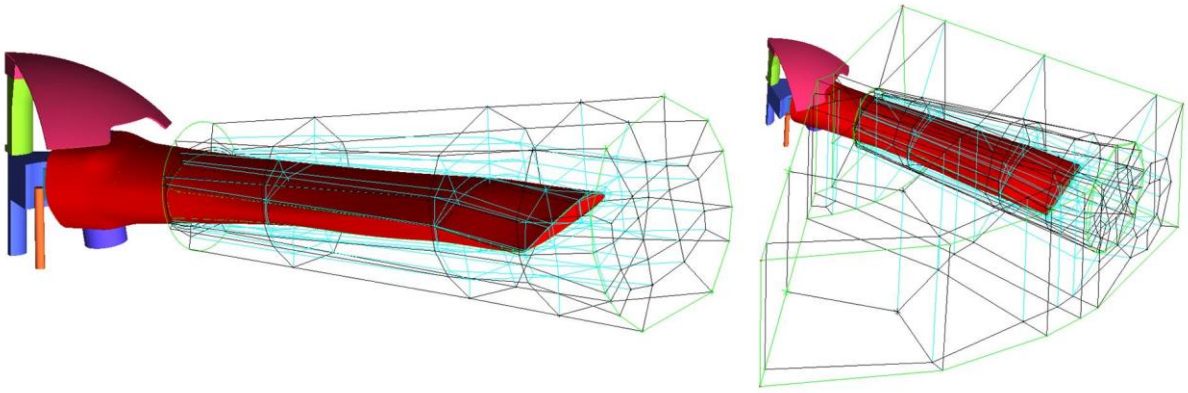

Figure 111: Blocking of one blade domain (left) and blocking of the disk segment domain with the embedded blade domain (right) [5].

After describing the structure of the blocking, the important parameters for the generation of the mesh are presented. In general, the values for the dimensionless wall distance of the first cell are set to approximately $y^+ = 1$ for each no-slip wall in all domains in order to resolve the velocity gradient at the wall appropriately and to avoid the application of a wall function. Concerning the settings of the cell sizes at the interfaces, the ratio of the lengths of the cells at both sides of the interface is set to approximately one. Ratios of approximately one can significantly reduce the numerical error at the interface and suppress the generation of non-physical wiggles. For the determination of the cell sizes in the wake region, the estimated turbulence length scale obtained from previous simulation runs is taken into account. The mesh in the symmetry plane of the helicopter plane is presented in Figure 112.

In Figure 113 (left), the whole mesh of the rotor heads is presented. A detailed view of the mesh of the rotor head is exhibited in Figure 113 (right). Therein, the structure due to the application of the periodicity is well visible. Caused by the complexity of the geometry, the cell growth ratios are high or even show peaks in some region. Nonetheless, these growth ratios do not lead to problems concerning the stability of the simulation run.

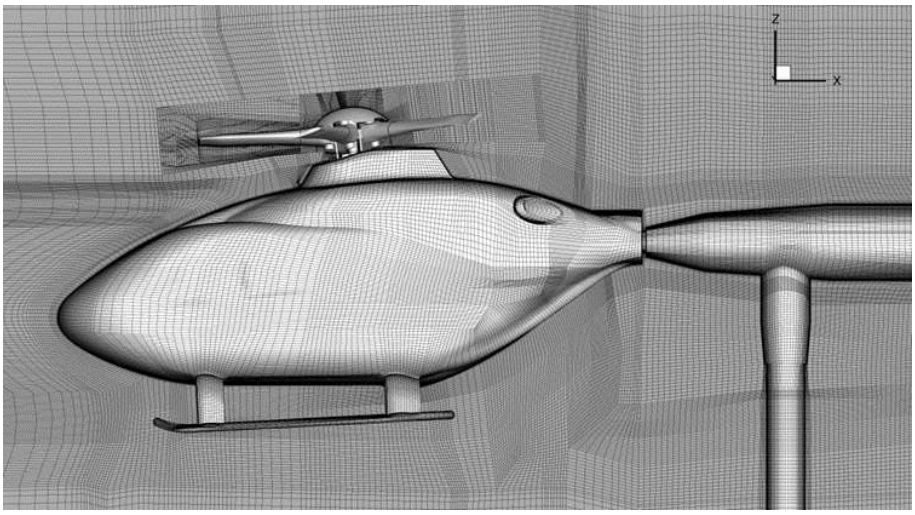

Figure 112: Mesh in the symmetry plane of the helicopter configuration excluding the empennage, but with included mounting sting.

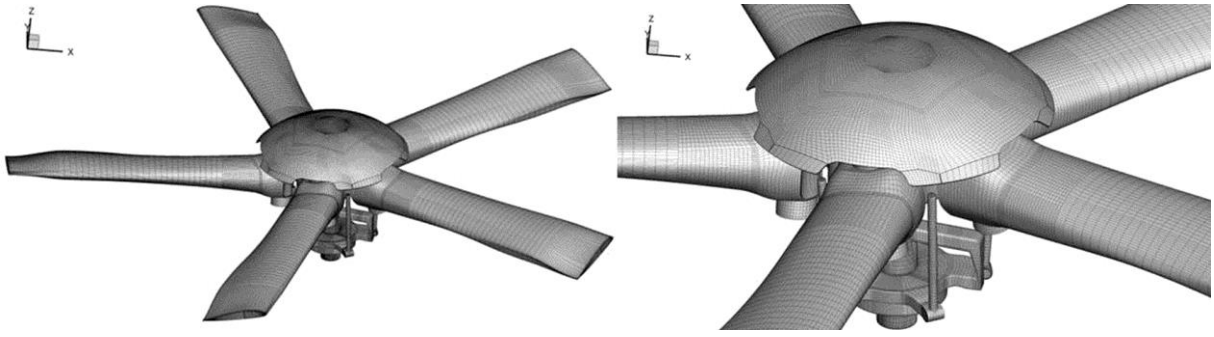

Figure 113: Surface mesh of the rotor head. The rotor head includes rotor mast, hubcap, scissors, damper, steering rods, and swash plate. The global view of the whole rotor head (left) and a detailed view of the rotor head (right) is shown.

The quality of the mesh is assessed by the representative determinants and the angles. In this context, the determinant refers to the ratio of the smallest determinant divided by the largest determinant of the Jacobian matrix evaluated for each cell. The minimum obtained value for all applied meshes within the whole computational domain is greater than 0.25. The angle designates the minimum internal angle for a cell. The angles are greater than 14 degrees for all applied meshes within the whole computational domain.

6.3.2 Application of the Mesh-Deformation Method

As presented in the previous section, the sliding mesh approach is used if possible. However, due to the small space between the different parts with relative motion in the URHD, a deforming mesh approach has to be applied. Therefore, the diffusion-based mesh-deformation method provided by ANSYS Fluent has been tested initially. A similar rotor head configuration has been successfully investigated with the comparable method of the flow solver ANSYS CFX by Grawunder et al. [6]. However, within these investigations some drawbacks were identified and procedures, like reloading the mesh after some time steps, had to be invented to obtain at least convergence. As stated in the previous chapter, the diffusion equation is a partial differential equation and requires a system of equations to be solved. For an unsteady case, it is has to be solved within each time step. Although the method allows for the application of an iterative solver and parallelization, the computational wall-clock times for deforming the mesh, within the present application, are even higher than for solving the flow equations for one time step. Furthermore, the convergence for calculating the mesh deformation in a parallel simulation depends strongly on the number of partitions as well as on the type of partitioning. In the worst case, the simulations are diverging for the present case. In order to avoid such issues, the analytical mesh-deformation is used for this investigation. The resulting speedup for the analytical mesh-deformation method is established up to an order of magnitude of two within this test case. The speedup is comparable as for the simple test case presented in section 5.3.

The method is applied for the URHD only. At first, several azimuthal divisions of the domain are obtained by the application of one analytical constraint. Therefore, the whole URHD is divided in five sectors by one analytical function. The green highlighted isosurface, representing the boundary of one sector to its neighboring sectors, is presented in Figure 114. In Figure 114 (left), the top view and in Figure 114 (right) the view along the blade in direction to the rotor head is shown. Each of these sectors contains one blade and allows for governing each blade pitch angle independently. The first described deforming function handles the mesh-deformation around each blade. Since the blade fulfills a cyclic, rotational motion, an inner radius r_{in} and an outer radius r_{out} are required for the deformation function. The mesh deformation is based on the angle $\theta_{def}(\psi, \dots) = F_{def}(\dots) \cdot \theta(\psi)$. Due to the complexity of the geometry of the rotor head, constant values for the radii cannot be applied. The space around a certain blade is limited by the surrounding blades as well as by the steering rod, the hubcap, and the mast. For the presented test case, 6 blade sections located along the spanwise direction of the blade y_{bl} are generated within the URHD. For each of the sections, the inner and the outer radius of a blade section, $r_{BS,in}(\phi_{BS})$ and $r_{BS,out}(\phi_{BS})$, respectively, are varied depending on the local circumferential direction ϕ_{BS}. Therefore, piecewise-defined curves are used to define the shape. Between the spanwise sections, a linear interpolation of the boundary radii is conducted. The second function handles the boundary of the deforming region at the inner part of

the blade. The function is solely depending on the spanwise position along the blade y_{bl}. The final deformation function is a result of the multiplication of the two deformation functions.

$$F_{def}(r_{BS}, \phi_{BS}, y_{bl}) = F_{\mathrm{def}\,1}(r_{BS}, \phi_{BS}, y_{bl}) \cdot F_{\mathrm{def}\,2}(y_{bl}) \tag{6.1}$$

In Figure 114, the resulting deforming regions are exhibited by two isosurfaces of the deformation function. The blue highlighted isosurface provides a value of the deformation function of $F_{def} = 0.01$ and the red highlighted isosurface of $F_{def} = 0.99$. The values are chosen instead of $F_{def} = 0.0$ and $F_{def} = 1.0$ to enable the depiction of the surface. The nodes outside of the blue highlighted isosurface are not moved cyclically, whereas the nodes inside the red highlighted isosurface are rotated with the blade. Consequently, the mesh of the boundary layer is not modified and subsequently, the quality of the mesh remains as is. The deforming law is applied for the mesh regions within the two isosurfaces.

Within this investigation, tests with an additional deformation function are performed. The idea is to generate a second deformation function that is superposed and allows for a movement of the nodes located between the blades and the interface between the URHD and the LRHD. The isosurfaces for $F_{defxp} = 0.01$ and $F_{defxp} = 0.99$ are presented in Figure 115 (left). This function enables a motion of the nodes at the grey interface in accordance with the circumferential component of the rotation of the blade. The function can be applied if the required pitch angles are large. For the present investigations the function is set to $F_{defxp} = 0.0$. In Figure 115 (right), the mesh at the interface between the URHD and the adjacent domains, the DD and the BD is depicted. The mesh is shown for a pitch angle close to the maximum. It is visible, that the quality of the mesh remains high.

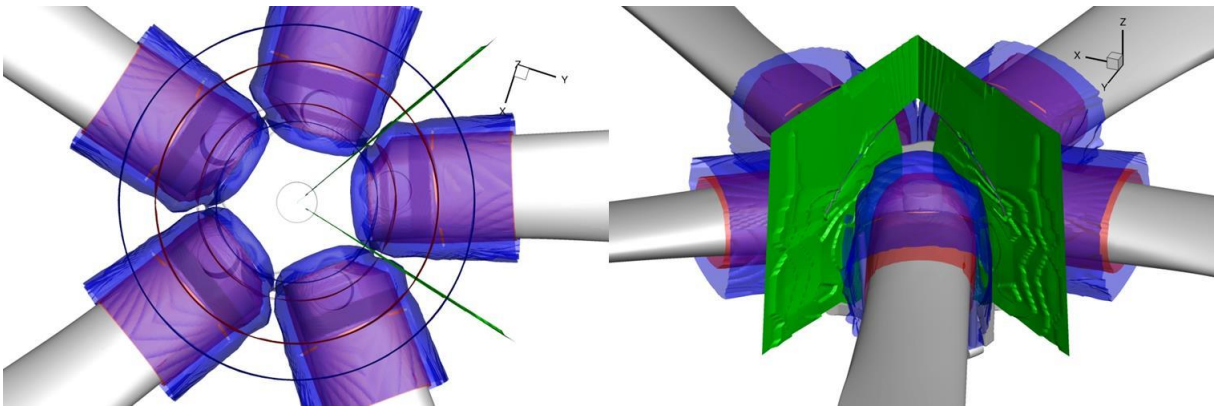

Figure 114: Definition of the deforming regions. Top view of the rotor (left) and view along the blade in direction of the rotor head (right) is presented. The isosurfaces covering the blades represent a deformation function of $F_{def} = 0.01$ (blue highlighted) and $F_{def} = 0.99$ (red highlighted). A sector, associated to a blade, is divided by the green highlighted isosurface.

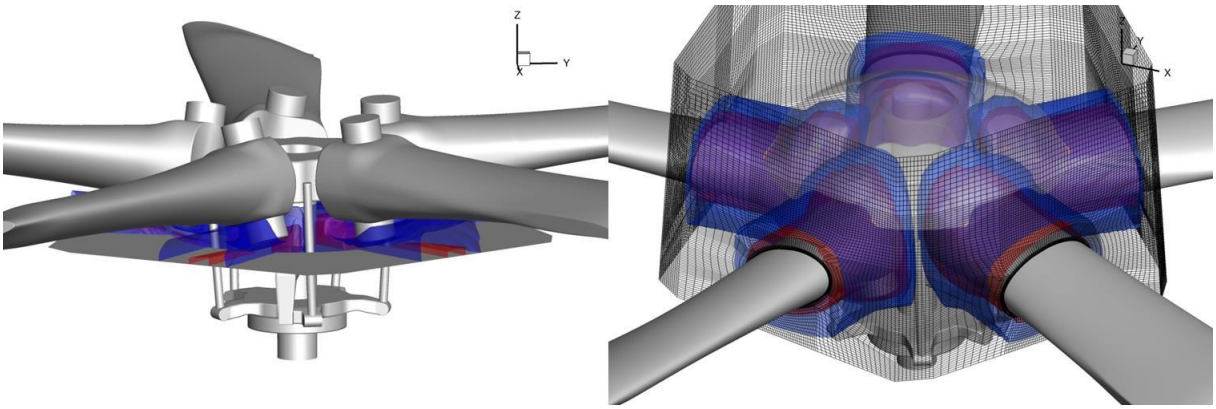

Figure 115: Additional deforming region (left) and actually used deforming region including the mesh (right) is shown. The isosurfaces of the additional deformation function of $F_{defxp} = 0.01$ (blue highlighted) and $F_{defxp} = 0.99$ (red highlighted) are presented (left).

The definition of the boundaries for the deforming domain is set manually within this investigation. Nevertheless, the boundaries can be determined by an automatic detection of the boundaries as well.

6.3.3 Solver Settings and Independency Studies

For the numerical simulations, the URANS equations are solved with the commercial flow solver ANSYS Fluent. Caused by a Mach number of $Ma < 0.3$ in the whole domain, the incompressible formulation of the governing flow equations is applied. Consequently, the pressure-based solver is chosen. During the simulation, the pressure-velocity coupling is treated by the application of the coupled or the SIMPLE algorithm. The absolute velocity formulation is chosen for all domains. A bounded second-order central difference scheme for the spatial discretization of the momentum equations is chosen in order to reduce the numerical dissipation. The boundedness of the solution is ensured by a local blending to a first-order upwind scheme. Moreover, spurious oscillations can be avoided. The standard pressure interpolation scheme of Fluent that takes into account the momentum equation coefficients is applied. The transport equations for the turbulent kinetic energy and the turbulence eddy frequency are discretized by a first-order upwind scheme. The modeling of turbulence is realized by the SAS model [146, 147] and the flow is assumed to be fully turbulent. The model is able to act as a statistical turbulence model in stable flow regions (e.g., boundary layers) and provides LES capabilities in unsteady flow regions (e.g., wake-flow region). The terms stable and unstable are in accordance with the publications. The method allows for resolving the turbulent structures comparable to a detached-eddy simulation. However, a dynamic adjustment of the turbulent length scale is used instead of an explicit dependence on the local mesh resolution. [146]. As a side note, the model is based on the SST model. An additional source term is added to the ω-equation for avoiding an overprediction of the turbulence eddy viscosity in regions of highly unsteady flow regimes.

The assumption of a fully-turbulent simulation is justified by the work of Grawunder et al. [148] for a comparable configuration. It was shown that the laminar-turbulent transition takes place at the front cabin section and consequently, the length of the boundary layer being laminar is small compared to that of being turbulent.

A comparison of the SST and the SAS model is provided by Stuhlpfarrer et al. in [145, 149]. In particular, the influence of the turbulence model on the separation of the flow at the backdoor section was detailed in [149]. The outcome is that the choice of the turbulence model is crucial.

While the SAS model leads to a symmetric region of separated flow, the results with the SST model show an asymmetric one. Moreover, the region of separated flow is predicted larger by the latter. The comparison of the numerical results with the experimental data obtained by PIV in several crossflow planes downstream of the cabin backdoor section was provided by Stuhlpfarrer et al. [150, 151, 152]. Due to the good agreement of the results generated by the SAS model, the latter is applied.

For the time-accurate solution, a two-step solution scheme is applied. At first, a steady state simulation with a fixed rotor head is performed to generate a developed flow field around the helicopter that features the turbulence decay appropriately also. In this step, the azimuthal angle of the rotor head is set to $\psi = 0°$ and the pitch angles of the blade cuffs are set in accordance to the steering law. The rotor head and the blade cuffs are meshed for one certain collective pitch angle, caused by the copying and rotating of the parts of the mesh during the mesh generation. Consequently, the cyclic pitch angle has to be adjusted to fulfill the steering law prior to the first time step. For the steady state solution, the coupled solver is applied. The latter calculates the flow quantities (u, v, w, p) in one coupled system of equations. The Courant number is set to $C = 5$ and the explicit-relaxation factors for the pressure and the momentum are set to $\alpha_p = \alpha_{mom} = 0.5$. The small values are necessary to obtain convergence for the complex geometry. The under-relaxation factors for the turbulent kinetic energy and specific dissipation rate are set to $\alpha_{tke} = \alpha_\omega = 0.8$. Following, the unsteady simulation with rotor head motion is performed. In order to reduce the numerical dissipation, a temporal second-order implicit scheme is chosen. The time-step size is set to obtain an incompressible Courant number of $\mathrm{C} < 1$ in the wake flow field [146, 147, 112]. For this case, a rotation of one degree azimuthal angle of the rotor head per time step is chosen. In order to speed up the simulation, for the unsteady part the SIMPLE algorithm is chosen. The under-relaxation factors for the pressure and the momentum are set to $\alpha_p = 0.1$ and $\alpha_{mom} = 0.6$, respectively. The under-relaxation factors for the turbulent kinetic energy and the specific dissipation rate are set to $\alpha_{tke} = \alpha_\omega = 0.4$. In order to obtain convergence within a time step, approximately 10 iterations are necessary. The fluid properties for the numerical simulations are set to a density of $\rho = 1.225\ kg/m^3$ and a molecular viscosity of $\mu = 1.7894 \cdot 10^{-5} kg/ms$. The boundary conditions are set in accordance to the experimental setup. The velocity at the inlet equals $u_{in} = U_\infty = 40\ m/s$ and the static pressure is set to $p_{in} = p_{amb} = 101325\ Pa$. At the outlet, as well as on the remaining boundaries of the calculation box, the pressure is set to $p = p_{amb}$. All physical surfaces are modeled with a no-slip boundary condition. The turbulence quantities at the inlet are determined by considering the turbulence decay in order to obtain comparable turbulence quantities at the model as in the wind-tunnel test. If backflow into the domain occurs locally at a pressure-based boundary condition, the direction of the inflow is established by the flow direction of its neighboring cell inside the domain.

Concerning the sensitivity of the grid resolution and the time-step size on the solution, both a mesh-independency study and a time-step-size independency study are conducted. The mesh-independency study is based on a medium mesh of 21.4 million cells. Basically, one coarsening and one refinement step with a factor of $1/1.2$ as well as 1.2, respectively, is executed. The mounting sting is included in the simulation, while the forces on the latter are not considered. As a side note, the author showed with a simulation applying the SAS model that the influence of the mounting sting on the flow at the cabin backdoor section is small [149]. Moreover, the cyclic pitch motion is not enabled. 13 rotor-head revolutions are simulated for the study and the time-averaged drag coefficients over the last two rotor-head revolutions are taken for the comparison. The coefficients

are considered to be converged, since the deviation in the coefficients between the 10th and the 13th revolution is less than 0.7%. The resulting drag coefficients read for the coarse mesh $C_D = 0.1952$, for the medium mesh $C_D = 0.1952$, and for the fine mesh $C_D = 0.1993$. The maximum relative deviation of the coefficients related to that of the finest grid is $\left|\Delta c_{D,rel}\right| < 2.1\%$. Although the relative deviation of the coefficients is acceptable, the biggest change is obtained from the medium to the fine grid. In order to ensure the result, an extra fine mesh with 66.7 million cells is generated that provides a drag coefficient of $C_D = 0.1995$. Consequently, the resulting relative deviation between all coefficients related to that of the finest grid reads $\left|\Delta C_{D,rel}\right| < 2.1\%$ and the medium grid is applied. As a side note, the obtained trend of the drag coefficient depending on the mesh resolution is caused by a counteracting behavior of different parts of the helicopter. A quantification of the contribution of the different parts of the helicopter to the overall trend is presented in [5]. For the time-step-size independency study, three different time-step sizes are chosen. The initial time-step size is $1°$ azimuthal rotor-head angle per time step. The larger time-step size equals $2°$ and the smaller $0.5°$ azimuthal rotor-head angle per time step. The drag coefficients read for the largest time-step size $C_D = 0.1927$, for the medium time-step size $C_D = 0.1952$, and smallest time-step size $C_D = 0.1951$. The maximum relative deviation between the largest and the smallest time-step size is $\left|\mathrm{C}_{D,rel}\right| < 1.3\%$. For the investigation, the time-step size is set to $1°$ azimuthal rotor-head angle per time step. In the following, a brief discussion of the choice of the mesh resolution and the time-step size and, in particular, of the connection of both is presented. The time-step size appears larger than in other works published, e.g. [128]. However, the mesh resolution is coarser also. As stated above, a Courant number of approximately one is set in the wake of the helicopter. Regarding the linear advection equation on an equidistant grid, the leading dispersive error term of the temporal and spatial discretization schemes is comparable for this Courant number. In this case, the dissipative error is caused by the temporal discretization scheme. It is a matter of fact that smaller time-step size leads to reduced numerical dissipation for this scheme also. However, since the focus is set in the course of this investigation on the near-wake flow field and verifying the applicability of the mesh-deformation approach, the time-step size is appropriate. For more detailed investigations of the far field downstream of the helicopter and the interaction with the tail, the mesh has to be refined and the time-step size has to be reduced, accordingly. Moreover, higher-order discretization schemes are beneficial to conserve the coherent vortical structures appropriately. As shown by Kowarsch et al. [153], for example, for a rotor-fuselage interaction, a fifth-order weighted essentially nonoscillatory discretization scheme (WENO5) is applied. This scheme reduces the dispersive error significantly compared to a second-order central difference scheme while applying dissipation only for high wave numbers.

6.4 Results and Analysis

In this section, the results of the experimental and numerical investigations are presented and compared. Firstly, the force and moment coefficients are discussed briefly and secondly, a detailed description of the flow field is presented. The investigations therefore are conducted for the FOC. Finally, numerical results as well as the quasi-volumetric PIV results are presented for the FHC.

6.4.1 Validation and Flow Field Description

The validation of the forces and moments is conducted with the time-averaged quantities of the numerical results and the wind-tunnel data for the FOC. In contrast to the mesh independency study, the cyclic pitch motion is included. In Table 20, the experimentally and numerically obtained coefficients for the six degrees of freedom are presented. The drag coefficient measured in the wind-tunnel experiment reads $C_D = 0.1827$ while the numerical result gives $C_D = 0.2020$. The obtained relative deviation is $\Delta C_{D,rel} \approx 10\%$ and is stated to agree reasonable according to other publications as reviewed by Reich et al. [124]. It is has to be remarked that if the cyclic motion of the rotor head is enabled, the resulting drag coefficient predicted by the numerical simulation is less by approximately $\Delta C_{D,rel} \approx -6.4\%$ related to the solely collective pitch motion. Considering the lift and the side-force coefficient, the magnitude of the values is very small related to that of the drag coefficient. Subsequently, the relative deviations are large. However, the absolute deviations are in the same order of magnitude as for the drag coefficient. Concerning the moment coefficients, the relative deviation shows a good agreement between the experimental data and the numerical results. The relative deviation of the coefficients reads $\Delta C_{m,rel} = -6.2\%$ for the pitching moment, $\Delta C_{l,rel} = -14.6\%$, for the rolling moment, and $\Delta C_{n,rel} = -9.1\%$ for the moment of yaw.

Table 20: Force and moment coefficients obtained by the wind-tunnel experiment and the numerical simulation according to Stuhlpfarrer et al. [5].

	C_D	C_L	C_Y	C_l	C_m	C_n
Experiment	0.1827	−0.0459	0.0083	−0.0206	−0.0484	−0.0022
Simulation	0.2020	−0.0162	−0.0360	−0.0176	−0.0454	−0.0020

In the following, the detailed description of the flow field as well as a validation of the numerical results with the experimental data for certain crossflow planes is provided. At the beginning, the occurring flow structures are presented and designated in Figure 116. The latter shows crossflow slice planes of the time-averaged velocity magnitude colored in the range of $1.5 \leq \frac{\overline{|\omega|} \cdot l_{ref}}{U_\infty} \leq 19.5$ and cut off at the limits. The flow structures related to the lower side of the helicopter are the forward skid landing gear wake at the side (FLWS), the forward skid landing gear wake at the bottom (FLWB), the wake of the skid landing gear (WSLG), the wake region between the strakes (WBS), and the wake downstream of each strake (WDS). The flow structures associated to the upper side of the helicopter are the blade tip vortices of the truncated blades (BTV), the mast fairing vortex pair (MFVP), and the hubcap vortex pair (HCVP). In general, the flow structures are designated in association to the part of its origin. The structure at the side of the helicopter, initiated by the visible edge, is not discussed.

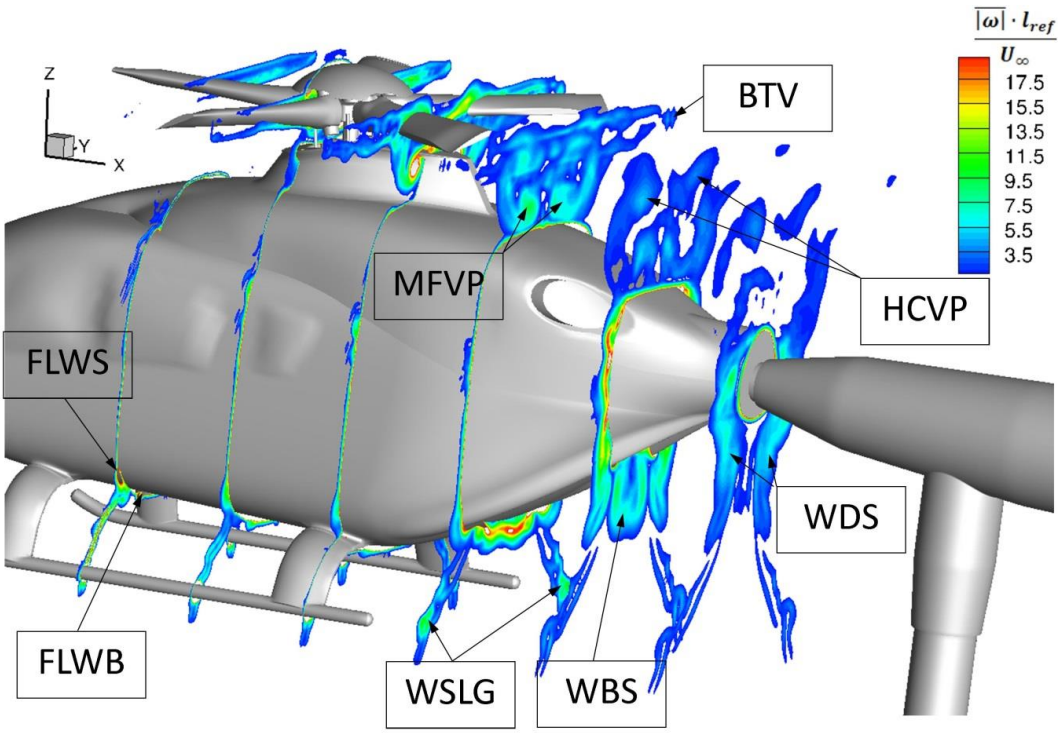

Figure 116: Crossflow planes colored by the time-averaged vorticity magnitude in order to determine the dominant flow structures [5]; $Re \approx 1 \cdot 10^6$, $\alpha = \beta = 0°$.

Concerning the topology of the flow at the lower side of the helicopter, the skid landing gear has a crucial influence. Initially, the shape of the forward bar of the skid landing gear governs the position of the separation as well as the size of the region of separated flow WBS. A small region of separated flow at the forward skid landing gear, resulting in the FLWB, is the origin for the separation between the strakes WBS. This issue was addressed in [149] and is reviewed later in this section. Moreover, the wake region WDS has its origin also at the forward bar of the skid landing gear. The connection of the bar with the cabin side causes a region of separated flow, resulting in the FLWS, which leads to the wake region WDS.
The dominating structures on the upper side of the helicopter are mainly the MFVP and the HCVP. Due to the averaging, the strength of the BTV is less compared to the aforementioned ones, since the vortices obviously are varying its position during one revolution. However, the BTV vorticity magnitude of the retreating blade (in forward flight on the left hand side) is less compared to that of the advancing side.

In the following, the validation of the numerical results with the experimental data is provided. Therefore, the representation of the flow field at six planes located in the wake of the helicopter is considered. Three planes are located downstream of the backdoor section and further three planes downstream of the rotor head as schematically depicted in Figure 117.

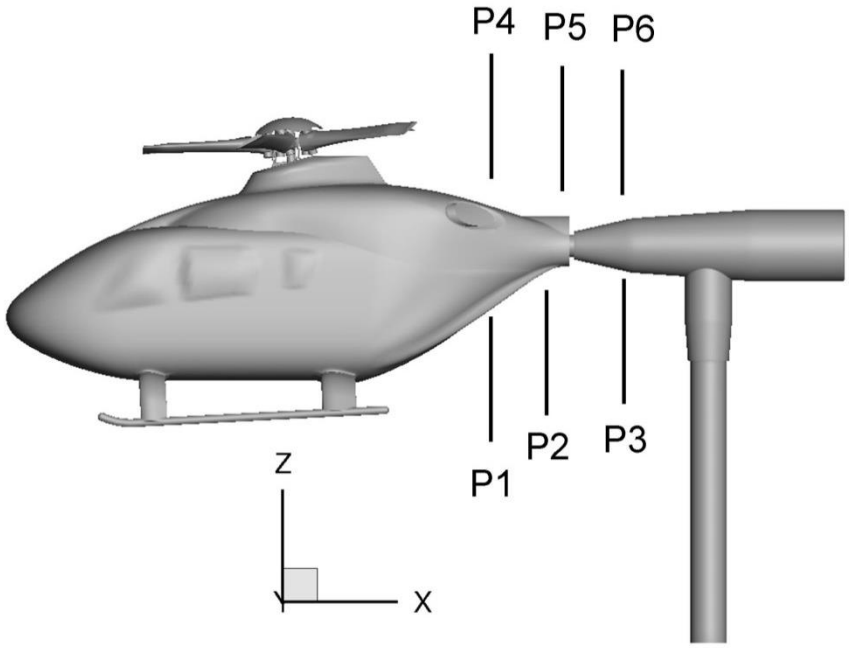

Figure 117: Definition of the crossflow planes. [5]

For the planes P1, P2, and P3, the normalized time-averaged axial velocity component is discussed and depicted in Figure 118. The discussion of the vertical velocity is referred to [5]. Figure 118 a), c), and e) depicts the experimental data while b), d), and f) show the results of the numerical simulation. Figure 118 a) and b) refer to P1, c) and d) to P2, and e) and f) to P3. Considering P1, the wake of the skid landing gear (WSLG) is provided by the experimental data as well as by the numerical solution as presented in Figure 118 a) and b). However, the magnitude of the velocity deficit is predicted higher by the numerical simulation. Furthermore, the region with the velocity deficit between the strakes at the aft body (WBS) is observed. The numerical simulation predicts the size of the velocity deficit region larger as well as the magnitude of the velocity deficit higher. Moreover, the region with velocity deficit downstream of each strake (WDS) is identified in the experimental data and the numerical result. The size of the region as well as the magnitude of the velocity deficit is more pronounced in the results of the numerical simulation. The WDS merges with the WSLG. In general, the numerical simulation provides the sizes of the regions larger and the associated magnitudes of the velocity deficits higher for P1. In Figure 118 c) and d), the same quantity is depicted at the further downstream positioned plane P2. The wake flow of the skid landing gear (WSLG) agrees well between the numerical results and the experimental data. The size and shape of the region of velocity deficit between the strakes (WBS) is provided similar by the experimental data and the numerical solution. However, the result of the numerical simulation provides a higher magnitude of the velocity deficit. The region of the velocity deficit downstream of each strake (WDS) is provided larger and with a higher magnitude of the velocity deficit by the numerical simulation. In accordance to the results of P1, the numerical simulation predicts the structures for P2 more pronounced than in the experiment. Figure 118 e) and f) depict the same quantity for P3. The wake of the skid landing gear (WSLG) is represented by the experimental data and the numerical results, but the magnitude of the velocity deficit is predicted higher by the numerical simulation. The region of the velocity deficit between the strakes (WBS) and the region of retarded velocity downstream of each strake (WDS) are predicted larger by the numerical simulation in contrast to the experimental data. Furthermore, the magnitude of the velocity deficit is predicted higher for the numerical results. For P3, the results of

the numerical simulation shows the structures more pronounced than the experimental data. In general, a higher velocity deficit in the wake is associated with a higher drag. Reconsidering the comparison of the drag coefficients, the relative deviation of the drag coefficient obtained by the numerical simulation related to that of the experimental data reads approximately $\Delta C_{D,rel} \approx 10\%$. Conclusively, the higher drag predicted by the numerical simulation can be declared.

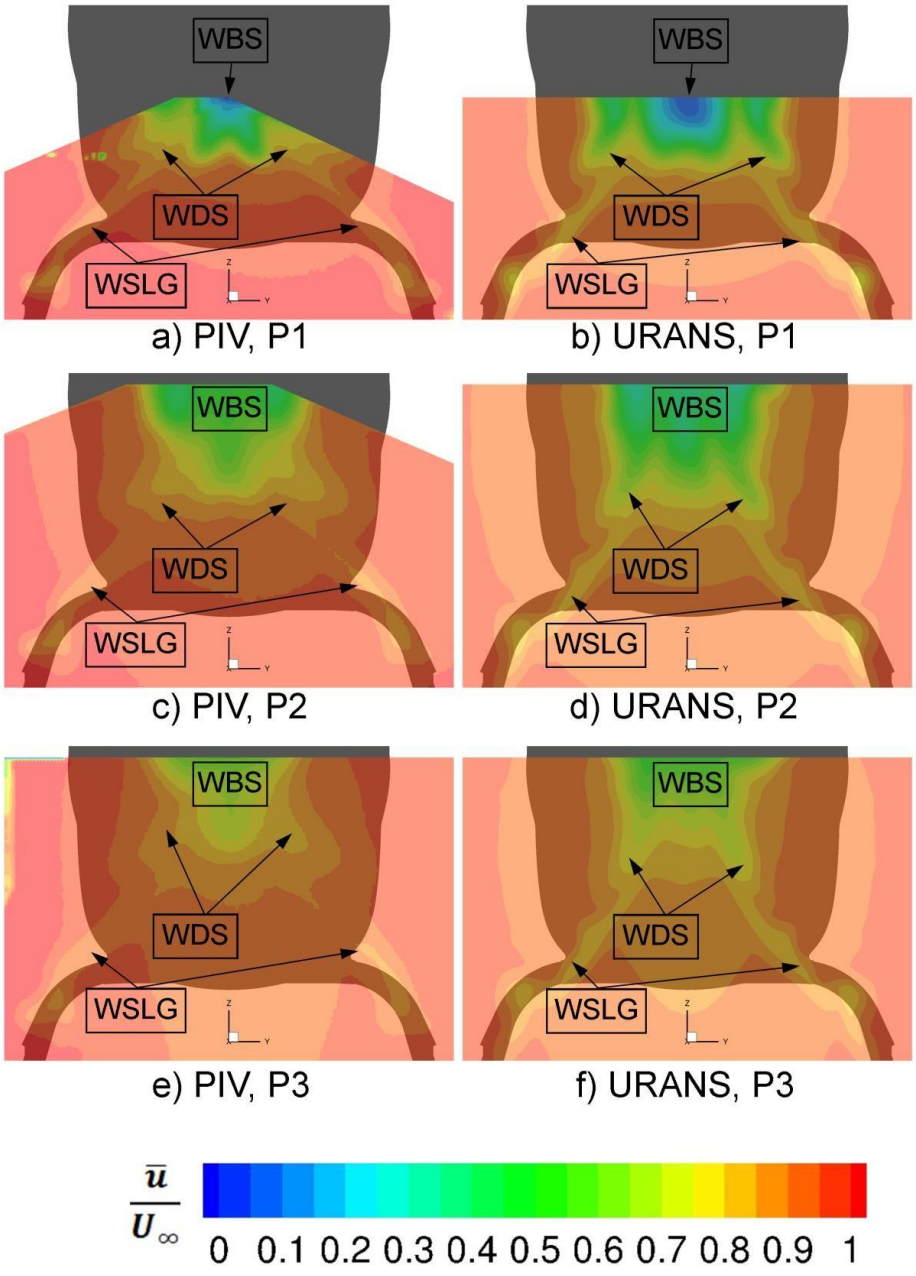

Figure 118: Normalized time-averaged axial velocity distribution for the crossflow planes P1, P2, and P3 in the wake flow of the backdoor section is shown [5]; $Re \approx 1 \cdot 10^6$, $\alpha = \beta = 0°$.

In the following, the review concerning the origin of the flow separation is described. Therefore, the flow at the bottom of the fuselage is analyzed in accordance to [149]. In Figure 119, the time-averaged surface streamlines at the bottom of the fuselage obtained by a numerical simulation with the SAS model are shown. In addition, slice planes of the time-averaged axial velocity colored and cut of by $0 \leq \frac{\overline{u}}{U_\infty} \leq 0.9$ as well as the isosurface of the quantity for $\frac{\overline{u}}{U_\infty} = 0$ are depicted. At first, the flow around the forward bar of the skid landing gear is considered. At the intersection of the fuselage and

the skid landing gear a separation of the flow occurs that is related to the FLWS. Moreover, a region of separated flow is detectable at the bottom of the fuselage that is caused by the curvature of the geometry. Both structures are of vortical flow type and provide a velocity deficit downstream of the separation. However, the structure at the bottom is less pronounced. Considering the surface streamlines, in particular at the bottom of the fuselage downstream of the forward bar of the skid landing gear, regions of convergence and divergence of the surface streamlines are visible. In the region of convergence, the boundary layer thickness is increased. Tracing the inwards located structure downstream, the influence on the separation at the cabin backdoor section is visible. The increased boundary layer thickness triggers the onset of the separation. The FLWS interacts with the backward bar of the skid landing gear as well. The resultant increase of the boundary layer thickness downstream of the backward bar leads to the WDS. The converging surface streamlines are detectable in this region also.

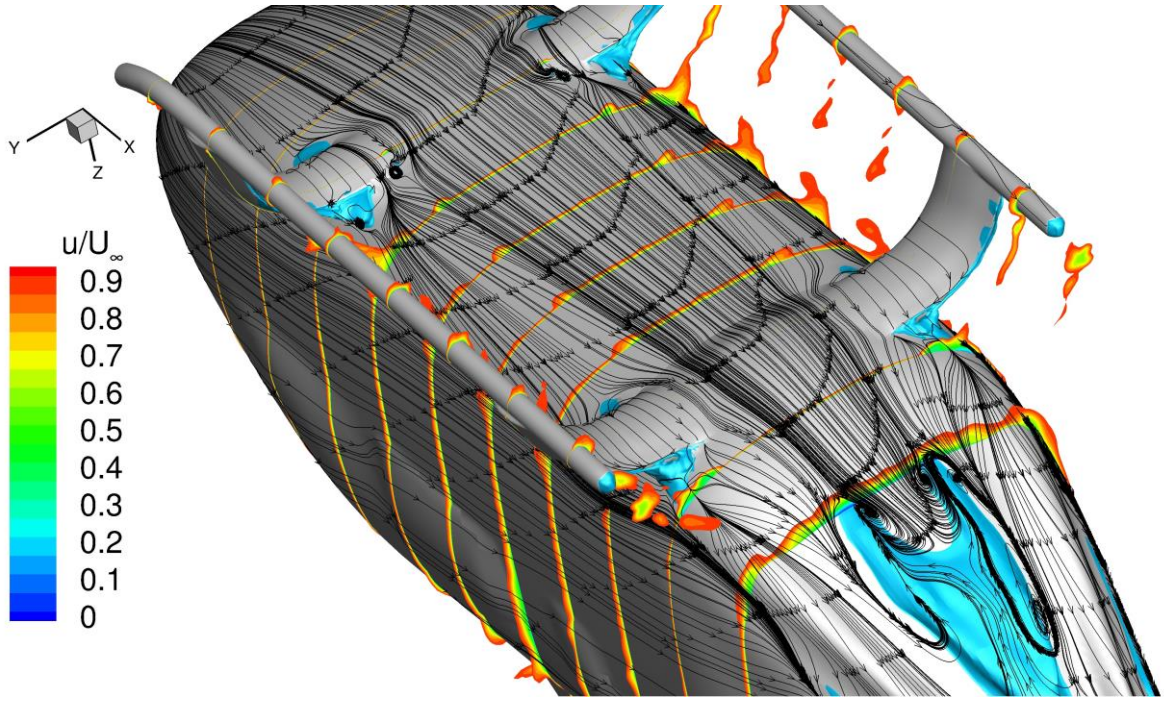

Figure 119: Surface streamlines obtained by a simulation with the SAS model. Blue highlighted isosurface of the normalized time-averaged axial velocity with the value $\overline{u}/U_\infty = 0$ is presented. Slice-planes colored and cut off by $0 \leq \overline{u}/U_\infty \leq 0.9$ are shown. The mounting sting is not included for this investigation; $Re \approx 1 \cdot 10^6$, $\alpha = \beta = 0°$.

After discussing the structure at the lower side of the helicopter, the wake flow of the rotor head is discussed in the following. Therefore, the normalized time-averaged axial velocity component, the normalized time-averaged axial vorticity component, and the turbulence intensity obtained by the experimental data and numerical results are presented at the three planes P4, P5, and P6. The discussion on the vertical velocity is referred to [5]. Figure 120 depicts the experimental data and the numerical results of the normalized time-averaged axial velocity component in the wake of the rotor head applying the same layout as presented for the backdoor section. The velocity field in plane P4 exhibits two regions of velocity deficits marked with A for the retreating blade side and B for the advancing blade side. Both regions are represented similar in size and shape by the experimental data and the numerical results. However, the numerical simulation predicts the size of region A slightly smaller. Considering the downstream located plane P5, the regions of velocity deficits, A and B, merge to one. The agreement between the experimental data and the numerical results is better

than in the upstream located plane P4, but the size of region A is still obtained slightly smaller by the experimental data. Finally, a similar behavior of the flow field as in plane P5 is obtained in plane P6.

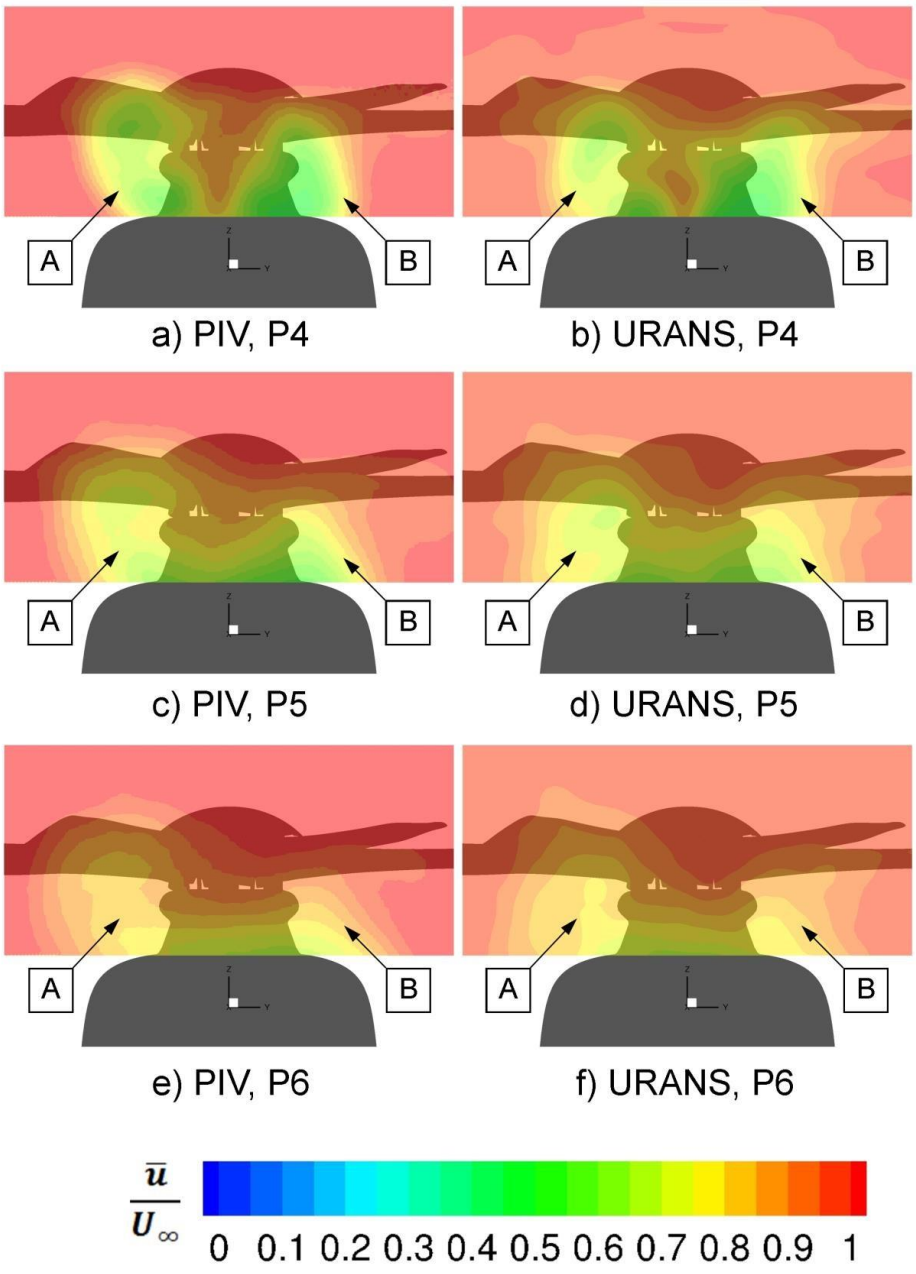

Figure 120: Normalized time-averaged axial velocity distribution for the crossflow planes P4, P5, and P6 in the wake flow of the rotor head [5]; $Re \approx 1 \cdot 10^6$, $\alpha = \beta = 0°$.

Figure 121 shows the experimental data and the numerical results of the normalized time-averaged axial vorticity component in planes P4, P5, and P6. As described above, the dominating vortical structures for the time-averaged consideration are the MFVP and the HCVP. The influence of the BTV is small due to the changing position during a revolution of the rotor head and the temporal averaging. The numerical simulation predicts the vortices at the plane P4 at a comparable position as provided by the experimental data, while the strengths and sizes of the vortical regions are different. In general, the numerical solution exhibits the vortical regions more concentrated than the experimental data. Both, the experimental data and the results of the numerical simulation show the strengths of the vortices at the retreating blade side higher than on the advancing blade side.

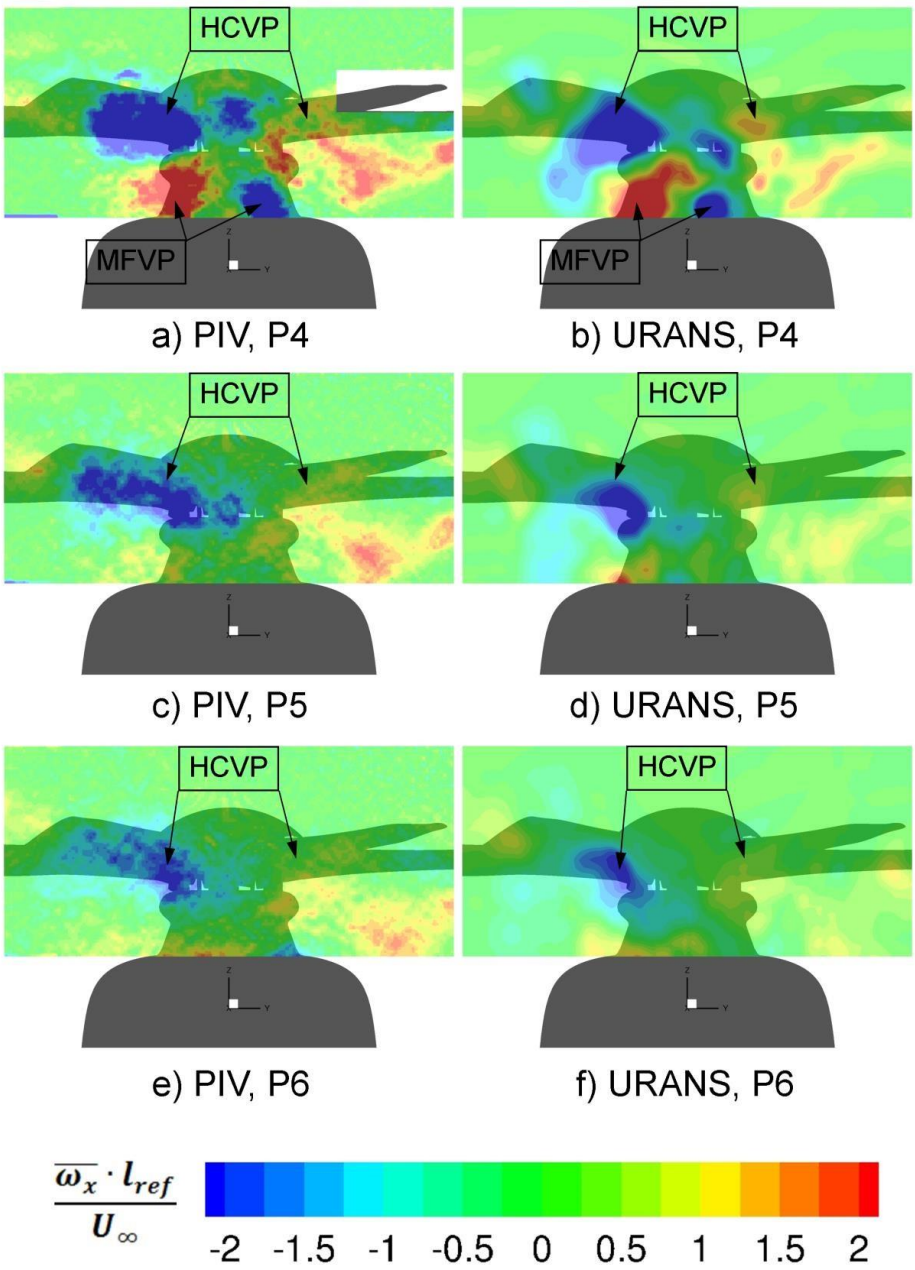

Figure 121: Normalized time-averaged axial vorticity distribution for the crossflow planes P4, P5, and P6 in the wake flow of the rotor head [5]; $Re \approx 1 \cdot 10^6$, $\alpha = \beta = 0°$.

The maximum negative axial vorticity is obtained within the hubcap vortex on the retreating blade side. The associated maximum value reads for the experimental data and the results of the numerical simulation $\frac{\overline{\omega_x}\, l_{ref}}{U_\infty} = -5.0$, but the location of the maximum differs within the vortex. The maximum positive axial vorticity magnitude is obtained within the mast fairing vortex on the retreating blade side. The associated maximum value predicted by the numerical simulation reads $\frac{\overline{\omega_x}\, l_{ref}}{U_\infty} = 5.9$, however, the experimental data provide a value of $\frac{\overline{\omega_x}\, l_{ref}}{U_\infty} = 4.6$. Again, the location of the maxima differs within the vortex. Considering the downstream positioned plane P5, the numerical results agree well with the experimental data also. The size of the hubcap vortex on the retreating blade side is predicted smaller and more concentrated by the numerical simulation, but the strength of the vortices is comparable. The size of the hubcap vortex on the advancing blade side is provided smaller

and the strength is predicted less by the numerical simulation. The MFVP is not visible for P5, since the vorticity magnitude is small and the structures move downwards. For the downstream located plane P6, the agreement between the numerical results and the experimental data is satisfactory also. Moreover, the convection of the vortices is captured also well. For example, the reduction of the maximum of the axial vorticity magnitude of the hubcap vortex on the retreating blade side during the convection is in good agreement between the experimental data and the numerical results. It is noted the spatial resolution of the numerical results and the experimental data is comparable. While the distance between two adjacent data points for the experimental data reads approximately $\Delta d \approx 3.5mm$, the range for the same quantity is provided for the numerical results with $2mm < \Delta d < 10mm$.

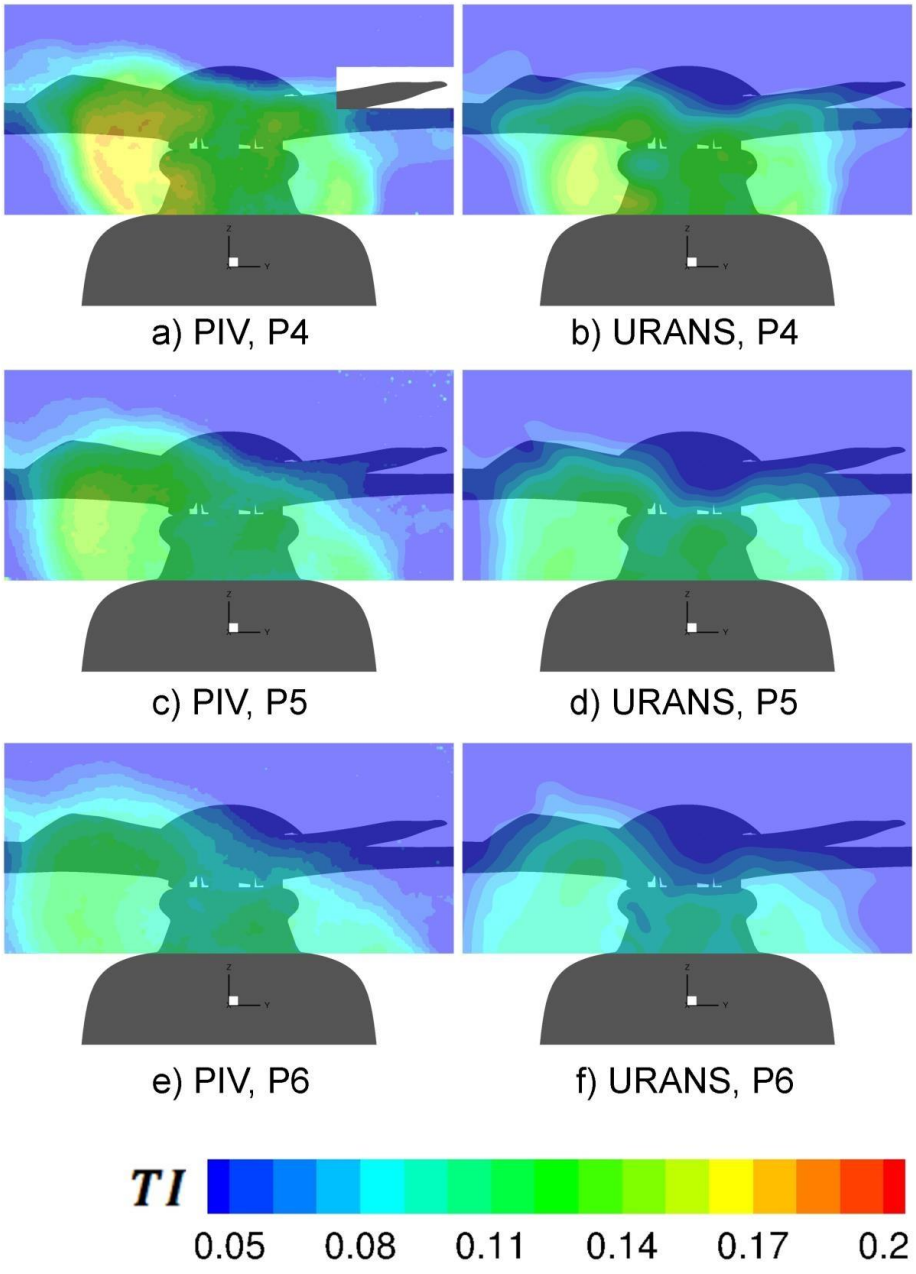

Figure 122: Turbulence intensity distribution for the crossflow planes P4, P5, and P6 in the wake flow of the rotor head [5]; $Re \approx 1 \cdot 10^6$, $\alpha = \beta = 0°$.

After discussing the mean values, the fluctuations are discussed. Therefore, the turbulence intensity distributions for the experimental data and the numerical results in the planes P4, P5, and P6 are presented in Figure 122. In plane P4, the distribution shows a good agreement between the experimental data and the numerical solution, although the region of increased turbulence intensities is provided larger by the experimental data. The maximum of the turbulence intensity occurs at the retreating blade side and reads for the experimental data $TI = 0.17$ and for the numerical simulation $TI = 0.16$. For the downstream located planes P5 and P6, a good agreement between the experimental data and the numerical results is obtained, but the regions are represented larger for the experimental data also. In plane P6, the maximum turbulence intensity determined by the experimental data is $TI = 0.12$ and for the results of the numerical simulation it reads $TI = 0.10$. The agreement is good by taken into account that the freestream turbulence varies up to an order of magnitude of minus two also.

In order to identify the dominant scales in the wake of the rotor head, the energy content for the spectral velocities depending on the spatial wave number is analyzed and assessed. For this purpose, the following procedure is applied for the planes P4, P5, and P6. For each plane, on 16 vertically positioned and laterally oriented lines, one-dimensional velocity spectra along the lateral direction are evaluated. The energy spectra are calculated from the velocity spectra for each line. Finally, the sum of the energy spectra depending on the wave number for one plane is determined. This procedure is performed for the 400 time-accurate samples of the data set and the temporal average is calculated. The raised-cosine function is applied as windowing function. For the PIV data, the results are smoothed to suppress noise. The applied method is similar to that presented by Foucaut et al. [154]. In Figure 123, the energy spectra of the axial and the vertical velocity component obtained by the experimental data and the numerical results are presented for the planes P4, P5, and P6. The wave number is nondimensionalized with the diameter of the hubcap. Figure 123 a) shows the energy spectra for the axial velocity component for plane P4. The dominant peak in the energy spectra is detected at a nondimensionalized wave number close to one $k\ D_{Hub} \approx 1$. The result is reasonable, since the size of the largest structure is associated to the diameter of the hubcap. A further characteristic peak in the energy spectra cannot be detected. However, the energy content at higher wave numbers is predicted too small by the numerical simulation compared to the experimental data. Due to the spatial resolution of the computational grid in the wake, the smaller scales related to higher wave numbers are not fully captured. Figure 123 b) exhibits the energy spectra for the vertical velocity component for plane P4. The dominant peak for $k\ D_{Hub} \approx 1$ and the energy content for low wave numbers is predicted higher, whereas for higher wave numbers, the energy content is presented lower by the numerical simulation in contrast to the experimental data. In Figure 123 c), d), e), and f), the energy spectra for the downstream positioned planes P5 and P6 are shown. Basically, due to the numerical dissipation of the smaller scales, the energy content for higher wave numbers is predicted too low by the numerical simulation the more downstream the plane is located. The trends can be detected easily by comparing the results for the planes P4, P5, and P6, for a high nondimensionalized wave number of, e.g., $k\ D_{Hub} = 8$. The statement is applicable for the axial as well as for the vertical velocity components.

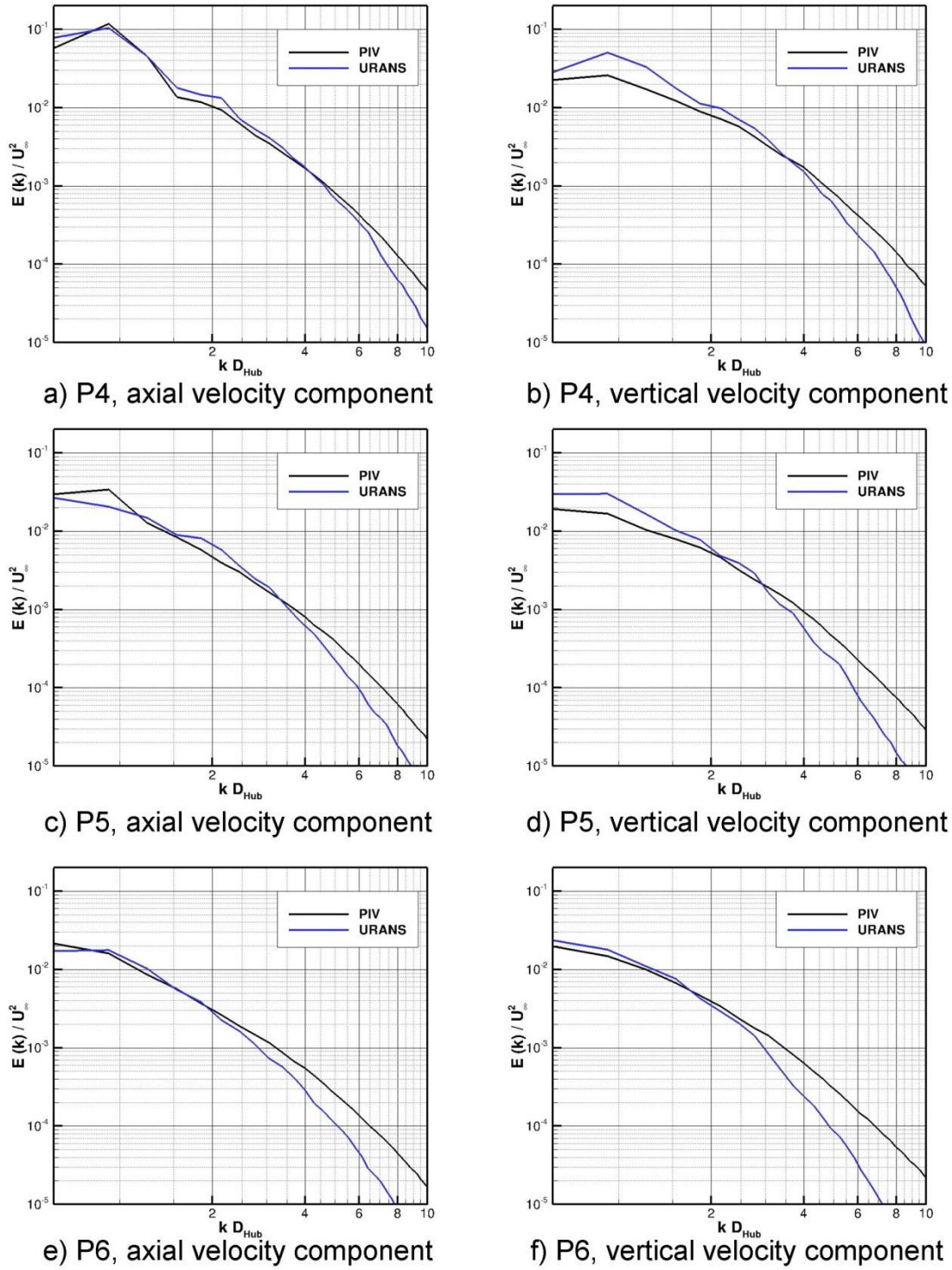

Figure 123: Energy spectra for the velocity components in dependence on the spatial wave number k multiplied by the diameter of the hubcap [5]; $Re \approx 1 \cdot 10^6$, $\alpha = \beta = 0°$.

6.4.2 Wake Flow Analysis

Within this section, the occurring flow structures for the FHC are discussed. At first, an overview of the occurring structures is presented on the basis of the numerical results. Thereafter, the phase-averaged quasi-volumetric PIV methodology is explained. Moreover, the data obtained by the latter are exhibited. A one-to-one comparison is not intended, since the blade pitch angles and the rotational speed for the numerical simulation are slightly different with respect to the experimental data.

In Figure 124, the flow structures are presented with the application of the Q criterion for the numerical result. Therefore, the isosurface of the nondimensionalized Q criterion is provided for a value of $Q \cdot \left(\frac{l_{ref}}{U_\infty}\right)^2 = 0.5$ (left) and for a value of $Q \cdot \left(\frac{l_{ref}}{U_\infty}\right)^2 = 10.0$ (right). The isosurfaces are colored by the nondimensionalized axial vorticity in the range of $-1 \leq \frac{\omega_x \cdot l_{ref}}{U_\infty} \leq 1$. The discussion is focused on the dominating vortical structures appearing in Figure 124. These are the blade tip vortices (BTV), the hubcap vortex pair (HCVP), the interactional vortical structure of the hubcap vortex (HCV) with the blade tip vortex on the retreating blade side (HTI), and the radially inwards of the blade tip positioned vortical structure (BIV). If applicable, the structures are associated to the number of the blade (B) causing the structure. The blades are numbered from 1 to 5 with increasing azimuthal rotor-head angle. At first, the blade tip vortices are discussed. The convection of the vortices, visualized by the lower level of the Q criterion, is represented well by the numerical simulation. The tracking can be performed on the advancing as well as on the retreating blade side easily. For the higher level of the Q criterion, the strength of the vortices enables the visualization solely in the vicinity of the blade. Nevertheless, for the lower level of the Q criterion, the interaction of the blade tip vortices of two adjacent blades is well visible for BTV2 and BTV3 on the advancing blade side in Figure 124 (middle, left). Furthermore, the interaction of BTV3 and B2 is shown. On the retreating blade side, the convection of the blade tip vortices, exhibited by the lower level of the Q criterion, is captured well also. The position of the HCVP is detectable on both sides of the hubcap. Basically, it cannot be identified as one unique vortical structure in this time-accurate capture. The interaction of the HCVs with the blade leads to small, higher-harmonic vortical structures. Nevertheless, the direction of the rotation of the vortices around the streamwise direction is provided reasonably. A further dominating structure results from the interaction of the HCV on the retreating blade side with the blade tip vortex of a certain blade. Consider the blade for an azimuthal rotor-head angle of $\psi = 180°$. Blade B3 is shown in approximately this position. If the blade is further rotating, the vortex is moving downstream with the local velocity of the flow. For an azimuthal rotor-head angle of approximately $\psi \approx 250°$, the blade tip vortex interacts with the hubcap vortex and leads to the structure HTI4. The position of blade B4 is shown in a state shortly after this interaction. The structure HTI4 is not shown in Figure 124, since it is hardly to detect in this initial state between the mast faring and the blade. Nevertheless, the evaluation of the structure downstream is captured well by both levels of the Q criterion. Finally, the second vortical structure originating radially inwards of the blade tip (BIV) is discussed. The vortical structure is initiated by a change of the airfoil section in radial direction. Radially outwards, the generated lift is higher than inwards. Consequently, a vortex arises. The direction of the rotation is opposed to that of the blade tip vortex. The vortex is captured well by the lower level of the Q criterion and interestingly, it is moving almost parallel to the blade tip vortex.

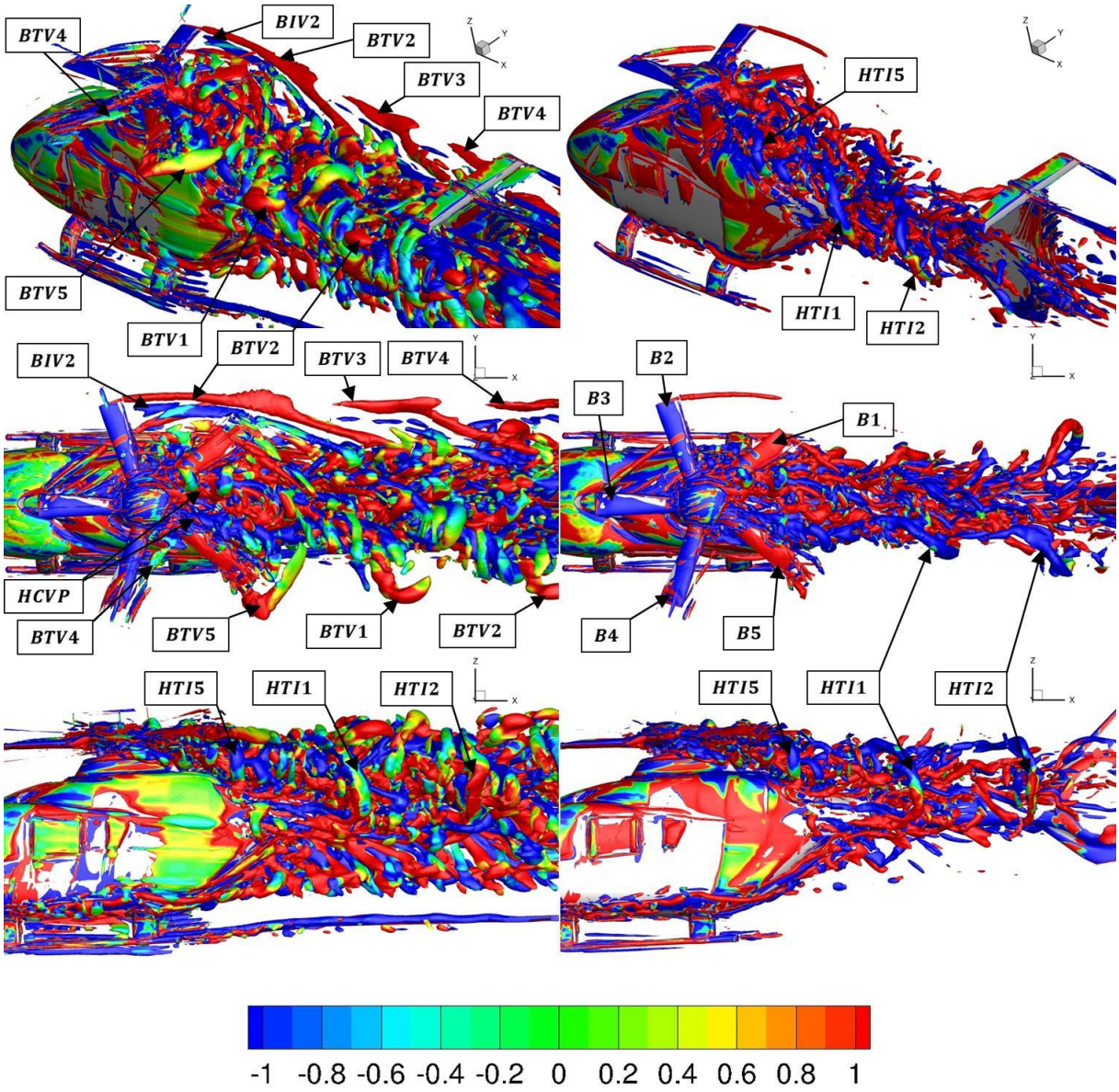

Figure 124: Wake structures for the FHC. The vortical structures are designated by the origin of the structure as well as the associated number of the blade (B) if applicable. BTV: Blade tip vortex; HCVP: Hubcap vortex pair; BIV: Inwards of the blade tip located vortex; HTI: Hubcap BTV interaction; $Re \approx 1 \cdot 10^6$, $\alpha = \beta = 0°$.

In the following, the reconstruction of the volumetric flow data from the measured two-dimensional, three-component PIV data is presented. Figure 126 exhibits the helicopter geometry, the grey highlighted PIV planes, and the blue highlighted cuboid. For the reconstruction, 15 crossflow PIV planes are used. The distance between the planes is set to $\Delta x = 50\ mm$ and the spatial resolution in the plane reads approximately $\Delta y \approx \Delta z \approx 3\ mm$. For the grid points of the cuboid, a spatial resolution of $\Delta x = 50\ mm$, $\Delta y = 10\ mm$, and $\Delta z = 10\ mm$ is chosen. The intention is that the PIV planes are aligned with planes of constant x-coordintate of the cuboid to simplify the interpolation. The PIV data are interpolated by an inverse-distance interpolation on the nodes of the cuboid. Therefore, the eight nearest nodes of a PIV plane are considered. In order to allow the investigation for the temporal evolution of the flow, the PIV data include azimuthal rotor-head angles of $\psi = 0°$, $\psi = 18°$, $\psi = 36°$, and $\psi = 54°$. Obviously, a temporal resolution in terms of azimuthal rotor-head

angle of $\Delta\psi = 18°$ is achieved due to periodicity. The PIV data for a certain azimuthal rotor-head angle are obtained by phase-averaging of 400 data samples. A similar approach, applying high-speed PIV for the evolution of the blade tip vortices, can be referenced to Bauknecht et al. [155].

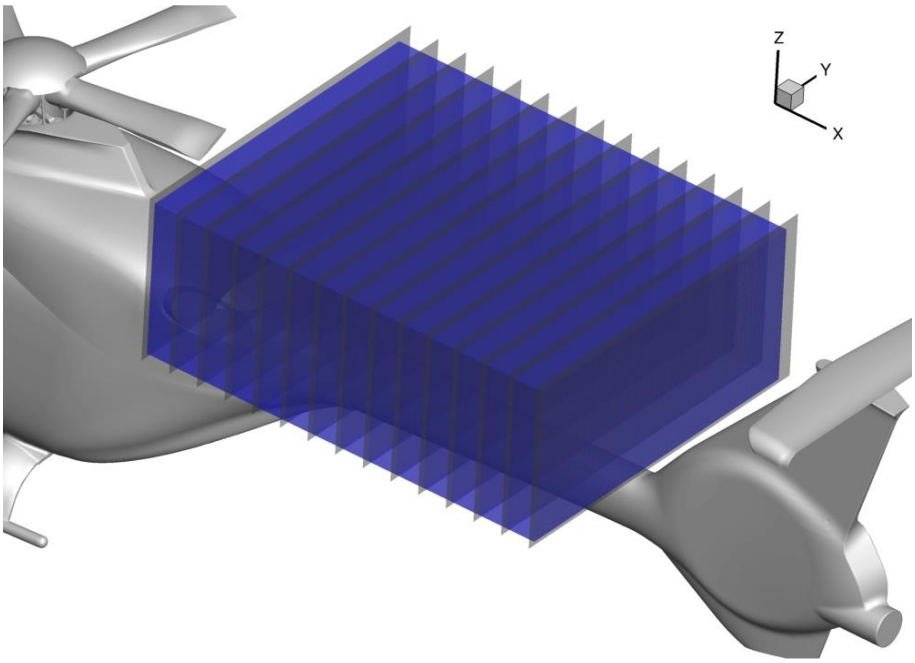

Figure 125: Quasi-volumetric PIV-setup. The grey highlighted planes show the measured planes, and the blue highlighted cuboid exhibits the volume for the reconstruction of the volumetric data.

Figure 126 shows the isosurface of the nondimensionalized Q criterion of $Q \cdot \left(\frac{l_{ref}}{U_\infty}\right)^2 = 0.5$ colored by the axial vorticity component in the range of $-1.0 \leq \frac{\omega_x \cdot l_{ref}}{U_\infty} \leq 1.0$ for the experimental data. The isosurface is presented for the azimuthal rotor-head angles of $\psi = 0°$ (top, left), $\psi = 18°$ (top, right) $\psi = 36°$ (bottom, left), and $\psi = 54°$ (bottom, right). The dominating structures are, like for the numerical results, the blade tip vortices (BTV), the hubcap vortex pair (HCVP), the interactional vortical structure of the hubcap vortex with the blade tip vortex on the retreating blade side (HTI), and the radially inwards of the blade tip positioned vortical structure (BIV). By comparing the results of the numerical simulation with the experimental data for the same level of the Q criterion, one major difference is well visible. Since the numerical simulation provides a time-accurate solution and the experimental data are phase-averaged, the latter shows mainly the periodic structures. The experimental data can be considered as a temporally-filtered flow field. Nevertheless, the experimental data represent the dominating structures well. Furthermore, the convection of the structures is visualized well. For a more detailed analysis, consider the BTVs on the advancing side at first. The blade tip vortices are designated according to the blade (B) of the origin. The blades are numbered from 1 to 5 with increasing azimuthal rotor-head angle. The volumetric PIV allows for tracking the position of the vortices during the convection easily, since the vortices are captured within the whole reconstructed domain. Basically, the lateral position of the vortex is determined mainly by the lateral position of the blade tip during the formation of the BTV. Since it is not possible to measure planes closer to the rotor head due to shading caused by the blade, the numerical results are taken into account for determining the origins of the vortical structures. While the blade tip

vortices on the advancing side are captured, the size of the measurement window is too small in the lateral direction in order to include the whole blade tip vortices on the retreating blade side also. As a remark, the goal of the investigation is the evaluation of the interaction of the vortical structures with the tail of the helicopter and therefore, the size of the window is sufficient. Nevertheless, the fragments of the BTVs are still depicted at the retreating side as well. The comparison with the numerical results shows a qualitatively well agreement for the strength and location of the BTVs. The HCVP is shown by the experimental data also. Compared to the numerical results, the phase-averaged data provide smoother structures. This issue is caused by the loss of the unsteady information during the averaging process. Consequently, the experimental data appear to be filtered by the application of a low-pass filter.

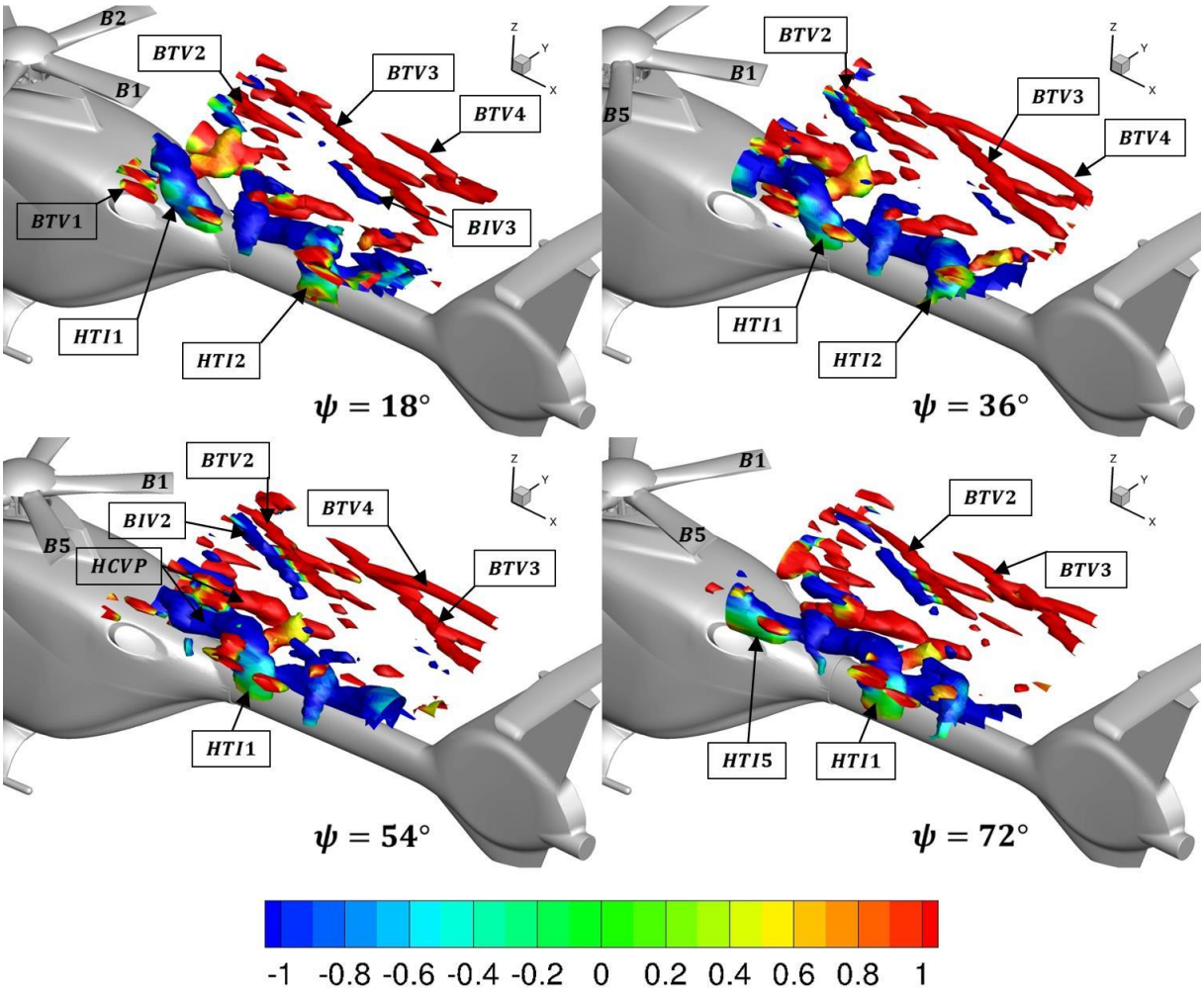

Figure 126: Isosurface of the normalized, phase-averaged Q criterion for an isovalue of $Q \cdot \left(\frac{l_{ref}}{U_\infty}\right)^2 = 0.5$ colored by the axial vorticity component in the range of $-1.0 \leq \frac{\omega_x \cdot l_{ref}}{U_\infty} \leq 1.0$. The vortical structures are designated by the origin of the structure as well as the associated number of the blade (B) if applicable. BTV: Blade tip vortex; HCVP: Hubcap vortex pair; BIV: Inwards of the blade tip located vortex; HTI: Hubcap BTV interaction; $Re \approx 1 \cdot 10^6$, $\alpha = \beta = 0°$.

The interaction of the HCV on the retreating blade side with the BTV of a certain blade, as previously discussed for the numerical results, is shown by the experimental data also. Basically, a similar behavior is provided. However, the structures are better to detect for the experimental data, since less structures appear, caused by the filtering. The structures are designated by HTI. Between two consecutive structures, e.g. HTI1 and HTI2, another structure is found that is not that distinctly

exhibited in the numerical solution. It is mentioned in the last paragraph that the HTIs are caused by the interaction of the HCV with the BTV. The other structure occurs by the interaction of the HCV with the blade itself. The second vortical structure, originating radially inwards of the blade tip (BIV), is presented by the experimental data as well. In particular, the behavior is comparable to that of the numerical solution. Due to lower strength of the structure, it is not fully captured for all azimuthal rotor-head angles.

In order to determine the strength of the structures, crossflow planes of the nondimensionalized vorticity magnitude in the range of $1.5 \leq \frac{|\omega| \cdot l_{ref}}{U_\infty} \leq 9.5$ are presented for the experimental data in Figure 127. The values are cut off below the lower limit. The data are provided comparably as in Figure 126 for the azimuthal rotor-head angles of $\psi = 0°$ (top, left), $\psi = 18°$ (top, right) $\psi = 36°$ (bottom, left), and $\psi = 54°$ (bottom, right). The structures, showing the highest strength, are the BTVs at the advancing blade side, the HCVP, and the HTIs. In particular, the highest values are exhibited for the hubcap vortex on the retreating blade side between two consecutive HTIs. The vorticity of the BIV is small compared to the previously mentioned structures.

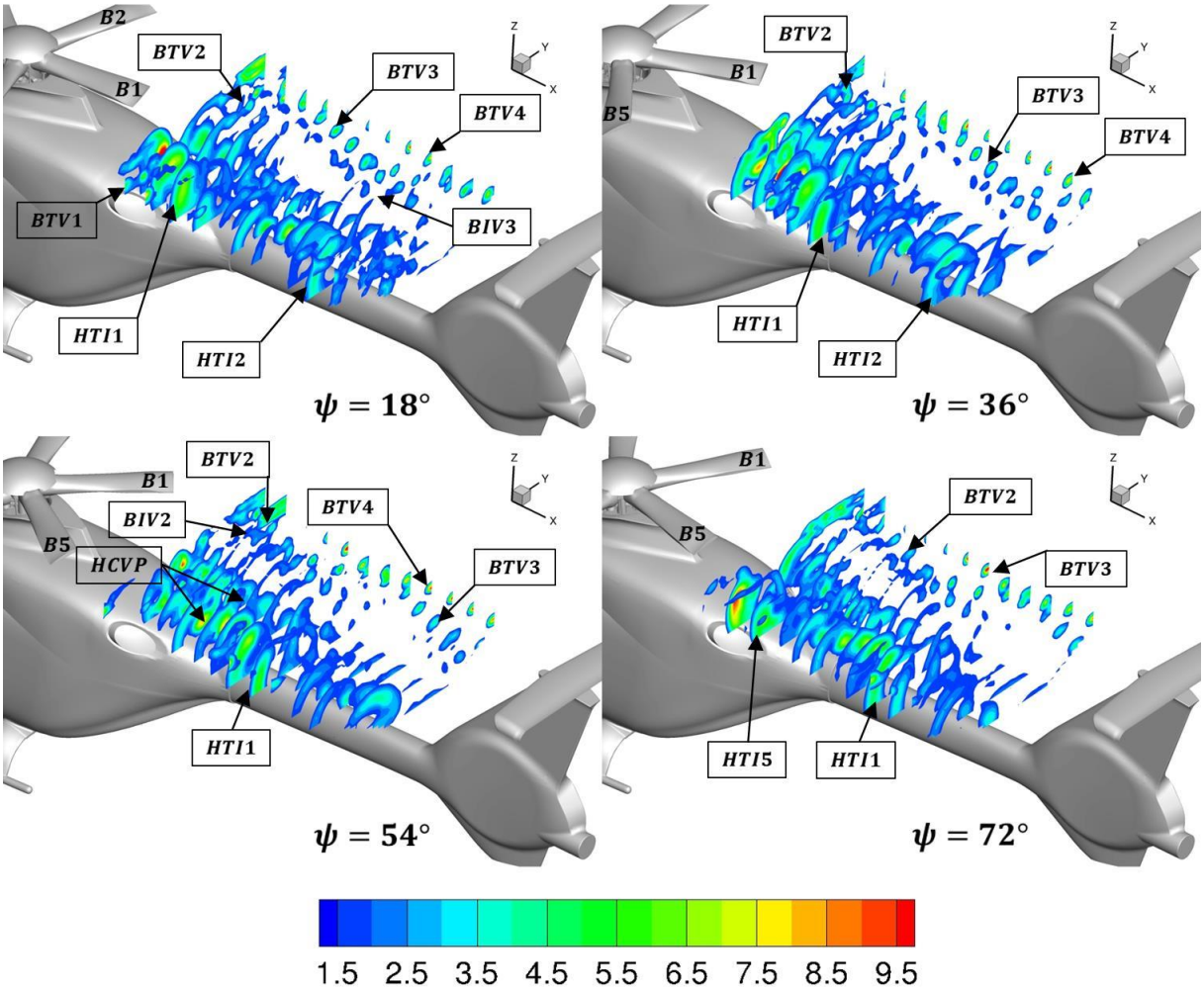

Figure 127: Crossflow planes colored by the phase-averaged, normalized vorticity magnitude in the range of $1.5 \leq \frac{|\omega| \cdot l_{ref}}{U_\infty} \leq 9.5$ cut off below the lower limit. The vortical structures are designated by the origin of the structure as well as the associated number of the blade (B) if applicable. BTV: Blade tip vortex; HCVP: Hubcap vortex pair; BIV: Inwards of the blade tip located vortex; HTI: Hubcap BTV interaction; $Re \approx 1 \cdot 10^6, \alpha = \beta = 0°$.

Finally, the velocity deficit in the wake is described. Therefore, crossflow planes of the nondimensionalized axial velocity component in the range of $0.4 \leq \frac{u}{U_\infty} \leq 0.9$ are presented for the experimental data in Figure 128. The values are cut off above an value of $\frac{u}{U_\infty} \geq 0.95$. The data are provided comparably as in Figure 126 for the azimuthal rotor-head angles of $\psi = 0°$ (top, left), $\psi = 18°$ (top, right) $\psi = 36°$ (bottom, left), and $\psi = 54°$ (bottom, right). The most important information obtained from the results is that the region of the velocity deficit in the wake of the rotor head does not change much in dependence on the azimuthal rotor-head angle. Nevertheless, slight deviations of the velocity deficit depending on the azimuthal rotor-head angle are present. Basically, the two regions already described for the FOC in a time-averaged manner, namely A and B in Figure 120, are detected. Resultantly, the axial velocity component impinging at the vertical stabilizer is changing slightly in time.

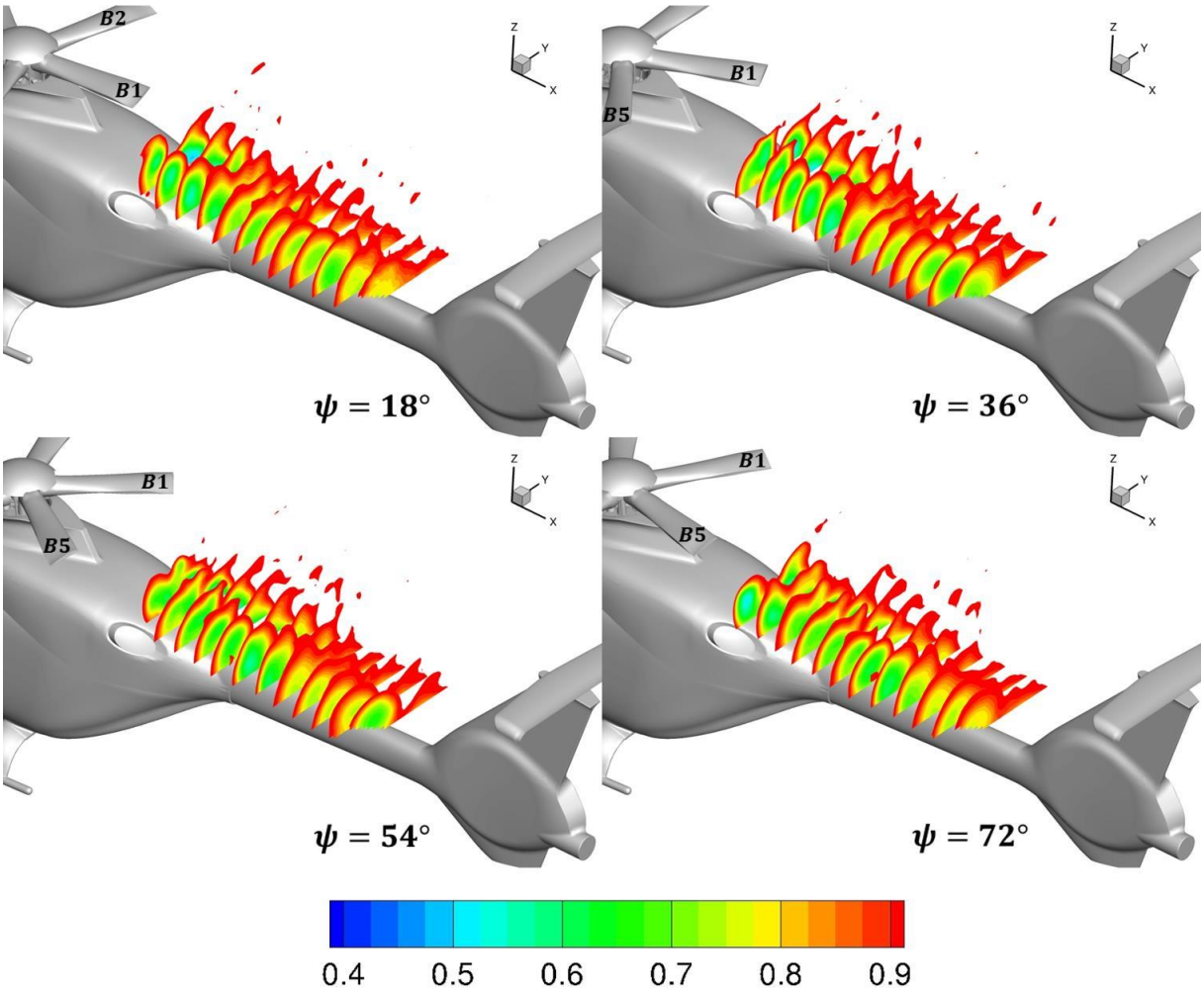

Figure 128: Crossflow planes colored by the phase-averaged, normalized axial velocity component in the range of $0.4 \leq \frac{u}{U_\infty} \leq 0.9$ cut off above $\frac{u}{U_\infty} \geq 0.95$. The blades are designated (B) ; $Re \approx 1 \cdot 10^6, \alpha = \beta = 0°$.

6.5 Conclusions

Complementary experimental and numerical investigations of a 1:5 scale model of a characteristic twin-engine utility helicopter were presented. Investigations for the helicopter configuration excluding the tail were applied for validating the numerical results in terms of the global forces and moments as well as of the velocity field in the wake flow. The full helicopter configuration was used for a characterization of the flow field and a comparison to the flow field reconstructed from PIV-data. Moreover, the application of the introduced mesh-deformation method was described in detail.

For the configuration without the empennage, the validation shows a reasonable to good agreement for the forces and moments. The prediction of the time-averaged axial velocity in the wake of the cabin backdoor section provides a good agreement between the experimental data and the numerical results. In addition, the origins of the separation of the flow at the cabin backdoor section were described. Concerning the wake flow of the rotor head, a validation of the time-averaged axial velocity and axial vorticity distribution as well as the turbulence intensity distribution was presented. The global behavior is in good agreement for all quantities between the experimental data and the numerical results. Nevertheless, the more dissipative character of the numerical simulation is detectable. In addition, the spectral energy content in the wake of the rotor head was investigated. While the energy content for the planes in the wake close to the rotor head is predicted well by the numerical simulation, the agreement with the experimental data is worse the higher wave numbers and the more downstream the plane is located. For the full configuration, the detailed analysis of the wake field was presented by the numerical simulation. The application of the phase-averaged quasi-volumetric reconstruction of the PIV-data for several azimuthal rotor-head angles allowed for a qualitative comparison with the numerical simulation. The dominating structures are captured comparably for the experimental data and the numerical results. Basically, the blade tip vortices, the hubcap vortex pair, and interactional structures are included. The convection of the structures is predicted also well. For a detailed investigation, the complementary investigation is highly beneficial for the characterization of the flow field.

7 Conclusions and Outlook

The fast and accurate prediction of lifting surfaces in rotational reference systems is important for many applications. The fields of application range from classical applications such as helicopters, propeller aircraft, or wind turbines to combined applications. The latter can be found, for example, within the growing field of urban air mobility. In general, the method for solving a given problem has to be suited for the specific needs. During the pre-design stage, a lot of designs have to be evaluated. The main objective therefore is the prediction of the trends for a certain modification. Within the subsequent stages, the focus is set on determining the absolute quantities correctly. Obviously, the requirements for the methods are different. However, the results for both questions have to be solved with the appropriate fidelity level in the context of efficient and reliable simulations.

The presented thesis provides enhanced solutions for both parts. Concerning the first part, the generalized actuator disc concept with certain modifications was presented. These were the application of a new Kernel function based on a raised cosine as well as a direct coupling for solving the blade characteristics in combination with the continuum simulation. As a further extension, the multi-domain approach was introduced. At the beginning, a very detailed literature review was provided. The theoretical basis was set by briefly summarizing the important ideas and equations of the momentum theories, the blade element theory, and as a combination of the latter, the blade element momentum theory. In the following, the fundamentals of the generalized actuator disc approach were described. For this thesis, in particular, the actuator disc (AD) and actuator line (AL) is important. In the next step, a brief description of the estimation of the airfoil data with the panel method coupled with the boundary layer integration method (PanBL) was presented. The latter method was used for the direct coupling with the generalized actuator disc approach. The actually implemented generalized actuator disc method in the course of this thesis was detailed thereafter. The workflow for the generalized actuator disc approach showed that three steps are important for the approach. The evaluation of the inflow condition, the generation of the airfoil data, and the calculation of the source terms for the continuum-based solution. At first, the steps for the actuator disc coupled directly with PanBL (AD-PanBL) were described as basis. Therefore, theoretical considerations concerning the best-suited position for the evaluation of the inflow conditions relative to the position of the disc in axial direction were made based on the momentum theory. Furthermore, the averaging process for determining the inflow conditions out of the cell quantities of the continuum-based solution was provided. Moreover, the definition and implementation of the Kernel function based on the raised-cosine function was presented in association with the distribution of the source terms. The difference in the determination of the inflow conditions and source terms for the actuator line coupled directly with PanBL (AL-PanBL) was presented subsequently. Therefore, theoretical considerations for the determination of the position of the averaging region in the plane normal to the spanwise direction of the blade were conducted based on potential theory. In addition, the spanwise distribution of the averaging regions was discussed also. Based on the previous information, the direct coupling of the three-dimensional continuum solution with the two-dimensional Reynolds-averaged Navier-Stokes simulations (2C) for generating the airfoil data within a multi-domain framework was described shortly. The multi-domain framework was applied for the actuator disc (AD-2C) and the actuator line (AL-2C). Therefore, solely the panel method coupled with the boundary layer integration method is substituted by the Reynolds-averaged Navier-Stokes simulation. However, due to the different size of the domains and the flow velocities through the domains, the practical realization needs a well-suited updating

scheme in order to obtain fast converging simulations. The applied schemes were presented in detail for the two-dimensional and three-dimensional test cases.

In order to evaluate the quality of the methods, several test cases with different complexity were established. The two-dimensional test case was used to evaluate the characteristics of a two-dimensional cascade of airfoils. Therefore, parameters related to the cascade like the advance ratio, the solidity, and the angle of attack were varied. In addition, the influence of the parameters associated to the generalized actuator disc model was investigated. The parameters are determined for the averaging and the source regions. For both regions, the width of the region, the widths of the smoothing region, and the center of the region has to be set. While for the actuator disc, the quantities are defined in one dimension, for the actuator line, two dimensions are required. For both parameter spaces, systematic studies were performed.
Concerning the parameters associated to the generalized actuator disc model, some findings can be concluded for the actuator disc:

- The forces acting on the blade are not dependent on the width of the averaging and source region if the latter are larger than five characteristic cell lengths.
- An independent result of the forces acting on the blade is obtained if the width of the averaging region related to that of the source region is greater than one.
- The resulting forces acting on the blade are not dependent on the width of the smoothing region if the region is larger than five characteristic cell lengths.
- By enabling the smoothing region, independence and smoothness of the forces acting on the blade are obtained for a relative motion of the actuator regions relative to the mesh.

While an independent solution of the forces on the blade is obtained for a wide range of the parameters for the actuator disc, for the actuator line, in particular for small widths of the averaging and source region, a decrease of the forces on the blades is detectable.
With the knowledge of these investigations, a well-suited parameter set for the generalized actuator disc was chosen for the calculations of the parameter field associated to the cascade. The simulations with the generalized actuator disc approach were conducted for a forward flight case as well as a static thrust test case and were compared to the resolved cascade simulations. Based on the latter, for the forward flight test case it can be stated:

- The higher the solidity, the smaller the forces acting on the blade.
- The higher the angle of attack, the higher the forces acting on the blade.
- For increasing advance ratios, the slope of the forces depending on the solidity becomes more negative.

For the resolved simulation of the static thrust test case it can be summarized:

- The higher the solidity, the smaller the forces acting on the blade.
- The higher the angle of incidence, the higher the forces acting on the blade.
- The slope of the forces depending on the solidity is more negative than for the forward flight test case.

For the test cases, the actuator disc and the actuator line models were directly coupled, on the one hand, with the PanBL, and on the other hand, within the multi-domain framework, with two-dimensional Reynolds-averaged Navier-Stokes simulations. In general, all modeling approaches

provided the trends correctly with respect to the resolved simulation. The PanBL-based models overestimate the lift and underestimate the drag which leads to different absolute values. For the AL-based models, the underestimated angle of attack obtained by the averaging procedure, in particular, for higher blade loadings results in a more positive slope of the forces depending on the solidity. One additional effect becomes visible for the static thrust test case. Since the PanBL-based approaches cannot handle the stall appropriately, the thrust is massively overpredicted for low solidities and high angles of incidence. Nevertheless, the modeled approaches show a good agreement with the resolved simulation for a wide range of input parameters for both the static thrust and the forward flight test case.

The three-dimensional cascade test case was based on the two-dimensional test case by adding a finite wing span. The purpose of this test case was to proof the quality of the methods including three-dimensional effects, in particular, in the blade tip region. For this test case, solely the forward flight state was investigated; however, the force distribution along the spanwise direction and the flow field was described also. The principal behavior is comparable to that of the two-dimensional test case and the modeled approaches capture the trends also well. Moreover, the overestimation of the lift and the underestimation of the drag by PanBL-based methods are detectable. The influence of the reduced angle of attack resulting by the averaging procedure for the AL-based methods for higher blade loadings is visible also. In addition, an overestimation of the lift by the AD-based methods is obtained for low solidities due to the not sufficiently accounted influence of the three-dimensional effects. The prediction of the spanwise distribution is covered appropriately by the modeled approaches also. However, the statements made for the two-dimensional test case are valid for the sections of the three-dimensional test case. In general, the agreement with the resolved simulation is better with the 2C-based methods than with the PanBL-based methods. In the blade tip region, the AL-based methods capture the three-dimensional effects better. The prediction of the circumferential force in the blade tip region is reasonable. Although the AL-based approaches agrees better with the resolved simulation, both the AD-based as well as the AL-based approaches cannot handle the increasing drag of the blade caused by the blade vortex interaction for higher solidities. Concerning the wake flow field, the principal behavior, like the flow contraction with increased segment loading, is predicted appropriately well by all modeled approaches. The agreement of the predicted positions of the vortices by the AL-based models is good related to the resolved simulation. However, the sizes of the vortex cores are presented too large depending on the applied widths of the actuator line.

As an increase in complexity, the three-dimensional propeller test case was conducted. The applied propeller was a three-bladed fixed-pitch propeller. The investigations included the resolved simulations for generating reference data as well as the modeled blade simulations using the AD-PanBL and the AL-PanBL approach. For this test case, different freestream velocities and rotational speeds were taken into account. In addition, the applicability of the approaches for non-axial inflow conditions was considered. For axial inflow conditions, the results for the thrust and efficiency of the modeled approach show a good agreement with those of the resolved propeller blade simulations. The distribution of the forces along the blade is represented well while discrepancies occur mainly due to the prediction of the airfoil data by PanBL. The overpredicted lift slope by PanBL leads to the more negative slope of the thrust coefficient depending on the advance ratio. Although the magnitude of the efficiency is not predicted correctly by the modeled approaches compared to that of the resolved propeller simulation, the advance ratio for the maximum is. Concerning the wake flow field, a good agreement of both modeled approaches with the resolved simulation is found also. The biggest differences in the results are detected in the wake of the aft body, since the interaction

of the modeled blades with the boundary layer of the latter is not captured appropriately. The strength and position of the blade wakes as well as of the blade tip vortices are in good agreement between the modeled approach and the resolved propeller simulation. It has to be remarked that the AD-PanBL approach is up to 400 times faster for generating the resulting forces and up to 800 times faster for generating the wake flow field compared to the time-accurate resolved blade simulation. The application of the methods for non-axial inflow conditions demonstrated a good agreement for moderate disc inflow angles regarding the forces and moments. For high disc inflow angles, the airfoil data are not provided appropriately by PanBL and consequently, the forces and moments are overestimated.

For the complex scenario within this thesis, a propeller-fuselage configuration was considered. Therefore, complementary numerical and experimental investigations were performed for a fuselage with mounted propeller of an electrically powered ultra-light aircraft. The wind-tunnel tests of the full-scale configuration have been conducted in the wind tunnel A of the Chair of Aerodynamics and Fluid Mechanics of the Technical University of Munich. The data served mainly as basis for the validation of the numerical approaches. For this test case, three different numerical setups with different approaches were applied. At first, AD-PanBL simulations incorporating the crucial parts of the wind-tunnel geometry (RANS/AD-W/T) are executed. At second, simulations of the isolated propeller using AD-PanBL (RANS/AD) were performed. At last, time-accurate simulations of the resolved propeller (URANS/RP) were conducted. This chain allows besides determining the overall characteristics of the different approaches, an isolated study of the occurring effects. Moreover, the procedure of the aerodynamic tare was discussed for the wind-tunnel tests and the “numerical wind-tunnel”. The URANS/RP result shows the best agreement with the W/T data of the applied numerical approaches, in particular, for the slope of the thrust coefficient depending on the advance ratio. The AD-based simulations provide a different slope due to the representation of the airfoil data as already seen for the other test cases. The thrust of the propeller-fuselage configuration in the “numerical wind-tunnel”, obtained by the application of the aerodynamic tare, is in accordance with that produced by the modeled propeller for the isolated propeller configuration. The detailed investigation of the contribution of forces, taken into account for the aerodynamic tare, shows that the increasing drag of the fuselage for higher thrust levels is compensated by the overestimated thrust due to the blockage of the fuselage and the small distance of the propeller to the floor of the test section.

For the modeling of the propeller, it can be concluded that the presented low to mid fidelity methods show good agreement with respect to the reference data for a wide range of input parameters by reducing the numerical effort drastically. Starting from the two-dimensional test case to the complex scenario, a good agreement is achieved for forces and moments as well as for the flow field prediction. Moreover, the procedure of the aerodynamic tare is applicable for the presented configuration despite mutual interference.

Nevertheless, certain aspects can be improved. For the PanBL-based approaches, the overestimation of the lift of the airfoil leads to overestimated forces of the propeller. As a result, the slope of the thrust and circumferential force depending on the advance ratio is predicted more negative. Therefore, PanBL can be substituted with XFoil which provides better airfoil data due to the inclusion of the boundary layer thickness by the two-way coupling. However, for the first estimation of results, PanBL has advantages caused by the high robustness.

For the AL-based approaches, the issue with the underestimated angle of attack caused by the averaging procedure is stated. Therefore, a dynamic adaption of the vortex center during the

iterations can be performed, for example, by subdividing the averaging region and determining the critical point of the flow topology and move the center of the averaging region to the position of the critical point.
The modeled approaches are best-suited for Cartesian grids. Consequently, the full potential of the method can be exploited by using these. In the last years, Fluent has enabled the generation of hexahedral core meshes within the field in combination with polyhedral meshes at the boundaries. By using bodies of influence for a local refinement of the mesh in the region of the propeller disc, the described modeling approach can be combined with the meshing process and can be completely automated. This allows, for example, the optimization of propeller positions for an aircraft.
Although the multi-domain approach was presented for the cascade test cases, the application for a three-dimensional propeller test case would be interesting. One question to be answered is, for example, if the stall of the blade can be captured appropriately for the AD and the AL modeling. For the latter, a further question is if the unsteady flow phenomena for a blade section can be captured also. Nevertheless, for both questions the numerical effort has to be taken into account. Furthermore, for achieving the highest benefit of such an enhancement, a high level of automation is required as already stated for the three-dimensional cascade test case.

The second part of the thesis dealt with the modeling of the flow around a helicopter including the rotor-head motion by introducing an analytical, fast, linear-scaling deforming-mesh approach. Furthermore, complementary numerical and experimental data were provided. In particular, phase-averaged quasi-volumetric particle image velocimetry measurements for analyzing the wake flow were conducted. At the beginning of this part, a detailed literature review was given. The focus of the latter was set on the one hand, on the flow around helicopters and on the other hand, on methods capturing mesh motion. In the following, a brief theoretical description of the methods for the motion of meshes was given. These were mainly the sliding mesh approach, the Chimera or overset mesh approach, and the deforming mesh approach. In particular, the subtypes of the deforming mesh approach realized in Fluent were discussed. Since the first investigations, prior to the development of the analytical mesh-deformation method, were made with the standard mesh approaches provided by Fluent, the latter served as basis for measure the quality and the speedup of the analytical mesh-deformation method. Thereafter, the analytical mesh-deformation method was detailed. The basic ideas were introduced and simple test cases were set to highlight the results graphically. The analytical mesh-deformation function is based on certain connected functions for rotation and translation of the mesh. The smoothing is based on a raised-cosine function. In order to determine the speedup compared to the diffusion-based mesh-deformation method provided by Fluent, a simple and well-suited test case was established. A relatively rotating cylinder was embedded in a squared domain and the space between was meshed by an O-grid. For the study, the number of cores as well as the number of nodes was varied. In general, a speedup in the order of magnitude of two is achieved by the analytical mesh-deformation. Furthermore, a linear scaling is obtained and the mesh quality remains visibly higher.

In the following, the detailed description of the main test case was provided. The investigations were conducted for a detailed, 1:5 scale model of a characteristic twin-engine light utility helicopter featuring collective and cyclic pitch motion of the blade cuffs governed by a fully functional swash plate. The model is based on Airbus Helicopters Green Rotorcraft Demonstrator Bluecopter. Two setups were considered. One setup included the whole helicopter and the other one excluded the tail boom as well as the vertical and horizontal stabilizer. The applied measurement techniques were

force and moment measurements with a six-component underfloor balance as well as flow field measurements with Stereo-PIV. The latter was used for the phase-averaged quasi-volumetric reconstruction of the flow field. The description of the numerical setup started with the applied meshing and blocking strategy. Thereafter, the application of the analytical mesh-deformation method for the test case was presented. For this test case, two multiplicatively connected deformation functions were applied. The first governed the rotation of the blade and the second described the mesh in the vicinity of the hub. Before the analyses of the results were provided, the solver settings were discussed in detail. For the configuration without the empennage, the validation shows a reasonable to good agreement for the forces and moments. The prediction of the time-averaged axial velocity in the wake of the cabin backdoor section provides a good agreement between the experimental data and the numerical results. In addition, the origins of the separation of the flow at the cabin backdoor section were described. Concerning the wake flow of the rotor head, a validation of the time-averaged axial velocity and axial vorticity distribution as well as the turbulence intensity distribution was presented. The global behavior is in good agreement for all quantities between the experimental data and the numerical results. Nevertheless, the more dissipative character of the numerical simulation is detectable. In addition, the spectral energy content in the wake of the rotor head was investigated. While the energy content for the planes in the wake close to the rotor head is predicted well by the numerical simulation, the agreement with the experimental data becomes worse with increasing wave numbers and the more downstream location of the plane. For this complex test case, the speedup of the analytical mesh-deformation method compared to the diffusion-based mesh-deformation method is in the order of magnitude of two which is in line with the simple test case. Moreover, no stability issues of the simulations with increasing rotor revolutions were detected. For the full configuration, the detailed analysis of the wake field was presented by the numerical simulation. The application of the phase-averaged quasi-volumetric reconstruction of the PIV-data for several azimuthal rotor-head angles allowed for a qualitative comparison with the numerical simulation. The dominating structures are captured comparably for the experimental data and the numerical results. The convection of the structures is predicted also well. For a detailed investigation, the complementary investigation is highly beneficial for the characterization of the flow field.

For the modeling of the flow around the helicopter, it can be concluded that the results of the presented method show a good agreement with the experimental data concerning the forces, moments, and the flow field. Nevertheless, for this test case enhancements can be made. Concerning the mesh generation, a Cartesian grid is beneficial for this case also, since the mesh-deformation method is working better, the better the quality of the initial mesh. For example, for a given angle of rotation, the final mesh quality remains higher and consequently, faster convergence rates are achievable. Moreover, the numerical error is also less for meshes of higher quality. For such simulations, the combination of hexahedral core meshes within the field in combination with polyhedral meshes at the boundaries is suggested as well.

List of References

[1] H. Glauert , "Airplane Propellers," in *Aerodynamic Theory*, Berlin, Springer Berlin Heidelberg, 1935, pp. 169-360.

[2] R. G. Rajagopalan and C. K. Lim, "Finite Difference Analysis of a Rotor In Hover and Axial Translation," in *24th Joint Propulsion Conference*, Massachusetts, Boston, 1988.

[3] M. Stuhlpfarrer, A. Valero-Andreu and C. Breitsamter, "Numerical and Experimental Investigation of the Propeller Characteristics of an Electrically Powered Ultralight Aircraft," *CEAS Aeronautical Journal,* vol. 8, no. 3, pp. 441-460, 2017.

[4] M. Grawunder, Aerodynamic Design Optimization for Utility Helicopter Drag Reduction, München: mediaTum, 2017.

[5] M. Stuhlpfarrer, A. Kümmel and C. Breitsamter, "Investigation of Helicopter Wake Flow Including Rotor-Head Motion," *Journal of Aircraft,* vol. 55, no. 5, pp. 2114-2126, 2018.

[6] M. Grawunder, R. Reß, V. Stein, C. Breitsamter and N. A. Adams, "Validation of a Flow Simulation for a Helicopter Fuselage Including a Rotating Rotor Head," in *New Results in Numerical and Experimental Fluid Mechanics X*, Springer International Publishing, 2016, pp. 303-313.

[7] W. Rankine, "On the mechanical principles of the action of propellers," *Transactions Institute of Naval Architects,* vol. 6, pp. 13-39, 1865.

[8] R. Froude, "On the Part Played in Propulsion by Differences of Fluid Pressure," *Transactions Institute of Naval Architects,* vol. 30, pp. 390-423, 1889.

[9] W. Froude, "On the Elmentary Relation Pitch, Slip and Propulsive Efficiency," *Transactions Institute of Naval Architects,* vol. 19, pp. 47-57, 1878.

[10] S. Drzewiecki, *Bulletin de l'Association Technique Maritime,* 1892 et seq..

[11] S. Drzewiecki, Theorie generale de l'Helice, Paris, 1920.

[12] A. Betz, "Die wichtigsten Grundlagen für den Entwurf von Luftschrauben.," *Zeitschrift für Flugtechnik und Motorluftschifffahrt,* no. 6, p. 97, 1915.

[13] G. de Bothezat, "The General Theory of Blade Screws.," *U.S. N.A.C.A. Technical Report,* no. 29, 1918.

[14] A. Fage und H. E. Collins, „An Investigation of the Magnitude of the Inlfow Velocity of the Air in the Immediate Vicinity of an Airscrew with a View to an Improvement in Accuracy of Prediction from Airfoil Data of the Perfomance of the Airscrew.," *Br. A.R.R R. and M. 328,* 1927.

[15] T. Y. Wu, "Flow Through a Heavily Loaded Actuator Disc," in *Symposium on Ship Theories, University of Hamburg, Institut für Schiffsbau*, 1962.

[16] T. Y. Wu, "Some Recent Developments in Propeller Theory," *Forschungshefte für Schiffsbau und Schiffsmaschinenbau,* vol. 12, no. 60, 1965.

[17] M. D. Greenberg und S. R. Powers, „Nonlinear Actuator Disc Theory and Flow Calculations, Including Nonuniform Loading.," *NASA CR 1672,* 1970.

[18] M. D. Greenberg, „Nonlinear Actuator Disc Theory," *Zeitschrift für Flugwissenschaften,* Bd. 3, Nr. 20, pp. 90-98, 1972.

[19] J. Conway, „Analytical Solution for the Actuator Disk with Variable Radial Distribution of Load.," *Journal of Fluid Mechanics,* Nr. 297, pp. 327-355, 1995.

[20] J. Conway, „Exakt Actuator Disk Solution for Non-Uniform Heavily Loading and Slipstream Contraction.," *Journal of Fluid Mechanics,* Nr. 365, pp. 235-267, 1998.

[21] H. A. Madsen, The Actuator Cylinder - A Flow Model for Vertical Axis Wind Turbines, Aalborg: The Insitute of Industrial Constructions and Energy Technology, Aalborg University Center, 1982.

[22] G. A. M. van Kuik, On the Limitations of Froude's Actuator Disc Concept, Eindhoven: Technische Universität Eindhoven, 1991.

[23] M. C. A. M. Peters, „The Actuator Disc with a Uniform, Axial Load Distribution: A Crtitical Study on 100 Years Doctroring on the Classical Theory (in Dutch)," Department of Physics, Technical University Eindhoven; Report R-982-A, 1989.

[24] R. Mikkelsen, Actuator Disc Methods Applied to Wind Turbines, Lynby, Denmark: DTU-Tryk, 2003.

[25] L. J. Vermeer, J. N. Sorensen and A. Crespo, "Wind Turbine Wake Aerodynamics," *Progress in Aerospace Sciences,* vol. 39, no. 6, pp. 467-510, 2003.

[26] J. G. Leishman, "Aerodynamics of Horizontal Axis Wind Turbines," in *Advances in Wind Energy Conversion Technology*, Berlin, Heidelberg, Springer, pp. 1-69.

[27] B. Sanderse, S. P. van der Pijl and B. Koren, "Review of CFD for Wind-Turbine Wake Aerodynamics," *Wind Energy,* vol. 14, no. 7, pp. 799-819, 2011.

[28] M. O. L. Hansen, J. N. Sorensen, S. Voutsinas, N. Sorensen and H. A. Madsen, "State of the Art Wind Turbine Aerodynamics and Aeroelasticity," *Progress in Aerospace Sciences,* vol. 42, no. 4, pp. 285-330, 2006.

[29] J. N. Sorensen, „General Momentum Theory for Horizontal Axis Wind Turbines," Springer Internation Publishing Switzerland, 2016.

[30] R. G. Rajagopalan and J. B. Fanucci, "Finite Difference Model for Vertical Axis Wind Turbine," *Journal of Propulsion,* vol. 1, no. 6, pp. 432-436, 1985.

[31] R. G. Rajagopalan und L. N. Wilson, „A Finite Difference Approach Suitable for Solving the Flow Fields of Rotors," in *5th Applied Aerodynamic Conference*, Monterey, 1987.

[32] R. G. Rajagopalan, T. L. Rickerl and P. C. Klimas, "Aerodynamic Interference of Vertical Axis Wind Turbines," *Journal of Propulsion,* vol. 6, no. 5, pp. 645-653, 1990.

[33] J. N. Sorensen, "Preliminary Results of Non-Linear, Unsteady Actuator Disc Model," in *4th Symposium on the Aerodynamics of Wind Turbins*, Rome, 1990.

[34] J. N. Sorensen and A. Myken, "Unsteady Actuator Disc Model for Horizontal Axis Wind Turbines," *Journal of Wind Engineering and Industrial Aerodynamics,* no. 39, pp. 139-149, 1992.

[35] J. N. Sorensen und C. W. Kock, „A Model for Unsteady Rotor Aerodynmics," *Journal of Wind Engineering and Industrial Design,* Nr. 58, pp. 259-275, 1995.

[36] C. Masson , I. Ammara and I. Paraschivoiu, "An Aerodynamic Method for the Analysis of Isolated Horizontal-Axis Wind Turbines," *International Journal of Rotating Machinery,* vol. 3, no. 1, pp. 21-32, 1997.

[37] I. Ammara, C. Leclerc and C. Masson, "A Viscous Three-Dimensional Differential/Actuator-Disk Method for the Aerdynamic Analysis of Wind Farms," *Journal of Solar Energy Engineering,* vol. 124, pp. 345-356, 2002.

[38] R. Mikkelsen, J. N. Sorensen and W. Z. Shen, "Modeling and Analysis of the Flow Filed around a Coned Rotor," *Wind Energy,* no. 4, pp. 121-135, 2001.

[39] C. Masson, A. Smaili and C. Leclerc, "Aerodynamic Analysis of HAWTs Operating in Unsteady Conditions," *Wind Energy,* vol. 4, no. 1, pp. 1-22, 2001.

[40] J. N. Sorensen and W. Z. Shen, "Numerical Modeling of Wind Turbine Wakes," *Journal of Fluids Engineering,* vol. 124, pp. 393-399, 2002.

[41] C. Leclerc and C. Masson, "Towards Blade-Tip Vortex Simulation with an Actuator-Lifting Surface Model," in *42nd AIAA Aerospace Sciences Meeting and Exhibit*, Reno, Nevada, 2004.

[42] N. Troldborg, Actuator Line Modelling of Wind Turbine Wakes, Lyngby: Technical University of Denmark, 2008.

[43] S. S. A. Ivanell, Numerical Computations of Wind Turbine Wakes, Stockholm: Royal Institute of Technology, 2009.

[44] W. Z. Shen, J. N. Sorensen und J. H. Zhang, „Actuator Surface Model for Wind Turbine Flow Computations," in *EWEC*, Mailand, 2007.

[45] W. Z. Shen, J. N. Zhang und J. N. Sorensen, „The Actuator-Surface Model: A New Navier-Stokes Based Model for Rotor Computations," *Journal of Solar Energy Engineering,* Bd. 131, pp. 011002-1-9, 2009.

[46] C. Sibuet Watters and C. Masson, "Recent Advances in Modeling of Wind Turbine Wake Vortical Structure Using a Differential Actuator Disk Theroy," *Journal of Physics: Conference Series,* vol. 75, p. 012037, 2007.

[47] C. Sibuet Watter and C. Masson, "Modeling Lifting-Device Aerodynamics Using the Actuator Surface Concept," *International Journal For Numerical Methods in Fluids,* vol. 62, pp. 1264-1298, 2010.

[48] P.-E. Rethore, Wind Turbine Wake in Atmospheric Turbulence, Roskilde: Riso National Labartory for Sustainable Energy, 2009.

[49] Y.-T. Wu und F. Porte-Agel, „Large-Eddy Simulation of Wind Turbine Wakes: Evaluation of Turbine Parametrisations," *Boundary-Layer Meteorology,* Bd. 138, Nr. 3, pp. 345-366, 2011.

[50] F. Porte-Agel, Y.-T. Wu, H. Lu und R. J. Conzemius, „Large-Eddy Simulation of Atmospheric Boundary Layer Flow Through Wind Turbines and Wind Farms," *Journal of Wind Engineering and Industrial Aerodynamics,* Bd. 99, Nr. 4, pp. 154-168, 2011.

[51] Y.-T. Wu und F. Porte-Agel, „Simulation of Turbulent Flow Inside and Above Wind Farms: Model Validation and Layout Effects," *Boundary-Layer Metereology,* Bd. 146, Nr. 2, pp. 181-205, 2013.

[52] F. Porte-Agel, H. Lu und Y.-T. Wu, „Interaction Between Large Wind Farms and the Atrmospheric Boundary Layer," *Procedia IUTUM,* Bd. 10, pp. 307-318, 2014.

[53] W. Z. Shen, W. J. Zhu und J. N. Sorensen, „Acturator Line/Navier-Stokes Computations for the MEXICO Rotor: Comparison with Detailed Measurements," *Wind Energy,* Bd. 15, Nr. 5, pp. 811-825, 2012.

[54] S. Aubrun, G. Espana, S. Loyer, P. Hayden and P. Hancock, "Is the Actuator Disc Concept Sufficient to Model the Far-Wake of a Wind Turbine?," in *Progress in Turbulence and Wind Energy IV, Springer Proceedings in Physics, vol 141.*, Berlin, Heidelberg, Springer, 2012, pp. 227-230.

[55] R. Johnstone, P. R. Spalart and G. N. Coleman, "DNS of Actuator Disk Arrays in Ekman Boundary Layers: Preliminay Results," in *Progress in Turbulence and Wind Energy IV, Springer Proceedings in Physics, vol 141.*, Berlin, Heidelberg, Springer, 2012, pp. 255-258.

[56] R. Malki, A. J. Williams, T. N. Croft and I. Masters, "A Coupled Blade Element Momentum - Computational Fluid Dynamics Model for Evaluating Tidal Stream Turbine Perfomance," *Applied Mathematical Modelling,* vol. 37, no. 5, pp. 3006-3020, 2013.

[57] E. Mahmoodi and A. P. Schaffarzyk, "Actuator Disc Modeling of the MEXICO Rotor Experiment," in *Wind Energy - Impact of Turbulence*, Berlin, Heidelberg, Springer, 2014, pp. 29-34.

[58] A. Jeromin , A. Bentamy and A. P. Schaffarzyk, "Actuator Disk Modeling of the Mexiko Rotor with OpenFOAM," in *First Symposium on OpenFOAM in Wind Energy 2013: Oldenburg, Germany, 20-21 March 2013*, Red Hook, NY, 2014.

[59] F. Castellani and A. Vignaroli, "An Application of the Actuator Disc Model for Wind Turbine Wakes Calcualions," *Applied Energy,* vol. 101, pp. 432-440, 2013.

[60] I. Masters, R. Malki, A. J. Williams und T. N. Croft, „The Influence of Flow Acceleration on Tidal Stream Turbine Wake Dynamics: A Numerical Study Using a Coupled BEM-CFD Model," *Applied Mathematical Modelling,* Bd. 37, Nr. 16-17, pp. 7905-7918, 2013.

[61] A. Makridis and J. Chick, "Validation of a CFD Model of Wind Turbine Wakes with Terrain Effects," *Journal of Wind Engineering and Industrial Aerodynamics,* vol. 123, pp. 12-29, 2013.

[62] L. A. J. Zori and R. G. Rajagopalan, "Navier-Stokes Calculations of Rotor-Airframe Interaction in Forward Flight," *Journal of the American Helicopter Society,* vol. 40, no. 2, pp. 57-67, 1995.

[63] S. Schmitz and P. K. Jha, "Modeling the Wakes of Wind Turbines and Rotorcraft Usinf the Actuator-Line Method in an OpenFoam - LES Solver," in *AHS International 69th Annual Forum*, Phoenix, Arizona, 2013.

[64] T. Nishino and R. H. J. Willden, "Low-Order Modelling of Blade-Induced Turbulence for RANS Actuator Disk Computations of Wind and Tidal Turbines," in *Wind Energy - Impact of Turbulence*, Berlin, Heidelberg, Springer, 2014, pp. 153-158.

[65] T. Kim, S. Oh and K. Yee, "Improved Actuator Surface Method for Wind Turbine Application," *Renewable Energy,* vol. 76, pp. 16-26, 2015.

[66] Q. Guo, L. Zhou and Z. Wang, "Comparison of BEM-CFD and Full Rotor Geometry Simulations for the Performance and Flow Field of a Marine Current Turbine," *Renewable Energy,* vol. 75, pp. 640-648, 2015.

[67] R. C. Storey, S. E. Norris und J. E. Cater, „An Actuator Surface Method for Efficient Transient Wind Turbine Simulation," *Wind Energy,* Bd. 18, Nr. 4, pp. 699-711, 2015.

[68] M. Edmunds, A. J. Williams, I. Masters und T. N. Croft, „An Enhanced Disk Averaged CFD Model for the Simulation of Horizontal Axis Tidal Turbines," *Renewable Energy,* Bd. 101, pp. 67-81, 2017.

[69] M. Shives and C. Crawford, "Adapted Two-Equation Turbulence Closures for Actuator Disk RANS Simulations of Wind & Tidal Turbine Wakes," *Renewable Energy,* vol. 92, pp. 273-292, 2016.

[70] R. J. A. M. Stevens, L. A. Martinez-Tossas and C. Meneveau, "Comparison of Wind Farm Large Eddy Simualtions Using Actuator Disk and Actuator Line Models with Wind Tunnel Experiments," *Renewable Energy,* vol. 116, pp. 470-478, 2018.

[71] M. H. Baba-Ahmadi and P. Dong, "Numerical Simulations of Wake Characteristics of Horizontal Axis Tidal Stream Turbine Using Actuator Line Model," *Renewable Energy,* vol. 113, pp. 669-678, 2017.

[72] M. H. Baba-Ahmadi and P. Dong, "Validation of the Actuator Line Method for Simulating Flow Through a Horizontal Axis Tidal Stream Turbine by a Comparison with Measurements," *Renewable Energy,* vol. 113, pp. 420-427, 2017.

[73] B. Ellie, G. Oger, P.-E. Guillerm and B. Alessandrini, "Simulation of Horizontal Axis Tidal Turbine Wakes Using a Weakly-Compressible Cartesian Hydrodynamic Solver with Local Mesh Refinement," *Renewable Energy,* vol. 108, pp. 336-354, 2017.

[74] J. Park, S. Oh, D. Park and M. Tai, "Improvement of Actuator Surface Method for Various Solidity Rotor Computations," in *6th Asian/Australien Rotorcraft Forum*, Kanazawa, Japan, 2017.

[75] X. Yang and F. Sotiropoulos, "A New Class of Actuator Surface Models for Wind Turbines," *Wind Energy,* vol. 21, no. 5, pp. 285-302, 2018.

[76] X. Yang, X. Zhang, Z. Li and G.-W. He, "A Smoothing Technique for Discrete Delta Funtions with Applications to Immersed Boundary Method in Moving Boundary Simulations," *Journal of Computational Physics,* vol. 228, no. 20, pp. 7821-7836, 2009.

[77] R. G. Rajagopalan and M. A. Moulton, "A Numerical Study of a Wing and Propeller in Mutual Interference," in *7th Applied Aerodynamics Conference*, Seattle, WA, 1989.

[78] R. G. Rajagopalan and S. R. Mathur, "Three Dimensional Analysis of a Rotor in Forward Flight," in *20th Fluid Dynamics, Plasma Dynamics and Lasers Conference*, Buffalo, NY, 1989.

[79] R. G. Rajagopalan and S. R. Mathur, "Three Dimensional Analysis of a Rotor in Forward Flight," *Journal of the American Helicopter Society,* vol. 38, no. 3, pp. 14-25, 1993.

[80] S. R. Mathur, Three Dimensional Analysis of a Rotor in Forward Flight, Ames, Iowa: Iowa State University, 1989.

[81] I. Fejtek and L. Roberts, "Navier-Stokes Computation of Wing/Rotor Interaction for a Tilt Rotor in Hover," *AIAA Journal,* vol. 30, no. 11, pp. 2595-2603, 1992.

[82] M. S. Chaffin and J. D. Berry, "Helicopter Fuselage Aerodynamics Under a Rotor by Navier-Stokes Simulation," *Journal of the American Helicopter Society,* vol. 42, no. 3, pp. 235-243, 1997.

[83] D. R. Poling, H. Rosenstein and G. Rajagopalan, "Use of a Navier-Stokes Code in Understanding Tiltrotor Flowfields in Hover," *Journal of the American Helicopter Society,* vol. 43, no. 2, pp. 103-109, 1998.

[84] N. Bettschart, "Rotor Fuselage Interaction: Euler and Navier-Stokes Computations with an Actuator Disk," in *AHS International 55th Annual Forum*, Montreal, 1999.

[85] Z. Tong and M. Sun, "Flow Analysis of Twin-Rotor Configuration by Navier-Stokes Simulation," *Journal of the American Helicopter Society,* vol. 45, no. 2, pp. 97-105, 2000.

[86] A. (. Filippone, "CFD Actuator Disk Solutions for a Helicotper Rotor in Hover Flight," University of Manchester, 2003.

[87] F. Le Chuiton, "Actuator Disc Modelling for Helicopter Rotors," *Aerospace Science and Technology,* vol. 8, no. 4, pp. 285-297, 2004.

[88] R. Schweikhard, "Actuator Disk for Helicopter Rotors in an Unstructured Flow Solver," *Journal of the American Helicopter Society,* vol. 52, no. 1, pp. 58-68, 2007.

[89] W. Khier, "Time-Accurate Versus Actuator Disk Simulations of Complete Helicopters," in *High Performance Computing in Science and Engineering' 05. Springer*, Berlin, Heidelberg, Springer, 2006, pp. 209-220.

[90] D. M. O'Brien and M. J. Smith, "Analysis of Rotor-Fuselage Interactions Using Various Rotor Models," in *43rd AIAA Aerospace Sciences Meeting and Exhibit*, Reno, Nevada, 2005.

[91] D. M. O'Brien, Analysis Of Computational Modeling Techniques For Complete Rotorcraft Configurations, Georgia Institute of Technology, 2006.

[92] T. Renaud, D. O'Brien, M. Smith and M. Potsdam, "Evaluation of Isolated Fuselage and Rotor-Fuselage Interaction Using Compuational Fluid Dynamics," *Journal of the American Helicopter Society,* vol. 53, no. 1, pp. 3-17, 2008.

[93] B. Benoit, A.-M. Dequin, K. Kampa, W. Grünhagen, P.-M. Basset and B. Gimonet, "HOST, a General Helicopter Simulation Tool for Germany and France," in *AHS 55th Annual Forum*, Virginia Beach, Virginia, 2000.

[94] A. Filippione and R. Mikkelsen, "Advances in CFD & Actuator Disk Models for Helicopter Aerodynamics," in *35th European Rotorcraft Forum 2009*, Hamburg, Germany, 2009.

[95] Y.-H. Kim and S.-O. Park, "Navier-Stokes Simulation of Unsteady Rotor-Airframe Interaction with Momentum Source Method," *International Journal of Aeronautical and Space Sciences,* vol. 10, no. 2, pp. 125-133, 2009.

[96] Y.-H. Kim and S.-O. Park, "Numerical Simulation of Rotor-Body Interaction with a New Momentum Source Method," in *1st Asian Australien Rotorcraft Forum and Exhibition 2012* , Busan, Korea, 2012.

[97] Y. H. Kim and S. O. Park, "Unsteady Momentum Source Method for Efficient Simulation of Rotor Aerodynamics," *Journal of Aircraft,* vol. 50, no. 1, pp. 324-327, 2013.

[98] T. Kim, S. Oh, K. Yee and H. J. Kang, "The Validation of OpenFOAM on the External Flow and the Extension of Algorithm for Rotor Inflow Analysis based on Actuator Disk Model," in *1st Asian Australien Rotorcraft Forum and Exhibition* , Busan, Korea, 2012.

[99] Y. Zhang, L. Ye and S. Yang, "Numerical Study on Flow Fields and Aerodynamics of Tilt Rotor Aircraft in Conversion Mode Based on Embedded Grid and Actuator Model," *Chinese Journal of Aeronautics,* vol. 28, no. 1, pp. 93-102, 2015.

[100] P. Li, Q. Zhao and Q. Zhu, "CFD Calculations on the Unsteady Aerodynamic Characteristics of a Tilt-Rotor in Conversion Mode," *Chinese Journal of Aeronautics,* vol. 28, no. 6, pp. 1593-1605, 2015.

[101] W. J. F. Koning, C. W. J. Acree and G. Rajagopalan, "Using RotCFD to Predict Isolated XV-15 Rotor Performance," in *AHS Technical Meeting on Aeromechanics Design for Vertical Lift*, San Francisco, CA, 2016.

[102] W. Johnson, "www.johnson-aeronautics.com," [Online]. Available: www.johnson-aeronautics.com/documents/CAMRADIIvolumeII.pdf. [Accessed 18 04 2021].

[103] D. Linton, G. Barakos, R. Widjaja and B. Thornber, "A New Actuator Surface Model with Improved Wake Model for CFD Simulations of Rotorcraft," in *AHS International 73rd Annual Forum & Technology Display*, Fort Worth, Texas, 2017.

[104] A. Raichle, Flusskonservative Diskretisierung des Wirkscheibenmodells als Unstetigkeitsfläche, Braunschweig: DLR-Forschungsbericht, 2017.

[105] J. J. Chiew and M. J. Aftomis, "A Conservative, Scalable, Space-Time Blade Element Rotor Model for Multi-Rotor Vehicles," in *AHS Technical Conference on Aeromechanics Design for Transformative Vertical Flight*, San Francisco, CA, 2018.

[106] B. Ortun, "A Coupled RANS/Lifting-Line Analysis for Modelling the Aerodynamics of Distributed Propulsion," in *AHS Technical Conference on Aeromechanics Design for Transformative Vertical Flight*, San Francisco, CA, 2018.

[107] A. Bottai, J. F. Horn, I. Oruc and J. Shipman, "Fully Coupled Flight Dynamics/CFD Simulations of a Helicopter with Actuator Disk Models for the Main Rotor and Tail Rotor," in *AHS Technical Conference on Aeromechanics Design for Transformative Vertical Flight*, San Francisco, 2018.

[108] C. Wauquiez, "Shape Optimization of Low Speed Airfoils using MATLAB and Automatic Differentiation," Royal Institute of Technology, Stockholm, 2000.

[109] J. Katz and A. Plotkin, Low-Speed Aerodynmics, n.p.: McGraw-Hill, 1991.

[110] J. N. Sorensen, W. Z. Shen and X. Munduate, "Analysis of Wake States by a Full-Field Actuator Disc Model," *Wind Energy,* vol. 1, no. 2, pp. 73-88, 1998.

[111] L. Prandtl, "Theorie des Flugzeugtragflügels im zusammendrückbaren Medium.," *Luftfahrt-Forschung,* vol. 13, pp. 313-319, 1936.

[112] ANSYS, Inc., "ANSYS Acadamic Research, Release 16.0, Help System," 2016.

[113] H. Schlichting and E. Truckenbrodt, Aerodynamik des Flugzeuges, 3 ed., vol. II, Berlin, Heidelberg: Springer, 2001.

[114] F. R. Menter, „Two-equtation Eddy-Viscosity Turbulence Models for Engeneering Applications," *AIAA Journal,* Bd. 32, Nr. 8, pp. 1598-1605, 1994.

[115] M. Stuhlpfarrer, A. Valero-Andreu and C. Breitsamter, "Numerical and Experimental Investigation of the Propeller Characteristics of an Electrically Powered UltraLight Aircraft," in *DLRK*, Augsburg, 2014.

[116] M. Stuhlpfarrer, A. Kümmel, A. Valero-Andreu and C. Breitsamter, "Numerische Simulation zur Propeller-Aerodynamik ein Ultraleicht-Elektroflugzeuges," in *Conference Proceedings - ANSYS Conference & 32. CADFEM Users' Meeting 2014, NCC Ost, Nürnberg Messe*, Grafing, 2014.

[117] R. Steijl and G. N. Barakos, "Computational Study of Helicopter Rotor-Fuselage Aerodyanmic Interaction," *AIAA Journal,* vol. 47, no. 9, pp. 2143-2157, 2009.

[118] P. W. Li Xu, "High Order Accurate and Low Dissipation Method for Unsteady Compressible Viscous Flow Computation on Helicopter Rotor in Forward Flight," *Journal of Computational Physics,* vol. 258, pp. 470-488, 2014.

[119] F. Vogel, Aerodynamische Analysen an Helikopter Zell-Ausleger Konfigurationen, München: Verlag Dr. Hut, 2016.

[120] M. Grawunder, R. Reß and C. Breitsamter, "Optimized Skid-Landing-Gears for Twin-Engine-Light-Utility helicopter," in *39th European Rotorcraft Forum 2013*, Moscow, 2013.

[121] M. Grawunder, R. Reß and C. Breitsamter, "Helicopter Aft-Body Drag Reduction by Passive Flow Control," in *40th European Rotorcraft Forum 2014*, Southampton, 2014.

[122] F. De Gregorio, "Helicopter Fuselage Model Drag Reduction by Active Flow Control Systems," *Journal of the American Helicopter Society,* vol. 64, no. 2, pp. 1-15, 2019.

[123] R. Shenoy, M. Holmes, M. J. Smith and N. Komerath, "Scaling Evaluations on the Drag of a Hub System," *Journal of the American Helicopter Society,* vol. 58, no. 3, pp. 1-13, 2013.

[124] D. Reich, R. Shenoy, M. Smith and S. Schmitz, "A Review of 60 Years of Rotor Hub Drag and Wake Physics: 1954-2014," *Journal of the American Helicopter Society,* vol. 61, no. 022007, pp. 1-17, 2016.

[125] S. Schmitz, D. Reich, M. J. Smith und L. R. Centolanza, „First Rotor Hub Flow Prediction Workshop Experimental Data Campaings and Computational Analysis,“ in *AHS International 73rd Annual Forum & Technology Display*, Fort Worth, Texas, 2017.

[126] D. B. Reich, B. R. Elbing, C. R. Berezin und S. Schmitz, „Water Tunnel Flow Diagnostics of Wake Structures Downstream of a Model Helicopter Rotor Hub,“ *Journal of the American Helicopter Society,* Bd. 59, Nr. 032001, pp. 1-12, 2014.

[127] J. G. Coder und N. F. Foster, „Structured, Overset Simulations for the 1st Rotor Hub Flow Workschop,“ in *AHS International 73rd Annual Forum & Technology Display*, Fort Woth, Texas, 2017.

[128] J. G. Coder, P. A. Cross and M. J. Smith, "Turbulence Modeling Strategies for Rotor Hub Flows," in *AHS International 73rd Annual Forum & Technology Display*, Fort Worth, Texas, 2017.

[129] E. M. Lee-Rausch and R. T. Biedron, "FUN3D Airloads Predictions for the Full-Scale UH-60A Airloads Rotor in a Wind Tunnel," *Journal of the American Helicopter Society,* vol. 59, no. 3, pp. 1-19, 2014.

[130] U. Kowarsch, C. Öhrle, M. Keßler and E. Krämer, "Aeroacoustic Simulation of a Complete H145 Helicopter in Descent Flight," *Journal of the American Heilcopter Society,* vol. 61, no. 4, pp. 1-13, 2016.

[131] U. Schäferlein (né Kowarsch), M. Keßler and E. Krämer, "Aeroelastic Simulation of the Tail Shake Phenomenon," *Journal of the Americal Helicopter Society,* vol. 63, no. 3, pp. 1-17, 2018.

[132] N. M. Chaderjian, "Navier-Stokes Simulation of UH-60A Rotor/Wake Interaction Using Adaptive Mesh Refinement," in *AHS International 73rd Annual Forum & Technology Display*, Fort Worth, Texas, 2017.

[133] R. Steijl, G. Barakos and K. Badcock, "A Framework for CFD Analysis of Helicopter Rotors in Hover and Forward Flight," *International Journal for Numerical Methods in Fluids,* no. 51, pp. 819-847, 2006.

[134] R. Renzoni, A. D'Alascio, N. Kroll, N. Peshkin, M. Hounjet, J.-C. Boniface, L. Vigevano, L. Morino, C. B. Allen, K. J. Badcock, L. Mottura, M. Scholl and . E. Kokkalis, "EROS - A common European Euler Code for the analysis of the helicopter rotor flowfield," *Progress in Aerospace Sciences,* no. 36, pp. 437-485, 2000.

[135] K. Pahlke and B. G. van der Wall, "Chimera Simulations of Mulitbladed Rotors in High-Speed Forward Flight with Weak Fluid-Structure Coupling," in *29th European Rotorcraft Forum*, Friedrichshafen, 2003.

[136] H. Pomin and S. Wagner, "Navier-Stokes Analysis of Helicopter Rotor Aerodynamics in Hover and Forward Flight," *Journal of Aircraft,* vol. 5, no. 39, pp. 813-821, 2002.

[137] H. Pomin and S. Wagner, "Aeroelastic Analysis of Helicopter Rotor Blades on Deformable Chimera Grids," *Journal of Aircraft,* vol. No.3, no. Vol 41, pp. 577-584, 2004.

[138] M. Potsdam, H. Yeo and W. Johnson, "Rotor Airloads Prediction Using Loose Aerodynamic/Structural Coupling," *Journal of Aircraft,* vol. 3, no. 43, pp. 732-742, 2006.

[139] M. Dietz, M. Keßler, E. Krämer and S. Wagner, "Tip Vortex Conservation on a Helicopter Main Rotor Using Vortex-Adapted Chimera Grids," *AIAA Journal,* vol. 45, no. 8, pp. 2062-2074, 2007.

[140] L. Dubac, F. Cantariti, M. Woodgate, B. Gribben, K. J. Badcock and B. E. Richards, "A Grid Deformation Technique for Unsteady Flow Computations," *International Journal for Numerical Methods in Fluids,* vol. 32, no. 3, pp. 285-311, 2000.

[141] Y. Park and O. Kwon, "Simulation of Unsteady Rotor Flow Field using Unstructured Adaptive Sliding Meshes," *Journal of the American Helicopter Society,* vol. 4, no. 49, pp. 391-400, 2004.

[142] F. Dehaeze and G. N. Barakos, "Mesh Deformation Methods for Rotor Flows," *Journal of Aircraft,* vol. 49, no. 1, pp. 82-92, 2012.

[143] M. Bebesel, A. D'Alascio, S. Schneider, S. Guenther, F. Vogel, C. Wehle and D. Schimke, "Bluecopter Demonstrator - An Approach of Eco-Efficient Helicopter Design," in *41st European Rotorcraft Forum*, München, 2015.

[144] Q. Zhang, A. Garavello, A. D'Alascio and D. Schimke, "Advanced CFD-based Optimization Methods Applied to the Industrial Design Process of Airframe Components at Airbus Helicopters," *American Helicopter Society 70th Annual Forum,* 2014.

[145] M. Stuhlpfarrer, A. Kümmel, J. Steck and C. Breitsamter, "Numerical and Experimental Investigations of Twin-Engine-Light Utility Helicopter Wake Flow," in *Proceedings of the 41st European Rotorcraft Forum*, München, 2015.

[146] F. Menter and Y. Egorov, "The Scale-Adaptive Simulation Method for Unsteady Turbulent Flow Predictions. Part 1: Theory and Model Description," *Journal Flow Turbulence and Combustion,* vol. 85, pp. 113-138, 2010.

[147] Y. Egorov, F. R. Menter, R. Lechner and D. Cokljat, "The Scale-Adaptive Simulation Method for Unsteady Turbulent Flow Predictions. Part 2: Application to Complex Flows," *Flow Turbulence Combustion,* vol. 85, pp. 139-165, 2010.

[148] M. Grawunder, R. Reß and C. Breitsamter, "Thermographic Transition Detection for Low-Speed Wind-Tunnel Experiments," *AIAA Journal,* vol. Vol. 54, no. No. 6, pp. 2011-2015, 2016.

[149] M. Stuhlpfarrer, A. Kümmel, J. Steck and C. Breitsamter, "Numerical and Expermental Investigations of Twin-Engine-Light Utility Helicopter Wake Flow," in *DLRK*, Rostock, 2015.

[150] M. Stuhlpfarrer, A. Kümmel, A. Buzica and C. Breitsamter, "Experimentelle und numerische Untersuchungen zur Nachlaufströmung einer Hubschrauberkonfiguration," in *Jahresbericht 2015 zum 17.STAB-Workshop*, Göttingen, 2015.

[151] M. Stuhlpfarrer, A. Kümmel and C. Breitsamter, "Numerische und experimentelle Untersuchungen der Nachlaufströmung einer Leichthubschrauberkonfiguration," in *Conference Proceedings - ANSYS Conference & 34. CADFEM Users' Meeting 2016, NCC Ost, Nürnberg Messe*, Grafing, 2016.

[152] M. Stuhlpfarrer, A. Kümmel and C. Breitsamter, "Numerical and Experimental Investigations of Twin-Engine-Light Utility Helicopter," in *Jahresbericht 2016 zum 20.DGLR-Fach-Symposium der STAB*, Göttingen, 2016.

[153] U. Kowarsch, M. Kessler and M. Krämer, "CFD-Simulation of the Rotor-Head Influence to the Rotor-Fuselage Interaction.," in *40th European Rotorcraft Forum*, Southampton, United Kingdom, 2014.

[154] M. Foucaut, J. Carlier und M. Stanislas, „PIV optimization for the study of the turbulent flow using spectral analysis,“ *Measurement Science and Technology,* Bd. 15, pp. 1046-1058, 2004.

[155] A. Bauknecht, B. Ewers, O. Schneider and M. Raffel, "Blade tip vortex measurements on actively twisted rotor blades," *Experiments in Fluids,* vol. 58, no. 5, p. 49, 2017.

[156] E. L. Houghton and P. W. Carpenter, Aerodynamics for Engineering Students, Oxford: Elsevier Butterwoth-Heinemann, 2003.

[157] B. Thwaites, "Approximate Calculation of the Laminar Boundary Layer," *Aero Quart,* vol. Vol.1, p. 245, 1949.

[158] T. Cebeci and P. Bradshw, Momentum Transfer in Boundary Layers, Washington: Hemisphere Publishing Cooporation, 1977.

[159] R. Michel, "Étude de la transition sur les profils d'ailes," *Tech. rep. 1/1578A ONERA,* 1951.

[160] M. R. Head, "Entrainment in the Turbulent Boundary Layers," *ARC R&M 3152,* 1958.

[161] H. Ludwieg and W. Tillmann, "Investigations of the Wall Shearing Stress in Turbulent Boundary Layers," *NACA Rept. TM 1285,* 1949.

[162] H. B. Squire and D. Young, "The Calculation of the Profile Drag of Airfoils," *Tech. rep. 1838. R. & M.,* 1938.

[163] M. Hepperle, "JavaFoil," [Online]. Available: http://www.mh-aerotools.de. [Accessed 20 04 2016].

[164] M. Drela and H. Youngren, "XFOIL Subsonic Airfoil Development System," [Online]. Available: http://web.mit.edu/drela/Public/web/xfoil/. [Accessed 22 07 2016].

[165] M. K. Rwigema, "Propeller Blade Element Momentum Theory With Vortex Wake Deflection," in *27th International Congress of the Aeronautical Sciences*, South Africa, 2010.

[166] A. Kümmel, M. Stuhlpfarrer and C. Breitsamter, "Methoden zur Propellerberechnung und -optimierung hinsichtlich maximalem Wirkungsgrad," in *Jahresbericht 2017 zum 18.STAB-Workshop*, Göttingen, 2017.

A Appendix

A.1 Normalized Cosine-Squared Function

Within this thesis, the normalized cosine-squared function is applied for different purposes due to its well-suited properties for the presented applications. It is used as a smoothing function for the actuator disk approach as well as the analytical grid-deformation method. The important properties are described as follows.

The cosine function $\cos(x_i)$ is a continuous function and is defined for all real numbers $x_i \in \mathbb{R}$ and subsequently, the cosine-squared function $\cos(x_i)^2$ as well. More accurate, the function $f(x) = \cos(x_i)^2$ is a mapping of the domains according to $f: \mathbb{R} \rightarrow \mathbb{R}_0^+$, in particular, $f(x_i) \in [0,1]$. In addition, the function $f(x)$ is a continuously differentiable function. Moreover, it is an even function with the maxima at $x_i = k \cdot \pi$ with $k \in \mathbb{Z}$. In the context of this work solely the domain of $x_i = \left[-\frac{\pi}{2}, \frac{\pi}{2}\right]$is of interest.

Another useful property is that after a substitution of $x_i = \frac{x\pi}{2}$, the integral

$$F = \int_{-1}^{1} \left(cos\left(\frac{x\pi}{2}\right)\right)^2 dx = 1, \tag{A.1}$$

over the interval of $x \in [-1,1]$ results to unity. Consequently, due to its even character, the integral over $x \in [0,1]$ gives $F = 0.5$. Figure 129 shows the normalized cosine-squared function for $x \in [-1,1]$. One can easily see the results of the integration by considering symmetry.

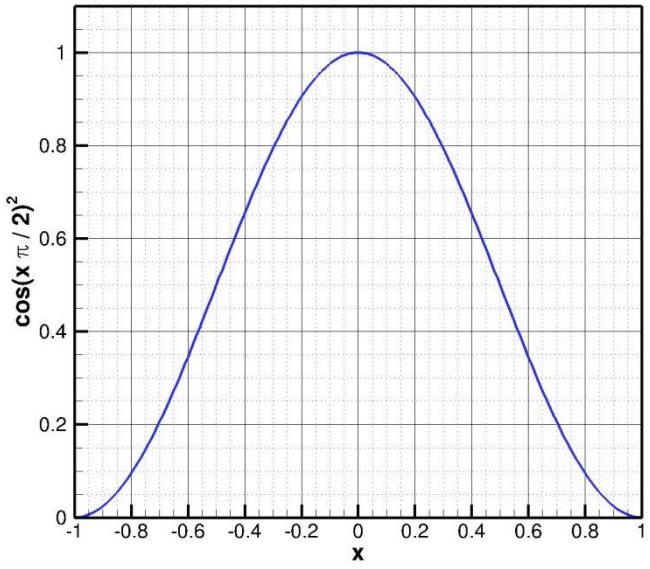

Figure 129: Normalized raised-cosine function for $x \in [-1, 1]$.

Piecewise Defined Smoothing/Distribution Function Based on the Raised Cosine

As presented in this thesis, some applications require a rectangular function for prescribing certain quantities. The rectangular function is defined as

$$\Pi(x) = \begin{Bmatrix} 0, & |x| > \frac{1}{2} \\ \frac{1}{2}, & |x| = \frac{1}{2} \\ 1, & |x| < \frac{1}{2} \end{Bmatrix}. \tag{A.2}$$

The function show discontinuities at $|x| = 1/2$. However, discontinuities in distributions functions in computational fluid dynamics lead to oscillations by using numerical schemes of reduced order.

The unitary Fourier transform of the rectangular function results in the sinc function. Consequently, it can be recognized that the rectangular function includes all wave number in spectral space. Applying a numerical scheme of reduced order which does not exactly handle all occurring wave numbers in spectral space appropriately, changes in phase and magnitude of the function lead to spurious oscillations in physical space.

In order to reduce spurious oscillations, the rectangular function is combined with a squared-cosine function to obtain the well-known raised-cosine function. The rectangular function is cut at the locations of the discontinuities and the positive and a negative part of the raised cosine is added at the respective position. The equation reads

$$F_{smooth} = \begin{Bmatrix} 0, & |x| > \frac{3}{2} \\ cos\left(\frac{(|x| - 0.5)\,\pi}{2}\right)^2, & |x| \geq \frac{1}{2}\ and\ |x| \leq \frac{3}{2} \\ 1, & |x| < \frac{1}{2} \end{Bmatrix}. \tag{A.3}$$

For a better imagination, the function is presented in Figure 130. Integrating this function over the interval of $x \in (-\infty, \infty)$ the solution is given to

$$F = \int_{-\infty}^{\infty} F_{smooth}\, dx = 2. \tag{A.4}$$

Obviously, the integral reaches the same results as a rectangular function with the discontinuities set at $|x| = 1$. After scaling the function by $1/2$, unity is obtained. That is a useful property, for a distribution function. Furthermore, the function F_{smooth} is bounded as well as continuously differentiable function. Moreover, the spectral representation is not a pure sinc function anymore and in particular, the spectral content at high wave numbers is decreased.

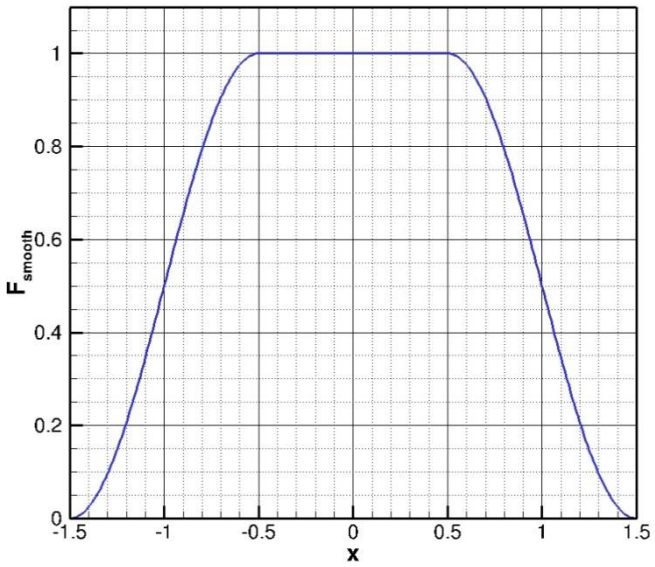

Figure 130: Normalized smoothing function for $x \in [-1.5, 1.5]$.

Moreover, to obtain a more general function for the application, additional scaling factors can be applied to vary the width of the rectangular part and the cosinusoidal part of the function. For this purpose, the function is modified by inventing the parameters d_1 and d_2 that represents the position of the start and the end of the cosinusoidal part. For the mesh deformation, the function is applied in accordance with this definition which reads

$$F_{smooth} = \left\{ \begin{array}{c} 0, \quad |x| > d_2 \\ cos\left(\frac{\pi}{2}\frac{(|x| - d_1)}{(d_2 - d_1)}\right)^2, |x| \geq d_1 \; and \; |x| \leq d_2 \\ 1, \quad |x| < d_1 \end{array} \right\}. \tag{A.5}$$

However, as easily can be determined, the integral of the function is not normalized. Furthermore, the center of the function is set to $x = 0$. Both properties are appropriate for a smoothing function, however, the distribution function has to allow for varying the center of the distribution as well as the integration has to provide unity. Since the function for the applications is assumed to be symmetrically, the set of parameters has to consist out of the center of the function d_c, the width of the underlying rectangular function d_w, and the width of the cosinusoidal part d_s. Finally, the distribution function gives

$$\mathrm{F}_{distr} = \left\{ \begin{array}{c} 0, \quad |x - d_c| > d_2 \\ \frac{1}{d_w}\cos\left(\frac{\pi}{2}\frac{(|x - d_c| - d_1)}{d_s}\right)^2, |x - d_c| \geq d_1 \; \wedge |x - d_c| \leq d_2 \\ \frac{1}{d_w}, \quad |x - d_c| < d_1 \end{array} \right\}, \tag{A.6}$$
$$with \; d_1 = \frac{d_w - d_s}{2} \; and \; d_2 = \frac{d_w + d_s}{2}.$$

The function fulfills the requirements formulated above. The integral over the interval of x ∈ $(-\infty, \infty)$ leads to unity independent of the parameters d_c, d_w, and d_s.

A.2 Panel Method Coupled with Boundary Layer Integration Method

A.2.1 Panel Method

The linear-strength vortex panel method according to Katz and Plotkin [109] is applied and described briefly. A more detailed description can be found in Stuhlpfarrer et al. [3]. The impermeability constraint is fulfilled at the boundaries by a Neumann boundary condition that reads

$$u_n = \frac{\partial \phi}{\partial \boldsymbol{n}} = 0, \tag{A.7}$$

with the surface orthogonal vector $\boldsymbol{n}$. The potential ϕ_P at a certain field point $P(x, y)$ is obtained by the freestream potential ϕ_∞ and the potential caused by the distribution of vortices with the strength ϕ_V located at the boundary of the airfoil:

$$\phi_P = \underbrace{U_\infty x + V_\infty y}_{\phi_\infty} + \int_S \underbrace{\frac{\gamma}{2\pi}\theta}_{\phi_V} ds \tag{A.8}$$

Applying the Neumann boundary condition and dividing the airfoil into n_p panels gives

$$(U_\infty, V_\infty) \cdot \boldsymbol{n} + \sum_{i=1}^{n_p} \int_{S_p} \frac{\partial \phi_V}{\partial \boldsymbol{n}} ds = (U_\infty, V_\infty) \cdot \boldsymbol{n} + (u, v) \cdot \boldsymbol{n} = 0. \tag{A.9}$$

with u and v being the induced velocity components due to vortex distribution at a certain panel. For the linear-strength vortex distribution, the vortex strength in the local panel coordinate system is defined as $\gamma(x_p) = \gamma_0 + \gamma_1 \cdot x_p$ and subsequently, the velocity components in the panel coordinate system read

$$u_p = \frac{y_p}{2\pi}\left(\frac{y_{j+1} - y_j}{x_{j+1} - x_j}\right) ln\frac{r_{j+1}}{r_j} + \frac{\gamma_j(x_{j+1} - x_j) + (\gamma_{j+1} - \gamma_j)(x_p - x_j)}{2\pi(x_{j+1} - x_j)}(\theta_{j+1} - \theta_j), \tag{A.10}$$

$$v_p = -\frac{\gamma_j(x_{j+1} - x_j) + (\gamma_{j+1} - \gamma_j)(x_p - x_j)}{2\pi(x_{j+1} - x_j)} ln\frac{r_j}{r_{j+1}} + \frac{y_p}{2\pi}\left(\frac{y_{j+1} - y_j}{x_{j+1} - x_j}\right)\left[\frac{x_{j+1} - x_j}{y_p} + (\theta_{j+1} - \theta_j)\right]. \tag{A.11}$$

Applying these equation to all panels, redistributing and transforming it into the global coordinate system, provides the influence coefficient matrix

$$a_{ij} = (u, v)_{i,j} \cdot n_i \tag{A.12}$$

as a set of N algebraic equations with the right hand side

$$RHS_i = -(U_{\infty,} V_{\infty,}) \cdot (cos\,\alpha_i, -sin\,\alpha_i). \tag{A.13}$$

In addition, the Kutta condition on the trailing edge is applied as follows

$$\gamma_1 + \gamma_{N+1} = 0. \tag{A.14}$$

The system of equations is solved by a lower-upper (LU) decomposition with partial pivoting (PLU) due to the higher numerical stability and the low computational effort of $O\left(\frac{2}{3}n^3\right)$ compared to other methods. With the resulting vortex distribution, the local tangential velocity at each panel is obtained and the pressure coefficient distribution can be calculated according to

$$c_p = 1 - \frac{U_e}{U_\infty}. \tag{A.15}$$

Finally, lift and drag coefficient are generated by summation and coordinate frame rotation.

A.2.2 Boundary Layer Integration Method

The boundary layer integration method is based on a similar formulation as described by Wauquiez [108]. Consider Prandtl´s boundary layer equations for incompressible flow [156]. Combining them to one integral equation and solving it along the y-direction from $y = 0$ to $y \to \infty$, the Kármán integral momentum equation results. Introducing the shape factors H, the latter equation reads

$$\frac{d\theta}{dx} + \frac{\theta}{U_e}(2 + H)\frac{dU_e}{dx} = \frac{1}{2}C_f. \tag{A.16}$$

Multiplying (A.16) with $\frac{\theta U_e}{\nu}$, substituting $L = \frac{\theta U_e}{\nu}\frac{C_f}{2}$, and $\lambda = \frac{Re\theta^2}{\nu}\frac{dU_e}{dx}$ gives

$$\frac{U_e}{\nu}\frac{d^2\theta}{dx^2} = 2(L - (2 + H)\lambda). \tag{A.17}$$

Using Thwaites´s approach [157, 158] for approximating the right hand side with $2(L - (2 + H)\lambda) \approx 0.45 - 6\lambda$ leads to

$$\frac{1}{\nu}\frac{d}{dx}(\theta^2 U_e^6) = 0.45 U_e^5. \tag{A.18}$$

The equation can be integrated by a 5-th order Gaussian quadrature along the streamwise direction of the airfoil, starting form the known value at the stagnation point. With the knowledge of θ, λ can be evaluated. Applying the semi-empirical formulas of Cebeci and Bradshaw [158], $H(\lambda)$ and $C_f(\lambda)$ can be determined. $C_f(\lambda)$ is used to check if laminar separation occurs. If separation is detected, a model for turbulent boundary layers is utilized downstream of the separation point. In addition, Michel´s criterion [159] is applied to estimate if laminar-turbulent transition occurs. Therefore, a critical Reynolds number based on the distance from the stagnation point is evaluated. If the critical Reynolds number is reached, laminar-turbulent transition is assumed. The formula reads

$$Re_\theta > Re_{\theta krit} = 1.174\left(1 + \frac{22400}{Re_x}\right) {Re_x}^{0.46}. \tag{A.19}$$

The turbulent boundary layer is estimated by Head´s model [160]. Therefore, the volume rate of fluid within the boundary layer at the streamwise position x is combined with the definition of the displacement thickness according to

$$\delta^* = \delta - \int_0^{\delta(x)} \frac{u(x,y)}{U_e}\, dy. \tag{A.20}$$

Using the shape factor H_1 and including the experimental data of Cebeci and Bradshaw [158], the following equations are obtained,

$$\frac{1}{U_e}\frac{d}{dx}(U_e \theta H_1) = 0.0306(H_1 - 3)^{-0.653}, \tag{A.21}$$

$$H_1 = \begin{cases} 3.3 + 0.8234(H - 1.1)^{-1.287} & if\ H \leq 1.6 \\ 3.3 + 1.5501(H - 0.6778)^{-3.064} & if\ H \geq 1.6. \end{cases} \tag{A.22}$$

The skin friction is determined by the Ludwig-Tillman skin friction law [161],

$$C_f = 0.246 \cdot 10^{-0.678H} \cdot Re_\theta^{-0.268}. \tag{A.23}$$

The equations are integrated from the transition point to the trailing edge, or in the case of turbulent separation, to the point of the separation. The drag coefficient is calculated with the Squire-Young [162] formula that reads

$$C_D = [2(\theta_{TE}/c)(U_e/U_\infty)_{TE}^{\frac{H_{TE}+5}{2}}]_{UP} + [2(\theta_{TE}/c)(U_e/U_\infty)_{TE}^{\frac{H_{TE}+5}{2}}]_{DOWN}. \tag{A.24}$$

A.2.3 Coupling of Panel Method with Boundary Layer Integration Method

A one-way coupling between the panel method (A.2.1) and a boundary layer integral method (A.2.2) (PanBL) is applied within this thesis. The implemented approach is based on [108]. At first, the inviscid potential flow around the airfoil is calculated. Secondly, the resulting boundary layer parameters are integrated along the streamwise direction and finally, the drag coefficient c_D is determined. No feedback of the calculated boundary layer displacement thickness to the panel method is provided. In addition, the Prandtl-Glauert compressibility correction can be applied for the panel method. Additionally, the Java-Foil stall correction [163] is applied in order to approximate the effect of the separation on lift and drag. A brief validation of the method with Xfoil [164] results for a NACA 0012 airfoil is presented in [3]. For angles of attack $\alpha < 8$, a good agreement is achieved between both methods. However, in the stall region, PanBL overestimates the lift coefficient drastically and the drag coefficient slightly.

A.3 Propeller Thrust and Torque Calculation with Blade Element Momentum Theory

A simple and fast tool to evaluate the thrust and torque of the propeller could by generated by the application of the blade element momentum theory. In the course of this thesis, the blade element theory has been coupled with PanBL (PropPanBL) in the well-known manner to obtain fast results. Within this code, the equations derived for the blade element momentum theory presented in chapter 2.4 are solved. However, for solving the equations numerically, the infinitely small differences have to be modified to finite differences $d \rightarrow \Delta$.

$$\Delta T = 4\,\pi\,\rho\,V^2(1+a)a\,r_P\,\Delta r_p,$$

$$\Delta Q = 4\,\pi\,\rho\,V\,\Omega(1+a)a' r_P^3\,dr_p.$$

$$\Delta T = \frac{1}{2}\,\rho\,V_{rel}^2 c\,B(\Delta c_L\cos(\phi) - \Delta c_D\sin(\phi))\,\Delta r, \tag{A.25}$$

$$\Delta Q = \frac{1}{2}\,\rho\,V_{rel}^2 c\,B\,(\Delta c_L\sin(\phi) + \Delta c_D\cos(\phi))\,r_P\,\Delta r_P.$$

Following the iterative procedure to solve this equation described in chapter 2.4 and summing the values for all sections accordingly provides the overall thrust and torque of the propeller.

$$T = \sum \Delta T,$$

$$Q = \sum\,\Delta Q. \tag{A.26}$$

In addition, to this procedure a modified set of equations can be solved, alternatively. A problem by solving the above presented equations for a and a' occurs if the inflow velocity becomes small. Since the inflow factors are normalized by the inflow velocity located infinite far upstream of the propeller. That means that the inflow factor will tend to infinity. In this case an absolute formulation has to be applied. The first two equations of the above presented system therefore are written as follows.

$$\Delta T = 4\,\pi\,\rho\,(V+u_{ind})u_{ind}\,r_P\,\Delta r_p,$$

$$\Delta Q = 4\,\pi\,\rho\,\Omega(V+u_{ind})w_{ind}\,r_P^3\,dr_p. \tag{A.27}$$

In this formulation, the values for u_{ind} and w_{ind} solved. The advantage of this formulation is that it allows for negative inflow velocities also. The requirement due to the chosen directions of the velocity vectors and to obtain correct signs is that $(V+u_{ind}) > 0$. The inequality implies $u_{ind} > -V$. This inequality imposes that the induced velocity for each section has to be higher than the negative inflow velocity. The result appears to be obvious; since the assumption for the theory is that there is no reversed flow through the propeller plane. Moreover, the results can be questionable if $-V \approx u_{ind}$, since the assumption of stream tubes and its neglected mutual interference may not be satisfied anymore. Nevertheless, the iterative solution can be obtained by rearranging the first equation to solve for u_{ind} and the second equation to solve for w_{ind}. However, the restrictions have to be kept in mind.

In order to estimate the thrust and torque for inclined inflow conditions, a simple modeling approach has been implemented in PropPanBL as well. This has been conducted with the contribution of A. Kümmel. For both of the formulations presented above, a simple vector decomposition of the inflow velocities depending on the angle of incidence of the propeller plane and the azimuthal angle of the propeller element is conducted. Therefore, the propeller disc is divided along the circumferential direction as well as in the radial direction. This approach is able to provide an approximation of the lateral moments caused by the propeller.

In order to optimize the shape of the propeller for prescribed airfoil geometries, a Betz optimum solver has been implemented according to [165] by Kümmel et al. [166] that has been used to generate the geometry for the generic test case.

A.4. Wind Tunnel A

The test section dimensions are $1.8\ m$ in height, $2.4\ m$ in width, and $4.8\ m$ in length. The closed return wind tunnel (Göttingen type) is operated with an open test section for the investigations conducted within this thesis. The uncertainty of the freestream velocity in the empty test section is less than 0.2%. The turbulence level is determined to be less than 0.4% and the uncertainty in the spatial and temporal mean velocity distribution less than 0.067%. [145]

Force and Moment Measurements

The aerodynamic forces and moments are measured by an external six-component underfloor balance. The measuring range for the forces reads $F_x = \pm 1500\ N$, $F_y = \pm 3000\ N$, and $F_z = \pm 3000\ N$ in the streamwise, lateral, and vertical direction, respectively. The measuring range for the moments are $M_x = \pm 700\ Nm$, $M_y \pm\ 500\ Nm$, and $M_z = \pm 700\ Nm$ for the rolling, pitching, and yawing moments, respectively. The load cell accuracy based on maximum loads provides a maximum error of less than 0.025% related to the full measurement range. In addition, the balance allows for a rotation of the model about the vertical axis.

In the course of this thesis the external balance has been applied for providing the reference data for the numerical simulations. It has been used for the propeller test case as well as the helicopter test case whereas different mounting strategies have been applied.

Wake Field Measurement

The wake flow field measurements are conducted with the Stereo-Particle Image Velocimetry technique (PIV). This method allows for generating velocity field data within defined planes. The PIV system used for the investigations in the course of this thesis contains a double cavity pulsed Nd:YAG laser. The maximum output energy per pulse is 325 mJ and the wavelength equals 532 nm. The maximum possible frequency of a double pulse is 15 Hz. The operating frequency range for maximum power output is between 13 Hz and 15 Hz. The pulse delay is set to $10\ \mu s$. An adjustable laser beam guiding arm with light sheet optics mounted on a three axis traverse system enables the displacement of the measurement plane. The light sheet thickness at the measurement plane is approximately 3 mm. The image acquisition is performed by two sCMOS cameras with a resolution of 2560 x 2160 pixels. The spatial resolution depends on the choice of the objective and the distance of the lens to the measuring plane as well as the size of the interrogation windows. Due to the synchronization with the blade passing frequency for the phase-averaged measurements, the least common multiple of the latter, the laser frequency, and the camera frequency is needed to determine the recording frequency. For the time-averaged measurement, the recording rate can be set in order to obtain maximum laser performance.